

ELECTROSTATIC CHARGE AND HUMIDITY EFFECTS
ON THE EFFICIENCY OF FIBROUS AUTOMOTIVE
AIR FILTERS USING LASER DOPPLER
ANEMOMETRY

By

TADESSE GEBREEGZIABHER

Bachelor of Science

Addis Ababa University

Addis Ababa, Ethiopia

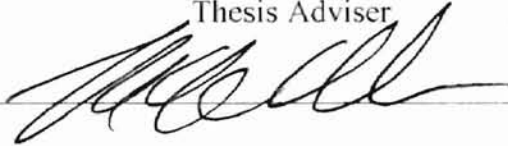
1986

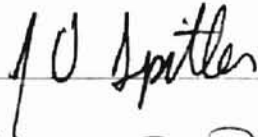
Submitted to the Faculty of the
Graduate College of the
Oklahoma State University
in partial fulfillment of
the requirements for
the Degree of
MASTER OF SCIENCE
July, 1999

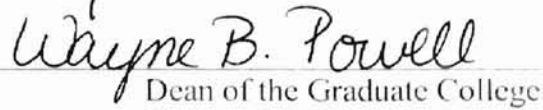
ELECTROSTATIC CHARGE AND HUMIDITY EFFECTS
ON THE EFFICIENCY OF FIBROUS AUTOMOTIVE
AIR FILTERS USING LASER DOPPLER
ANEMOMETRY

Thesis Approved:


Thesis Adviser






Dean of the Graduate College

ACKNOWLEDGMENTS

I would like to express my heart felt gratitude to my major advisor Dr. R. L. Dougherty for his relentless guidance, advice and encouragement throughout my graduate studies at the Oklahoma State University. Dr. Dougherty is a special person whom I admire for his patience, kindness, all round know-how, and academic excellence. I also extend my sincere appreciation to my other committee members Dr. F. W. Chambers and Dr. J. D. Spitler for their valuable suggestions and support.

Thanks are due to my colleagues, P. Saxena, S. H. Yao, A. Al-Sarkhi, and R. Srinivasan for their help and support. I would also like to thank James Davis and other MAE North Lab Workshop personnel for their help and cooperation.

I want to use this opportunity to thank my spiritual parents Dr. Karl Rosenfeld and the Rev. Dagmar Schmidt for their financial support and encouragement. I also extend my special appreciation to the Rev. Russell Bennett and through him to his congregation for their support during my stay in Tulsa, Oklahoma.

My special thanks go to my uncles G. Gebresellasie, E. Gebresellasie, and B. Gebresellasie and to my parents A. Gebresellasie and G. Berhe (posthumously).

Finally, I extend my gratitude to Dayco-Purolator Products, Inc. and the Oklahoma Center for the Advancement of Science and Technology (OCAST) for supporting this study financially.

TABLE OF CONTENTS

Chapter	Page
I. INTRODUCTION	1
1.1 Objectives and Methodologies	4
1.2 Thesis Organization	8
II. FUNDAMENTALS OF FIBROUS FILTRATION	9
2.1 Introduction	9
2.2 Basic Principles of Filtration	10
2.2.1 Assessment of Filter Performance	11
2.2.2 Filter Layer Efficiency for Monodisperse Aerosols	13
2.2.3 Quality Factor	14
2.2.4 Single Fiber Efficiency	15
2.2.5 The Single Fiber Efficiency Model	18
2.2.6 The Isolated Fiber Theory	20
2.2.7 Mechanisms of Filtration	22
2.3 Fibrous Filter Models	24
2.3.1 Capillary Tube Models	26
2.3.2 The Barrier Models	27
2.3.3 Pore Theory	30
2.3.4 The Three-Dimensional Offset Screen Model	31
2.4 Mechanical Filtration Mechanisms	31
2.4.1 Diffusive Deposition	31
2.4.2 Direct Interception	34
2.4.3 Inertial Impaction	36
2.4.4 Gravitational Deposition	40
2.5 Combined Effects of Mechanical Filtration Mechanisms	42
2.6 Basic Electrostatic Mechanisms of Action	43
III. LITERATURE REVIEW	46
3.1 Introduction	46
3.2 Electrostatic Charge Generation and Neutralization	47
3.2.1 Charging Aerosol Particles	47
3.2.1.1 Static Electrification	48
3.2.1.2 Diffusion Charging	50
3.2.1.3 Field Charging	51
3.2.1.4 Charging by Radioactive Sources	53
3.2.2 Charging Mechanisms of Filter Fiber Materials	55

3.2.2.1	Triboelectric Charging of Filter Materials	55
3.2.2.2	Corona Charging of Filter Materials	56
3.2.2.3	Induction Charging	57
3.2.3	Charge Neutralization	57
3.3	Electrostatic Filtration Mechanisms	61
3.3.1	Single Fiber Efficiencies	63
3.3.2	Combined Effect of Electrostatic and Mechanical Mechanisms	66
3.4	Overall Filter Efficiency	67
3.5	Pressure Drop	67
3.6	Factors that Affect Electrostatic Charge Generation in Duct Flows	68
3.7	Air Filter Test Standards	69
3.7.1	The ASTM F 1215-89 Standard Test Code	70
3.7.2	The SAE J726 Standard Test Code	70
3.7.3	The SAE J1669 Standard Test Code	72
3.8	Experimental Studies	75
3.8.1	Electrostatic Charge Effects	75
3.8.2	The Effect of Humidity	82
3.8.2.1	Efficiency	82
3.8.2.2	Humidity Effects on Charged Materials	84
3.8.3	Research at OSU	85
3.9	Theories of Adhesion of Particles	90
3.9.1	Van der Waals Forces	91
3.9.2	Electrostatic Forces	91
3.9.3	Humidity	91
3.10	Present Study	94
IV.	THE LDA INSTRUMENTATION, EXPERIMENTAL FLOW SETUP AND PROCEDURES	96
4.1	General Description	96
4.2	LDA Instrumentation	97
4.2.1	Laser Unit	98
4.2.2	Fiber Drive Unit	98
4.2.3	Data Receiving and Processing Unit	99
4.3	Local Filter Efficiency Measurements	103
4.4	Stability of the LDA System	106
4.5	Experimental Flow Setup	113
4.5.1	General	114
4.5.2	Seeding Aerosols by Atomization	114
4.5.3	Air Humidity and Temperature Control	117
4.5.4	Electrostatic Charge Neutralization	118
4.6	Air Flow Rate and Pressure Drop Measurements	122
4.7	Small Angle Diffuser Housing	122
4.8	A13192 Test Filter	124
4.9	Experimental Procedure	126
V.	ELECTROSTATIC VOLTAGE, HUMIDITY, AND CONSISTENCY MEASUREMENTS	130

5.1	Introduction	130
5.2	Electrostatic Charge Investigation	131
5.2.1	Factors that Affect Charge Polarity and Quantity	132
5.2.2	Electrostatic Charge Measurements	132
5.2.2.1	Experimental Work for Summer Season	133
5.2.2.2	Experimental Work for Winter Season	138
5.2.2.3	The Time Dependence of Electrostatic Charge	144
5.2.3	Electrostatic Discharging of the Experimental Housing and Particles	147
5.3	Humidity and Moisture Measurements	155
5.3.1	Composition of Air and Basic Concepts of Humidity	156
5.3.2	Humidity and Temperature Variation of the Air Flow	157
5.3.3	Humidity Control	162
5.3.4	Determination of Moisture Content in Air	163
5.3.5	Determination of Moisture for Fibrous Filters	164
5.4	Consistency Measurements	167
5.4.1	Number Density Variation and Electrostatic Charge	168
5.4.2	Humidity Effects	175
5.4.3	Atomization Rate and Concentration of Solutions	182
VI.	RESULTS AND DISCUSSION	185
6.1	Effects of Electrostatically Charged Particles on Filtration	186
6.1.1	Velocity, Number Density, and Efficiency Profiles	193
6.1.2	Efficiency Variation with Flow Rate	202
6.1.3	Pressure Drop Variation with Flow Rate	203
6.2	Humidity Effects on Fibrous Filtration Using Neutralized PSL Particles	205
6.2.1	Low Humidity Effects	211
6.2.2	High Humidity Effects	219
6.2.2.1	Velocity, Number Density and Efficiency Profiles	219
6.2.2.2	Efficiency Variation with Flow Rate and Pressure Drop	223
6.3	Single Fiber Efficiency	226
6.4	Comparison of Results	231
6.4.1	Comparison with Theoretical Results	231
6.4.2	Comparison with Previous Experimental Studies	234
VII.	SUMMARY, CONCLUSIONS AND RECOMMENDATIONS	236
7.1	Summary	236
7.1.1	The Stability of the LDA System	236
7.1.2	Number Density Measurements	237
7.1.3	Electrostatic Charge Generation and Voltage Measurement	239
7.1.4	Humidity Measurements	242
7.2	Conclusions	243
7.3	Recommendations for Future Work.....	247
	REFERENCES	251
	APPENDICES	260
	APPENDIX A LETTER TO NATARAJAN ET AL. FROM E. R. FREDERIC	261

APPENDIX B	SWEPT VOLUME TECHNIQUE	263
APPENDIX C	ERROR ANALYSIS	265
APPENDIX D	ELECTROSTATIC CHARGE EFFECTS: VELOCITY, NUMBER DENSITY AND EFFICIENCY RESULTS FOR 0.966 μm DIAMETER PSL PARTICLES IN THE SMALL ANGLE DIFFUSER HOUSING	268
APPENDIX E	HUMIDITY EFFECTS: VELOCITY, NUMBER DENSITY AND EFFICIENCY RESULTS FOR 0.966 μm DIAMETER PSL PARTICLES IN THE SMALL ANGLE DIFFUSER HOUSING	287
APPENDIX F	BASIC TERMS AND DEFINITIONS RELATED TO HUMIDITY MEASUREMENTS	324
APPENDIX G	MOISTURE ESTIMATION PROCEDURE	327
APPENDIX H	HUMIDITY MEASUREMENTS	330
APPENDIX I	STOKES NUMBER CALCULATION	340
APPENDIX J	LIST OF EQUIPMENT	342
APPENDIX K	SINGLE FIBER EFFICIENCY CALCULATION.....	344
APPENDIX L	LANGMUIR'S SINGLE FIBER EFFICIENCY EQUATION FOR DIFFUSION	346
APPENDIX M	SINGLE FIBER EFFICIENCY EQUATION FOR INTERCEPTION	348
APPENDIX N	CALIBRATION OF HUMIDITY AND TEMPERATURE MEASUREMENTS	350
APPENDIX O	ELECTROSTATIC CHARGE VOLTAGE MEASUREMENTS ...	354

LIST OF TABLES

Table	Page
3.1 Triboelectric Series of Materials [McAteer, 1989]	49
3.2 Chemical Composition (Analysis) of Standard Test Dusts [SAE, 1998]	72
3.3 Standard Test Dust Particle Size Distribution by Weight, % [SAE, 1998]	72
3.4 SAE Dust Particle Size Distribution in % by Volume [SAE, 1998]	72
3.5 Particle Size Distribution by Volume, % [SAE, 1998]	73
4.1 Optical Parameters of the LDA System [Liang, 1997]	100
4.2 Selected Technical Parameters of Test Filter A13192	124
4.3 Pressure Drop Variation across a New Filter As a Function of Air Flow Rate	126
5.1 Polarity of Charged Particles	154
5.2 Composition of Dry Air [McQuiston and Parker, 1994]	156
6.1 Summary of Test Results on Electrostatic Charge Effects for the Model A13192 Dayco-Purolator Automotive Air Filter Using 0.966 μm PSL Particles in the Small Angle Diffuser Housing	189
6.2 Summary of Test Results for Electrostatic Charge Effects: Single Fiber Efficiency and Stokes Number for the Model A13192 Dayco-Purolator Automotive Air Filter Using 0.966 μm PSL Particles in the Small Angle Diffuser Housing	192
6.3 Summary of Test Results on Humidity Effects for the Model A13192 Dayco-Purolator Automotive Air Filter Using 0.966 μm Diameter Neutralized PSL Particles in the Small Angle Diffuser Housing	206
6.4 Humidity Effects: Summary of Test Results, Single Fiber Efficiency and Stokes Number Analysis for the Model A13192 Dayco-Purolator Automotive Air Filter Using 0.966 μm Diameter PSL Particles in the Small Angle Diffuser Housing	208

LIST OF FIGURES

Figure	Page
2.1 Geometry Used to Help Relate Single Fiber and Overall Efficiencies of a Filter [Crawford, 1976]	17
2.2. Definition of Single Fiber Efficiency, $E_s = y/R_f$ [Davies, 1973]	19
2.3 Filtration by an Isolated Fiber of Radius 5 μm over a Range of Air Velocities: (a) Domains in Which the Various Mechanisms of Filtration Are Predominant (b) Isolated Fiber Efficiency Contours [Davies, 1973]	22
2.4 Collision and Secondary Mechanisms in Aerosol Filtration [Jaroszczyk and Wake, 1991]	23
2.5 Photomicrograph of a Real Fibrous Filter [Khan, 1995]	25
2.6 Langmuir's Parallel Cylinder Filter Model [Khan, 1995]	28
2.7 The Cell Model for High Porosity Filters as Employed by Langmuir (Parallel Flow), Happel and Kuwabara (Transverse Flow) [Brown, 1993]	28
2.8 Calculation by Benarie Showing the Tendency for the Flow Through a Fibrous Filter to Seek the Larger Pores. The Percentage of the Total Flow, Q , Passing Through the Upper 1, 5, and 10% of Pores Plotted Against the Geometrical Standard Deviation, σ_g , of the Pore Size [Davies, 1973]	30
2.9 Single-Fiber Collection by Brownian Diffusion [Hinds, 1982]	32
2.10 Single-Fiber Collection by Direct Interception [Hinds, 1982]	35
2.11 Single-Fiber Collection Efficiency by Inertial Impaction [Hinds, 1982]	37
2.12 Performance of Electrostatically Charged and Neutral Filters of Identical Geometry: (1) Neutral Filter Material; (2) Charged Filter Material [Brown, 1993]	44
3.1 Field and Diffusion Charging: (a) Number of Charges Acquired Versus	

N_{ict} for Various Particle Diameters at a Field Strength of 5000 V/cm, (b) Number of Charges Acquired Versus Particle Size for Various Field Strengths at $N_{ict} = 10^7$ ion-s/cm³ and $\epsilon_r = 5.1$ [Hinds, 1982]	51
3.2 Electric Field Lines for a Conducting Particle in a Uniform Field (Negative Ions and Negative Plate at Left). (a) An Uncharged Particle; (b) A Partially Charged Particle; and (c) A Particle at Saturation [Hinds, 1982] ...	52
3.3 Unipolar Charger Using Alpha-ray Radioactive Source [Adachi et al., 1990a]	54
3.4 General Triboelectrification of Materials [Chapman Catalog, 1997]	55
3.5 Illustration of Charge Configuration on Electrically Charged Filter Material: Resin Wool Material (Single-fiber); (b) Mixed Fiber Material; (c) Split Fiber Electret Material; (d) Electret Material Charged in Felt Form [Brown, 1993]	56
3.6 Corona Neutralizer [Adachi et al., 1990b]	59
3.7 Mechanisms of Particle Capture by a Fiber [Frederick, 1996]	62
3.8 Single Fiber Efficiency Versus the Relevant Dimensionless Parameter: (1) Uniformly Charged Fiber, Charged Particle; (2) Uniformly Charged Fiber, Neutral Particle; (3) Line Dipole Charged Fiber, Neutral Particle; (4) Line Quadruple Charged Fiber, Neutral Particle [Brown, 1993]	66
3.9 Schematic of the Performance of a Typical Electret Filter Versus Time [Hseih et al., 1996]	76
3.10 A Schematic of Particle Deposition on Single Fiber with and without Electrical Forces [Hseih et al., 1996]	77
3.11 A Schematic of Particle Deposition on Charged and Non-charged Filter Media [Hseih et al., 1996]	78
3.12 Collection Efficiency for Nonelectret and Electret Samples [Davies, 1994]	79
3.13 Collection Efficiency Versus Filtration Velocity for Nonelectret and Electret Filter Media for Different Particle Sizes [Davies, 1994]	80
3.14 Charge Effect on Filtration Efficiency and Particle Size [Kalatoor et al., 1997] ...	81
3.15 Effect of Relative Humidity on Filter Efficiency [Matteson, 1987]	83
3.16 Log of Resistivity Versus Relative Humidity for Various Materials [Henry, 1971]	84

3.17 Log of Voltage Versus Relative Humidity for Various Materials [Henry, 1971]	85
3.18 Overall Efficiency Versus Flow Rate for Non-neutralized Aerosols and Neutral Filter [Natarajan, 1995]	87
3.19 Overall Efficiency of a 'Neutral Flat Filter' with Non-neutralized 0.966 μm PSL Particles [Anand, 1997]	88
3.20 Efficiency Versus Flow Rate for a 'Neutral Pleated Filter' and Non-neutralized 0.966 μm PSL Particles [Jadbabaei, 1997]	89
3.21 Efficiency Versus Flow Rate for 'Neutral Pleated Filters' with Non-Neutralized PSL Particles Having Different Diameters [Saxena, 1998]	90
3.22 A Spherical Particle Attached to a Plane by Capillary Forces [Brown, 1993]	92
3.23 The Influence of Atmospheric Humidity on the Forces of Adhesion by Corn [Davies, 1966]	93
4.1 Schematic of the Laser Doppler Instrumentation	97
4.2 Probe Volume and Fringe Pattern [Liang, 1997]	100
4.3 High Frequency Component Superimposed on the Pedestal	101
4.4 Sample Signals Displayed on Oscilloscope	103
4.5 Two-Dimensional Filter Measurement Grid	104
4.6 Dependence of Number Density upon Laser Power [Natarajan, 1995]	107
4.7 Variation of Laser Power with Bread Board Temperature as Humidity and Cooling Water Outlet and Inlet Temperatures into Laser Tube Jacket Remained Stable within 1°C (June, 1997)	108
4.8 Variation of Laser Power with Bread Board Temperature as Humidity and Cooling Water Outlet and Inlet Temperatures into Laser Tube Jacket Remained Stable within 1°C (May, 1997)	109
4.9 Fiber Drive Setup on an Insulated Metal Table	110
4.10 Power Variation As a Function of Time for Shifted and Unshifted Beams	111
4.11 A Cylindrical Tube for Holding Pinhole Apertures	112

4.12 Laser Setup on an Insulated Metal Table	113
4.13 Experimental Setup	115
4.14 Behavior of Charged Materials: (a) Ungrounded Charged Conductor, (b) Ungrounded Charged Insulator, (c) Grounded Conductor, (d) Grounded Insulator	119
4.15 Charge Neutralization Setup (Upper Half of Housing)	120
4.16 Small Angle Diffuser Housing Construction Details	123
4.17 Schematic Drawing of the Model A13912 Test Filter	125
4.18 Initial Pressure Drop across Filter Versus Flow Rate	127
5.1 Variation of Electrostatic Voltage with Air Flow Rate at the Mixing Box for 0.5 μm Diameter PSL Particles (conc. = 3/500, Summer, 1997)	135
5.2 Variation of Electrostatic Voltage with Air Flow Rate Upstream of Filter for 0.5 μm Diameter PSL Particles (conc. = 3/500, Summer, 1997)	135
5.3 Variation of Electrostatic Voltage with Air Flow Rate at the Mixing Box and Upstream of Filter for 0.966 μm Diameter PSL Particles (conc. = 3/500, Summer, 1997)	136
5.4 Variation of Humidity and Temperature with Preheated Air Flow Rate (Summer, 1997)	138
5.5 Electrostatic Voltage Measurement at the Mixing Box and Filter for 0.5 μm Diameter PSL Particles (conc. = 3/500, Winter, 1997)	139
5.6 Electrostatic Charge Voltage Measurement for 0.966 μm Diameter PSL Particles (conc. = 3/500, Winter, 1998)	140
5.7 Electrostatic Voltage Variation with Flow Rate for 0.966 μm Diameter PSL Particles (conc. = 6/500, Winter, 1998)	141
5.8 Electrostatic Charge Variation with Flow Rate for 2.04 μm Diameter PSL Particles (conc. = 12/500, Winter, 1998)	142
5.9 Variation of Electrostatic Charge Voltage, Absolute and Relative Humidities, and Temperature with Air Flow Rate for 2.04 μm Diameter PSL Particles (conc. = 12/500; Winter, 1998)	143

5.10	Electrostatic Voltage As a Function of Time for 0.966 μm Diameter PSL Particles at a Flow Rate of 60.8 m^3/hr (conc. = 5/500, Winter, 1998)	145
5.11	Electrostatic Charge Voltage Variation with Time for Wire Grounded Housing at an Air Flow Rate of 60.8 m^3/hr for 0.966 μm Diameter PSL Particles (conc. = 5/500, Winter, 1998)	146
5.12	Electrostatic Charge Voltage Generation and Variation with Time for Ungrounded Housing Using Clean Air (Flow Rate = 60.8 m^3/hr , Winter, 1998)	147
5.13	Electrostatic Charge Neutralization of 0.966 μm Diameter PSL Particles for Grounded Housing Using Aluminum Foil at a Flow Rate of 60.8 m^3/hr (conc. = 5/500, Winter, 1998)	148
5.14	Electrostatic Charge Voltage Growth with Time for Ungrounded Housing and Air Flow Rate of 60.8 m^3/hr Using Glass Beads of 1.5 μm Diameter (Mean Size Distribution) (conc. = 8.3/500, Winter, 1998)	150
5.15	Electrostatic Discharging of an Initially Charged Plexiglass Filter Housing with Time (without Grounding, Winter, 1998)	151
5.16	Electrostatic Discharging Using Grounded Aluminum Foil for Air at a Flow Rate of 60.8 m^3/hr (Winter, 1998)	152
5.17	Electrostatic Discharging Using Grounded Aluminum Foil for 1.5 μm Diameter Glass Beads (conc. = 5/500, Winter, 1998)	153
5.18	Temperature and Humidity Variations (before the Mixing Box) of Preheated Air at 6.97 m^3/hr (Atomizer off, Winter, 1998)	157
5.19	Temperature and Humidity Variations (before the Mixing Box) of Preheated Air at 42 m^3/hr (Atomizer off, Date: 01/23/98)	158
5.20	Temperature and Humidity Variations (before the Mixing Box) of Preheated Air at 40 m^3/hr (Atomizer off, Date: 01/23/98)	158
5.21	Temperature and Humidity Variations (before the Mixing Box) of Preheated Air at 60 m^3/hr (Atomizer off, Date: 01/23/98)	159
5.22	Temperature and Humidity Variations (before the Mixing Box) with Air Flow Rate Using a New Inlet Duct (Atomizer off, Heater on, Date: 01/25/98)	160
5.23	Temperature and Humidity Variations (before the Mixing Box) of Preheated Air while Atomizing Distilled Water (Atomizer on,	

Heater on, Date: 01/25/98)	160
5.24 Temperature and Humidity Variations of Preheated Air (6 cm from Filter Downstream Surface) (Atomizer off, Heater on, Date: 01/28/98)	161
5.25 Temperature and Humidity Variations of Air (6 cm from Filter Upstream Surface) while Atomizing Distilled Water (Heater on, Date: 01/28/98)	162
5.26 Laser Power Variation with Time as Coupler Temperature Changes	169
5.27 Laser Power Variation with Time as the Temperature at the Couplers Remains Stable	170
5.28 Laser Power Variation as Temperature at Couplers Changes	170
5.29 Variation of Number Density with Time as Coupler Temperature Changes for a Constant Flow Rate of 103.7 m ³ /hr	172
5.30 Variation of Number Density with Time at Constant Coupler Temperature and Constant Air Flow Rate of 103.7 m ³ /hr (Date: 05/30/98)	172
5.31 Number Density, Relative Humidity, Coupler Temperature, and Electrostatic Charge Voltage Variations with Time (Flow Rate of 103.7 m ³ /hr, 0.966 μm Diameter PSL Particles)	173
5.32 Variation of Number Density, Coupler Temperature, Relative Humidity, and Electrostatic Charge Voltage, and Relative Humidity of Air inside the Housing (Constant Flow Rate of 103.7 m ³ /hr, 0.966 μm Diameter PSL Particles)	174
5.33 Minimum and Maximum Relative Humidity Variations with Flow Rate (Humidity Control: Using Humidifier, Heater, and Atomization of Distilled Water; Test Date: 06/09/98)	176
5.34 A Humidity Control Experiment to Maintain Maximum and Minimum Humidity (Using Humidifier, Heater, and Atomizer; Test Date: 06/09/98)	177
5.35 Consistency Measurements on Room Air: Number Density Variations at the Center of Filter with Flow Rate (Heater off, Atomizer off, and Humidifier off, Test Date: 03/21/98)	179
5.36 Consistency Measurements on Room Air: Number Density Variations at the Center of Filter with Flow Rate (Heater on, Atomizer on, and Humidifier on; Test Date: 03/22/98)	180

5.37	Temperature Correlation at the Mixing Box and Upstream of the Filter	181
5.38	Humidity Correlation at the Mixing Box and Upstream of the Filter	181
5.39	Atomizer Consistency Test Results for 0.966 μm Particles [Saxena, 1998]	183
5.40	Number Density for Different Particle Concentrations [Anand, 1997]	184
6.1	Electrostatic Voltage, Temperature, and Humidity Variation with Air Flow Rate for 0.966 μm PSL Particles at the Mixing Box and Filter without Grounding (conc. = 6/500, Winter, 1998)	187
6.2	Upstream Velocity Distribution for Test No. ESH10.2 at an Air Flow Rate of 13.53 m^3/hr	194
6.3	Downstream Velocity Distribution for Test No. ESH10.2 at an Air Flow Rate of 13.53 m^3/hr	194
6.4	Upstream Number Density Distribution for Test No. ESH10.2 at an Air Flow Rate of 13.53 m^3/hr	196
6.5	Downstream Number Density Distribution for Test No. ESH10.2 at an Air Flow Rate of 13.53 m^3/hr	196
6.6	Local Filtration Efficiency Profile for Test No. ESH10.2 at an Air Flow Rate of 13.53 m^3/hr	197
6.7	Upstream Velocity Distribution for Test No. ESH75.1 at an Air Flow Rate of 103.7 m^3/hr	198
6.8	Downstream Velocity Distribution for Test No. ESH75.1 at an Air Flow Rate of 103.7 m^3/hr	198
6.9	Upstream Number Density Distribution for Test No. ESH75.1 at an Air Flow Rate of 103.7 m^3/hr	199
6.10	Downstream Number Density Distribution for Test No. ESH75.1 at an Air Flow Rate of 103.7 m^3/hr	199
6.11	Local Filtration Efficiency Distribution for ESH75.1 at an Air Flow Rate of 103.7 m^3/hr	200
6.12	Electrostatic Charge Effects on Fibrous Filtration Efficiency Using Electrostatically Charged and Neutral PSL Particles (Summer, 1998)	202
6.13	Electrostatic Charge Effects: Pressure Drop Variation with Flow Rate	204

6.14	Upstream Velocity Distribution for Test No. NESH10.1 at Low Humidity and an Air Flow Rate of 13.53 m ³ /hr	212
6.15	Downstream Velocity Distribution for Test No. NESH10.1 at Low Humidity and an Air Flow Rate of 13.53 m ³ /hr	213
6.16	Upstream Number Density Distribution for Test No. NESH10.1 at an Air Flow Rate of 13.53 m ³ /hr	213
6.17	Downstream Number Density Distribution for Test No. NESH10.1 at an Air Flow Rate of 13.53 m ³ /hr	214
6.18	Filtration Efficiency Distribution for Test No. NESH10.1 at Low Humidity and an Air Flow Rate of 13.53 m ³ /hr	214
6.19	Upstream Velocity Distribution for Test No. NESH125.3 at Low Humidity and an Air Flow Rate of 187.7 m ³ /hr	216
6.20	Downstream Velocity Distribution for Test No. NESH125.3 at Low Humidity and an Air Flow Rate of 187.7 m ³ /hr	216
6.21	Upstream Number Density Distribution for Test No. NESH125.3 at Low Humidity and an Air Flow Rate of 187.7 m ³ /hr	217
6.22	Downstream Number Density Distribution for Test No. NESH125.3 at Low Humidity and an Air Flow Rate of 187.7 m ³ /hr	217
6.23	Filtration Efficiency Distribution for Test No. NESH125.3 at Low Humidity and an Air Flow Rate of 187.7 m ³ /hr	218
6.24	Upstream Velocity Distribution for Test No. NESH10.4 at High Humidity and an Air Flow Rate of 13.53 m ³ /hr	220
6.25	Downstream Velocity Distribution for Test No. NESH10.4 at High Humidity and an Air Flow Rate of 13.53 m ³ /hr	221
6.26	Upstream Number Density Distribution for Test No. NESH10.4 at High Humidity and an Air Flow Rate of 13.53 m ³ /hr	221
6.27	Downstream Number Density Distribution for Test No. NESH10.4 at High Humidity and an Air Flow Rate of 13.53 m ³ /hr	222
6.28	Filtration Efficiency Distribution for Test No. NESH10.4 at High Relative Humidity and an Air Flow Rate of 13.53 m ³ /hr	223

6.29 Humidity Effects on Fibrous Filtration Efficiency Using Electrostatically Neutral PSL Particles (Summer, 1998)	224
6.30 Humidity Effects on Fibrous Filtration: Filter Efficiency Variation with Pressure Drop for Electrostatically Neutral Filter and Particles	225
6.31 Humidity Effects: Total Single Fiber Efficiency Versus Stokes Number for Dayco-Purolator A13192 Filters Using Neutralized 0.966 μm Diameter PSL Particles	228
6.32 Total Single Fiber Efficiency for Dayco-Purolator A13192 Filters Using Electrostatically Charged 0.966 μm Diameter PSL Particles in the Small Angle Diffuser Housing at Low Humidity	229
6.33 Single Fiber Efficiencies Versus Stokes Number for Charged and Neutralized 0.966 μm Diameter PSL Particles at Different RH for the Dayco-Purolator A13192 Filter (Small Angle Diffuser Housing)	230
6.34 Comparison of Experimental Results of Present Study (Humidity and Electrostatic Charge Effects) with a Theoretical Model Based on Perfect Adhesion Theory [Duran, 1995] for Interception Parameter = 0.018, Fiber Diameter = 51.7 μm , and Packing Density = 0.23	232
6.35 Comparison of Experimental Filtration Efficiency Results with a Theoretical Model Based on Perfect Adhesion [Duran, 1995] for 0.966 μm Diameter Particles and A13192 Filter with Interception Parameter = 0.018, Fiber Diameter = 51.7 μm , and Packing Density = 0.23]	233
6.36 Comparison of Filtration Efficiencies for the Model A13192 Filter Using 0.966 μm Charged and Neutral Particles at High and Low Air Humidities with Jadbabaei's [1997] Result	234
7.1 Schematic Drawing of an Electrostatic Charger/Ionizer	249
B.1 Swept Volume Technique [Liang, 1997]	264
D.1 Electrostatic Charge Effect on Efficiency of Pleated Fibrous Filter: (a) Upstream No. Density, (b) Downstream No. Density, (c) Upstream Velocity, (d) Downstream Velocity, (e) Local Efficiency. Pressure Drop Δp [mm Water] = 3, RH = 43.5%, Temperature [$^{\circ}\text{C}$] = 38, Electrostatic Voltage at Filter [v] = 100, Air Flow Rate = 13.5 m^3/hr , Test # ESH10.1, Test Date: 08/20/98	270

D.2 Electrostatic Charge Effect on Efficiency of Pleated Fibrous Filter: (a) Upstream No. Density, (b) Downstream No. Density, (c) Upstream Velocity, (d) Downstream Velocity, (e) Local Efficiency. Pressure Drop Δp [mm Water] = 3, RH = 39%, Air Temperature [$^{\circ}\text{C}$] = 39, Electrostatic Voltage at Filter [v] = 150, Air Flow Rate = 13.5 m ³ /hr, Test # ESH10.2, Test Date: 08/20/98	271
D.3 Electrostatic Charge Effect on Efficiency of Pleated Fibrous Filter: (a) Upstream No. Density, (b) Downstream No. Density, (c) Upstream Velocity, (d) Downstream Velocity, (e) Local Efficiency. Pressure Drop Δp [mm Water] = 3, RH = 33%, Air Temperature [$^{\circ}\text{C}$] = 43, Electrostatic Voltage at Filter [v] = 150, Air Flow Rate = 29.5 m ³ /hr, Test # ESH20.1, Test Date: 08/21/98	272
D.4 Electrostatic Charge Effect on the Efficiency of Pleated Fibrous Filter: (a) Upstream No. Density, (b) Downstream No. Density, (c) Upstream Velocity, (d) Downstream Velocity, (e) Local Efficiency. Pressure Drop Δp [mm Water] = 3, RH = 32%, Air Temperature [$^{\circ}\text{C}$] = 44, Electrostatic Voltage at Filter [v] = 200, Air Flow Rate = 29.5 m ³ /hr, Test # ESH20.2, Test Date: 08/21/98	273
D.5 Electrostatic Charge Effect on Efficiency of Pleated Fibrous Filter: (a) Upstream No. Density, (b) Downstream No. Density, (c) Upstream Velocity, (d) Downstream Velocity, (e) Local Efficiency. Pressure Drop Δp [mm Water] = 3, RH = 33%, Air Temperature [$^{\circ}\text{C}$] = 52, Electrostatic Voltage at Filter [v] = 200, Air Flow Rate = 60.81 m ³ /hr, Test # ESH40.1, Test Date: 08/22/98	274
D.6 Electrostatic Charge Effect on Efficiency of Pleated Fibrous Filter: (a) Upstream No. Density, (b) Downstream No. Density, (c) Upstream Velocity, (d) Downstream Velocity, (e) Local Efficiency. Pressure Drop Δp [mm Water] = 5, RH = 33%, Air Temperature [$^{\circ}\text{C}$] = 49.5, Electrostatic Voltage at Filter [v] = 200, Air Flow Rate = 60.81 m ³ /hr, Test # ESH40.2, Test Date: 08/22/98	275
D.7 Electrostatic Charge Effect on Efficiency of Pleated Fibrous Filter: (a) Upstream No. Density, (b) Downstream No. Density, (c) Upstream Velocity, (d) Downstream Velocity, (e) Local Efficiency. Pressure Drop Δp [mm Water] = 5, RH = 35%, Air Temperature [$^{\circ}\text{C}$] = 52, Electrostatic Voltage at Filter [v] = 500, Air Flow Rate = 77.1 m ³ /hr, Test # ESH50.1, Test Date: 08/23/98	276
D.8 Electrostatic Charge Effect on Efficiency of Pleated Fibrous Filter: (a) Upstream No. Density, (b) Downstream No. Density, (c) Upstream Velocity, (d) Downstream Velocity, (e) Local Efficiency. Pressure Drop Δp [mm Water] = 8, RH = 35%, Air Temperature [$^{\circ}\text{C}$] = 52,	

Electrostatic Voltage at Filter [v] = 750, Air Flow Rate = 77.1 m ³ /hr, Test # ESH50.2, Test Date: 08/13/98	277
D.9 Electrostatic Charge Effect on Efficiency of Pleated Fibrous Filter:	
(a) Upstream No. Density, (b) Downstream No. Density, (c) Upstream Velocity, (d) Downstream Velocity, (e) Local Efficiency. Pressure Drop Δp [mm Water] = 13, RH = 39%, Air Temperature [°C] = 47, Electrostatic Voltage at Filter [v] = 750, Air Flow Rate = 103.7 m ³ /hr, Test # ESH75.1, Test Date: 08/24/98	278
D.10 Electrostatic Charge Effect on Efficiency of Pleated Fibrous Filter:	
(a) Upstream No. Density, (b) Downstream No. Density, (c) Upstream Velocity, (d) Downstream Velocity, (e) Local Efficiency. Pressure Drop Δp [mm Water] = 13, RH = 39%, Air Temperature [°C] = 48, Electrostatic Voltage at Filter [v] = 750, Air Flow Rate = 103.7 m ³ /hr, Test # ESH75.2, Test Date: 08/24/98	279
D.11 Electrostatic Charge Effect on Efficiency of Pleated Fibrous Filter:	
(a) Upstream No. Density, (b) Downstream No. Density, (c) Upstream Velocity, (d) Downstream Velocity, (e) Local Efficiency. Pressure Drop Δp [mm Water] = 30, RH = 42%, Air Temperature [°C] = 43, Electrostatic Voltage at Filter [v] = 500, Air Flow Rate = 145.7 m ³ /hr, Test # ESH100.1, Test Date: 08/25/98	280
D.12 Electrostatic Charge Effect on Efficiency of Pleated Fibrous Filter:	
(a) Upstream No. Density, (b) Downstream No. Density, (c) Upstream Velocity, (d) Downstream Velocity, (e) Local Efficiency. Pressure Drop Δp [mm Water] = 30, RH = 42%, Air Temperature [°C] = 42, Electrostatic Voltage at Filter [v] = 500, Air Flow Rate = 145.7 m ³ /hr, Test # ESH100.2, Test Date: 08/25/98	281
D.13 Electrostatic Charge Effect on Efficiency of Pleated Fibrous Filter:	
(a) Upstream No. Density, (b) Downstream No. Density, (c) Upstream Velocity, (d) Downstream Velocity, (e) Local Efficiency. Pressure Drop Δp [mm Water] = 38, RH = 45%, Air Temperature [°C] = 37, Electrostatic Voltage at Filter [v] = 500, Air Flow Rate = 187.7 m ³ /hr, Test # ESH125.1, Test Date: 08/28/98	282
D.14 Electrostatic Charge Effect on Efficiency of Pleated Fibrous Filter:	
(a) Upstream No. Density, (b) Downstream No. Density, (c) Upstream Velocity, (d) Downstream Velocity, (e) Local Efficiency. Pressure Drop Δp [mm Water] = 38, RH = 45%, Air Temperature [°C] = N/A, Electrostatic Voltage at Filter [v] = 500, Air Flow Rate = 187.7 m ³ /hr, Test # ESH125.2, Test Date: 08/28/98	283

D.15	Electrostatic Charge Effect on Efficiency of Pleated Fibrous Filter: (a) Upstream No. Density, (b) Downstream No. Density, (c) Upstream Velocity, (d) Downstream Velocity, (e) Local Efficiency. Pressure Drop Δp [mm Water] = 48, RH = 50%, Air Temperature [°C] = N/A, Electrostatic Voltage at Filter [v] = 400, Air Flow Rate = 229.7 m ³ /hr, Test # ESH150.1, Test Date: 08/27/98	284
D.16	Electrostatic Charge Effect on Efficiency of Pleated Fibrous Filter: (a) Upstream No. Density, (b) Downstream No. Density, (c) Upstream Velocity, (d) Downstream Velocity, (e) Local Efficiency. Pressure Drop Δp [mm Water] = 48, RH = 50%, Air Temperature [°C] = 34, Electrostatic Voltage at Filter [v] = 400, Air Flow Rate = 229.7 m ³ /hr, Test # ESH150.2, Test Date: 08/27/98	285
D.17	Electrostatic Charge Effect on Efficiency of Pleated Fibrous Filter: (a) Upstream No. Density, (b) Downstream No. Density, (c) Upstream Velocity, (d) Downstream Velocity, (e) Local Efficiency. Pressure Drop Δp [mm Water] = 122, RH = 50%, Air Temperature [°C] = 31, Electrostatic Voltage at Filter [v] = 500, Air Flow Rate = 313.8 m ³ /hr, Test # ESH200.1, Test Date: 08/27/98	286
E.1	Humidity Effect on Efficiency of Electrostatically Neutral Pleated Fibrous Filter: (a) Upstream No. Density, (b) Downstream No. Density, (c) Upstream Velocity, (d) Downstream Velocity, (e) Local Efficiency. Pressure Drop Δp [mm Water] = 3, RH = 43.5%, Air Temperature [°C] = 38, Air Flow Rate = 13.5 m ³ /hr, Test # NESH10.1, Test Date: 03/22/98	289
E.2	Humidity Effect on Efficiency of Electrostatically Neutral Pleated Fibrous Filter: (a) Upstream No. Density, (b) Downstream No. Density, (c) Upstream Velocity, (d) Downstream Velocity, (e) Local Efficiency. Pressure Drop Δp [mm Water] = 3, RH = 95%, Air Temperature [°C] = 27, Air Flow Rate = 13.5 m ³ /hr, Test # NESH10.2, Test Date: 03/22/98	290
E.3	Humidity Effect on Efficiency of Electrostatically Neutral Pleated Fibrous Filter: (a) Upstream No. Density, (b) Downstream No. Density, (c) Upstream Velocity, (d) Downstream velocity, (e) Local Efficiency. Pressure Drop Δp [mm Water] = 3, RH = 45%, Air Temperature [°C] = 39, Air Flow Rate = 13.5 m ³ /hr, Test # NESH10.3, Test Date: 08/15/98	291
E.4	Humidity Effect on Efficiency of Electrostatically Neutral Pleated Fibrous Filter: (a) Upstream No. Density, (b) Downstream No. Density, (c) Upstream Velocity, (d) Downstream Velocity, (e) Local Efficiency. Pressure Drop Δp [mm Water] = 3, RH = 85%, Air Temperature [°C] = 29, Air Flow Rate = 13.5 m ³ /hr, Test # NESH10.4, Test Date: 08/15/98	292
E.5	Humidity Effect on Efficiency of Electrostatically Neutral Pleated Fibrous	

Filter: (a) Upstream No. Density, (b) Downstream No. Density, (c) Upstream Velocity, (d) Downstream Velocity, (e) Local Efficiency. Pressure Drop Δp [mm Water] = 5, RH = 35%, Air Temperature [°C] = 43, Air Flow Rate = 29.5 m ³ /hr, Test # NESH20.1, Test Date: 06/18/98	293
E.6 Humidity Effects on Efficiency of Electrostatically Neutral Pleated Fibrous Filter: (a) Upstream No. Density, (b) Downstream No. Density, (c) Upstream Velocity, (d) Downstream Velocity, (e) Local Efficiency. Pressure Drop Δp [mm Water] = 5, RH= 31.5%, Air Temperature [°C] = 48, Air Flow Rate = 29.5 m ³ /hr, Test # NESH20.2, Test Date: 07/06/98	294
E.7 Humidity Effect on Efficiency of Electrostatically Neutral Pleated Fibrous Filter: (a) Upstream No. Density, (b) Downstream No. Density, (c) Upstream Velocity, (d) Downstream Velocity, (e) Local Efficiency. Pressure Drop Δp [mm Water] = 5, RH = 79%, Temperature [°C] = 35, Air Flow Rate = 29.5 m ³ /hr, Test # NESH20.3, Test Date: 07/06/98	295
E.8 Humidity Effect on Efficiency of Electrostatically Neutral Pleated Fibrous Filter: (a) Upstream No. Density, (b) Downstream No. Density, (c) Upstream Velocity, (d) Downstream Velocity, (e) Local Efficiency. Pressure Drop Δp [mm Water] = 5, RH = 33%, Air Temperature [°C] = 43, Air Flow Rate = 29.5 m ³ /hr, Test # NESH20.4, Test Date: 06/22/98	296
E.9 Humidity Effect on Efficiency of Electrostatically Neutral Pleated Fibrous Filter: (a) Upstream No. Density, (b) Downstream No. Density, (c) Upstream Velocity, (d) Downstream Velocity, (e) Local Efficiency. Pressure Drop Δp [mm Water] = 5, RH = 80%, Air Temperature [°C] = 31, Air Flow Rate = 29.5 m ³ /hr, Test # NESH20.5, Test Date: 07/22/98	297
E.10 Humidity Effect on Efficiency of Electrostatically Neutral Pleated Fibrous Filter: (a) Upstream No. Density, (b) Downstream No. Density, (c) Upstream Velocity, (d) Downstream Velocity, (e) Local Efficiency. Pressure Drop Δp [mm Water] = 5, RH = 17%, Air Temperature [°C] = 55, Air Flow Rate = 60.81 m ³ /hr, Test # NESH40.1, Test Date: 03/01/98	298
E.11 Humidity Effect on Efficiency of Electrostatically Neutral Pleated Fibrous Filter: (a) Upstream No. Density, (b) Downstream No. Density, (c) Upstream Velocity, (d) Downstream Velocity, (e) Local Efficiency. Pressure Drop Δp [mm Water] = 5, RH = 85%, Air Temperature [°C] = 37, Air Flow Rate = 60.81 m ³ /hr, Test # NESH40.2, Test Date: 03/05/98	299
E.12 Humidity Effect on Efficiency of Electrostatically Neutral Pleated Fibrous Filter: (a) Upstream No. Density, (b) Downstream No. Density, (c) Upstream Velocity, (d) Downstream Velocity, (e) Local Efficiency. Pressure Drop Δp [mm Water] = 5, RH = 85%, Air Temperature [°C] = 38, Air Flow Rate = 60.81 m ³ /hr, Test # NESH40.3, Test Date: 08/16/98	300

- E.13 Humidity Effect on Efficiency of Electrostatically Neutral Pleated Fibrous Filter: (a) Upstream No. Density, (b) Downstream No. Density, (c) Upstream Velocity, (d) Downstream Velocity, (e) Local Efficiency. Pressure Drop Δp [mm Water] = 5, RH = 35%, Air Temperature [$^{\circ}$ C] = 53, Air Flow Rate = 60.81 m³/hr, Test # NESH40.4, Test Date: 06/22/98 301
- E.14 Humidity Effect on Efficiency of Electrostatically Neutral Pleated Fibrous Filter: (a) Upstream No. Density, (b) Downstream No. Density, (c) Upstream Velocity, (d) Downstream Velocity, (e) Local Efficiency. Pressure Drop Δp [mm Water] = 5, RH = 42%, Air Temperature [$^{\circ}$ C] = 46, Air Flow Rate = 77.1 m³/hr, Test # NESH50.1, Test Date: 06/11/98 302
- E.15 Humidity Effect on Efficiency of Electrostatically Neutral Pleated Fibrous Filter: (a) Upstream No. Density, (b) Downstream No. Density, (c) Upstream Velocity, (d) Downstream Velocity, (e) Local Efficiency. Pressure Drop Δp [mm Water] = 8, RH = 35%, Air Temperature [$^{\circ}$ C] = 53, Air Flow Rate = 77.1 m³/hr, Test # NESH50.2, Test Date: 06/13/98 303
- E.16 Humidity Effect on Efficiency of Electrostatically Neutral Pleated Fibrous Filter: (a) Upstream No. Density, (b) Downstream No. Density, (c) Upstream Velocity, (d) Downstream Velocity, (e) Local Efficiency. Pressure Drop Δp [mm Water] = 8, RH = 80%, Air Temperature [$^{\circ}$ C] = 34, Air Flow Rate = 77.1 m³/hr, Test # NESH50.3, Test Date: 06/13/98 304
- E.17 Humidity Effect on Efficiency of Electrostatically Neutral Pleated Fibrous Filter: (a) Upstream No. Density, (b) Downstream No. Density, (c) Upstream Velocity, (d) Downstream Velocity, (e) Local Efficiency. Pressure Drop Δp [mm Water] = 8, RH = 85%, Air Temperature [$^{\circ}$ C] = 35, Air Flow Rate = 77.1 m³/hr, Test # NESH50.4, Test Date: 08/16/98 305
- E.18 Humidity Effect on Efficiency of Electrostatically Neutral Pleated Fibrous Filter: (a) Upstream No. Density, (b) Downstream No. Density, (c) Upstream Velocity, (d) Downstream Velocity, (e) Local Efficiency. Pressure Drop Δp [mm Water] = 23, RH = 35%, Air Temperature [$^{\circ}$ C] = 47, Air Flow Rate = 103.7 m³/hr, Test # NESH75.1, Test Date: 06/09/98 306
- E.19 Humidity Effect on Efficiency of Electrostatically Neutral Pleated Fibrous Filter: (a) Upstream No. Density, (b) Downstream No. Density, (c) Upstream Velocity, (d) Downstream Velocity, (e) Local Efficiency. Pressure Drop Δp [mm Water] = 18, RH = 45%, Air Temperature [$^{\circ}$ C] = 44, Air Flow Rate = 103.7 m³/hr, Test # NESH75.2, Test Date: 06/09/98 307
- E.20 Humidity Effect on Efficiency of Electrostatically Neutral Pleated Fibrous Filter: (a) Upstream No. Density, (b) Downstream No. Density, (c) Upstream Velocity, (d) Downstream Velocity, (e) Local Efficiency. Pressure Drop Δp [mm Water] = 23, RH = 80%, Air Temperature [$^{\circ}$ C] = 34,

	Air Flow Rate = 103.7 m ³ /hr, Test # NESH75.3, Test Date: 06/09/98	308
E.21	Humidity Effect on Efficiency of Electrostatically Neutral Pleated Fibrous Filter: (a) Upstream No. Density, (b) Downstream No. Density, (c) Upstream Velocity, (d) Downstream Velocity, (e) Local Efficiency. Pressure Drop Δp [mm Water] = 23, RH = 80%, Air Temperature [°C] = 31, Air Flow Rate = 103.7 m ³ /hr, Test # NESH75.4, Test Date: 08/17/98	309
E.22	Humidity Effect on Efficiency of Electrostatically Neutral Pleated Fibrous Filter: (a) Upstream No. Density, (b) Downstream No. Density, (c) Upstream Velocity, (d) Downstream Velocity, (e) Local Efficiency. Pressure Drop Δp [mm Water] = 41, RH = 73%, Air Temperature [°C] = 33. Air Flow Rate = 145.7 m ³ /hr, Test # NESH100.1, Test Date: 06/25/98	310
E.23	Humidity Effect on Efficiency of Electrostatically Neutral Pleated Fibrous Filter: (a) Upstream No. Density, (b) Downstream No. Density, (c) Upstream Velocity, (d) Downstream Velocity, (e) Local Efficiency. Pressure Drop Δp [mm Water] = 43, RH = 74%, Air Temperature [°C] = 33, Air Flow Rate = 145.7 m ³ /hr, Test # NESH100.2, Test Date: 06/25/98	311
E.24	Humidity Effect on Efficiency of Electrostatically Neutral Pleated Fibrous Filter: (a) Upstream No. Density, (b) Downstream No. Density, (c) Upstream Velocity, (d) Downstream Velocity, (e) Local Efficiency. Pressure Drop Δp [mm Water] = 40, RH = 35%, Air Temperature [°C] = 40, Air Flow Rate = 145.7 m ³ /hr, Test # NESH100.3, Test Date: 07/12/98	312
E.25	Humidity Effect on Efficiency of Electrostatically Neutral Pleated Fibrous Filter: (a) Upstream No. Density, (b) Downstream No. Density, (c) Upstream Velocity, (d) Downstream Velocity, (e) Local Efficiency. Pressure Drop Δp [mm Water] = 41, RH = 38%, Air Temperature [°C] = 39, Air Flow Rate = 145.7 m ³ /hr, Test # NESH100.4, Test Date: 07/13/98	313
E.26	Humidity Effect on Efficiency of Electrostatically Neutral Pleated Fibrous Filter: (a) Upstream No. Density, (b) Downstream No. Density, (c) Upstream Velocity, (d) Downstream Velocity, (e) Local Efficiency. Pressure Drop Δp [mm Water] = 64, RH = 87%, Air Temperature [°C] = 28, Air Flow Rate = 187.7 m ³ /hr, Test # NESH125.1, Test Date: 06/29/98	314
E.27	Humidity Effect on Efficiency of Electrostatically Neutral Pleated Fibrous Filter: (a) Upstream No. Density, (b) Downstream No. Density, (c) Upstream Velocity, (d) Downstream Velocity, (e) Local Efficiency. Pressure Drop Δp [mm Water] = 61, RH = 80%, Air Temperature [°C] = 28, Air Flow Rate = 187.7 m ³ /hr, Test # NESH125.2, Test Date: 06/30/98	315
E.28	Humidity Effect on Efficiency of Electrostatically Neutral Pleated Fibrous Filter: (a) Upstream No. Density, (b) Downstream No. Density,	

- (c) Upstream Velocity, (d) Downstream Velocity, (e) Local Efficiency.
 Pressure Drop Δp [mm Water] = 56, RH = 43%, Air Temperature [°C] = 37,
 Air Flow Rate = 187.7 m³/hr, Test # NESH125.3, Test Date: 07/11/98 316
- E.29 Humidity Effect on Efficiency of Electrostatically Neutral Pleated Fibrous
 Filter: (a) Upstream No. Density, (b) Downstream No. Density,
 (c) Upstream Velocity, (d) Downstream Velocity, (e) Local Efficiency.
 Pressure Drop Δp [mm Water] = 56, RH = 48%, Air Temperature [°C] = 37,
 Air Flow Rate = 187.7 m³/hr, Test # NESH125.4, Test Date: 07/12/98 317
- E.30 Humidity Effect on Efficiency of Electrostatically Neutral Pleated Fibrous
 Filter: (a) Upstream No. Density, (b) Downstream No. Density,
 (c) Upstream Velocity, (d) Downstream Velocity, (e) Local Efficiency.
 Pressure Drop Δp [mm Water] = 74, RH = 43.5%, Air Temperature [°C] = 35,
 Air Flow Rate = 229.7 m³/hr, Test # NESH150.1, Test Date: 07/02/98 318
- E.31 Humidity Effect on Efficiency of Electrostatically Neutral Pleated Fibrous
 Filter: (a) Upstream No. Density, (b) Downstream No. Density,
 (c) Upstream Velocity, (d) Downstream Velocity, (e) Local Efficiency.
 Pressure Drop Δp [mm Water] = 71, RH = 43.5%, Air Temperature [°C] = 36,
 Air Flow Rate = 229.7 m³/hr, Test # NESH150.2, Test Date: 07/11/98 319
- E.32 Humidity Effect on Efficiency of Electrostatically Neutral Pleated Fibrous
 Filter: (a) Upstream No. Density, (b) Downstream No. Density,
 (c) Upstream Velocity, (d) Downstream Velocity, (e) Local Efficiency.
 Pressure Drop Δp [mm Water] = 104, RH = 43.5%, Air Temperature [°C] = 35,
 Air Flow Rate = 273.6 m³/hr, Test # NESH175.1, Test Date: 07/02/98 320
- E.33 Humidity Effect on Efficiency of Electrostatically Neutral Pleated Fibrous
 Filter: (a) Upstream No. Density, (b) Downstream No. Density,
 (c) Upstream Velocity, (d) Downstream Velocity, (e) Local Efficiency.
 Pressure Drop Δp [mm Water] = 107, RH = 48.5%, Air Temperature [°C] = 35,
 Air Flow Rate = 273.6 m³/hr, Test # NESH175.2, Test Date: 07/07/98 321
- E.34 Humidity Effect on Efficiency of Electrostatically Neutral Pleated Fibrous
 Filter: (a) Upstream No. Density, (b) Downstream No. Density,
 (c) Upstream Velocity, (d) Downstream Velocity, (e) Local Efficiency.
 Pressure Drop Δp [mm Water] = 122, RH = 45%, Air Temperature [°C] = 34,
 Air Flow Rate = 313.8 m³/hr, Test # NESH200.1, Test Date: 07/03/98 322
- E.35 Humidity Effect on Efficiency of Electrostatically Neutral Pleated Fibrous
 Filter: (a) Upstream No. Density, (b) Downstream No. Density,
 (c) Upstream Velocity, (d) Downstream Velocity, (e) Local Efficiency.
 Pressure Drop Δp [mm Water] = 124, RH = 44%, Air Temperature [°C] = 32,
 Air Flow Rate = 313.8 m³/hr, Test # NESH200.2, Test Date: 07/04/98 323

G-1	Absolute Humidity Variation with Time at a Constant Air Flow Rate	329
H.1	Temperature and Humidity Variations Downstream of Filter As a Function of Air Flow Rate: (a) without Both Heat Addition and Atomization of Distilled Water (b) with Both Heat Addition and Atomization of Distilled Water	331
H.2	Temperature and Humidity Variations Downstream of Filter As a Function of Air Flow Rate: (a) without Heat Addition and Atomization of Distilled Water (b) with Heat Addition But No Atomization of Distilled Water	332
H.3	Temperature and Humidity Variations Upstream of Filter As a Function of Air Flow Rate: (a) with Both Heat Addition and Atomization of Distilled Water (b) with Both Heat Addition and Atomization of Distilled Water	333
H.4	Temperature and Humidity Variations Upstream of Filter As a Function of Air Flow Rate: (a) with Heat Addition and Atomization of Distilled Water (b) with Heat Addition and Atomization of Distilled Water	334
H.5	Temperature and Humidity Variations Near Mixing Box As a Function of Air Flow Rate: (a) with Both Heat Addition and Atomization of Distilled Water (b) with Heat Addition and Atomization of Distilled Water	335
H.6	Temperature and Humidity Variations of Preheated Air As a Function of Time: (Heater on, But without the Atomization of Distilled Water; Date: 01/23/98) (a) at an Air Flow Rate of 77 m ³ /hr (b) at an Air Flow Rate of 103 m ³ /hr	336
H.7	Temperature and Humidity Variations of Preheated Air As a Function of Time Downstream of Filter (Heater on, But without Atomization of Distilled Water): (a) at an Air Flow Rate of 15 m ³ /hr (b) at an Air Flow Rate of 29 m ³ /hr	337
H.8	Temperature and Humidity Variations As a Function of Time Upstream of Filter (with Heat Addition, But without Atomization of Distilled Water): (a) at an Air Flow Rate of 15 m ³ /hr (b) at an Air Flow Rate of 13 m ³ /hr	338
H.9	Temperature and Humidity Variations As a Function of Time Downstream of Filter (Heater on, But without the Atomization of Distilled Water): (a) at an Air Flow Rate of 12 m ³ /hr (b) at an Air Flow Rate of 17 m ³ /hr	339
N-1	Humidity Calibration Curve for SunBeam Based on Omega RH20 Humidity Sensor (Date: 07/14/98)	352

N-2 Temperature Calibration Curve for SunBeam Based on Omega
RH20 Temperature Sensor (Date: 07/14/98) 353

NOMENCLATURE

a_1	lower limit of integration (initial time) [s]
A	unfolded filter area [m^2]
A_1	diffusion term
A_p	cross-sectional area of probe volume [m^2]
b	half of the distance between the centers of two fibers [m]
b_1	upper limit of integration (final time) [s]
B_1	hydrodynamic factor
B_w	van der Waals constant [dynes cm^7]
c_e	cumulative fractional error in number density
C	particles (count) concentration [m^{-3}]
C_0	particle concentration upstream of fiber [m^{-3}]
C_1	particle (count) concentration entering filter [m^{-3}]
C_2	particle (count) concentration leaving filter [m^{-3}]
C_c	Cunningham slip correction factor
d_{pv}	minor diameter of the cross-section of probe volume [μm]
d_s	stopping distance for a particle [m]
D	diffusion coefficient [m^2/s]
D_a	hydrodynamic diameter [$\text{kg}^{1/2}\text{m}^{-1/2}$]
D_f	fiber diameter [μm]

D_p	particle diameter [μm]
e	a constant number called the natural number ($e = 2.7182818284\dots$)
e_c	the elementary unit charge ($= 1.6 \times 10^{-19}$ Coulomb)
E	particle (count) collection efficiency
E_{adh}	adhesion efficiency or probability
E_{coll}	collision efficiency
E_D	single fiber efficiency due to diffusion
E_f	field strength or intensity [v/cm]
E_G	single fiber efficiency due to gravitational forces
E_I	single fiber efficiency due to inertial impaction
E_i	single fiber-efficiency due to i th filtration mechanism
$E_{i\dots j}$	the combined single fiber efficiency due to filtration mechanisms i through j
E_{is}	isolated fiber efficiency
E_m	mass collection efficiency
E_R	single fiber efficiency due to interception
E_s	single fiber collection efficiency
f	frequency [$1/\text{s}$]
F	electrostatic force [N]
F_{ad}	adhesion force [dynes]
F_e	resultant of external forces applied to a particle [N]
F_G	force on a particle due to its weight [N]
F_M	resistance force exerted on particle due to the medium [N]
F_u	dimensionless inter-fiber distance ($=R_f/b$)

g	acceleration due to gravity [m/s^2]
H	height of filter [m]
I	electric current [A]
k	Boltzmann constant [$\text{Jm}^{-3}\text{K}^{-4}$]
k_1	empirical constant for pressure drop across a filter [m^{-3}]
k_2	empirical constant for pressure drop across a filter [m^{-4}]
k_c	the Kozeny constant
K_0	filter permeability [m^2]
K_u	the Kuwabara hydrodynamic constant
L	filter thickness [m]
L_f	total length of fiber per unit volume of filter [m^{-2}]
L_{pv}	major diameter (length) of the cross-section of probe volume [μm]
L_s	swept volume length [m]
m	mass of one particle [kg]
m_a	mass of dry air [kg]
m_{da}	mass of displaced air by particle [kg]
m_g	mass of gas [kg]
m_{ma}	mass of mixture (moist air) [kg]
m_v	mass of water vapor [kg]
M_1	mass concentration entering filter [gm/m^3]
M_2	mass concentration leaving filter [gm/m^3]
M_a	molecular weight of vapor [kg/mole]
MF	mass of moisture loss or gain by filter [kg]

MF_E	equilibrium moisture content of air [kg]
MF_I	initial moisture content of air [kg]
M_g	molecular weight of gas [kg/mole]
M_v	molecular weight of vapor [kg/mole]
$M_{v(\text{down})}$	moisture content of air downstream of filter [kg]
$M_{v(\text{up})}$	moisture content of air upstream of filter [kg]
n	amount of electric charge [Coulomb]
n_i	number of particles counted at grid location i
n_s	limiting or saturation charge [Coulomb]
n_p	number of particles per unit volume [m^{-3}]
N	general dimensionless parameter for intensity of particle deposition by electrostatic charge
N_D	dimensionless parameter for diffusion [$N_D = Pe^{-1}$]
N_G	dimensionless parameter for intensity of deposition by gravity
N_i	number density at grid location ' i ' [m^{-3}]
N_{ic}	ion density or concentration [cm^{-3}]
$N_{i\text{down}}$	local number density downstream of filter [m^{-3}]
$N_{i\text{up}}$	local number density upstream of filter [m^{-3}]
N_{oq}	dimensionless parameter for electrostatic deposition due to image forces (neutral fibers and charged particles)
$N_{Q'o}$	dimensionless parameter for electrostatic deposition due to image forces (charged fibers and neutral particles)

$N_{Q,q}$	dimensionless parameter for electrostatic deposition due to Coulombic forces (charged fibers and charged particles)
N_R	dimensionless parameter for intensity of deposition by interception [$N_R = D_p/D_f$]
N_v	flow rate of particle count [s^{-1}]
p_g	gas pressure [Pa]
p_{sat}	partial pressure of water vapor for saturated condition [Pa]
p_t	total pressure [Pa]
p_v	partial pressure of water vapor [Pa]
p_1	static air pressure upstream of the filter [Pa]
p_2	static air pressure downstream of the filter [Pa]
P_a	partial pressure of air [Pa]
P	particle penetration (count basis)
Pe	Peclet number, a dimensionless number that characterizes the intensity of deposition by diffusion [$Pe = D_f U_0/D$]
P_i	penetration due to i th filtration mechanism ($P_i=1-E_i$)
P_m	particle penetration (mass basis)
P_s	total penetration ($P_s=1-E_s$)
q	charge on a particle (Coulomb)
Q	flow rate of air [m^3/hr or m^3/min]
Q'	charge on a fiber per unit length (Coulomb/m)
Q_F	quality factor [m^2/N]
r	radius or radial distance in a polar coordinate [m]
r_m	intermolecular distance [cm]

R	universal gas constant [8314 J/kg-mole-K]
R _a	gas constant of air [287 J/kg-K]
R _d	number density ratio [$N_{i\text{down}}/N_{i\text{up}}$]
Re	Reynolds number [= $\rho_a D_f U / \mu$]
R _f	fiber radius [μm]
R _p	radius of particle [μm]
R _v	gas constant of vapor [462 J/kg-K]
R _w	water film radius [cm]
S ₁	total wetted surface area per unit volume of filter bed [m^{-1}]
S _f	fringe spacing [μm]
SF	solidity factor
St	Stokes no. [$St = C_c \rho_p (D_p)^2 U_0 / (18 \mu D_f)$] a parameter for intensity of deposition by inertia
St _{cr}	Critical Stokes number
t	time [s]
t _i	run time, data collection time at grid location 'i' [s]
T	temperature [$^{\circ}\text{K}$ or $^{\circ}\text{C}$]
U	velocity of air inside filter [m/s]
U ₀	velocity of air inside filter far upstream of the fiber [m/s]
U ₁	upstream average face velocity (based on unfolded filter area) [m/s]
U ₂	upstream average face velocity (based on duct/folded filter area) [m/s]
U ₃	upstream average face velocity (based on LDA measurements) [m/s]
U _f	velocity of air at the face of the filter prior to entering the filter [m/s]

V	velocity of particle [m/s]
V_e	velocity of charged particles [m/s]
V_g	volume of gas [m ³]
V_i	average measured velocity of particles at grid location 'i' [m/s]
V_{ic}	average speed of charging ions [= 2.4×10^4 cm/s]
V_s	settling velocity of particle [m/s]
W	width of filter [m]
x	linear axis
X	axis along the centerline of the LDA transceiver
y	distance of limiting trajectory from the centerline of fiber [m], also linear axis
Y	axis perpendicular to the center-line of the LDA transceiver
z	compressibility factor of gas
z_i	ion mobility [cm ² /v-s, or cm ² /statv-s]
Z	vertical axis along the center-line of the housing
Greek	
α	filter solidity, packing density
α_p	the angle between two crossing laser beams [radians]
γ	fractional capture per unit depth of filter [1/m]
$\Delta N_{i\text{down}}$	deviation (error) in downstream number density [m ⁻³]
$\Delta N_{i\text{up}}$	deviation (error) in upstream number density [m ⁻³]
Δp	pressure drop across filter [Pa]
ϵ	filter porosity, ($\epsilon = 1 - \alpha$)
ϵ_0	permittivity of free space [Farads/m]

ϵ_1	dielectric constant of particle
ϵ_2	dielectric constant of fiber
η_i	local efficiency
η_{overall}	overall efficiency averaged over all of the grid points
θ	angle of contact between the particle and the water film [radians]
θ	polar angle [radians]
λ_w	wavelength of light [nm]
λ	free mean path of air molecules [μm]
μ	dynamic viscosity of air [Pa-s]
π	a mathematical constant [$\pi = 3.14159265\dots$]
ρ	particle-cylinder fiber distance [μm]
ρ_a	density of air [kg/m^3]
ρ_{ma}	density of moist air (air-vapor mixture) [kg/m^3]
ρ_p	particle density [kg/m^3]
ρ_r	electrical resistivity [ohm m]
σ	the surface tension of water [dynes/cm]
σ_g	standard deviation of the pore size [μm]
τ_s	stopping time for particle [s]
Φ	particle capture per unit fiber length per unit time [$\text{m}^{-1}\text{s}^{-1}$]
ψ	stream function [m^2/s]
ϖ	a constant parameter dependent on the velocity of air [s^{-1}]
Ω	humidity ratio [kg vapor/kg dry air]

ABBREVIATIONS

AH	absolute humidity [kg vapor /kg mixture]
Ci	an abbreviation for Curie (a unit of radioactivity)
conc.	concentration of solution (by volume) [ml of suspension/ ml of solution]
K.E.	kinetic energy
PSL	spherical polystyrene latex
RH	relative humidity (p_v/p_{sat})
Temp.	temperature [$^{\circ}$ C, K]
∇^2	Laplacian operator

CHAPTER I

INTRODUCTION

In the automobile industry, the development of an automotive air filter is related to the development and improvement of the performance and reliability of the vehicle (automobile) itself. Fodor [1979] found out that about 80% of all internal combustion engine failures were attributed to engine wear due to contaminating dust particles having various concentrations and sizes. Thus for its high performance and endurance, a modern automotive engine requires the intake of clean air, preferably free from submicron abrasive and contaminating particulate matter. Many studies have revealed that the life span, wear, efficiency (power loss), lube oil consumption, and emission of an internal combustion engine are closely related to the efficiency or capability of an air induction filter to remove abrasive dust particles under various environmental conditions.

Engine designers and engineers are increasingly concerned about the type, size and concentration of contaminants that could be ingested by the engine. Other than industrial and atmospheric dusts, the contaminants that can be ingested by the engine, depending upon the geographical location and environmental conditions, include mud, snow, water (mist), sand, fine metal debris, sticky hydrocarbons and soot. Jaroszczyk et al. [1993a] report that there are about 50 to 400 billion submicron particles per cubic meter of air, to which another 1.2 billion pollen particles may be added seasonally.

The concentration of the contaminants that may reach the filter, depending upon the environment, ranges from 0.01-10 mg/m³ of air. In industrial areas, the average concentration is 0.1-0.3 mg/m³. In agricultural environments and dusty roads, the concentration even reaches 1000 mg/m³ Jaroszczyk et al. [1993a]. These contaminants of various sizes, shapes, types, and concentration, as well as different electrical (charge), chemical and physical properties, complicate the design of an air induction filter or system. Hence the design of an air induction system in general, and an air induction filter for the removal of abrasive aerosols in particular, still remains as an integral part of the problems and challenges of internal combustion engine designs. However, according to Bugli [1997], air induction filter designs have dramatically changed over the last few years to meet the following requirements:

1. filtration efficiency,
2. flow restriction,
3. dust holding capacity,
4. sound attenuation,
5. overall emission,
6. service requirement.

From a macroscopic point of view, the filtration process is characterized by several parameters as outlined above. However, the basic performance characteristics of a filtration process are filtration (dust collection) efficiency, airflow restriction or pressure drop, dust holding capacity, air cleaner structural integrity and cost.

Filtration efficiency is the measure of the filter's ability to remove contaminants from the air stream. Pressure drop is the difference between the static pressures

measured immediately upstream and downstream of the filter at a certain airflow rate. Dust holding capacity is defined as the amount of dust particles that the filter can hold before reaching a certain terminal pressure drop. Efficiency and pressure drop are highly dependent upon the properties of the porous medium used and the fluid for a clean filter. As filtration proceeds, pressure drop and efficiency also depend upon the properties of the deposited particles.

In the automotive industry, fibrous filters are commonly used in the air induction systems of engines and recently as cabin air filters for the removal of abrasive and contaminating aerosol particles from the air stream. This is solely for their high depth filtration efficiency, low resistance to airflow, high dust capacity and low cost. The fact that filtration by fibrous filters has been studied the most, both theoretically and experimentally, also contributes to its wide application. Fibrous filters are pads of fibers in an open 3-dimensional network. The inter-fiber distances are usually large in relation to fiber diameters, and fibrous filters can have considerable rigidity even though the packing fraction (the fraction of the perceived volume of the filter that is actually occupied by the fibers) is only a few percent [Brown, 1993].

The mechanisms of filtration or particle capture in fibrous filters can be divided into mechanical and electrostatic type. The effects of the mechanical filtration mechanisms (diffusion, inertial impaction, interception, and gravity) and the flow velocity across the filter media have been extensively studied for a number of years both theoretically and experimentally since the times of Albrecht [Orr, 1977]. Thus many mathematical models for predicting the flow field around fibers, different single and overall efficiency parameters and pressure drop are well developed and found in the

literature. Similarly the capture of particles by electrical forces (Coulombic and polarization) in fibrous filtration using different charging mechanisms of the fibers or the contaminating dust particles has attracted several researchers to enhance the efficiency of fibrous filters. [Polarization is the charging of filter fibers and particles by induction. For example, when a charged particle approaches a neutral filter fiber, it induces a dipole (negative and positive charge) on the fiber. On the other hand, when a neutral particle approaches a charged filter fiber, the fiber can induce a dipole on the particle. Thus a polarized particle or fiber has both negative and positive charges far apart from each other. However, for Coulombic action to take place, a net charge on the particle and fiber is of paramount importance Davies (1973)].

Profound research work in electrostatics reveals that, when metals and semiconductors are electrically isolated from the ground, they easily become charged due to rubbing against surfaces where friction or contact followed by separation as in duct or channel flows may play an important role in the triboelectrification phenomena. Even the resuspension by atomization of contaminants from liquid solutions and then drying them can produce a high electrostatic charge that may influence the filtration efficiency significantly. For that matter, it is a routine and standard task for a filtration researcher to neutralize electrostatically charged particles that are used in the evaluation of the performance of fibrous filters.

1.1 Objectives and Methodologies

The School of Mechanical and Aerospace Engineering at Oklahoma State University has been doing research on automotive air induction systems and filters for the

last several years. The studies that have been performed in the local efficiency measurement of fibrous filters have used a Laser Doppler Anemometry (LDA) system to measure particle counts (concentration) and velocities, by atomizing and drying high pressure solutions of monodisperse spherical polystyrene latex (PSL) particles. These studies have focused on the overall initial efficiency of engine filters. Investigation into the effects of parameters like humidity, temperature and, above all, electrostatic charge (that may arise from the triboelectric effects of the PSL particles in the duct flow or atomization process) on filtration was not performed until this work. The experimental results in some cases showed variations from one experiment to the other. The necessity of addressing these problems of inconsistency became clear when Anand [1997] and Jadbabaei [1997] examined previous experimental work and did some additional consistency measurements. They attributed a few of the problems to housing leakage and the stability of the LDA system. Previously Frederick [1996], a senior researcher in fabric filtration at the Mellon Institute, in his letter [refer to Appendix A] written to Natarajan and coauthors, commenting on the published paper by Natarajan et al. [1996], emphasized and recommended the need to study the effects of triboelectric charge. In his thesis, Anand [1997] also recommended that electrostatic charge effects on filtration efficiency be investigated.

In this study, to explore the effects of humidity and electrostatic charge on filtration efficiency at different flow rates (face velocities), Dayco-Purolator A13192 pleated automotive air filters made from non-woven filter media were tested with 0.966 μm diameter spherical polystyrene latex particles as the contaminant. Since humidity highly influences electrostatic charge quantity and stability, prior to the local efficiency

measurements, the author had established a graphical correlation between electrostatic voltage level, humidity, and the contaminant size, type, and concentration before and after the particles reach the filter as a function of airflow rate. Thus, in this study, electrostatic charge refers to the static charge produced either due to the resuspension of the PSL particles by atomization or the triboelectric effects (friction, contact and separation) of the PSL particles as they flow through the duct/filter housing. Measurements of electrostatic voltage and humidity were performed both in the summer and winter over a one-year period to confirm the consistency of the measurements before the investigation was conducted to document the effects of electrostatic charge and humidity on filtration efficiency. The time dependence of charge accumulation and decay was also investigated during and after the experimental filtration processes, respectively, at different locations along the duct and test housing (at the mixing box and filter – to be detailed later in this thesis). Humidity variations of the air stream close to the test filter at both upstream and downstream locations were also investigated, and the time needed to reach equilibrium (between the air stream and the filter) was established for each flow rate.

One of the challenges in investigating electrostatic charge effects on fibrous filtration is neutralizing the charged particles. The neutralization or control of the electrostatically charged particles in this research was carried out mainly by covering the outside of the test housing with conducting aluminum foil, without resorting to the use of any radioactive radiation source or ionized air. Experiments were conducted on electrostatic charge neutralization by covering the experimental plexiglass housing with thin aluminum foil and grounding the whole system using a copper conductor. The

housing and the filter support (aluminum sheet) were mounted were also grounded and experimental results showed an effective charge neutralization/reduction from the surface of the housing for all flow rates. However, the theory behind the discharging mechanism remains unexplained and beyond the scope of this study. Some literature indicates that this discharging mechanism is valid, but does not provide sufficient theoretical background. In addition, the humidity of the air at different flow rates was controlled using a heater and humidifier in combination. A hygrometer-thermometer device was also installed inside the air stream in a mixing chamber to monitor the humidity and temperature of the flow. Pressure drop changes (volume flow rate), electrostatic voltage and humidity were also recorded and monitored during the local efficiency measurements.

This research was specifically conducted on a small angle diffuser housing similar in concept to the test housing specified in the revised J1669 Test Code of the SAE [1998]. The research was divided into two parts. In the first part of the experimental study, electrostatic charge (produced due to the resuspension of PSL particles or triboelectric effects) was eliminated (minimized) from the small angle diffuser housing using the grounded aluminum foil. Then the effect of humidity was investigated experimentally by varying the humidity between two achievable maximum and minimum humidity values for each flow rate to study the effect on mechanical filtration mechanisms. In the second part of the research, the electrostatic charge on the spherical polystyrene latex particles was retained and maximized by lowering the humidity of the flow for each flow rate. The correlation of these two results allowed the investigation of the electrical (electrostatic charge) and humidity effects on fibrous filtration.

1.2 Thesis Organization

This thesis work is divided into seven chapters. The following chapter mainly focuses on the fundamentals of fibrous filtration and mechanical filtration theories. Chapter III is devoted to the literature review on electrical mechanisms of filtration in fibrous filters and the models for predicting the single fiber efficiencies, and on the effect of humidity on fibrous filtration and pressure drop. It also presents related previous experimental studies. Chapter IV presents the experimental setup and procedures used to carry out this study. All of the consistency measurements related to electrostatic voltage, humidity, the stability of the Laser Doppler Anemometry (LDA) system (laser power and number density) and the atomizer for seeding particles are presented in Chapter V. Chapter VI delineates the experimental results and discussions. Chapter VII discusses the summary, conclusions and recommendations for future work. Other selected experimental results, relevant material and a list of test equipment are provided in the Appendices.

CHAPTER II

FUNDAMENTALS OF FIBROUS FILTRATION

2.1 Introduction

Fibrous filtration is a complicated fluid-particle separation process that involves several mechanical and electrical (electrostatic) separation mechanisms as the fluid passes through a porous media. The capture of aerosol particles by fibrous filtration is the most common method of air cleaning. At low dust concentration levels, fibrous filters are the most economical means of achieving high efficiency collection of submicron particles. Theoretical models for predicting mainly the overall filtration efficiency and pressure drop of a filter are found in the vast scientific literature on filtration. Today experimental and theoretical filtration is a dynamic area of research. Significant progress has been made in this field with the advent of fast computers, which enable computational and viscous fluid dynamics experts to solve (numerically) viscous and potential fluid flow problems in order to determine the trajectories of the particles. Once the trajectories of the particles are found, the theoretical individual and total single fiber efficiencies can be evaluated. However, to date, the gap between theory and experiment remains wide.

Instead of beginning with the literature review for electrostatic mechanisms of filtration and humidity effects on filtration efficiency, the author has opted to first present

the fundamentals of fibrous filtration that are common to both mechanical and electrostatic mechanisms of filtration. After a brief description of the fundamentals of filtration efficiency and pressure drop across the filter in Section 2.2, fibrous filtration models upon which both classical and modern filtration theories are based will be reviewed briefly in Section 2.3. The mechanical filtration mechanisms are covered in Section 2.4. The electrical particle capture mechanisms and humidity effects, to which this study is most devoted and related, will be reviewed in Chapter III in detail, while an introduction to the basic electrical mechanisms will be presented in Section 2.6.

2.2 Basic Principles of Filtration

Macroscopic investigation of a filter shows that a fibrous filter consists of a mat of fine fibers arranged in such a way that most of them are oriented perpendicular to the direction of air flow. The orientation of fibers in a thin element at right angles to the flow may be at random. It is also possible to think of a fibrous filter as a large number of woven or non-woven layers of fibers. Though a single layer may not have a good particle capture efficiency due to the large inter-fiber distances (compared to the particle size), the filter as a whole can perform well, owing to the tortuous path the fluid-particle suspension has to follow within the filter. Thus depending upon the constitution of the filter media, particle retention may take place at the surface of the filter (hence termed surface filtration) or throughout the entire depth of filter media - depth filtration [Brown, 1993].

The porosity of fibrous filters ranges from 60% to greater than 99%, while the size of the fibers may range from one to several hundred micrometers. Some of the most

commonly used fibers include cellulose fibers (wood fibers), glass fibers, and plastic fibers. Because of their open structure, fibrous filters are permeable to the air and they render a low resistance to airflow. Fibrous filters have the capability to capture aerosol particles that are too small to be sieved out. Thus, due to its high porosity and the rare chance of a submicron particle coming into contact with more than one fiber at a time, one can infer that particle capture must involve only one fiber. Hence the theory of particle capture in fibrous filters is based on the single fiber theory [Brown, 1993; Davies, 1973].

2.2.1 Assessment of Filter Performance

The methods of filtration efficiency assessment and the type of filter to be used depend upon the purpose of the filter and what is to be done with the captured particles. The ability of filters to collect aerosol particles in fluid (air) sampling is usually expressed in terms of an efficiency of collection, the fraction of entering particles that are retained by the filter. Since the recovery of the particles is of paramount importance, a surface filtration is favored. This efficiency can be expressed either in terms of particle (or count) collection efficiency, E , or mass collection efficiency, E_m .

$$E = \frac{C_1 - C_2}{C_1} \quad (2-1)$$

$$E_m = \frac{M_1 - M_2}{M_1} \quad (2-2)$$

where C_1 and C_2 refer to the respective number concentration of particles [particle count per unit volume of air] entering and leaving the filter and M_1 and M_2 refer to the mass

concentrations of particles [mass of particles per unit volume of air] entering and leaving the filter, respectively. The performance of filters that are used for air cleaning, engine protection or any other similar purposes in which the filtered air is of vital importance can be quantified in terms of particle number penetration, P , and mass penetration of particles, P_m , the respective fractions of entering particles (count or mass) that exit or penetrate the filter.

$$P = \frac{C_2}{C_1} = 1 - E \quad (2-3)$$

$$P_m = \frac{M_2}{M_1} = 1 - E_m \quad (2-4)$$

In this study, the performance of an automotive air filter is reported in terms of collection efficiency rather than penetration, as some researchers here at OSU and elsewhere in the USA, including the Society of Automotive Engineers, prefer to do.

The pressure drop of a filter is defined as the difference in static pressures of the filter measured immediately upstream and downstream of the filter:

$$\Delta p = p_1 - p_2 \quad (2-5)$$

where p_1 is the static fluid (air) pressure before the filter and p_2 is the static pressure after the filter. The velocity of the fluid (air) at the face of the filter prior to entering the filter is called the face velocity, U_f . It is calculated by dividing the volume flow rate, Q , of the air by the filter area, A as:

$$U_f = \frac{Q}{A} \quad (2-6)$$

Inside the filter, the velocity of the air, U , is larger than the face velocity, U_f , due to the reduction of the size of the passage by the volume of filter fibers.

$$U = \frac{Q}{A(1-\alpha)} \quad (2-7)$$

where α is the volume fraction of fibers, called packing density, or solidity. It is the ratio of the volume of all of the fibers to the total volume of the filter.

$$\alpha = \frac{\text{volume of all fibers}}{\text{total volume of filter}} = 1 - \varepsilon \quad (2-8)$$

where ε is the porosity of filter defined as: $\varepsilon = \frac{\text{void volume in filter}}{\text{total volume of filter}}$.

The flow inside a filter is most usually laminar. The dimensionless Reynolds number, Re that characterizes the flow around the fiber based on fiber diameter, D_f , and the velocity, U , of the air inside the filter, is calculated by

$$Re = \frac{\rho_a D_f U}{\mu} \quad (2-9)$$

where ρ_a and μ refer to the density and dynamic viscosity of air. For fibrous filters, typical values of Re at low velocities are on the order of 1 or smaller.

2.2.2 Filter Layer Efficiency for Monodisperse Aerosols

A fibrous filter is made up of several layers. The efficiency or penetration of monodisperse particles in a homogenous fibrous filter that captures particles throughout its depth is dependent upon its thickness, L [Brown, 1993].

Hinds [1982] defines γ as a fractional capture per unit depth of a filter for a differentially thin element, dx , and then computes the number of particles, n_p , captured when a unit volume of air with aerosols enters the filter element.

$$n_p = C\gamma dx \quad (2-10)$$

where C is the particle count concentration [number of particles per unit volume] entering the filter element. The decrease in the number of particles penetrating the filter is n_p .

$$dC = -n_p = C\gamma dx \quad (2-11)$$

The integration of the above differential equation yields:

$$\ln\left(\frac{C_2}{C_1}\right) = -\gamma L \quad (2-12)$$

$$\text{or } P = e^{-(\gamma L)} \quad (2-13)$$

This implies that particle penetration decreases exponentially as the thickness or depth of the filter, L , increases. The relation of the above filter efficiency model to the single fiber efficiency due to all possible filtration mechanisms will be presented in Subsection 2.2.4.

2.2.3 Quality Factor

Filtration researchers have established a criterion, the filter quality factor, Q_F , to compare different filters. Liu et al. [1995] call this the figure of merit. It is a function of both pressure drop and penetration (or efficiency). The pressure drop across a filter is dependent upon the face velocity (U_f), thickness (L), solidity (α), and the properties of the fluid. The best filter is the one that gives the highest efficiency at low pressure drop. Pressure drop is related to the amount of energy expenditure. Thus Q_F is a useful measure of the quality of a filter. The higher the Q_F value, the better the filter. The disadvantage of this criterion is that it is not dimensionless as shown below:

$$Q_F = \frac{\gamma L}{\Delta p} = \frac{-\ln(P)}{\Delta p} \quad (2-14)$$

2.2.4 Single Fiber Efficiency

The factors that affect filtration are fiber diameter, $D_f = 2R_f$, packing density α , face velocity U_f , and particle diameter D_p . In modern filtration theory, the influence of these factors is calculated using the methods of fluid mechanics, kinetic theory and electrostatic theory, taking into account the effect of neighboring fibers. On the other hand, the classical filtration theory is based on the isolated fiber theory as if the neighboring fibers do not exist. The overall filter efficiency can also be related to the single fiber efficiency [Davies, 1973].

According to Hinds [1982], the single fiber efficiency is defined as a dimensionless aerosol particle deposition rate on a unit length of a fiber. It is the fraction of aerosol particles approaching a fiber in the region defined by the projected area of fiber that ultimately sticks to the fiber:

$$E_s = \frac{\text{number of particles collected on a unit length}}{\text{number of particles geometrically incident on a unit length}}$$

Using the assumption that all of the fibers in a filter have the same size, the total length of a fiber in a unit volume of filter, L_f , can be obtained from the definition of solidity from Eq. (2-8):

$$L_f = \frac{4\alpha}{\pi D_f^2} \quad (2-15)$$

The number of particles collected when a unit volume of aerosol passes through a unit cross-section and differential thickness dx is

$$n_p = CE_s D_f L_f dx \quad (2-16)$$

where D_f , is fiber diameter and others as defined before. Comparing Eqs. (2-10) and (2-16), one can establish the relation between the single fiber efficiency, E_s , and the layer efficiency, γ , as follows (with the help of Eq. (2-15)):

$$\gamma = \frac{4\alpha E_s}{\pi D_f} \quad (2-17)$$

Other authors give a slightly different relationship between layer and single fiber efficiencies based on the velocity inside the filter as reported by Brown [1993]:

$$\gamma = \frac{4\alpha E_s}{\pi D_f(1-\alpha)} \quad (2-18)$$

Brown [1993] argues that both equations are correct, provided E_s is defined in a manner appropriate to each. The discrepancy is mainly due to the fact α is not defined for air flow ahead of the filter, and so the mean velocity inside the filter is higher by a factor of $(1-\alpha)^{-1}$ than the velocity of the air approaching the filter. Finally, the relation between the efficiency of a filter and the single fiber is found by introducing Eqs. (2-17) or (2-18) into Eq. (2-13) to get the respective equations for the filter efficiency, E , as:

$$E = 1 - e^{-\left(\frac{4E_s\alpha}{\pi D_f}\right)L} \quad (2-19a)$$

$$E = 1 - e^{-\left(\frac{4E_s\alpha}{\pi D_f(1-\alpha)}\right)L} \quad (2-19b)$$

Equation (2-19b) can also be derived from Crawford's [1976] approach as shown below. In Fig. 2.1, the cross-section of a filter, with dimensions W by H and thickness L , is in a plane normal to the air flow. It is assumed that all of the filter fibers have the same single fiber efficiency, E_s , uniform packing density, α , and fiber diameter, D_f . The flow rate of particles, N_v , past any section, is

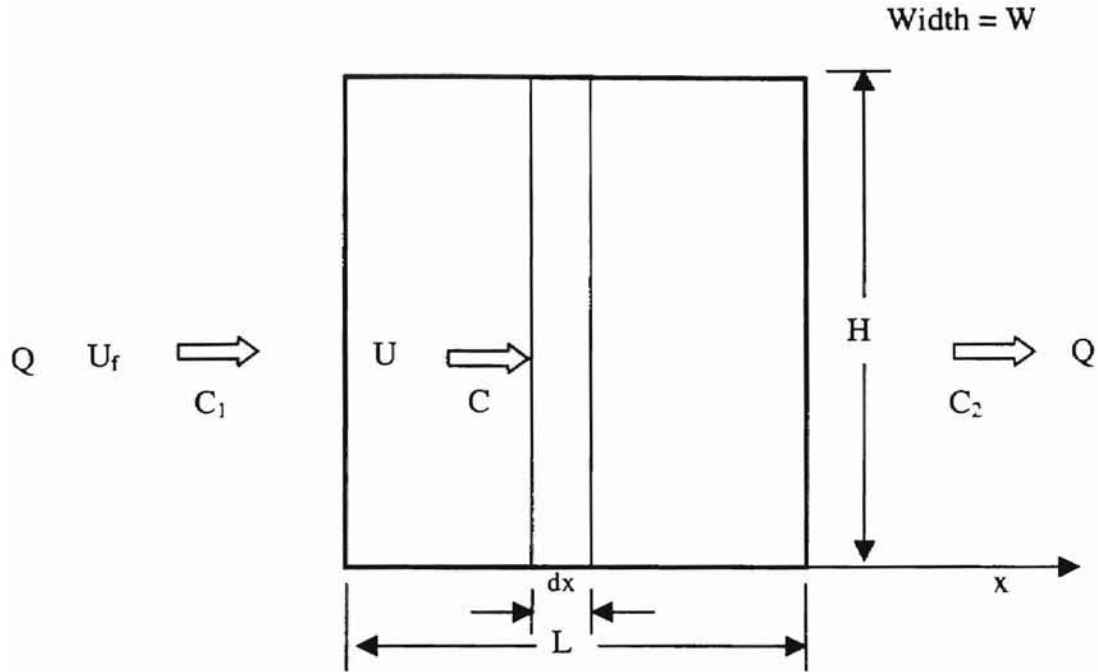


Figure 2.1 Geometry Used to Help Relate Single Fiber and Overall Efficiencies of a Filter [Crawford, 1976].

$$N_v = CQ \quad (2-20)$$

where C is the number of particles per unit volume of air, and Q is the volume flow rate of air. The rate at which particles are removed from the stream in the section of thickness dx is calculated as follows [Crawford, 1976]:

$$dN_v = -E_s C U D_f L_f W H dx \quad (2-21)$$

where L_f is the total length of a fiber in a unit filter volume obtained from Eq. (2-15), the filter area, $A = WH$, and U is the velocity of air inside the filter, obtained from Eq. (2-7). Assuming dN_v is a change in the particle flow rate due only to a change (decrease) in the concentration of particles C and combining Eqs. (2-7), (2-20) and (2-21) yields,

$$\frac{dC}{C} = -E_s \frac{D_f L_f dx}{1 - \alpha} \quad (2-22a)$$

$$\frac{dC}{C} = -\frac{4\alpha E_s dx}{\pi(1-\alpha)D_f} \quad (2-22b)$$

(Note: The negative sign in Eqs. (2-22a) and (2-22b) is introduced to show the rate of decrease in concentration with distance, x). Integrating the left hand side of Eq. (2-22b) with respect to C between C_1 and C_2 and the right hand side with respect to x between 0 (zero) and L , one gets the equation for penetration, P , which is related to the overall filter efficiency, E , as follows:

$$\frac{C_2}{C_1} = P = e^{-\left(\frac{4\alpha E_s}{\pi(1-\alpha)D_f}\right)L} \quad (2-23)$$

$$E = 1 - e^{-\left(\frac{4\alpha E_s}{\pi(1-\alpha)D_f}\right)L} \quad (2-24)$$

2.2.5 The Single Fiber Efficiency Model

Assuming a nearly laminar flow, the single fiber efficiency is the ratio of the distance between two limiting streamlines approaching a fiber to the diameter, $D_f = 2R_f$, of the fiber.

$$E_s = y/R_f \quad (2-25)$$

Equation (2-25) can be expressed as a function of the air flow streamline and velocity distribution inside the filter. For uniform flow as shown in Fig. 2.2, the streamlines upstream of the fiber can be expressed as [Brown, 1993]:

$$\Psi = Uy \quad (2-26)$$

(The stream function, ψ , has a value of $\psi = 0$ at the centerline and on the fiber surface.)

$$E_s = \Psi/UR_f \quad \text{or} \quad E_s = 2\Psi/UD_f \quad (2-27)$$

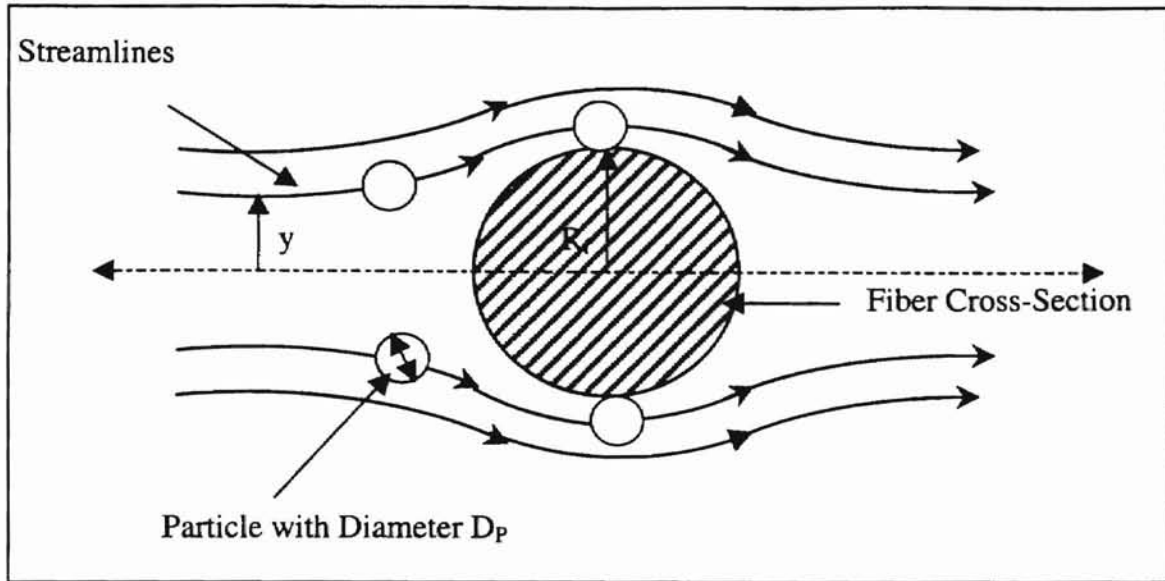


Figure 2.2. Definition of Single Fiber Efficiency, $E_s = y/R_f$ [Davies, 1973].

The above definition holds, provided that the fiber under consideration is isolated or almost isolated and that a limiting trajectory can be defined in such way that aerosols originating nearer to the fiber's central axis than this trajectory will be captured and those beyond that trajectory will not.

For diffusion deposition, where the limiting trajectories can not be well determined, the single fiber efficiency E_D can be related to the concentration of particles in the air, C_0 , of the fiber and the velocity of approach, U_0 , and the rate of capture of particles per unit time per unit length of fiber, Φ , as:

$$E_D = \frac{\Phi}{C_0 U_0 D_f} \quad (2-28)$$

Thus the single fiber efficiency is a dimensionless parameter. Usually it is less than unity but in some cases, it can be greater than 1.0 (for example, single fiber efficiency due to electrostatic mechanisms). In most of the literature, filtration researchers assume that particles that strike the fiber remain adhered to it, hence the terminology perfect

adhesion. However, in reality, a particle that strikes the fiber can be removed or detached due to several particle removal mechanisms such as aerodynamic drag, bouncing and blow off effects when the Stokes number is greater than 1. Jaroszczyk et al. [1993a] made a distinction between collection efficiency and collision efficiency in their efforts to determine the single fiber efficiency. In general, Jaroszczyk et al. [1993a] define the single fiber collection (deposition) efficiency, E_s , as a function of the collision efficiency, E_{coll} , and the adhesion (retention) probability, E_{adh} . The single fiber collection or deposition efficiency refers to the amount of particles retained or adhered to the fiber. On the other hand, the collision efficiency refers to the total amount of particles coming in contact with the fiber, and the adhesion (retention) probability E_{adh} , is the probability (or efficiency) of particles remaining attached to a fiber after contact with the fiber. Hence the single fiber efficiency is

$$E_s = E_{coll} E_{adh} \quad (2-29)$$

2.2.6 The Isolated Fiber Theory

To calculate the elemental or overall efficiency of a filter using Eq. (2-24), it was stated that the single fiber efficiency takes into account the effects of surrounding fibers and packing density or solidity. However, the isolated fiber efficiency, E_{is} , disregards the mutual effects of neighboring fibers and the packing density of the filter. Many researchers of classical filtration theory have used this concept to calculate the fiber efficiency by calculating the trajectories of the particles for different flow conditions and mechanisms. The isolated fiber theory is accurate only for mechanisms of deposition like diffusion and electrostatics, which operate only near the fiber surface. The equations

developed from this theory by Lamb [Davies, 1973] for the flow field round an isolated cylinder were not satisfactory for calculating the trajectories of particles with inertia. They are only valid for low values of Reynolds number. However, Yoshika and his colleagues [Davies, 1973] who have attempted to adjust the results by comparing with experiments, have developed the isolated fiber theory. The diagrams in Figs. 2.3(a) and 2.3(b) are presented by Emi and Yoshioka [Davies, 1973], which depict clearly the domains over which the various mechanisms of filtration are dominant. The curves have been calculated from Emi and Yoshika's results for isolated fibers. From the curves, it can be seen that inertial effects come into play only for velocity greater than 20 cm/sec and particle diameter greater than 0.3 μm , while gravity is important for velocities less than 20 cm/sec and particle diameter higher than 0.2 μm . Diffusion is dominant in the region of small particles over a wide range of velocity but decreases as velocity increases. The most penetrating particle at a certain flow velocity is found from Fig. 2.3(b) [Davies, 1973] by finding the particle diameter with the lowest E_{is} at that specific velocity.

Ptak and Jaroszczyk [1990] have experimentally established the correlation between isolated and single fiber efficiencies by determining a solidity factor, SF , that takes into account the effect of neighboring fibers. It is determined as follows:

$$SF = \frac{0.9}{\alpha^{0.3}} \quad (2-30)$$

where α is the packing density or solidity. Then the single fiber efficiency, E_s , is expressed as:

$$E_s = E_{is} SF \quad (2-31)$$

in which E_{is} is the isolated fiber efficiency.

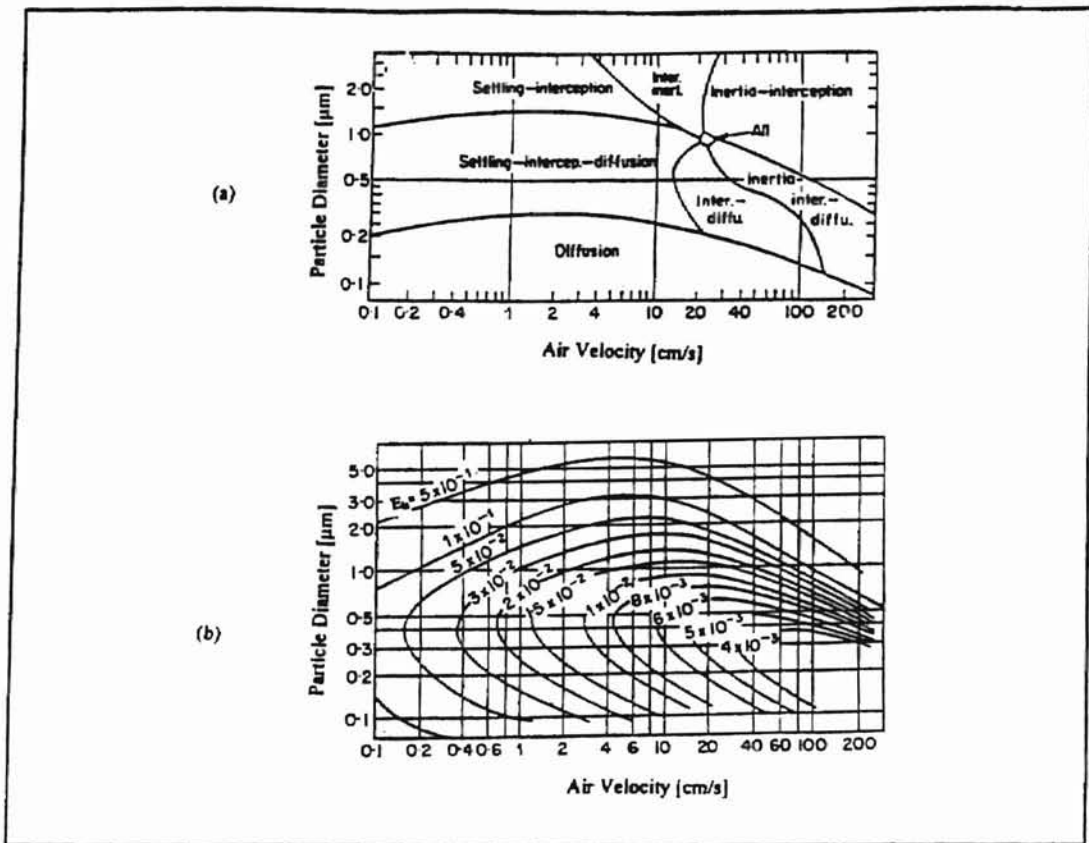


Figure 2.3 Filtration by an Isolated Fiber of Radius 5 μm over a Range of Air Velocities: (a) Domains in Which the Various Mechanisms of Filtration Are Predominant (b) Isolated Fiber Efficiency Contours [Davies, 1973].

2.2.7 Mechanisms of Filtration

The capture of particles from a flowing fluid involves several mechanisms. The most important mechanisms of filtration other than mechanical blockage and sieving action are as follows:

- Direct interception,
- Inertial impaction,
- Brownian diffusion,

- Gravitational settling,
- Electrostatic deposition.

The first four mechanisms of deposition signify particle capture by mechanical means, while the last mechanism is categorized as an electrical means of particle capture. Figure 2.4 illustrates these mechanisms for a flow past a cylinder fiber. Calculating the overall single fiber coefficient due to an individual mechanism requires knowledge of particle trajectories in the vicinity of the fiber. The trajectory of a particle traveling through a fluid is governed by Newton's law of motion [Pich, 1977]:

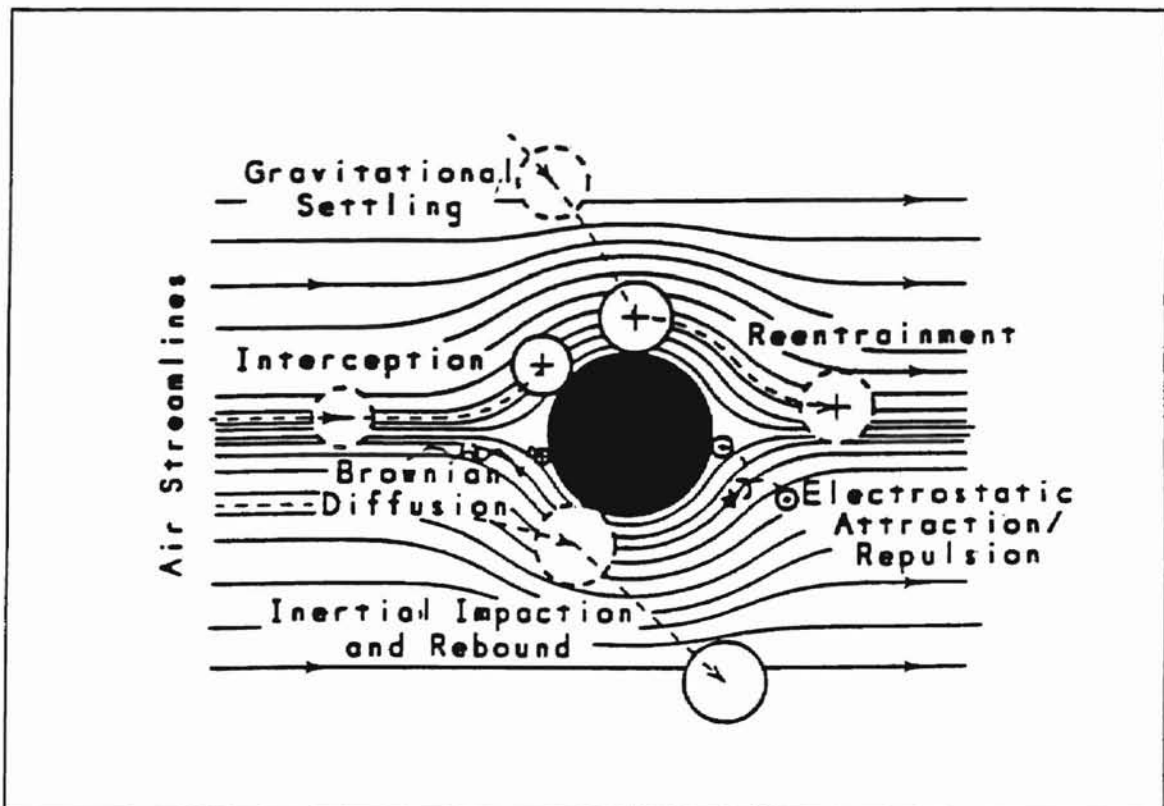


Figure 2.4 Collision and Secondary Mechanisms in Aerosol Filtration [Jaroszczyk and Wake, 1991].

$$m \frac{dV}{dt} = F_e - F_M \quad (2-32)$$

where F_e is the resultant of the external forces applied to the particles (e.g., gravitational and electrostatic forces), F_M is the resultant force due to the resistance of the medium, and m and V are the mass and velocity of the particle, respectively. The scheme for calculating the efficiency of a filter is outlined as follows by Pich [1977]:

1. Calculate the velocity field around the fiber cylinder or around the model by which the filter is approximated.
2. Calculate the single fiber efficiency due to the various filtration mechanisms.
3. If several capture mechanisms are involved simultaneously, the resulting (total) single fiber efficiency is estimated
4. For isolated cylinder models, the influence or the interference effect of neighboring fibers is estimated on the deposition process.
5. Finally, relate the single fiber efficiency of a fiber in the filter to the filter efficiency.

The next subsection concentrates on a brief review of fibrous model filters, which are essential for approximating the real filter in the prediction of filtration efficiency and pressure drop.

2.3 Fibrous Filter Models

In solving the basic problem of filtration theory, it is necessary to express both the pressure drop and efficiency of the filter as functions of the properties of the aerosol particles, the dispersing medium and the filter [Pich, 1977].

The study of fluid flow characteristics and dynamics of particle capture in filter media is necessary from both theoretical and practical points-of-view to the complete understanding and quantification of the filter media performance under varying conditions. The structure of a real filter is highly complex, whereas the systems chosen to simulate them at a laboratory scale are usually over-simplified, and this implies that a direct comparison between theory and experiment for a real filter is not easy. Filtration theory requires approximations of real filter structures that are sufficiently simple to be handled mathematically but sufficiently complicated to represent the realistic description of filters used in practice. A photomicrograph of the structure of a real fibrous filter is shown in Fig. 2.5.

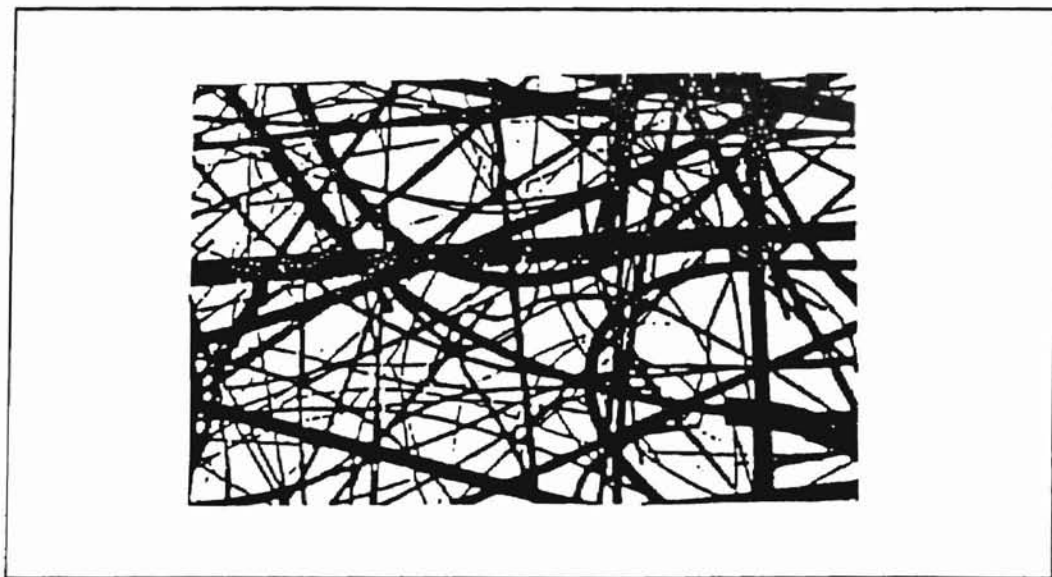


Figure 2.5 Photomicrograph of a Real Fibrous Filter [Khan, 1995].

Most of the filter and filtration models that have been developed over the last 50 years or more to simulate real filters are two-dimensional and do not account for the microscale inhomogeneities and the three-dimensional random distribution of pores or collectors essentially present in a real filter media. Recently a three-dimensional filter

model has been proposed which addresses some of the fundamental shortcomings of the traditional filter models. In his review of the filtration theories in fibrous media, Khan [1995] presents a summary of the theories in the study of air filtration in non-woven fibrous filter media. Khan argues that the traditional approaches to predict pressure and particle capture efficiencies in fibrous filters, based on the highly idealized two-dimensional filter models, have led most of the time to the overprediction of the performance of a real fibrous filter. The traditional fibrous filter models upon which both the classical and modern filtration theories are based are divided into four broad categories. Most of the filter models are highly idealized and two-dimensional except for the fourth category, the three-dimensional screen model. They are enumerated as follows [Khan, 1995]:

1. capillary tube models,
2. barrier models,
3. pore theory,
4. three-dimensional offset screen model.

2.3.1 Capillary Tube Models

Khan [1995] reports that this model originally evolved from that of Darcy's work who first experimentally studied the seepage of water through sand under gravity. Darcy established the following famous relationship for predicting pressure drop across porous media:

$$\Delta p = \frac{U L \mu}{K_0} \quad (2-33a)$$

where Δp is the pressure drop, K_0 is the permeability, U_f is the face velocity, μ is the viscosity of the fluid, and L is the thickness or depth of the filter. However, early improvement by Dupuit, that was later further developed by Kozeny, and finally modified by Carman [Khan, 1995] have refined Darcy's equation further by taking into account the solidity and modeling the filter (porous media) as a bundle of capillary tubes. Thus the Kozeny-Carman equation for the prediction of pressure drop is given by

$$\Delta p = \frac{1}{\epsilon^3} k_c S_1^2 \mu U_f L \quad (2-33b)$$

where ϵ is the porosity of the porous medium, k_c is the Kozeny constant and S_1 is the total wetted surface area per unit volume of filter bed. The Kozeny constant k_c is approximately 5.

2.3.2 The Barrier Models

Most of the models used in formulating the mathematical modern and classical filtration models are based on this category of filter models. Albrecht [Khan, 1995] for the first time proposed a single cylinder model to study particle capture in fibrous filter media assuming a potential flow around the fiber in solving particle trajectory equations. Since then, many improvements have been made in the simplest model geometry and the inviscid flow equations employed by Albrecht in modeling a real filter. Langmuir [1942] was the first to propose an array of parallel rows of cylinders as a model, which accounted for the interfiber effects. Langmuir [1942] was able to visualize a filter model consisting of parallel rows of cylinders oriented along the fluid flow as shown in Fig. 2.6.

Filter models are further classified according to low and high porosity. In this respect, the ordered inter-fiber distance and fiber diameter are very important parameters.

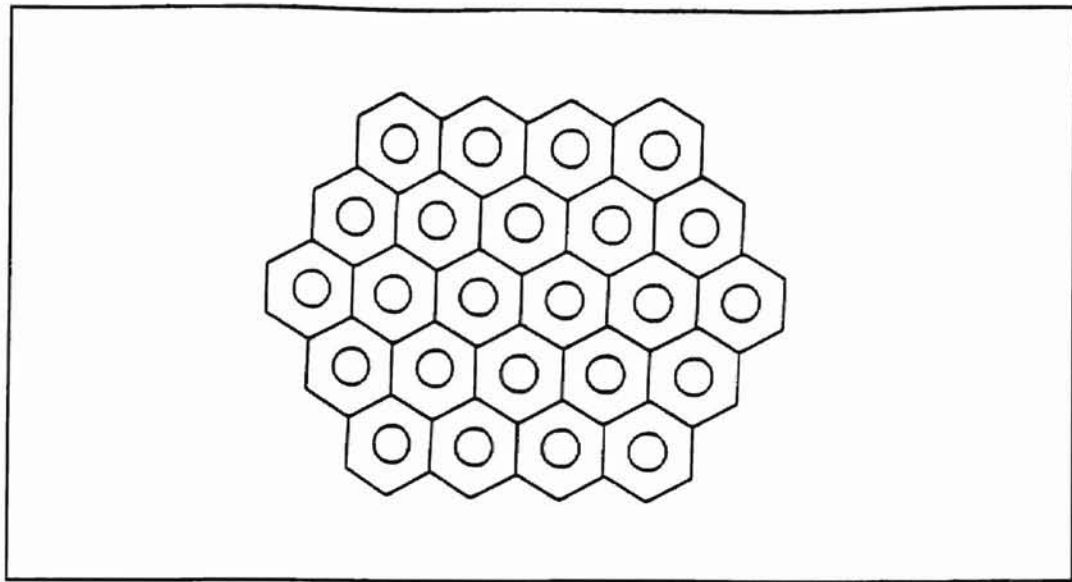


Figure 2.6 Langmuir's Parallel Cylinder Filter Model [Khan, 1995].

Figure 2.7 shows a cell model for high porosity filters as employed by Langmuir [Khan, 1995]. The inter-fiber distance is expressed in terms of a dimensionless number, F_u . It is the ratio of the distance, $2b$ between two cylindrical fibers and the fiber diameter, $D_f = 2R_f$.

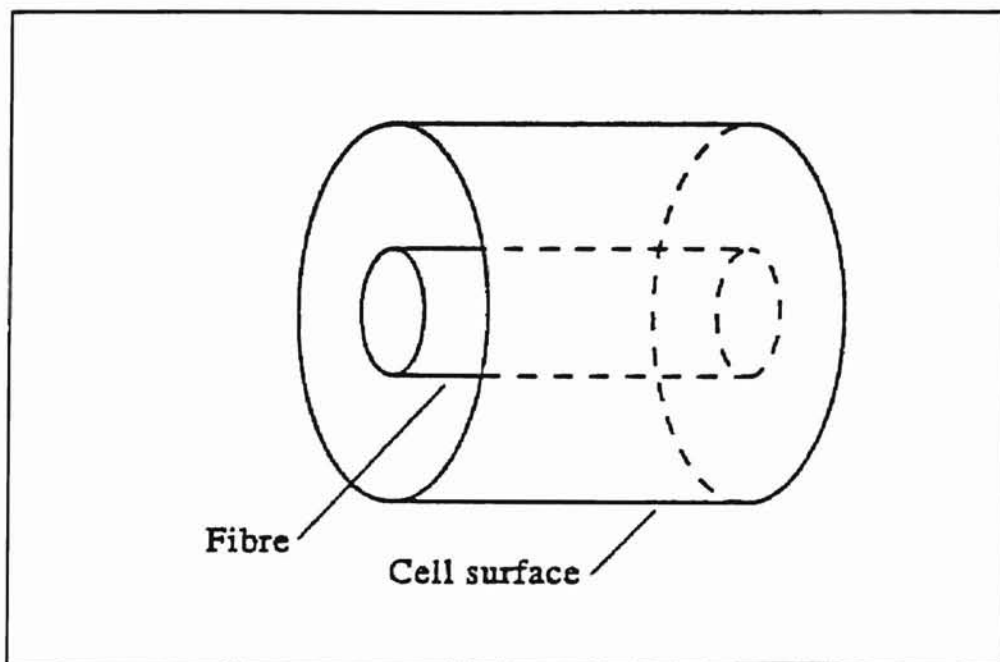


Figure 2.7 The Cell Model for High Porosity Filters as Employed by Langmuir (Parallel Flow), Happel and Kuwabara (Transverse Flow) [Brown, 1993].

$$Fu = \frac{D_f}{2b} = \frac{R_f}{b} \quad (2-35)$$

The porosity of a filter is related to Fu by the following relations, depending upon the arrangement of the cylindrical fibers [Orr, 1977].

An infinite array of cylinders (structure of the first order): $\varepsilon = 1 - \frac{\pi}{4} Fu$

A system of an infinite array of cylinders (structure of the second order):

(1) For a square structure: $\varepsilon = 1 - \frac{\pi}{4} (Fu)^2$

(2) For a triangular structure (staggered arrangement): $\varepsilon = 1 - \frac{\pi}{2\sqrt{3}} (Fu)^2$

(3) For a nonaligned structure ($2b$ is not constant); according to Orr's [1977] report,

Fuchs and Stechkina express the porosity as: $\varepsilon = 1 - (Fu)^2$

A summary of barrier models, including cell models, is given below as presented by Khan [1995].

1. Isolated Cylinder Models; used in inviscid or viscous flow,
2. In-line-cylinder Array Models,
 - High-porosity ($Fu \ll 1$ or $\alpha \ll 1$) models
 - Low-porosity ($(1 - Fu) \ll 1$ or $\varepsilon \ll 1$) models
3. Staggered Cylinder Array Models
 - High-porosity ($Fu \ll 1$ or $\alpha \ll 1$) systems of cylinders in transverse flow,
 - High porosity ($Fu \ll 1$ or $\alpha \ll 1$) systems of cylinders in longitudinal flow,
 - Low-porosity ($(1 - Fu) \ll 1$ or $\varepsilon \ll 1$) systems in transverse flow,
4. Single Array Model with nonuniform cylinder spacing,

5. Fan Model with nonparallel arrangement of cylinders,
6. Other Models.

2.3.3 Pore Theory

The pore sizes of real fibrous filters are not uniform throughout the filter. According to Benarie [Davies, 1973], the porosity of a filter is a mean value. Benarie also showed that, for viscous flow, since the pressure gradient along a pore is inversely proportional to the fourth power of its radius, the distribution of flow through the channels must also be lognormal. Therefore Benarie concluded that most of the flow passes through the larger pores. Using this model, several researchers have predicted the pressure drop of real filters. Figure 2.8 shows the tendency of a fluid to seek larger pores.

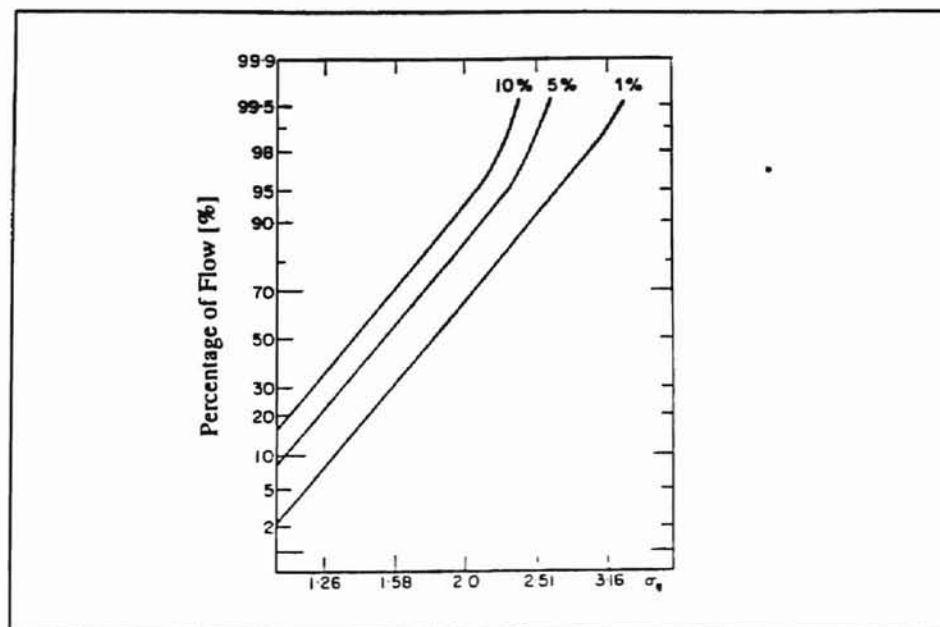


Figure 2.8 Calculation by Benarie Showing the Tendency for the Flow Through a Fibrous Filter to Seek the Larger Pores. The Percentage of the Total Flow, Q , Passing Through the Upper 1, 5, and 10% of Pores Plotted Against the Geometrical Standard Deviation, σ_g , of the Pore Size [Davies, 1973].

2.3.4 The Three-Dimensional Offset Screen Model

Khan [1990] proposed this model in his dissertation from the Mechanical Engineering Department, University of Rhode Island. His new model accounted for structural properties of the filter, namely fiber size, solidity, and degree of isotropy of the filter, and also utilized a three-dimensional flow field.

2.4 Mechanical Filtration Mechanisms

In the previous sections, the basic principles of filtration common to both mechanical and electrical particle capture mechanisms have been introduced. The single and isolated fiber (early filtration theory) efficiency models have also been discussed, from which the single fiber efficiencies of a fiber can be calculated (due to all mechanisms) to predict the overall filtration efficiency of a new filter. In this section, the theoretical efficiency of a fiber will be reviewed due to various mechanical mechanisms as presented by several researchers.

In mechanical filtration, the commonly encountered filtration mechanisms are diffusive deposition, interception, inertial impaction and gravitational settling.

2.4.1 Diffusive Deposition

Under certain circumstances, owing to Brownian (random) motion, the trajectories of aerosol particles smaller than 0.2 μm diameter do not coincide with the streamlines of the fluid (air). The aerosol particles can diffuse from the flow streams to the fibers and get deposited thereon. As the particle size decreases, the intensity of the Brownian motion increases thereby increasing the collision efficiency. In developing the

collection efficiency due to this mechanism, the particles are assumed as point masses; and the concentration at the surface of the collecting fibers is zero.

The efficiency of deposition, E_D , is calculated as follows:

$$E_D = \frac{\Phi}{C_0 U_0 D_f} \quad (2-28)$$

where Φ is the number of particles deposited on the unit length of the fiber in a unit time, C_0 is the concentration of particles in the air upstream of the fiber, and U_0 is the upstream velocity of air inside the filter far removed from the effect of the fiber. U_0 is not the same

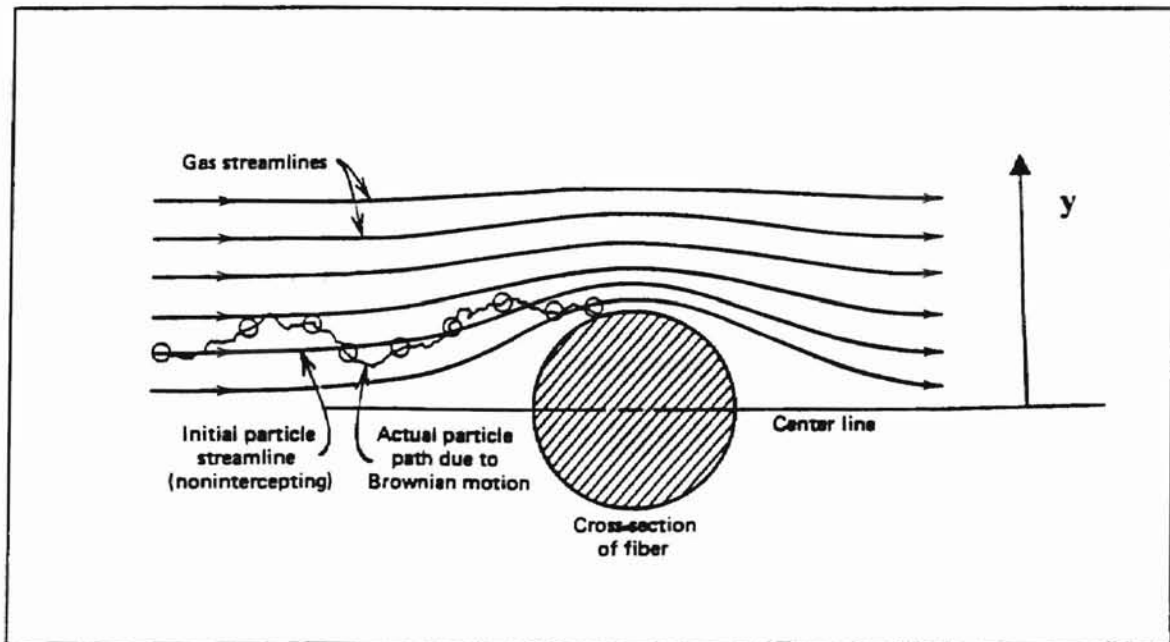


Figure 2.9 Single-Fiber Collection by Brownian Diffusion [Hinds, 1982].

as the face velocity U_f or the average velocity U inside the filter. U is obtained by dividing the flow rate by the filter area (for flat filters) or by spreading the flow over the unfolded filter area (for pleated filters), taking into account the filter packing density.

To calculate the efficiency of deposition E_D , one needs to solve the basic differential equation governing diffusive deposition [Pich, 1987].

$$\frac{\partial C}{\partial t} + \text{div}(CV) = D \nabla^2 C \quad (2-36)$$

where V is the velocity of the particles, C is the particle concentration and ∇^2 is the Laplacian operator. Introducing the relation $\text{div}(CV) = C\text{div}(V) + V\text{grad}(C)$ into Eq. (2-36) and setting $\text{div}(V) = 0$ for an incompressible fluid (even air is considered incompressible under low pressure) yields

$$\frac{\partial C}{\partial t} + V\text{grad}(C) = D \nabla^2 C \quad (2-37)$$

In non-dimensionalizing Eq. (2-37), a dimensionless term, Pe known as the Peclet number is introduced, which is defined as $Pe = \frac{D_f U_0}{D}$, where D_f is the fiber diameter, D is the diffusion coefficient, and U_0 is the velocity of fluid far ahead (upstream) from the fiber. The Peclet number Pe or its reciprocal $N_D = Pe^{-1}$ is used as the dimensionless number that characterizes the intensity of diffusion deposition. Various researchers have found the solution of Eq. (2-37) for different Pe and Re values.

Case 1. $Pe \ll 1$ and $Re < 1$:

For small Pe and viscous flow conditions, the equation for diffusion efficiency E_D was derived by Stechkina [Pich, 1987] as:

$$E_D = \frac{2\pi}{Pe(1.502 - \ln Pe)} \quad (2-38)$$

Case 2. $Pe \gg 1$ and $Re < 1$:

This case was investigated by Langmuir [Pich, 1987]. According to Langmuir, says Pich, the efficiency of diffusion on a fiber is

$$E_D = \frac{1}{2(2 - \ln \text{Re})} \left[2(1 + A_1) \ln(1 + A_1) - (1 + A_1) + \frac{1}{1 + A_1} \right] \quad (2-39)$$

where, $A_1 = 1.308 \left[(2 - \ln \text{Re})^{1/3} / \text{Pe}^{1/3} \right]$. As A_1 tends to zero (or $A_1 \ll 1$), Eq. (2-39)

reduces to [refer to Appendix L on the steps followed to prove it],

$$E_D = 1.71 \frac{1}{(2 - \ln \text{Re})^{1/3}} \text{Pe}^{-2/3} \quad (2-40)$$

Other researchers, Friedlander and Natason [Pich, 1987], derived an equation for E_D based on modern concepts of boundary layer diffusion and found the same solution as that of Langmuir's reduced equation. Stechkina [Pich, 1987] also calculated the equation for case 2, believed to be the most accurate and valid for $\text{Pe} > 80(2 - \ln \text{Re})$ as:

$$E_D = \frac{2.9}{(2 - \ln \text{Re})^{1/3}} \text{Pe}^{-2/3} + 0.624 \text{Pe}^{-1} \quad (2-41)$$

Case 3. $\text{Pe} \gg 1$ and $\text{Re} \gg 1$:

In this diffusive deposition region, Fuchs and Stechkina [Pich, 1987] reported the diffusion efficiency for parallel cylinders by employing the Kuwabara and Happel [Brown, 1993] flow field

$$E_D = \frac{2.9}{(B_1)^{1/3}} \text{Pe}^{-2/3} \quad (2-42)$$

where $B_1 = -[0.75 + (\ln \alpha)/2]$ (Kuwabara) and $B_1 = -[0.50 + (\ln \alpha)/2]$ (Happel).

2.4.2 Direct Interception

The mechanism of direct interception occurs when aerosol particles behave in a

passive way with respect to the airflow, without being subjected to any inertial effects, diffusive motion or any other external forces, including gravitational forces [Brown, 1993]. A particle that follows the streamline is intercepted as soon as it approaches the fiber within a distance equal to half of its own diameter, D_p . Figure 2.10 shows the mechanism of single fiber collection by direct interception. The mechanism of direct interception is characterized by a dimensionless parameter $N_R = D_p/D_f$, where D_p is the diameter of the particle and D_f is the fiber diameter.

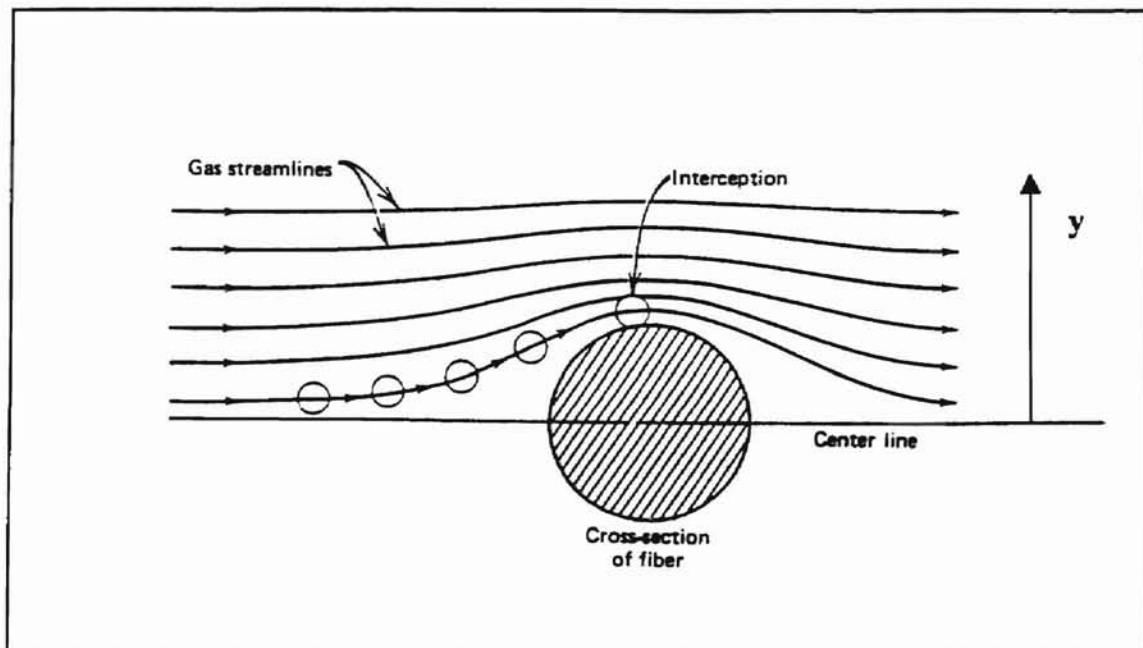


Figure 2.10 Single-Fiber Collection by Direct Interception [Hinds, 1982].

Based on Eq. (2-27), the efficiency of deposition due to this mechanism for incompressible, ideal, irrotational (potential) flow is [Brown, 1993]

$$E_R = \frac{2\Psi(r, \theta)}{U_0 D_f} \quad (2-43)$$

(The stream function, ψ , has a value of $\psi = 0$ at the centerline and surface of the fiber).

The value of the limiting stream function $\Psi(r,\theta)$ is evaluated at $r = R_f + D_p/2$ and $\theta = \pi/2$.

In calculating E_R , different models may have different values of $\Psi(r,\theta)$. For the Kuwabara model, the single fiber efficiency due to interception [Brown, 1993] is

$$E_R = \frac{1}{2Ku} \left\{ 2(1 + N_R) \ln(1 + N_R) - (1 + N_R)(1 - \alpha) + (1 + N_R)^{-1}(1 - \alpha/2) - \frac{\alpha}{2}(1 + N_R)^3 \right\} \quad (2-44a)$$

$$Ku = -\frac{1}{2}\alpha \ln(\alpha) - 0.75 + \alpha + \frac{\alpha^2}{4} \quad (2-44b)$$

where Ku is the Kuwabara hydrodynamic constant. When the value of N_R is small, the above equation can be reduced to [refer to Appendix M on the steps followed to prove it],

$$E_R = \frac{N_R^2(1 - \alpha)}{Ku} \quad (2-45)$$

In general, utilizing the Kuwabara flow field and applying it to other models gives the general equation as follows [Brown, 1993]:

$$E_R = \frac{N_R^2(1 - \alpha)}{Ku[1 + N_R]^{2/3(1 - \alpha)}} \quad (2-46)$$

2.4.3 Inertial Impaction

As the streamlines of air undergo convergence, divergence or curvature due to an obstacle, the air experiences acceleration. The trajectories of the aerosol particles may not coincide with the streamlines, and the particles can move relative to the fluid depending upon the inertia of the individual particles and then get deposited on the obstacle (i.e., the fiber). The single fiber efficiency due to inertia, E_I , is defined as the ratio of the number of particles collected by the fiber to the number of particles that would be captured if the particles moved in a straight line. The single fiber efficiency

can be expressed using Eq. (2-25) as $E_I = y/R_f$. Figure 2.11 shows the single fiber collection by inertial impaction.

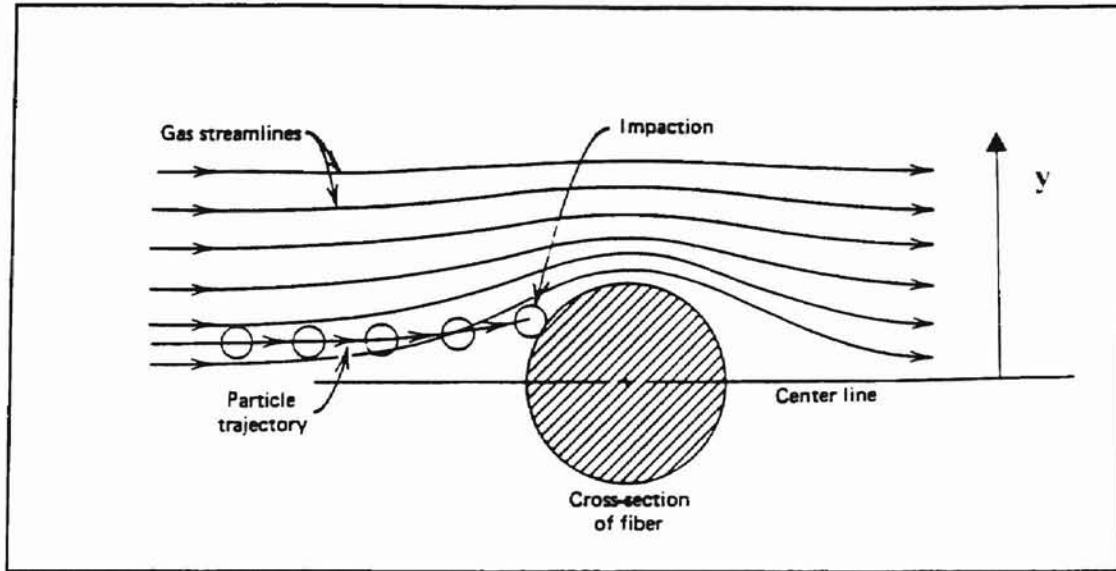


Figure 2.11 Single-Fiber Collection Efficiency by Inertial Impaction [Hinds, 1982].

The dimensionless parameter that characterizes the inertial deposition of particles is the Stokes number, St , that appears in the basic equation of motion (dimensionless) of the particle in the fluid. The basic motion is given by Eq. (2-32) as:

$$m \frac{dV}{dt} = F_e - F_M \quad (2-32)$$

For a spherical particle projected at a velocity V into a stationary fluid medium without the presence of external forces, F_e , the above equation reduces to

$$m \frac{dV}{dt} = -F_M \quad (2-47a)$$

$$m \frac{dV}{dt} = -3\pi \mu D_p V \quad (2-47b)$$

where, $F_M = 3 \pi \mu D_p V$ is the Stokes drag, m is the mass of the particle, D_p is the diameter of particle and V is the velocity of the particle. Stokes' assumption for Eq. (2-47b) is that the fluid velocity at the surface of the sphere is zero. However, this assumption is not met for small particles having diameters on the order of the mean free path of the air. There is some slip at the surface of such spherical particles. Cunningham provided a correction and modified Eq. (2-47b) by introducing a slip correction factor, C_c , the Cunningham correction factor

$$C_c = 1 + 2.52 \frac{\lambda}{D_p} \quad (2-48)$$

where λ is the mean free path of the molecules of the dispersing medium (in this case air). The Cunningham correction factor is always greater than one and reduces the drag force, F_M , by the factor of C_c . Therefore Eq. (2-47b) becomes

$$m \frac{dV}{dt} = \frac{-3 \pi \mu D_p V}{C_c} \quad (2-49)$$

The solution of the above equation yields the stopping time τ_s required for a particle's velocity to drop by a factor of e (2.7182818284...), and the stopping distance, d_s , of the particle is found as follows. Equation (2-49) can be expressed as

$$\left(\frac{4}{3} \pi \frac{D_p^3}{8} \rho_p \right) \frac{dV}{dt} = \frac{-3 \pi \mu D_p V}{C_c} \quad (2-50)$$

After rearranging, $\frac{dV}{V} = \frac{-18 \mu}{D_p^2 C_c \rho_p} dt$ and then the integral of $\int_V^{V/e} \frac{dV'}{V'} = \frac{-18 \mu}{D_p^2 C_c \rho_p} \int_0^{\tau_s} dt$

between V and V/e with respect V' (left hand side) and between 0 (zero) and τ_s (for right hand side) with respect to t yields

$$\tau_s = \frac{D_p^2 \rho_p C_c}{18\mu} \quad (2-51)$$

Multiplying Eq. (2-51) by the velocity, V , gives the distance d_s traveled by the particle as

$$d_s = \frac{VD_p^2 \rho_p C_c}{18\mu} \quad (2-52)$$

where ρ_p is the density of the particle and μ is the dynamic viscosity of air. The parameter describing the behavior of a particle suspended in an air stream that moves at a velocity U_0 (upstream of the fiber far removed from the effect of the fiber) will be given by substituting U_0 for V in Eq. (2-52). Then the dimensionless parameter, St , is obtained by dividing d_s by the diameter of the fiber to get

$$St = \frac{d_s}{D_f} = \frac{\rho_p D_p^2 U_0 C_c}{18 D_f \mu} \quad (2-53)$$

In the early theories of filtration, Albrecht [Davies, 1973] introduced and defined the Stokes number, St , simply as the dimensionless ratio of the kinetic energy, K.E., of a particle travelling with a velocity U_0 to the work done against viscous drag, F_M , over a distance R_f (equal to the radius of the filter fiber) by moving relative to the air. Thus the Stokes number,

$$St = \frac{K.E.}{(F_M R_f)} = \frac{\frac{1}{2} m U_0^2}{[(3\pi\mu D_p U_0) R_f]} = \frac{D_p^2 \rho_p U_0}{9\mu D_f} \quad (2-54)$$

Anand [1997] reports seeing the same equation as Eq. (2-54), which is based on early theories and differs from Eq. (2-53) where the factor 18 is replaced by 9. This could have been due to an error that arose to write out Eq. (2-53) in terms of the radii of the fiber and particle. However, Eq. (2-53), derived based on Brown's [1993] modern

definition of the Stokes number is widely used for calculating the Stokes number in studying filtration efficiency due to inertial effects as flow rate increases.

The single fiber efficiency for the inertial deposition as a function of the Stokes number as obtained from theoretical and experimental work by Landahl and Hermann [Pich, 1987] for $Re = 10$ is given by

$$E_i = \frac{St^3}{St^3 + 0.77St^2 + 0.22} \quad (2-55)$$

Critical Values of Stokes Number: For particle deposition to take place at an obstacle, a particle must have the minimum inertia given by the St_{cr} .

$$\text{for } St < St_{cr}, \quad \text{then } E_i = 0 \quad (2-56a)$$

According to Langmuir and Blodgett [Davies, 1966] the critical Stokes number, St_{cr} , for a potential flow is given by

$$St_{cr} = \frac{1}{16} \quad (2-56b)$$

2.4.4 Gravitational Deposition

Suspended aerosol particles in air tend to settle as the suspending medium flows through the porous medium. During this process, particles can be deposited under the influence of gravitational force on the fibers. The intensity of deposition of particles by gravity is considered to increase for large sized particles and small velocities. The intensity of deposition of the mechanism is described by a dimensionless parameter, N_G ,

$$N_G = \frac{V_s}{U_0} \quad (2-58)$$

where V_s is the settling velocity and U_0 is the velocity of the fluid on the upstream side far from the fiber. The settling velocity V_s is obtained from the equilibrium of the gravity force $F_G = (m - m_{da})g$, (where m_{da} is the displaced mass of air creating buoyancy) and the drag force F_M (equal and opposite to F_G) acting on the particle as follows [Hinds, 1982]:

$$(m - m_{da})g = \frac{\pi D_p^3 (\rho_p - \rho_a)g}{6} = \frac{3\pi\mu D_p V_s}{C_c} \quad (2-59)$$

neglecting the density of air (i.e. $\rho_a \ll \rho_p$) and solving Eq. (2-59) for V_s , yields

$$V_s = \frac{D_p^2 \rho_p g C_c}{18\mu} \quad (2-60)$$

Substituting into Eq. (2-58) results in:

$$N_G = \frac{D_p^2 \rho_p g C_c}{18\mu U_0} \quad (2-61)$$

The single fiber efficiency, E_G , due to gravity is [Brown, 1993; Pich, 1987]

$$E_G = N_G = \frac{D_p^2 \rho_p g C_c}{18\mu U_0} \quad (2-62)$$

However, Stechkina [Pich, 1987] states that the deposition due to gravity for upward flow and downward flow take the following forms:

$$E_G = (1 + N_R)N_G = (1 + N_R) \frac{D_p^2 \rho_p g}{18\mu U_0} \quad (\text{for downward flow}) \quad (2-63)$$

$$E_G = -(1 + N_R)N_G = -(1 + N_R) \frac{D_p^2 \rho_p g}{18\mu U_0} \quad (\text{for upward flow}) \quad (2-64)$$

where $N_R = D_p/D_f$, and other terms are as defined earlier. Equations (2-63) and (2-64) can yield the same result as Eq. (2-62) when N_R tends to zero, except for the sign and the Cunningham slip correction factor.

2.5 Combined Effects of Mechanical Filtration Mechanisms

Theoretically it is incorrect to add the single-fiber efficiencies due to individual mechanisms to obtain the total (overall) single-fiber efficiency, E_s , due to the fact that different mechanisms compete for the same particle and its capture could be counted twice or more. However, it is possible that one mechanism may predominate over the others depending upon the different conditions of particle size and face velocity. Under these circumstances, the overall single-fiber efficiency may be assumed to depend wholly upon that particular mechanism. Hence it is a common and widespread approach to assume that individual single fiber efficiencies E_i ($i = 1, 2, 3, \dots, m$) can be arithmetically added provided they are considered to be mutually exclusive [Pich, 1987; Hinds, 1982].

$$E_s = E_1 + E_2 + \dots + E_m \quad (2-65)$$

On the other hand, Brown [1993] argues that when the dispersing fluid flows past the cylindrical fiber, several mechanisms may act simultaneously. Thus his approach is to assume that the filtration mechanisms act independently and evaluate the single fiber efficiencies E_i ($i = 1, 2, 3, \dots, m$). For example, for two mechanisms with single fiber efficiencies E_1 and E_2 , a fraction $(1-E_1)$ particles would escape capture by mechanism 1, while a fraction of $(1-E_2)$ of $(1-E_1)$ [i.e. $(1-E_1)(1-E_2)$] escape mechanism 2. Thus by defining the total penetration P_s of all by $P_s = 1 - E_s$, one can formulate the following:

$$P_s = 1 - E_s = P_1 P_2 P_3 \dots P_m \quad (2-66)$$

where P_i stands for penetration due to the i th filtration mechanism (effect), and is defined by $P_i = 1 - E_i$ ($i = 1, 2, 3, \dots, m$). In a rigorous form, Eq. (2-66) becomes

$$E_s = E_{1, \dots, j} = 1 - \prod_i^j (1 - E_i) \quad (2-67)$$

where $E_{i...j}$ is the combined single fiber efficiencies due to the i th through j filtration mechanisms (effects). For example, for three mechanisms (inertia, diffusion and interception), the overall single fiber efficiency using Eq. (2-67) becomes

$$E_s = 1 - (1 - E_I)(1 - E_D)(1 - E_R) \quad (2-68)$$

Expanding Eq. (2-68) yields the following equation:

$$E_s = E_I + E_D + E_R - E_I E_D - E_I E_R - E_I E_D E_R \quad (2-69)$$

For $E_I E_D$, $E_I E_R$, $E_I E_D E_R \ll E_I$, E_D , E_R (the products are negligible), Eq. (2-69) yields

$$E_s = E_I + E_D + E_R \quad (2-70)$$

Thus Eqs. (2-70) and (2-65) have the same form and can lead to the same result.

2.6 Basic Electrostatic Mechanisms of Action

Electrically charged fibers can attract both charged and uncharged particles. When the fiber and particles are oppositely charged, they are attracted to each other by Coulombic forces. The attraction of neutral particles by a charged filter fiber takes place due to polarization forces. Thus when charged particles already deposited at the fiber and the charged fiber itself induce a dipole in a neutral particle as it approaches the filter, the particles are said to be attracted by a polarization force. The same also holds true, if the particles are charged and the filter is neutral. The strength of the induced dipole depends upon the volume of the particle and the dielectric constant of its constituent material. The efficiency of this mechanism and that of the Coulombic interaction depends upon the quotient of the drift velocity of the particles under the influence of an attractive electric force and the convective velocity of the flow field tending to take it past the fiber. This implies that all electrostatically charged filters operate well at low

filtration velocities over a limited particle size range [Brown, 1993]. As shown in Fig. 2.12, the capture efficiency for 5 μm diameter particles is higher than that of 1 μm particles.

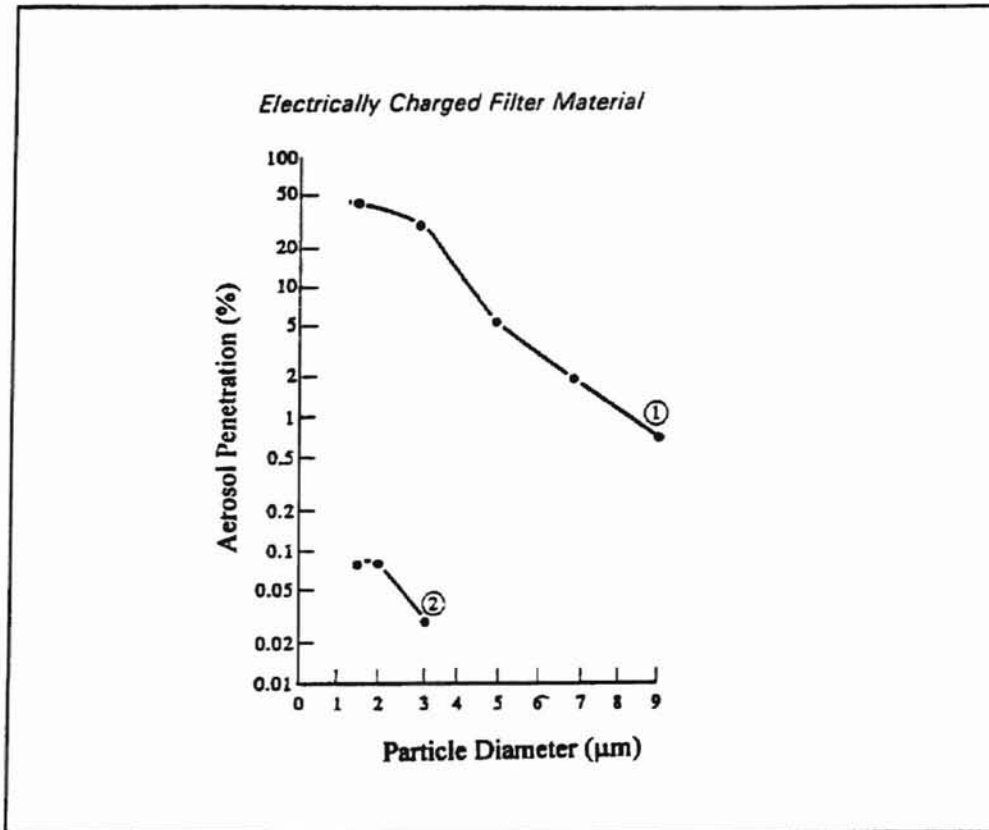


Figure 2.12 Performance of Electrostatically Charged and Neutral Filters of Identical Geometry: (1) Neutral Filter Material; (2) Charged Filter Material [Brown, 1993].

In the filtration of aerosol particles, it is customary to charge the filter fibers and/or the aerosol particles in order to enhance filtration efficiency. Aerosol particles can acquire charge by the following mechanisms: (1) static electrification, (2) diffusion charging, (3) field charging, and (4) charging using radioactive sources. Mechanisms (2) and (3) require the generation of unipolar ions (atoms with excess or a deficiency of electrons) by corona discharge. Charge carried by aerosol particles is estimated on the

basis of the charging mechanism. Filter materials can also be charged by different methods: triboelectric charging, corona charging, and charging by induction.

CHAPTER III

LITERATURE REVIEW

3.1 Introduction

The high mobility of corona charged aerosol particles in an electric field has been used in electrostatic precipitators in industrial air or gas cleaning since about 1900. Two decades later, the application of electrostatic charge in the development of conventional two stage electrostatic precipitators for commercial and residential applications was evident. Electrostatic precipitation has also been used in aerosol sciences in a variety of aerosol sampling devices and in the measurement and classification of aerosol size distribution [Whitby and Liu, 1966]. However the most important discovery in the application of electrostatic charge, pertinent to the study of fibrous air filtration, was the discovery of the first electrostatically augmented air filter, the Hanson filter, in 1930 [Davies, 1973].

Aerosol particles and filter fibers often carry electrostatic charge that may considerably influence the deposition of particles during the filtration process. The electrostatic charge on the fibers of a filter is, in the majority of cases, unstable and decreases with time mainly due to the conductivity of the fibers, passage of ionized gases or radioactive radiation, deposition of charged particles, and humidity [Pich, 1977].

Electrostatic charge may affect particle separation performance of a filter in two ways: (1) particles may be attracted to the fibers from a distance in the air stream, (2) and the electrostatic forces may increase the ability of a fiber to retain a particle once it is attracted (adhesion).

In the following sections and subsections, some of the theories in electrostatic charge generation, particle capture mechanisms, and the mathematical theory of capture will be reviewed. Experimental studies on the effects of electrostatic mechanisms of filtration will also be presented, and comparisons will be also made between charged and uncharged fibrous filters in air filtration in Section 3.8.

3.2 Electrostatic Charge Generation and Neutralization

In the next sections and the subsections to follow, this author will review those mechanisms of action related to the generation of electrostatic charge on aerosols and filter materials and the methods employed to neutralize them. However, the author's emphasis will be on the generation of electrostatic charge by the atomization of solutions of suspensions of spherical polystyrene latex particles and electrostatic charge due to high velocity flow of other contaminant loaded gases through ducts which are related to this research.

3.2.1 Charging Aerosol Particles

There are numerous methods to charge aerosol particles. Mechanical atomization of liquids in atomizers, nozzles, etc, is one of the common sources of electrostatically low to moderately charged aerosols. On the other hand, aerosols can be highly charged by the

application of corona charge and radioactive radiation. There are four mechanisms by which aerosol particles can acquire charges: static electrification, diffusion, field charging (the latter two depend on corona charge), and charging by radioactive radiation.

3.2.1.1 Static Electrification

This is one of the mechanisms by which electrostatic charge can be generated. Static electrification causes particles to be charged as they are separated from bulk material or other surfaces. It can give rise to highly charged particles under the right circumstances. Particles are usually charged by this mechanism during formation, resuspension, or high-velocity transport (as in duct and channel flows). The mechanism of static electrification consists of three mechanisms that can charge aerosol particles during generation, namely, electrolytic charging, spray electrification, and contact charging [Hinds, 1982].

Electrolytic Charging: Electrolytic charging results when highly dielectric liquids are separated from solid surfaces. One good example is the atomization of a suspension of aerosols. Pure water as a highly dielectric fluid can be electrostatically charged easily during atomization. During atomization, these liquids strip off charge from the surface of the atomizer and produce slightly to moderately charged droplets as they are separated from these surfaces.

Spray Electrification: This results from the disruption of charged liquid surfaces. Some liquids, due to surface effects, have a charged surface layer; and when this surface is disrupted during the formation of droplets by atomization or bubbling, charged droplets are produced.

Contact Charging: This charging mechanism occurs during the separation of dry nonmetallic particles from solid surfaces. This is sometimes referred to as triboelectric charging - charging due to contact followed by separation and friction. When the particles are separated from surfaces, they have an excess or deficiency of electrons. Polarity and amount of charge depend on the kind of materials involved and their relative position in the triboelectric series of materials. The triboelectric series is the classification of materials according to the ease of a material to become positively charged when it comes in contact with another material. The triboelectric series for some materials is given in Table 3.1. Rubbing and sliding against surfaces that involve friction

Table 3.1 Triboelectric Series of Materials [McAteer, 1989].

Positive	Acetate
+	Glass
	Nylon
	Wool
	Silk
	Aluminum
	Polyester
	Paper
	Cotton
	Steel
	Nickel, Copper, Silver
	Zinc
	Rubber
	Acrylic
	Polyurethane Foam
	PVC (Vinyl)
-	Teflon
Negative	

are some of the common examples of this mechanism. This mechanism requires dry surfaces; otherwise relative humidity values above 60% can inhibit the development of charges. Resuspending dry powders involves some friction between the powder and the apparatus and consequently produces charged aerosols.

3.2.1.2 Diffusion Charging

Charging of aerosol particles due to the random collision of unipolar gaseous ions and the neutral particles is called diffusion charging. As the unipolar ions diffuse toward the surfaces of neutral particles, they impart their electric charges to the neutral particles. This diffusion charging is as a result of the Brownian motion of the ions and particles. According to White, as reported by Whitby et al. [Davies, 1966] and Hinds [1982], the amount of charge, n , on a particle that has been exposed to unipolar ions with an average concentration of N_{ic} ions/cm³ charged by diffusion charging for a specified time, t , is estimated by the following equation:

$$n = \frac{D_p k T}{2e_c^2} \ln \left(1 + \frac{D_p V_{ic} \pi e_c^2 N_{ic} t}{2kT} \right) \quad (3-1)$$

where N_{ic} is ion density, t is the charging time, D_p is the diameter of the particle, V_{ic} is the average speed of the charging ions ($V_{ic} = 2.4 \times 10^4$ cm/s), k is the Boltzmann constant, e_c is the elementary unit charge ($e_c = 1.6 \times 10^{-19}$ Coulomb), and T is the absolute temperature in °K. The discussion of the charging of aerosol particles by field charging (due to corona discharge) is next.

3.2.1.3 Field Charging

The process of charging neutral particles due to wandering unipolar ions in the presence of a strong electric field is called field charging. The rapid motion of ions in an electric field causes an increase in the number of collisions between the ions and the neutral particles. According to Hinds [1982], the uniform electric field lines experience distortion when a spherical particle is placed between the negative and positive plates. Figure 3.1 shows a combination of field and diffusion charging. As shown in Fig. 3.1(a), at constant $N_{ic}t$, as the diameter of particles increases the amount of charge acquired also increases proportionally. On the other hand in Fig 3.1(b), for a constant particle diameter, the amount of elementary charge increases as the charging field strength increases.

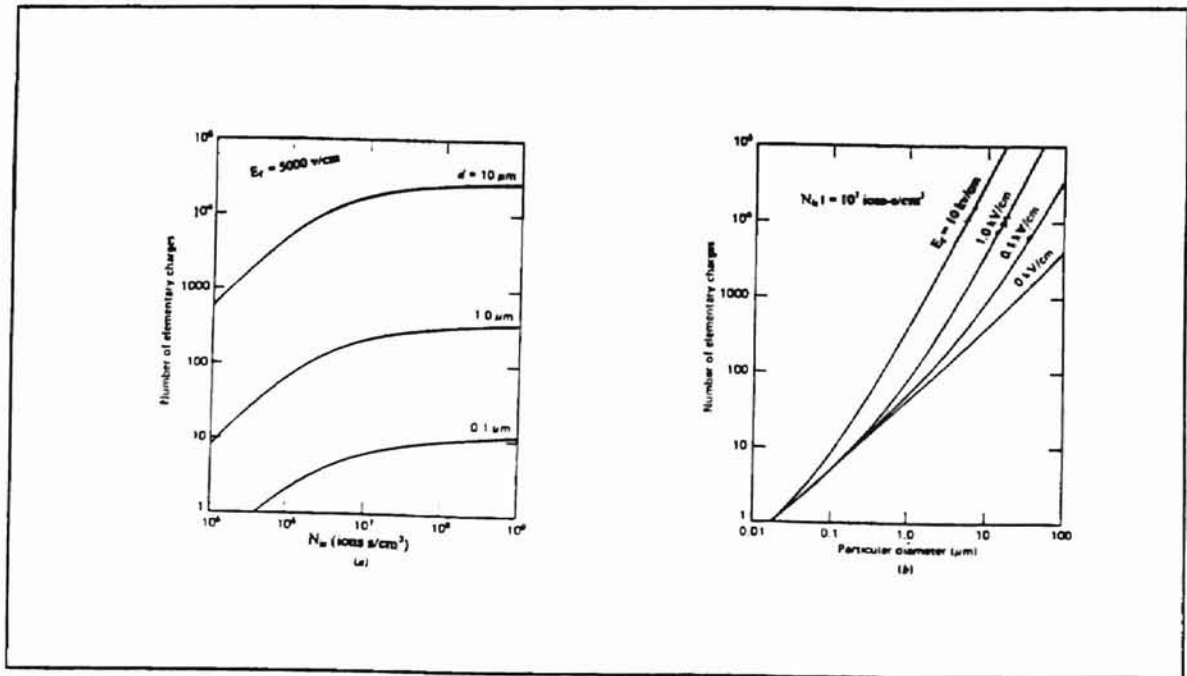


Figure 3.1 Field and Diffusion Charging: (a) Number of Charges Acquired Versus $N_{ic}t$ for Various Particle Diameters at a Field Strength of 5000 V/cm, (b) Number of Charges Acquired Versus Particle Size for Various Field Strengths at $N_{ic}t = 10^7$ ion-s/cm³ and $\epsilon_1 = 5.1$ [Hinds, 1982].

The field lines as shown in Fig. 3.2 depict the trajectories of the ions. The extent of distortion depends on the dielectric constant, ϵ_1 , of the particle material and the charge of the particle. Ions in this field travel along the field lines and collide with the particle where the field lines intersect the particle. As the particle charge builds up, the field lines

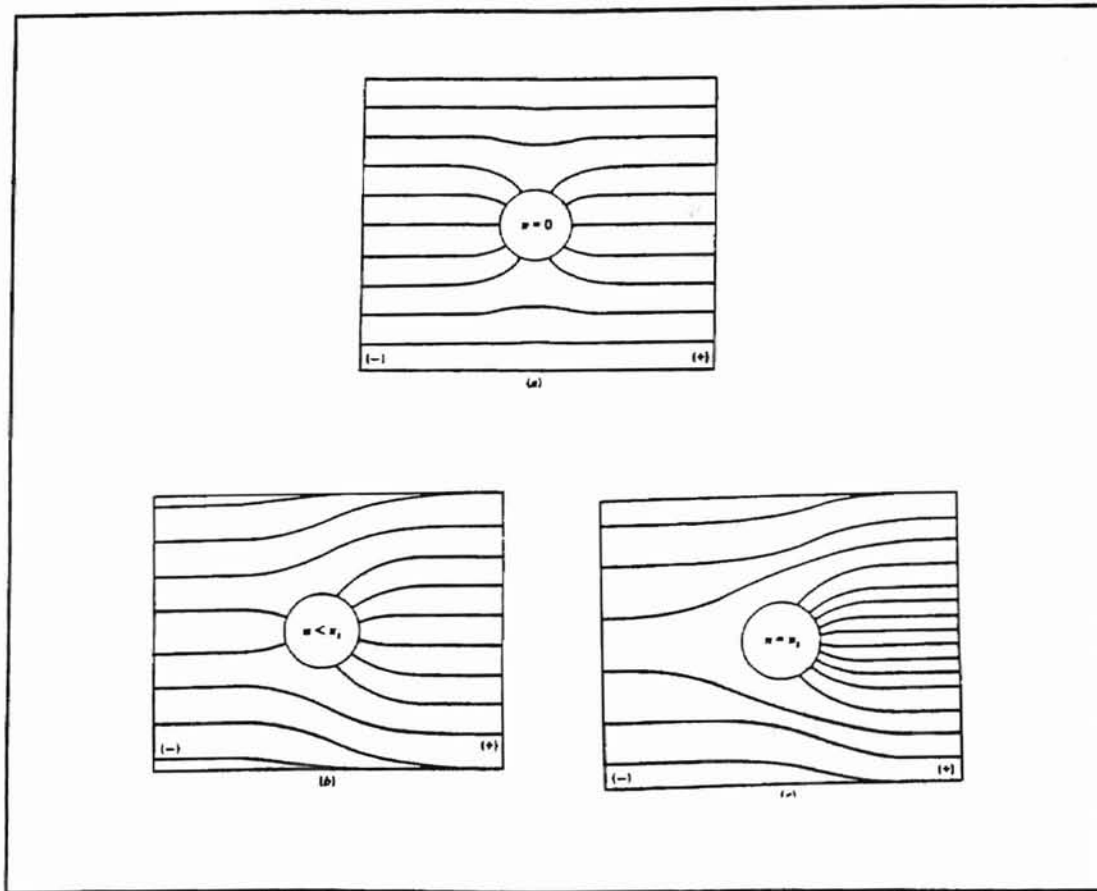


Figure 3.2 Electric Field Lines for a Conducting Particle in a Uniform Field (Negative Ions and Negative Plate at Left). (a) An Uncharged Particle; (b) A Partially Charged Particle; and (c) A Particle at Saturation [Hinds, 1982].

change, and the rate of ion flow rate decreases until the particle is ultimately charged to its limiting value. When the particle reaches its limiting value, there is no flow of ions and convergence of field lines at the particle. The amount of charge, n , acquired by the particle is estimated by the following equation [Hinds, 1982]:

$$n = \left(\frac{3\varepsilon_1}{\varepsilon_1 + 2} \right) \left(\frac{E_f D_p^2}{4e_c} \right) \left(\frac{\pi e_c z_i N_{ic} t}{1 + \pi e_c z_i N_{ic} t} \right) \quad (3-2)$$

where ε_1 is the dielectric constant of the particle, z_i is the mobility of the ions ($z_i = 1.50 \text{ cm}^2/\text{v-s} = 450 \text{ cm}^2/\text{stv-s}$), and E_f stands for electric field.

A charged particle experiences an electrical force when it is placed in an electrical field, E_f . Due to this force, the charged particle experiences motion at a velocity, V_e . Therefore the mobility of a particle (ability to move in an electric field), z_i is defined as:

$$z_i = \frac{V_e}{E_f} \quad (3-3)$$

The limiting value of the electrostatic charge, n_s , that can be acquired by a particle is given by:

$$n_s = \left(\frac{3\varepsilon_1}{\varepsilon_1 + 2} \right) \left(\frac{E_f D_p^2}{4e_c} \right) \quad (3-4)$$

where n_s is the limiting or the saturation charge after a certain charging time, t , D_p is the particle diameter, E_f is the electric field, and e_c is the elementary unit charge.

3.2.1.4 Charging by Radioactive Sources

A high efficiency unipolar charger using an alpha-ray source has been developed by Adachi et al. [1990a] for charging very small aerosol particles. The new charger has low particle losses and works well for ultrafine aerosol particle charging better than a corona charger. In the charger, the ions are generated by the irradiation of alpha-rays from the radioactive source Am^{241} , and the direction of the ion flow attracted by a d.c. electric field and the aerosol flow direction are the same. This design feature helps control the deposition losses of charged particles by electrophoresis. Figure 3.3 shows a

schematic drawing of the charger. The charger has a wire mesh at each end of the cylindrical tube where the alpha-ray radioactive source is placed. The cylindrical tube is made of an insulator. The two wire meshes at both ends serve as electrodes. The entrance mesh is connected to a d.c. power supply to generate an electric field, while the second is connected to an electrometer. (An electrometer is used to measure the amount of charge carried by particles in a fluid flow.) The radioactive source Am^{241} of activity $10 \mu\text{Ci}$ near electrode 1 ionizes the air around it (within a radius of 4 cm) and produces bipolar ions. The d.c voltage pushes the positive ions to be attracted by electrode 2. This

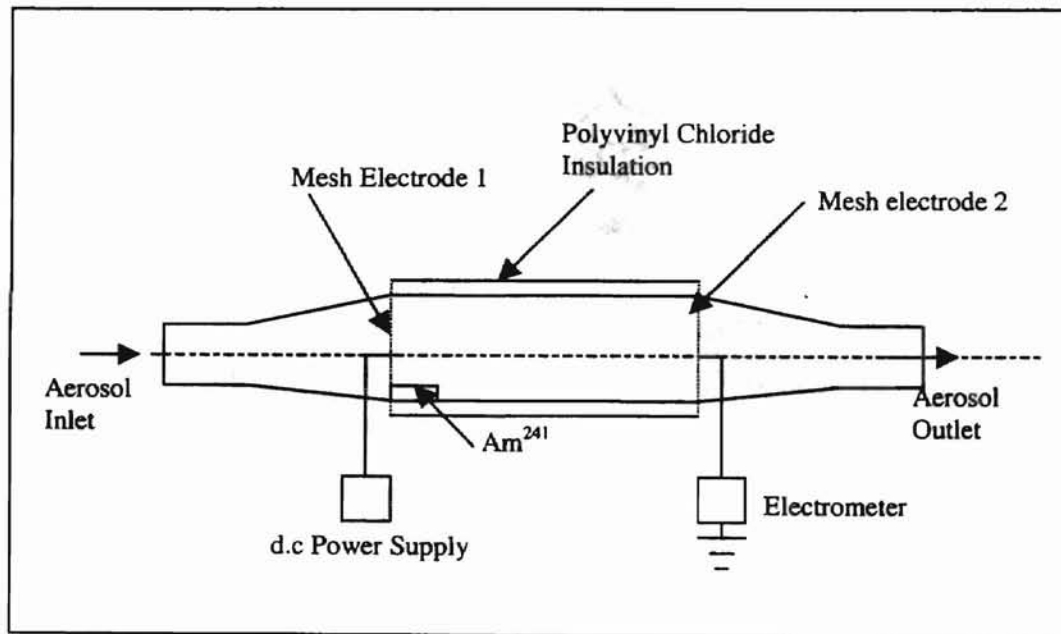


Figure 3.3 Unipolar Charger Using Alpha-ray Radioactive Source [Adachi et al., 1990a].

leaves the entering aerosol particles to be exposed only to unipolar ions. Changing the intensity of the electric field or the flow rate can change the particle charge.

3.2.2 Charging Mechanisms of Filter Fiber Materials

Filter materials can be charged through three main charging processes: triboelectric charging, corona charging, and charging by induction [Brown, 1993]. In the next three subsections, the charging mechanisms of filter fibers will be reviewed. Figure 3.4 shows generation of charge by triboelectric processes.

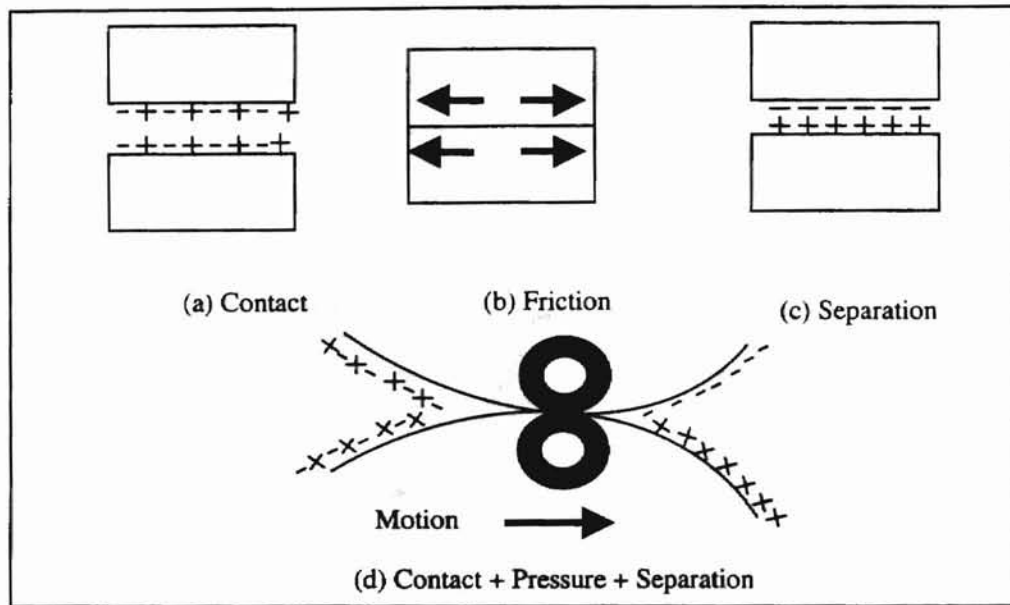


Figure 3.4 General Triboelectrification of Materials [Chapman Catalog, 1997].

3.2.2.1 Triboelectric Charging of Filter Materials

The transfer of electrostatic charge between two materials due to contact followed by separation and rubbing action has been known for a long time. Some common examples of electrification by triboelectric charging include rubbing an amber rod on wool and the combing of hair by a plastic comb, which we are aware of daily.

The first electrostatic filter, the resin-wool or Hansen filter is based on the triboelectrification phenomena of rubbing for its charging process. Figure 3.5 depicts the configuration of charge in a resin wool filter material. Amber is fossilized resin; and

particles of the resin in its native form, when carded with fibers of wool in a filter, exchange charge in such a way that the resin obtains an excess of electrons while the wool encounters deficiency of electrons to become positively charged. Since resin is a good insulator, its low conductivity helps in the stability of the charges. It was this phenomenon that brought about the discovery of electrostatic fibrous filtration in 1930 by

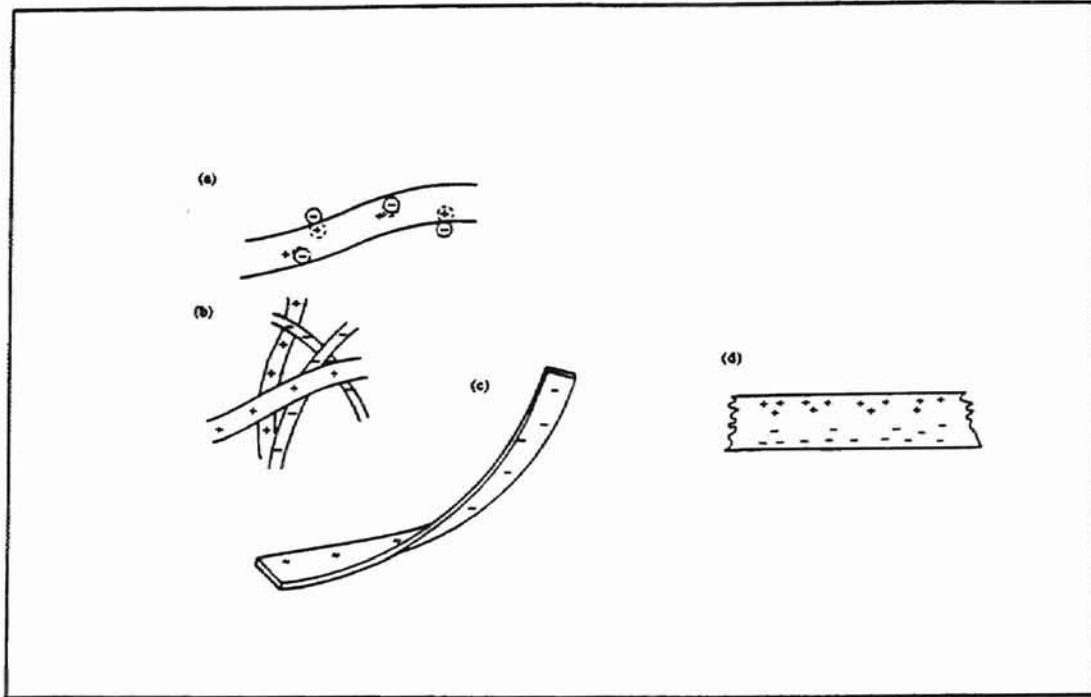


Figure 3.5 Illustration of Charge Configuration on Electrically Charged Filter Material: (a) Resin Wool Material (Single-fiber); (b) Mixed Fiber Material; (c) Split Fiber Electret Material; (d) Electret Material Charged in Felt Form [Brown, 1993].

Hansen. The contribution of triboelectric charging to the enhancement of the efficiency of fibrous filters, though a measurable quantity, is rather small [Brown, 1993].

3.2.2.2 Corona Charging of Filter Materials

Corona discharge refers to the emission of ions by a point electrode at high electric potential. The ions which have the same sign as the electrode drift under the

influence of the electric field caused by the electrode to a collecting surface of a lower potential as in electrostatic precipitation. If the surface is an insulator or a thin sheet of polymer placed on a conductor, this leads to the agglomeration of abundant electrostatic charge on one side and a compensating charge of the opposite sign on the other side, creating a dipolar configuration. Corona discharge can impart electric charge to filter fibers made of polymers. The dipolar charge can be imparted by freezing in a polarization charge after the material has been felted to produce what is called the real electret filter. An electret filter is a filter with permanent dipolar charge [Brown, 1993].

3.2.2.3 Induction Charging

Another charging mechanism for filter materials is called induction charging. It is similar to the mechanism of producing electrically charged sprays. Electrostatic spraying involves the production of charged liquid particles, where the processes of detachment and charging occur simultaneously. In a similar way, if we have melts or solution of polymers, due to the high viscosity, the fragmentation of the spray is delayed and the solidification of the polymer into a fiber may take place, yielding a charged fiber. The fibers produced by electrostatic extrusion may have diameters of 2 or 3 μm or even less. This mechanism is believed to yield fibers with unipolar charge, but they may have bipolar charge.

3.2.3 Charge Neutralization

In aerosol science and filtration, aerosol neutralization is routine; but it is an important task that a researcher may need to perform in order to avoid unwanted

electrostatic effects in laboratory tests. A researcher in fluid filtration is undoubtedly required to monitor electrostatic charge quantities on the aerosols and the filter itself at various fluid flow rates and its effects on the performance of filters (e.g., the use of atomized dry particles). According to Whitby's [Davies, 1966] technique, the establishment of charge equilibrium of an aerosol with bipolar ions is the basis for neutralization of highly charged aerosols. Generating dry aerosols by the evaporation of atomized liquid suspensions of particles or a solution of solids has been found to carry a high residual electrical charge. Such high electrical charge is not desirable in experimental filtration. So far there are two commonly used methods in the neutralization of electrostatically charged aerosols. They are radioactive radiation and the use of unipolar ions from corona charging of gases.

The technique of neutralizing charged aerosols by Whitby and Liu [Davies, 1966] emphasizes mixing of the highly charged aerosols with a stream of high concentration bipolar ions produced by a sonic generator and allowing sufficient time until Boltzmann equilibrium is established. The use of a radioactive source extensively in experimental aerosols and filtration in some research institutes and universities is facing strict controls from safety enforcement bodies and the regulations on the use of such items is very strict. The search for reliable alternative solutions is continuing.

Recently, a corona-neutralizing unit has been developed by Adachi et al. [1990b] as shown in Fig. 3.6. The corona neutralizer consists of three parts: one is for generating bipolar ions; the other part, the mixing chamber, is for mixing the unipolar ions and the aerosol particles to be neutralized. The third part is the charging chamber where the collision of the particles and ions takes place until the particles are neutralized and leave

the chamber. In the ionization chamber, the two unipolar ionizers produce negative and positive ions respectively. The ionizers are in the form of needles facing an orifice. High voltage application on the needles produces a corona discharge. The passage of compressed air forces the ions to enter into the mixing chamber through an orifice, where

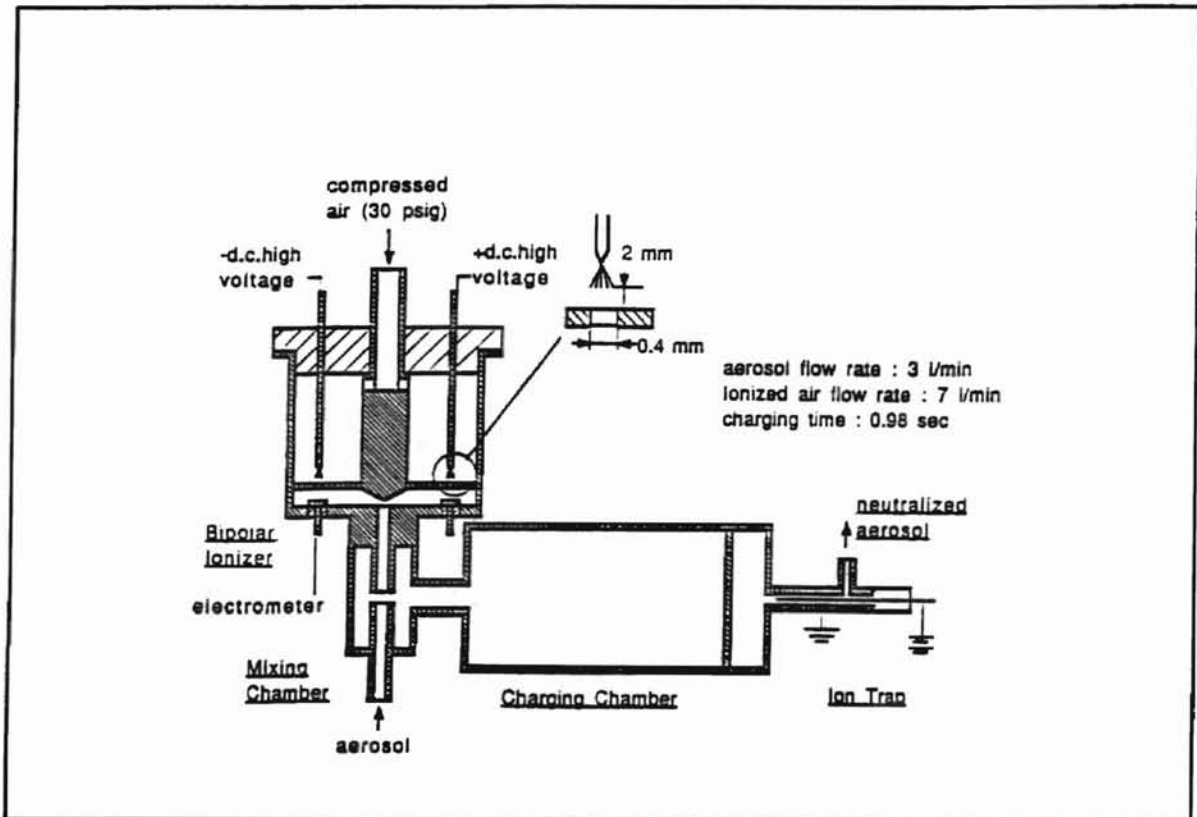


Figure 3.6 Corona Neutralizer [Adachi et al., 1990b].

bipolar ions are mixed with the aerosol particles. The neutralization of the aerosol particles takes place at the charging chamber by diffusion or collision between the ions and aerosols [Adachi et al., 1990b].

Liu and Pui [1974] also emphasized the necessity of neutralizing highly charged aerosols that are produced by laboratory aerosol generators. To reduce the level of charge on aerosol particles, bipolar ions can be employed to avoid any unwanted

electrostatic effects. By the exposure of an aerosol to a source of ionizing radiation, small ions can be created; and the gaseous medium around the particles can be made electrically conductive. The particles can then discharge themselves by capturing ions of opposite polarity. Small bipolar ions can also be produced using an a.c. corona discharge and then be mixed with the charged aerosol to be neutralized.

In the design or application of aerosol neutralizers, the time, t , necessary to neutralize a particle is estimated using Gunn's equation [Liu and Pui, 1974] as follows:

$$t = \frac{1}{4\pi N_{ic} e_c z_i} \quad (3-5)$$

However, Liu and Pui [1974] argue that Eq. (3-5) provides only a rough estimate of the required neutralization time. They point out that neutralization time is dependent upon both the initial particle charge and the kinetics of the charge neutralization process. In their study, they present some considerations on their choice of Kr^{85} (Krypton-85) as the radioactive source in the charge neutralizing unit. The Kr^{85} radioactive neutralizer consists of a radioactive source (Kr^{85}) placed along the center of a cylindrical metal container. The radioactive source, Kr^{85} gas, is inserted and sealed in a stainless cylindrical tube of 3 mm diameter and 0.076 mm thickness. The β -radiation from the Kr^{85} penetrates through the stainless cylindrical wall to ionize the gas molecules surrounding the tube. The functions of the outer metal cylinder are (1) to confine the β -radiation from the inner cylinder and (2) to provide the necessary volume for the neutralization of the incoming charged aerosols. They also emphasized the safety and long life of this radioactive source. Kr^{85} has a maximum energy of only 0.695 MeV, which can be easily contained by the 1.6 mm thick outer cylinder that can shield the lab personnel from any health hazard.

The charge neutralization of aerosols of DOP (di-octyl phtalate) in isopropyl alcohol using a vibrating orifice droplet generator was tested on this neutralizer [Liu and Pui, 1974]. The solution droplets were first allowed to evaporate. Results at various aerosol flow rates by varying the activity of the neutralizer showed that, at a given constant value of the product, $N_{ic} t = 6 \times 10^6$ ion s/cm³, the higher the aerosol flow rate, the higher the activity of the neutralizer should be in order to effectively neutralize the particles. When the DOP aerosols (2.53 μ m diameter) were passed through the Kr⁸⁵ neutralizer (with an activity of 2 mCi) at various flow rates ranging from 23.6 to 94.41 liters/min, the corresponding residence time of the aerosol in the neutralizer was found to be between 3.83 and 0.95 seconds.

The charge of the incoming aerosols was measured by spraying the solution droplets directly into a Faraday cup and measuring the current with an electrometer. The number of droplet charge, n , was calculated from the equation [Liu and Pui, 1974],

$$n = I / f e_c \quad (3-6)$$

where I is the current, f is the operating frequency of the generator, and $e_c = 1.6 \times 10^{-19}$ Coulomb.

3.3 Electrostatic Filtration Mechanisms

This section deals with the electrostatic mechanisms of filtration and the corresponding single fiber efficiency equations. Figure 3.7 shows both the mechanical and electrostatic mechanisms of filtration.

Recall from the preceding subsections of this chapter the discussion on the different charging mechanisms of aerosol particles and filter materials, and the neutralizing procedures and methods. The methodologies employed to solve the equations of motion for trajectories of the electrostatically charged particles and the single fiber efficiencies therein are more or less similar to that of the mechanical mechanisms. To understand the mechanical mechanisms of deposition of aerosol particles on the fibers of a filter and the single fiber efficiencies of the individual mechanisms based on the single fiber theory, the reader is advised to read Section 2.4 of Chapter II.

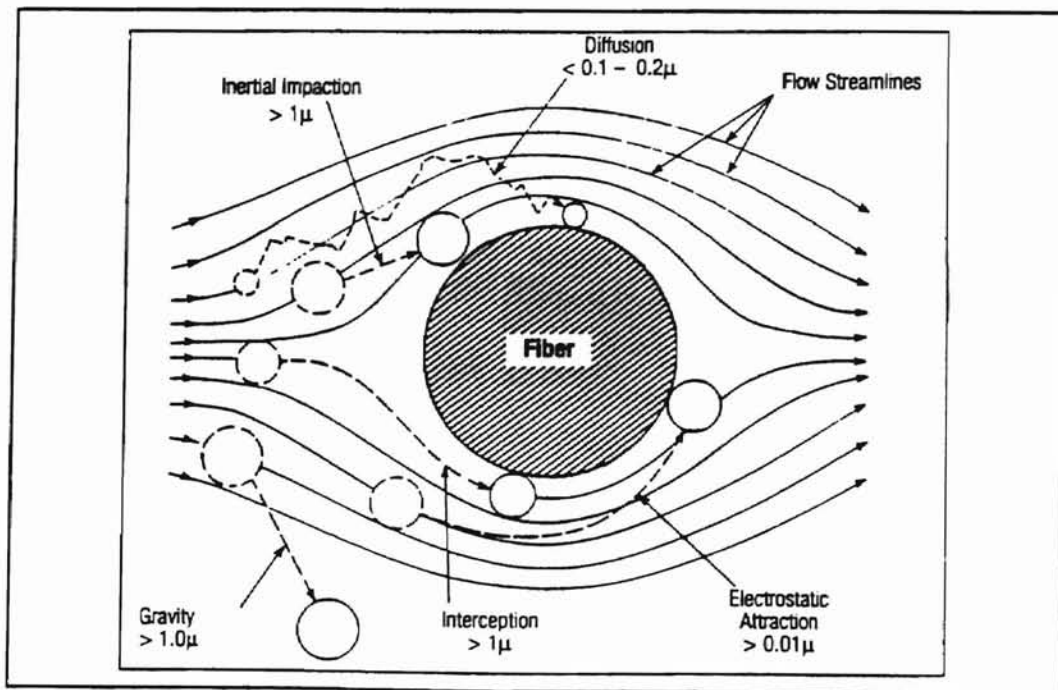


Figure 3.7 Mechanisms of Particle Capture by a Fiber [Frederick, 1996].

All single fiber efficiencies are derived from the same fundamental equation, Newton's second law of motion. As in the mechanical deposition mechanisms, the procedures for calculating the single fiber efficiencies are based on dimensionless

parameters. To describe the process of electrostatic deposition, knowledge of the electrical forces between the particle and the fiber is indispensable. The electrostatic interaction between a fiber and a particle have been studied and described by Zebel, Gillespie, Natason, Whitby and Liu [Pich, 1987]. Accordingly there are three cases of electrostatic interaction between a fiber and a particle, depending upon whether the particle, or the fiber or both are electrostatically charged.

3.3.1 Single Fiber Efficiencies

1. Charged Particle - Charged Fiber

Natason and Gillespie [Pich, 1987] described the Coulombic attraction between a charged particle and a charged fiber with opposite charges as:

$$F(\rho) = \frac{2Q'q}{\rho} \quad (3-7)$$

where Q' is the charge per unit length of the fiber, q is the particle charge, and ρ is the distance between the particle and the cylindrical fiber.

2. Neutral Particles - Charged Fiber

The force of interaction between a charged fiber and a neutral particle is called a polarization force and is described according to Natason [Davies, 1966] by

$$F(\rho) = 4Q'^2 \left(\frac{\epsilon_1 - 1}{\epsilon_1 + 2} \right) \frac{R_p^3}{\rho^3} \quad (3-8)$$

where ϵ_1 is the dielectric constant of the particle, and R_p is the radius of the particle. The fiber charge appears in the above equation as a squared term because it first induces the dipole and then it interacts with it.

3. Neutral Fiber - Charged Particle

Natason and Gillespie [Pich, 1987] describe the force of interaction between an electrically charged particle and its image on a cylindrical fiber as:

$$F(\rho) = \frac{q^2}{4(\rho - R_f)^2} \frac{\epsilon_2 - 1}{\epsilon_2 + 1} \quad (3-9)$$

where ϵ_2 is the dielectric constant of the fiber, and R_f is the radius of the fiber. The force of interaction is called an image force.

Now that the forces have been determined, it remains to express the single fiber efficiency of the fiber due to different electrostatic mechanisms in terms of dimensionless numbers that denote the intensity of deposition of particles on the fiber. The dimensionless parameters for Stokes particles are the ratio of electrostatic forces to drag forces of the medium according to Wanz and Wong's [Davies, 1996] approach. The second approach due to Pich, consists of non-dimensionalizing the equation of motion of the particle as a whole [Pich, 1987]. Both approaches lead to the same result. The basic equation of motion for Stokes particles is formulated as:

$$m \frac{dV}{dt} = F_e - F_M \quad (3-10)$$

where m is the mass of the particle, V is the velocity of the particle, F_e is the external force and F_M is the resistance of the medium. The dimensionless parameter describing the intensity of particle deposition due to Coulombic forces, $N_{Q'q}$ is given by

$$N_{Q'q} = \frac{4Q'q}{3\pi \mu D_p D_f U_0} \quad (3-11)$$

where U_0 is the velocity of the flow of the medium (air) far from the fiber.

The dimensionless parameter $N_{Q'o}$ for the electrostatic deposition of particles due to the image forces between neutral particles and charged fibers is

$$N_{Q^o} = \frac{4}{3\pi} \left(\frac{\epsilon_1 - 1}{\epsilon_1 + 2} \right) \frac{D_p^2 Q^2}{D_f^3 U_0 \mu} \quad (3-12)$$

On the other hand, the dimensionless parameter N_{oq} describing deposition due to image forces between the neutral fibers and charged particles is given by

$$N_{oq} = \frac{q^2}{3D_p D_f^2 U_0} \left(\frac{\epsilon_2 - 1}{\epsilon_2 + 1} \right) \quad (3-13)$$

The single fiber efficiencies are calculated in terms of the corresponding dimensionless parameters. E_{Q^o} for the deposition of particles due Coulombic forces as derived by Kraemer, Johnstone, and Natason [Pich, 1987] is

$$E_{Q^o} = \pi N_{Q^o} = \frac{4Q^o q}{3\mu D_p D_f U_0} \quad (3-14)$$

The single fiber efficiency E_{Q^o} due to the polarization (image) forces between the charged fiber and a neutral particle is given as:

$$E_{Q^o} = \left[\left(\frac{\epsilon_1 - 1}{\epsilon_1 + 2} \right) \frac{2D_p^2 Q^2}{D_f^3 U_0 \mu} \right]^{\frac{1}{3}} = \left(\frac{3\pi}{2} \right)^{\frac{1}{3}} N_{Q^o}^{\frac{1}{3}} \quad (3-15)$$

Finally the single fiber efficiency E_{oq} for neutral fiber - charged particle (potential flow) as derived by Natason is

$$E_{oq} = \left[\frac{2q^2}{D_p D_f^2 U_0} \left(\frac{\epsilon_2 - 1}{\epsilon_2 + 1} \right) \right]^{\frac{1}{3}} = (6\pi)^{\frac{1}{3}} N_{oq}^{\frac{1}{3}} \quad (3-16a)$$

For viscous flow, the single fiber efficiency is given as [Pich, 1987]:

$$E_{oq} = \frac{2}{[2 - \ln(\text{Re})]^{\frac{1}{2}}} N_{oq}^{\frac{1}{2}} \quad (3-16b)$$

Figure 3.8 shows the single fiber efficiencies as a function of the relevant dimensionless parameter.

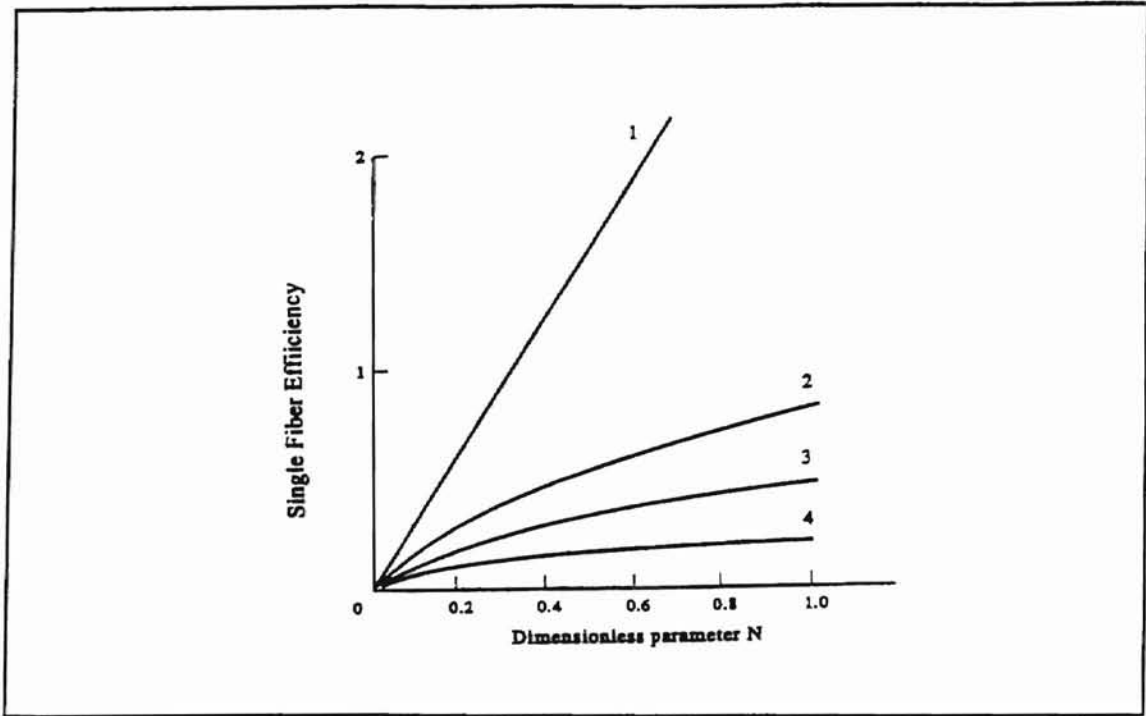


Figure 3.8 Single Fiber Efficiency Versus the Relevant Dimensionless Parameter: (1) Uniformly Charged Fiber, Charged Particle; (2) Uniformly Charged Fiber, Neutral Particle; (3) Line Dipole Charged Fiber, Neutral Particle; (4) Line Quadruple Charged Fiber, Neutral Particle [Brown, 1993].

3.3.2 Combined Effect of Electrostatic and Mechanical Mechanisms

Electrostatic Forces and Interception: For the combined effect of image forces (between a charged particle and a neutral fiber) and interception, the expression for the single fiber efficiency is given by Brown (1993) as:

$$E_{Roq} = \left[\frac{\sin^2(\theta) N_R^4}{\xi^2} + 2 \frac{N_{\infty} (1 + \cos(\theta))}{\xi} \right]^{1/2} \quad (3.17)$$

where $\epsilon_0 = \frac{10^{-9}}{36\pi}$ [Farads/m] is the permittivity of free space, $\xi = \frac{(1-\alpha)}{Ku}$ (in which Ku is

the Kuwabara constant), θ is the polar angle, and $N_{\infty} = \frac{q^2}{12\pi^2 \epsilon_0 D_p D_f^2 U_0} \left(\frac{\epsilon_2 - 1}{\epsilon_2 + 1} \right)$.

3.4 Overall Filter Efficiency

The single fiber efficiencies due to the mechanical and electrostatic mechanisms have been calculated theoretically in the preceding section. By combining the single fiber efficiencies due to all of the mechanisms, the overall single fiber efficiency E_s is obtained using Eqn. (2-65) by adding the single fiber efficiencies as if they act independently (refer to Section 2.5 of Chapter II) as:

$$E_s = E_1 + E_2 + \dots + E_n \quad (3-18)$$

Therefore the overall filter efficiency can be calculated as follows:

$$E = 1 - e^{-\left(\frac{4 \alpha E_s}{\pi(1-\alpha)D_f}\right)L} \quad (3-19)$$

3.5 Pressure Drop

The pressure drop of a new filter can be predicted from several theoretical and empirical formulas. The pressure drop across a filter varies with its thickness, L , the velocity, U , the fiber radius, R_f , the coefficient of viscosity, μ , and the packing density (solidity), α . Using dimensional analysis, the final equation for the pressure drop, Δp is given as [Brown, 1993]:

$$\Delta p = \frac{\mu L U F(\alpha)}{R_f^2} \quad (3-20)$$

The value of the dimensionless function $F(\alpha)$ is a function of α that depends upon the kind of model employed to predict filter performance characteristics. The above equation for pressure drop is in agreement with the first law of filtration theory, Darcy's law. On the other hand, the cell models of Kuwabara and Happel predict pressure drop of a model filter as follows:

$$\Delta p = \frac{4\mu LU\alpha}{R_f^2 \left[\frac{1}{2} \ln(\alpha) - \frac{1}{2} \frac{(1-\alpha^2)}{(1+\alpha^2)} \right]} \quad (\text{Happel}) \quad (3-21)$$

$$\Delta p = \frac{4\mu LU\alpha}{R_f^2 \left[-\frac{1}{2} \ln(\alpha) - 0.75 + \alpha - \frac{\alpha^2}{4} \right]} \quad (\text{Kuwabara}) \quad (3-22)$$

(Note: in all cases the flow is assumed to be normal to the axis of the fiber). For flows parallel to the axis of the fiber, one half of Kuwabara's model above gives the pressure drop [Brown, 1993] as:

$$\Delta p = \frac{2\mu LU\alpha}{R_f^2 \left[-\frac{1}{2} \ln(\alpha) - 0.75 + \alpha - \frac{\alpha^2}{4} \right]} \quad (3-23)$$

Empirical models have also been developed to predict pressure drop across filters. The function $F(\alpha)$ in Eq. (3-20) has been determined for various filter media to be of the following form [Brown, 1993]:

$$F(\alpha) = 16\alpha^{3/2} (1 + 56\alpha^3) \quad (3-24)$$

The pressure drop across the filter can also be represented by the following empirical equation [Society of Automotive Engineers, 1998]:

$$\Delta p = k_1 \mu Q + k_2 \rho_a Q^2 \quad (3-25)$$

In which k_1 and k_2 are empirical constants, ρ_a is the air density and Q is the air flow rate.

3.6 Factors that Affect Electrostatic Charge Generation in Duct Flows

Experiments performed on the study of static charge generation by contaminant loaded fluid flow in pipes indicate that the static charge quantity and polarity depend upon several factors. Some of them are listed as follows:

- (a) the type of contaminants,
- (b) the concentration of contaminants,
- (c) the amount of moisture in the fluid,
- (d) the flow velocity,
- (e) the surface roughness of the pipe and
- (f) the conductivity or resistivity of the pipes.

The studies also show that electrical resistivity, dielectric constants and the viscosity of the fluid are very important in the electrification process [Gibson, 1971].

3.7 Air Filter Test Standards

The selection of a filter test housing design (geometry and material), filter media and its treatment, as well as the nature and size of the seeding contaminants used, highly influence the performance characteristics of fibrous filters. A monodisperse test aerosol used for evaluating the performance of a filter may result in different performance characteristics for the same filter media under the same conditions but with different test housing geometries. It is also possible for the same filter media tested with the same aerosol size and similar housing geometries, but under different test conditions to exhibit different filter performances. In view of this, the need to present a uniform method for determining and reporting air cleaner performance and to establish and specify uniform testing procedures, conditions and equipment have led to the introduction and development of several filter test standards in many developed countries at national and international levels. Some of the common standard test codes used in North and South America, including the United States of America, for testing or evaluating the

performance of modern automotive air induction filters (circular and panel type) are the SAE J726, SAE J1669, and ASTM F 1215-89. The ISO-5011 and JIS-D-1612 Standard Test Codes are practiced in Europe and Japan, respectively [Bugli, 1997]. Efforts are underway to commonize the SAE J726 Standard Test Code with the ISO Standard.

3.7.1 The ASTM F 1215-89 Standard Test Code

This standard test method was developed by the American Society for Testing and Materials Committee F21 for determining the initial efficiency of flat sheet filter media in air flow using latex spherical particles. The standard code covers techniques for measuring the initial particle size efficiency of flat sheet filter media using a light scattering particle counting system for particle size ranges from 0.5 to 5 μm . This standard test is applied to testing filters with face velocities ranging from 1 to 25 cm/s and with expected efficiencies lower than 99.9% at 1 μm . The test standard code also specifies a humidity range of 30 to 50% to ensure drying of the PSL particles [ASTM, 1989]. The aerosol particles produced by atomizing suspensions of monodisperse latex spherical particles are neutralized by a radioactive source. An ionization flux of 10^3 mCi/(m^3/s) provides the neutralization of 10^7 to 10^8 aerosol particles/ m^3 before they are mixed and diluted with preconditioned air and finally introduced to the test filter.

3.7.2 The SAE J726 Standard Test Code

The Society of the Automotive Engineers (SAE) in the United States is one of the leading societies that has established and compiled standardized air cleaners and an air cleaner test code [SAE, 1998]. The SAE J1141 Air Cleaner Elements [SAE, 1997],

provides listings of recommended round and panel type filters for the United States domestic passenger cars and light trucks. The SAE J726 test code [SAE, 1998] provides a standardized method of determining and reporting air filter performance and provides specifications for testing filters using a standard filter test housing.

However, previous studies made here at the School of Mechanical and Aerospace Engineering by Sabnis [1993], Newman [1994], and Liu et al. [1995] have shown that the test housing as specified in the SAE J726 Test Code does not provide uniform flow over the test filter. Flow visualization techniques and velocity distribution measurements using a Laser Doppler Anemometry system have confirmed that the flow within the test housing above and below the test filter undergoes recirculation and separation which implies nonuniform flow and hence nonuniform pressure distribution. Nonuniform flow in turn yields nonuniform local efficiency measurements.

The OSU School of Mechanical and Aerospace Engineering in cooperation with the SAE Air Cleaner Test Code Subcommittee has addressed the above problems of this nonuniform flow in the SAE J726 test housing. Duran [1995] reports that those previous investigations and recommendations led to the revision of the SAE J726 Test Code and the development of a new filter test housing similar to that specified under the SAE J1669 Passenger Compartment Air Cleaner Test Code [SAE, 1993] approved in December of 1994. The Society of Automotive Engineers recommends the use of two types of dust namely, the SAE fine and SAE coarse dusts for the evaluation of the performance of filters. Table 3.2 shows the chemical composition (analysis) of standard test dusts. Tables 3.3 and 3.4 show particle size distributions by percent weight and volume, respectively.

Table 3.2 Chemical Composition (Analysis) of Standard Test Dusts [SAE, 1998].

CHEMICAL ANALYSIS OF TEST DUST	
CHEMICAL	%WEIGHT
SiO ₂	65-76
Al ₂ O ₃	11-17
Fe ₂ O ₃	2.5-5.0
Na ₂ O	2-4
CaO	3-6
MgO	0.5-1.5
TiO ₂	0.5-1.0
V ₂ O ₃	.10
ZrO	.10
BaO	.10
Loss on ignition	2-4

Table 3.3 Standard Test Dust Particle Size Distribution by Weight, % [SAE, 1998].

Size Range, μm	Fine Grade	Coarse Grade
0-5	39±2	12±3
5-10	18±3	12±3
10-20	16±3	14±3
20-40	18±	23±3
40-80	9±3	30±3
80-200	-	9±3

Table 3.4 SAE Dust Particle Size Distribution in % by Volume [SAE, 1998].

Size, μm	Fine Grade (% less than)	Coarse Grade (% less than)
5.5	38±3	13±3
11	54±3	24±3
22	71±3	37±3
44	89±3	56±3
88	97±3	84±3
176	100	100

3.7.3 The SAE J1669 Standard Test Code

The objective of this test code is to maintain a uniform test method for evaluating the performance characteristics of air filters used in automotive interior ventilation

systems. Though the SAE J1669 was originally designed for the cabin air filters, it can also be used to test other type of filters. It is also possible to measure the overall efficiency, incremental efficiency, and fractional efficiency (for a range of particle sizes) of filters using particle sizing and counting instruments (for example, as in LDA systems by light scattering techniques). Standard Dusts are used for testing the dust holding capacity and overall efficiencies. The difference between the SAE J726 and SAE J1669 test housings is the fact that the later has a small diffuser angle of 7° . This allows a uniform flow condition at the filter face, which excludes recirculation.

For dust loading and holding capacities, ultrafine dust particles with size distribution as given in Table 3.5 below are used by the SAE J1669 Standard Test Code.

Table 3.5 Particle Size Distribution by Volume, % [SAE, 1998].

SIZE	ULTRA FINE GRADE (%)
2.0	85-88
3.2	65-71
5.0	26-34
10.0	0-2

In the SAE J1669 test code, monodisperse or polydisperse latex particles, lycopodium and other aerosols may also be used for special filter performance tests. Some of the test conditions with regard to temperature and humidity are specified as $20^{\circ}\text{C} \pm 5^{\circ}\text{C}$ and $65\% \pm 15\%$, respectively. Prior to the filter performance test, the air filter is subjected to a cycle of varying temperature and humidity conditions. In the first cycle, the filter is subjected to a temperature of $80^{\circ}\text{C} \pm 5^{\circ}\text{C}$ for 8 hours, then brought to room conditions followed by another cycle of exposure to a temperature of $38^{\circ}\text{C} \pm 5^{\circ}\text{C}$ and a humidity of $90\% \pm 5\%$ for 8 hours. After the completion of the second cycle, the filter is again brought to room conditions and then subjected to an environment with a

temperature of $-40\text{ }^{\circ}\text{C} \pm 5\text{ }^{\circ}\text{C}$ for 8 hours and allowed to adjust to room conditions. After the final cycle, the filter is stabilized to test conditions for not less than 5 hours. For more details, the reader is advised to read SAE test codes SAE J726 and SAE J1669 provided in the SAE handbooks.

There are two recommended particle-counting methods for the SAE J1669 test standard. They are (1) the sequential counting system and (2) the simultaneous counting system. For stable aerosol generating systems (in which the aerosol generation varies less than 2% from one sample period to the next), a single upstream-downstream counting system is sufficient. In the simultaneous counting system, the particles upstream and downstream of the filter are counted and recorded simultaneously [SAE, 1998].

Generally, experimental studies for the evaluation of the performance of real filters are conducted on the basis of a standard test code. However, experiments conducted on model filters (carefully made in the laboratory) to verify mathematical models may not follow strict standard test code procedures. All test standards have their own testing procedures, equipment, and standard dust particles to simulate a real filtration process under different test conditions.

Saxena [1998], Anand [1997], Jadbabaei [1997], Williams [1996], and Natrajan et al. [1995], have used a housing similar to the J1669 test housing in evaluating the performance of pleated automotive air induction filters and flat filter media. All of these researchers have reported almost uniform flow upstream of the filter, while observing the presence of recirculation zones downstream of the filter, due to area reduction at the edges of the filter by the rubber mounting.

3.8 Experimental Studies

Experimental measurements on fibrous filters provide the most reliable information on the actual performances of filters. Comparison of experimental and theoretical results for the evaluation of filter media and the verification of mathematical models on both real and model filters show that fibrous filtration theories usually tend to underpredict the performance of filters. However, the contribution of those theories to the prediction of the performance of fibrous filters is quite significant.

3.8.1 Electrostatic Charge Effects

There is limited literature on experimental studies in triboelectrostatically charged particles and their effects on conventional fibrous filtration. However, many researchers have conducted several experiments to evaluate the enhancement of conventional fibrous filters both by employing charged filter fibers (electret) and neutral particles and by employing charged particles and electret (charged) filters. Whatever the case may be, the author believes that the basic principle remains the same and emphasizes sticking to the main electrostatic mechanism of action, which is of paramount importance.

Experiments conducted by Hseih et al. [1996] on electret filters, made from a combination of coarse and electrostatically charged fibers and used in high filtration efficiency systems, have helped to verify how electrostatic mechanisms might be significant in enhancing filter efficiencies as shown in Fig. 3.9. In their experimental work, they found that the performance of electret filters due to electrostatic mechanisms is only dominant during the initial filtration process. As time proceeds and more particles are deposited on the filter, the efficiency decreases until it reaches its minimum value in

the transition region. In the transition region, as mechanical effects start dominating the filtration process where the combined action of electrostatic and mechanical filtration mechanisms take place, the efficiency starts to rise once again to its maximum value.

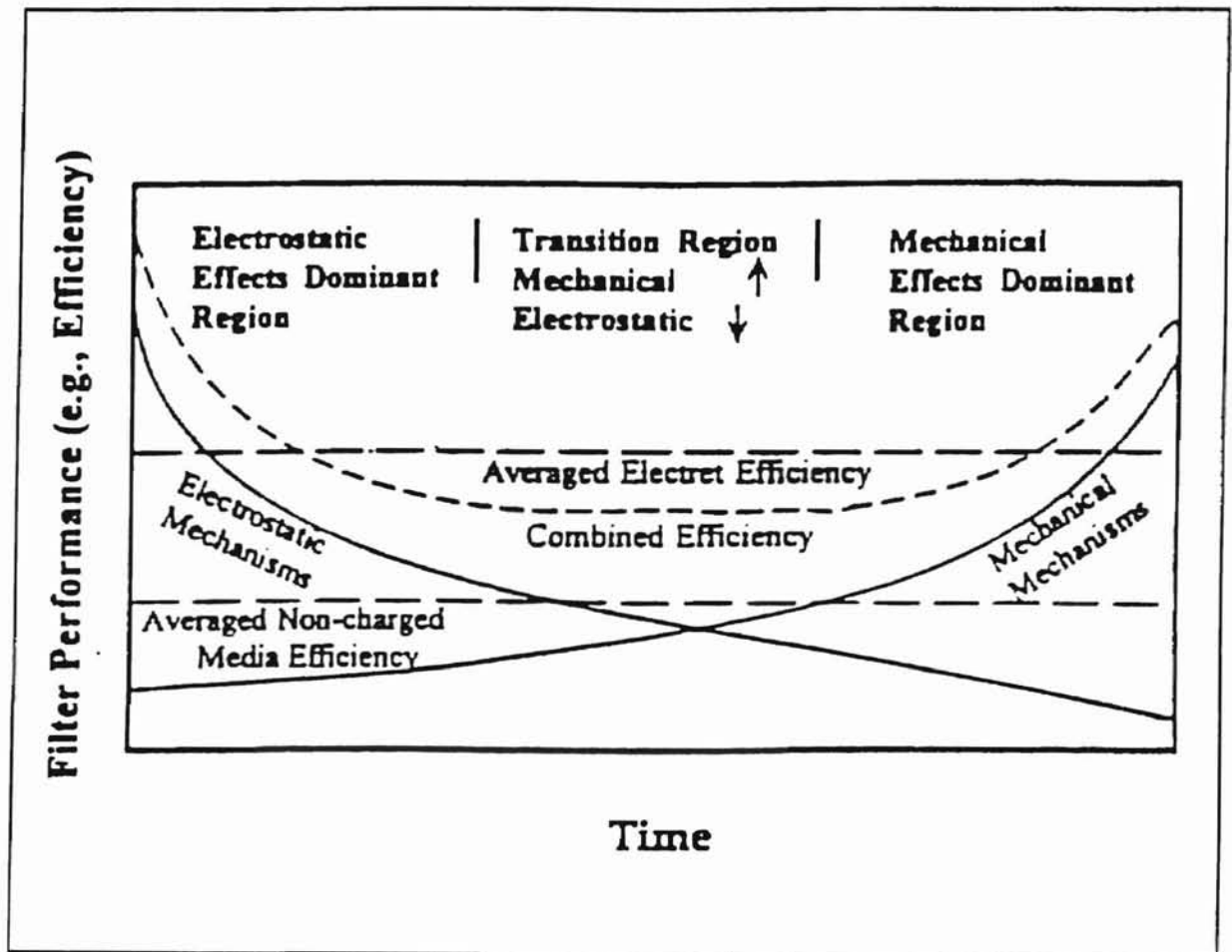


Figure 3.9 Schematic of the Performance of a Typical Electret Filter Versus Time [Hsieh et al., 1996].

Particle deposition on electret media is characterized by (1) more uniform particle deposition around the fibers and (2) quasi-gradient filter structure in which the structure of the electret filter is more open at its entrance and tighter at the exit. Unlike conventional non-charged media, the distribution of the collected particles on typical electret filters is more uniform around the fibers due to the electrostatic effects. Figure

3.10 illustrates the difference in the deposition of collected particles between a charged fiber and a non-charged fiber. For the uncharged filter media, the majority of particles are collected on the upstream side of the fiber, which faces the airflow. The deposited particles tend to form dendritic (string like) structures faster, which cause drag forces. It is the drag forces that cause a faster pressure drop increase. Particles on the fibers of electret filters are uniformly distributed, and the rise in pressure drop is lower than for the uncharged filter media.

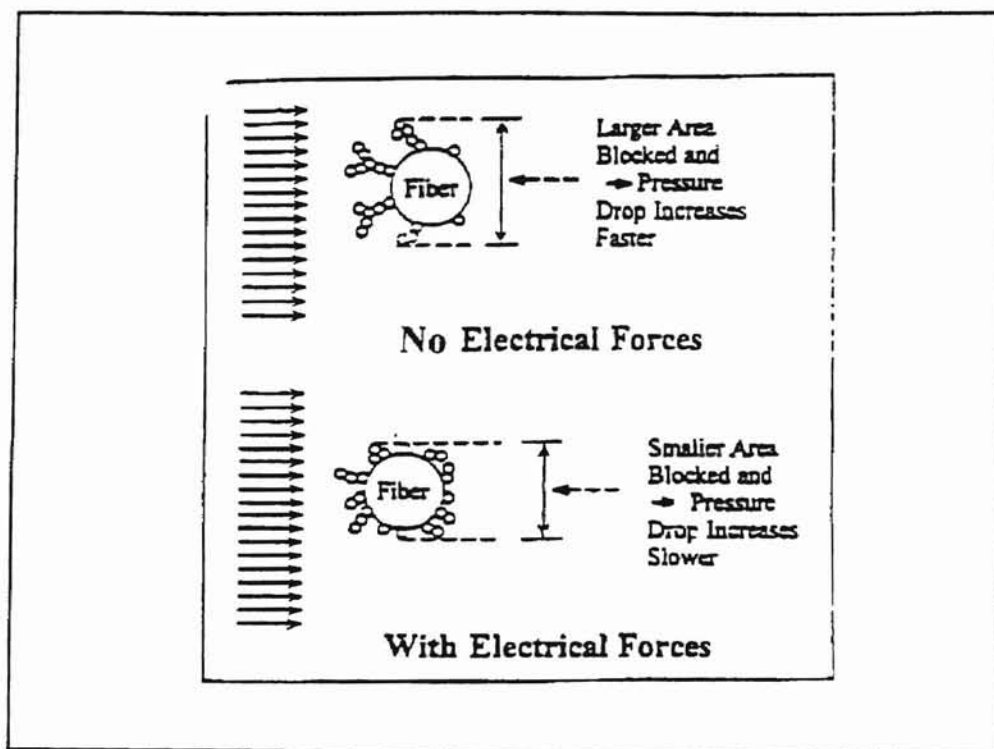


Figure 3.10 A Schematic of Particle Deposition on Single Fiber with and without Electrical Forces [Hseih et al., 1996].

The second feature of an electret filter as listed in (2) is the quasi-gradient filter structure as shown in Fig. 3.11. A typical filter material has uniform structure throughout its depth, whereas a gradient filter has an open structure at the top and a tighter structure at the bottom. This gradient structure can slow down the increase of pressure drop and also increase the dust holding capacity of the filter [Hseih et al., 1996]. Thus more

uniform particle deposition around the fibers and the quasi-gradient filter property have positive impacts on the filter lifetime.

Hseih et al. [1996] also conducted different experiments with different electret filters by using cigarette smoke as the main aerosol. They found that the charge of some electret filters was destroyed easily by the oily aerosols from the cigarette smoke.

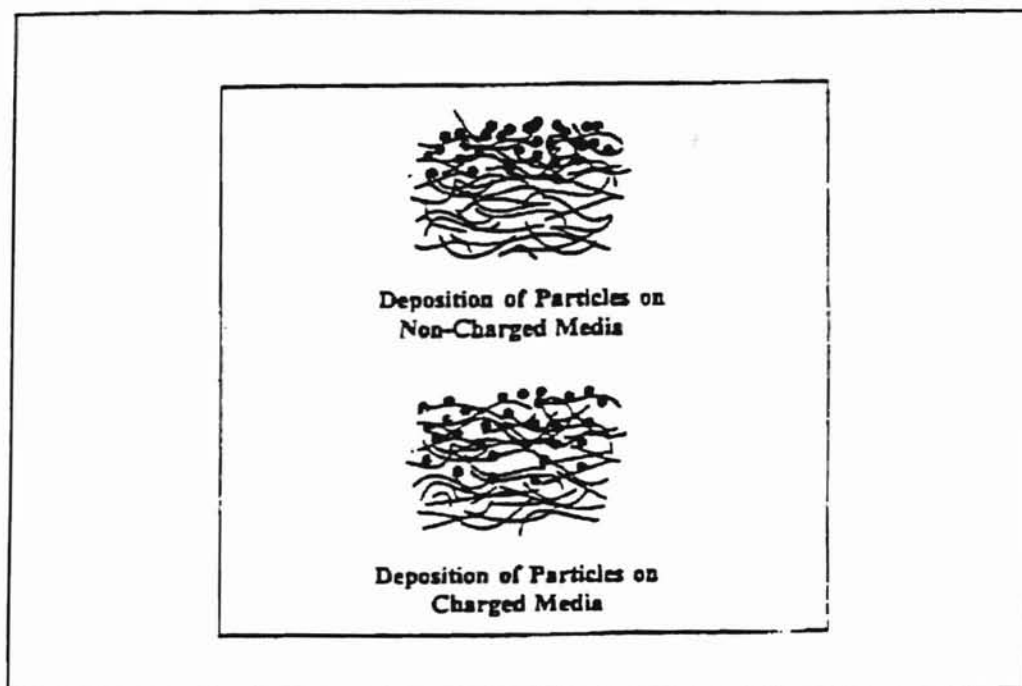


Figure 3.11 A Schematic of Particle Deposition on Charged and Non-charged Filter Media [Hseih et al., 1996].

The effect of face velocity and particle size on electrostatic mechanisms of filtration (non-woven electret and nonelectret filter media) was investigated by Davies [1994] using the ASTM F 1215-89 test standard. To illustrate the utility of this standard for the evaluation of the filtration performance of filter media, tests were conducted on two filter media. Both media were identical except one was electret and the other nonelectret. The two media consisted of melt-blown polypropylene filters with an approximate thickness of 390 μm and a geometric fiber diameter of 2.1 μm . The particle

sizes used were 1, 2, and 3 μm PSL particles with a filter face velocity up to 40 cm/s. Figure 3.12 shows a comparison of efficiency between nonelectret media (test numbers 14-21) and electret media (test numbers 23-30) at a constant face velocity of 20 cm/s.

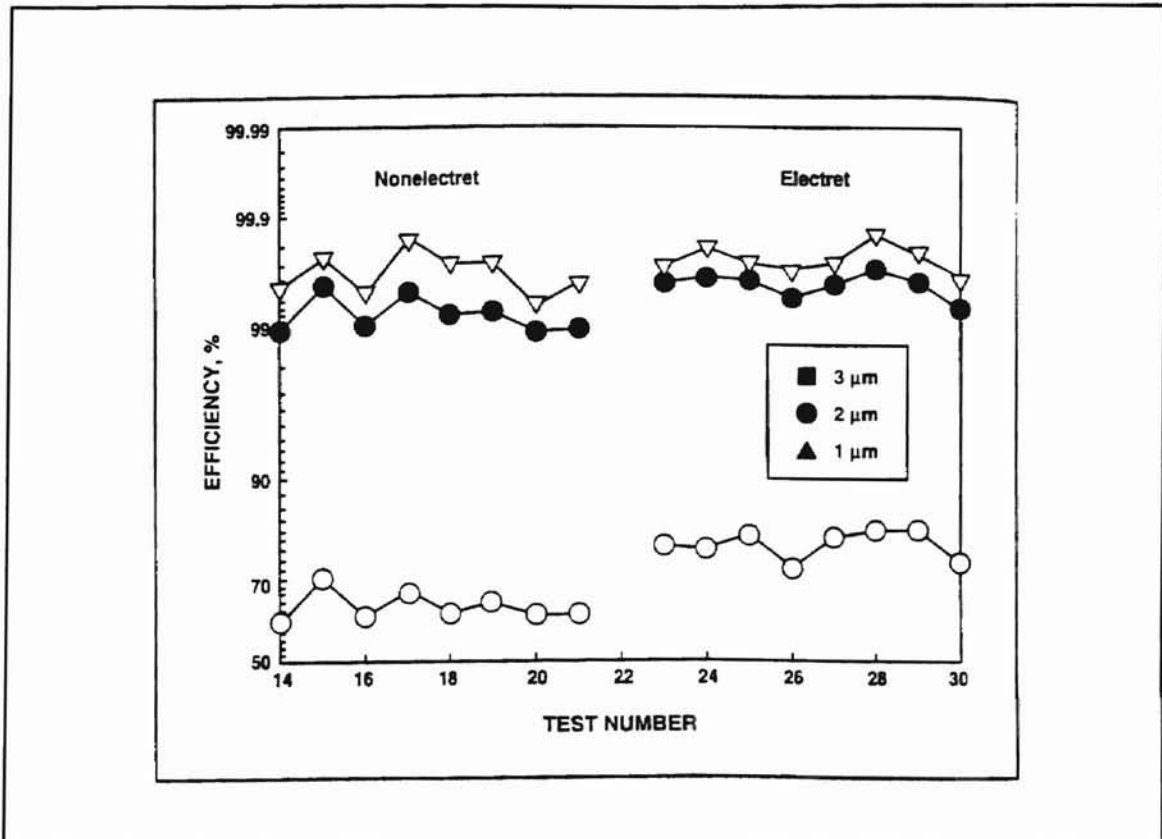


Figure 3.12 Collection Efficiency for Nonelectret and Electret Samples [Davies, 1994].

One concludes from this test that, at this velocity the electret filter was slightly more efficient than the nonelectret with average efficiencies of 78.5%, 99.52% and 99.71% for 1.0, 2.0, and 3.0 μm particle sizes.

Results of Davies' [1994] experimental investigation of particle size effects for velocity ranging from 1.2 cm/s to 40 cm/s on both types of filter media is shown on Fig. 3.13. The results show that the electret filter had significantly greater efficiencies than the non-electret filter at the low velocities where the electrostatic mechanisms of action

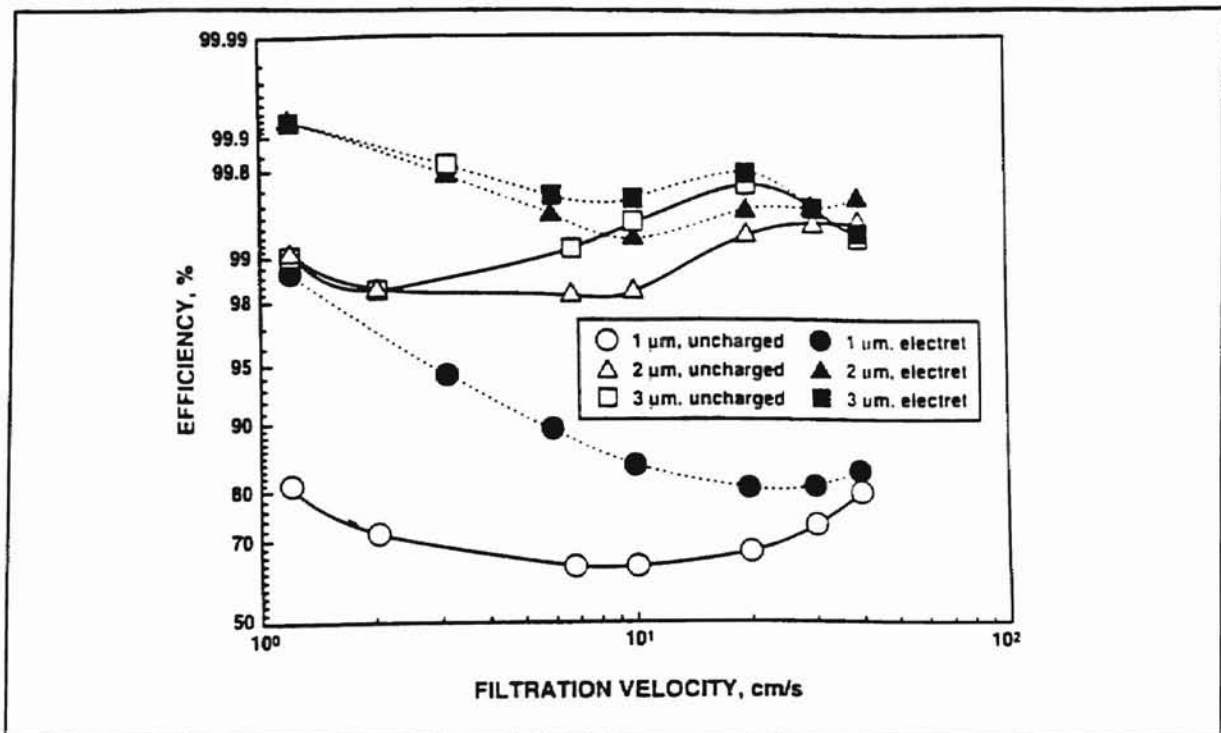


Figure 3.13 Collection Efficiency Versus Filtration Velocity for Nonelectret and Electret Filter Media for Different Particle Sizes [Davies, 1994].

and diffusion are dominant. As the velocity increased, the efficiency for both media decreased. As velocity continued to increase, then the efficiency started to increase, showing that the mechanism of inertial impaction was starting to dominate. At 40 cm/s, the difference in efficiency for both types of filter media was very small. This implies the dominance of inertial impaction over both the diffusive and electrostatic mechanisms.

Kalatoor et al. [1997] tested the effect of neutralized and non-neutralized dust particles on a new electrostatically charged and pleated depth filter media (Tribex Plus) for modern automotive ventilation systems using SAE ultra fine dust (Powder Technology Inc., Burnsville, Minnesota). The new media contained fine fibers of average diameter less than 5 μm , which were lodged (placed) into a depth filter medium with larger average diameter fibers of 15 to 20 μm . A Fluidized Bed Aerosol Generator

(TSI Model no. 34001) generated the test aerosol. Charge neutralization was effected by a Kr^{85} radiation source. Figure 3.14 illustrates filtration efficiency variation as function of particle size for the electrostatically neutralized and non-neutralized SAE ultrafine aerosol particles.

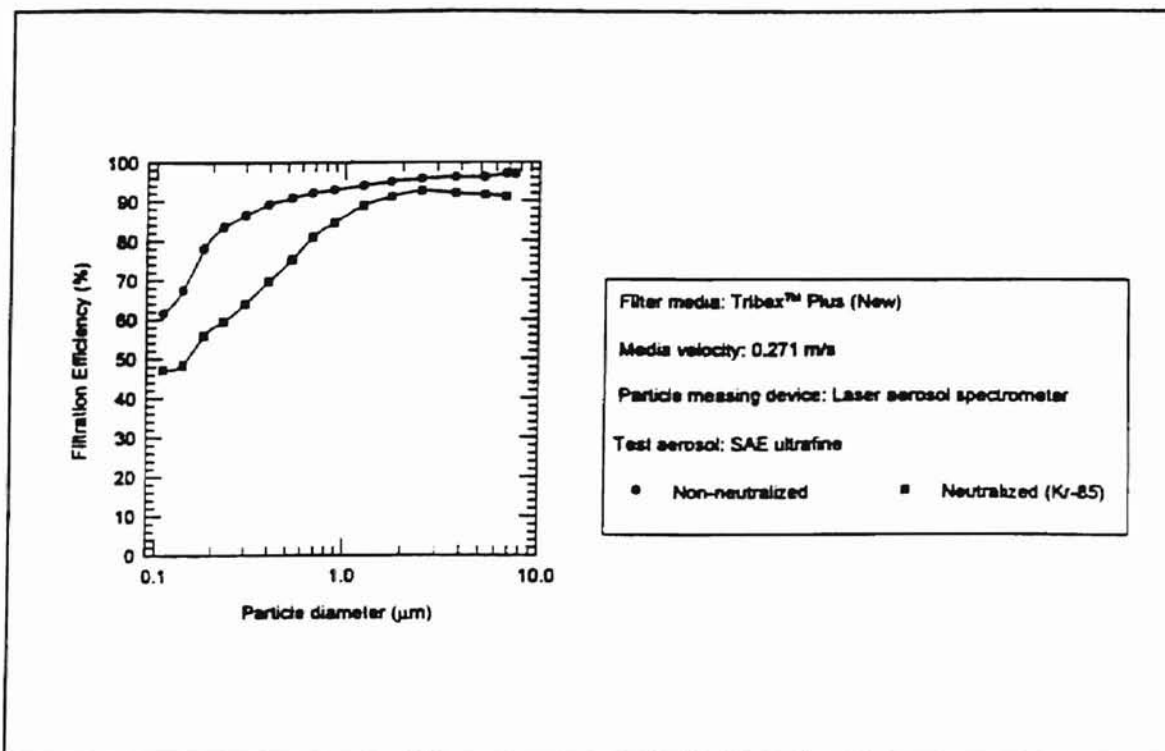


Figure 3.14 Charge Effect on Filtration Efficiency and Particle Size [Kalatoor et al., 1997].

The media show higher efficiencies for non-neutralized particles in the submicron range due to the contribution of Coulombic forces of attraction. Kalatoor et al. [1997] argue that the probability of an electrostatically neutral particle to be deposited on the fiber (due to polarization effects of the electric field of the electret) was less than that of an already charged particle. However, the electret media demonstrated high particle collection efficiency for both the neutralized and non-neutralized particles. The media velocity was 0.271 m/s. The results indicate that the media have excellent dust loading

characteristics typical of depth filter media, which capture particles throughout their depth as the contaminant loaded medium (air) flows through.

3.8.2 The Effect of Humidity

Humidity affects the efficiency of fibrous filters depending upon the type of particles and the fiber. The type, shape, surface roughness, type of contaminant and the contact time of both the contaminant and the fiber are very important to the adhesion of particles to the fibers by the surface tension of the water films from the humid air. As the water vapor condenses, the surface tension at the junction of the fiber and dust particles helps the adhesion of particles.

3.8.2.1 Efficiency

Humidity affects filtration both favorably and adversely depending upon the history of the filter. The fact that humidity destroys electrostatic charge by increasing the conductivity of materials may lead us to the conclusion that there will be a fall in the efficiency of previously charged filters at higher relative humidity, RH, values. However the general trend for the particulate retention (efficiency) of neutral filters is to increase steadily with humidity due to the adhesion between the particles and the fibers as a result of surface tension of the condensing water vapor. This is dependent upon the type, nature, and shape of the dust particles used and the filter fiber material.

According to Matteson [1987], Dorman conducted some experiments on the effects of humidity on fibrous filters using B.S. No. 2 (British Standard No. 2) dust which is composed of 60 to 80% by weight 3.5-7 μm , 99.5% finer than 13 μm , and 2% finer

than 2.5 μm diameter particles. The results indicated that, for dry fibrous filters the efficiency was markedly dependent upon the relative humidity of the air, although tests on oil-wetted filters with dry dust showed little change in efficiency. Figure 3.15 shows the gravimetric efficiency of a fibrous filter as a function of the relative humidity. This indicates that dry fibrous filters are unsuitable for the capture of dry dusts unless humidity is high. On the other hand, tests carried out on ASHRAE dusts (aluminum oxide dusts) showed no significant changes on the efficiency of filters over the humidity range of 30 to 65% RH. This implies that particle nature plays an important role in establishing the effect of humidity on particle capture.

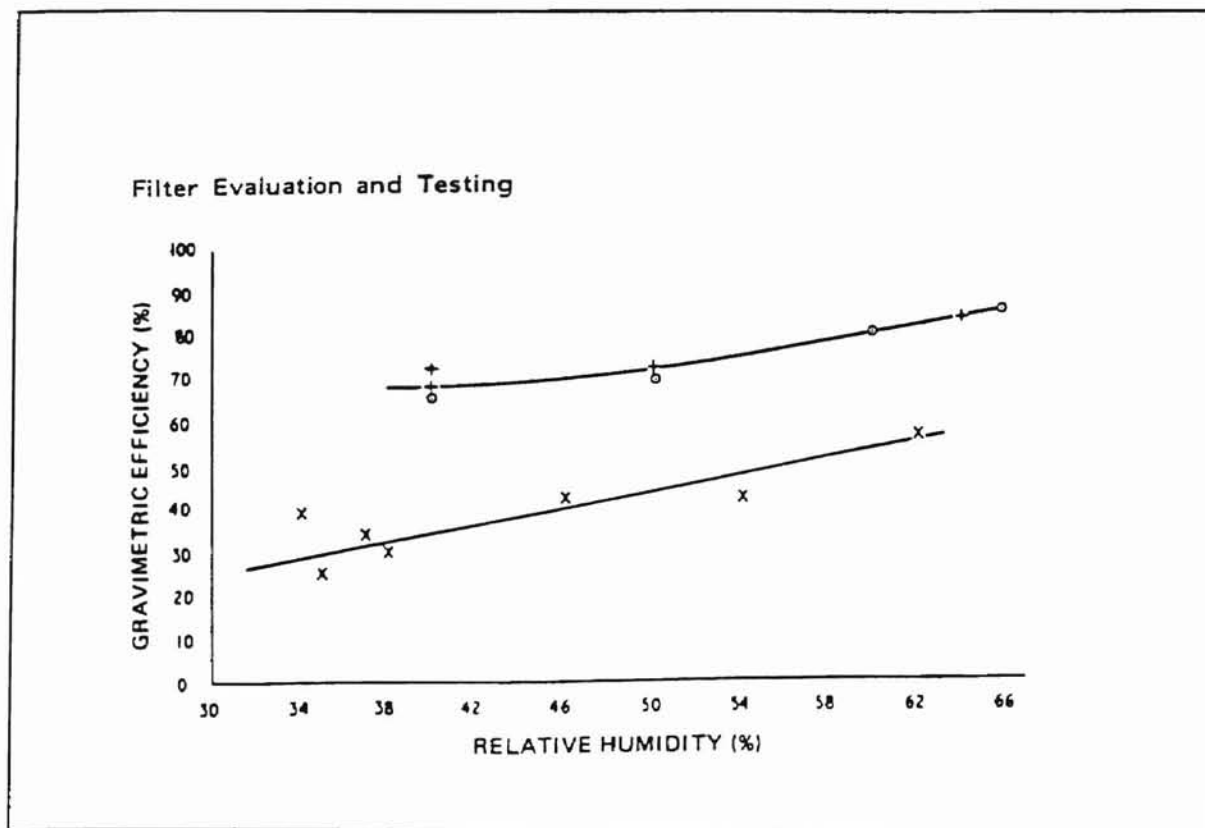


Figure 3.15 Effect of Relative Humidity on Filter Efficiency [Matteson, 1987].

3.8.2.2 Humidity Effects on Charged Materials

In the previous sections, we have seen that electrostatic charge enhances filter efficiency. However, electrostatic charge can be destroyed when the humidity of the medium increases. It is believed that, as humidity increases, the conductivity of materials increases as well.

Henry [1971] did an extensive experimental study to investigate the risks of ignition due to high triboelectrostatic voltage on outer clothing because of contact and separation with other bodies. From the experimental work, he established the dependence of resistivity and electrostatic voltage of different materials on humidity as shown in Fig. 3.16. The experimental studies done on selected materials (cotton, new

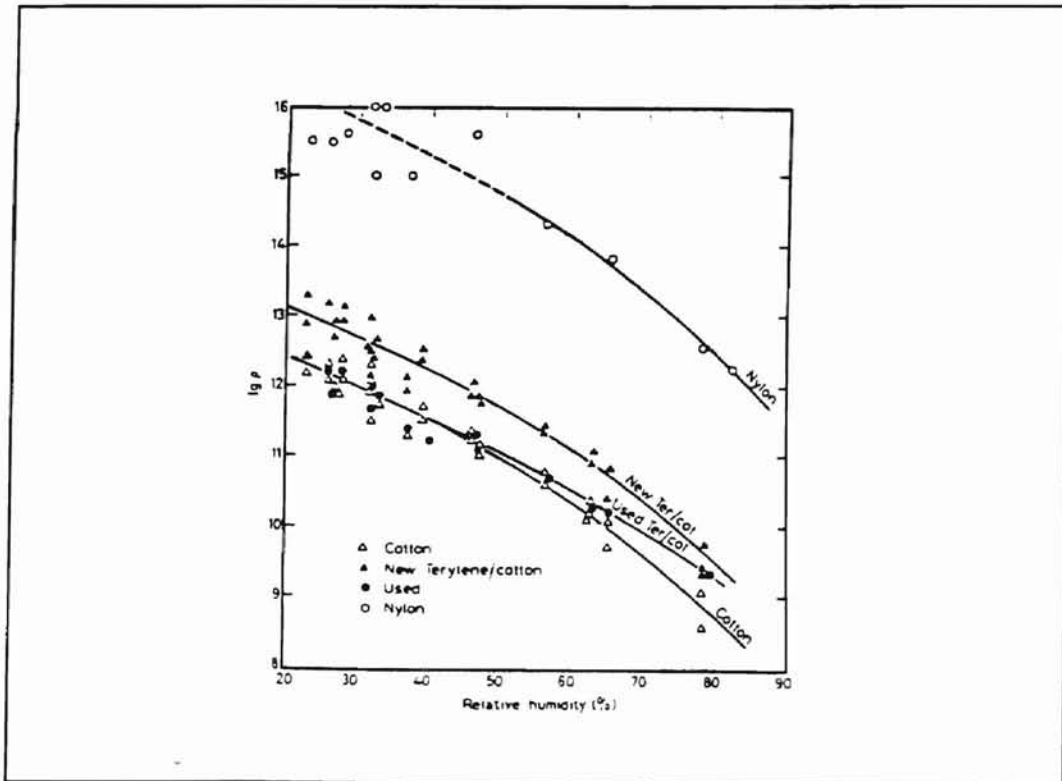


Figure 3.16 Log of Resistivity Versus Relative Humidity for Various Materials [Henry, 1971].

and used terylene/cotton, and nylon), using an electrometer to measure the electrostatic charge, showed that there is a steady fall in the resistance of the materials as the humidity increases. Similarly the corresponding voltage was found to steadily decrease as the relative humidity increased as shown in Fig. 3.17.

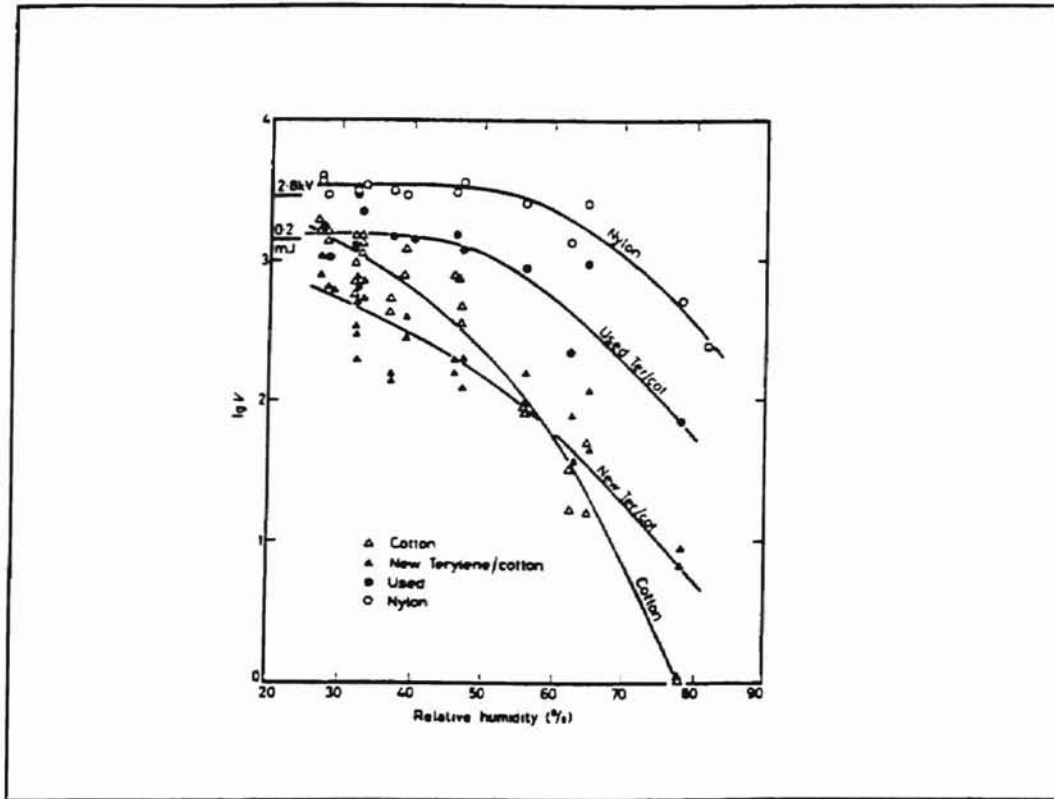


Figure 3.17 Log of Voltage Versus Relative Humidity for Various Materials [Henry, 1971].

3.8.3 Research at OSU

The research work in the field of fibrous filtration at OSU's School of Mechanical and Aerospace Engineering has been in the performance evaluation and testing of air induction systems and filters (pleated and flat filter media) both theoretically and

experimentally. Some of the research work has been devoted to air induction system (flow and housing geometry) evaluation and selection based on CFD (Computational Fluid Dynamics) analysis. Most of the experimental work has also been done on the overall initial efficiency measurements of flat and pleated automotive filter media using state-of-the-art flow measurement technology – Laser Doppler Anemometry. Many of the previous researchers in experimental filtration have reported some inconsistency problems in measurement of number densities and hence local efficiencies of the filters.

There has not been any previous investigation related to the study herein. This study has tried to tackle the inconsistency problems from the outset by dealing with the possible root causes of the inconsistencies - stability of the Laser Doppler Anemometer, stability of the contaminant seeding, and, as the title suggests, investigating the 'Effect of Electrostatic Charge and Humidity'.

Next, the author would like to present the efficiency measurements on 'non-charged automotive pleated and flat filter media' in general and the inconsistencies as reported by the respective authors. Anand [1997] and Williams [1996] conducted experimental local efficiency measurements on electrostatically neutral flat filter media. Saxena [1998], Jadbabaei [1997] and Natarajan [1995] also conducted similar experiments on a neutral A13192 pleated filters. None of them did any charge neutralization, humidity or temperature measurement and control immediately after the atomization and drying of the aerosol particles prior to the efficiency measurements.

Figure 3.18 shows Natarajan's overall efficiency versus flow rate measurements. Natarajan admittedly reports that his measurements suffered for consistency due to the instability of the laser power. After addressing laser stability and air leakage as the root

causes of the inconsistency problems, Anand [1997] went on to verify the repeatability of his measurements. Both Anand and Jadbabaei [1997] attributed the instability of the laser power to temperature variations around the laser couplers and to vibration induced

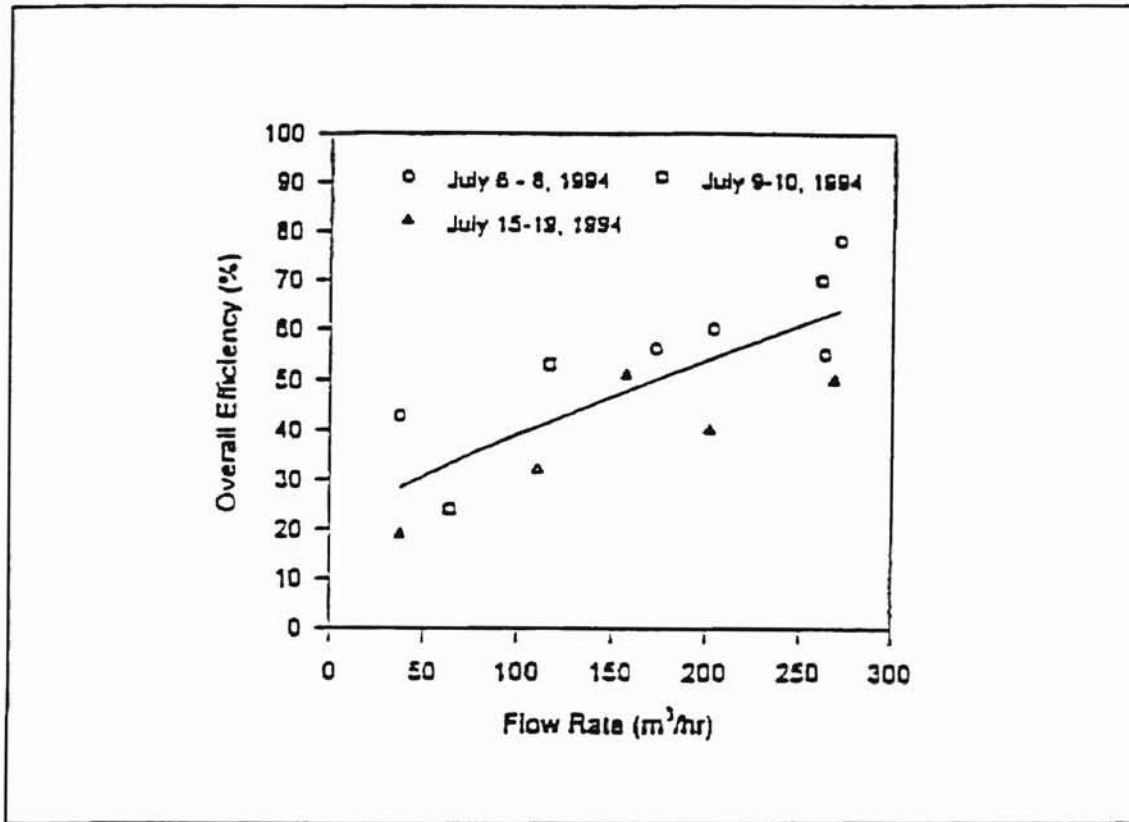


Figure 3.18 Overall Efficiency Versus Flow Rate for Non-neutralized Aerosols and Neutral Filter [Natarajan, 1995].

by the blower. Later, the author together with Saxena [1998], after some experimental work, refuted vibration as a cause of the laser power instability. Anand [1997] measured the efficiency of flat filter media and established a correlation between flat and pleated media. Figure 3.19 delineates his work on flat filters and his comparison with the theoretical work of Lee [1977]. Jadbabaei [1997] also did some experiments on the filtration efficiency of automotive air filters. Though Anand and Jadbabaei were quite aware of the instability of the laser power and attributed the instability to variable

temperature and vibration, their efforts to maintain constant temperature and eliminate vibration by installing shock absorbers did not prove to be the final solution. Jadbabaei's

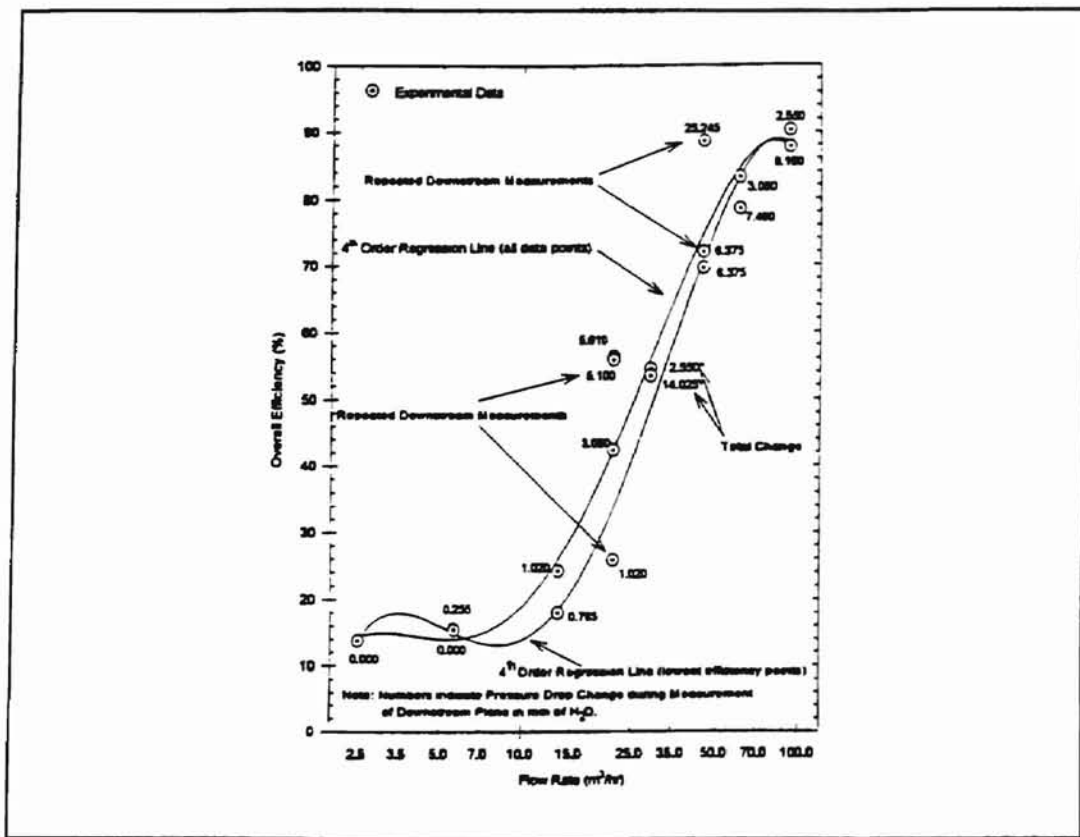


Fig 3.19 Overall Efficiency of a 'Neutral Flat Filter' with Non-neutralized 0.966 μm PSL Particles [Anand, 1997].

[1997] experiments on the performance of uncharged (neutral) pleated filters were conducted in the small angle diffuser housing with the atomization and drying of 0.996 μm PSL particles, as shown in Fig. 3.20. As in the work of other researchers, the PSL particles were not neutralized, for there was not any means to do so. Saxena [1998] also conducted experiments on the comparison of efficiencies of fibrous filters using different particle diameter (0.5, 1.0 and 2.0 μm) on different housings including the SAD (small

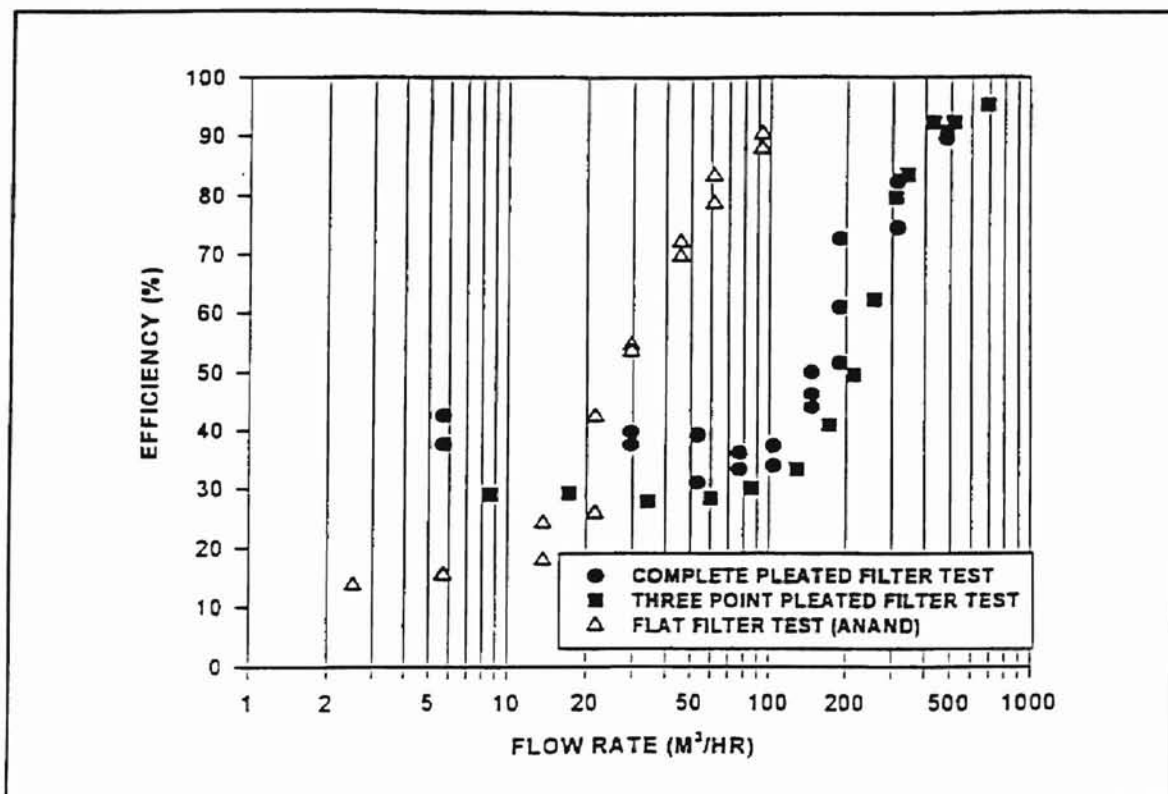


Figure 3.20 Efficiency Versus Flow Rate for a 'Neutral Pleated Filter' and Non-neutralized 0.966 μm PSL Particles [Jadbabaei, 1997].

angle diffuser) filter housing, the simulated automotive housing, and the SAE J726 filter housing.

Though the stability of the laser system was far better than for any previous testing, there were some marked irregularities in the local efficiency measurements of the filters in the low and high flow rate regions that could not be explained. Figure 3.21 shows results from Saxena's work on the variation of efficiency with flow rate. In all of the studies that have been conducted in the experimental filtration of fibrous filters, control of humidity, temperature, and charge have not been addressed until this research.

Oklahoma State Univ. Library

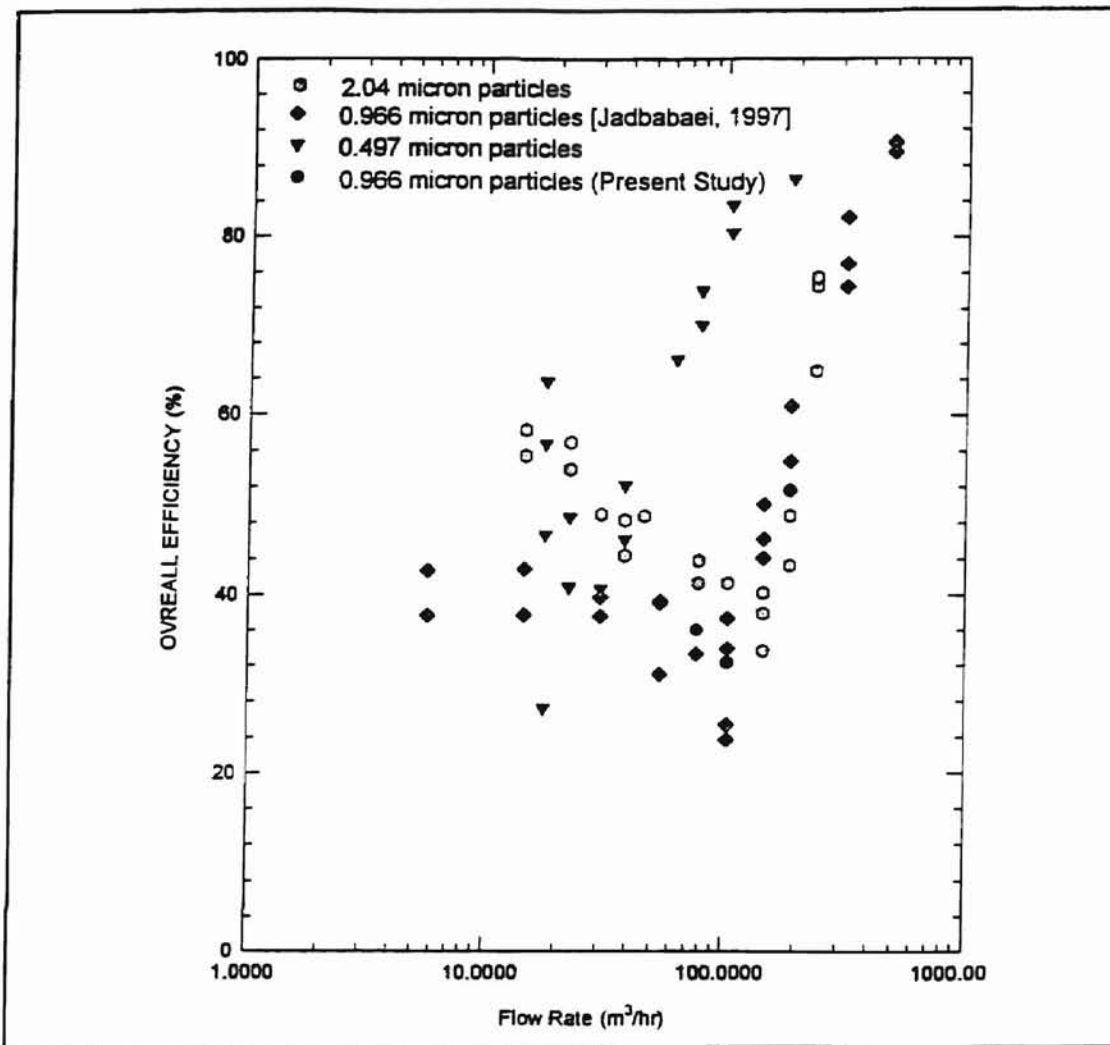


Figure 3.21 Efficiency Versus Flow Rate for 'Neutral Pleated Filters' with Non-Neutralized PSL Particles Having Different Diameters [Saxena, 1998].

3.9 Theories of Adhesion of Particles

Particles of submicron size are believed to adhere to the fibers of filters mainly due to van der Waals forces. However, the other factors that may influence the retention of particles are electrostatic forces, surface tension of absorbed films, contamination, the shapes of the particles and fibers, the surface roughness, and the contact time.

3.9.1 Van der Waals Forces

The van der Waals forces are connected to molecules and are comprised of forces between polar molecules, and between molecules polarized by fields of other molecules and by the London – van der Waals dispersion forces. The force due to the van der Waals effect is estimated by [Matteson, 1987]

$$F_{ad} = B_w r_m^{-7} \quad (3.26)$$

where B_w is a van der Waals constant, and r_m is the intermolecular distance.

3.9.2 Electrostatic Forces

Loeffler [Matteson, 1987] performed some experiments using 1 μm and 10 μm diameter particles to investigate the effects of electrostatic charge on adhesion. He concluded that, even under high charge densities, the contribution of electrostatic force to adhesion is lower than that of van der Waals forces. However, electrostatic charge has a marked effect on the adhesion of particles.

3.9.3 Humidity

Several researchers have investigated the forces of adhesion between a spherical particle and a plate in the presence of a water film. The magnitude of the forces shows that adhesion between particles in air usually increases as the relative humidity of the air is increased, due to a layer of condensed water surrounding the point of contact. Studies made on spherical particles between 21 μm and 90 μm in diameter showed that adhesive

forces increased linearly with humidity, indicating that humidity is a major factor influencing the adhesion of particles to uncoated particles [Matteson, 1987].

Most materials adsorb liquid molecules on their surfaces, and there is an attractive force between the particles and the surface of fibers because of the surface tension of the liquid drawn into the capillary space at the point of contact as shown in Fig. 3.22. For

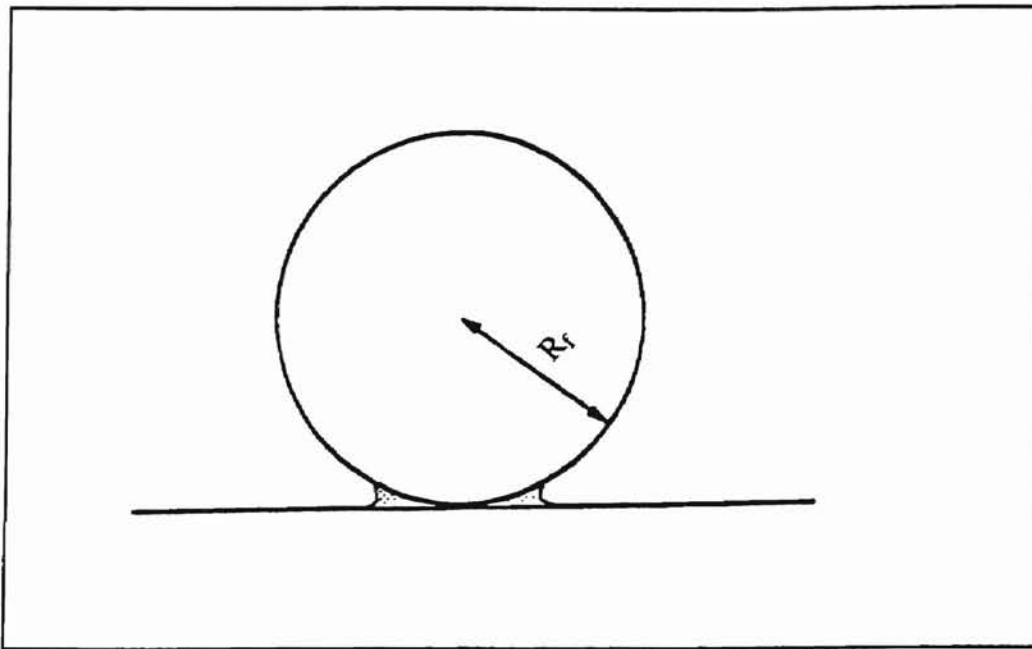


Figure 3.22 A Spherical Particle Attached to a Plane by Capillary Forces [Brown, 1993].

relative humidities above 90%, the force of adhesion, F_{ad} , is estimated [Hinds, 1982] using Eqn. (3-27)

$$F_{ad} = 2\pi\sigma D_p \quad (3-27)$$

where σ is the surface tension of water in dynes/cm. Experimental measurements of adhesive forces are made by determining the forces necessary to detach the particles. For hard materials and clean surfaces, Hinds [1982] found a useful expression for estimating

the adhesive force, F_{ad} , at 25 °C as a function of the diameter of the particles and the relative humidity, RH, by

$$F_{ad} = 150D_p (0.5 + 0.0045(\%RH)) \quad (3-28)$$

where F_{ad} is in dynes/cm, D_p is the diameter of the particle in cm, and %RH is the relative humidity in percent.

Matteson [1987], on the other hand calculated the force of adhesion, F_{ad} , as

$$F_{ad} = 4\pi\sigma R_w \cos(\vartheta) \quad (3-29)$$

where R_w is the radius of the water film surrounding the lower part of the spherical particle and ϑ is the angle of contact between the particle and the water film. The magnitude of the adhesion force due to a water film is between 0.1 and 1.0 dynes [Matteson, 1987].

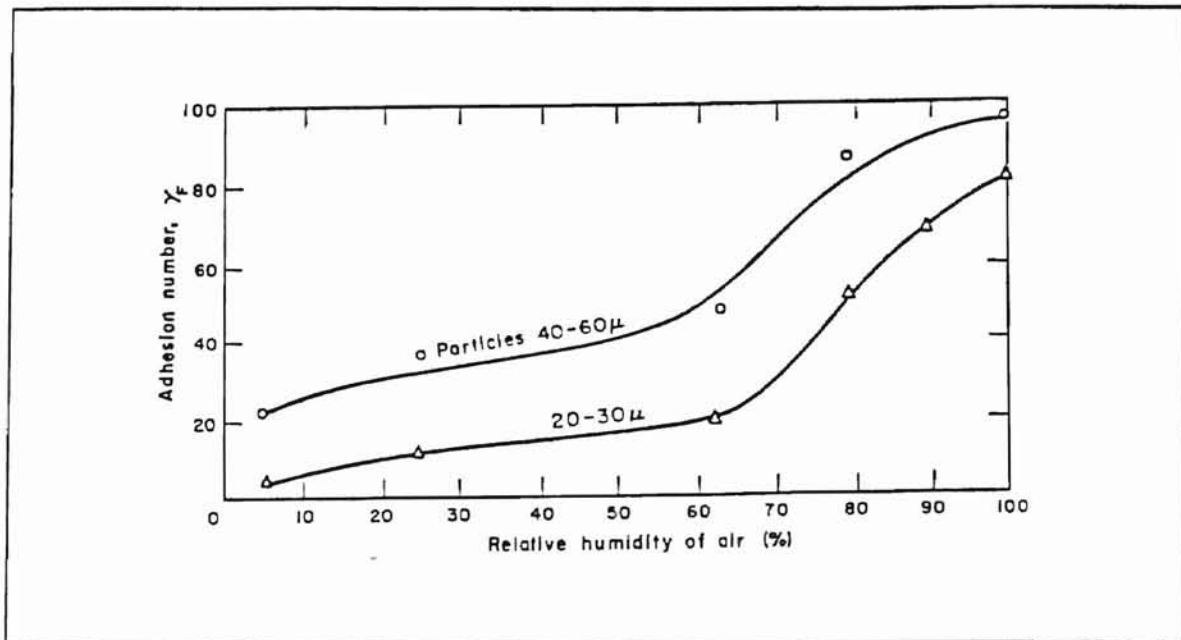


Figure 3.23 The Influence of Atmospheric Humidity on the Forces of Adhesion by Corn [Davies, 1966].

3.10 Present Study

As outlined in the introductory part of this thesis, the main objective of this study has been broad and was mainly devised to see the interdependence of both humidity and electrostatic charge (generated from triboelectric effects and the atomization of suspensions of spherical polystyrene latex particles) and their independent effects on fibrous filtration. This study concentrates on local filtration efficiency measurements for automotive filters (non-charged Dayco-Purolator A13192) using 1.0 μm diameter particles that are seeded into a preheated airflow by the atomization of a high-pressure solution of spherical polystyrene latex (PSL) particles while monitoring electrostatic charge (voltage) and humidity.

In the first part of this experimental study, the effect of humidity on fibrous filtration is investigated by neutralizing the charged particles using a grounded aluminum foil that covers the external surface of the small angle diffuser test housing. In the second part, the electrostatic charge resulting from the atomization followed by drying and the triboelectrostatic effects of the PSL particles in the duct flow are maximized by minimizing the humidity, and then their effects on filtration efficiency are investigated.

The most important tasks are outlined as follows:

1. Search for a new, simple, cheap and hazard free approach to charge neutralization.
2. Establish a correlation between the electrostatic charge voltage and the contaminant loaded airflow rate, contaminant concentration and humidity of the air.
3. Verify and compare the effects of electrostatic charge and humidity on

filtration efficiency by measuring the local efficiency of a filter using an optical light scattering system based on Laser Doppler Anemometry.

4. Model a real filter as a medium in continuous exchange of moisture (possibly including other thermodynamic properties) with the contaminated air until the establishment of equilibrium between the air and the filter.

CHAPTER IV

THE LDA INSTRUMENTATION, EXPERIMENTAL FLOW SETUP AND PROCEDURES

4.1 General Description

The LDA (Laser Doppler Anemometry) system represents the state-of-the-art technology for the measurement of particle concentration in a flow by detecting and counting the contaminant particles and their respective velocities over a period of time using optical light scattering techniques. Thus from the particle count, velocity, and data collection time, the concentration of particles upstream and downstream of the filter is calculated, from which the efficiency of the filter can be found.

The LDA system in this study operates in the fringe mode, which requires the interference of two intersecting laser beams. The Laser Doppler Anemometer (manufactured by Aerometrics, Inc.) used in these experiments utilizes a 5-watt Argon-ion laser (Innova 70-A) manufactured by Coherent, Inc. as a source of coherent light for the detection of particles by reflected light signals. The experimental flow set up consists of an air heater, humidifier, atomizer, mixing box, test housing, aluminum foil (for charge neutralization), filter and filter mountings, a TSI flow meter and control panel, and a suction blower.

Oklahoma State Univ. Library

In this chapter, a comprehensive explanation of the LDA instrumentation and its working principles, as well as the experimental flow setup used in investigating the effects of electrostatic charge and humidity on fibrous filtration efficiency will be presented. The problems associated with the stability of the laser system that directly or indirectly affect consistent filter efficiency measurements, and the efforts made to control will also be discussed.

4.2 LDA Instrumentation

The LDA has the following major units and the detailed components are shown in Fig. 4.1 below:

1. laser unit
2. fiber drive unit

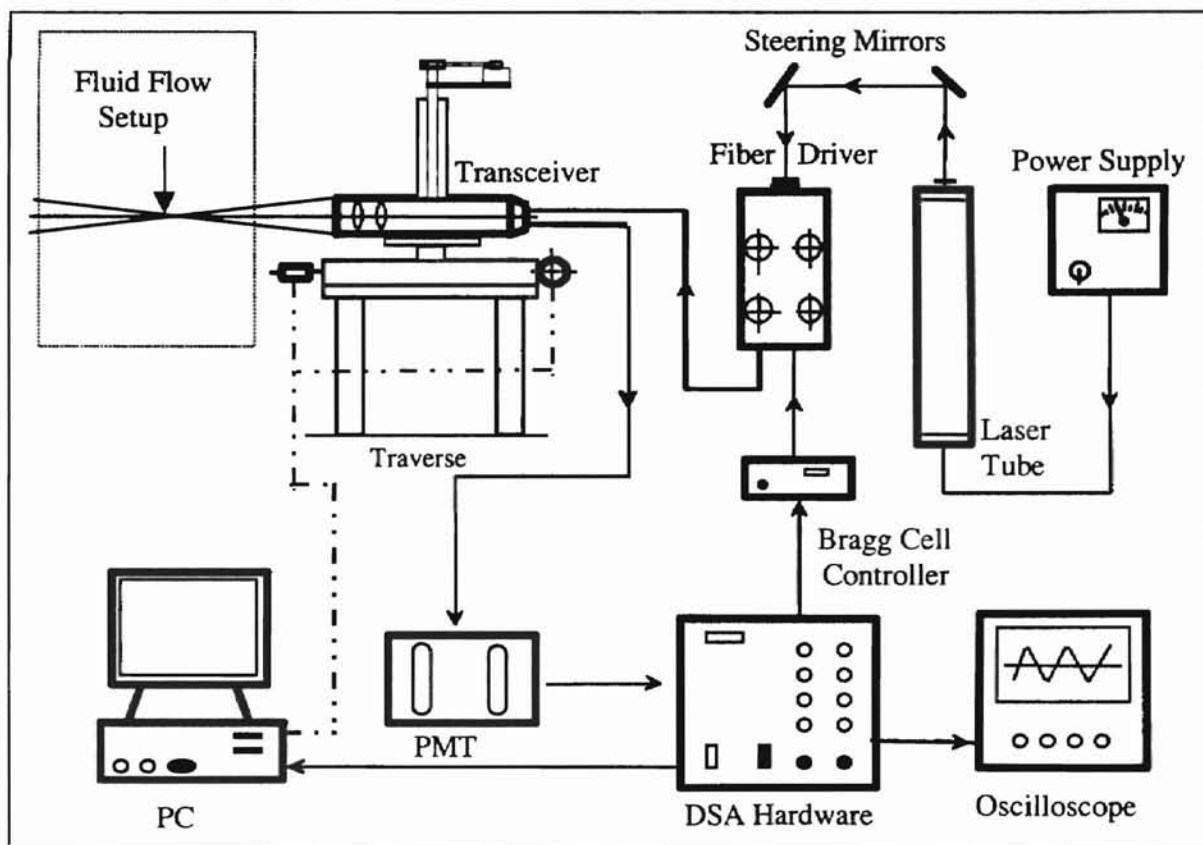


Figure 4.1 Schematic of the Laser Doppler Instrumentation.

Oklahoma State Univ. Library

3. data receiving and processing unit

The LDA system operates in the fringe mode with two colors (wavelengths) and is designed to measure two velocity components. The respective wavelengths, λ_w , of the two beams, namely blue and green, that come from the Argon-ion laser are $\lambda_w = 488$ nm and $\lambda_w = 514.5$ nm.

4.2.1 Laser Unit

The laser unit consists of the power supply and the water-cooled Argon-ion laser tube with a nominal lasing power capacity of 5 watts. It generates a multi-line or multi-wavelength beam of light. The main components of the beam that are used for the two component LDA systems are the blue and green beams. The laser beam is directed from the exit of the laser tube to the fiber drive unit by the external steering mirrors as shown in Fig. 4.1.

4.2.2 Fiber Drive Unit

The fiber drive unit consists of the fiber drive including the couplers and a Bragg cell (for frequency shifting) controlled by a bragg cell controller and many other internal prisms and mirrors for the dispersion and steering of the beams respectively. The fiber drive receives the laser beam directed by the external steering mirrors from the laser tube as shown in Fig. 4.1. As it enters the Bragg cell at the fiber drive, the beam is split into shifted and unshifted (first and zero order) beams. Each shifted and unshifted beam consists of two colors (green and blue). The beams are frequency shifted by 40 MHz. Generally, frequency shifting of the beams is the most convenient method of

discriminating (determining) the direction of velocity in LDA systems by generating moving fringes [Drain, 1980]. After the dispersion of the beam into individual colors, the laser light beams are coupled into the 4 μm diameter fiber optic cables by the focusing lenses housed inside the couplers that are mounted at the top of the fiber drive. Then the four beams are transmitted via the four separate fiber optic cables to the transceiver. The fiber optic cables are jacketed by a 3-mm Kevlar-reinforced thermoplastic tube. The jacketed fibers are also covered by stainless steel reinforced coil tubing with liquid-tight PVC outer covers.

4.2.3 Data Receiving and Processing Unit

This unit consists of the transceiver probe mounted on the three-dimensional transverse optical table, the photomultiplier tubes (PMT), DSA hardware, the monitoring computers, and the digital oscilloscope as shown in Fig. 4.1.

The transceiver probe is an optical system that contains transmitting and receiving components of the LDA system in a single package. The transceiver probe contains all of the optics necessary to form the probe volume and collect the light scattered from that region for processing by the DSA hardware. The light beams exiting from the fiber drive are divergent in nature as they come out of the fiber optic cables inside of the transceiver probe. These divergent beams exiting from the fibers are collimated (converted into parallel beams) by collimating lenses. The pairs of beams of the same color are made parallel to each other until they reach the focussing lens (called the transmitter lens) at the end of the transceiver probe. At the focal point, which lies inside the flow regime of interest, the shifted and unshifted beams of each color intersect to form an ellipsoidal

volume called the probe volume as shown in Fig. 4.2(a). The focal point is about 500 mm from the transmitter lens, which is located at the end of the transceiver head. The interference of the two beams also forms a bright-dark-bright light interference pattern called the fringe pattern as shown in Fig. 4.2(b). Some of the optical parameters of the LDA system are tabulated in Table 4.1.

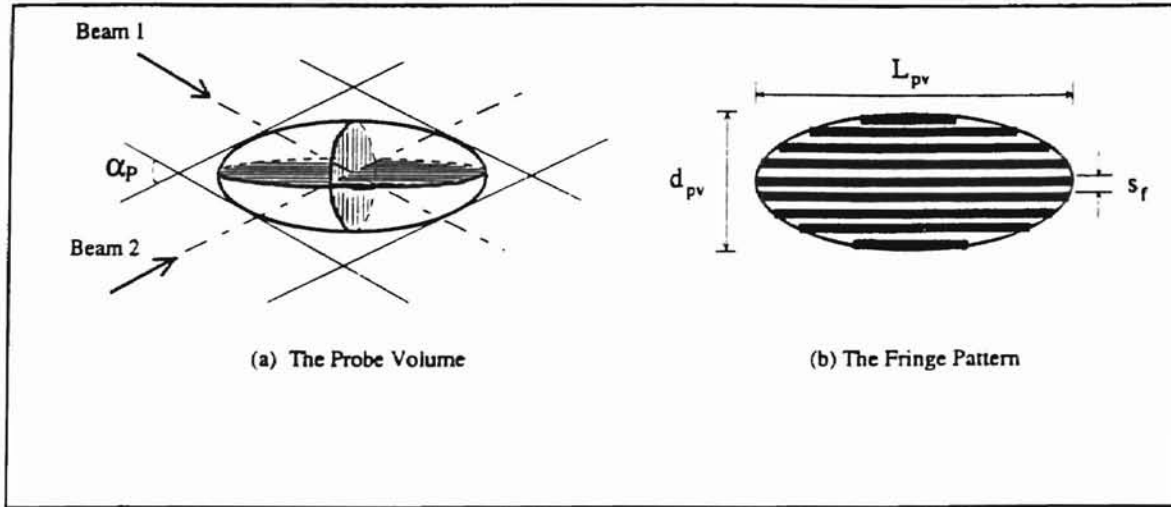


Figure 4.2 Probe Volume and Fringe Pattern [Liang, 1997].

Table 4.1 Optical Parameters of the LDA System [Liang, 1997].

Optic Parameters	Green Beams	Blue Beams
Wavelength [nm]	514.5	488
Beam diameter at the focusing lens [mm]	5	5
Angle between crossing beams [degrees]	10.32	10.32
Diameter of probe volume [μm]	66	62
Length of probe volume [μm]	733.8	689.4
Cross-section of probe volume [μm^2]	3.804×10^4	3.357×10^4
Volume of probe volume [μm^3]	1.674×10^6	1.388×10^6
Fringe spacing [μm]	2.86	2.71
Number of fringes	~23	~23

The light intensity within the probe volume has a Gaussian distribution. At the center of the probe volume, the intensity reaches its peak value and then falls to zero as the distance from the center increases infinitely. The boundary of the probe volume is defined by a limiting light intensity of $1/e^2$ [Drain, 1980] from which detectable light signals can be generated as a seeding particle passes through it.

When a seeding particle in the test flow passes through the probe volume, the light will be scattered back by the particle and the signal will match the incident bright-dark-bright light pattern superimposed on a low frequency high amplitude pedestal as shown in Fig. 4.3. The scattered light (optical signals) from a seed particle at the probe volume is received and collimated by the transmitter lens of the transceiver probe and is

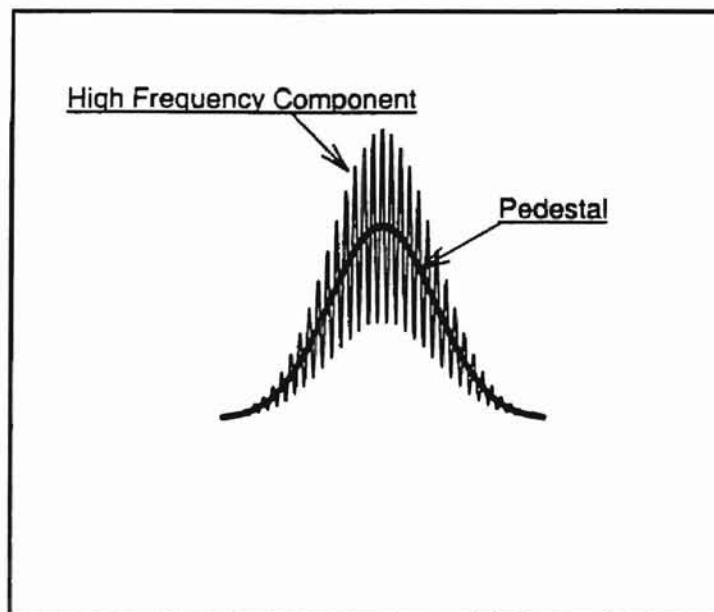


Figure 4.3 High Frequency Component Superimposed on the Pedestal.

focused into a multimode fiber. This fiber, also called the receiver fiber, directs the light away from the transceiver head back through the fiber cable to the photomultiplier tube

Oklahoma State Univ. Library

for photo detection. At the PMT the light signals are converted into analog electronic signals to be processed by the DSA hardware and software using a Fast Fourier Transform in order to calculate the velocities of the particles. The DSA parameters for operating the LDA system are set within the DSA software installed at the monitoring computer. A digital oscilloscope helps monitor the raw signals from the PMT and the processed (output) signals from the DSA hardware at various stages of the process.

Four signals are displayed on the oscilloscope screen during the experiment. The first signal (1) in Fig. 4.4 is the raw and unprocessed signal after the PMT and pre-amplifier. Next the DSA processes the removal of the Gaussian pedestal. The high pass filter removes the Gaussian pedestal and the high frequency component only is left for velocity calculations of the particles. Therefore signal (2) on the oscilloscope indicates the high pass filtered signal, which is the Doppler burst without the pedestal. Signal (3) as displayed on the oscilloscope is the log signal. It is the condition of the signal after a logarithmic amplification is done on it to increase the amplitude of the signal and compress its dynamic range. The final signal (4) on the oscilloscope is the burst detector signal, which helps to locate the burst and issue a signal to the controller to transfer the sampled signal to the buffer for processing. A digital signal processor board inside the DSA hardware box is used to compute the Discrete Fourier Transform (DFT) using a Fast Fourier Transform (FFT) algorithm. This is done to compute the frequency spectrum of the signal and hence, the velocity of the particle by inverting the frequency. The signals for each of the two channels or velocity components can be viewed independently on the oscilloscope through the BNC connectors for each channel provided on the front panel of the DSA hardware.

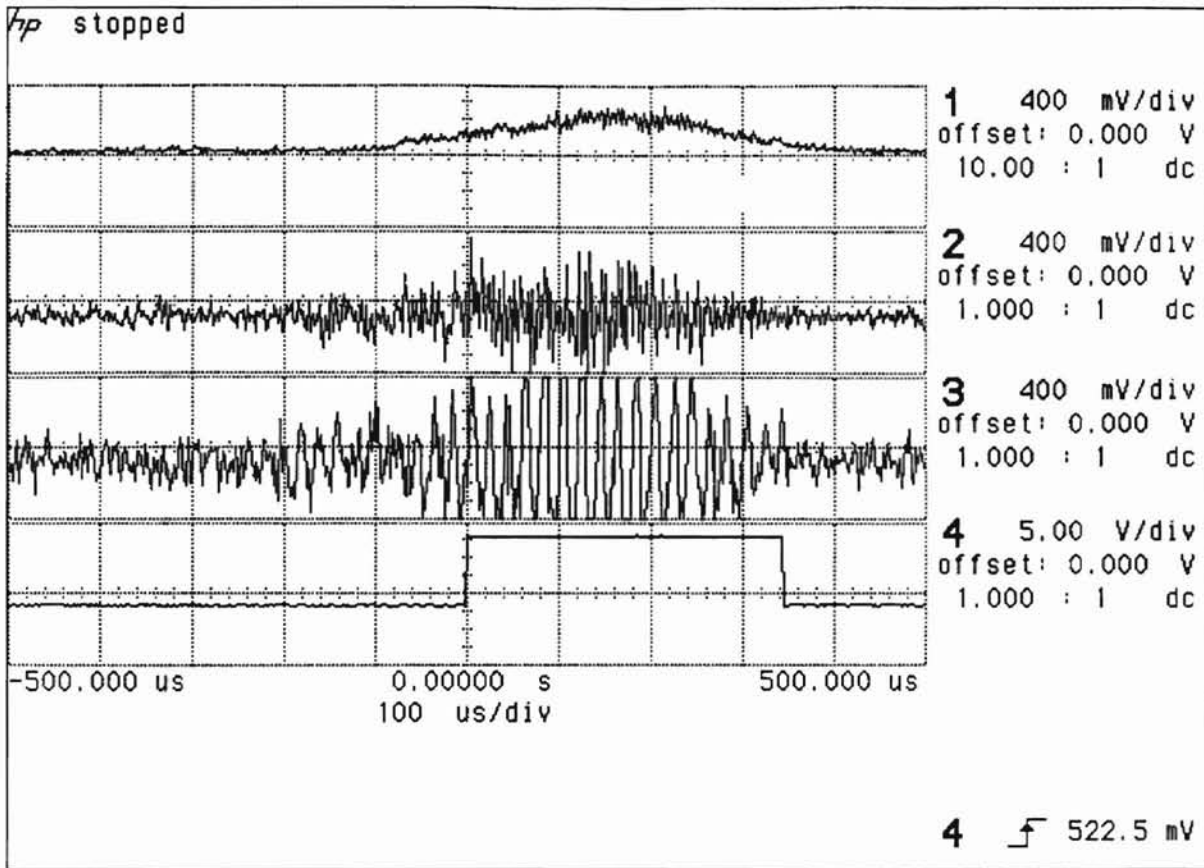


Figure 4.4 Sample Signals Displayed on Oscilloscope.

4.3 Local Filter Efficiency Measurements

The local efficiency measurements of the filter from which the overall efficiency can be found were obtained by calculating the local upstream and downstream number densities at several points on the filter using the "swept volume technique" developed by Liang [1996]. The filter was divided into a 5x7 grid point system as shown in Fig. 4.5.

Using the swept volume technique [see Appendix B], the number density, N_i , the (concentration of particles per unit volume swept out) at the i^{th} grid point, is calculated from the processed data as obtained from the computer. Thus the number density is the number of particles, n_i , divided by the volume swept out by the average velocity, V_i , of the particles collected in time, t_i , and the cross-sectional area of the probe volume, A_p .

Oklahoma State Univ. Library

The number density is calculated upstream and downstream of the filter to find the local filtration efficiency.

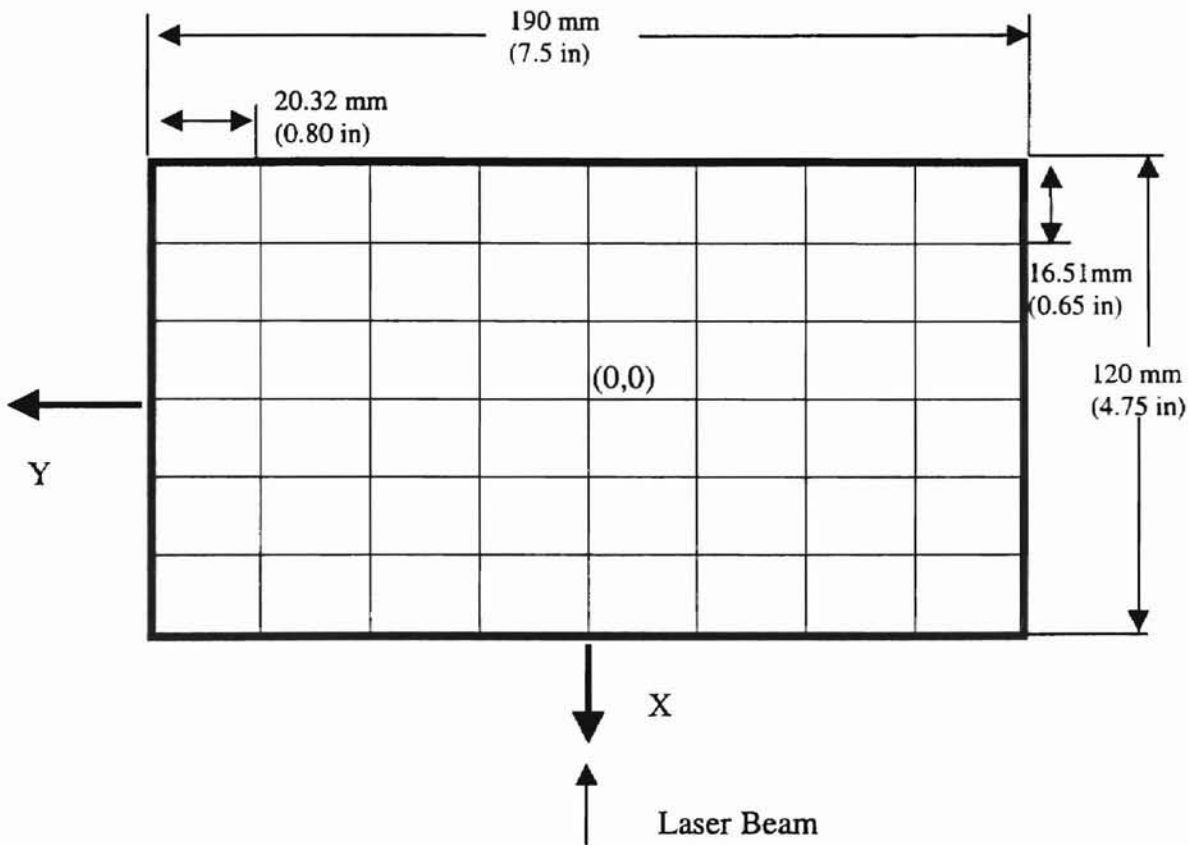


Figure 4.5 Two-Dimensional Filter Measurement Grid.

$$N_i = \frac{n_i}{V_i t_i A_p} \quad (4-1)$$

The probe volume generated by the intersecting beams can be moved around the two-dimensional filter grid system upstream and downstream of the filter by moving the transceiver probe using the three-dimensional traverse. DC stepper motors (one for each direction), controlled by a computer to which a stepper software is installed, control the motion of the transceiver (probe volume).

In calculating the number density using the swept volume technique, it is imperative to note that the number of particles (samples), n_i , be the sum of the rejected

and validated particles in order to keep track of the mass balance of the particles and minimize errors in local efficiency measurements. The maximum number density for low flow rates (less than 13 m³/hr) is of the order of 10¹¹ particles/m³ both upstream and downstream of the filter. It is also true that two or more particles may cross the probe volume at a time (simultaneously), and the LDA system may receive the light signals from all of the particles as a single signal only. At low flow rates, with a large number of particles per unit volume of the air, this could lead to negative efficiencies. Thus more than one particle may cross the probe volume simultaneously due to the high concentration of particles in the airflow which can cause high collection time upstream of the filter with consequent lower number densities. However, downstream of the filter, due to a lower concentration of particles caused by filtration, this problem is less likely to occur. In this regard, it is advisable not to heavily seed the airflow for lower flow rates.

The local filtration efficiency, η_i , can be calculated by taking the number densities upstream and downstream of the filter at the i^{th} grid location as:

$$\eta_i = \frac{N_{iup} - N_{idown}}{N_{iup}} = 1 - \frac{N_{idown}}{N_{iup}} \quad (4-2)$$

where N_{iup} and N_{idown} are the respective upstream and downstream number densities calculated using Eq. (4-1).

The overall filter efficiency, η_{overall} , is calculated from averaging the local efficiencies.

$$\eta_{\text{overall}} = \frac{\sum_{i=1}^{\text{Total Grid Points}} \eta_i}{\text{Total Grid Points}} = 1 - \frac{1}{\text{Total Grid Points}} \sum_{i=1}^{\text{Total Grid Points}} \frac{N_{idown}}{N_{iup}} \quad (4-3)$$

Natarajan [1995] calculated the overall efficiency, $\eta_{overall}$, in a different way by taking the summation of the number densities upstream and downstream of the filter as follows:

$$\eta_{overall} = 1 - \frac{\sum_{i=1}^{Total\ Grid\ Points} N_{idown}}{\sum_{i=1}^{Total\ Grid\ Points} N_{iup}} \quad (4-4)$$

The two equations give slightly different results.

4.4 Stability of the LDA System

Consistency measurements conducted by Natarajan [1995] suggest that the number density measurement at the center of the duct was dependent upon the laser power. As shown in Fig. 4.6, the number density increased steadily and then flattened out as the power was steadily increased. Since the usage of higher laser power is also a major concern to the safety of personnel, the laser power was set to a nominal operating power around 1 watt. In this and all other previous experiments, the laser power used was 0.8 watt measured at the exit of the laser tube. However, due to losses during coupling at the fiber drive and inside the optic fiber cables, the transmitted power efficiency measured at the transceiver probe may not exceed 50%.

From Natarajan's [1995] poor repeatability results and Anand's [1997] consequent work on the stability of the laser, there was a need to investigate the stability of the laser power so that the size (light intensity) of the probe volume remained constant throughout the experiment in order to get consistent number density measurements. Consistency measurements in the present study (see Chapter V) reveal that as the laser power changes with time, the number density also changes, because of the low intensity

of scattered light (signals) and hence low detection of particles which can lead to inconsistent local and overall efficiency measurements.

The author together with Saxena [1998] conducted several experiments to determine the potential sources of the unstable laser power. The following factors were considered first for investigation:

1. variation of temperature of the laser cooling water,
2. vibration due to the blower,
3. air currents around the laser and fiber drive,
4. and temperature variation around the couplers and fiber drive including the aluminum breadboard mounting.

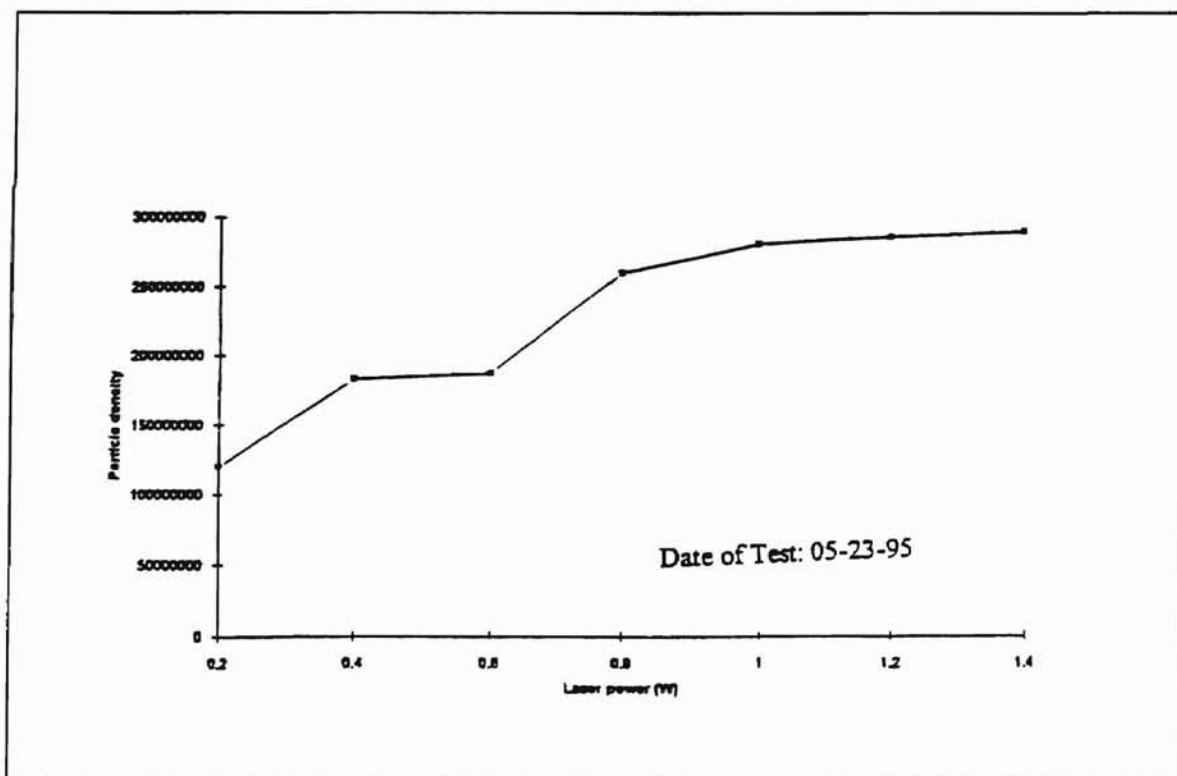


Figure 4.6 Dependence of Number Density upon Laser Power [Natarajan, 1995].

The effect of laser tube cooling water temperature variation on laser power measured at the transceiver was monitored while other factors were not controlled. A

thermometer was also installed to monitor the temperature variation of the cooling water at the inlet and outlet of the laser tube. However, experimental results as shown in Figs. 4.7 and 4.8 indicated that there was a power variation, even if the cooling water temperature remained steady at the inlet and outlet of the laser tube for some time. Thus the effect of the cooling water temperature was excluded as a major source of problems provided that the cooling water temperature and pressure were maintained within the recommended operational ranges as supplied by the manufacturer.

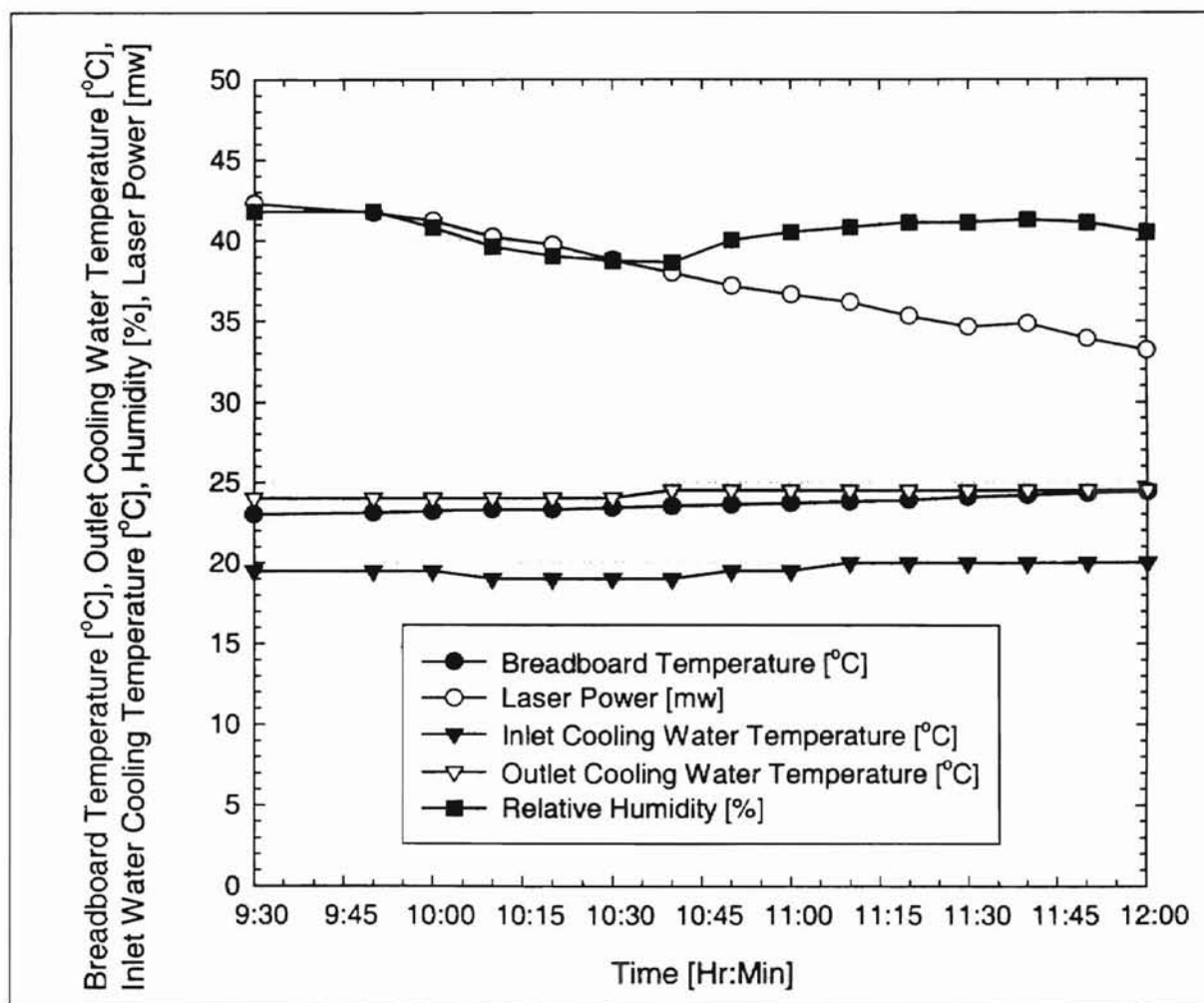


Figure 4.7 Variation of Laser Power with Bread Board Temperature as Humidity and Cooling Water Outlet and Inlet Temperatures into Laser Tube Jacket Remained Stable within 1°C (June, 1997).

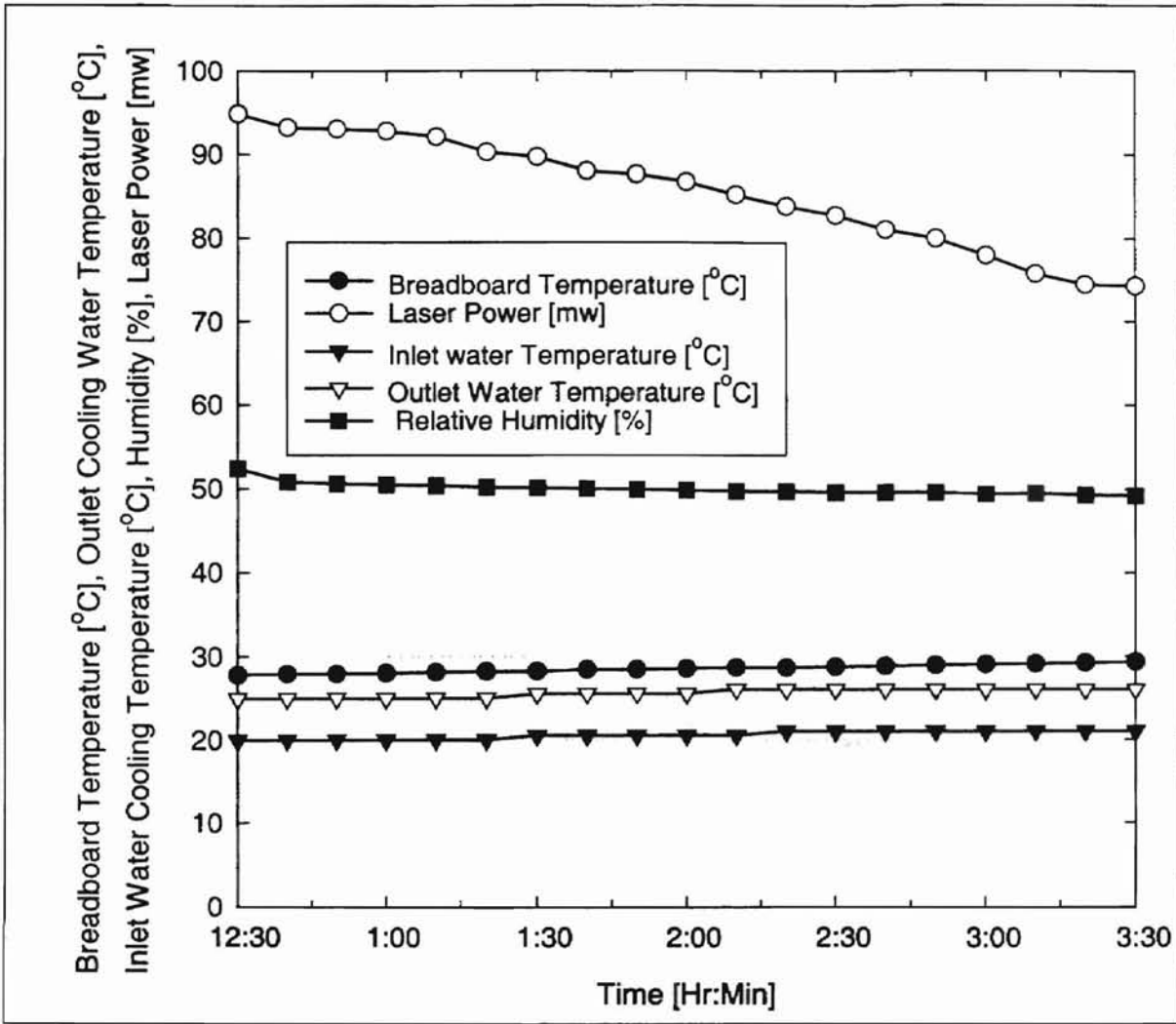


Figure 4.8 Variation of Laser Power with Bread Board Temperature as Humidity and Cooling Water Outlet and Inlet Temperatures into Laser Tube Jacket Remained Stable within 1°C (May, 1997).

The effect of vibration (due to the blower) on the stability of the laser was also investigated. Repeated experiments on the measurement of the power of the shifted and unshifted beams, while the blower was on or shut off, showed that there was not any direct or induced (resonance) vibration effects from the isolated but vibrating electric motor of the blower. The power of the shifted and unshifted beams suffered losses, whether the blower was on or shut off, whenever the temperature at the couplers changed

[Saxena, 1998]. Hence Anand's [1997] speculation that the vibration from the blower was one of the major causes could not be verified. The humidity of the air inside the room was also monitored and plotted against time, but did not contribute to the instability of the laser system.

The other possible cause behind the laser power fluctuations was temperature variations around the fiber drive unit (couplers and internal mirrors), the breadboard, and external steering mirrors as shown in Fig. 4.9.

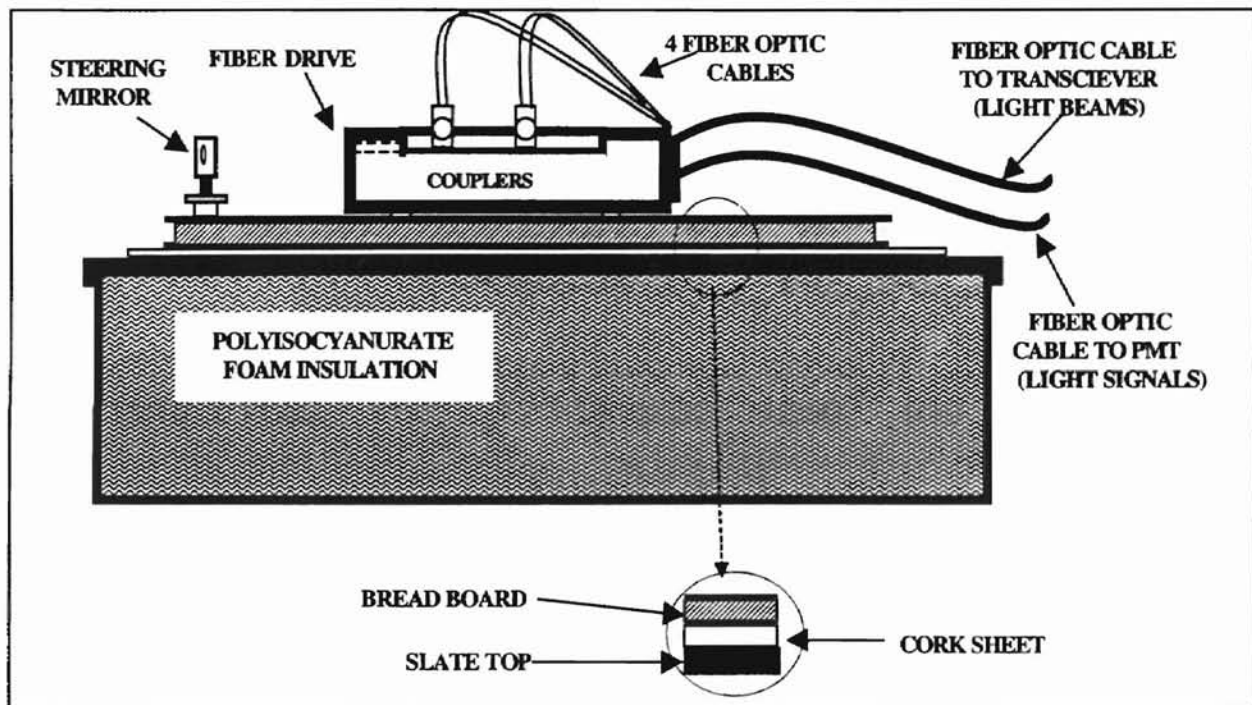


Figure 4.9 Fiber Drive Setup on an Insulated Metal Table.

Figure 4.10 shows the variation of laser power measured at the transceiver probe as the breadboard or coupler temperature changed with time. From the laser stability experiments, it was understood that, to maintain stable laser power, it was important that the temperature around the breadboard, couplers, and laser drive unit remained stable.

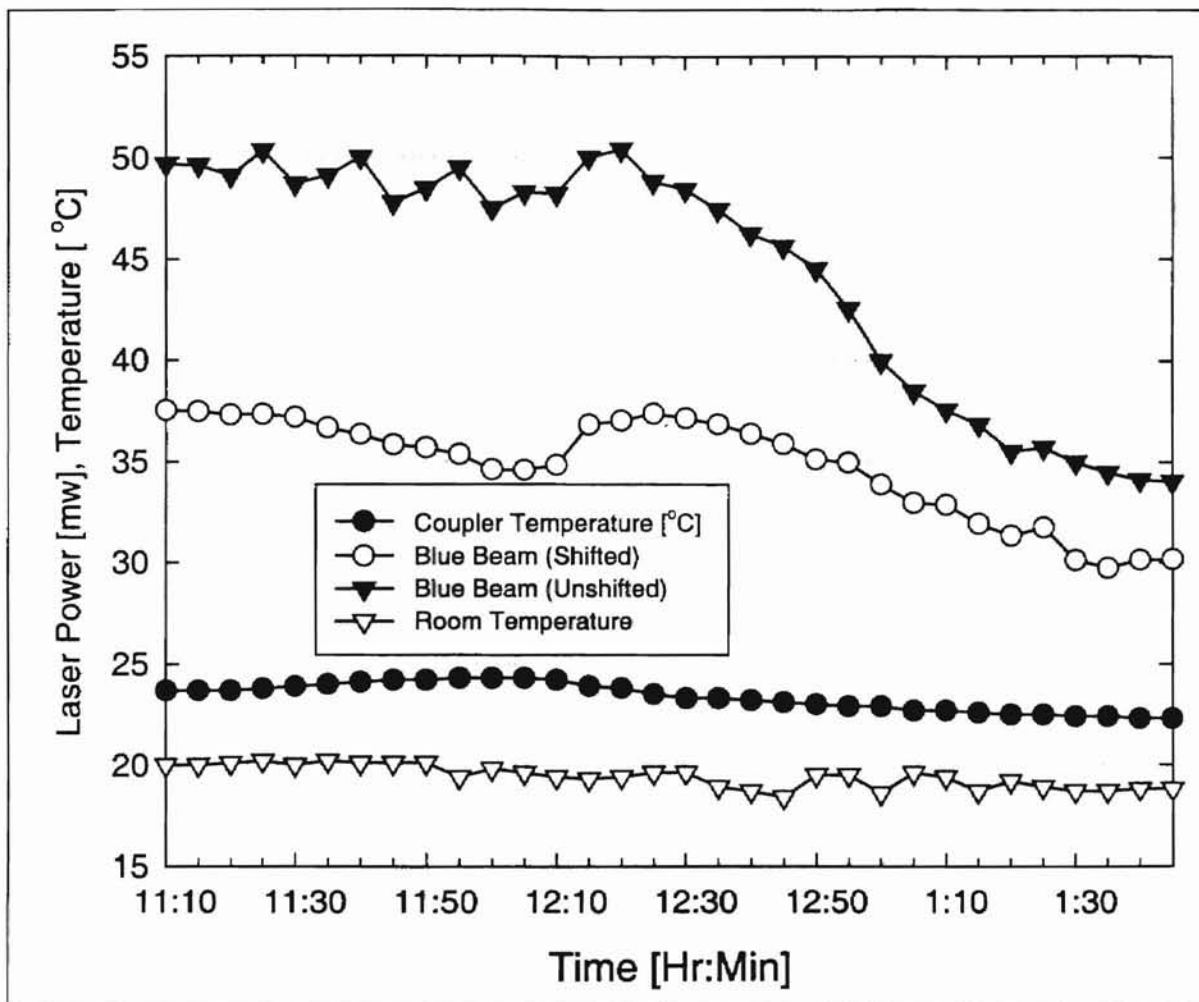


Figure 4.10 Power Variation As a Function of Time for Shifted and Unshifted Beams.

Some experiments using pinhole apertures were also conducted by preparing a cylindrical tube shown in Fig. 4.11 as a pinhole aperture holder at both extreme ends to simulate the couplings and misalignment of the light beams inside the couplers. The coupler of each beam was replaced each time by the cylindrical tube to see the effect of temperature on the misalignment of the light beams. The apertures used were with 200 and 50 μm pinholes press fitted into the tube and located at both ends of the cylindrical tube. As the temperature varied, the beams suffered power losses as measured at the transceiver probe. This indicates that misalignment of the beams due to temperature variation could be a

crucial factor. Thus maintaining stable temperature at the couplers and fiber drive units is critically important.

To maintain stable temperature and offset the continuous heat load that comes from the blower and air heater, an additional air conditioner was installed in the data acquisition room. A partition was made between the data acquisition room and the test stand room using a tarp so that the air conditioner effectively maintained the desired temperature at the couplers. The tarp helped to confine the conditioned air and stop any convective heat transfer between the two rooms.

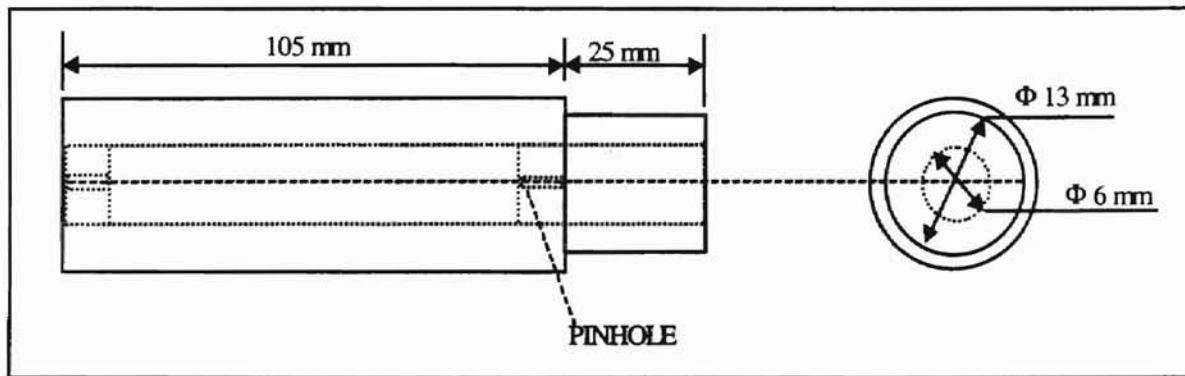


Figure 4.11 A Cylindrical Tube for Holding Pinhole Apertures.

However, after some repeated experiments, the author found that there had been at times some laser power loss (up to 12%) even after all of these solutions and procedures were implemented. Further observations and experiments showed that uneven temperature variation around the table (metal), upon which the fiber drive and laser tube were mounted also could be responsible for the power loss. The author believed that uneven thermal expansion and contraction of the table legs could change the level of the table and the breadboard, and thus could cause misalignment of the beams.

From these experiments, the author decided to put a polyisocyanurate insulation foam board (galvanized by aluminum foil) around the table as shown in Figs. 4.9 and 4.12.

The author finally concluded that monitoring the temperature around the couplers is the most crucial task that must be given due attention in order to produce relatively stable laser beam power. Therefore the temperature of the couplers was monitored during the real filtration experiments by installing an Omega RH21 thermometer (temperature sensor) having an accuracy of ± 0.1 °C.

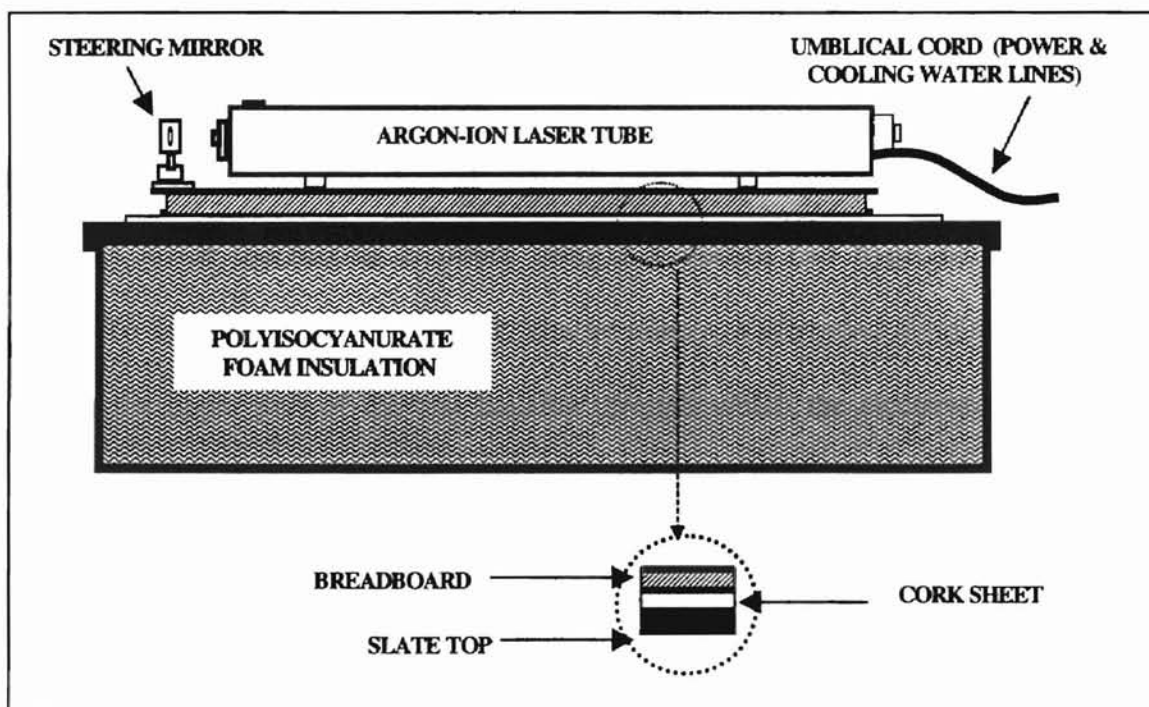


Figure 4.12 Laser Setup on an Insulated Metal Table.

4.5 Experimental Flow Setup

In this section the experimental setup used for the local filtration efficiency measurements will be presented.

4.5.1 General

The schematic of the experimental flow setup for conducting experiments on the effect of electrostatic charge and humidity on the overall efficiency of the A13192 filters is shown in Fig. 4.13. A suction blower draws air from the room through an electric air heater that preheats the air to a few degrees above the room temperature, and the air then flows towards the filter through the PVC piping, the mixing chamber, and the upper housing. A suspension of 0.966 μm PSL particles is injected into the preheated air flow by a six-jet atomizer at an atomization pressure of 248 kPa (36 psi). The preheated air dries the atomized water droplets and particles. To ensure uniform mixture of the air and particles, a mixing chamber is used. The humidity and temperature of the air are also monitored inside the mixing chamber using a Sunbeam hair hygrometer-thermometer device. To investigate the electrostatic charge effects, a grounded aluminum foil is used to cover the upper part of the test housing through which the electrostatically charged aerosol particles flow to the filter. At the filter, the required number of particles is detected using the LDA system upstream and downstream of the filter. Finally the filtered air with some trace of the contaminant particles passes through an absolute filter to be discharged to the atmosphere by the blower. The pneumatically operated control panel sets the amount of air that passes through the TSI flow meter via the filter.

4.5.2 Seeding Aerosols by Atomization

In fluid flow measurements, the velocity of the fluid is of primary interest; and the LDA system uses light scattering particles for this purpose. This implies that the LDA actually measures the speed of the particles. Hence it is important that there is consistent

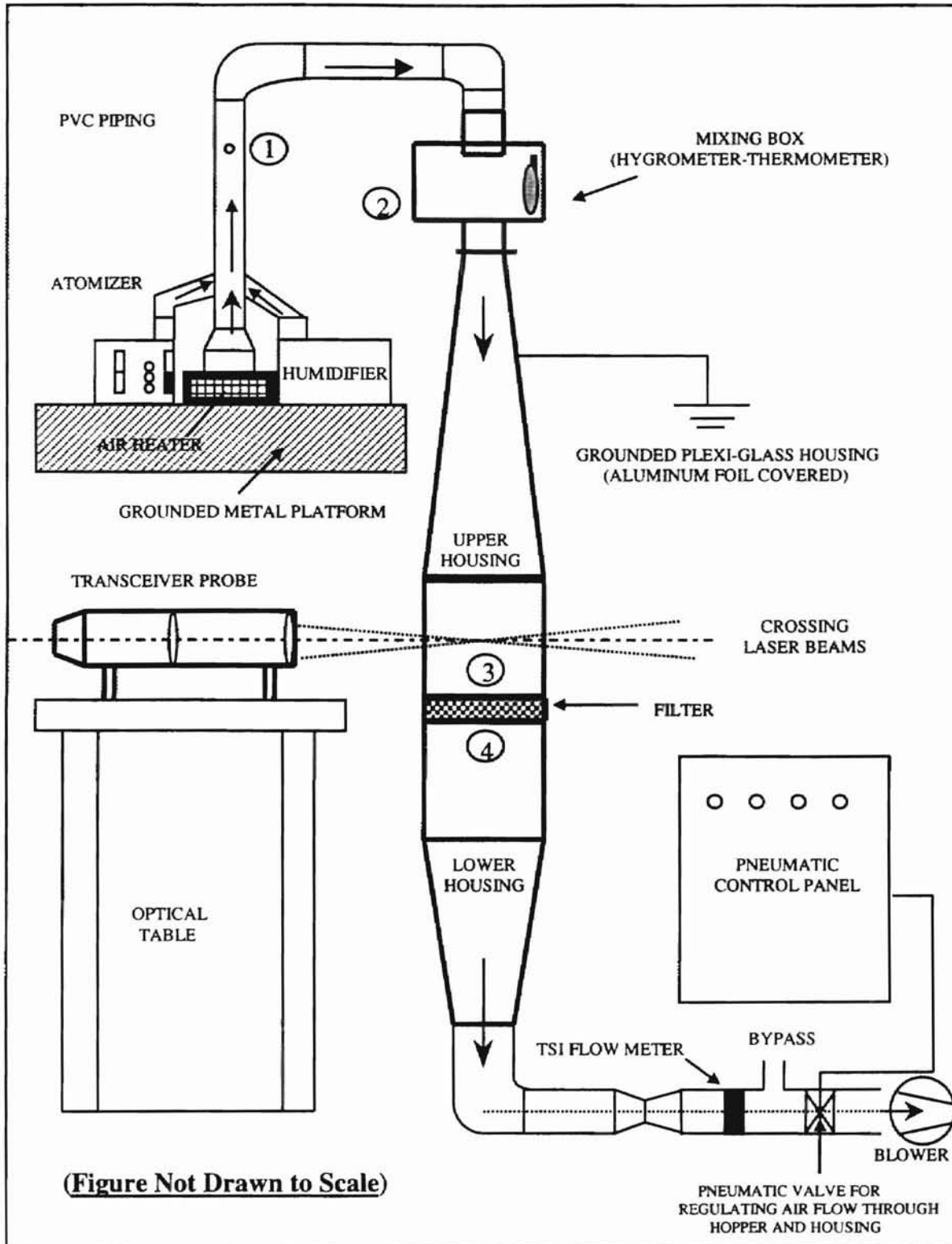


Figure 4.13 Experimental Setup.

particle generation, and a sufficient number of particles with appropriate size and density.

Some of the requirements of the seed particles include:

- (a) ability to scatter sufficient light;
- (b) the tendency to follow the flow measured by an aerodynamic diameter, D_a as: $D_a = D_p \sqrt{\rho_p}$ where D_p is particle size and ρ_p is particle density. D_a should be small;
- (c) a sufficient concentration to produce the desired data rate for the LDA system;
- (d) suitable physical and chemical properties (inert and non toxic);
- (e) ability to survive the environment; and
- (f) low cost.

The method used for the generation of the aerosol particles was the pressure atomization of suspensions of PSL particles by an atomizer with subsequent evaporation of the suspended liquid droplets. Atomization is a process in which a high velocity air jet produces a fine spray of droplets by shearing off a liquid film. The model 9306 TSI atomizer consists of three control valves, a pressure regulator, a liquid level gauge and a reservoir with a capacity of 700 ml. In the body of the atomizer, there are six atomizer assemblies that can be used at one time. The atomizer assembly consists of a liquid tube, a spherical impactor to break the atomized droplets by impaction, and an atomizer jet. The control valves control the atomizer jets. Each control valve is labeled with the number of jets that it can control. The valve labeled "1 Jet" controls one jet; the valve labeled "2 Jets" controls two additional jets, whereas the valve labeled "3 Jets" controls three additional jets. The total aerosol (particle) output is proportional to the number of

jets used and the input pressure.

In this experimental study, a PSL suspension of 5 ml at a concentration of 10% (by weight) solids was used for every 995 ml of distilled water in order to prepare a solution of 1000 ml for flow rates below and including 77.1 m³/hr. For higher flow rates (above 77.1 m³/hr), the amount of solution used was 10 ml for every 990 ml of water. The atomizer was operated with purified air at a pressure of 248 kPa (36 psi), which may also be used to change the dilution ratio of the air-liquid solution, using the dilution system of the atomizer.

4.5.3 Air Humidity and Temperature Control

The humidity and temperature of the air (used for the filtration process), as it is drawn into the housing, is controlled by the settings of the heating and humidifying devices installed at the inlet of the experimental setup as shown in Fig. 4.10. While the electric heater, with alternate power capacities of 1300 and 1500 watts, was used to control the temperature and humidity, an ultrasonic humidifier was installed to help achieve higher humidity requirements. This humidifier injected mists of distilled water for lower air flow rates below 229.7 m³/hr (150 scfm). A regulating valve was installed to regulate the amount of vapor or mist entering the system depending upon the desired humidity of the air. A room air conditioner and a heater also helped to condition the room air so that the temperature of the room remained stable for most of the experiment. A mechanical hygrometer-thermometer device installed at the mixing box was used to monitor the instantaneous humidity and temperature variations of the air. Prior to the investigation of the effect of humidity on the efficiency of fibrous filters, several

preliminary humidity measurements upstream and downstream of the filter were taken so that one can predict the amount of water that can be removed or absorbed by the filter. Thus two Omega model RH21 (digital temperature and humidity sensing devices) were installed upstream and downstream of the filter to simultaneously record the temperature and humidity changes with time as the air flowed in the duct for different flow rates.

4.5.4 Electrostatic Charge Neutralization

The neutralization of the electrostatic charge in this experiment was accomplished by securing a firm contact between the external surface of the plexiglass housing and an aluminum foil covering that was grounded by a copper wire connected to a water pipe. The neutralization process involves the transfer of charge from the statically charged particles and plexiglass to the ground. The most interesting concept here is that, even though plexiglass is a poor conductor of electricity, it does not appear to seriously hinder the discharging (maybe by induction) of the electrostatically charged particles in the duct.

To explain the principle of charge neutralization, it may be important to see the discharging mechanisms of a charged conductor (metal) and a charged insulator (nonmetal) as shown in Fig. 4.14. From Fig. 4.14(a), in the absence of external field influences, the charge on a conductor will be uniform in magnitude and polarity. For a charged insulator, the charge distribution is localized as shown in Fig. 4.14(b); i.e., the charge in different locations can be different in magnitude and polarity. This major difference in the behavior of conductors and insulators is due to the high mobility of charge in conductors and the almost nonexistent mobility of charge in insulators. By the same token, this difference in the mobility of charge explains why a conductor loses its

charge quickly when grounded; and an insulator remains charged as shown in Figs. 4.14(c) and 4.14(d) [McAteer, 1989].

The author of this study tried the above grounding system (using a single grounded copper wire to the surface of the charged plexiglass housing) to neutralize the charges and partially verified the above theory. However, it must be clear that if an effort is made to connect as many grounded conducting wires as there are localized charged surfaces (pockets), it is possible to transfer charge both ways from those local surfaces of

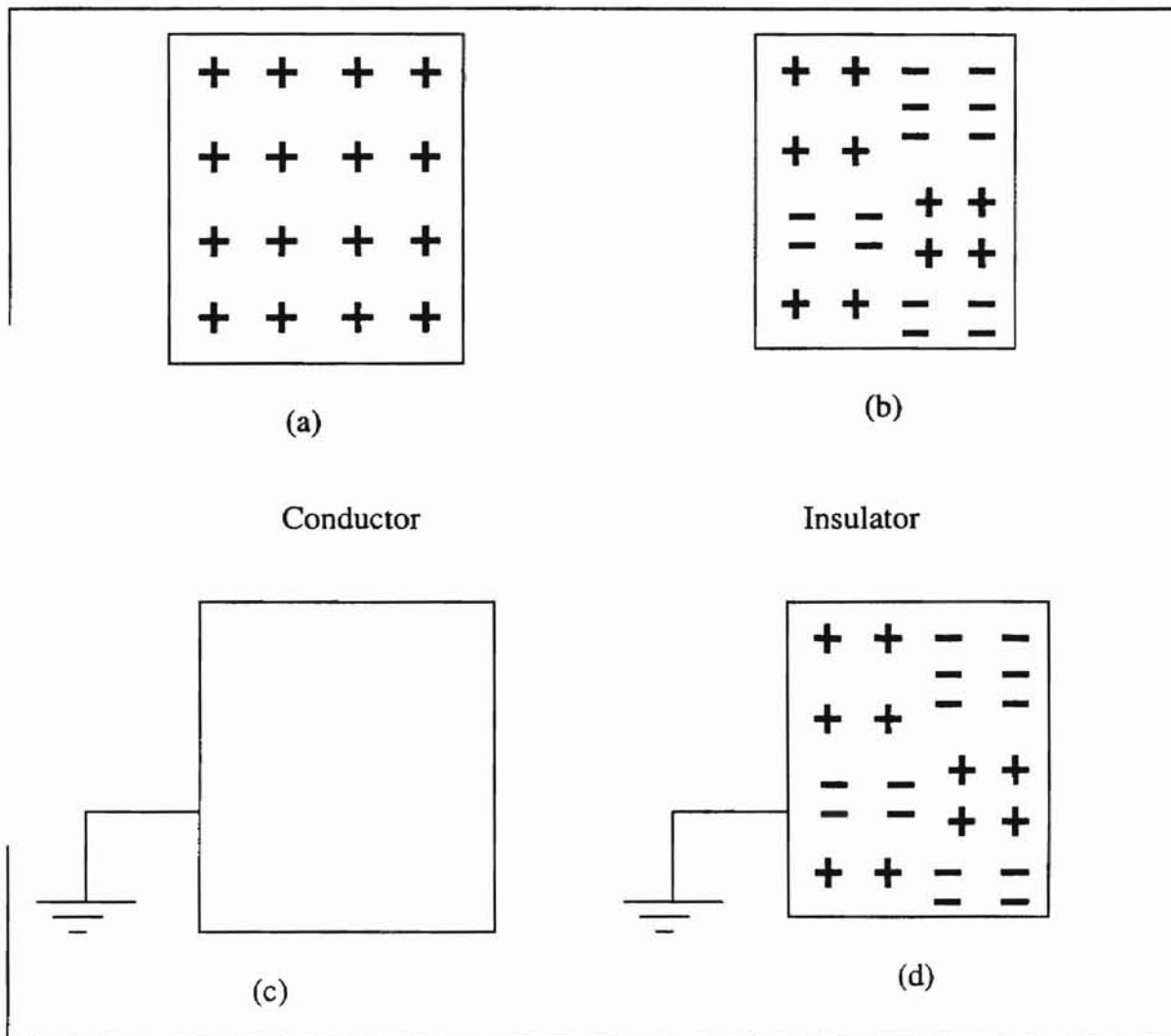


Figure 4.14 Behavior of Charged Materials: (a) Ungrounded Charged Conductor, (b) Ungrounded Charged Insulator, (c) Grounded Conductor, (d) Grounded Insulator.

insulator until it is completely neutralized. Thus the limit of putting many conducting wires on the surface of the charged insulator as the number of local surface areas tend to infinity, implies the need to completely cover the insulator surface with a conductor. It is this analogy that led the author to the successful discharging of the charged particles and plexiglass housing by covering it with grounded aluminum foil.

Another question the reader may raise concerns the transfer of charge from inside of the plexiglass housing and from the charged particles inside the flow to the conducting aluminum foil as diagrammed in Fig. 4.15. The mechanism of charge transfer or neutralization seems to be a complicated phenomenon. However, the author believes that

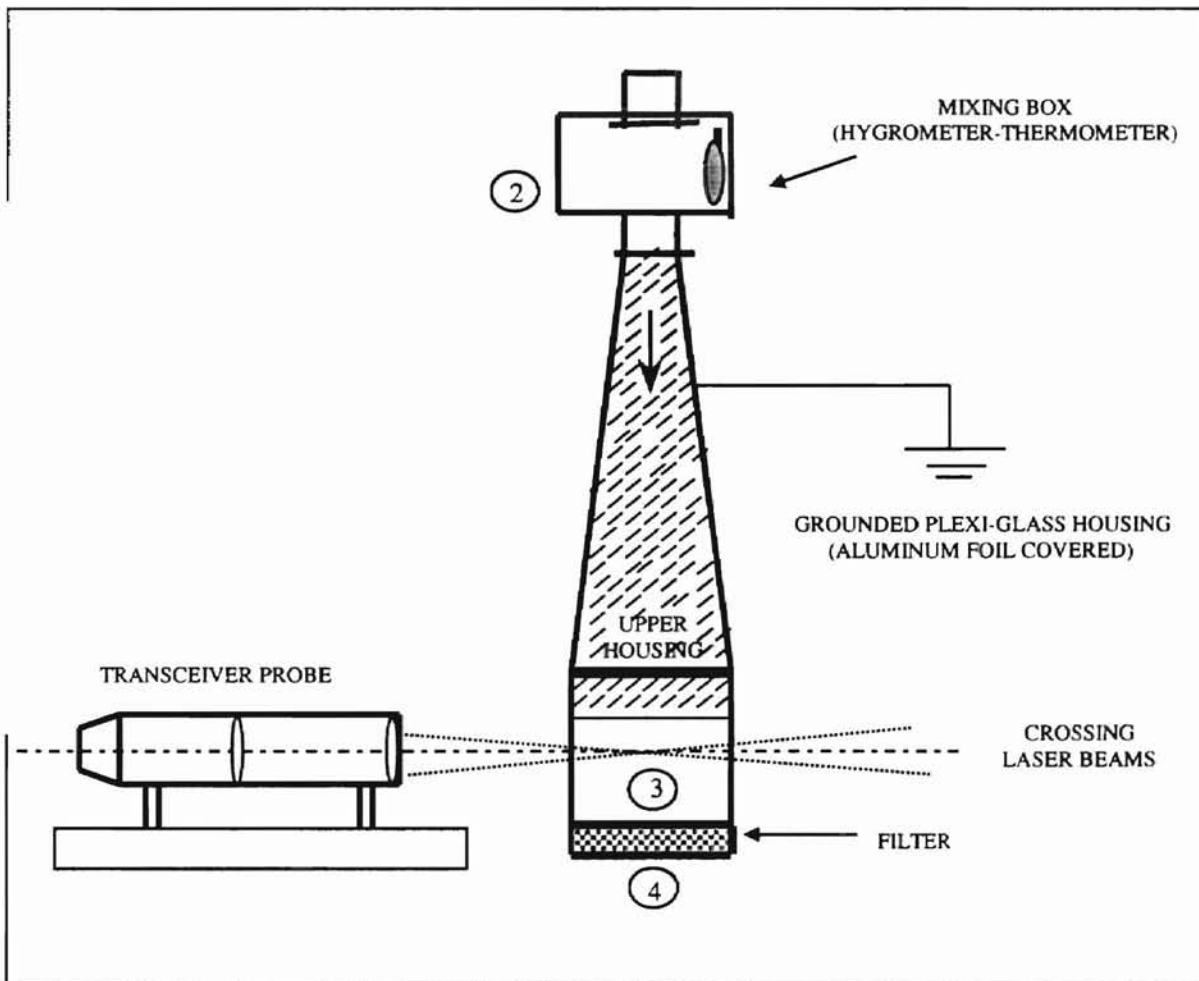


Figure 4.15 Charge Neutralization Setup (Upper Half of Housing).

the transfer of charge may occur by induction or polarization effects. This implies that the electric field of the charged particles or the charged internal surface of the plexiglass can induce opposite charge on the surface of the grounded aluminum foil or the vice versa. One must also remember that the ground is the source of unlimited negative charge. Also the charged particles, as they flow through the duct, can induce an opposite charge on the aluminum foil, which in turn is discharged by the grounded aluminum foil, while rendering opposite charge in the particles to neutralize them.

To support this argument, the author would like to present a study done by Bouguila et al. [1993] on the painting of insulators using conventional electrostatic painting techniques and the simulation of the decay of charge using corona discharge by ionized air to effectively and qualitatively paint the insulators. They have confirmed that a grounded counter electrode on the back face of the sample speeds up the decay of charge, and that the better the contact the faster the decay. Hence grounding the opposite face of the insulator with a conductor enhanced uniform painting by avoiding the accumulation of charge that can prevent the accumulation of charged paints with consequent nonuniform painting.

In this study, the measurement of electrostatic charge quantity was indirectly determined using an electrostatic field meter manufactured by ETS Electro-tech Systems, Inc. The electrostatic field meter was used to measure the electrostatic potential of the charge inside the flow by bringing the meter to a distance of about 5.1 cm (~2 inches) from the external surface of the plexiglass housing. Electrostatic voltage measurements were taken at three different locations, namely at the mixing box, upstream, and downstream of the filter. The electrostatic charge voltage reading is proportional to the

amount of charge on the surface of the charged body, distance of the electrostatic field meter from the charged surface, and the surface area of the charged body.

4.6 Air Flow Rate and Pressure Drop Measurements

The constant airflow across the filter was monitored using a model 2018 TSI flow meter, which was installed in the fully developed section of the duct far from the downstream side of the filter. The manually operated pneumatic control panel (with automatic option) controls the amount of air passing through the filter during the experimental filtration process. The experimental setup was designed for a constant mass flow rate by maintaining constant air properties (temperature and pressure). The TSI flow meter readings were in standard cubic feet per minute that can give the corresponding mass flow rates for a constant air density at standard conditions (at a temperature of 21 °C and a pressure of 1 atmosphere). The pressure drop across the filter was measured at the initial and final stages of the filtration experiment, using a graduated manometer (water column) with an accuracy of a tenth of an inch connected to pressure taps located at about 1.3 and 0.8 m upstream and downstream of the filter, respectively.

4.7 Small Angle Diffuser Housing

The filter test housing was built in the laboratory and was reasonably similar in construction to the housing specified in the SAE J1669 Cabin Air filtration Code [SAE, 1993], except for minor changes in the dimensions and the angle of divergence of the walls of the diffuser section. The diffuser section of the upper housing has a gradual angle of divergence of 6.34° to avoid recirculation and separation of the flow due to an

unfavorable pressure gradient that consequently could generate nonuniform pressure and velocity distributions upstream of the filter surface. Figure 4.16 shows some of the constructional features of the small angle diffuser housing.

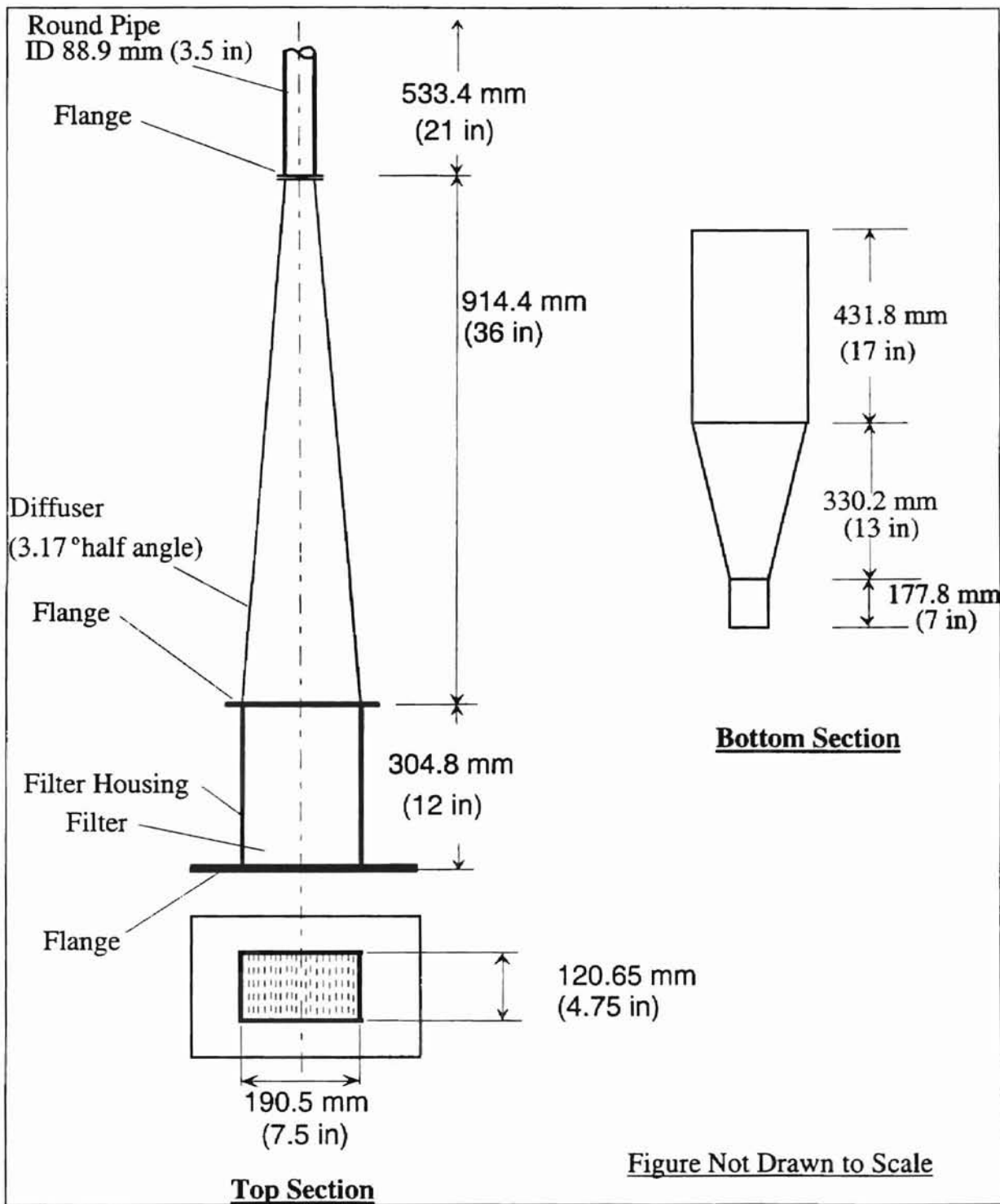


Figure 4.16 Small Angle Diffuser Housing Construction Details.

4.8 A13192 Test Filter

The filters that were employed in this study were the Dayco-Purolater model A13192 pleated test filters. The test filter is composed of fibrous cellulose paper with a nominal design flow rate of 187.7 m³/hr. Some of its technical parameters are listed in Table 4.2 below [Duran, 1995].

The supporting wire mesh of the filter (shown in Fig. 4.17) is used for the reinforcement of the filter might have a paramount importance in the discharging of electrostatic charge. Though the filter wire mesh is isolated from the ground by glass mounts and seals, the author believes that, due to the wire mesh's high conductivity and possible induction (polarization) effects, it may play a big role in evenly distributing the

Table 4.2 Selected Technical Parameters of Test Filter A13192.

Filter Parameters	Values
Width	121 mm
Height	193 mm
Pleat Height	30 mm
Pleat Pitch	3.125 mm
Fiber Diameter (Estimated)	51.78 um
Packing Density (Estimated)	0.345

electrostatic charge. The source of charge on the wire mesh could be due to charged particles flowing past it or due to previously deposited charged particles on the upstream side of the filter by induction. The author believes that the wire mesh might have contributed to the low detection (measurement) of electrostatic voltage downstream of the filter due to its high conductivity of charge to the neighboring metal structure that supports the filter housing. Figure 4.17 shows the schematic drawing of the filter and the wire mesh.

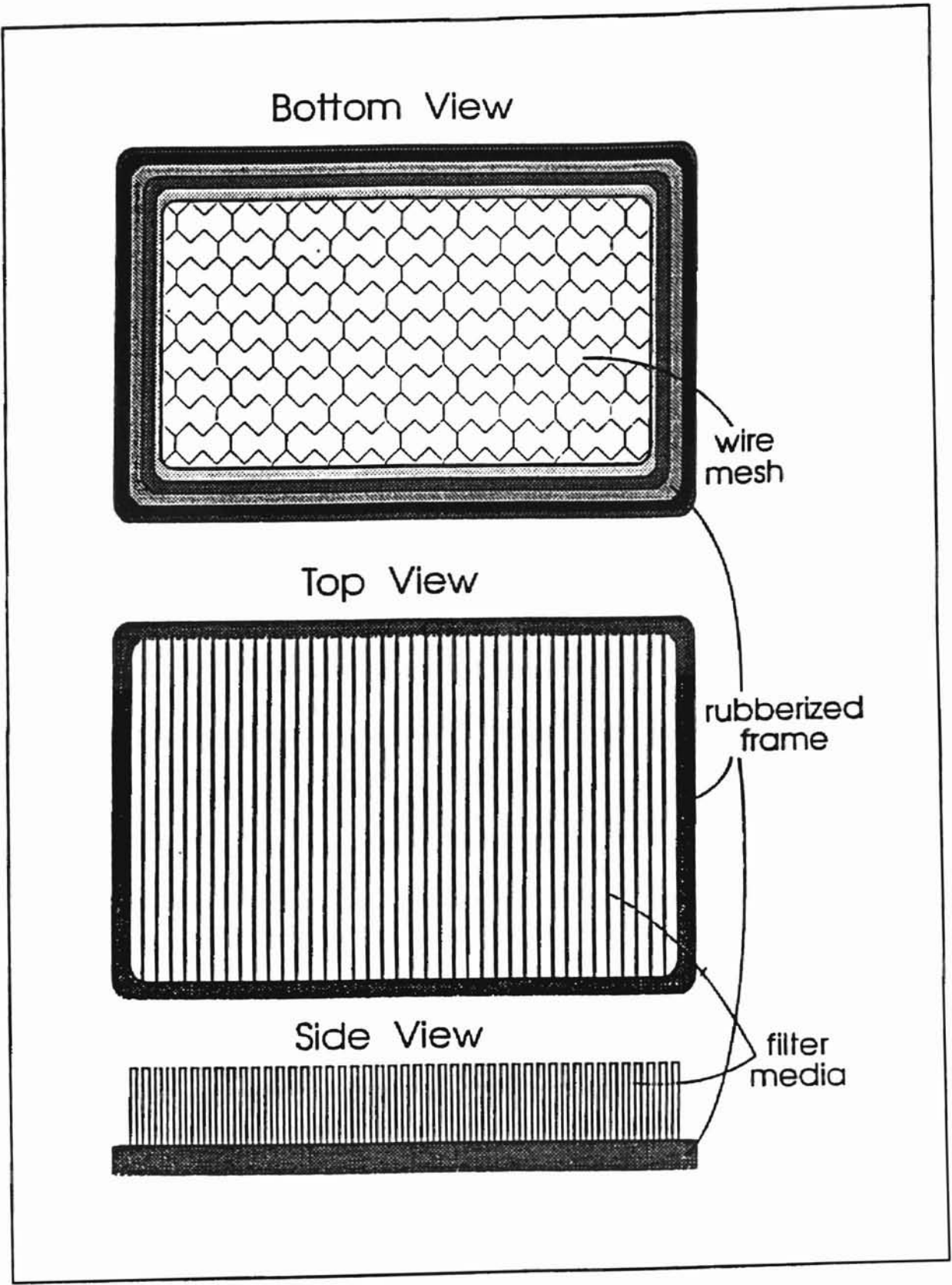


Figure 4.17 Schematic Drawing of the Model A13912 Test Filter.

4.9 Experimental Procedure

In this subsection, the procedure for efficiency measurements in investigating electrostatic and humidity effects using the LDA system will be presented. The following general procedure was followed:

1. A new filter is placed in the experimental setup and tested for any leakage using the soapy water test, by blowing air into the housing to pressurize the system. The soapy water was applied on the external surface of the housing including the duct system. Usually the leakage testing along the filter housing and duct system all the way up to the TSI flow meter took about 45 minutes.
2. For each experiment, after replacing the filter, improper filter seating and leakage problems were also indirectly checked by measuring the pressure drop across the filter at a certain flow rate and comparing it to a previously measured pressure drop for the same flow rate. Thus, for this purpose, pressure drop versus flow rate data (as shown in Table 4.3) or pressure versus flow rate (plotted in Fig. 4.18) for new filters was established before hand.

Table 4.3 Pressure Drop Variation across a New Filter As a Function of Air Flow Rate.

Flow Rate (m ³ /hr)	21.4	29.3	37.2	45.0	60.8	76.6	92.3	95.2	103.6	112.0	128.7	145.4
Pressure Drop (mm H ₂ O)	1	5	5	5	5	8	10	17	18	20	23	28
Flow Rate (m ³ /hr)	162.1	178.9	195.6	212.3	229.1	270.9	312.7	354.5	396.4	438.2	480.0	521.8
Pressure Drop (mm H ₂ O)	33	37	43	52	61	84	109	135	163	198	234	282

3. The humidity and temperature of the room were recorded each time before conducting any filtration efficiency experiment in order to help regulate the

humidity and temperature of the flow by selecting the appropriate settings of the heater and humidifier.

4. The blower, heater and humidifier (depending upon the condition of the inlet air and its flow rate to meet high humidity requirements) were turned on. Before the experiment was initiated, the atomizer was also filled with distilled water and turned on to atomize the distilled water so that a steady-state condition was established in the filter housing before the actual atomization of the PSL solution. The flow rate of air was set at the pneumatic control panel (see Fig. 4.13) to the desired flow rate with the help of the TSI flow meter (see Fig. 4.13).

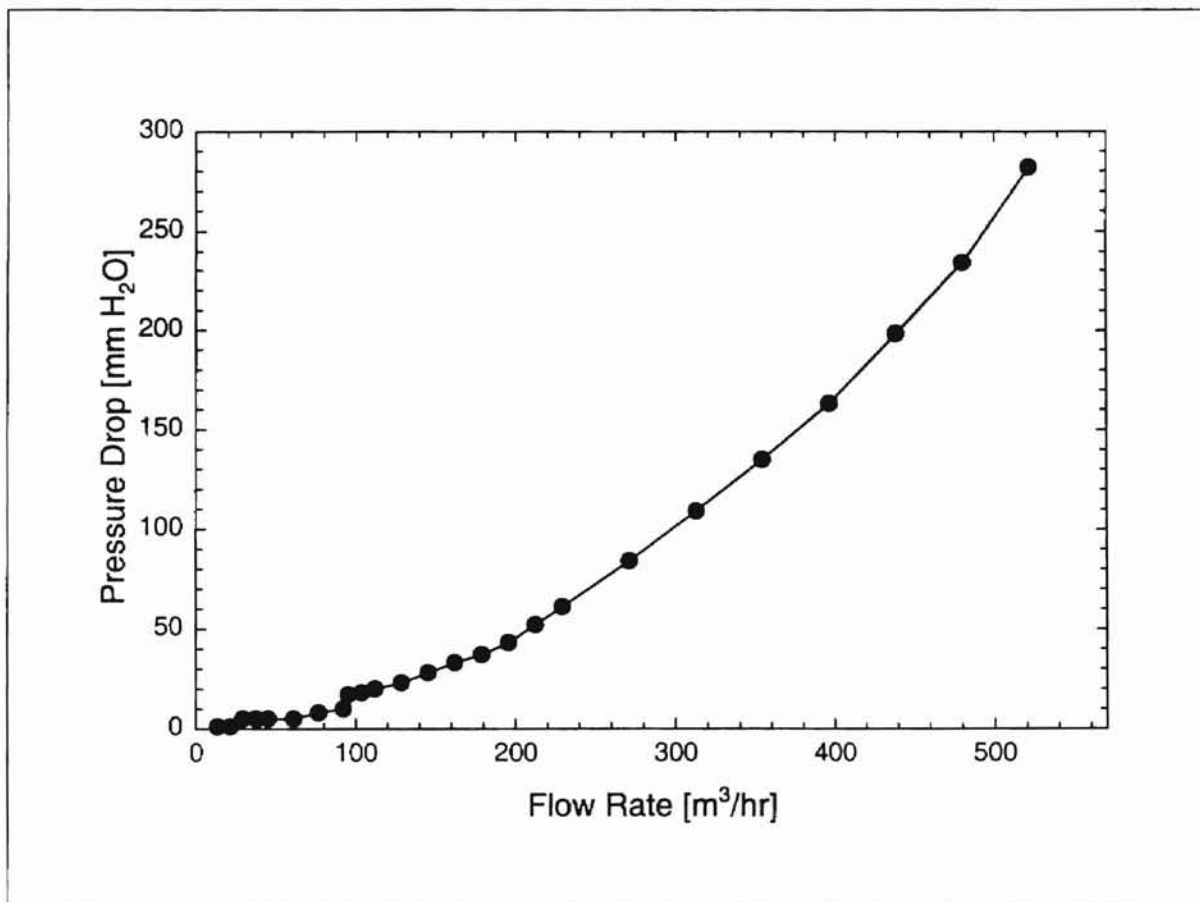


Figure 4.18 Initial Pressure Drop across Filter Versus Flow Rate.

5. Following the operational manual of the LDA system [Aerometrics, 1992], the laser was started and left idle until its power stabilized (at least for 30 minutes). Simultaneously the temperature of the couplers, breadboard and data acquisition room reached steady-state (within 25-30 °C) within 45 minutes by recirculating the air within the room using two fans.
6. In the mean time, 500 to 750 ml of PSL solution was prepared at the required concentration and placed in the atomizer, which was connected to a compressed air supply at a pressure of 248 kPa (36 psi).
7. Once the temperature of the room was stabilized (within 50 minutes), the laser beams were focused using the focusing knobs at the couplers for an efficient coupling of the beams to the respective fiber optic cables for each beam.
8. The compressed air supply valve was opened to start the atomization of the PSL particles so that the probe volume created by the crossing beams could be seen wearing laser goggles to bring it to the center of the filter (about 15 mm above its upstream surface and about 50 mm (~2 inches) downstream of the filter). [Even though for technical reasons (due to the cumulative thickness of the filter rubber seal and filter support and the need to avoid the clipping of laser beams) the measurements are taken far away from the downstream surface of the filter, efficiency measurements are not adversely affected as one would think. Since the cross-sectional area of the duct remains constant within a length of 430 mm (17 inches), the flow velocity due to the jet effect of the air flow downstream of the filter and the concentration of the particles inside the jet flow are believed to remain unchanged over a short length]. Then the optimum DSA parameters

were set by trial and error until good signals were displayed on the oscilloscope. These signals include the raw unprocessed signal after the photomultiplier tube and amplifier, the Doppler burst without the Gaussian pedestal, the logarithmic amplification of the signal (to increase the signal), and the burst detector signal [Aerometrics, 1992]. The typical and critical DSA parameters [for definition refer to the Aerometrics manual] for low and high flow rates that needed careful selection to get good signals were the high voltage, the sampling rate, number of samples and the measurement range (maximum and minimum velocity range).

9. For the investigation of humidity effects on filtration efficiency, the required constant humidity was controlled by both the heater and humidifier and monitored using the SunBeam hygrometer-thermometer device (mechanical type, see Appendix J).
10. For the investigation of electrostatic charge effects on filtration efficiency, the humidity was lowered as much as possible by maximizing the heat supply and monitoring the temperature and humidity of the air in the room and that of the air flow inside the mixing box.
11. Once the required humidity and temperature of the air flow was achieved, the probe volume was moved sequentially to each grid point upstream and downstream of the filter by moving the transceiver probe using the three-dimensional motion controller. The number of samples, collection time and average velocity of the particles were taken for each grid location from which the number density of the particles was computed using Eq. 4.1, which then allowed finding the overall efficiency of the filter by Eq. 4.3.

CHAPTER V

ELECTROSTATIC VOLTAGE, HUMIDITY, AND CONSISTENCY

MEASUREMENTS

5.1 Introduction

In this chapter is presented the major preliminary work that was undertaken prior to the investigation of the local filtration efficiencies with respect to electrostatic charge and humidity. The electrostatic charge was generated either as a result of the atomization of suspensions of different particles (PSL, sodium chloride, and glass beads) or other triboelectric mechanisms due to separation and contact of the particles between the housing surfaces and the filter. Investigation and measurement of electrostatic voltage were carried out at different locations along the filter housing using these different particles with different diameters and concentrations. Then a correlation was established between the main factors that affect the electrostatic voltage level for different air flow rates in the housing.

Several experiments were also conducted to confirm the consistency (repeatability) of the measurements at different times and flow rates to investigate both the electrostatic and humidity effects. The fact that humidity highly influenced the electrostatic charge generation and quantity was another factor that led the author to

carrying out this parallel research. Initially, the author had speculated that high humidity variations could have been one of the problems of inconsistent efficiency measurements in the past research work here [Natrajan, 1995] at the School of Mechanical and Aerospace Engineering. Thus this interest has helped synchronize the studies on both electrostatic charge and humidity effects and establish their correlation.

The electrostatic charge investigation is presented in Section 5.2 whereas the variation of the humidity of the air, the estimation of moisture in the filter, consistency measurements on the LDA, and other factors related to filtration efficiency are discussed in Sections 5.3 and 5.4. The experimental procedures for investigating the electrostatic and humidity effects on the local filtration efficiencies of the Dayco-Purolator A13912 fibrous filters are presented in Section 5.5.

5.2 Electrostatic Charge Investigation

The investigation involves the measurement of electrostatic voltage at different locations using different types of particles with various diameters as they flow through the PVC piping, plexiglass housing, and test filter at different air flow rates and humidities. The electrostatic voltage level is dependent upon the amount of charge and the distance between the static field meter and the charged surface. It is also dependent upon the surface area or size of the charged surface.

In this section, the author presents the variation of electrostatic voltage with flow rate and its correlation with humidity for various types of particles. The results on the time dependence of the electrostatic charge voltage (charge decay and accumulation) have also been investigated as the particles flow through the experimental setup. Indeed

a significant portion of the discussion and experimentation delves into the work on charge accumulation and decay (neutralization).

5.2.1 Factors that Affect Charge Polarity and Quantity

The author did several experiments using 0.5, 0.966, and 2.04 μm diameter PSL particles, 1.5 μm diameter glass beads, sodium chloride salt, and air by itself without any artificial seeding (contamination). Some of the factors that affect the polarity are the intrinsic chemical properties of the particles. The experimental results for PSL particles showed negative polarity for all diameters, concentrations, and flow rates. Sodium chloride was found to be neutral. However, the glass beads showed positive polarity for all air flow rates and concentrations of solutions. The air drawn from the room showed positive polarity at the filter for all flow rates at lower humidities. As outlined in the literature review, the main factor that determines the polarity and amount of the charge or the electrostatic voltage quantity is the relative positions of the particles or materials in the triboelectric series [see Chapter III]. Thus the triboelectric series of the materials and particles is the most determinant factor. However, high relative humidity (> 60%) can also cause the reduction/elimination of the electrostatic charge by enhancing the conductivity of air, which enhances the grounding of the charged materials and particles.

5.2.2 Electrostatic Charge Measurements

There are different ways of measuring electrostatic charge. One of the methods applied to fluid flows is the use of an electrometer [Bensch, 1977]. On the other hand, for the electrostatic charge on the surface of web handling materials and in areas where it

is difficult to use the electrometer, electric field meters are used to measure the electrostatic charge voltage or electrostatic field [Chubb, 1993; Durkin, 1993; Sudarshan and Jaitly, 1988; Electro-tech Systems, Inc. Catalog, 1996]. From the electrostatic voltage or electric field information, the amount of charge can be obtained by solving some complex differential equations governing the electric field distribution of the materials with known boundary conditions. Thus static field meters are easy to use, and they measure both the electrostatic voltage and the polarity of the charge even for areas with difficult access.

In this study an electrostatic field meter has been used to measure or monitor the electrostatic charge voltage and the polarity of the charge while the experimental filtration process was under way. In both the summer and winter seasons of the years 1997 and 1998, the author conducted some experiments using different particles as contaminants. These included PSL particles of different diameters and concentrations, glass beads, and sodium chloride. The room air by itself without subjecting it to artificial contamination was also tested for charge polarity and electrostatic voltage level revealing interesting results.

5.2.2.1 Experimental Work for Summer Season

Most of the experiments were conducted on PSL particles both in the summer and winter seasons of the year. This was in tune with the fact that, in fibrous filtration efficiency measurements, monodisperse PSL particles are commonly used as the challenge contaminants in addition to some other standard test dusts [Matteson, 1987]. Polymerizing styrene, vinyltoluene, or butadiene in various combinations is one of the

several methods to produce uniform spherical latex particles. Some of the physical properties of PSL particles used in the experiment include:

1. low specific gravity of 1.05,
2. refractive index of 1.59,
3. 10% solids by weight in deionized water as packaged and received from the supplier (Duke Scientific).

Since the humidity is relatively higher in the summer than in the winter, the trend is higher electrostatic voltage in the latter than in the former.

0.5 μm PSL particles: The first experiment on voltage measurement was conducted by taking 3 ml of a suspension of 0.5 μm PSL particles at 10% by weight and 447 ml of distilled water to prepare a 500 ml test solution. After the blower and air heater were started, a 30 minute stabilizing time was allowed, to some extent less than that normally practiced in the actual experimental procedure (outlined in the last section of Chapter IV) for local efficiency measurements. The relative humidity and the room temperature were recorded as 47% and 26.3 $^{\circ}\text{C}$, respectively, before the voltage measurement and the atomization process began. The experiment started at a low air flow rate of 5.65 m^3/hr and the atomization pressure of the PSL particles into the flow of the preheated air was 2.45 atmospheres. Measurements of the electrostatic voltage were taken at three locations (at the mixing box, and upstream and downstream of the test filter) while changing the flow rate of the air. The results for two of the locations (at mixing box and upstream side of the filter) are presented in Figs. 5.1, and 5.2. There was not any voltage detected downstream of the filter.

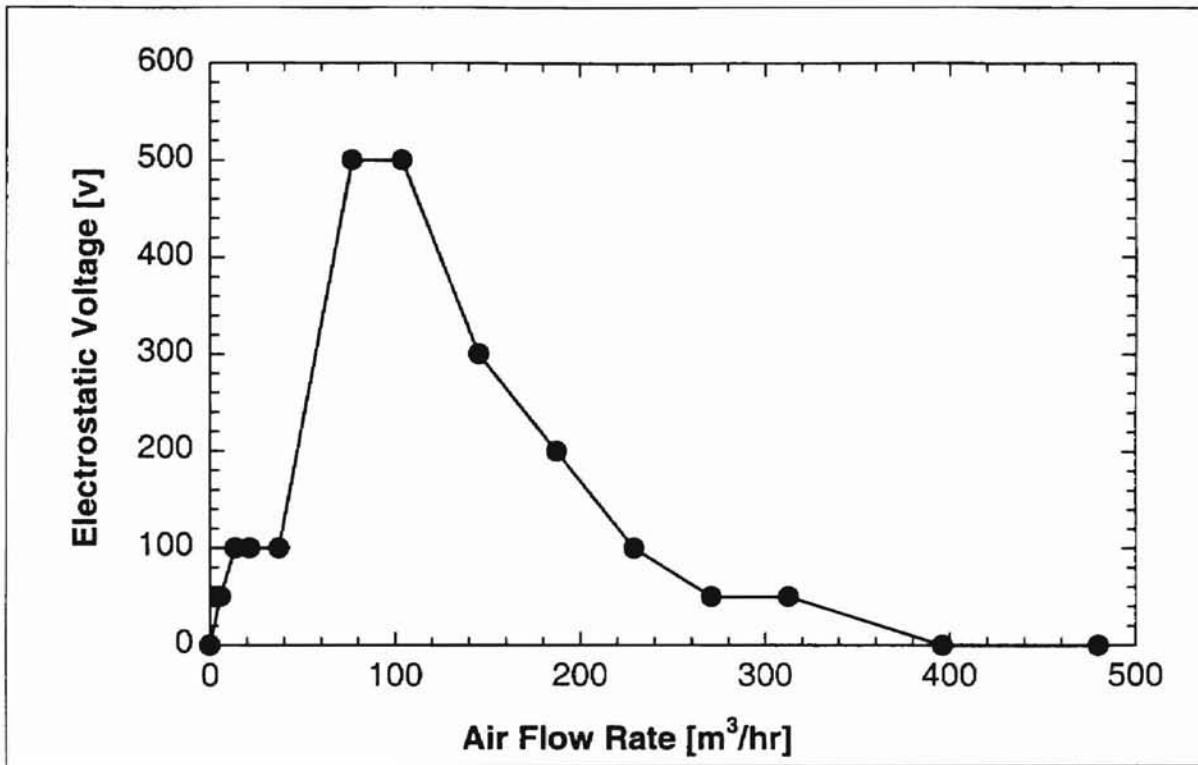


Figure 5.1 Variation of Electrostatic Voltage with Air Flow Rate at the Mixing Box for 0.5 μm Diameter PSL Particles (conc. = 3/500, Summer, 1997).

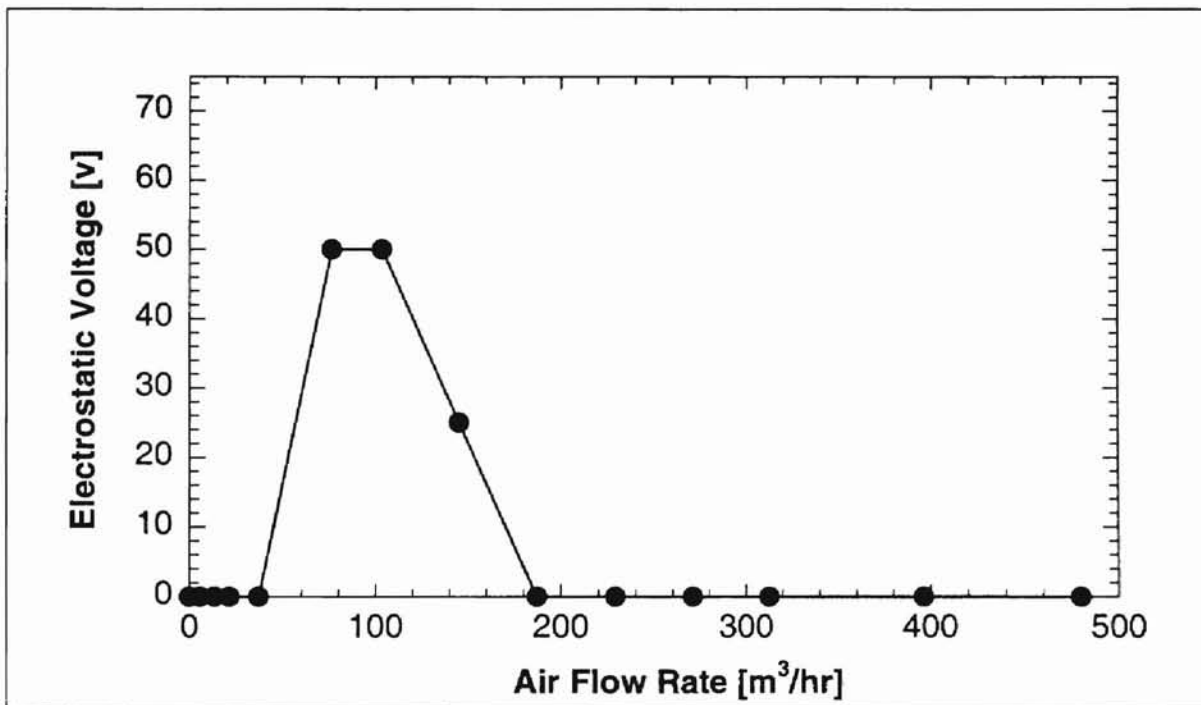


Figure 5.2 Variation of Electrostatic Voltage with Air Flow Rate Upstream of Filter for 0.5 μm Diameter PSL Particles (conc. = 3/500, Summer, 1997).

0.966 μm PSL Particles: The objective of this experiment was to see how the sizes of the particles affect the electrostatic charge voltage level. By adding 3 ml of 10% solids by weight of the 0.966 μm diameter PSL suspension to 447 ml of distilled water, a 500 ml solution was prepared to conduct the experiment at different flow rates. Accordingly, electrostatic voltage measured at the same two locations was relatively higher than that of the 0.5 μm PSL particles for the same concentration. For all cases, the polarity of the charge was negative. Figure 5.3 shows the electrostatic voltage variation with flow rate.

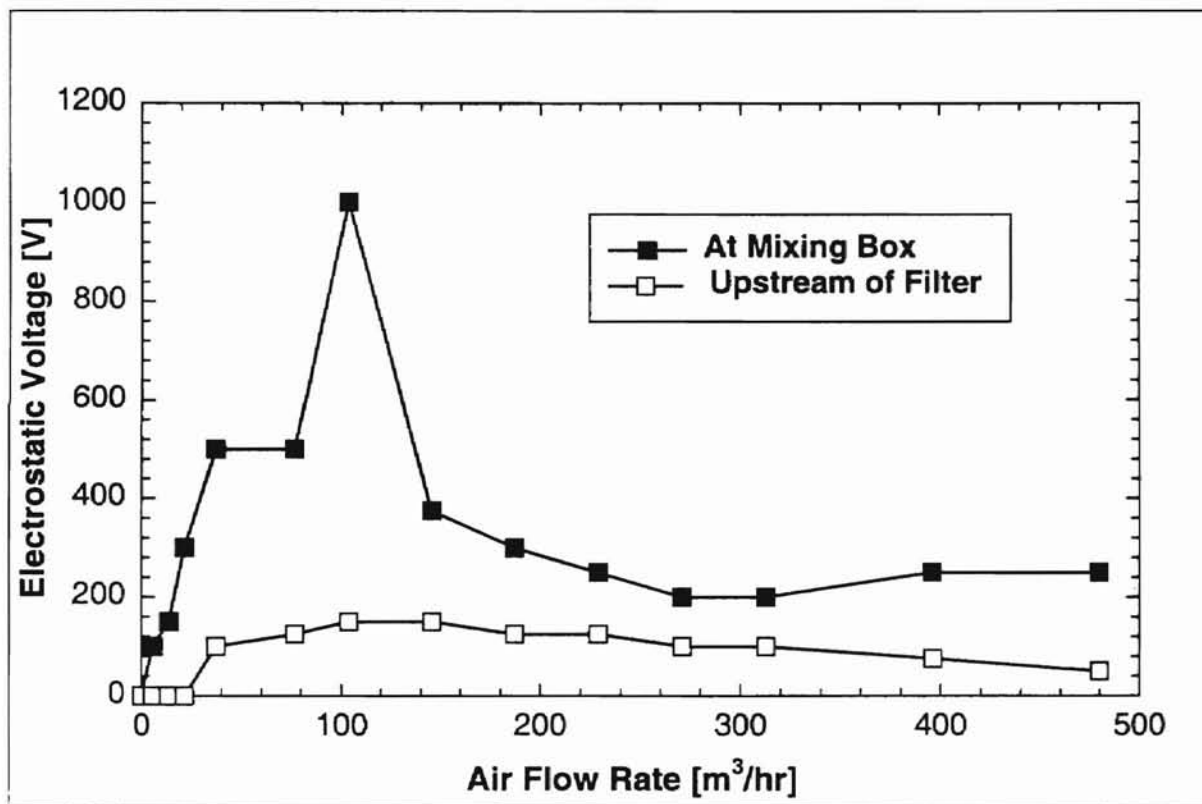


Figure 5.3 Variation of Electrostatic Voltage with Air Flow Rate at the Mixing Box and Upstream of Filter for 0.966 μm Diameter PSL Particles (conc. = 3/500, Summer, 1997).

Sodium Chloride Particles: An experiment to investigate the electrostatic charge generation as crystals of sodium chloride (suspended in air) flow through the housing as well as the filter showed neutrality (zero charge). However, according to the triboelectric

series or theory of electrostatics, there should be an exchange of charge between two dissimilar materials, even if the charge is very small. Hence the author thinks that the hygroscopic (water absorption) nature of sodium chloride, that can destroy electrostatic charge by absorbing moisture from the humid air, could be responsible for the absolute zero readings of electrostatic charge voltage for all of the flow rates. In addition, many other researchers have also reported sodium chloride crystals as neutral particles that can be used for testing initial filter efficiencies in the laboratory.

Glass Beads: An experiment was conducted on 1.5 μm diameter particles by preparing a solution of 5 grams of glass beads in 495 ml of distilled water. The maximum electrostatic voltage measured upstream of the filter was 50 and 75 volts with positive polarity at flow rates of 77.1 and 103.7 m^3/hr , respectively. For the rest of the flow rates and the other two locations (at the mixing box and downstream of the filter), the electrostatic voltage was zero.

Clean Air: For this test, the air from the room that was drawn into the flow setup was preheated without any injection or atomization of contaminants into it. Efforts to measure static charge did not yield any measurable quantities for all of the flow rates. Unlike the winter results, the electrostatic charge voltage measured at the three locations was zero (see Section 5.2.2.2).

The corresponding humidity and temperature variations of the air flow through the housing and filter are given in Fig. 5.4. Figure 5.4 was plotted after measuring the humidity and temperature of the air for each of the flow rates while atomizing distilled water and preheating the air flow with a 1250 watt electric heater (which is normally used for drying the PSL particles). To measure the temperature and humidity of the air flow,

an Omega RH21 digital hygrometer-thermometer device was installed half way between the mixing box or about 1.2 m above the inlet of the experimental setup where the heater

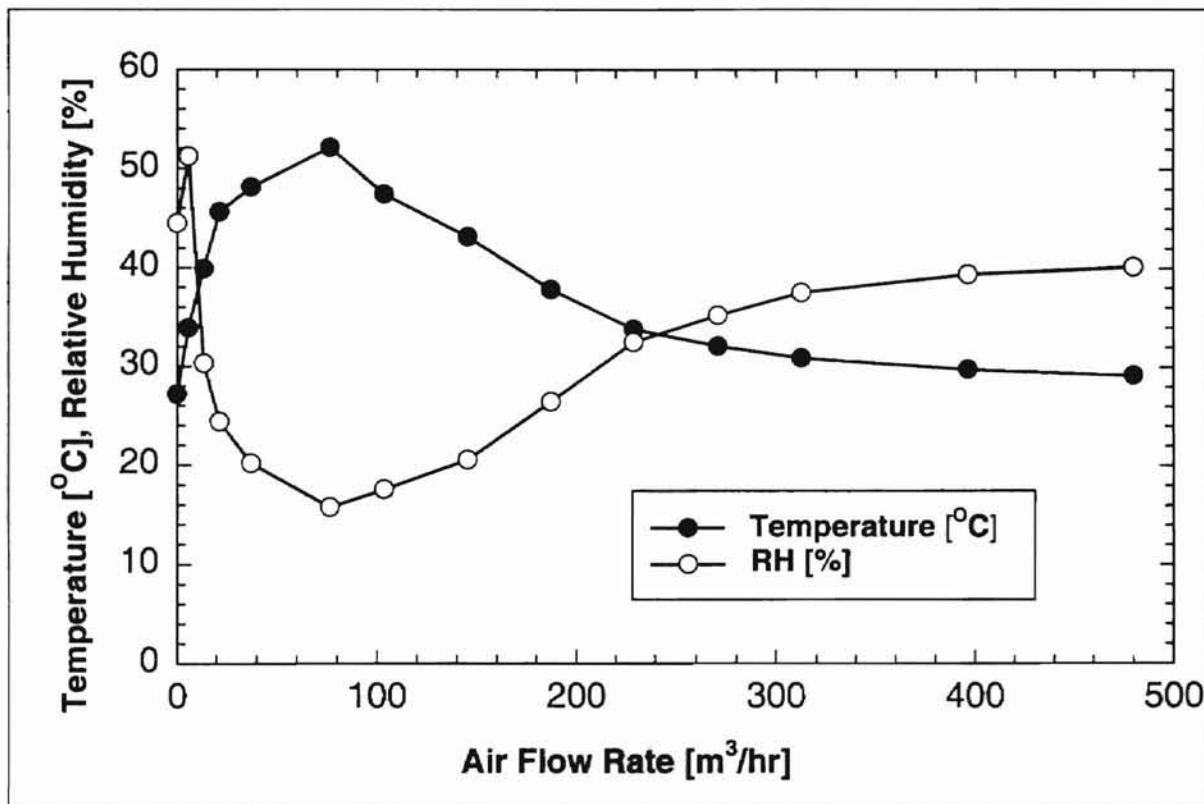


Figure 5.4 Variation of Humidity and Temperature with Preheated Air Flow Rate (Summer, 1997).

humidifier and atomizer are located in order to conform with the safe operating or working environment and ranges of the device (see list of equipment, Appendix J). The temperature-humidity probe was inserted into the flow by drilling a hole into the PVC piping, which was later sealed in order to avoid any leakage.

5.2.2.2 Experimental Work for Winter Season

These experiments were mainly conducted from November of 1997 through March of 1998 as a continuation of the summer season experiments and in a quest for more and

comprehensive information about the nature and level of the electrostatic charge that can be attained. The experiments were performed with PSL, glass beads, and sodium chloride as well as clean air. Clean air refers to the air flowing through the experimental set up without using (atomizing) any contaminants. The results are presented and discussed one by one for each type of particle.

0.5 μm PSL particles: To compare the electrostatic charge voltage level (quantity) and polarity in winter and summer at different flow rates for the same concentration and particle diameter, tests were done on 0.5 μm particles following the same procedure as for the summer season. As shown in Fig. 5.5, electrostatic charge voltage measurements

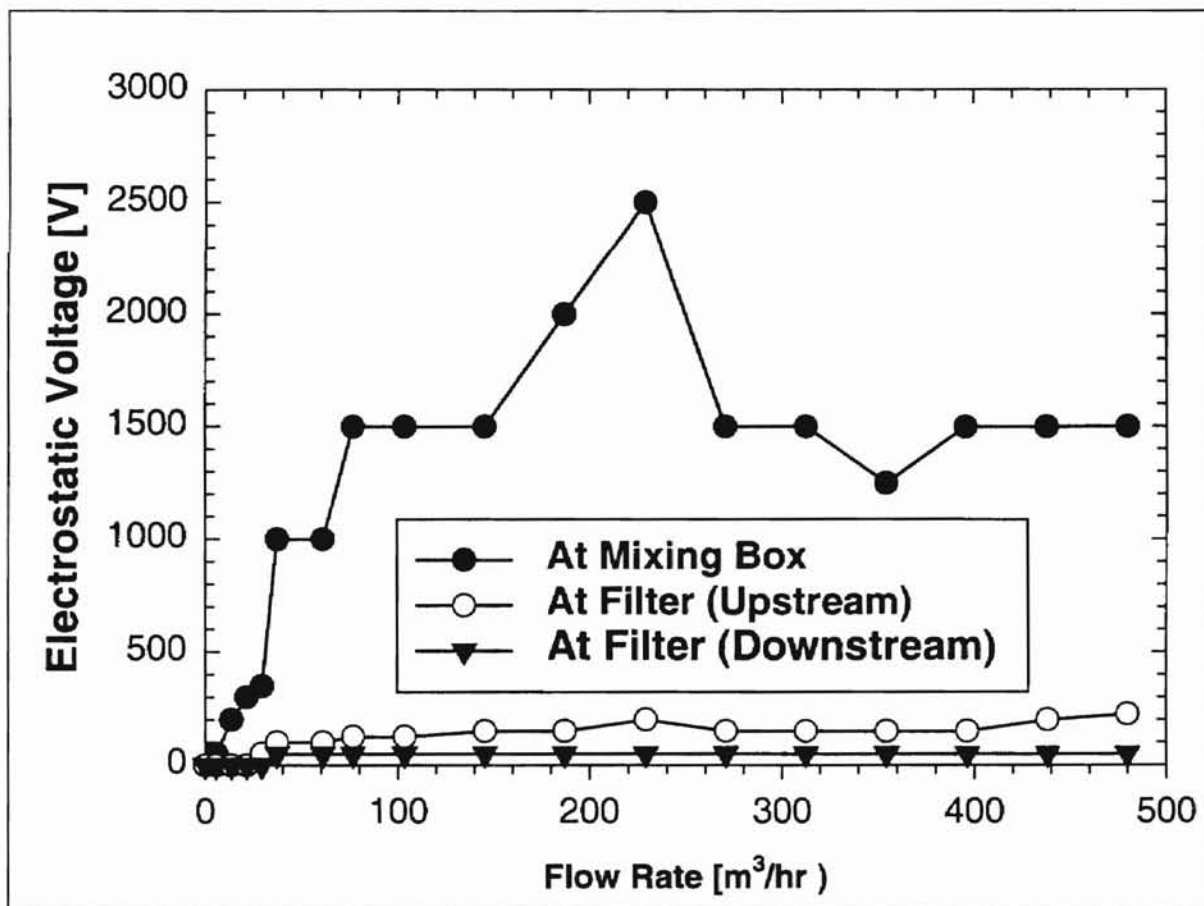


Figure 5.5 Electrostatic Voltage Measurement at the Mixing Box and Filter for 0.5 μm Diameter PSL Particles (conc. = 3/500, Winter, 1997).

in the winter were much higher than those recorded in the summer season (see Fig. 5.2).

0.966 μm PSL particles: To explore the effect of particle diameter and concentration on electrostatic charge quantity, an experiment was also performed using 0.966 μm diameter particles. The results are presented in Figs. 5.6 and 5.7. Comparison of Figs. 5.5 and 5.6 show that the electrostatic charge voltage for the 0.966 μm diameter particles is higher than that of the 0.5 μm diameter particles. On the other hand, comparison of the summer and winter results for the 0.966 μm diameter particles shows that the electrostatic charge voltage is higher in the winter than in the summer season. Thus electrostatic voltage depends upon the diameter and concentration of particles. However, humidity and other test conditions must be taken into account when we compare the electrostatic voltage of

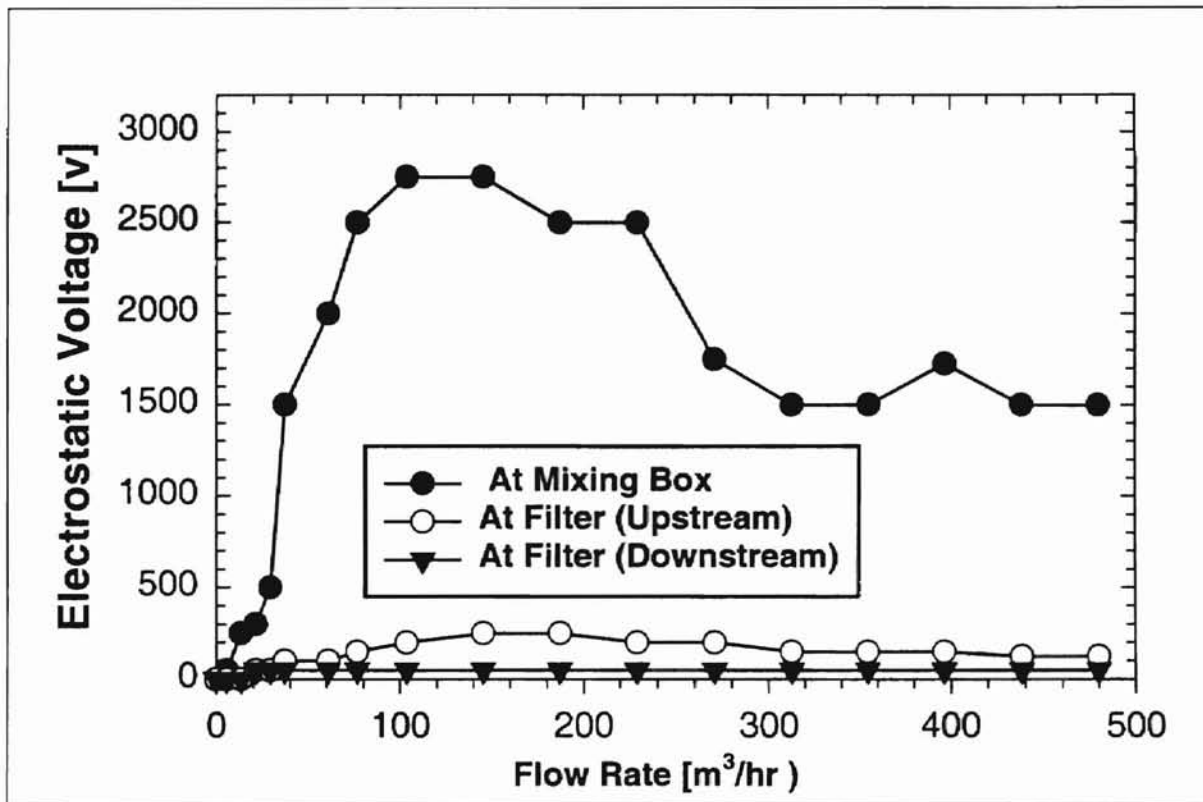


Figure 5.6 Electrostatic Charge Voltage Measurement for 0.966 μm Diameter PSL Particles (conc. = 3/500, Winter, 1998).

the particles. If the test conditions are not the same, then the test results may be misleading and inconsistent.

Figure 5.7 shows electrostatic charge voltage variation with flow rate for the 0.966 μm diameter particles at a concentration of 6/500 suspension of PSL particles. The electrostatic voltage steadily increases between 0 and 100 m^3/hr and then tends to decrease beyond 200 m^3/hr . This may be due to the fact that the electrostatic charge is related to the relative humidity and temperature of the air. As the air flow rate increases, the humidity of the air inside the flow approaches the humidity of the room, because the heater cannot significantly change the humidity of the incoming air at high flow rates. Otherwise, it is believed that, when the fluid velocity increases, electrostatic voltage also

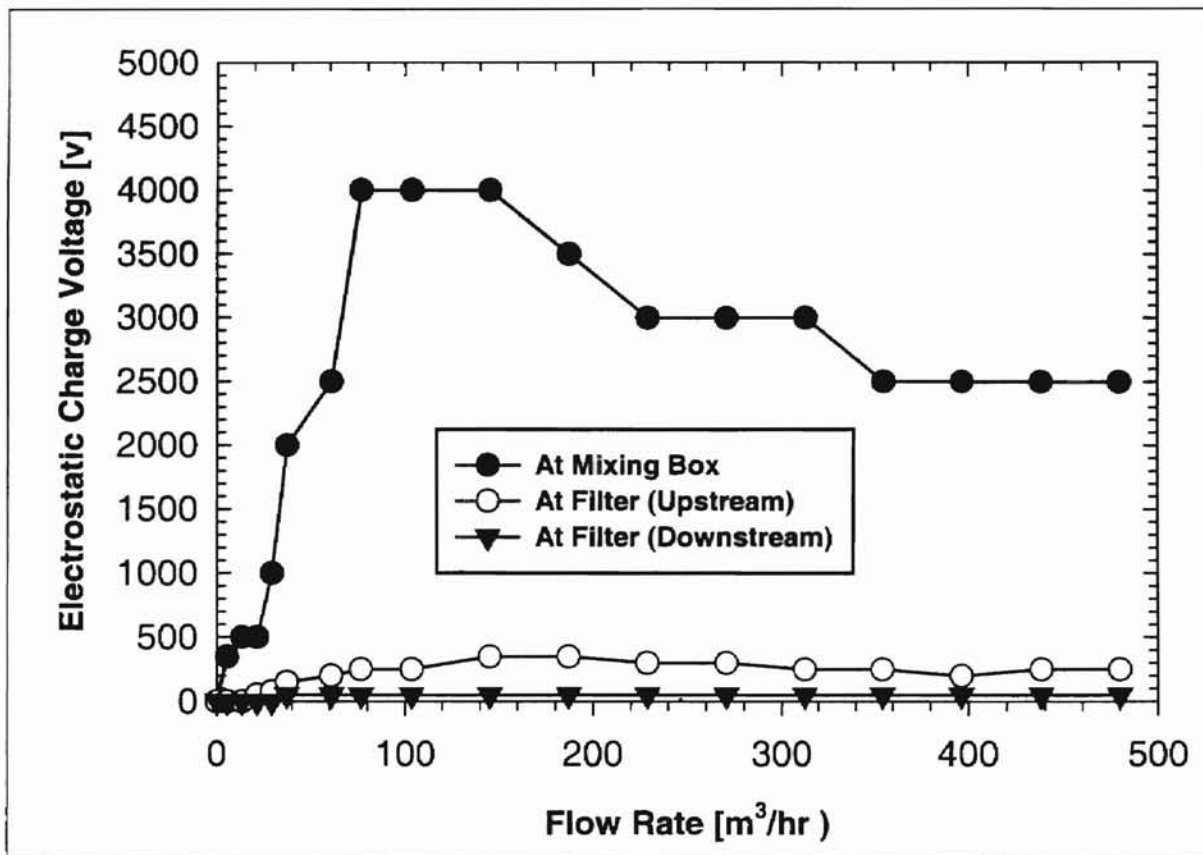


Figure 5.7 Electrostatic Voltage Variation with Flow Rate for 0.966 μm Diameter PSL Particles (conc. = 6/500, Winter, 1998).

increases due to the turbulent behavior of the fluid that can enhance charge generation due to friction, fast rate of separation, and contact.

From these experimental results with the 0.5 and 0.966 μm diameter particles both in the summer and winter seasons, one can observe that the electrostatic voltage is dependent on the size, concentration of particles, air flow rate and test conditions (humidity and temperature). Theoretical and experimental work [Davies, 1973] also indicate that electrostatic charge is proportional to the square of particle diameter. However, the author believes that further experiments may be needed to verify these results by measuring the electrostatic charge using other charge measuring devices.

2.04 μm PSL Particles: Similarly, the experiments for the 2.04 μm diameter PSL particles (as shown in Fig. 5.8) were performed by taking a concentration twice that for

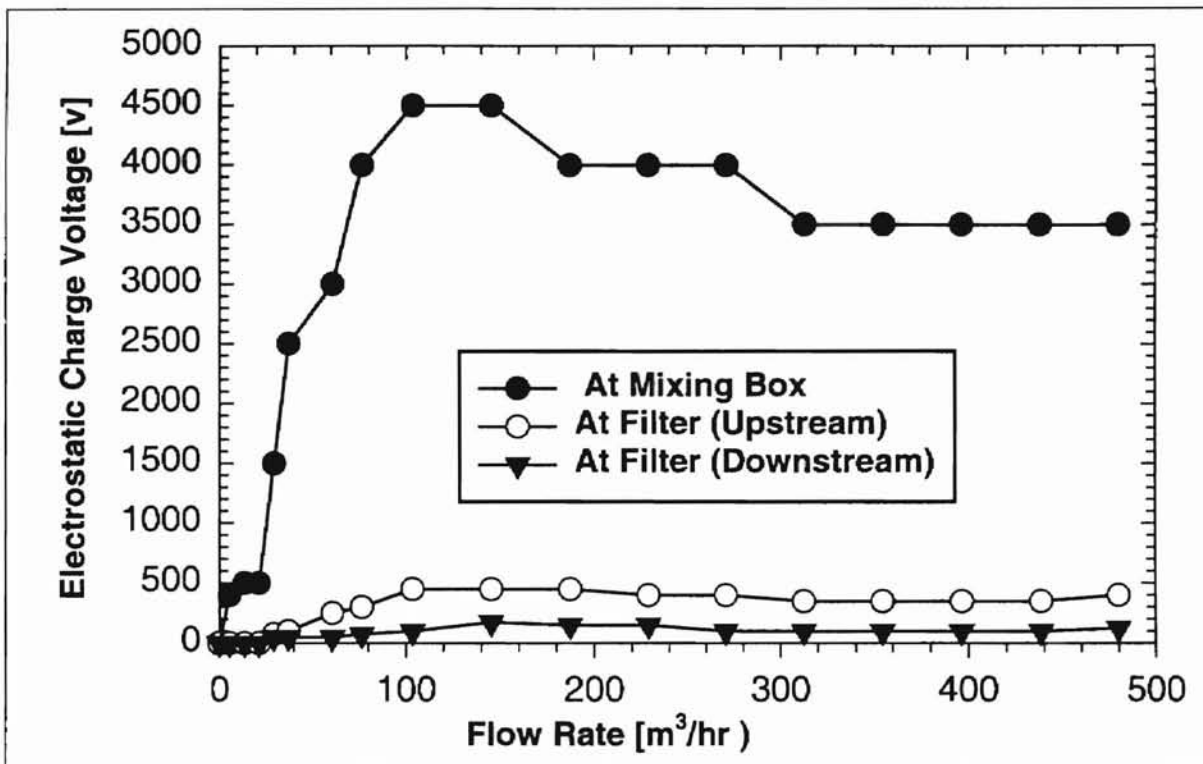


Figure 5.8 Electrostatic Charge Variation with Flow Rate for 2.04 μm Diameter PSL Particles (conc. = 12/500, Winter, 1998).

the 0.966 μm diameter particles. The electrostatic voltage variation with flow rate for the 2.04 μm diameter PSL particles are plotted. The experiment was conducted by mixing a 12 ml suspension of the 10% solids by weight of the 2.04 μm diameter PSL particles with 488 ml of distilled water in order to prepare a 500 ml solution.

Correlation of Electrostatic Voltage and other Parameters: As shown in Fig. 5.9, there is a correlation among the electrostatic voltage, the rate of flow of the contaminant loaded air, and the relative humidity of the air inside the flow. The author also believes that the humidity of the air inside the room directly or indirectly affects the amount of electrostatic voltage. Thus the average relative humidity inside the housing is dependent

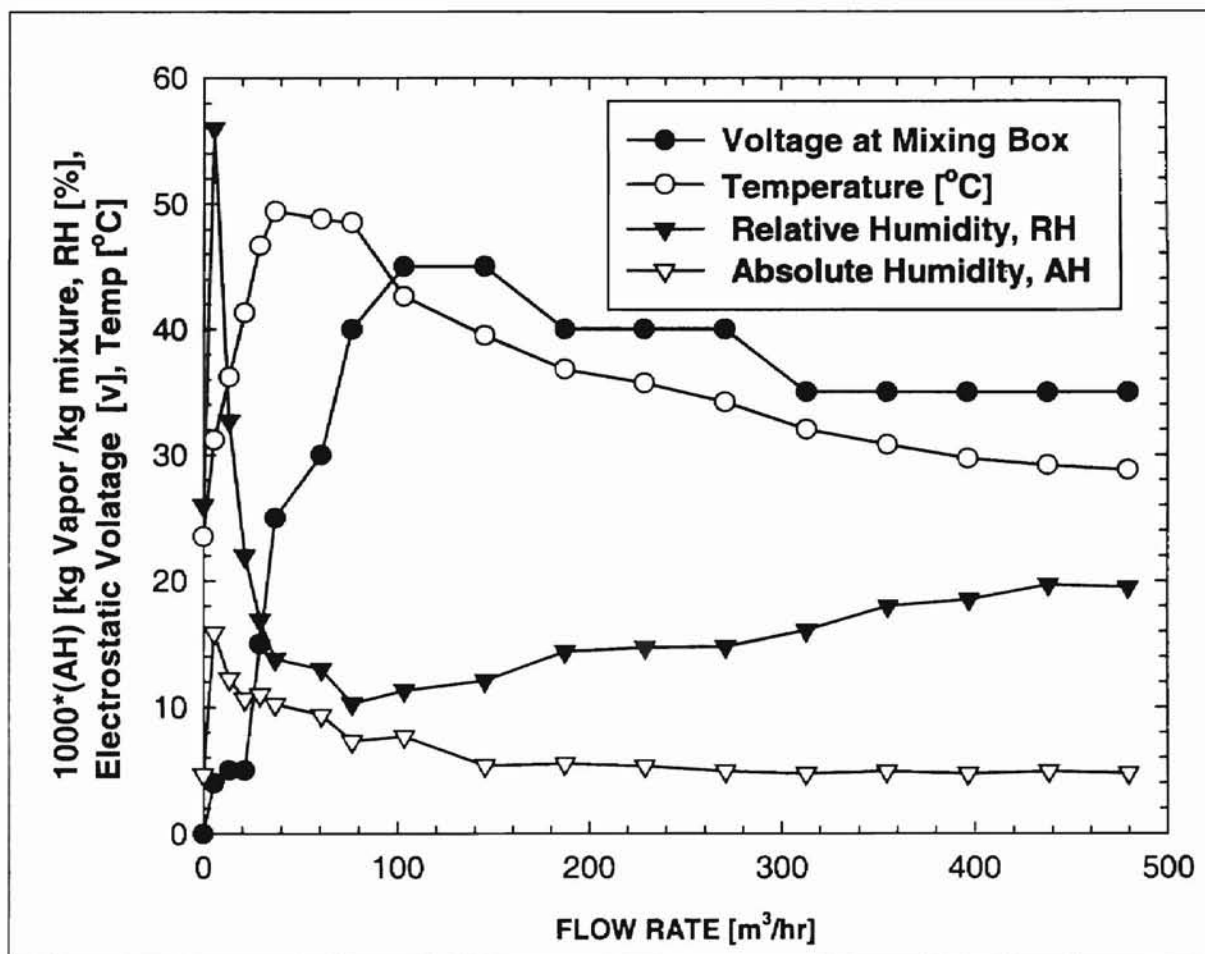


Figure 5.9 Variation of Electrostatic Charge Voltage, Absolute and Relative Humidities, and Temperature with Air Flow Rate for 2.04 μm Diameter PSL Particles (conc. = 12/500; Winter, 1998).

Oklahoma State University

upon the initial inlet air conditions, the amount of solution atomized into the flow and the heat supply from the heater. Therefore the electric heater's constant heat supply (with a maximum of 1500 w), to lower considerably the humidity of the incoming flow of air for higher flow rates, is not sufficient. The same holds true also for both the humidifier and the atomizer to considerably change (increase) the humidity of the air at high flow rates (beyond 300 m³/hr). Thus the relative humidity of air for higher flow rates remains relatively unchanged. As shown in Fig. 5.9, the absolute humidity also remains constant as the flow rate increases steadily.

5.2.2.3 The Time Dependence of Electrostatic Charge

Experimental measurements show that, during the actual filtration process, the measured electrostatic voltage increases with time. This author did some experiments on the accumulation and decay of charge using 0.966 μm diameter PSL particles, glass beads and clean air (without injecting any contaminants).

To investigate the accumulation of charge, a 5 ml suspension of 10% solids of PSL particles by weight was mixed with 495 ml of distilled water to make 500 ml of solution. After turning on the heater and the blower and filling the atomizer with the 5/500 solution of PSL particles, the TSI flow meter was adjusted to a constant air flow rate of 60.8 m³/hr (by manually operating the pneumatic control panel that controls a pneumatic valve). The housing was not grounded and the electrostatic charge voltage was recorded for about one and one-half hours at an interval of 5 minutes. This is the average time necessary to take data for the downstream side of the filter during the local efficiency measurement. The results (as plotted in Fig. 5.10) show a steady growth of electrostatic

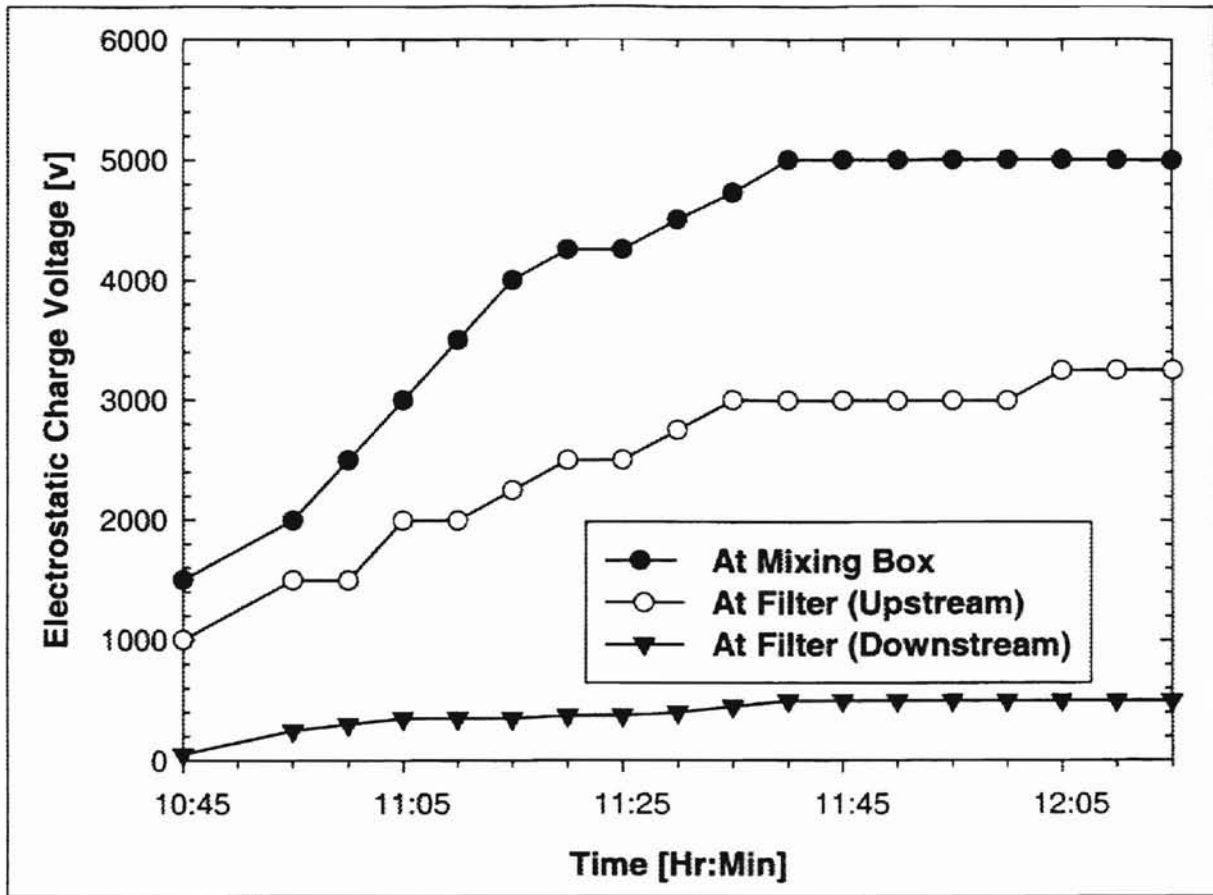


Figure 5.10 Electrostatic Voltage As a Function of Time for 0.966 μm Diameter PSL Particles at a Flow Rate of 60.8 m^3/hr (conc. = 5/500, Winter, 1998).

voltage with time. Thus due to the accumulation of charged particles on the upstream side of the filter with time, the electrostatic voltage on the upstream side also steadily increased with time. Another test was conducted using the 0.966 μm PSL particles to see the reduction of charge from the experimental setup by grounding the surface of the plexiglass housing with a single grounded copper wire. This time the grounding did not result in the decay of the charge (neutralization of the particles) as expected. Figure 5.11 shows the variation of the electrostatic voltage at the mixing box, upstream and downstream of filter with time at a constant air flow rate of 60.8 m^3/hr for the wire grounded housing.

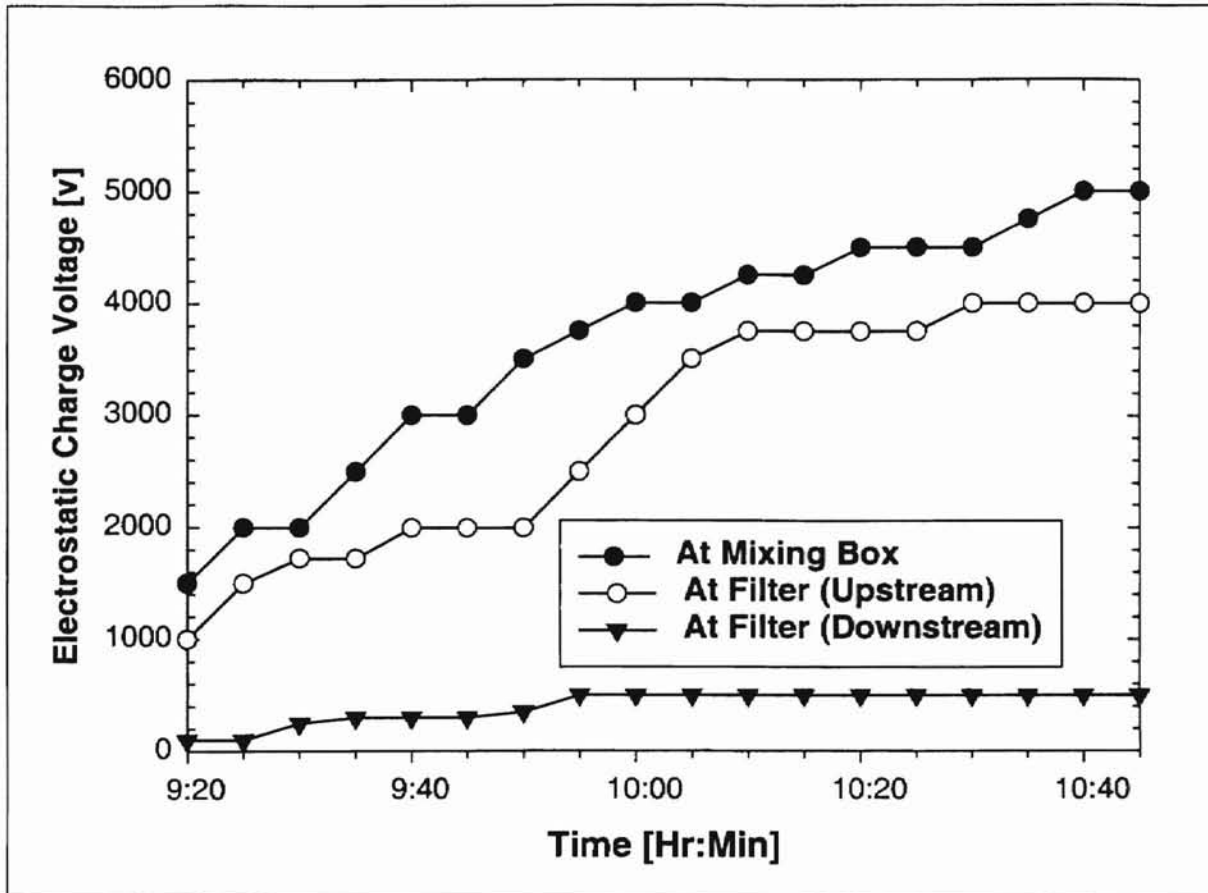


Figure 5.11 Electrostatic Charge Voltage Variation with Time for Wire Grounded Housing at an Air Flow Rate of $60.8 \text{ m}^3/\text{hr}$ for $0.966 \text{ }\mu\text{m}$ Diameter PSL Particles (conc. = 5/500, Winter, 1998).

An experiment involving electrostatic voltage measurement with time was also performed with room air (without particle seeding) and a new filter. Results show that the electrostatic charge, generated from triboelectric effects between the filter and air, had positive polarity. The electrostatic charge voltage at the mixing box was found to be zero, while the electrostatic charge voltage readings upstream and downstream of the filter were of the same polarity and magnitude and varied as a function of time. The electrostatic charge voltage at the filter was also gradually increasing with time as shown in Fig. 5.12. For this experiment, the heater was turned on and there was no atomization of any other particles or distilled water.

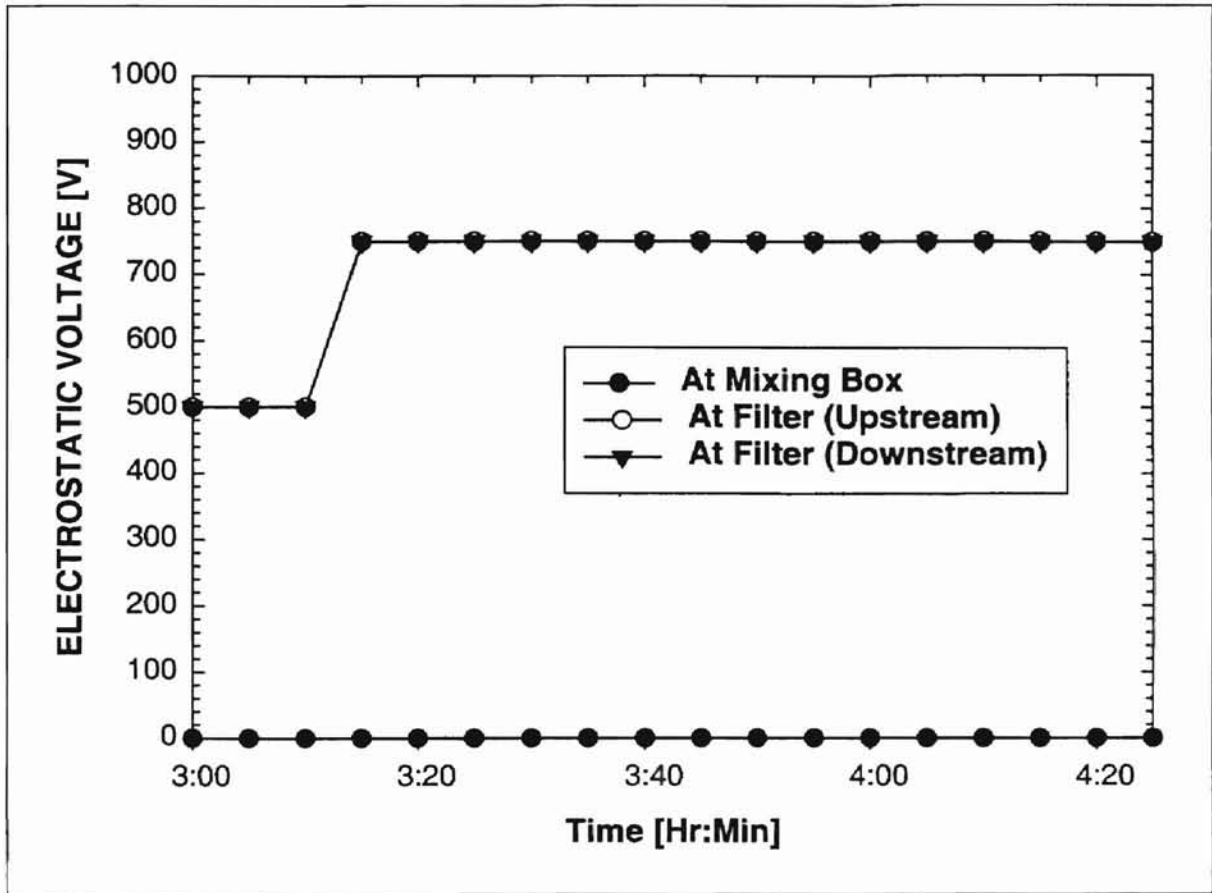


Figure 5.12 Electrostatic Charge Voltage Generation and Variation with Time for Ungrounded Housing Using Clean Air (Flow Rate = 60.8 m³/hr, Winter, 1998).

This experimental result suggests that the contact between the filter and the submicron particles present in the air may be responsible for the electrostatic voltage. However, many atmospheric researchers have reported that the atmospheric air has also naturally charged particles (atoms and dust) due to radioactive radiation or other factors.

5.2.3 Electrostatic Discharging of the Experimental Housing and Particles

Discharging of the housing and the PSL particles was one of the challenges of this research work. The next experiment was done to verify the effectiveness of the grounded

aluminum foil in neutralizing electrostatic charge from the surface of the plexiglass housing and the PSL particles.

The upper part of the filter housing (plexiglass) covered with the aluminum foil, was grounded using a copper wire attached to a water pipe. Then the measurement of electrostatic voltage followed at intervals of 10 minutes for about an hour and a half. Figure 5.13 shows the experimental results using 0.966 μm diameter PSL particles. The experiment was also conducted more or less by strictly adhering to the experimental procedures (see Chapter IV) used to carry out the actual filtration efficiency experiments.

The author was also interested in monitoring the rate of discharge of electrostatic

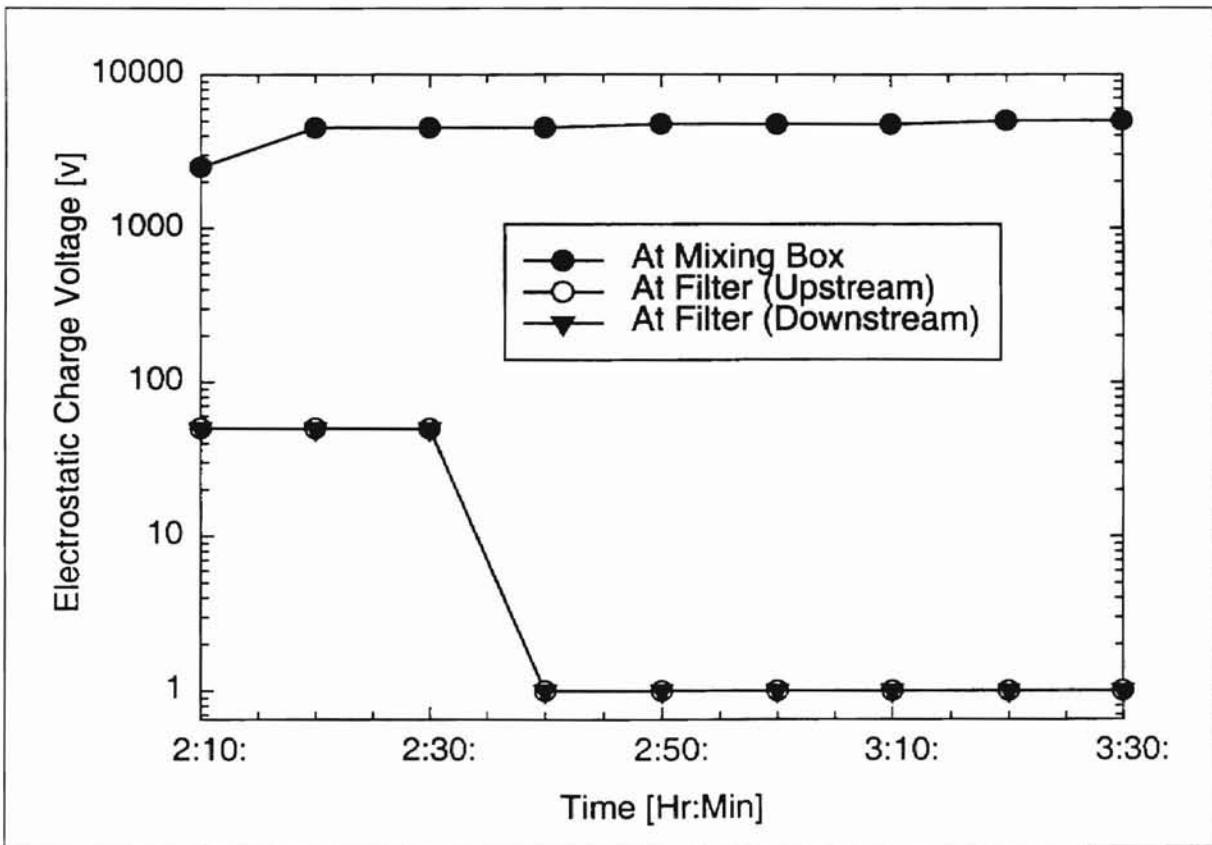


Figure 5.13 Electrostatic Charge Neutralization of 0.966 μm Diameter PSL Particles for Grounded Housing Using Aluminum Foil at a Flow Rate of 60.8 m^3/hr (conc. = 5/500, Winter, 1998).

charge from the mixing box (ungrounded part of the housing) after shutting of the system (blower, heater, and atomizer). To do so, the author started to measure the electrostatic voltage, time, and the humidity of the stationary air inside the mixing box immediately after shutting off the system. The electrostatic voltage on both sides of the filter remained zero, while at the mixing box, it fell to 2500 volts after 50 minutes as humidity monitored inside the box increased gradually. The average humidity of the room was recorded as 25%.

Electrostatic voltage measurement on glass beads was another task that attracted the attention of this author, as there was a plan in the laboratory to carry out efficiency measurements using these particles in order to minimize cost, with the glass beads replacing the more expensive PSL particles.

Before the test, 8.3 grams of glass beads were added to 500 ml of water in order to prepare a 500 ml solution. The glass beads had an average median diameter of $1.5 \mu\text{m}$ and a specific gravity of about 1.5. The air flow rate was set at $60.8 \text{ m}^3/\text{hr}$ and the heater and atomizer were turned on and left running for 3 minutes. The measurement of electrostatic voltage was performed at the three locations, namely at the mixing box, upstream and downstream of the filter. The readings were recorded every 5 minutes and plotted against time. Figure 5.14 shows the electrostatic charge voltage growth for glass beads as a function of the running time of the blower, atomizer and heater for the ungrounded filter housing.

As shown in Fig. 5.14, the electrostatic voltage upstream of the filter was much higher than that at the mixing box or at the bottom of the filter. Unlike the PSL particles, which generated high electrostatic voltage at the mixing box, glass beads exhibited a

relatively low electrostatic voltage at the mixing box, while a considerable amount of voltage was measured on the upstream side of the filter. The next experiment was a continuation of the above experiment.

The aim of this experiment was to find out how long it would take for the highly charged plexiglass housing to be discharged after stopping the atomization and drying of

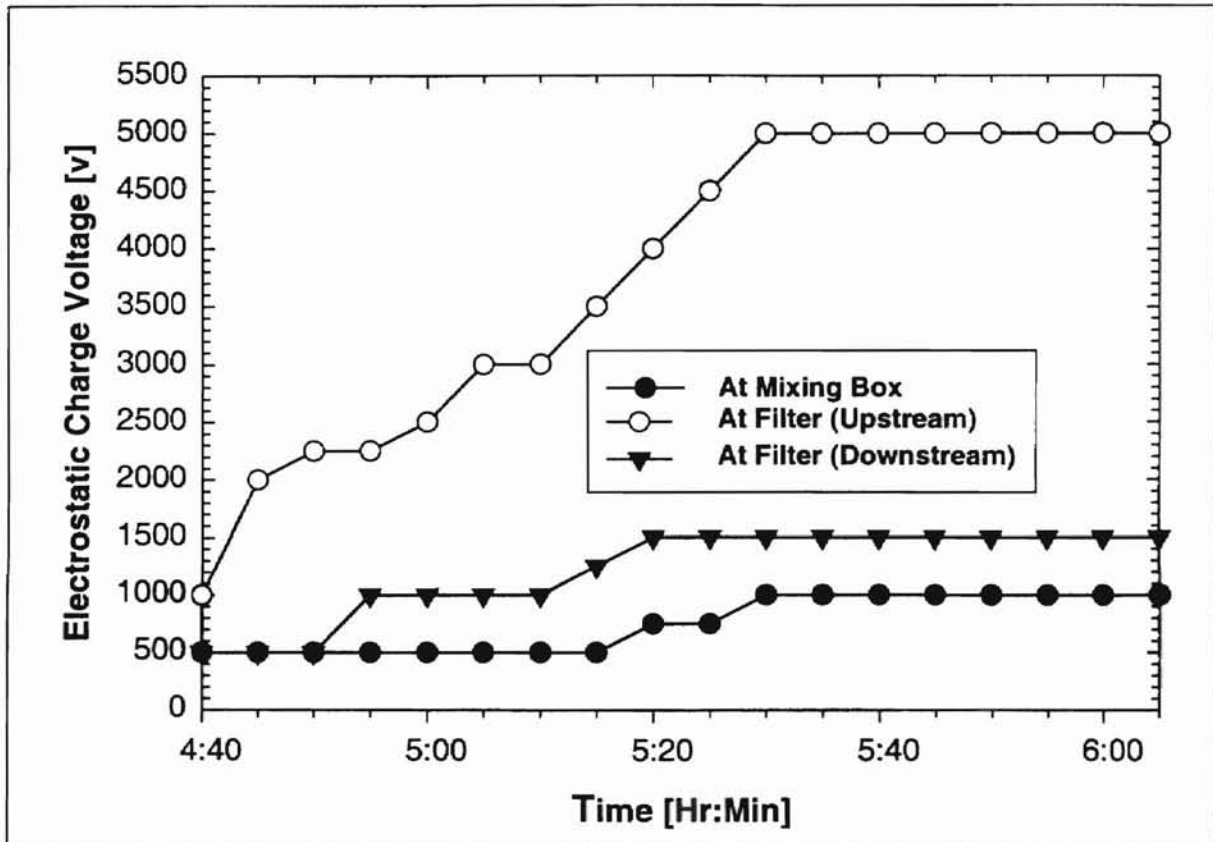


Figure 5.14 Electrostatic Charge Voltage Growth with Time for Ungrounded Housing and Air Flow Rate of $60.8 \text{ m}^3/\text{hr}$ Using Glass Beads of $1.5 \mu\text{m}$ Diameter (Mean Size Distribution) (conc. = $8.3/500$, Winter, 1998).

PSL particles and shutting off the blower. Accordingly the measurement started immediately after shutting off the system (blower, atomizer and heater), and the electrostatic charge voltage was recorded and plotted as function of time to investigate the rate of reduction of charge without grounding the housing. The electrostatic charge

voltage was recorded at intervals of 5 minutes and the results were plotted as shown in Fig. 5.15. The author later found out that there was a relatively sharp decrease in the electrostatic voltage over the first 20 minutes and for the rest of the time, the curve was flat where the rate of charge dissipation was low. Figure 5.15 shows the decay progress with time.

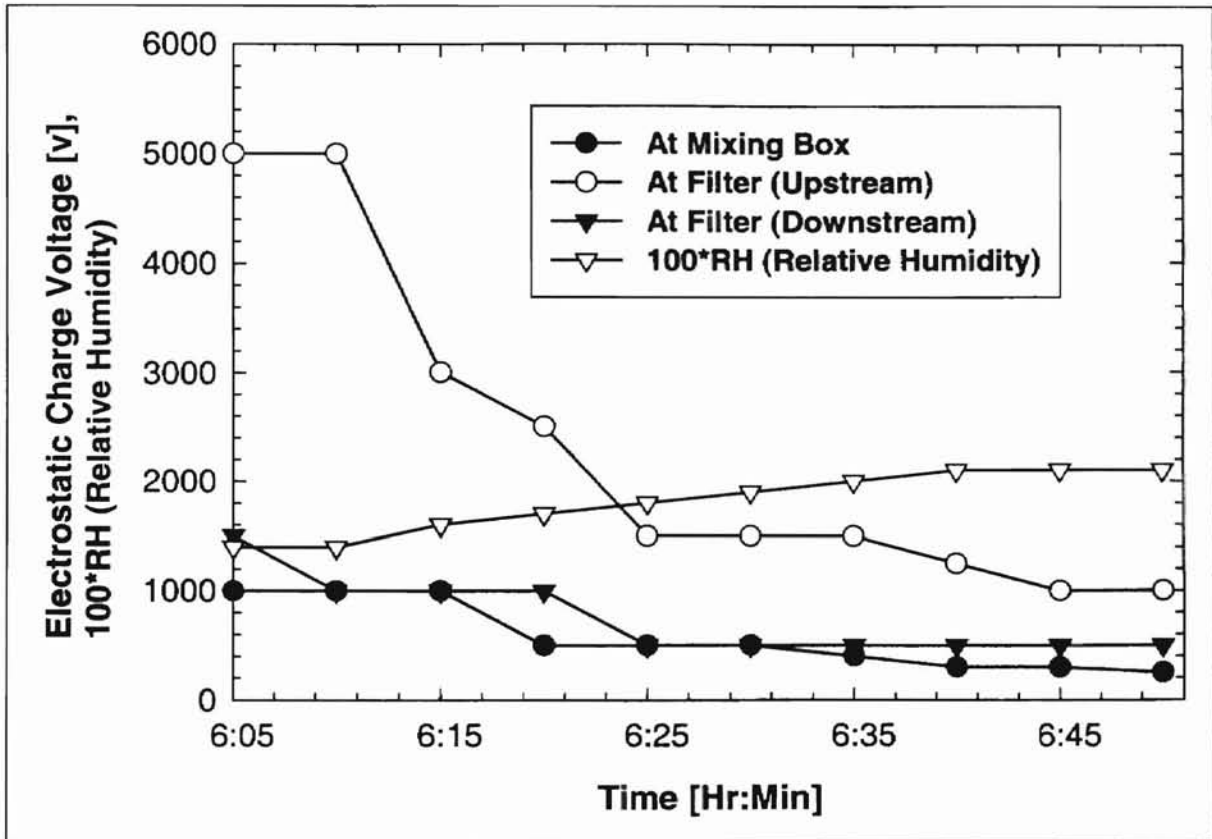


Figure 5.15 Electrostatic Discharging of an Initially Charged Plexiglass Filter Housing with Time (without Grounding, Winter, 1998).

The author believes that the discharging process is dependent upon the initial charge density and the relative humidity, which influences the conductivity of the air both inside and outside of the plexiglass housing. The humidity in the mixing box was also recorded and plotted as function of time. From this experiment, one can see how long it may take to neutralize the charge from an ungrounded filter housing.

The discharging of the filter housing as clean air flows through the filter housing and filter (without the use of any artificial contaminants) was also tested. The TSI flow meter was set at $60.8 \text{ m}^3/\text{hr}$, and the heater was turned on. After recording the average humidity of the air inside the mixing box as 29%, the continuous reduction of charge at the filter and zero electrostatic voltage at the mixing box was observed throughout the experiment (shown below in Fig. 5.16). The polarity of the charge generated at the filter was positive. The grounding of the housing proved effective in neutralizing the charge of the housing. From this experiment, one can infer by deduction that the atmospheric air is not quite clean and consists of a considerable amount of contaminants. Had it not been for the contaminants, the electrostatic voltage reading would have been zero.

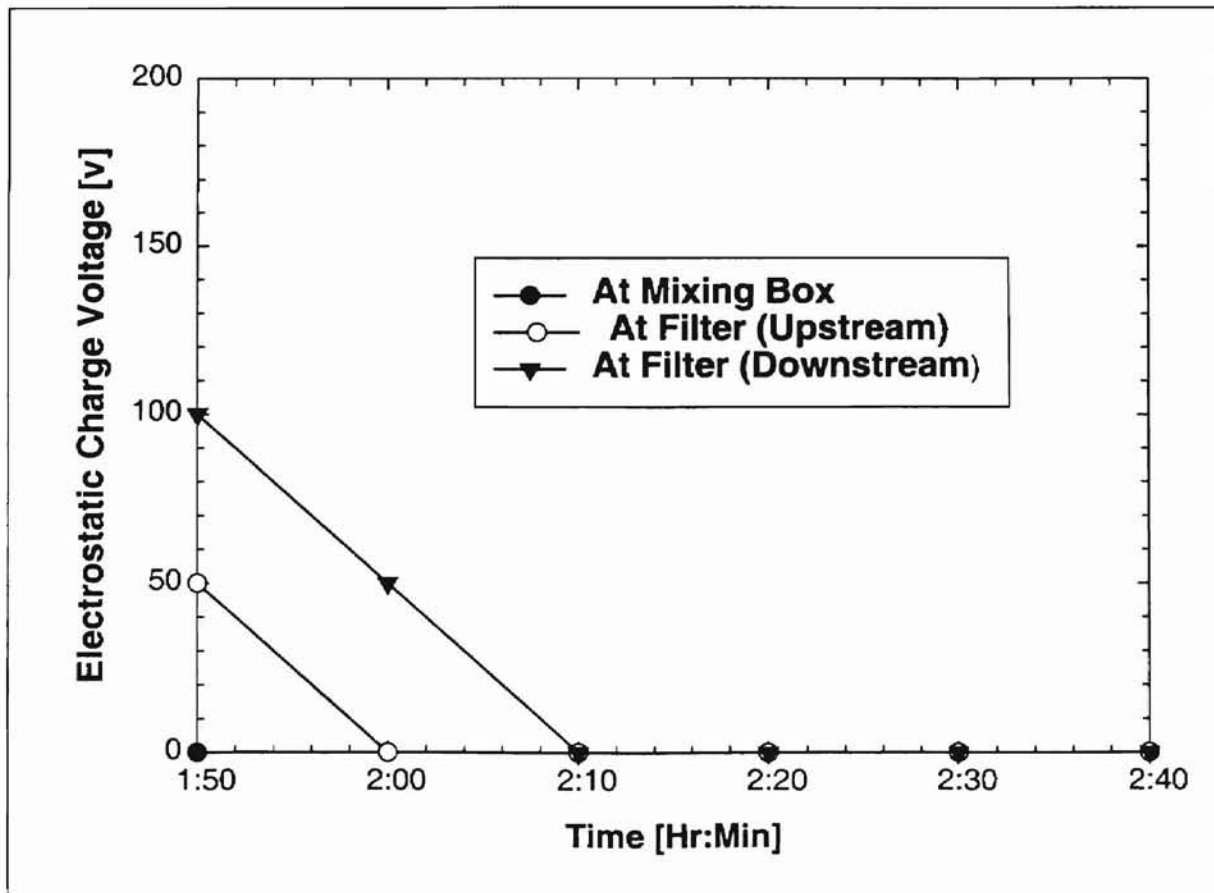


Figure 5.16 Electrostatic Discharging Using Grounded Aluminum Foil for Air at a Flow Rate of $60.8 \text{ m}^3/\text{hr}$ (Winter, 1998).

Another interesting experiment on the neutralization of charge from the test housing was conducted using glass beads at a low concentration (5 grams per 500 ml of distilled water). The use of a low concentration solution of glass beads as contaminants resulted in an electrostatic voltage measurement at the mixing box that followed an increasing-decreasing function with time (unlike that of the PSL particles) as shown in Fig. 5.17. Prior to the test, the TSI flow meter was set to a $60.8 \text{ m}^3/\text{hr}$, the heater and atomizer were also turned on, and the test continued as measurements were taken at intervals of 10 minutes. While the maximum electrostatic charge was limited only to 50 volts on the upstream and downstream sides of the filter, the electrostatic voltage at the ungrounded mixing box followed a parabolic shape (increasing-decreasing function) for

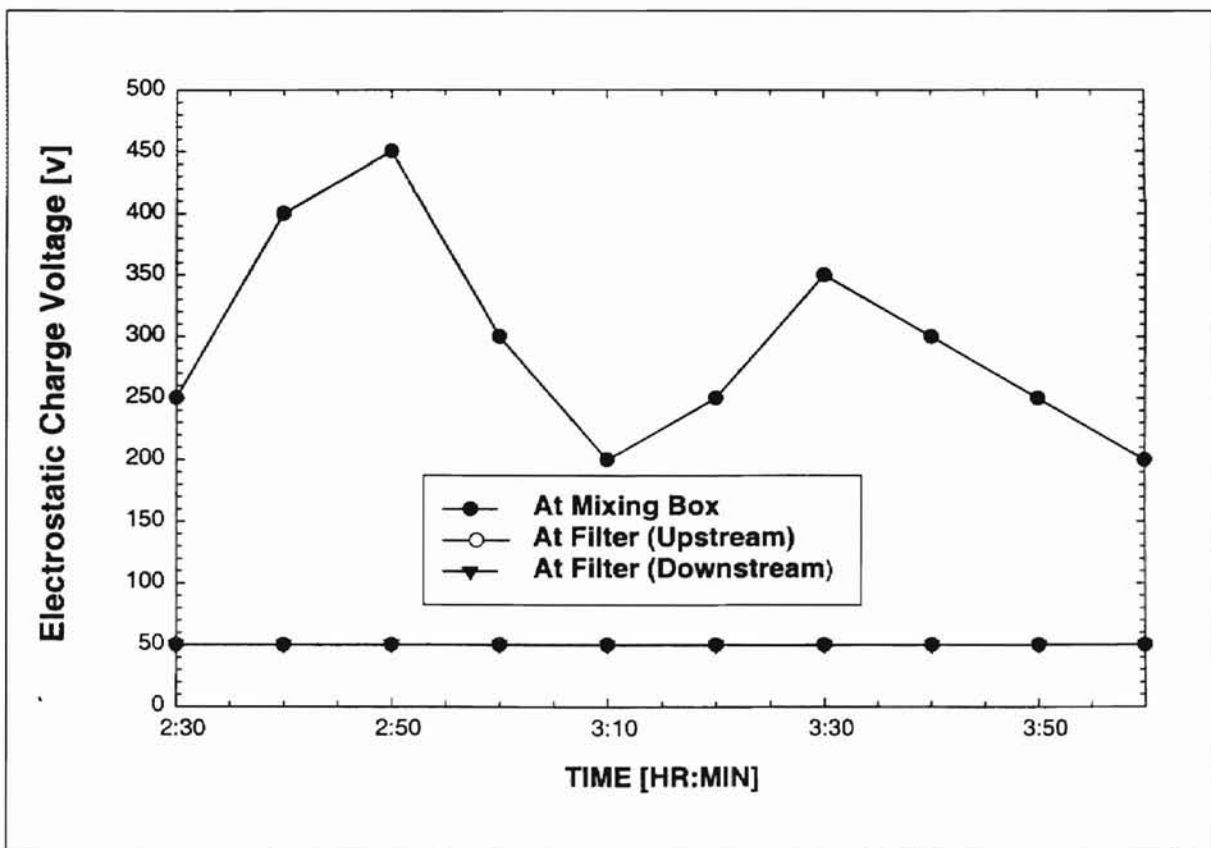


Figure 5.17 Electrostatic Discharging Using Grounded Aluminum Foil for $1.5 \mu\text{m}$ Diameter Glass Beads (conc. = 5/500, Winter, 1998).

the first 30 minutes. To find out if this was associated with the settling of the particles as a function of time, the atomizer was agitated by hand at 3:05 hours and as the atomization proceeded, it was possible to observe another similar increasing-decreasing trend beyond 3:10 hours (see Fig. 5.17). Thus as the particles tend to settle in the reservoir (tank) of the atomizer, the amount of particles injected into the flowing air decreases. This test indirectly helped to explain that electrostatic charge voltage is proportional to the concentration of particles injected to the flow.

The following can be summarized from Subsection 5.2 on the electrostatic charge investigation and consistency/repeatability measurements:

- The level (amount) of electrostatic voltage depends on type, size, particle concentration and humidity of the air flow and found repeatable.
- The polarity of the charge depends upon the type of contaminant. Following the atomization and drying of the solutions or the suspensions of different artificial contaminants and the flow of these particles through the PVC pipes (bends and elbows) and the plexiglass housing, electrostatic charge of varying magnitude may be generated. The electrostatic charge carried by the particle could be of either negative or positive polarity; or the particle may remain neutral, depending upon the type of the contaminant used (as shown in Table 5.1).

Table 5.1 Polarity of Charged Particles.

Type of Contaminant	Polarity
Salt (NaCl)	Neutral
PSL Particles of Different Diameters	Negative
Glass Beads	Positive
Room air	Positive

- Electrostatic charge voltage values depend upon time. At a constant air flow rate, the electrostatic charge voltage grows with time. The decay (discharging) of

electrostatic charge from the surface of the charged plexiglass housing also shows time dependence.

- Charge neutralization by covering the plexiglass housing with a conducting aluminum foil shows that electrostatic charge can be minimized provided the aluminum foil is grounded and has firm contact with the surface of the plexiglass housing.

5.3 Humidity and Moisture Measurements

In this section, humidity measurements performed upstream and downstream of the filter and procedures for the determination of moisture content of the air and the filter (at a certain air flow rate) will be presented. This is aimed at simulating the real filtration process with respect to the absorption of water moisture by excluding the solid dust particles. Humidity as discussed in the literature review, significantly affects the efficiency of fibrous filters by enhancing or discouraging the adhesion of particles to the fibers, depending upon the nature of the particles and the filter material. However in this section, the solid pollutants are neglected and the vapor-air mixture will be treated as a perfect gas obeying the gas laws for simplification.

The composition of the air and some important experimental humidity measurements, from which moisture content in the air or the filter may be estimated, are discussed in this subsection. Experimental humidity measurements of air (upstream of the mixing box as well as upstream and downstream of the filter) as functions of time and flow rate are presented in Subsection 5.3.2. Absolute humidity versus time plots can be obtained from the equivalent relative humidity versus time data (plots) with the help of

psychrometric charts or some calculations to estimate the moisture content. The estimate of the amount of moisture in the air at a constant flow rate will be demonstrated using simple numerical integral methods in Appendix G. Based on the procedure for determining moisture in the air (Subsection 5.3.4), simple mathematical formulas for predicting the moisture content of a fibrous filter are provided in Subsection 5.3.5.

5.3.1 Composition of Air and Basic Concepts of Humidity

Atmospheric air is a mixture of many gases and water vapor as well as a multitude of submicron solid pollutants, depending upon the geographical location and altitude. However, the standard composition of dry air as fixed by the International Committee on Psychrometric Data [McQuiston and Parker, 1994] is limited to only four main constituents as given below in Table 5.2.

Table 5.2 Composition of Dry Air [McQuiston and Parker, 1994].

Constituent	Molecular Mass	Volume Fraction
Oxygen	32	0.2095
Nitrogen	28.016	0.7809
Argon	39.944	0.0093
Carbon Dioxide	44.01	0.0003

The author finds it appropriate to go through the basic terms and definitions related to humidity and psychrometric parameters before any discussion of the experimental results and related investigations. Some of the basic terms and definitions of humidity or psychrometric parameters such as relative and absolute humidity (or humidity ratio), dry and wet bulb temperatures, dew point, gas law, etc., are provided in Appendix F.

5.3.2 Humidity and Temperature Variation of the Air Flow

In this subsection, measurement of humidity and temperature variation of the air, inside the PVC pipe before the mixing box and inside the test housing across the test filter under different conditions, will be presented.

The locations selected for temperature and humidity measurements are shown in the experimental flow setup in Chapter IV at positions, about 1.2 m above the heater and atomizer setup, 1, at the mixing box, 2, upstream of the filter, 3, and downstream of the filter, 4. Some representative plots of humidity and temperature variation with time or flow rate, before the air enters the mixing box or at the downstream and upstream of the filter, are presented in Figs. 5.18 through 5.25.

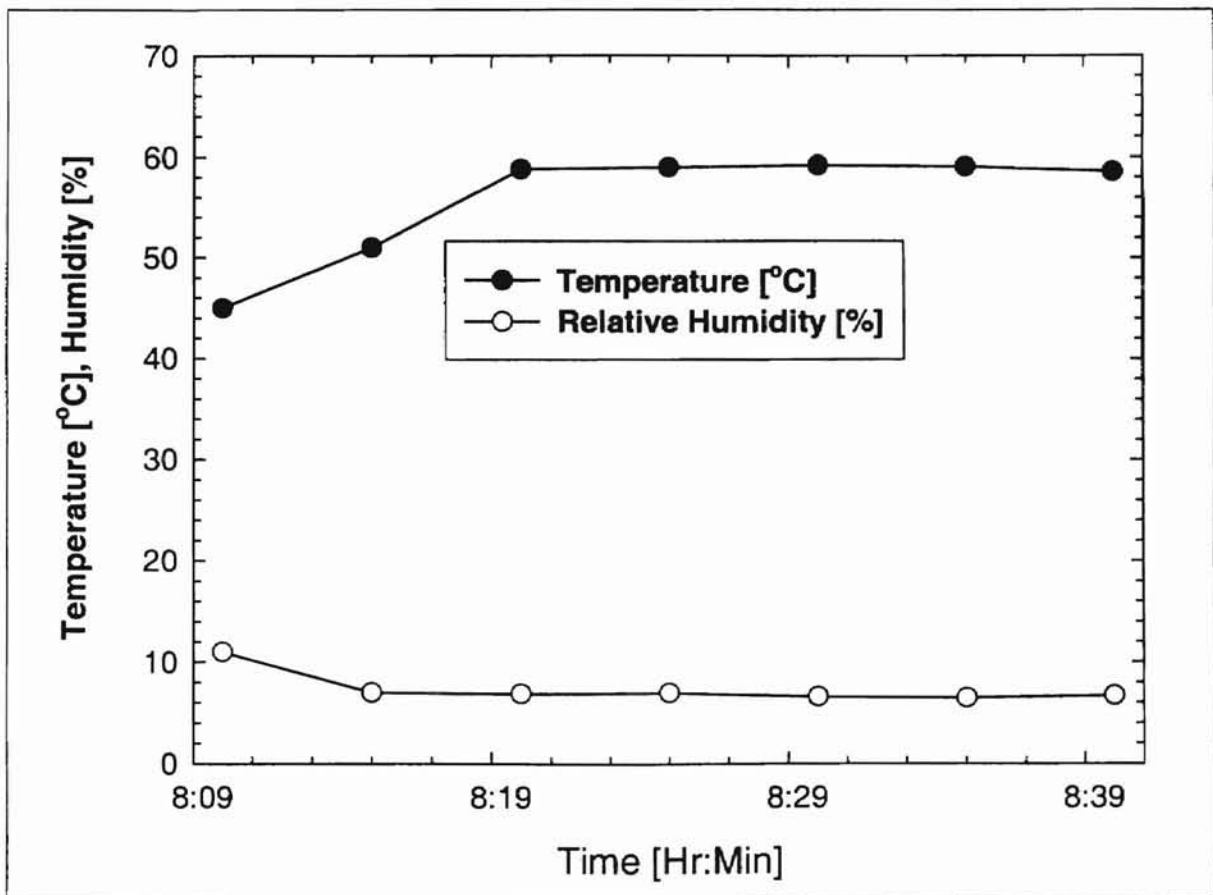


Figure 5.18 Temperature and Humidity Variations (before the Mixing Box) of Preheated Air at $6.97 \text{ m}^3/\text{hr}$ (Atomizer off, Winter, 1998).

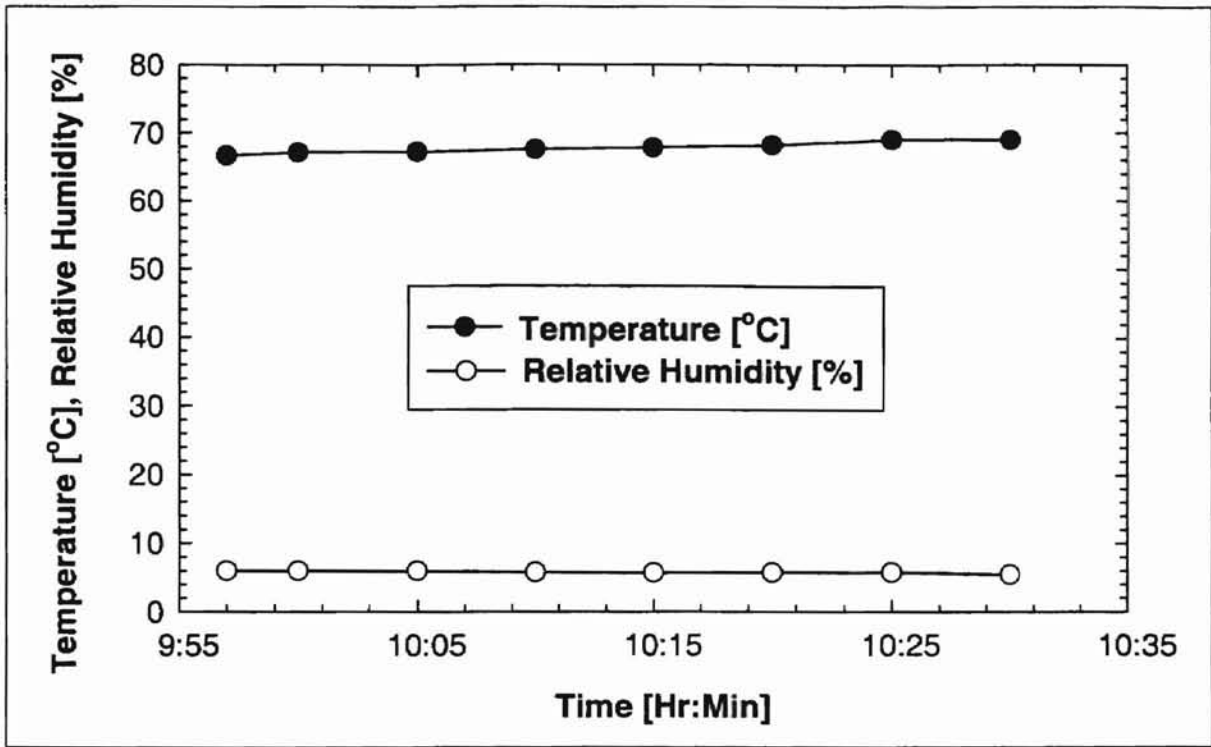


Figure 5.19 Temperature and Humidity Variations (before the Mixing Box) of Preheated Air at 42 m³/hr (Atomizer off, Date: 01/23/98).

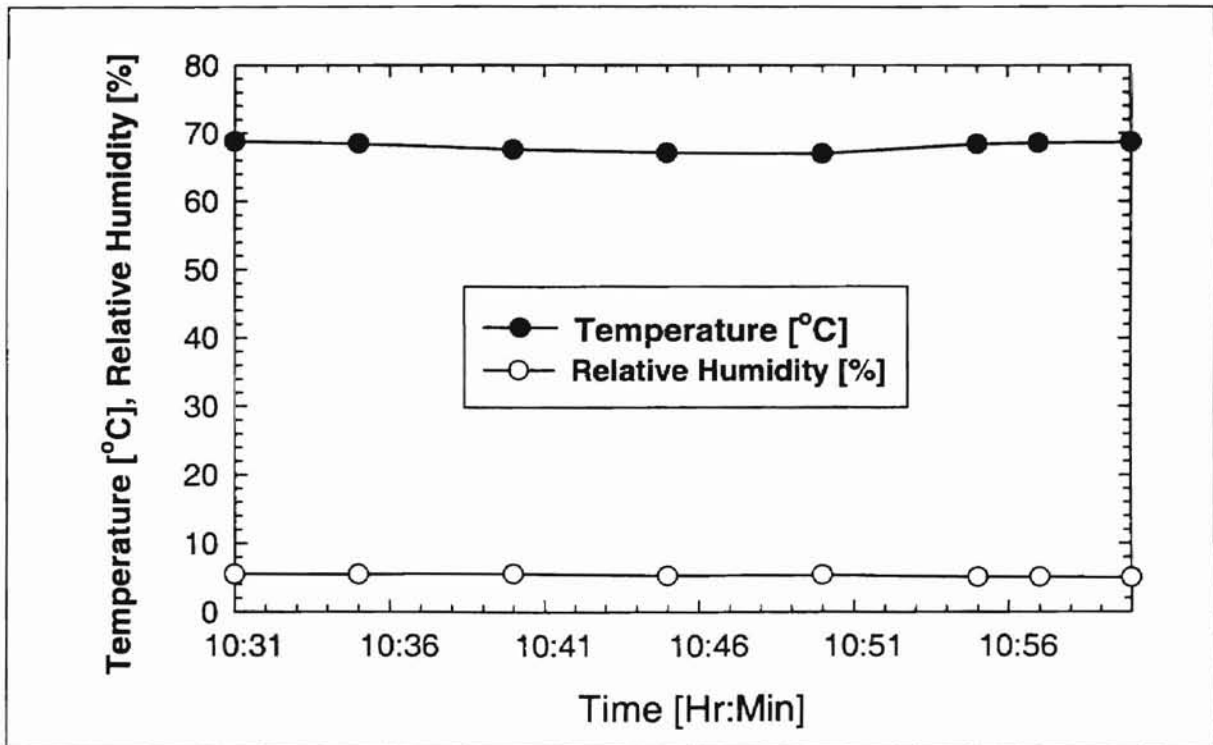


Figure 5.20 Temperature and Humidity Variations (before the Mixing Box) of Preheated Air at 40 m³/hr (Atomizer off, Date: 01/23/98).

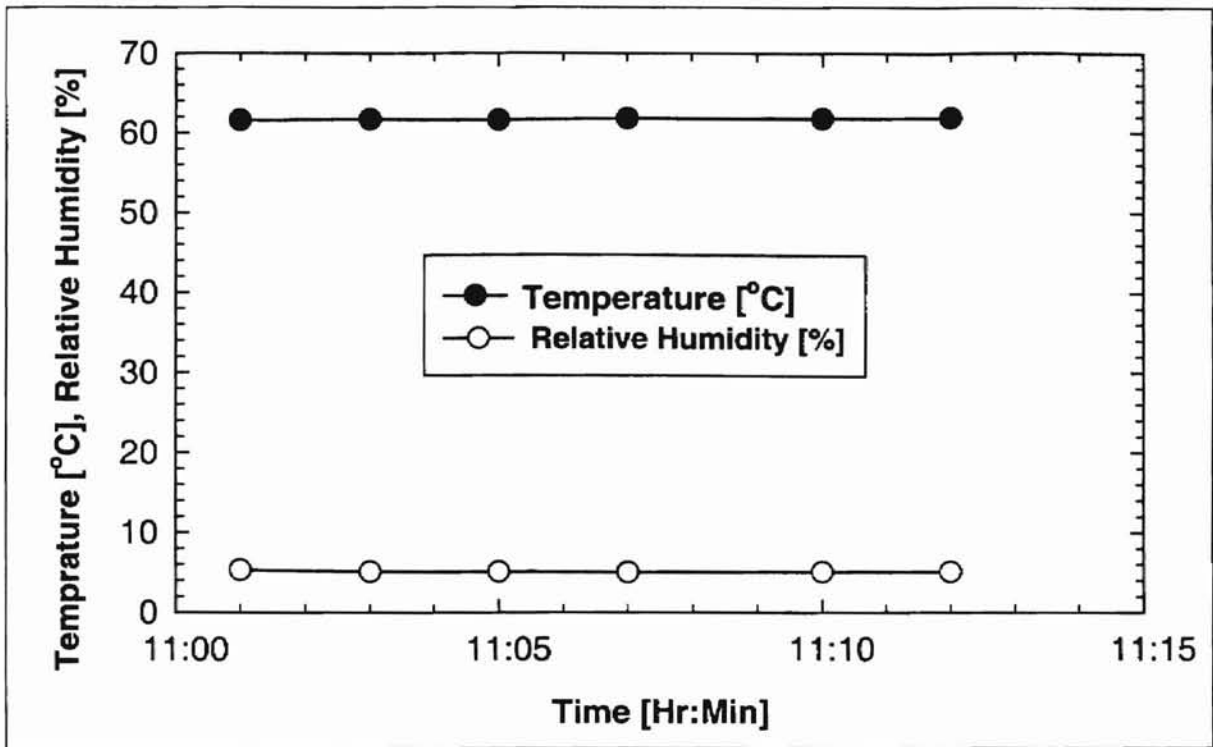


Figure 5.21 Temperature and Humidity Variations (before the Mixing Box) of Preheated Air at $60 \text{ m}^3/\text{hr}$ (Atomizer off, Date: 01/23/98).

A close comparison of Figs. 5.18 through 5.21, shows that the steady-state temperature of the preheated air was lower for low flow rates than the steady-state temperature for the intermediate flow rates. This inconsistency was attributed to the leakage of unpreheated air into the PVC duct through the unsealed duct-heater setup. The air flowing through the duct was not coming entirely through the heater. To offset this problem, some improvements were made to the setup by installing a new inlet duct. Since the capacity of the heater was also small, it became necessary to replace it with a new electric heater having a larger heating capacity. Thus the corrective measures on the inlet duct system ensured the passage of air through the heater so that the air was sufficiently heated to vaporize the atomized water and dry the PSL particles. Hence the steady-state humidity and temperature variations with flow rate improved for the new setup as shown in Fig. 5.22. Figure 5.23 shows relative and absolute humidity variations.

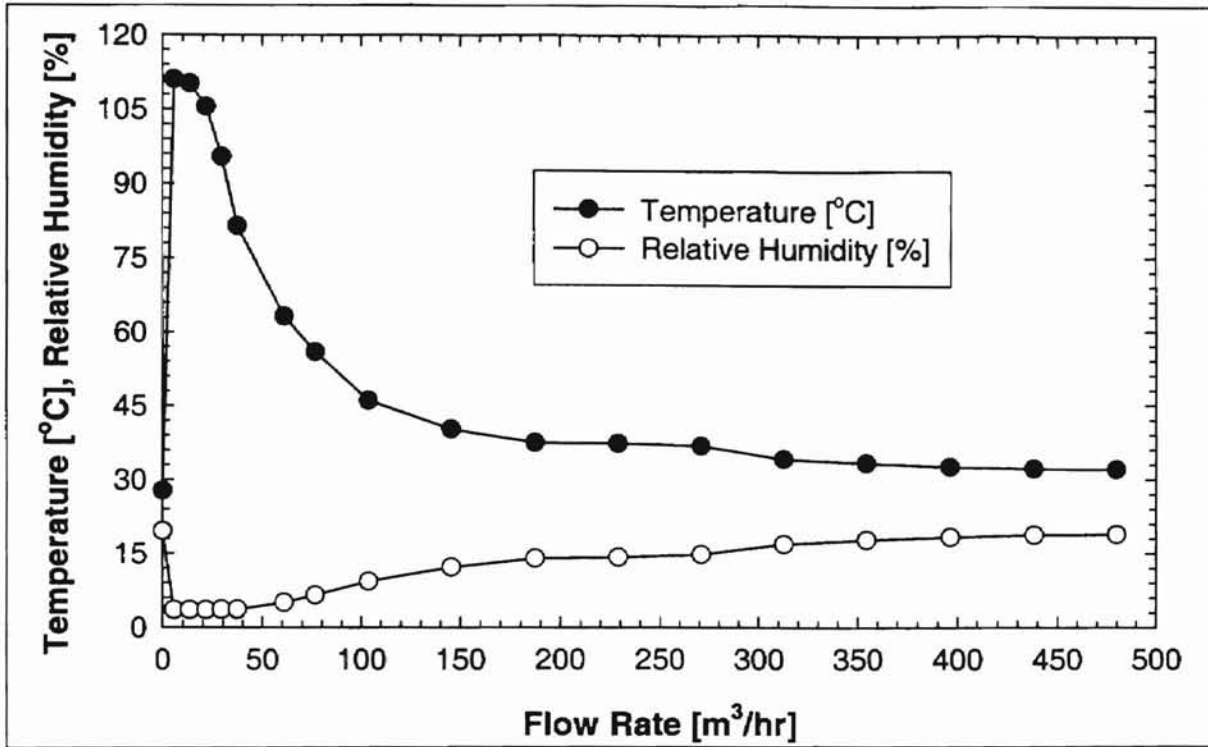


Figure 5.22 Temperature and Humidity Variations (before the Mixing Box) with Air Flow Rate Using a New Inlet Duct (Atomizer off, Heater on, Date: 01/25/98).

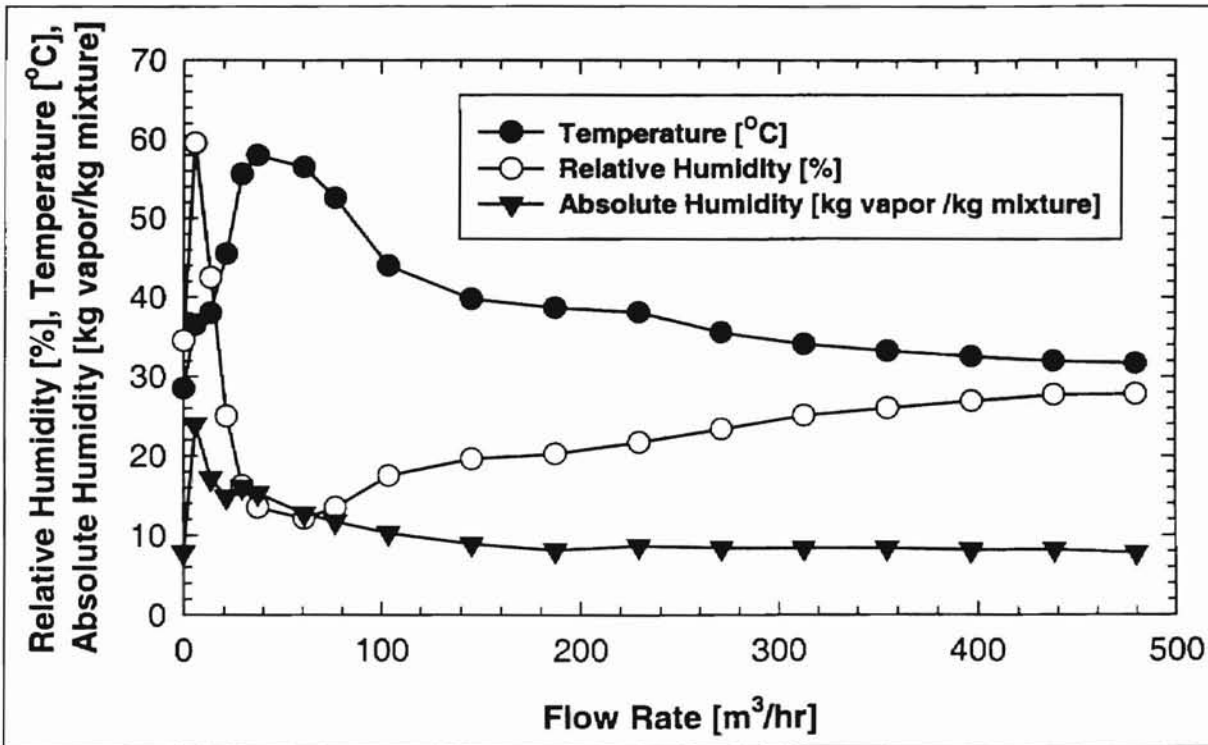


Figure 5.23 Temperature and Humidity Variations (before the Mixing Box) of Preheated Air while Atomizing Distilled Water (Atomizer on, Heater on, Date: 01/25/98).

The temperature and humidity variations for each flow rate in all cases were recorded as a function of time until the readings reached steady-state. The time taken to reach steady-state was longer for lower flow rates than for higher flow rates.

Figure 5.24 shows the variation of absolute and relative humidities and temperature of the air as a function of the air flow rate downstream of the filter. The atomizer was shut off while the heater was turned on.

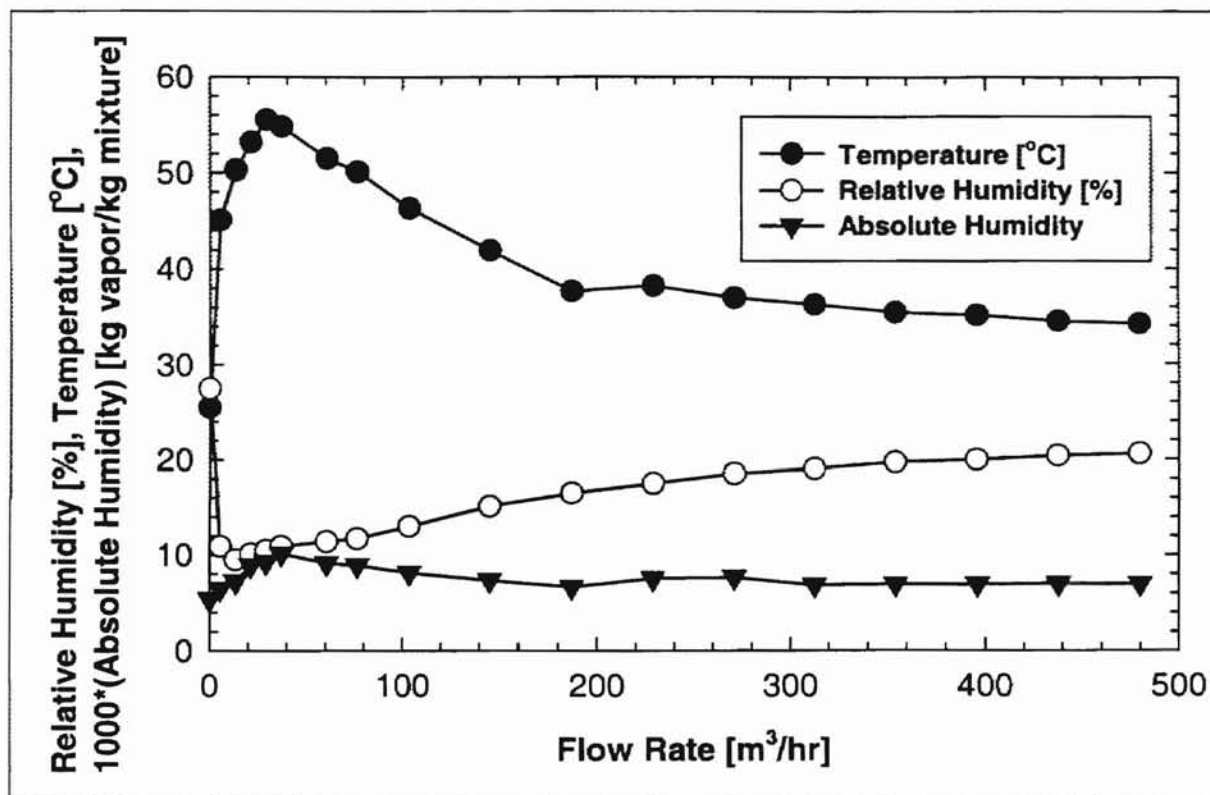


Figure 5.24 Temperature and Humidity Variations of Preheated Air (6 cm from Filter Downstream Surface) (Atomizer off, Heater on, Date: 01/28/98).

Humidity and temperature variation was also measured about 6 cm upstream of the filter surface. The shapes of the plots for the upstream case are more or less similar to that downstream of the filter or at the mixing box. Figure 5.25 is a plot of the temperature and humidity variations obtained by atomizing distilled water and preheating the air.

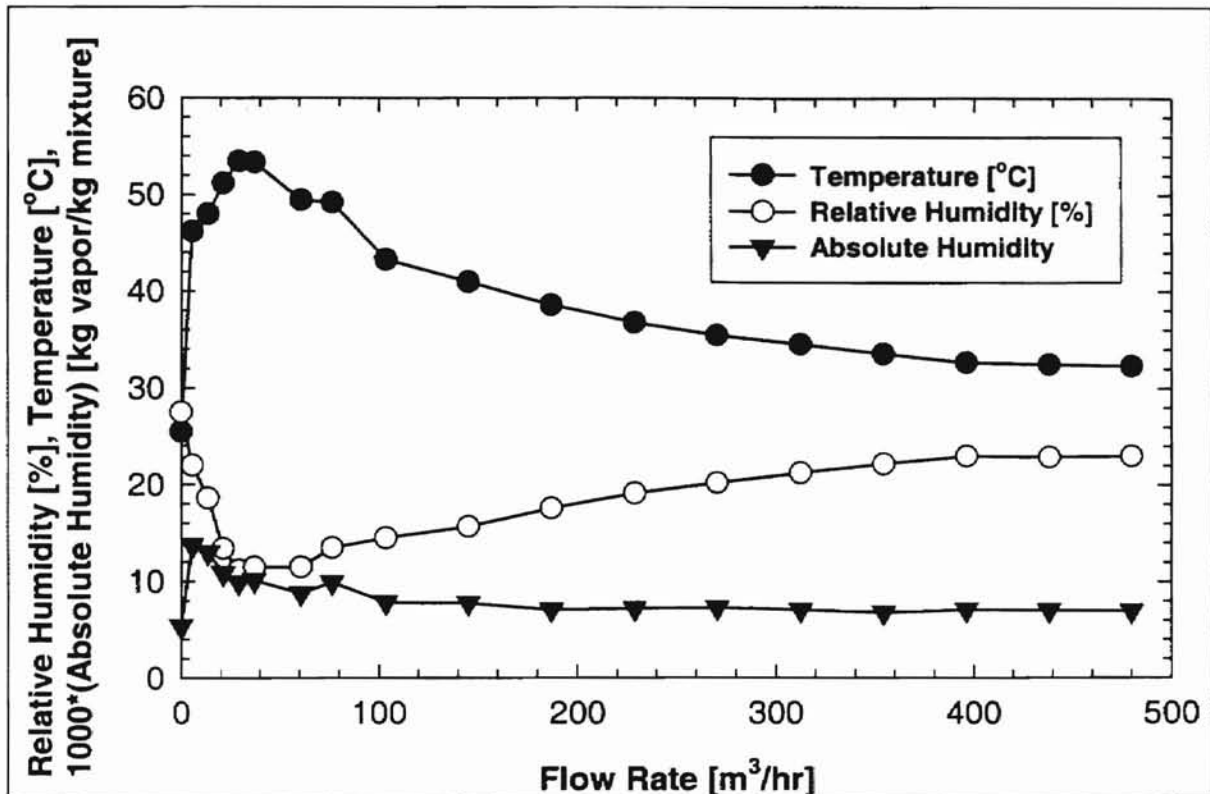


Figure 5.25 Temperature and Humidity Variations of Air (6 cm from Filter Upstream Surface) while Atomizing Distilled Water (Heater on, Date: 01/28/98).

5.3.3 Humidity Control

In fibrous filtration, it is important that the humidity of the air is known and kept constant to within $\pm 5\%$. As shown in many of the humidity and temperature variation plots in Subsection 5.3.2, not only does the humidity of the air vary with flow rate but it also exhibits time dependence.

The temperature and humidity of the air inside the laboratory is mainly affected by the heat loads from the blower and air heater. However, weather conditions outside the building also contribute their share. This implies that there is fluctuation in the humidity of the air inside the room due to temperature changes, which makes it essential

to introduce humidity control mechanisms. Thus to control the humidity of the air reaching the filter and to maintain the required average humidity inside the test housing, an ultrasonic humidifier was used. The humidifier generated clouds of water vapor (mist) using ultrasonic vibration. The humidifier was installed near the inlet duct below the entrance of the atomized particles and above the heater as shown in the experimental set up [refer to Fig. 4.13]. The humidifier was also connected to the PVC piping and a valve was installed at the connecting tube to regulate the flow of the mist.

The ultrasonic humidifier helped increase the humidity of the air flow substantially for low flow rates up to $187.7 \text{ m}^3/\text{hr}$ in the summer season and up to $103.7 \text{ m}^3/\text{hr}$ during the winter season. The maximum limiting humidity that could be achieved was 50% for both flow rates (103.7 and $187.7 \text{ m}^3/\text{hr}$). However, one had to learn some additional techniques to increase or decrease the humidity by controlling the heat supply to the incoming air and by monitoring the temperature and humidity of the air by a hygrometer-thermometer device installed at the mixing box. The movable inlet duct mounted on the heater, shifting of the heater around, and switching between minimum and maximum heating capacities of the air heater were some of the effective methods used in the regulation of the heat supplied into the air flow to control the humidity.

5.3.4 Determination of Moisture Content in Air

In the previous sections and subsections of this chapter, the humidity and temperature variations of the air at different locations along the filter housing were presented as a function of time or flow rate. From these, one has a clear picture of how the humidity and temperature vary with time and flow rate. In this subsection, the

author's interest is to present some techniques that might help in the determination of moisture from the experimental humidity measurements. Figures 5.18 through 5.21 show time dependent temperature and humidity plots at constant flow rates. From these plots, we can estimate the moisture content in the air that can be transferred or given up to the filter, depending upon the previous history of the filter. The procedures are as follows:

1. Transform the relative humidity functions into the corresponding absolute humidity function.
2. Use numerical methods to integrate the absolute humidity versus time curve to estimate the amount of moisture carried by the air in that period of time.

The details of the procedures for estimating the moisture content in air that can help to evaluate the amount of moisture (water film) inside the filter or moisture lost from the filter to the air are provided in Appendix G.

5.3.5 Determination of Moisture for Fibrous Filters

Though it may be possible to determine the amount of moisture in fibrous filters using some other techniques (for example, gravimetric analysis) before and after the filtration test, mathematically predicting the moisture contents in a filter becomes a useful and reliable means for several other investigations of adhesion models.

A real automotive filter may undergo incessant exchange of moisture with the induction air depending on the environmental conditions. For special tests, the amount of moisture absorbed or lost can be determined by monitoring the humidity and temperature of the airflow upstream and downstream of the filter during the filtration process. Hence applying the procedures listed in Appendix G upstream and downstream of the filter the

procedures filter, one can obtain the moisture loss or gain, MF of the filter by,

$$MF = M_{V(UP)} - M_{V(DOWN)} \quad (5-1)$$

where $M_{V(UP)}$ and $M_{V(DOWN)}$ are the respective moisture contents of the air on the upstream and downstream of the filter over a certain experimental run time.

For humidity controlled experiments, it might be also important to consider using empirical equations based on experiments to estimate the instantaneous moisture content. One important assumption is that moisture absorption is proportional to the moisture concentration or gradient between the air and the filter. From the experimental results, the author has observed that the time taken to reach equilibrium in moisture and temperature between the filter and the dispersing medium (in this case, air) is much shorter for high flow rates than for low flow rates. Thus a mathematical equation by Young et al. [1965] used in the tobacco industry for predicting the moisture content of tobacco under controlled conditions may be used for this purpose to begin with. It has been derived from drying operations, which states that the rate of drying of a slab is directly proportional to the moisture content. The basic differential equation is given by,

$$\frac{d(MF)}{dt} = \varpi(MF_E - MF) \quad (5-2)$$

Integration yields,
$$\frac{MF_E - MF}{MF_E - MF_i} = e^{-\varpi t} \quad (5-3)$$

Rearranging the above equation and solving for MF yields,

$$MF = MF_E - (MF_E - MF_i)e^{-\varpi t} \quad (5-4)$$

where MF = the moisture content at time t

MF_i = initial moisture content

MF_E = moisture content at equilibrium

ω = is a parameter dependent on the velocity of the air

ω may be determined for each desired flow rate in a controlled experiment, it may also depend upon the type of filter material, and the initial and final (equilibrium) moisture content. Both the initial and final moisture content can also be determined using gravimetric analysis.

Humidity and temperature measurements upstream and downstream of the filter have revealed that, as time becomes larger and larger, the temperature and humidity upstream and downstream of the filter approach each other. This implies that equilibrium in humidity and temperature is eventually established between the two media. At equilibrium, the rate of moisture transfer with time becomes zero. In the rate of moisture transfer, some of the important parameters that may need to be considered are the flow rate or velocity of the air, the running (exposure) time and the type of filter material. A filter or filter material that is chemically treated as water-resistant and repellent may not behave the same way as the untreated filter material.

From Section 5.3 on humidity and moisture measurements, the following can be summarized:

- All humidity measurement experiments were found repeatable.
- The humidity and temperature of the air at any location along the duct show time dependence as the air flows with constant heat supply to it by the heater.
- At low flow rates, the time taken for a flow to reach steady-state temperature and humidity is longer than that for high flow rates.

- As the flow rate increases indefinitely, the humidity and temperature of the air flow approach room conditions.
- By calculating and establishing absolute humidity variation with time from the relative humidity curves for a constant flow rate, it is possible to estimate the amount of moisture held in the air.
- Monitoring the relative humidity and temperature of the air upstream and downstream of the filter may help estimate the amount of moisture absorbed by the filter using numerical methods under especial conditions to study adhesion models.

5.4 Consistency Measurements

In Chapter IV, some of the problems related to the stability of the laser that can result in inconsistent number density or efficiency measurements were discussed. Other potential sources of poor repeatability are as follows:

- (1) particle seeding (atomization) rate,
- (2) electrostatic charge,
- (3) air humidity,
- (4) air leakage into the filter test housing.

There have been reports of inconsistent particle counting, sizing and filter efficiency measurements by previous researchers [Liang, 1997; Natarajan, 1995] here at the School of Mechanical and Aerospace Engineering Air Filtration Laboratory. Initially water droplets generated by an ultrasonic humidifier were used as seeding particles. A suction blower drew the air along with the water droplets from the humidifier into the

duct. However, the results obtained by seeding with water droplets as contaminants were inconsistent and contradictory from test to test. Thus the repeatability of the experiments was poor. This might have been due to the evaporation of the water droplets when the air was dry (low humidity) and the condensation of additional water droplets when the humidity of the air was high. There were many unsuccessful efforts to solve the problems of inconsistencies associated with the use of water droplets from a humidifier as seed particles until the humidifier was replaced by a new TSI Model 9306 six-jet atomizer [Liang, 1997]. Though the atomizer is capable of generating particles from any fluid, the atomization and drying of suspensions of PSL particles was preferred for several reasons and introduced about 6 years ago.

In this section, in addition to the presentation of the consistency measurements on humidity, electrostatic charge, particle seeding and concentration, the author briefly presents some of the test results showing how laser power instability affects the number density. In Chapter IV, the discussions of the stability of the laser power and the main factors that affect it have been established through experiments. The experimental results of the laser instability due to temperature effects, which this author and Saxena [1998] jointly performed are reported and documented in the appendix of his thesis work. For this reason, the author will not discuss these tests in detail; but three plots are presented in order to demonstrate these effects in the next subsection.

5.4.1 Number Density Variation and Electrostatic Charge

The variation of the laser power with temperature has been a major concern until this author finally improved and verified the solutions of the instability problems as discussed

in Chapter IV of this thesis. Non-neutralized particles are also believed to contribute to the inconsistencies of filtration efficiencies. Figures 5.26 through 5.28 show the effect of coupler temperature variation on the stability of the laser power. The laser beams under investigation were the shifted and unshifted green or blue beams. Two pairs of beams of the same color but of different orders (shifted or unshifted) were simultaneously tested for power stability with time, as the temperature at the couplers changed or remained stable within ± 0.5 °C. Figure 5.28 clearly shows how the power of each laser beam responds to temperature changes. For the first few minutes as the laser temperature steadily increases, the power for both laser beams decreases. But later, as the coupler temperature decreased, the power tended to increase.

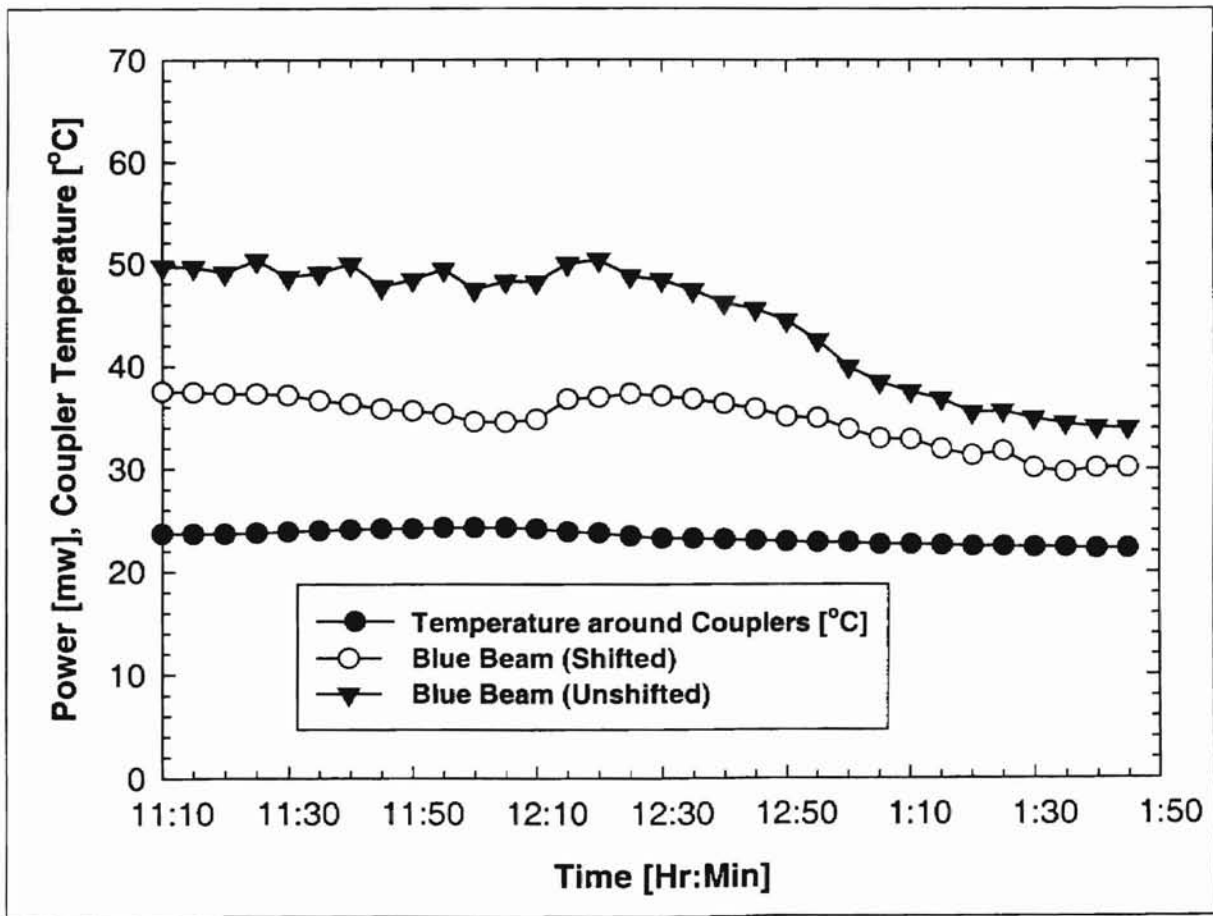


Figure 5.26 Laser Power Variation with Time as Coupler Temperature Changes.

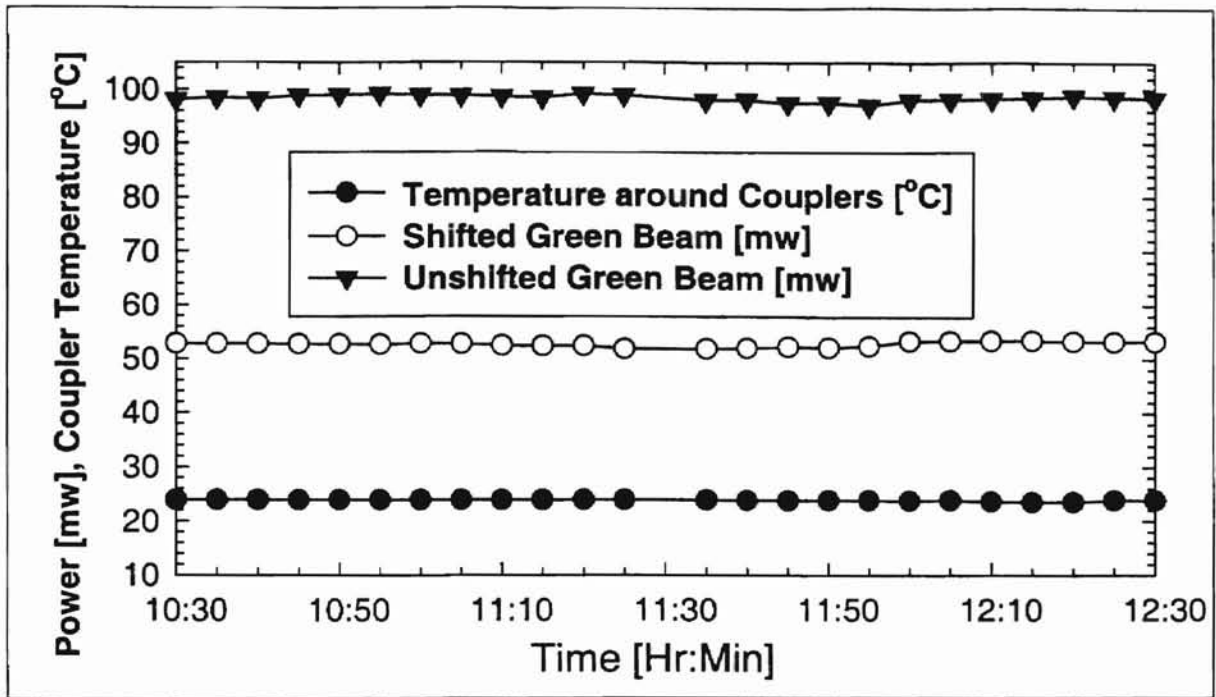


Figure 5.27 Laser Power Variation with Time as the Temperature at the Couplers Remains Stable.

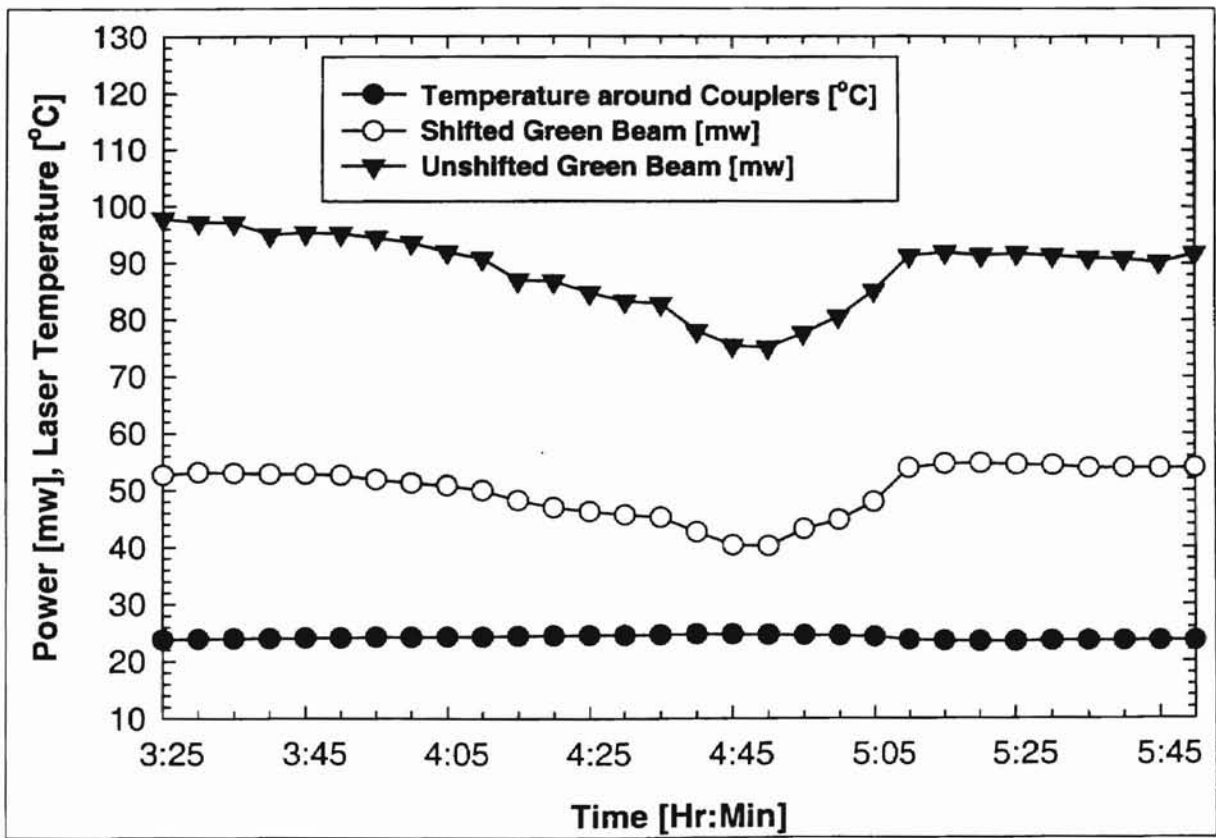


Figure 5.28 Laser Power Variation as Temperature at Couplers Changes.

The verification of the aluminum foil's ability and reliability to produce the electrostatic charge neutralization was also simultaneously carried out with the consistency measurement of number density. The following initial experiment was conducted to see the variation of number density with laser (coupler) temperature. By maneuvering the laser transceiver probe using the three-dimensional motion controller, the probe volume of the laser was brought to the center of the filter inside the housing about 10 to 12 mm above the filter surface. After starting the blower (adjusted to 103.7 m³/hr) and aligning the laser beams at a reference temperature, the atomization of the 0.966 μm diameter PSL particles proceeded, and the proper DSA parameters for collecting the signals were set. The temperature of the laser was monitored so that it remained constant throughout the experiment by turning on the air conditioner [Saxena, 1998] depending upon the necessity or the temperature changes inside the plexiglass laser cover that houses the laser tube and fiber drive unit. During the experiment, the data (the velocity, number of samples collected and run time) from the computer and laser temperature were recorded simultaneously every 2 to 3 minutes. Figure 5.29 shows the plot of number density and laser temperature variation with time.

To further verify that temperature change causes the laser power to vary, which in turn affects the detection of particles or number density, another test was performed by holding the temperature at the couplers constant. As shown in Fig. 5.30, the number density tends to oscillate about an average value of approximately $7 \times 10^8 \text{ m}^{-3}$. This was indeed a good verification that constant coupler temperature helped to maintain constant laser power and hence consistent number density and efficiency measurements.

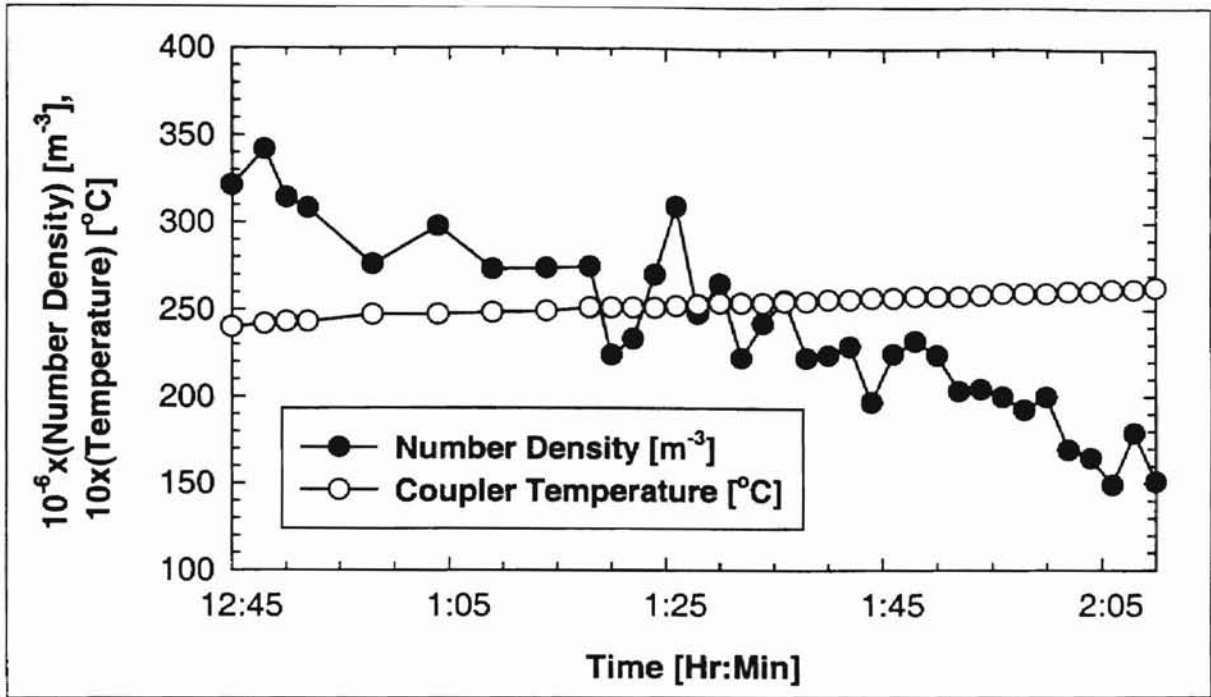


Figure 5.29 Variation of Number Density with Time as Coupler Temperature Changes for a Constant Flow Rate of $103.7 \text{ m}^3/\text{hr}$.

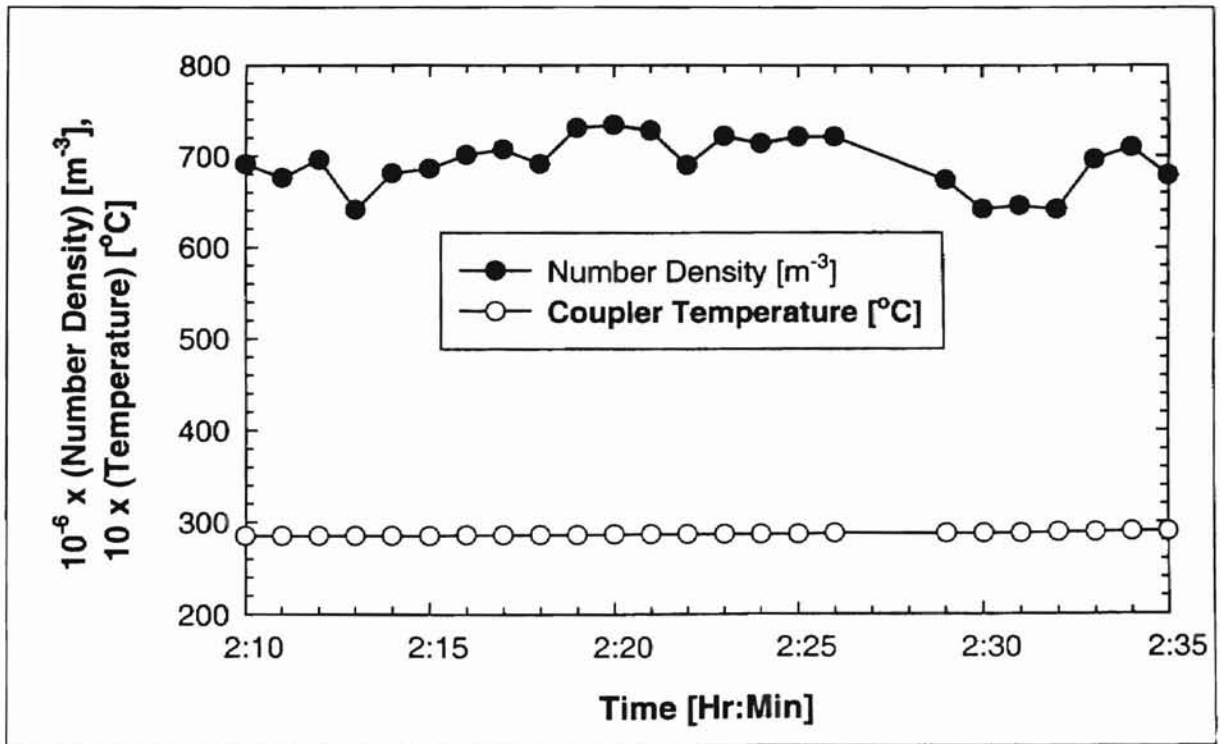


Figure 5.30 Variation of Number Density with Time at Constant Coupler Temperature and Constant Air Flow Rate of $103.7 \text{ m}^3/\text{hr}$ (Date: 05/30/98).

Electrostatic charge has been listed by many researchers [Liu and Pui, 1974] as a potential source of inconsistency in the efficiency measurements of fibrous filters. Hence to avoid unwanted electrostatic charge effects in the laboratory, charge neutralization becomes an essential task. Thus the following experiment was performed in order to evaluate and further investigate the effectiveness of the aluminum foil in the neutralization of electrostatic charge and monitor the variation of number density as coupler temperature and humidity vary with time. Figure 5.31 shows the test results.

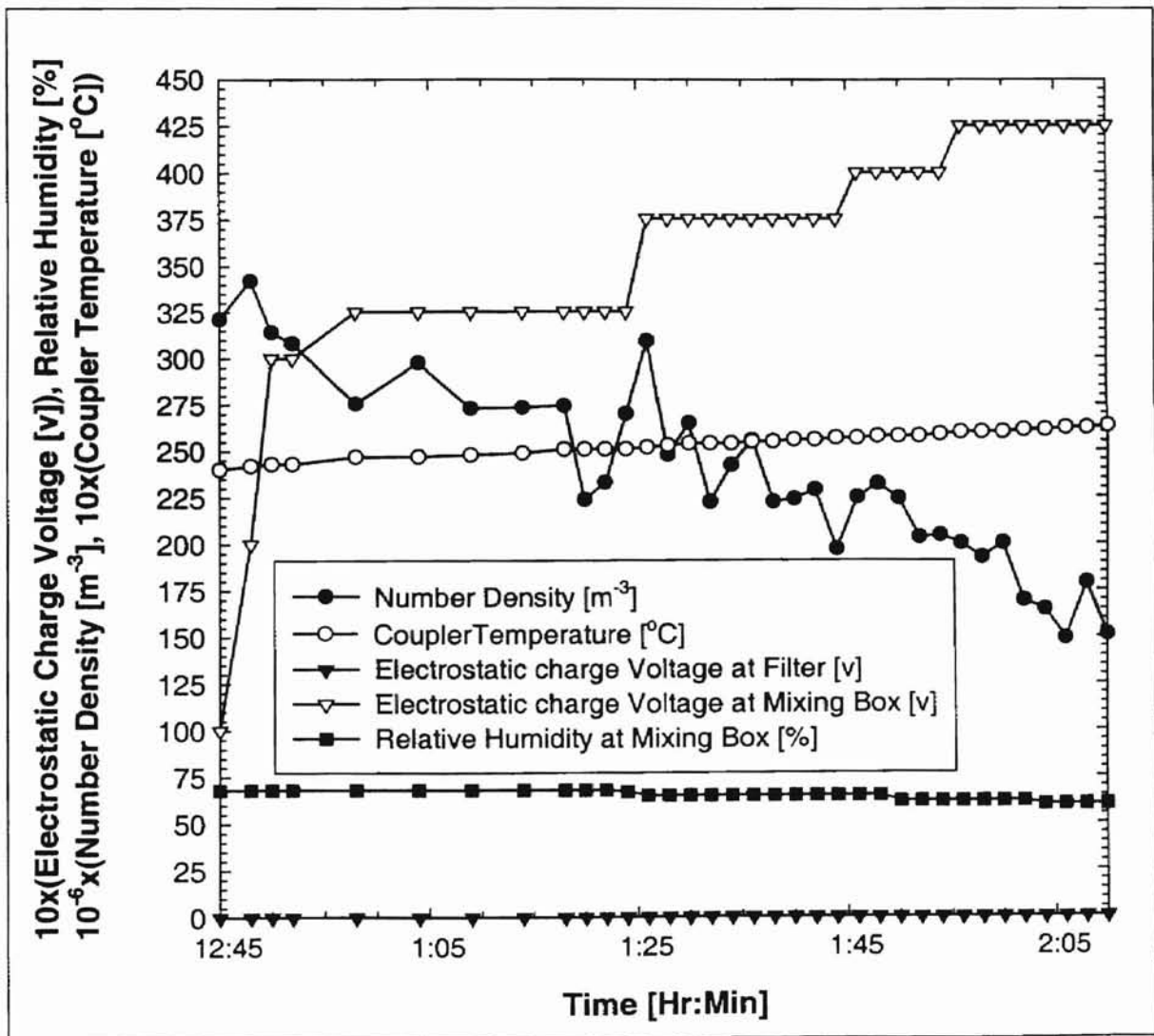


Figure 5.31 Number Density, Relative Humidity, Coupler Temperature, and Electrostatic Charge Voltage Variations with Time (Flow Rate of $103.7 \text{ m}^3/\text{hr}$, $0.966 \mu\text{m}$ Diameter PSL Particles).

The results were simultaneously monitored, at a constant air flow rate of $103.7 \text{ m}^3/\text{hr}$. The electrostatic voltage at the filter remained zero throughout the experimental time period. While proving the effectiveness of the grounded aluminum foil in reducing electrostatic charge from the grounded surface of the pelexiglass housing above the filter, the ungrounded mixing box showed a time dependent charge growth. The number density of the particles decreased as the temperature of the couplers gradually changed.

On the other hand, Fig. 5.32 shows plots of test results for the repeatability of the previous test on the effectiveness of aluminum foil in neutralizing charge as time goes by.

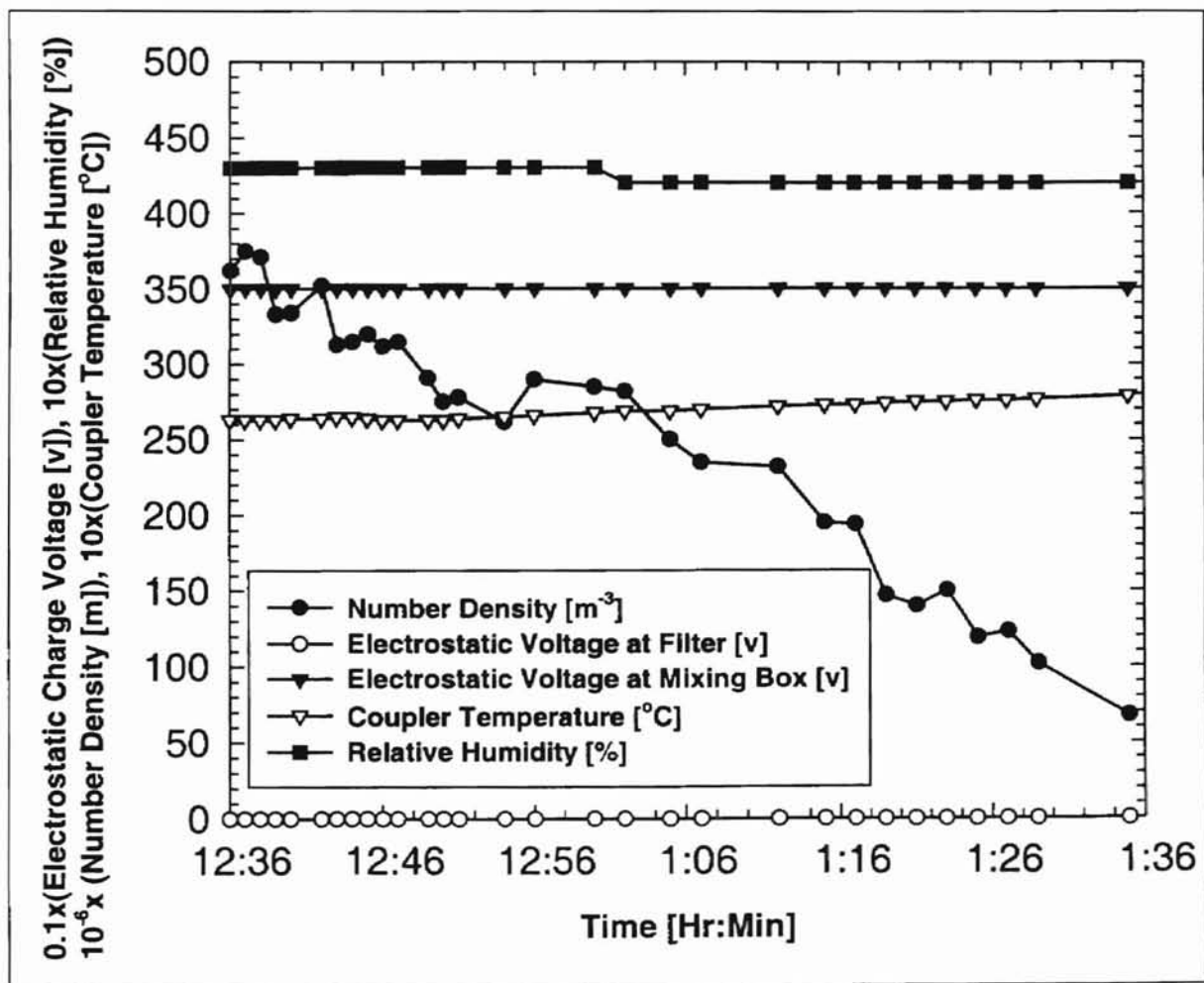


Figure 5.32 Variation of Number Density, Coupler Temperature, Relative Humidity, and Electrostatic Charge Voltage, and Relative Humidity of Air inside the Housing (Constant Flow Rate of $103.7 \text{ m}^3/\text{hr}$, $0.966 \mu\text{m}$ Diameter PSL Particles).

It also shows electrostatic charge voltage growth with time after running the system for one hour by turning on the blower, heater and atomizer (for the atomization of 0.966 μm diameter PSL particles). The variations were closely monitored and recorded. From this plot, one can see that the coupler temperature had changed appreciably, while the electrostatic charge voltage at the ungrounded mixing box increased to 3500 v, but the voltage at the filter remained zero. The number density of the particles was further decreasing with time as the coupler temperature gradually increased. Unlike the reports of the previous studies by Anand [1997], which stated that maintaining the bread board temperature within ± 0.1 $^{\circ}\text{C}$ (using the Omega RH21 digital thermometer) would guarantee to maintain constant number density, in this study, maintaining coupler temperature within ± 0.5 $^{\circ}\text{C}$ was important in order to keep the number density constant.

The conclusion to be drawn from the test was that the number density varied as the temperature changed. On the other hand, the electrostatic charge voltage at the filter was minimized by the installation of grounded aluminum foil showing its effectiveness.

5.4.2 Humidity Effects

The author believes that uncontrolled humidity is one of the sources of inconsistency in filter efficiency measurements during the filtration process.

In order to study how the humidity and temperature of the air flow change with flow rate without controlling the humidity and temperature, an experiment was performed and the test results plotted. Figure 5.33 is a typical example of a humidity curve for maximum and minimum humidities for various flow rates by simply maintaining constant heat supply or constant injection rate of mist (water vapor) into the air flow.

The minimum humidity curve was obtained by supplying a constant heat supply to the air flow at different flow rates and atomizing distilled water (to simulate the atomization of solutions of suspensions of PSL particles). On the other hand, the maximum humidity curve was obtained by injecting a constant flow of mist into the duct in addition to the constant supply of heat. Thus for both cases, at low flow rates, there is relatively higher humidity than at the intermediate flow rates, due to the injection of distilled water to the air. However, as the flow rate increases steadily, the temperature and humidity changes for higher flow rates are smaller than those for intermediate or low flow rates.

In order to compare the efficiencies of a filter at different flow rates, it is important that the humidity of the air flow be maintained constant. To test the reliability of the experimental setup, an experiment was carried out to see how possible it would be

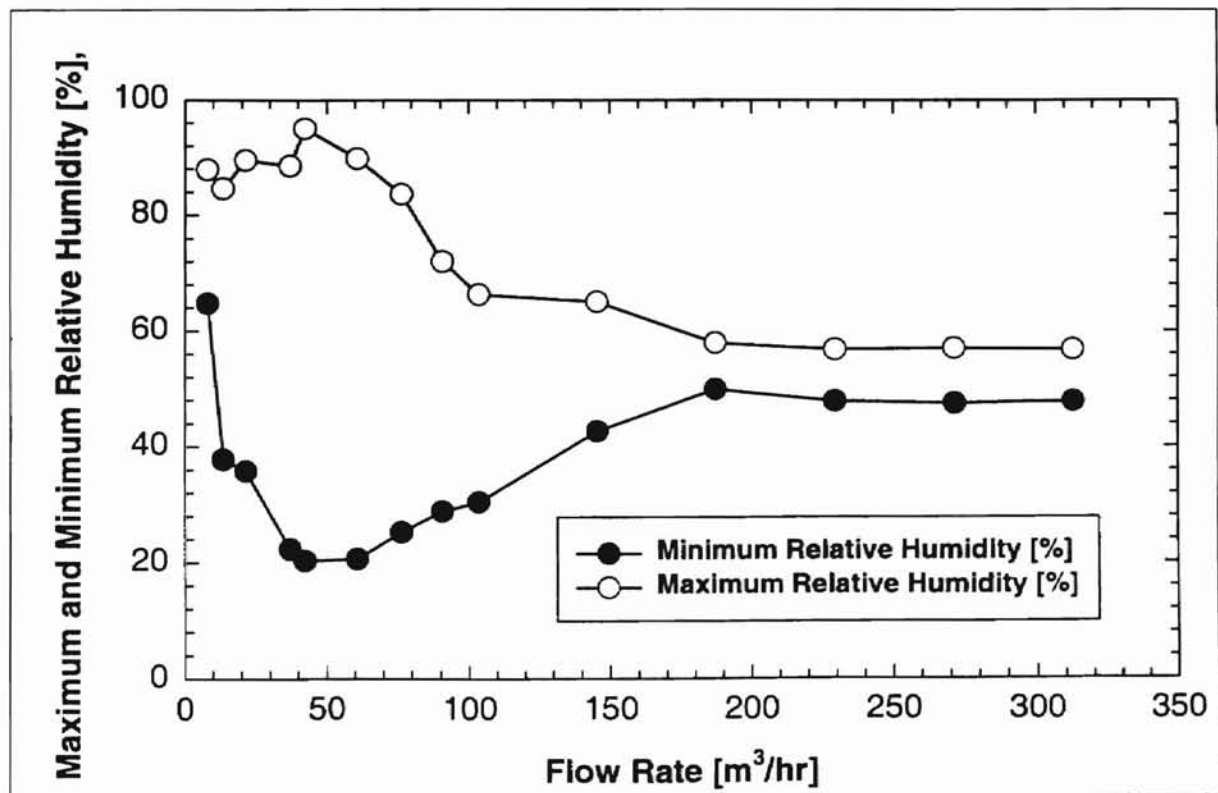


Figure 5.33 Minimum and Maximum Relative Humidity Variations with Flow Rate (Humidity Control: Using Humidifier, Heater, and Atomization of Distilled Water; Test Date: 06/09/98).

to maintain constant minimum and maximum humidity curves for all flow rates. The ultrasonic humidifier was turned on with the option of controlling the amount of mist flow into the system in order to maximize the humidity of the air, while the heat supply was held constant to make sure that all of the water droplets of the atomized water were vaporized. The humidity versus flow rate curve shows the possible experimental maximum and minimum humidity variations that can be attained for air inlet conditions of 70% relative humidity and temperature of 27 °C. The test results were plotted in Fig. 5.34. From the plot, one can infer that the curves can shift up or down depending upon the inlet air conditions. For higher flow rates, it was difficult to change (maximize or lower) the humidity. As the flow rate increased infinitely, the humidity and temperature of the air measured at the mixing box approached room conditions.

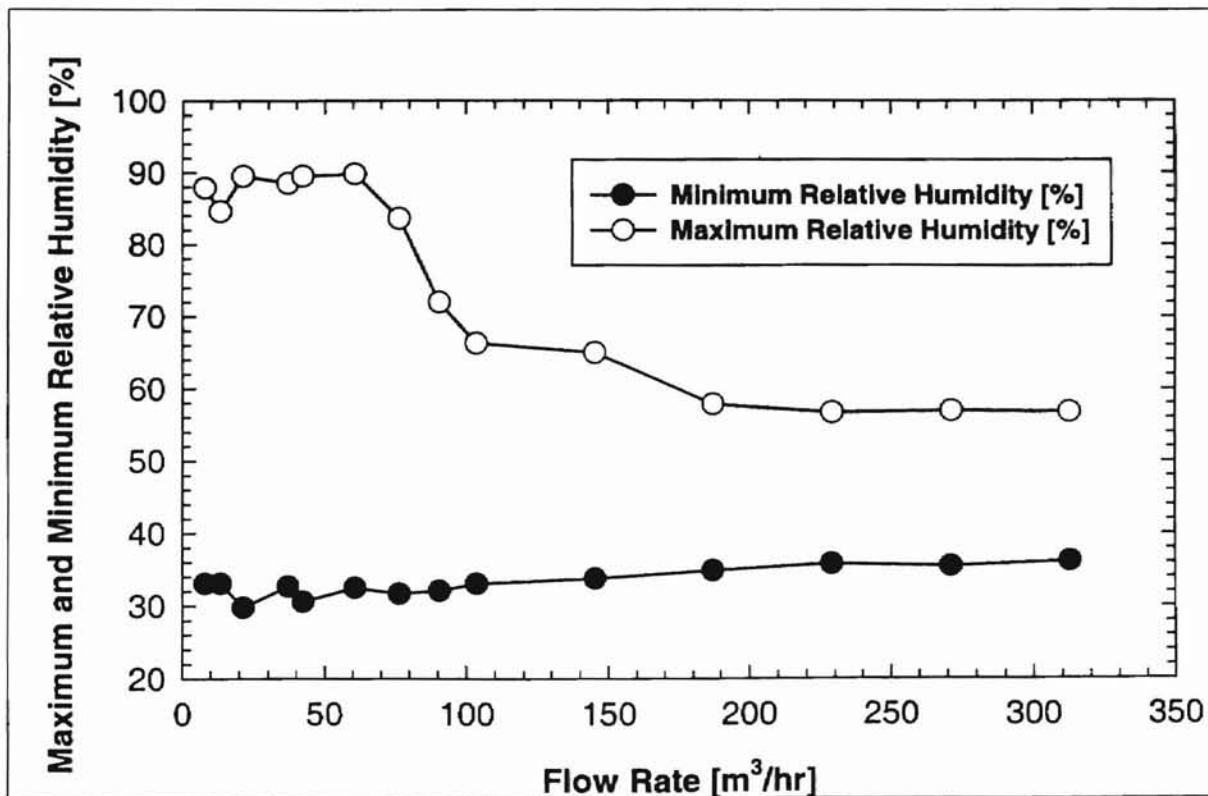


Figure 5.34 A Humidity Control Experiment to Maintain Maximum and Minimum Humidity (Using Humidifier, Heater, and Atomizer; Test Date: 06/09/98).

In filter efficiency measurements, the importance of maintaining consistent and uniform humidity is essential when comparing efficiencies for the same or various flow rates. In this thesis, the effects of humidity on the efficiency of filters was investigated by comparing the efficiencies of a filter measured at low and high humidities. In the discussion to follow and in this study in general, high humidity refers to relative humidities above 70%, while low humidity refers to values below 50%. To realize this goal, monitoring the daily humidity of the air inside and outside the room was also very important.

The next two experiments were done to estimate the margin of error of the LDA system. Thus particle counting and detecting had to be performed using the LDA system to check the presence of condensed water vapor or unvaporized water droplets from the atomizer. Unless the water droplets are vaporized, they may reach the filter together with the PSL particles and contribute to the inconsistency of the filtration efficiency measurements.

In the first experiment, the detection of particles in room air was performed without the atomization of distilled water and preheating the air flowing into the experimental housing. The resulting number densities were compared to expected number densities for each flow rate. The number of particles detected for each flow rate were very insignificant; only between 2 to 5 particles were detected every 200 seconds. The corresponding number densities were plotted in Fig. 5.35 as a function of flow rate. The number density errors for each flow rate were less than 0.01% as compared to the actual number densities (that range from 10^7 for high flow rates to 10^{10} m^{-3} for a low flow

rate of $10 \text{ m}^3/\text{hr}$) obtained by atomizing a 5 ml suspension of 10% solids by weight of PSL particles in 495 ml of distilled water.

The other experiment was done to find out the worst possible errors that might occur due to unvaporized and or condensed water particles that may reach the filter. Thus unlike the first experiment, this experiment was conducted with the atomization of distilled water followed by vaporization of the atomized water droplets using an electric

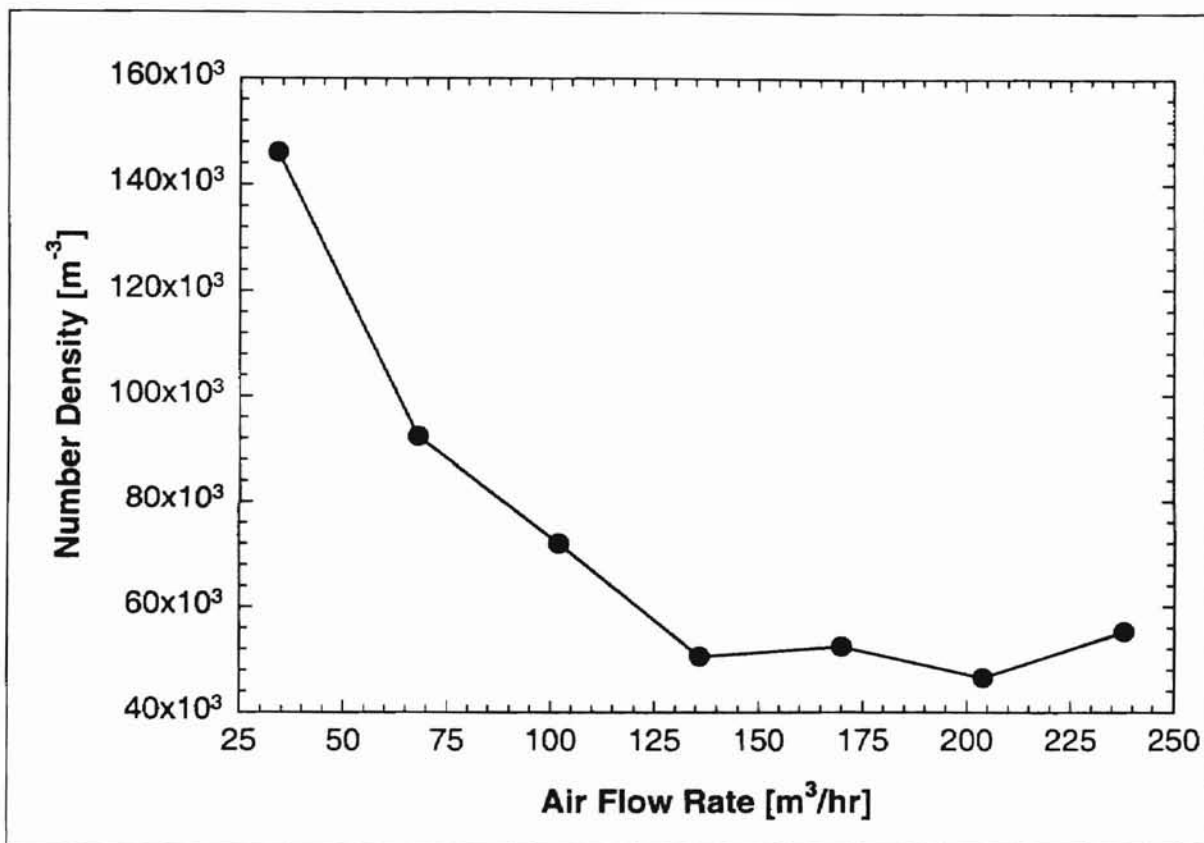


Figure 5.35 Consistency Measurements on Room Air: Number Density Variations at the Center of Filter with Flow Rate (Heater off, Atomizer off, and Humidifier off, Test Date: 03/21/98).

Heater while the humidifier helped increase the humidity of the flow to the maximum.

For each flow rate, the number of particles counted was slightly higher than that for room air, but still did not bring about significant errors in the measurement of number

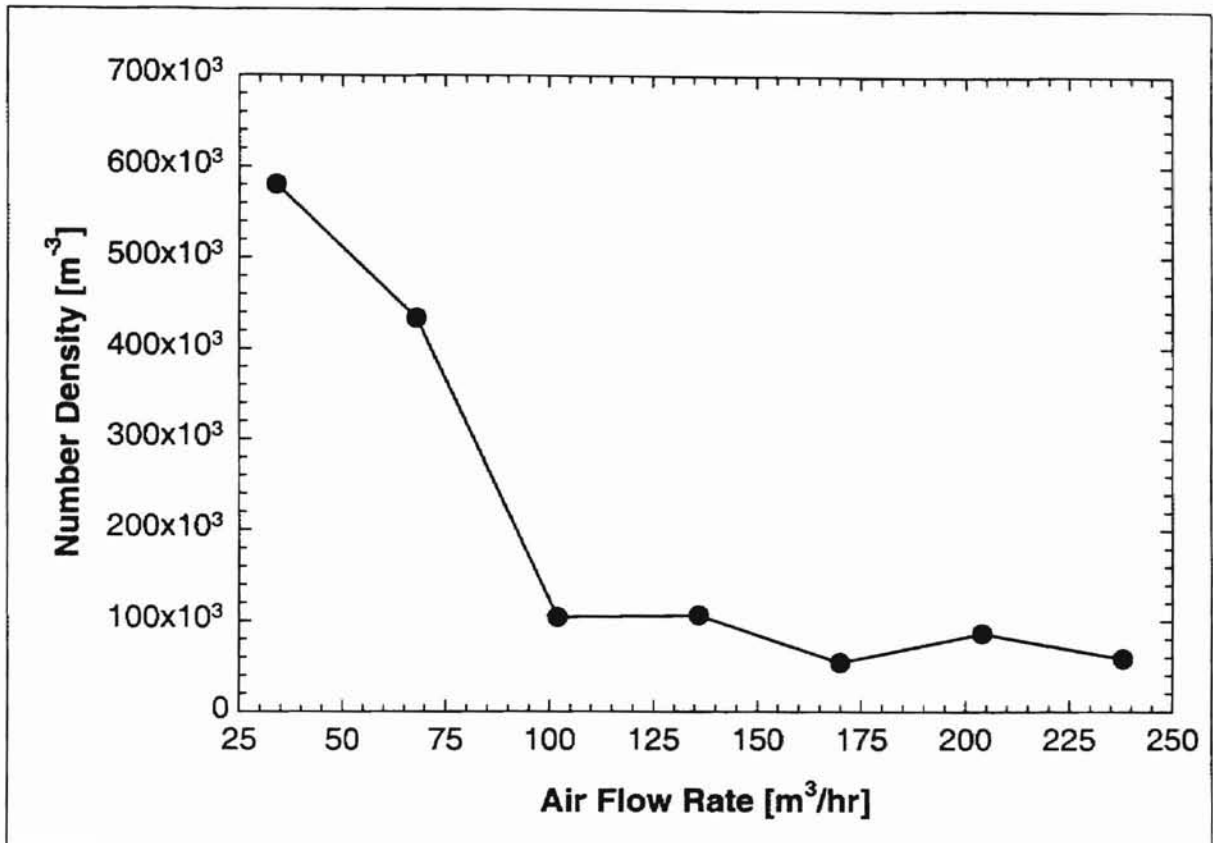


Figure 5.36 Consistency Measurements on Room Air: Number Density Variations at the Center of Filter with Flow Rate (Heater on, Atomizer on, and Humidifier on; Test Date: 03/22/98).

densities. The collection time was also on the order of 150 to 200 seconds. Yet the error never exceeded the 1% mark as compared to the corresponding actual number densities obtained by atomizing 0.966 μm diameter PSL. Figure 5.36 is the plot of number density variation with flow rate.

Efforts were also made to find out to what extent the humidity of the air measured at the mixing box changed when it reached the filter. The experimental results that were found show that the correlation of the temperatures and humidities at the filter and mixing box were linear as shown in the interpolating curves of Figs. 5.37 and 5.38. Thus these measurements confirm that the variations of humidity and temperature at the two

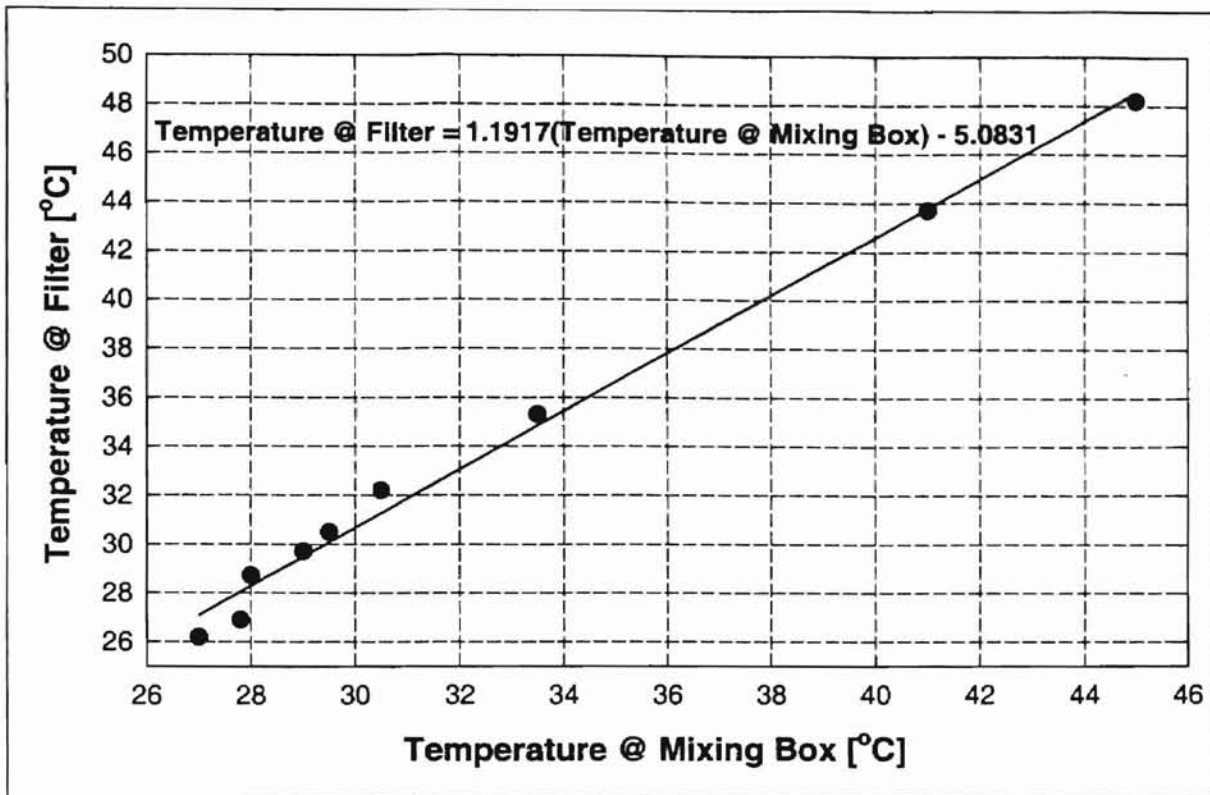


Figure 5.37 Temperature Correlation at the Mixing Box and Upstream of the Filter.

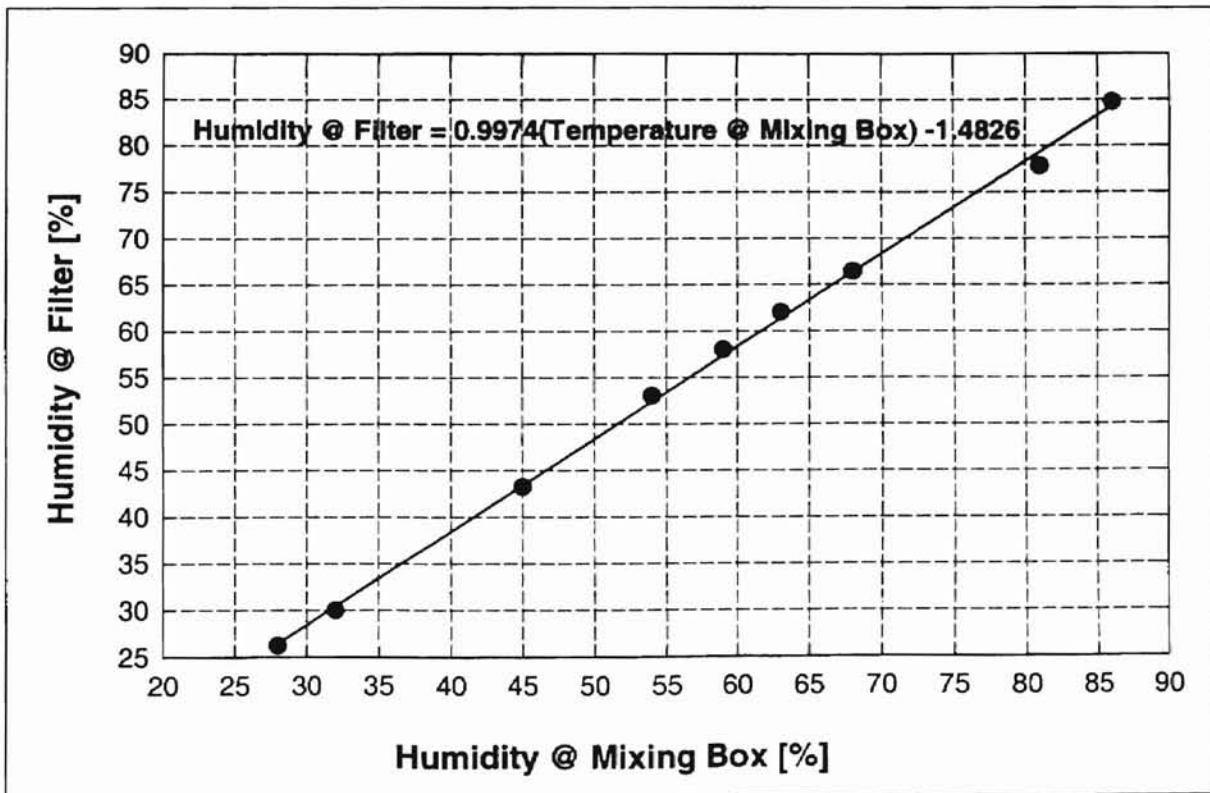


Figure 5.38 Humidity Correlation at the Mixing Box and Upstream of the Filter.

locations (at the filter and mixing box) are minimal. Hence as the air flows through the mixing box and plexiglass housing to the filter, it does not shed its vapor in the form of moisture due to temperature changes (cooling effect). This test again verifies that there is no condensation of water vapor, which can cause errors in number densities.

5.4.3 Atomization Rate and Concentration of Solutions

In order to get consistent number density and local and overall filtration efficiency measurements, the rate of atomization of the particles should remain constant throughout the experiment. Constant atomization rate can be maintained provided that the atomization pressure and the concentration of the solution remain constant. Though the PSL particles with a specific gravity of 1.05 may have a very low probability of settling (sedimentation), there are chances that variations in the atomization pressure of the solution may affect the atomization rate.

Saxena [1998] carried out some tests to check on consistency of the atomization rate of the particles and his test results are presented in Fig. 5.39. He calculated the sampling rate of the particles, which is the number of samples divided by the run time (time necessary to collect samples by the LDA system). Using 0.966 μm diameter PSL particles, he showed that the sampling rate data was within $\pm 5\%$. This error could be the cumulative of all errors, if there are any, that can be attributed to minor atomization pressure fluctuations and fluctuations in concentration at lower temperatures that enhance the sedimentation of the PSL particles. The following relation as discussed by Anand [1997] relates the record length and the sampling rate:

$$\text{Record Length} = \frac{\text{Number of Samples}}{\text{Sampling Rate}} \quad (5-5)$$

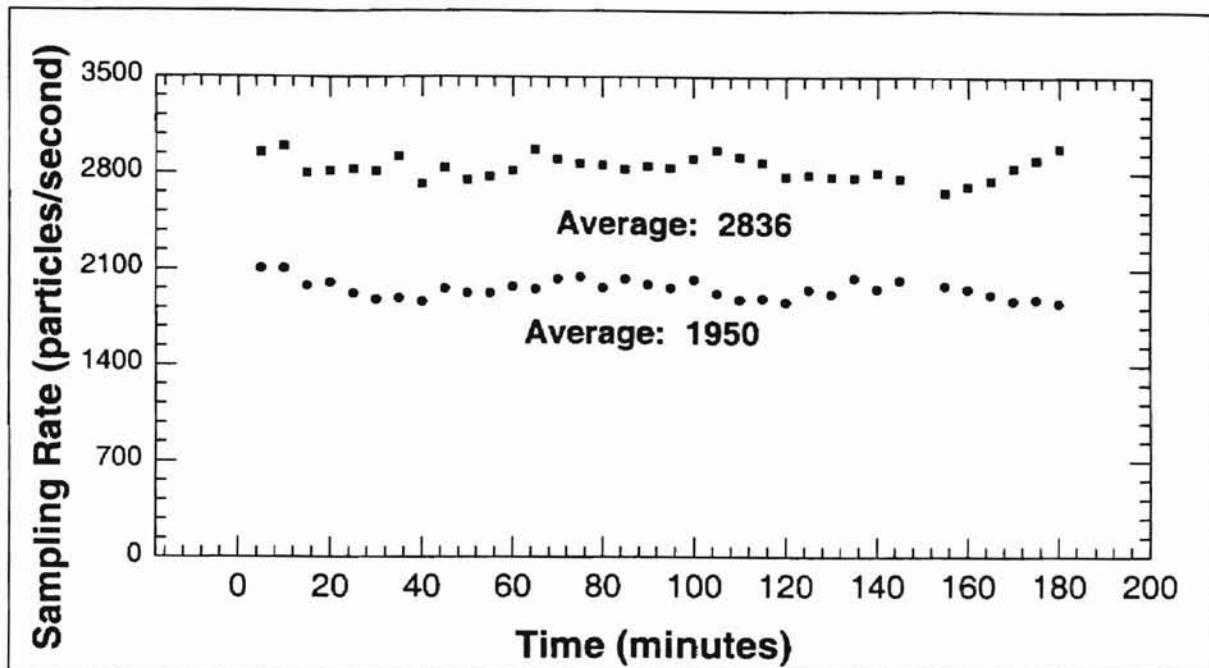


Figure 5.39 Atomizer Consistency Test Results for 0.966 μm Particles [Saxena, 1998].

Anand [1997] also carried out some consistency measurements on the effect of the concentration of the PSL solutions. The experimental results are presented in Fig. 5.40. Anand found a linear correlation between the number density measured at the center of the housing and the concentration of the solution. This suggested that the atomization rate and the LDA instrumentation were stable and have high accuracy.

Although the stability of the system has been improved more than ever before, the author had measured negative efficiencies at lower flow rates. This might be attributed to the increase in the optical density of the medium due to high particle concentration (number of particles per unit volume of air flow), which can be calculated as follows:

$$\text{Particle Concentration} = \frac{\text{Number of Particles Atomized Per Unit Time}}{\text{Volume Flow Rate of Air}} \quad (5-6)$$

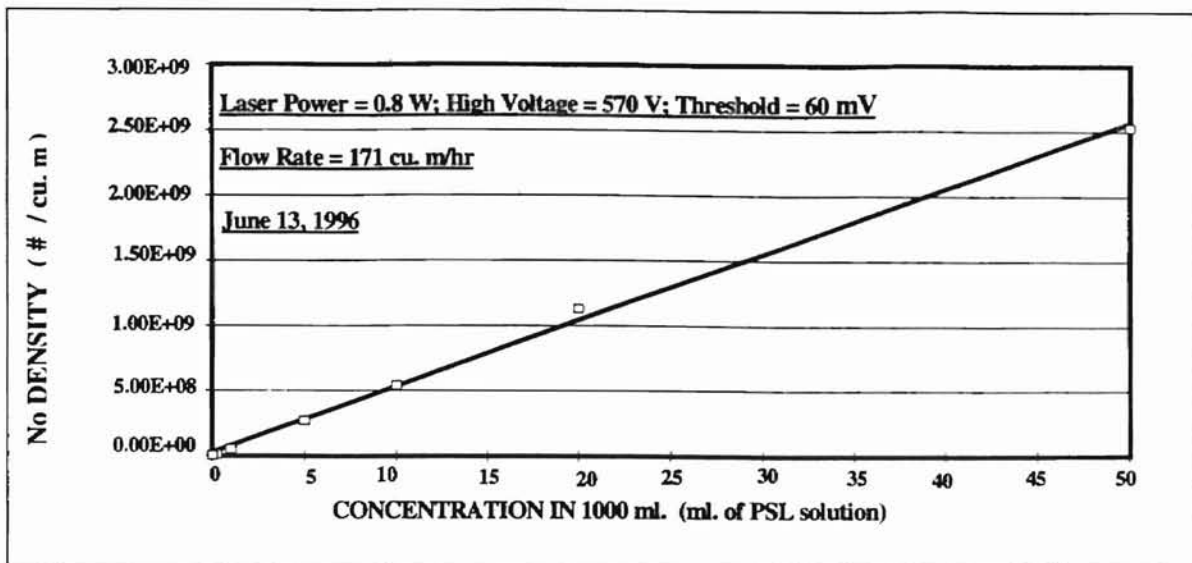


Figure 5.40 Number Density for Different Particle Concentrations [Anand, 1997].

When the particle concentration is high (greater than 5/1000) for low flow rates, the LDA system can generate negative efficiencies. Hence the author did overcome this problem by halving the concentration of the solution (from 10/1000 to 5/1000 by volume) for lower flow rates. Since the PSL particle seeding rate is proportional to atomization pressure and the dilution ratio, other possible options to minimize the particle seeding rate include lowering (regulating) the atomization pressure or changing the dilution ratio (i.e., the ratio of air to solution) using the dilution system of the atomizer. Thus these methods can help to obtain the optimum particle concentration necessary for the LDA system in order to prevent the overseeding of the air flow.

CHAPTER VI

RESULTS AND DISCUSSION

In this chapter, investigation results of electrostatic charge (due to triboelectric effects or the resuspension of PSL particles by atomization) and humidity effects on the performance of the A13192 fibrous automotive air filters (manufactured by Dayco-Purolator Inc.) are presented. The study has been divided into two main sections and has been carried out on the small angle diffuser housing. In the first section, the experimental results and the discussion thereof on the effect of the electrostatically charged 0.966 μm diameter PSL particles on the efficiency of fibrous filters at different air flow rates are provided. In Section 6.2, results for the effects of humidity at low relative humidities (less than 50%) and high relative humidities (greater than 70%) on the efficiency of the pleated filters using electrostatically neutral 0.966 μm size PSL particles at different flow rates will be presented. Upstream and downstream velocity, number density and efficiency profiles for low, intermediate and high flow rates will also be presented and discussed. In the rest of the sections of this chapter, investigation of the variation of single fiber efficiencies (calculated from the overall experimental efficiencies) as a function of Stokes number will be assessed. Comparison of the results of both studies will also be made separately and with other previous experimental and theoretical work to see how efficiencies vary with Stokes number or flow rate.

6.1 Effects of Electrostatically Charged Particles on Filtration

In Chapter V, the experimental results concerned with the variation of electrostatic charge voltage as a function of flow rate and time, and the factors that affect its level (quantity) and polarity have been presented in detail. In order to show the overall picture of the electrostatic charge variation along the air duct and filter housing at different locations, a summary of the factors (flow rate, particle concentration and humidity) associated with the level of the electrostatic voltage and their correlation is graphically presented below. Figure 6.1 depicts the variation of the electrostatic charge voltage, particle concentration of the contaminating PSL particles per unit volume of air, relative and absolute humidities, and temperature as functions of the air flow rate.

Since the rate of injection of the PSL solution into the air flow is constant for all of the flow rates, the concentration of the PSL particles (weight per unit volume of air) follows a decreasing function with increasing flow rate. This graph has been added to the previous graphs presented in Chapter V in an effort to consolidate the most important factors and to help in understanding the trend of the electrostatic charge voltage variation with flow rate.

The particle concentration (mg of solution/unit volume of air) curve was determined by dividing the mass rate of injection (using the atomizer) of PSL particles into the air duct by the air flow rate. The rate of atomization of PSL solution into the air flow has been determined experimentally as 2.6 ml of solution/min at a pressure of 248 kpa when all 6 jets of the atomizer are fully open. This atomization rate when changed into the corresponding mass flow rate of PSL particles for 6 ml of 10% solution in 494 ml of distilled water is about 3.276 milligrams per minute, which is about 8.7×10^8 particles

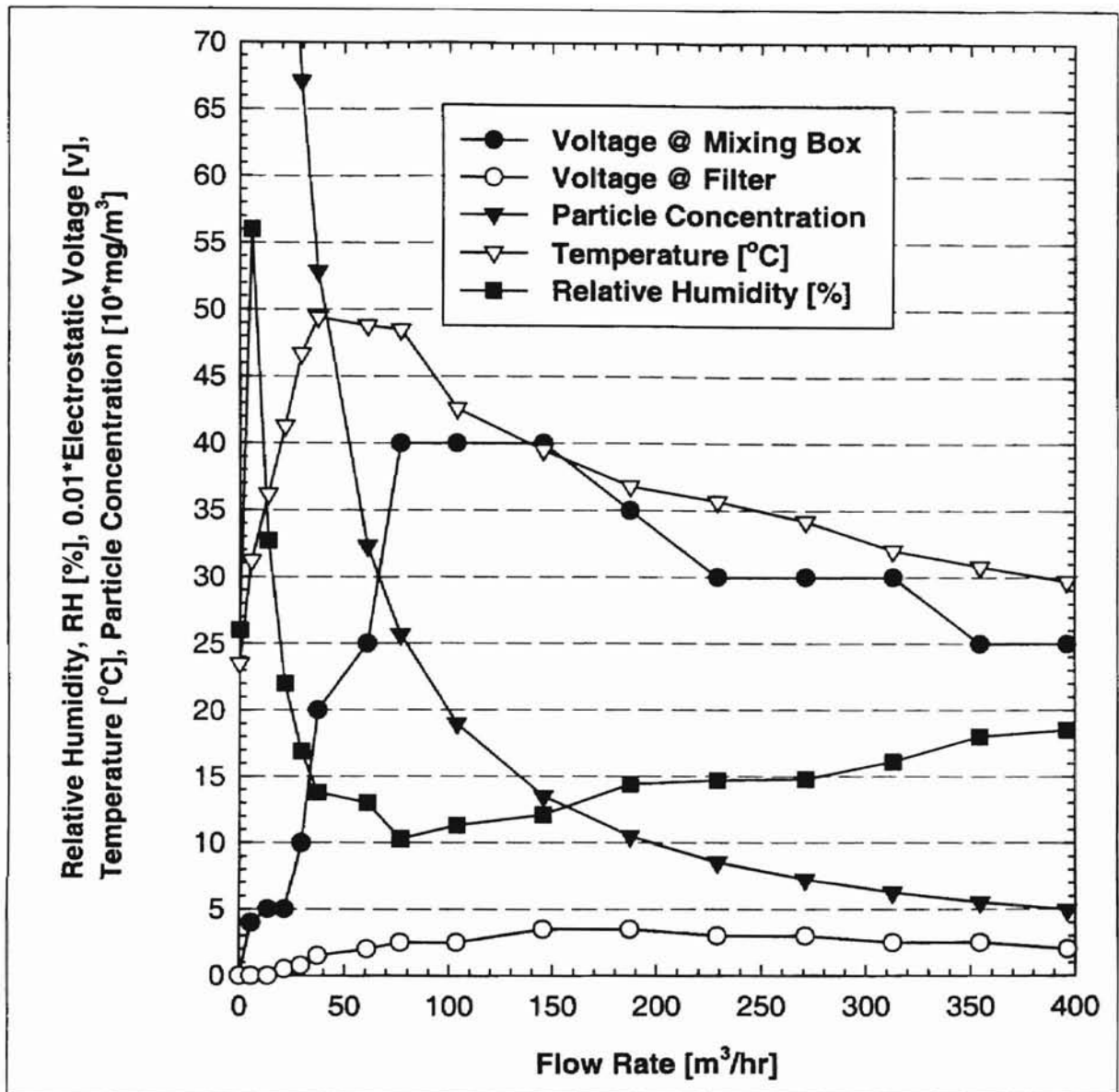


Figure 6.1 Electrostatic Voltage, Temperature, and Humidity Variation with Air Flow Rate for 0.966 μm PSL Particles at the Mixing Box and Filter without Grounding (conc. = 6/500, Winter, 1998).

(of 0.966 μm diameter) per minute. In calculating the particle concentration or number, one should not mistake aerosol flow rate (air + atomized water + particles) as provided in the instruction manual of the model 9306 TSI Atomizer, which is about 52.08 liter/minute (or 8.68 liter/minute per jet) at 248 kPa for the experimentally determined atomization rate of 2.6 ml of solution/minute. It is these atomized particles that are

injected into the air inside the duct at different flow rates which are responsible for the high triboelectrostatic charge voltage at the filter, the surface of filter housing, and the mixing box as shown in Fig. 6.1.

Table 6.1 provides a summary of the experimental test results on the effect of the electrostatically charged 0.966 μm diameter PSL particles in determining the performance of the A13192 filter. Various experimental tests were carried out at nine different flow rates of the dispersing medium (air) ranging from 13.5 to 313.8 m^3/hr using a new filter for each test. For each flow rate, the humidity of the air was maintained at the lowest possible value by heating the incoming air. At each flow rate, two tests were also carried out to see the consistency of the results. The readings for evaluating the local efficiency of the filter were taken at 35 grid points both upstream and downstream of the filter as shown in Fig. 4.5. The local number densities upstream and downstream of the filter were calculated from Eq. 4.1 using the collection time, number of attempted samples, and average velocity of the samples as obtained from the LDA instrumentation data acquisition system and the cross-sectional area of the probe volume based on the swept volume technique (see Appendix B). Two sets of readings (runs) were taken for each grid point.

During the experiment to determine the initial efficiency of the filter, data collection was taken downstream of the filter first instead of upstream of the filter, in order to avoid the fast clogging of the filter. Hence the electrostatic voltage readings of Table 6.1 were taken at the end of the data collection downstream of the filter. During an experiment, all parameters (humidity, pressure, electrostatic voltage, and temperature) were also recorded and monitored for each flow rate. The flow rates in the tables and

Table 6.1 Summary of Test Results on Electrostatic Charge Effects for the Model A13192 Dayco-Purolator Automotive Air Filter Using 0.966 µm PSL Particles in the Small Angle Diffuser Housing.

Test Number	Test Date	Flow Rate [m ³ /hr]	RH [%]	Average No. Density [m ⁻³]		Average Velocity [m/s]		Pressure Drop [mm water] Initial (Final)	Static Voltage [V] Upstream of Filter (with Negative Polarity)	Filter Efficiency [%]
				Upstream	Downstream	Upstream	Downstream			
ESH10.1	08/20/98	13.53	43.5	2.89X10 ⁹	1.84X10 ⁹	0.286 (0.164)	0.376 (0.445)	3 (3)	100	35.64
ESH10.2	08/20/98	13.53	39	3.65X10 ⁹	2.22X10 ⁹	0.283 (0.164)	0.475 (0.445)	3 (3)	150	38.97
ESH20.1	08/21/98	29.5	33	1.57X10 ⁹	1.06X10 ⁹	0.590 (0.357)	0.975 (0.971)	3 (3)	150	31.75
ESH20.2	08/21/98	29.5	32	1.87X10 ⁹	1.15X10 ⁹	0.600 (0.357)	0.959 (0.971)	3 (3)	200	38.47
ESH40.1	08/22/98	60.81	33	7.76X10 ⁸	5.87X10 ⁸	1.018 (0.735)	1.666 (2.002)	5 (5)	200	35.71
ESH40.2	08/22/98	60.81	33	9.94X10 ⁸	6.21X10 ⁸	1.120 (0.735)	1.743 (2.002)	5 (5)	300	37.56
ESH50.1	08/23/98	77.1	35	1.26X10 ⁹	5.63X10 ⁸	1.410 (0.932)	2.253 (2.538)	5 (5)	500	35.30
ESH50.2	08/13/98	77.1	35	1.24X10 ⁹	6.94X10 ⁸	1.487 (0.932)	2.314 (2.538)	8 (8)	750	43.88
ESH75.1	08/24/98	103.7	39	1.00X10 ⁹	5.38X10 ⁸	2.086 (1.253)	3.518 (3.414)	13 (13)	750	46.34
ESH75.2	08/24/98	103.7	39	1.14X10 ⁹	5.84X10 ⁸	1.984 (1.253)	3.239 (3.414)	13 (13)	750	43.82
ESH100.1	08/25/98	145.7	42	4.55X10 ⁸	1.79X10 ⁸	3.038 (1.761)	5.194 (4.797)	30 (30)	500	60.69
ESH100.2	08/25/98	145.7	42	4.79X10 ⁸	1.90X10 ⁸	3.392 (1.761)	5.143 (4.797)	30 (30)	500	57.50
ESH125.1	08/28/98	187.7	45	5.85X10 ⁸	2.15X10 ⁸	3.550 (2.269)	5.646 (6.179)	38 (38)	500	62.59
ESH125.2	08/28/98	187.7	45	4.30X10 ⁸	1.57X10 ⁸	3.540 (2.269)	5.768 (6.179)	38 (38)	500	64.29
ESH150.1	08/27/98	229.7	50	3.26X10 ⁸	6.82X10 ⁷	4.549(2.776)	6.723 (7.562)	51 (53)	400	78.73
ESH150.2	08/27/98	229.7	50	4.4X10 ⁸	8.20X10 ⁷	4.638 (2.776)	7.380 (7.562)	57 (61)	400	81.06
ESH200.1	08/27/98	313.8	50	2.86X10 ⁸	3.88X10 ⁷	6.302 (3.973)	9.014 (10.33)	122 (135)	500	86.43

discussion to follow refer to standard conditions at sea level, namely 101 kPa and 21 °C. They are the corrected flow rates obtained from the TSI mass flow meter calibration curves developed by Anand [1997] and Jadbabaei [1997]. The initial and final pressure drops measured using a U-tube manometer (connected to pressure taps located at the two extreme ends of the filter housing upstream and downstream of the filter) were also recorded at the beginning and end of each experiment for each flow rate. For most of the experiments, the pressure drop across the filter remained constant at low flow rates, while for high flow rates, the change in pressure drop increased steadily. For example, at 313.8 m³/hr, the initial pressure drop across the filter changed by 13 mm from 122 to 135 mm of water column measured by the manometer with an accuracy to the nearest millimeter.

The electrostatic charge voltage reading with a negative polarity upstream of the filter increased with flow rate from 100 v at low flow rates to a maximum of 750 v at both 77.1 and 103.7 m³/hr flow rates. Then the electrostatic charge declined gradually for higher flow rates. The humidity of the air ranged from a low humidity value of 32 % for intermediate flow rates to a 50 % value for high flow rates of 187.7 and 313.8 m³/hr. This has been due to the limited heating capacity of the electric heater to meet the heating demand as the flow rate steadily increases. The average number density downstream of the filter ranged from the order of $\sim 10^9$ at low flow rates to the order of $\sim 10^7$ for high flow rates. However the number density upstream of the filter ranged from the order of $\sim 10^9$ at low flow rates to the order of $\sim 10^8$ for higher flow rates. The filtration efficiency of the filter increased steadily with flow rate.

The test number for each experiment has been alphanumerically designated for easy handling and differentiation purposes to specify the type of test, the kind of filter

housing used, and the flow rate. For example, test number ESH10.1 stands for electrostatic charge effect test conducted on the small angle diffuser housing at a standard air flow rate of 10 cubic feet per minute ($13.53 \text{ m}^3/\text{hr}$); and it was the first test for that experiment. The number density and velocity profiles upstream and downstream of the filter, as well as the efficiency profiles for all of the flow rates other than those presented in this section, are listed in Appendix D.

In Table 6.2 the single fiber efficiency and Stokes number are tabulated for each experimental test. The single fiber efficiency is calculated from the experimental overall efficiency of the filter after solving Eq. (2-24) for single fiber efficiency. The Stokes number is determined based upon the calculated and measured (LDA) flow velocities. The average duct velocity obtained by uniformly distributing the flow over the entire pleated filter or duct cross-sectional area ($121 \text{ mm} \times 191 \text{ mm}$) is less than the average velocity of the particles (measured using the LDA system at the 35 grid points) by almost half. This is due to the fact that the LDA measurement is carried out on representative grid points that cover only 55% of the filter area. On the other hand, the average velocities obtained by spreading the flow over the unfolded pleated filter area, which is 19.3 times the area of the pleated filter [Jadbabaei, 1997], is much lower than the average velocity obtained from the LDA measurement or that calculated by uniformly distributing the flow over the duct cross-sectional area. The calculated Stokes number is proportional to the average velocity used. In this thesis, the Stokes number calculated based on the duct velocity [Jadbabaei, 1997] have been used for all of the investigations and analyses to follow.

Table 6.2 Summary of Test Results for Electrostatic Charge Effects: Single Fiber Efficiency and Stokes Number for the Model A13192 Dayco-Purolator Automotive Air Filter Using 0.966 µm PSL Particles in the Small Angle Diffuser Housing.

Test No.	FLOW RATE [m ³ /hr]	Upstream Velocity [m/s] Based on			Pressure [in] Initial (Final)	Pressure [mm] Initial (Final)	Overall Filter Efficiency [%]	Single Fiber Efficiency [%]	Stokes Number Based on (U ₁)	Stokes Number Based on (U ₂)	Stokes Number Based on (U ₃)
		Unfolded Filter Area (U ₁)	Duct/Folded Filter Area (U ₂)	LDA (U ₃)							
ESH10.1	13.53	0.008	0.164	0.286	0.1 (0.1)	3 (3)	35.64	0.002	0.0007	0.0144	0.0251
ESH10.2	13.53	0.008	0.164	0.283	0.1 (0.1)	3 (3)	38.97	0.003	0.0007	0.0144	0.0249
ESH20.1	29.5	0.018	0.357	0.59	0.1 (0.1)	3 (3)	31.75	0.002	0.0016	0.0313	0.0518
ESH20.2	29.5	0.018	0.357	0.6	0.1 (0.1)	3 (3)	38.47	0.003	0.0016	0.0313	0.0527
ESH40.1	60.81	0.038	0.735	1.018	0.2 (0.2)	5 (5)	35.71	0.002	0.0033	0.0645	0.0894
ESH40.2	60.81	0.038	0.735	1.120	0.2 (0.2)	5 (5)	37.56	0.003	0.0033	0.0645	0.0984
ESH50.1	77.1	0.048	0.932	1.41	0.2 (0.2)	5 (5)	35.3	0.002	0.0042	0.0818	0.1238
ESH50.2	77.1	0.048	0.932	1.487	0.3 (0.3)	8 (8)	43.88	0.003	0.0042	0.0818	0.1306
ESH75.1	103.7	0.065	1.253	2.086	0.5 (0.5)	13 (13)	46.34	0.003	0.0057	0.1101	0.1832
ESH75.2	103.7	0.065	1.253	1.984	0.5 (0.5)	13 (13)	43.82	0.003	0.0057	0.1101	0.1742
ESH100.1	145.7	0.091	1.761	3.308	1.2 (1.2)	30 (30)	60.69	0.005	0.0080	0.1546	0.2905
ESH100.2	145.7	0.091	1.761	3.392	1.2 (1.2)	30 (30)	57.5	0.005	0.0080	0.1546	0.2979
ESH125.1	187.7	0.118	2.269	3.55	1.5 (1.5)	38 (38)	62.59	0.005	0.0103	0.1992	0.3117
ESH125.2	187.7	0.118	2.269	3.54	1.5 (1.5)	38 (38)	64.29	0.006	0.0103	0.1992	0.3108
ESH150.1	229.7	0.144	2.776	4.549	2.0 (2.1)	51 (53)	78.73	0.009	0.0126	0.2438	0.3994
ESH150.2	229.7	0.144	2.776	4.638	2.3 (2.4)	57 (61)	81.06	0.009	0.0126	0.2438	0.4073
ESH200.1	313.8	0.197	3.793	6.302	4.8 (5.3)	122 (135)	86.43	0.011	0.0173	0.3330	0.5534

6.1.1 Velocity, Number Density, and Efficiency Profiles

The local velocity, number density, and efficiency distributions mainly depend upon the flow rate of the air in the duct, provided that the seeding rate and the laser power remain constant, as discussed in the Consistency Measurement Section of Chapter V. However, unlike the average velocity of the particles (measured by the LDA system), the number density highly depends upon the stability of the laser power, and this problem has been controlled effectively by maintaining constant temperature around the laser system throughout the experiment. In this subsection, the velocity, number density, and efficiency profiles for some representative flow rates in the low, intermediate and high flow rate regions are selected and presented. All of the upstream and downstream profiles are restricted to the central region of the filter, within the central 55% of its total upstream surface area.

Figures 6.2 and 6.3 show the velocity profiles upstream and downstream of the filter at a low air flow rate of $13.53 \text{ m}^3/\text{hr}$. The average downstream velocity is about 1.7 times greater than the average upstream velocity. The explanation for this is that the effective cross-sectional area of the bottom of the filter through which the air flows is reduced by the rubber mounting that provides support and sealing for the filter. Hence, a close look at the geometric size downstream of the filter shows that the cross-sectional area is about $98 \text{ mm} \times 171 \text{ mm}$, which is about 72% of the cross-sectional area of the upstream side of the filter. Again this area is further reduced by about 50% due to the wire mesh that is implanted (embedded) in the rubber mounting to support and guard the bottom of the cellulose filter paper against rupture. Thus, it is this cumulative area reduction and recirculation effect at the edges of the filter that yield higher velocity near

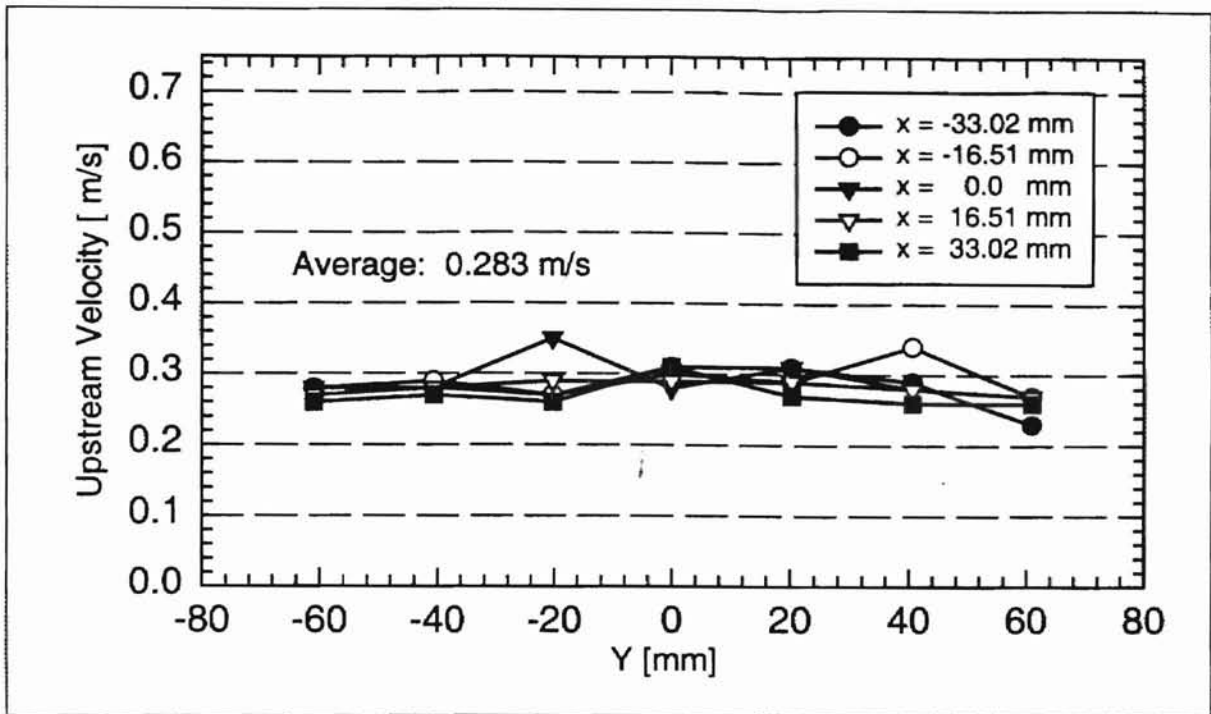


Figure 6.2 Upstream Velocity Distribution for Test No. ESH10.2 at an Air Flow Rate of $13.53 \text{ m}^3/\text{hr}$.

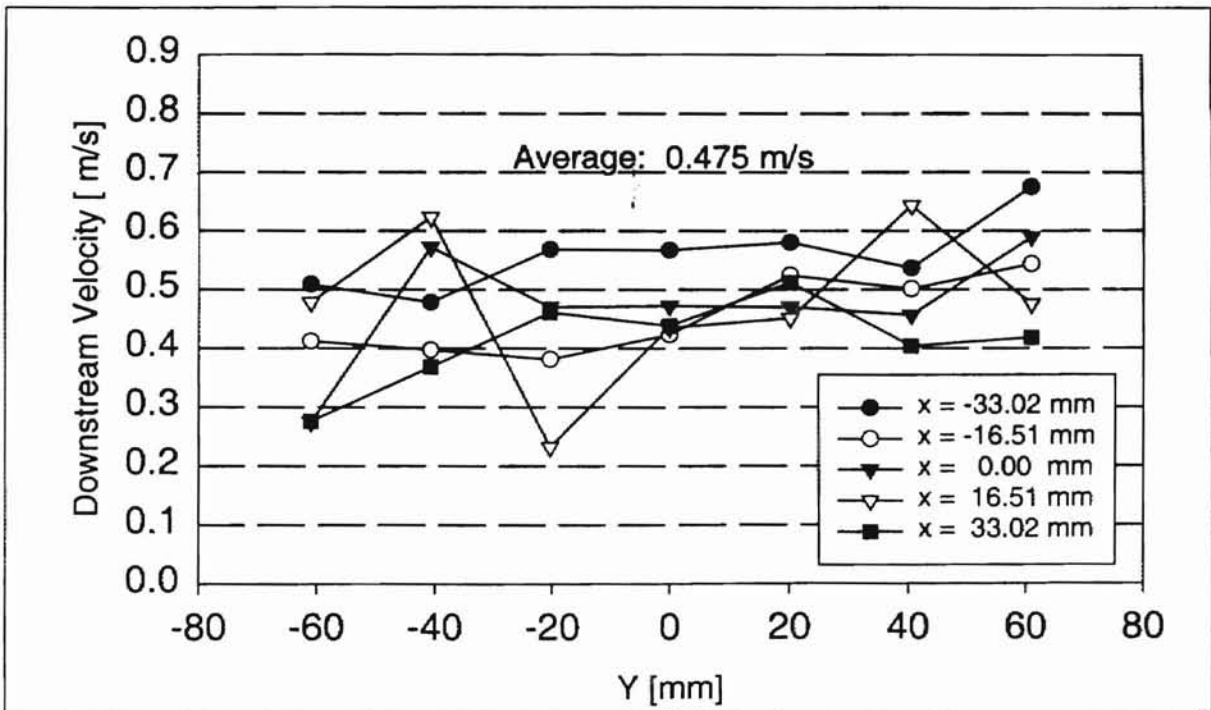


Figure 6.3 Downstream Velocity Distribution for Test No. ESH10.2 at an Air Flow Rate of $13.53 \text{ m}^3/\text{hr}$.

the central region downstream of the filter and very low velocities near the edges, respectively.

Number density and velocity profiles are closely related. The respective number density profiles corresponding to the velocity profiles of Figs 6.2 and 6.3 are provided in Figs. 6.4 and 6.5. A close look at Figs. 6.4 and 6.5 show that, in most cases, those grid points with high number densities correspond to grid points with low velocities. These have been some of the problems that were also found to lead to negative efficiencies. To offset such problems, one has at times to move closer to the neighboring grid point by about half of the step size towards the central zone. However, since number density is inversely proportional to sample collection time as given by Eq. (4-1), it is also possible at times that high sample collection time due to clogging or recirculation effects can also suppress (lower) the number density. Thus number densities inside the recirculation zone are often higher than those outside of the zone mainly due to the low average velocity of the particles. Most downstream number density profiles are not symmetric to each other with respect to the geometric centerline of the filter. This is mainly due to the unsymmetrical velocity profile and the clogging of the filter over a period of time, which influences the collection time for the particles. The corresponding filtration efficiency profile of Fig. 6.6 is obtained by calculating the local efficiency η_i from the upstream and downstream number densities at the i th grid point using Eq. (4.2) as follows:

$$\eta_i = \frac{N_{iup} - N_{idown}}{N_{iup}} = 1 - \frac{N_{idown}}{N_{iup}} \quad (6.1)$$

where N_{iup} and N_{idown} are the respective upstream and downstream number densities at the i th grid point.

The local filtration efficiency distribution of the filter shown in Fig. 6.6 for an air

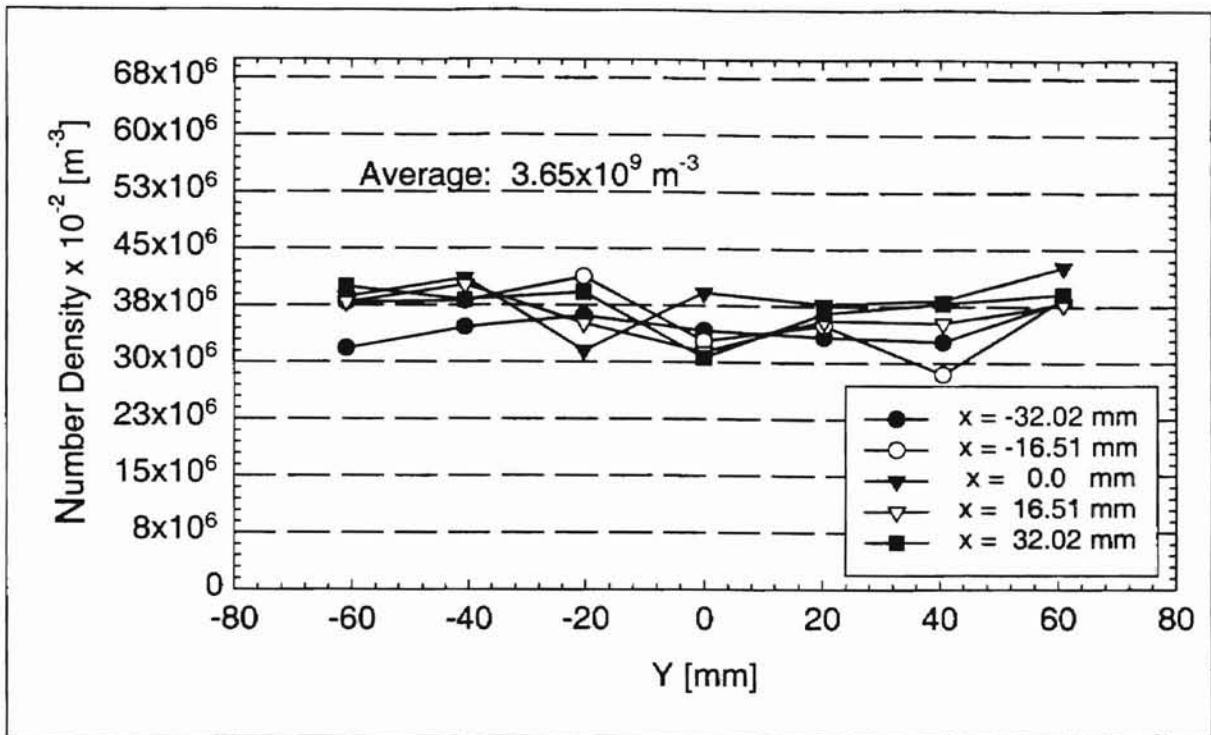


Figure 6.4 Upstream Number Density Distribution for Test No. ESH10.2 at an Air Flow Rate of $13.53 \text{ m}^3/\text{hr}$.

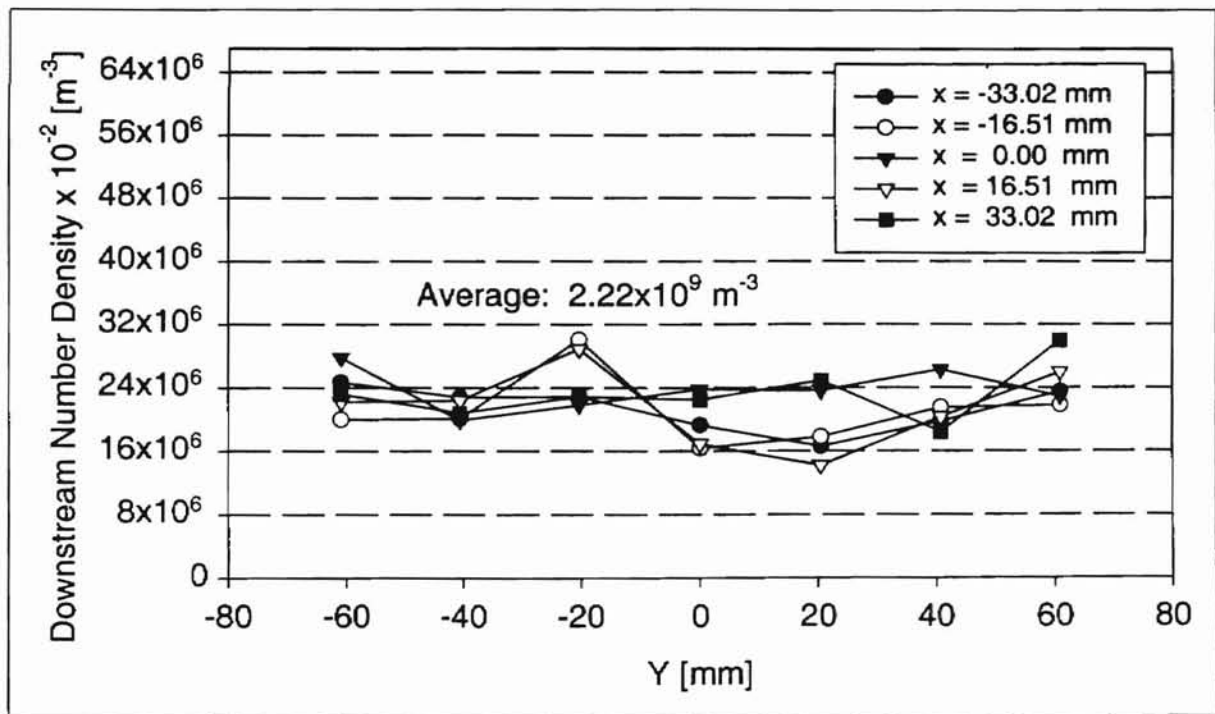


Figure 6.5 Downstream Number Density Distribution for Test No. ESH10.2 at an Air Flow Rate of $13.53 \text{ m}^3/\text{hr}$.

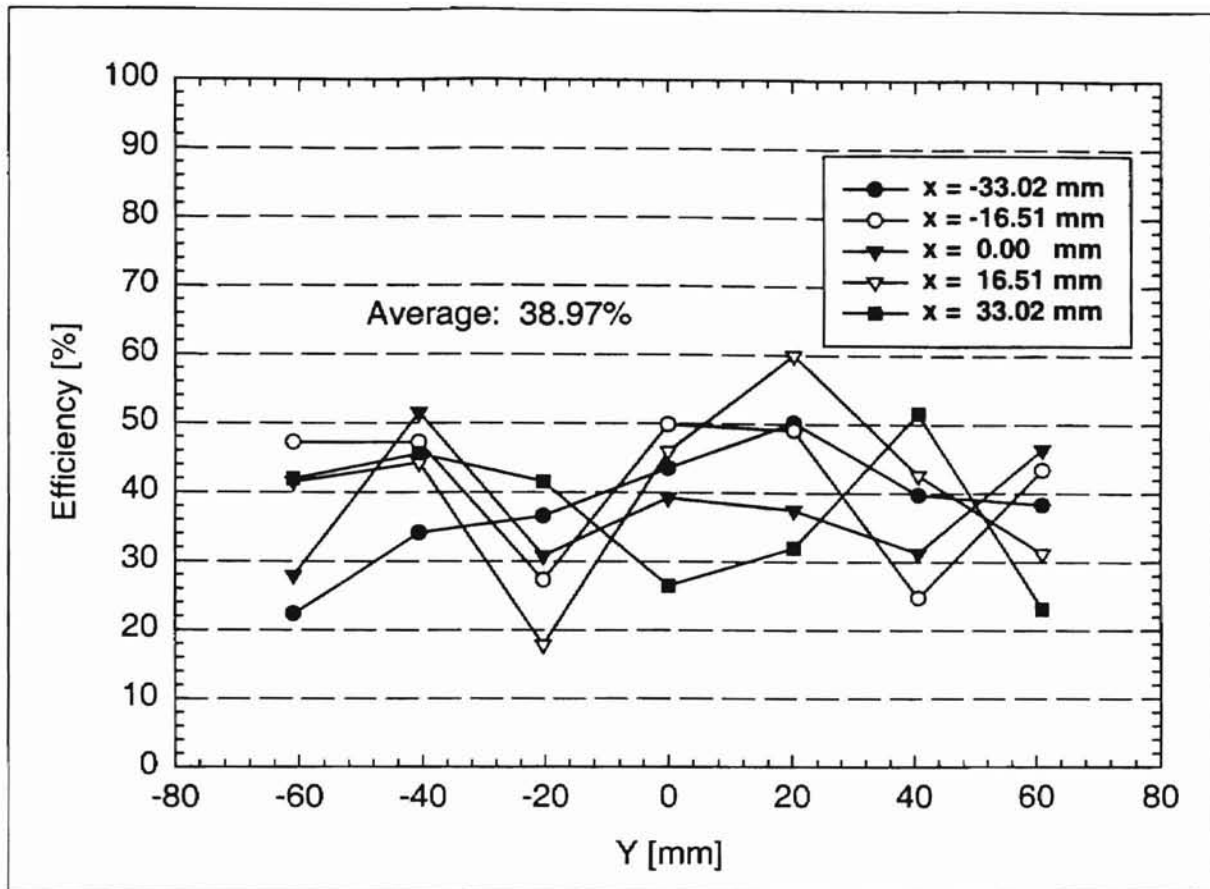


Figure 6.6 Local Filtration Efficiency Profile for Test No. ESH10.2 at an Air Flow Rate of $13.53 \text{ m}^3/\text{hr}$.

flow rate of $13.53 \text{ m}^3/\text{hr}$ is not uniform. The local filtration efficiencies vary between minimum and maximum values of 18 and 58%, respectively, with an average of 38.97%.

The velocity, number density, and efficiency profiles for the low intermediate flow rate of $103.7 \text{ m}^3/\text{hr}$ for the same model A13192 filter tested with the same $0.966 \mu\text{m}$ diameter particles to test electrostatic charge effects under monitored conditions (humidity and temperature) are presented in Figs. 6.7 through 6.11. Figures 6.7 and 6.8 show the velocity profiles, while Figs. 6.9 and 6.10 are the corresponding number density profiles. Figure 6.11 shows the local filtration efficiency distribution as calculated from the local upstream and downstream number densities.

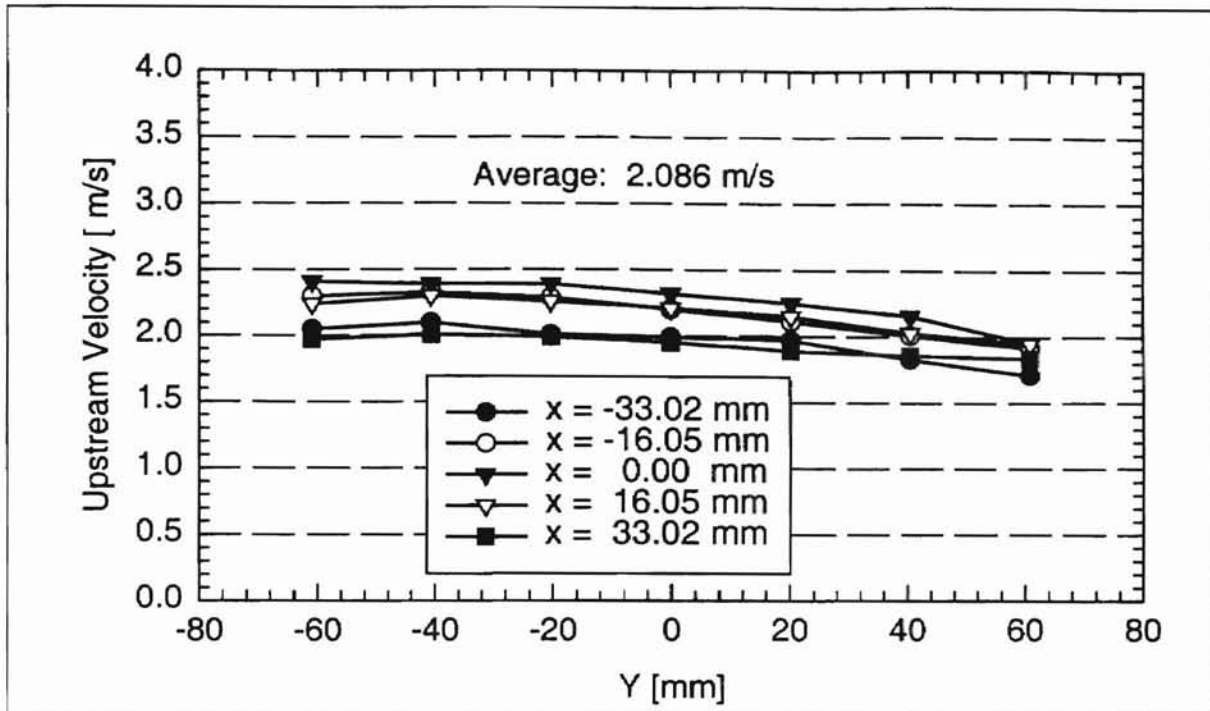


Figure 6.7 Upstream Velocity Distribution for Test No. ESH75.1 at an Air Flow Rate of 103.7 m³/hr.

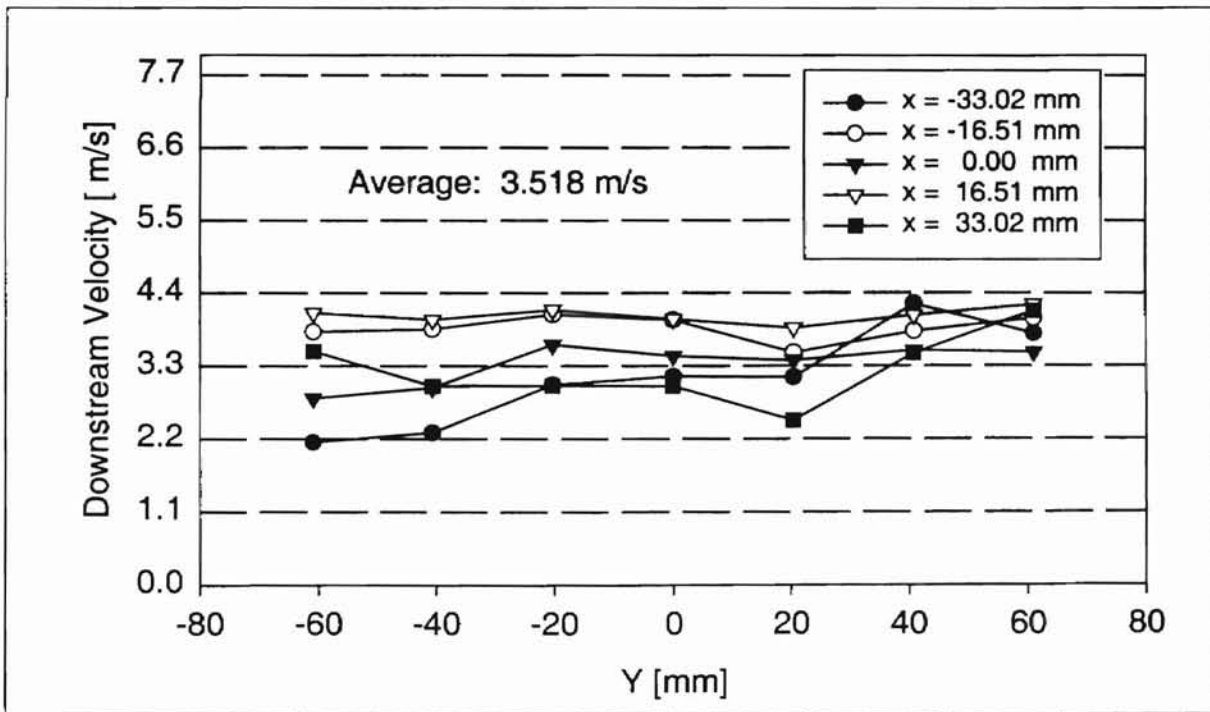


Figure 6.8 Downstream Velocity Distribution for Test No. ESH75.1 at an Air Flow Rate of 103.7 m³/hr.

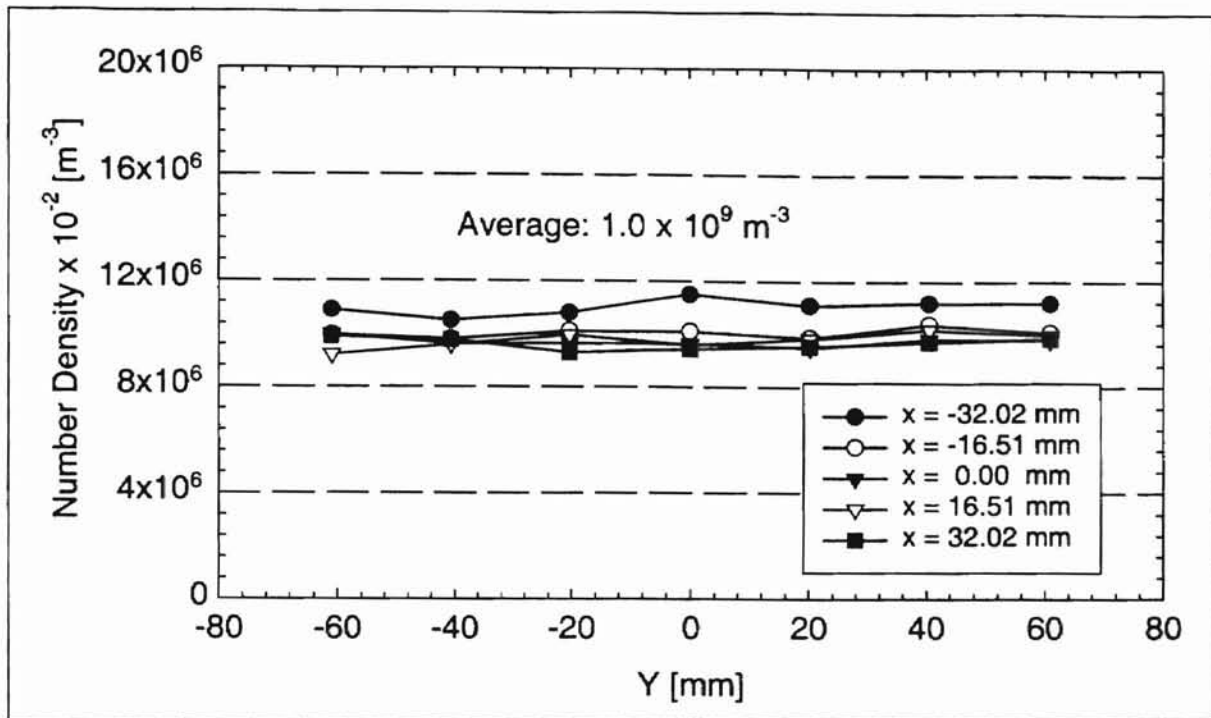


Figure 6.9 Upstream Number Density Distribution for Test No. ESH75.1 at an Air Flow Rate of $103.7 \text{ m}^3/\text{hr}$.

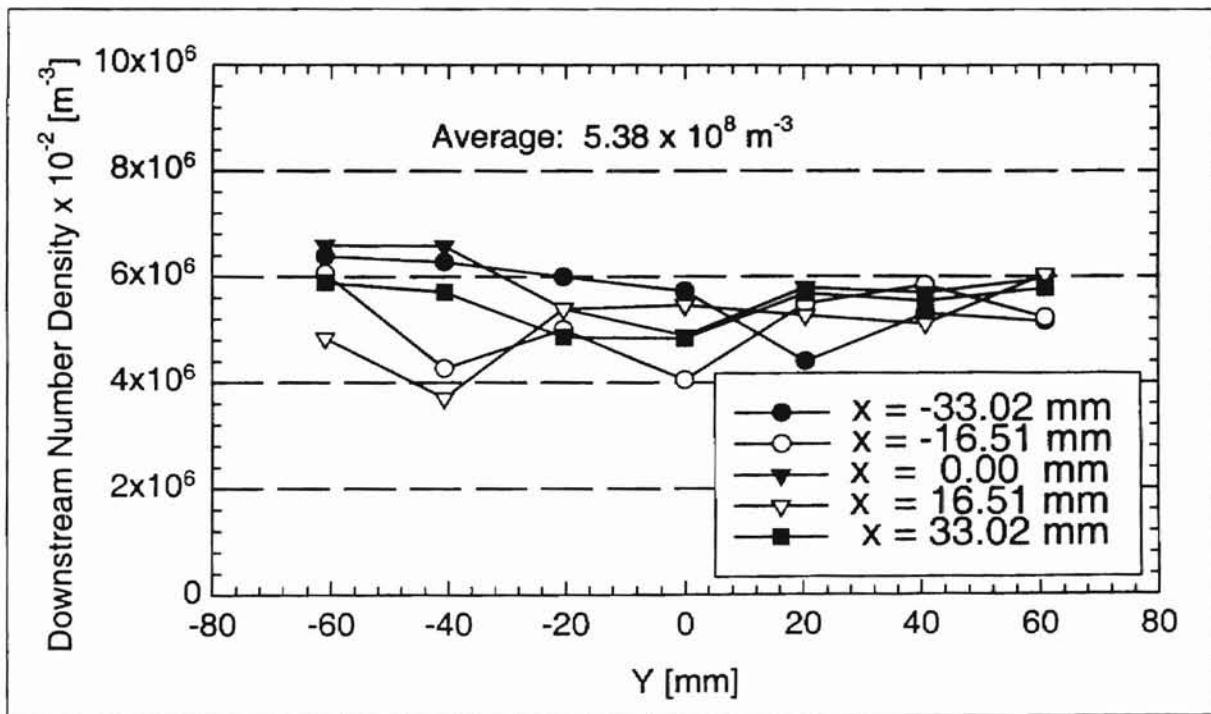


Figure 6.10 Downstream Number Density Distribution for Test No. ESH75.1 at an Air Flow Rate of $103.7 \text{ m}^3/\text{hr}$.

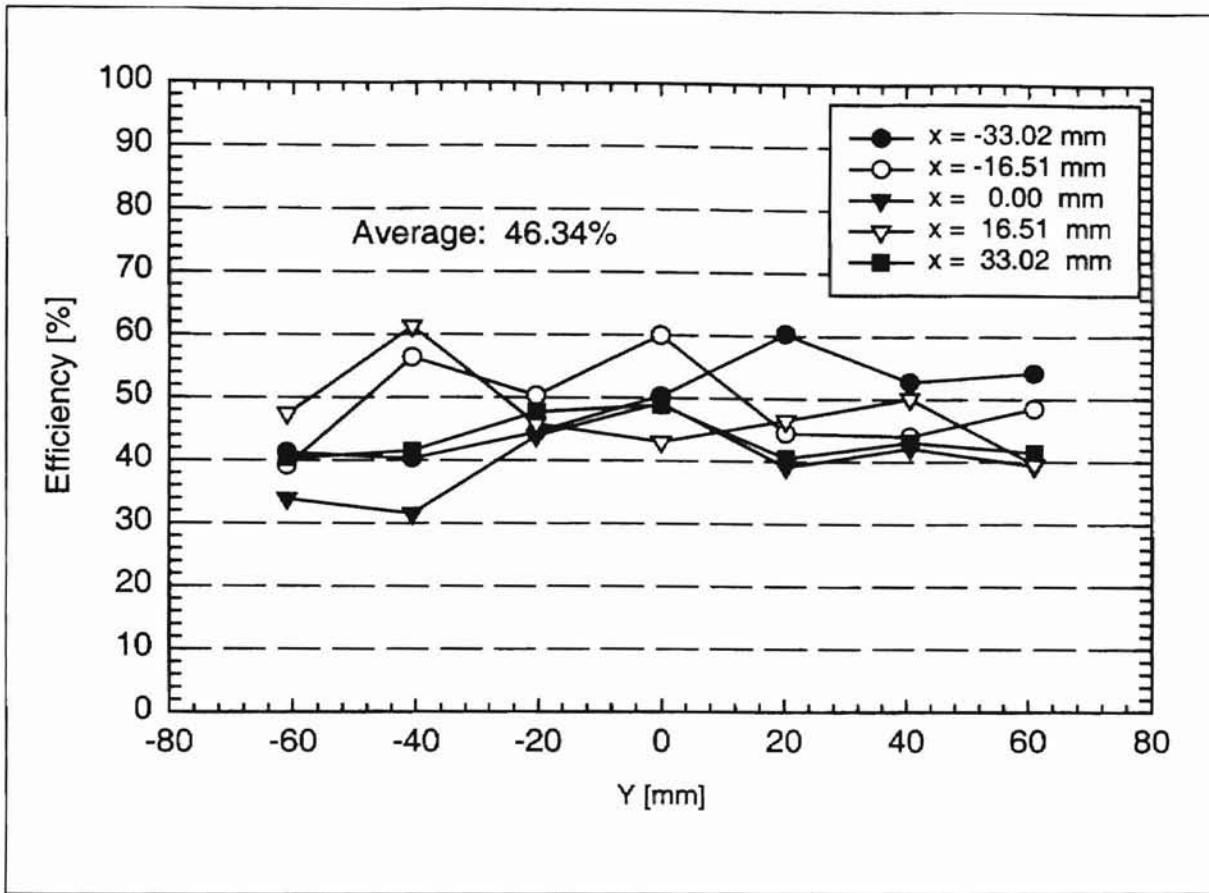


Figure 6.11 Local Filtration Efficiency Distribution for ESH75.1 at an Air Flow Rate of $103.7 \text{ m}^3/\text{hr}$.

The efficiency profile of Fig. 6.11 with an average of 46.34% is more uniform than the efficiency profile of Fig. 6.6 measured at the low air flow rate of $13.53 \text{ m}^3/\text{hr}$. Thus the efficiency profile of Fig 6.6 obtained from its respective upstream and downstream number densities, is not in a tight band compared to the efficiency profile of Fig. 6.11 measured at a high flow rate. A slight change in the velocity distribution can cause a significant change in the efficiency distribution of the filter at low flow rates than at higher flow rates. This may be explained in terms of the number density ratio (ratio of downstream to upstream number densities) and further investigation of Eq. (6-1) as follows:

$$\eta_i = 1 - \frac{N_{idown}}{N_{iup}} = 1 - R_d \quad (6.2)$$

where N_{iup} and N_{idown} are the number densities upstream and downstream of the filter as defined previously, and R_d is the downstream to upstream number density ratio. From this expression, the fact that local filtration efficiencies are higher at higher flow rates implies that as η_i tends toward 1, the density ratio R_d tends towards zero or the ratio of the downstream to upstream densities becomes very low. By the same token, it is not difficult to prove that for lower flow rates, since the efficiency is low, the number density ratio is higher than those of high flow rates. This can also briefly explain how a small percentile changes in the downstream or upstream number densities can easily affect the local and overall efficiencies of the filter. For most low flow rates, the number densities upstream and downstream of the filter are very close to each other, unlike the number densities for high flow rates.

The velocity distribution for the upstream velocity profile of Fig 6.2 ranges between the minimum and maximum values of 0.24 and 0.36 m/s, respectively, while the corresponding upstream number density varies between approximately $3.2 \times 10^9 \text{ m}^{-3}$ and $4.3 \times 10^9 \text{ m}^{-3}$. However, the velocity and number density ranges downstream of the filter are much higher. The velocity, downstream of the filter, varies approximately between 0.23 and 0.7 m/s. while the downstream number density varies between $1.5 \times 10^9 \text{ m}^{-3}$ and $3.0 \times 10^9 \text{ m}^{-3}$. On the other hand, the velocity and number density profiles upstream of the filter for the intermediate flow rate (103.7 m^3/hr) are more uniform than the corresponding downstream velocity and number density profiles.

6.1.2 Efficiency Variation with Flow Rate

The variation of overall filtration efficiency with flow rate for the electrostatically charged and unneutralized PSL particles as they flow in the atomized and dried state through the duct and fibrous filter is shown in Fig. 6.12. The overall efficiencies of the filter using neutralized PSL particles at low humidities are provided in Subsection 6.2 of

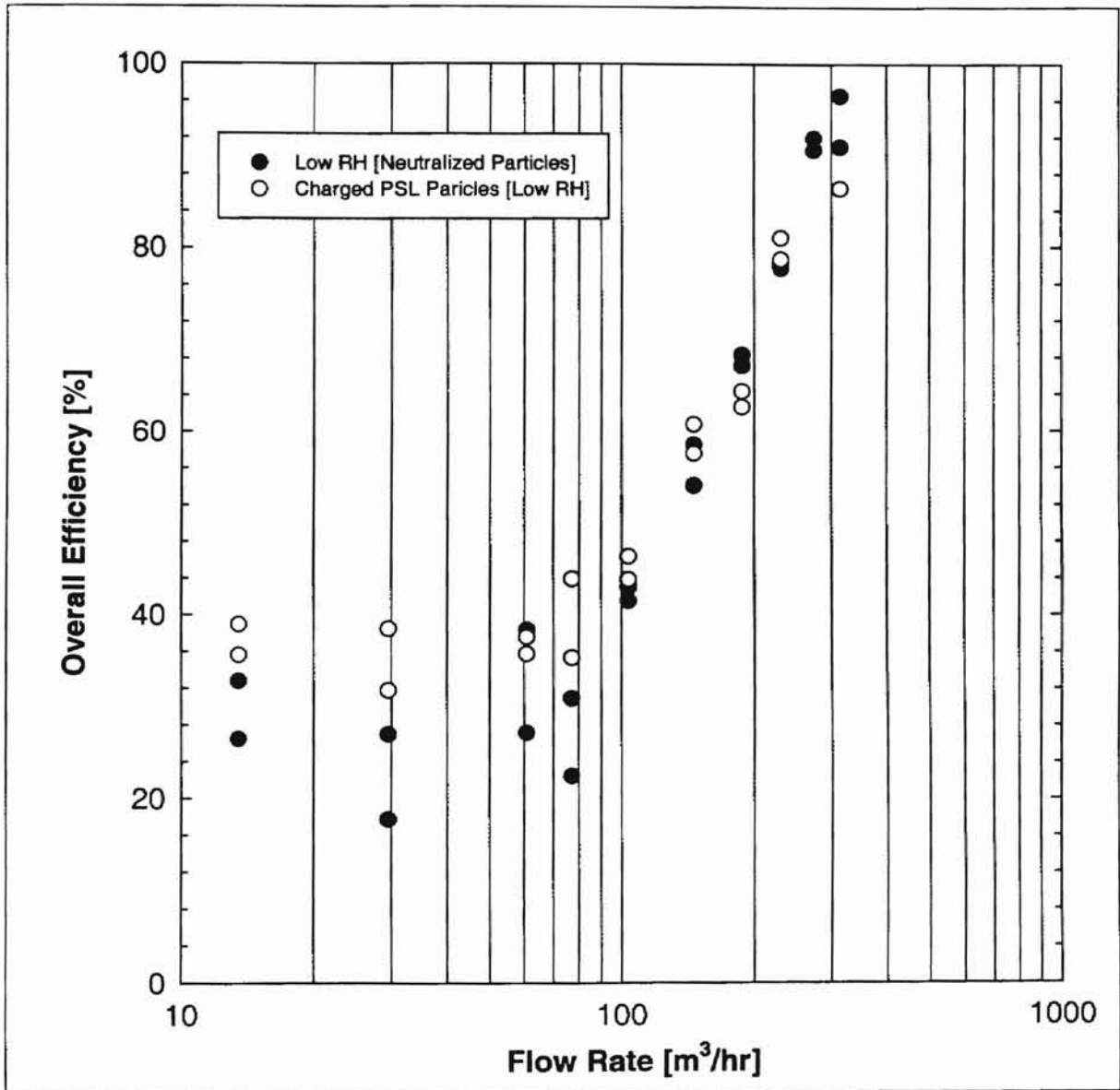


Figure 6.12 Electrostatic Charge Effects on Fibrous Filtration Efficiency Using Electrostatically Charged and Neutral PSL Particles (Summer, 1998).

of this chapter. As the flow rate increases, the efficiency increases for both charged and neutralized PSL particles. However, at low flow rates, tests with electrostatically charged particles show slightly higher efficiencies than with neutral particles. The efficiency at low flow rates was found to be extremely low even at times leading to negative efficiencies for solutions with high PSL concentrations (10 ml of PSL solution at 10% solids mixed with 990 ml of distilled water to make 1000 ml of solution). As explained in the experimental consistency measurements in Chapter V, the author is of the opinion that this might be due to the high optical density and other properties of the contaminant loaded air. Hence it was found important to reduce the dense seeding rate of the particles by cutting the concentration of the PSL particle in half for all of the flow rates less than or equal to $77 \text{ m}^3/\text{hr}$. Thus to prepare a 1000 ml of solution, only 5 ml of PSL suspension at 10% solids has been used. Low filtration efficiencies have been attributed to over seeding, which might have created a high optical density that obstructs or affects the particle counting or the reflectivity of the seeding particles at the intended grid point of interest.

From the logarithmic scale, one can see that the efficiency steadily increases with flow rate in the high flow rate region. Hence, from this experiment, the conclusion that can be drawn is that the electrostatic charge effect on the efficiency of the filter has been found to be dependent upon flow rate. The electrostatic effect is higher at low flow rates than at high flow rates. At high flow rates, electrostatic charge effects become negligible. Thus the electrostatic filtration action decreases as the flow rate steadily increases.

6.1.3 Pressure Drop Variation with Flow Rate

The pressure drop across the test filter has been found to be dependent upon the

flow rate of the air. In the literature, many filtration researchers explain that the pressure drop for electrostatically charged filters is less than for uncharged filters. However, in this experiment, it has been difficult to corroborate this fact due to the limited accuracy of the water manometer and the low electrostatic charge voltage. A plot of the actual (measured) pressure drops against flow rate for the investigation of electrostatic charge effects is provided in Fig 6.13.

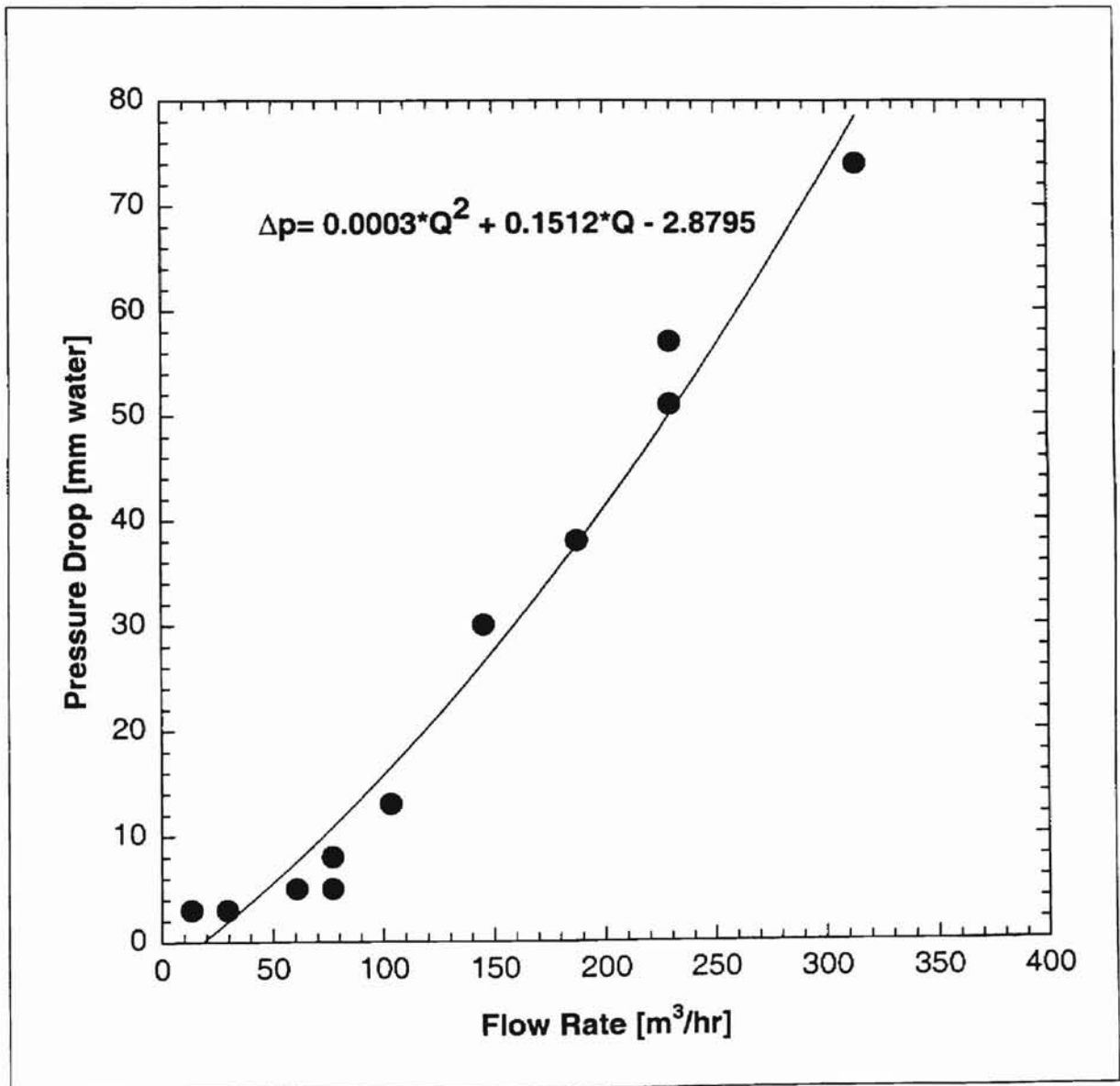


Figure 6.13 Electrostatic Charge Effects: Pressure Drop Variation with Flow Rate.

As shown in the plot, the pressure drop changes quadratically with flow rate. The best filter is a filter that can provide low pressure drop and high filtration efficiency. High pressure drop across a filter implies high energy expenditure (requirement) to draw air through the filter, which in turn calls for a high capacity blower in industrial installations or high suction pressure inside automotive engines to meet the high demand for filtered air.

6.2 Humidity Effects on Fibrous Filtration Using Neutralized PSL Particles

Experiments on the performance of the model A13192 fibrous filters at high and low humidities by neutralizing the electrostatic charge of the particles as they flow along the duct, following the experimental flow set up of Chapter IV, have been conducted and the results are presented in Tables 6.3 and 6.4. Table 6.3 shows the summary of humidity, average number densities and velocities of the flow upstream and downstream of the filter, initial pressure drop, electrostatic charge voltage, and the overall filtration efficiency of the test filters as function of air flow rate. Table 6.4 summarizes the test results for these electrostatically neutralized particles at different air flow rates subjected to different humidity conditions. The calculated single fiber efficiencies at low and high humidities and the Stokes number based on the different face velocities (calculated from folded and unfolded filter area and for LDA measurements) are also tabulated.

As in the previous section, the experimental tests on the effect of humidity using electrostatically neutralized PSL particles for each flow rate are designated alphanumerically. For example As shown in Tables 6.3 and 6.4, NESH10.1 designates a test carried out on electrostatically neutralized particles at 10 scfm ($13.53 \text{ m}^3/\text{hr}$) in the

Table 6.3 Summary of Test Results on Humidity Effects for the Model A13192 Dayco-Purolator Automotive Air Filter Using 0.966 μm Diameter Neutralized PSL Particles in the Small Angle Diffuser Housing.

Test Number	Test Date	Flow Rate [m ³ /hr]	RH [%]	Average No. Density [m ⁻³]		Average Velocity [m/s]		Pressure Drop [mm water] Initial (Final)	Static Voltage [V] Upstream of Filter (with Negative Polarity)	Filter Efficiency [%]	
				Upstream	Downstream	Upstream	Downstream			Low RH	High RH
NESH10.1	03/22/98	13.53	43.5	3.65X10 ⁹	2.68X10 ⁹	0.31 (0.164)	0.460 (0.445)	3 (3)	0	26.49	
NESH10.2	03/22/98	13.53	95	4.16X10 ⁹	2.55X10 ⁹	0.234 (0.164)	0.434 (0.445)	3 (3)	0		38.26
NESH10.3	08/15/98	13.53	45	2.77X10 ⁹	1.83X10 ⁹	0.226 (0.164)	0.301 (0.445)	3 (3)	0	32.80	
NESH10.4	08/15/98	13.53	85	2.41X10 ⁹	1.52X10 ⁹	0.227 (0.164)	0.363 (0.445)	3 (3)	0		36.43
NESH20.1	06/15/98	29.5	35	2.28X10 ⁸	1.94X10 ⁹	0.782 (0.3576)	1.188 (0.971)	5 (5)	0	14.59	
NESH20.2	07/06/98	29.5	31.5	2.67X10 ⁸	1.96X10 ⁹	0.715 (0.357)	1.231 (0.971)	5 (5)	0	26.49	
NESH20.3	06/21/98	29.5	79	1.82X10 ⁹	1.26X10 ⁹	0.660 (0.357)	0.994 (0.971)	5 (5)	0		30.50
NESH20.4	06/22/98	29.5	33	1.22X10 ⁹	9.99X10 ⁸	0.721 (0.357)	1.122 (0.971)	5 (5)	0	17.73	
NESH20.5	07/06/98	29.5	80	1.87X10 ⁹	1.30X10 ⁹	0.699 (0.357)	1.272 (0.971)	5 (5)	0		30.40
NESH40.1	03/01/98	60.8	17	5.96X10 ⁸	4.34X10 ⁸	1.311 (0.735)	1.980 (2.002)	5 (5)	50	27.13	
NESH40.2	03/05/98	60.8	85	9.42X10 ⁸	5.35X10 ⁸	1.322 (0.735)	2.214 (2.002)	5 (5)	0		42.54
NESH40.3	08/16/98	60.8	85	1.07X10 ⁹	6.21X10 ⁸	0.908 (0.735)	1.420 (2.002)	5 (5)	0		41.48
NESH40.4	06/22/98	60.8	35	1.11X10 ⁹	6.60X10 ⁸	1.392 (0.735)	2.350 (2.002)	5 (5)	50	38.33	
NESH50.1	06/11/98	77.1	42	1.18X10 ⁹	8.11X10 ⁸	1.980 (0.932)	3.05 (2.538)	5 (5)	0	30.86	
NESH50.2	06/13/98	77.1	35	9.76X10 ⁸	7.55X10 ⁸	1.707 (0.932)	2.583 (2.538)	8 (8)	50	22.43	
NESH50.3	06/13/98	77.1	80	1.01X10 ⁹	6.79X10 ⁸	1.792 (0.932)	3.422 (2.538)	8 (8)	0		31.91
NESH50.4	08/16/98	77.1	85	8.92X10 ⁸	5.71X10 ⁸	1.34 (0.932)	2.350 (2.538)	8 (8)	0		35.98
NESH75.1	06/09/98	103.7	35	6.42X10 ⁸	3.56X10 ⁸	2.594 (1.253)	4.041 (3.414)	23 (23)	0	42.96	
NESH75.2	06/09/98	103.7	45	7.49X10 ⁸	4.36X10 ⁸	2.625 (1.253)	4.177 (3.414)	18 (18)	0	41.49	
NESH75.3	07/14/98	103.7	80	7.62X10 ⁸	3.92X10 ⁸	3.118 (1.253)	4.967 (3.414)	23 (23)	0		43.30
NESH75.4	08/17/98	103.7	80	6.77X10 ⁸	3.66X10 ⁸	2.074 (1.253)	3.31 (3.414)	23 (23)	0		45.87

Table 6.3 (Cont'd): Summary of Test Results on Humidity Effects for the Model A13192 Dayco-Purolator Automotive Air Filter Using 0.966 µm Diameter Neutralized PSL Particles in the Small Angle Diffuser Housing.

Test Number	Test Date	Flow Rate [m ³ /hr]	High Low RH [%]	Average No. Density [m ⁻³]		Average Velocity [m/s]		Pressure Drop [mm water] Initial (Final)	Static Voltage [V] Upstream of Filter (with Negative Polarity)	Filter Efficiency [%]	
				Upstream	Downstream	Upstream	Downstream			Low RH	High RH
NESH100.1	06/25/98	145.7	73	3.31X10 ⁸	9.36X10 ⁷	4.799 (1.761)	7.511 (4.797)	41 (41)	0		71.80
NESH100.2	06/25/98	145.7	74	2.75X10 ⁹	9.65X10 ⁷	4.955 (1.761)	7.409 (4.797)	43 (43)	0		64.52
NESH100.3	07/12/98	145.7	35	4.49X10 ⁹	1.86x10 ⁸	4.359 (1.761)	6.878 (4.797)	41 (41)	0	58.47	
NESH100.4	07/13/98	145.7	38	3.74X10 ⁸	1.72X10 ⁸	4.628 (1.761)	7.237 (4.797)	41 (41)	0	54.05	
NESH125.1	06/29/98	187.7	87	2.38X10 ⁸	4.02X10 ⁷	5.638 (2.269)	8.308 (6.179)	64 (64)	0		83.03
NESH125.2	06/30/98	187.7	80	2.15X10 ⁸	6.38X10 ⁷	5.284 (2.269)	7.924 (6.179)	61 (61)	0		70.20
NESH125.3	07/11/98	187.7	43	3.76X10 ⁸	1.22X10 ⁸	5.431 (2.269)	8.429 (6.179)	56 (56)	0	67.08	
NESH125.4	07/12/98	187.7	48	3.54X10 ⁸	1.12X10 ⁸	5.100 (2.269)	8.355 (6.179)	56 (56)	0	68.31	
NESH150.1	07/02/98	229.7	43.5	1.27X10 ⁸	3.07X10 ⁷	6.370 (2.776)	9.359 (7.562)	74 (74)	0	77.75	
NESH150.2	07/11/98	229.7	43.5	2.28X10 ⁸	4.83X10 ⁷	6.235 (2.776)	9.500 (7.562)	71 (71)	0	78.21	
NESH175.1	07/02/98	273.6	43	1.30X10 ⁸	1.17X10 ⁷	7.688 (3.307)	10.51 (9.007)	104 (104)	0	90.64	
NESH175.2	07/07/98	273.6	48.5	1.41X10 ⁸	1.25X10 ⁷	7.42 (3.307)	10.56 (9.007)	107 (107)	0	91.95	
NESH200.1	07/03/98	313.8	45	1.02X10 ⁸	8.82X10 ⁶	8.251 (3.793)	11.02 (9.007)	122 (135)	0	91.02	
NESH200.2	07/04/98	313.8	45	1.12X10 ⁸	3.91X10 ⁶	8.046 (3.793)	11.539 (9.01)	124 (145)	0	96.52	

Table 6.4 Humidity Effects: Summary of Test Results, Single Fiber Efficiency and Stokes Number Analysis for the Model A13192 Dayco-Purolator Automotive Air Filter Using 0.966 μm Diameter PSL Particles in the Small Angle Diffuser Housing.

Test No.	FLOW RATE [m ³ /hr]	Upstream Velocity [m/s] Based on			Pressure Drop [in] Initial (Final)	Pressure Drop [mm] Initial (Final)	Overall Filter Efficiency [%]	Single Fiber Efficiency [%]	Stokes Number Based on (U ₁)	Stokes Number Based on (U ₂)	Stokes Number Based on (U ₃)
		Unfolded Filter Area (U ₁)	Duct/Folded Filter Area (U ₂)	LDA (U ₃)							
NESH10.1	13.53	0.008	0.164	0.310	0.1 (0.1)	3 (3)	26.49	0.002	0.0007	0.0144	0.0272
NESH10.2	13.53	0.008	0.164	0.234	0.1 (0.1)	3 (3)	38.26	0.003	0.0007	0.0144	0.0205
NESH10.3	13.53	0.008	0.164	0.226	0.1 (0.1)	3 (3)	32.8	0.002	0.0007	0.0144	0.0198
NESH10.4	13.53	0.008	0.164	0.227	0.1 (0.1)	3 (3)	36.43	0.002	0.0007	0.0144	0.0199
NESH20.1	29.5	0.018	0.357	0.782	0.2 (0.2)	5 (5)	14.59	0.001	0.0016	0.0313	0.0687
NESH20.2	29.5	0.018	0.357	0.715	0.2 (0.2)	5 (5)	26.49	0.002	0.0016	0.0313	0.0628
NESH20.3	29.5	0.018	0.357	0.660	0.2 (0.2)	5 (5)	30.5	0.002	0.0016	0.0313	0.0580
NESH20.4	29.5	0.018	0.357	0.721	0.2 (0.2)	5 (5)	17.73	0.001	0.0016	0.0313	0.0633
NESH20.5	29.5	0.018	0.357	0.699	0.2 (0.2)	5 (5)	30.4	0.002	0.0016	0.0313	0.0614
NESH40.1	60.8	0.038	0.735	1.311	0.2 (0.2)	5 (5)	27.13	0.002	0.0033	0.0645	0.1151
NESH40.2	60.8	0.038	0.735	1.322	0.2 (0.2)	5 (5)	42.54	0.003	0.0033	0.0645	0.1161
NESH40.3	60.8	0.038	0.735	0.908	0.2 (0.2)	5 (5)	41.48	0.003	0.0033	0.0645	0.0797
NESH40.4	60.8	0.038	0.735	1.392	0.2 (0.2)	5 (5)	38.33	0.003	0.0033	0.0645	0.1222
NESH50.1	77.1	0.048	0.932	1.980	0.2 (0.2)	5 (5)	30.86	0.002	0.0042	0.0818	0.1739
NESH50.2	77.1	0.048	0.932	1.707	0.3 (0.3)	8 (8)	22.43	0.001	0.0042	0.0818	0.1499
NESH50.3	77.1	0.048	0.932	1.792	0.3 (0.3)	8 (8)	31.91	0.002	0.0042	0.0818	0.1574
NESH50.4	77.1	0.048	0.932	1.34	0.3 (0.3)	8 (8)	35.98	0.002	0.0042	0.0818	0.1177
NESH75.1	103.7	0.065	1.253	2.594	0.9 (0.9)	23 (23)	42.96	0.003	0.0057	0.1101	0.2278
NESH75.2	103.7	0.065	1.253	2.625	0.7 (0.7)	18 (18)	41.49	0.003	0.0057	0.1101	0.2305
NESH75.3	103.7	0.065	1.253	3.118	0.9 (0.9)	23 (23)	43.3	0.003	0.0057	0.1101	0.2738
NESH75.4	103.7	0.065	1.253	2.074	0.9 (0.9)	23 (23)	45.87	0.003	0.0057	0.1101	0.1821
NESH100.1	145.7	0.091	1.761	4.799	1.6 (1.6)	41 (41)	71.8	0.007	0.0080	0.1546	0.4214

Table 6.4 (Cont'd): Humidity Effects: Summary of Test Results, Single Fiber Efficiency and Stokes Number Analysis for the Model A13192 Dayco-Purolator Automotive Air Filter Using 0.966 μm diameter PSL Particles in the Small Angle Diffuser Housing.

Test No.	FLOW RATE [m ³ /hr]	Upstream Velocity [m/s] Based on			Pressure Drop [in] Initial (Final)	Pressure Drop [mm] Initial (Final)	Overall Filter Efficiency [%]	Single Fiber Efficiency [%]	Stokes Number Based on (U ₁)	Stokes Number Based on (U ₂)	Stokes Number Based on (U ₃)
		Unfolded Filter Area (U ₁)	Duct/Folded Filter Area (U ₂)	LDA (U ₃)							
NESH100.2	145.7	0.091	1.761	4.955	1.7 (1.7)	43 (43)	64.52	0.006	0.0080	0.1546	0.4351
NESH100.3	145.7	0.091	1.761	4.359	1.6 (1.6)	41 (41)	58.47	0.005	0.0080	0.1546	0.3828
NESH100.4	145.7	0.091	1.761	4.628	1.6 (1.6)	41 (41)	54.05	0.004	0.0080	0.1546	0.4064
NESH125.1	187.7	0.118	2.269	5.638	2.5 (2.5)	64 (64)	83.03	0.010	0.0103	0.1992	0.4951
NESH125.2	187.7	0.118	2.269	5.284	2.4 (2.5)	61 (61)	70.2	0.007	0.0103	0.1992	0.4640
NESH125.3	187.7	0.118	2.269	5.431	2.2 (2.3)	56 (56)	67.08	0.006	0.0103	0.1992	0.4769
NESH125.4	187.7	0.118	2.269	5.100	2.2 (2.3)	56 (56)	68.31	0.006	0.0103	0.1992	0.4478
NESH150.1	229.7	0.144	2.776	6.370	2.9 (3.1)	74 (74)	77.75	0.008	0.0126	0.2438	0.5594
NESH150.2	229.7	0.144	2.776	6.235	2.8 (2.8)	71 (71)	78.21	0.008	0.0126	0.2438	0.5475
NESH175.1	273.6	0.171	3.307	7.688	4.1 (4.3)	104 (104)	90.64	0.013	0.0150	0.2904	0.6751
NESH175.2	273.6	0.171	3.307	7.42	4.2 (4.4)	107 (107)	91.95	0.014	0.0150	0.2904	0.6516
NESH200.1	313.8	0.197	3.793	8.251	4.8 (5.3)	122 (135)	91.02	0.013	0.0173	0.3330	0.7245
NESH200.2	313.8	0.197	3.793	8.046	4.9 (5.7)	124 (145)	96.52	0.018	0.0173	0.3330	0.7065

small angle diffuser housing. Thus NE stands for electrostatically neutralized and SH stands for the small angle diffuser housing in which the test was conducted.

The experiments in these tests were performed while monitoring the test conditions of the air flow (humidity and temperature) and by reducing the electrostatic charge voltage from the surface of the filter housing by grounding it using the experimental setup of Chapter IV. More or less, these tests on the effect of humidity, especially those which were conducted under low humidities to see electrostatic charge effects, were performed under conditions similar to those of the previous experiments using electrostatically charged particles to test electrostatic charge effects. On the other hand, during the tests that were carried out to test the effect of high humidity on filtration efficiency, the author had closely monitored the temperature and the maintenance of high humidity of the flow throughout the experimental test. Thus the test conditions (for low humidity tests) remained more or less similar for all the tests. However, while the electrostatic charge voltage was zero for most of the flow rates, at times there were electrostatic charge voltage readings up to 50 v for a few of the intermediate flow rates, since the housing and metallic structure around the housing were grounded. Downstream of the filter, the electrostatic charge voltage was zero for all flow rates. However, the electrostatic charge voltage for the ungrounded mixing box remained significantly high (2500-4000 v), depending upon the humidity of the room and flow rate of air. The concentration of PSL particles used in these experiments in determining the performance of the filters was also maintained at the same value as the concentration of the particles used for studying charged PSL particle effects (i.e., 5 or 10 ml suspension of PSL particles at 10% solids by weight, depending upon the flow rate of air).

In this section, the number density, velocity and efficiency profiles for selected low and high flow rates will be presented. The efficiency and pressure drop variations across the filter will also be examined. The rest of the experimental results for the number density, velocity, and efficiency profiles are provided in Appendix E.

6.2.1 Low Humidity Effects

Low humidity refers to relative humidities much lower than the critical relative humidity of 60% [Chapman Catalog, 1996] above which electrostatic charge may not exist. Hence, in these experimental tests, low relative humidity values would include those relative humidities below 50%. By heating the incoming air, the humidity of the air flow has been lowered as much as possible, depending upon the air inlet conditions and flow rate. These experimental results were conducted to see how well fibrous filters perform under relatively low humidities as compared to high humidity conditions using neutralized PSL particles. These results will be in turn compared with the previous results for electrostatically charged PSL particles in Section 6.4.

The velocity, number density and efficiency profiles for some representative flow rates are discussed in this subsection. Figures 6.14 and 6.15 show the velocity distribution upstream and downstream of the filter at an air flow rate of 13.53 m³/hr and low humidity. The number densities upstream and downstream of the filter are shown in Figs. 6.16 and 6.17. The local filtration efficiency distribution at low humidity and a flow rate of 13.53 m³/hr has been plotted in Fig 6.18. Comparison of upstream and downstream velocity profiles shows that the upstream velocity profile is more uniform than the downstream velocity profile. On the other hand, comparing the respective

velocity profiles for the experimental tests performed using charged PSL particles (see Section 6.1) with the velocity distribution of the test results for neutralized PSL particles (both cases at low air humidity) shows that there are no marked differences in the velocity distributions. For both cases, the upstream velocity profiles remain more uniform than the downstream velocity profiles. The concentration of the PSL particle solution used in the experiment to test low humidity effects was low (i.e. 5 ml suspension at 10% solids) for low flow rates and high (10 ml suspension at 10% solids) for high flow rates when preparing a 1000 ml solution in distilled water. This was in order to offset the problems of extremely low, and at times negative, local and overall efficiencies at low flow rates due to the dense seeding of particles that can change the optical density of the medium significantly as has been explained in Chapter V.

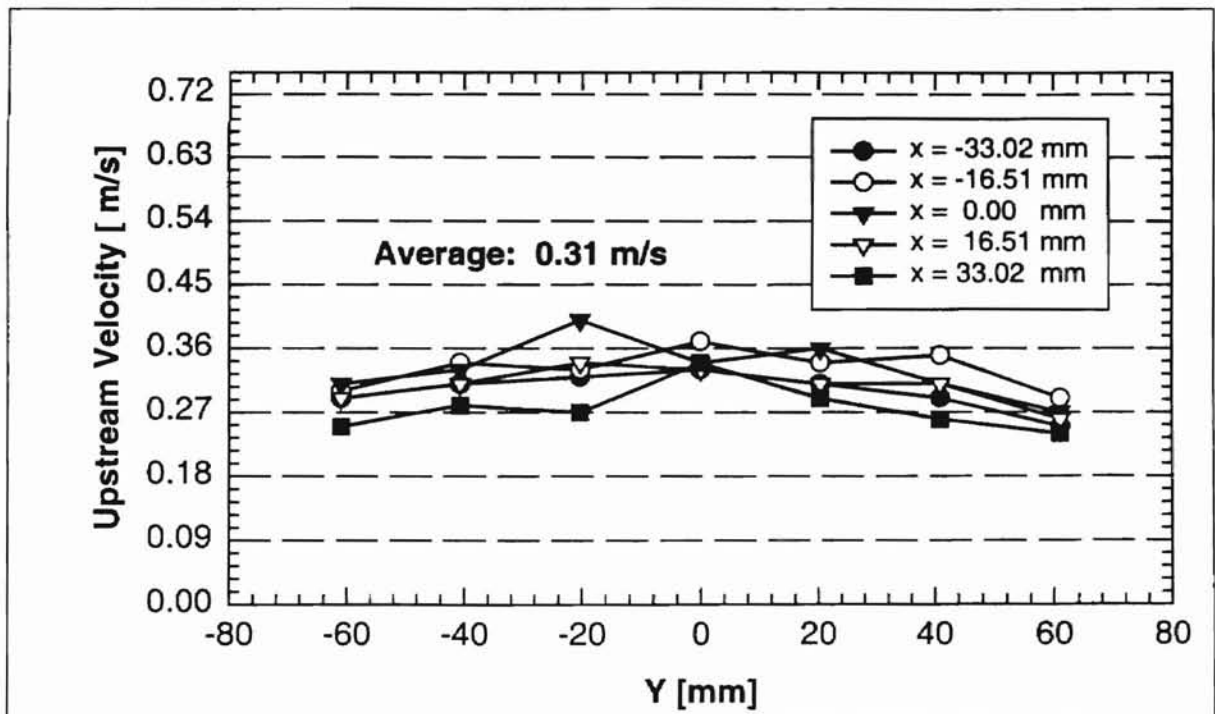


Figure 6.14 Upstream Velocity Distribution for Test No. NESH10.1 at Low Humidity and an Air Flow Rate of 13.53 m³/hr.

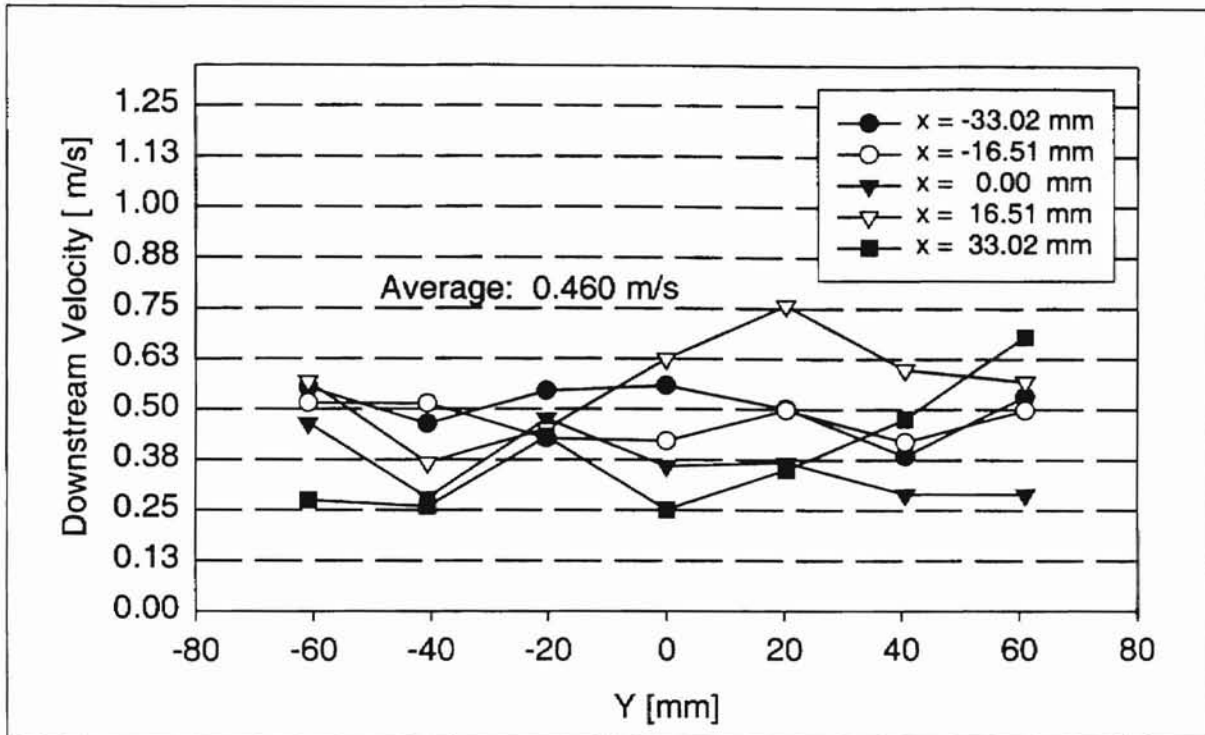


Figure 6.15 Downstream Velocity Distribution for Test No. NESH10.1 at Low Humidity and an Air Flow Rate of 13.53 m³/hr.

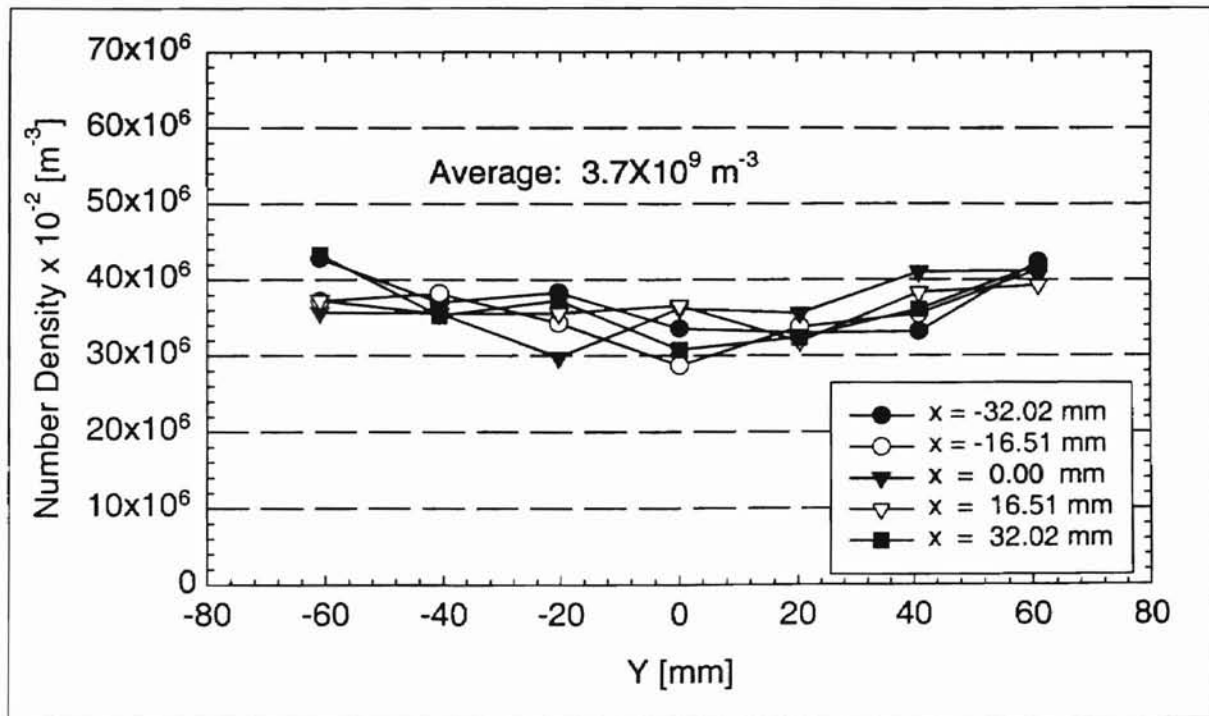


Figure 6.16 Upstream Number Density Distribution for Test No. NESH10.1 at an Air Flow Rate of 13.53 m³/hr.

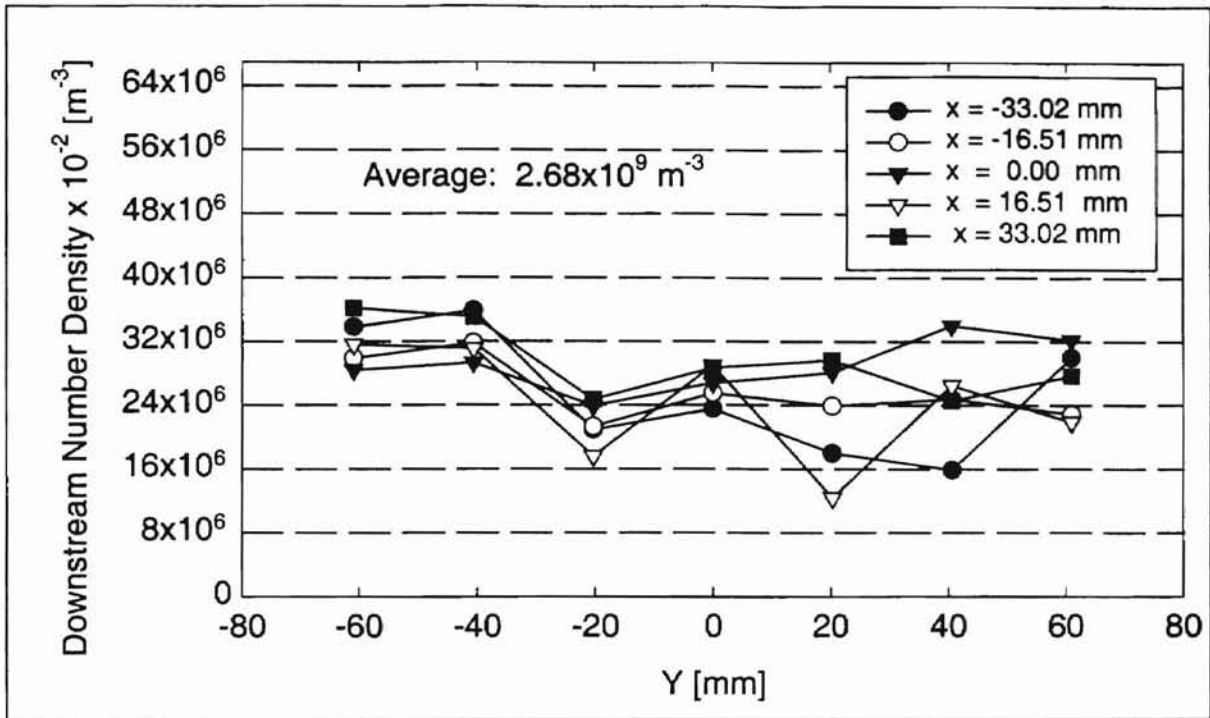


Figure 6.17 Downstream Number Density Distribution for Test No. NESH10.1 at an Air Flow Rate of $13.53 \text{ m}^3/\text{hr}$.

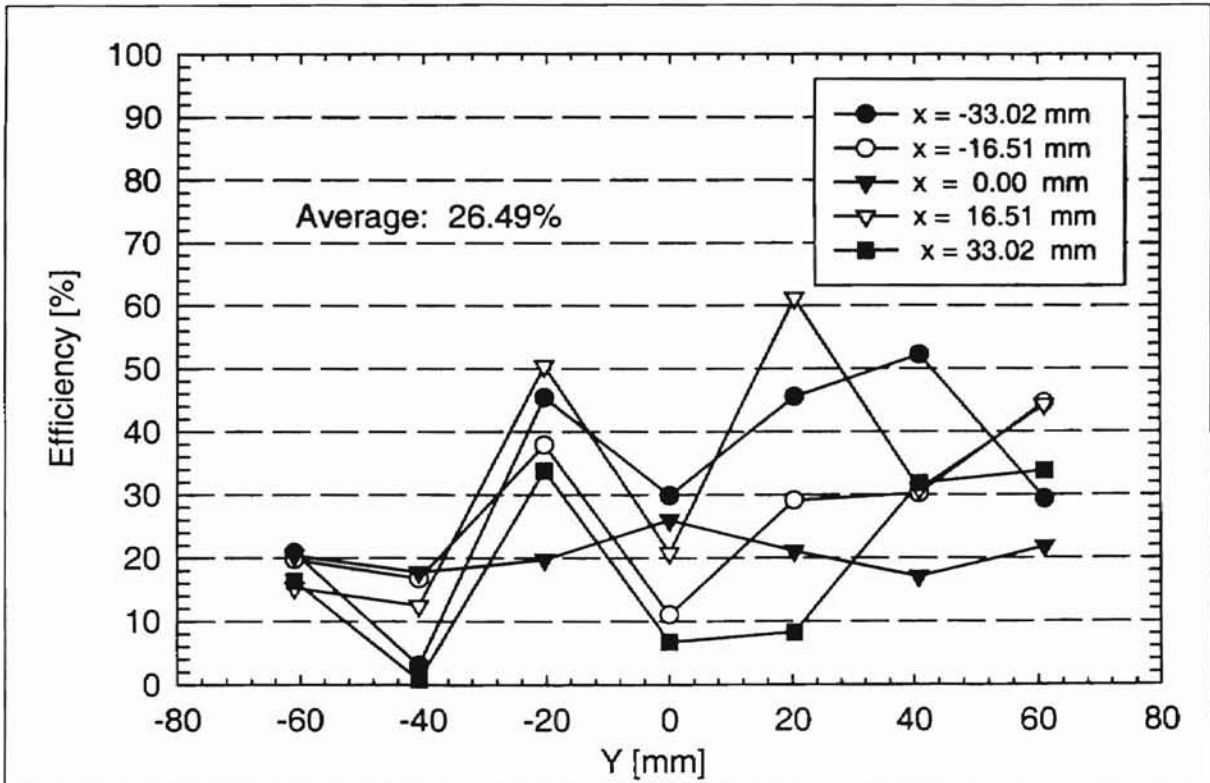


Figure 6.18 Filtration Efficiency Distribution for Test No. NESH10.1 at Low Humidity and an Air Flow Rate of $13.53 \text{ m}^3/\text{hr}$.

Figures 6.19 through 6.23 show the respective upstream and downstream velocity, number density and efficiency profiles for a high flow rate of 187.7 m³/hr at a low relative humidity of 43%. Both the upstream and downstream velocity profiles of Figs. 6.19 and 6.20 for the low humidity air flow (loaded with the PSL contaminants) are characterized by uniform and nonuniform velocity distributions upstream and downstream of the filter, respectively. The average downstream velocity (8.429 m/s) is higher than the average upstream velocity (5.431 m/s). This marked difference in the average upstream and downstream velocities has been attributed to the geometric construction of the filter and filter housing. The wire mesh and rubber mount that reinforce the structural integrity of the filter play an important role in the average velocity of the flow downstream of the filter.

The local upstream and downstream number density distributions, with corresponding average number densities of 3.76×10^8 and $1.22 \times 10^8 \text{ m}^{-3}$, are presented in Figs. 6.21 and 6.22, respectively. In the experimental test to determine the effect of low humidity on the efficiency of filters, the observation of the author was that the time taken to collect the data (number of samples) downstream has always been most important. In comparison to tests carried out at high humidity, data collection downstream of the filter has required less time at low humidity than at high humidity. This implies that, for the LDA data acquisition system to collect the same number of samples downstream of the filter at low and high humidities, the run times (data collection times) were found to be different. This trend has been observed for all flow rates, unlike the electrostatic charge effect, which was limited only to low flow rates (less than 77.1 m³/hr).

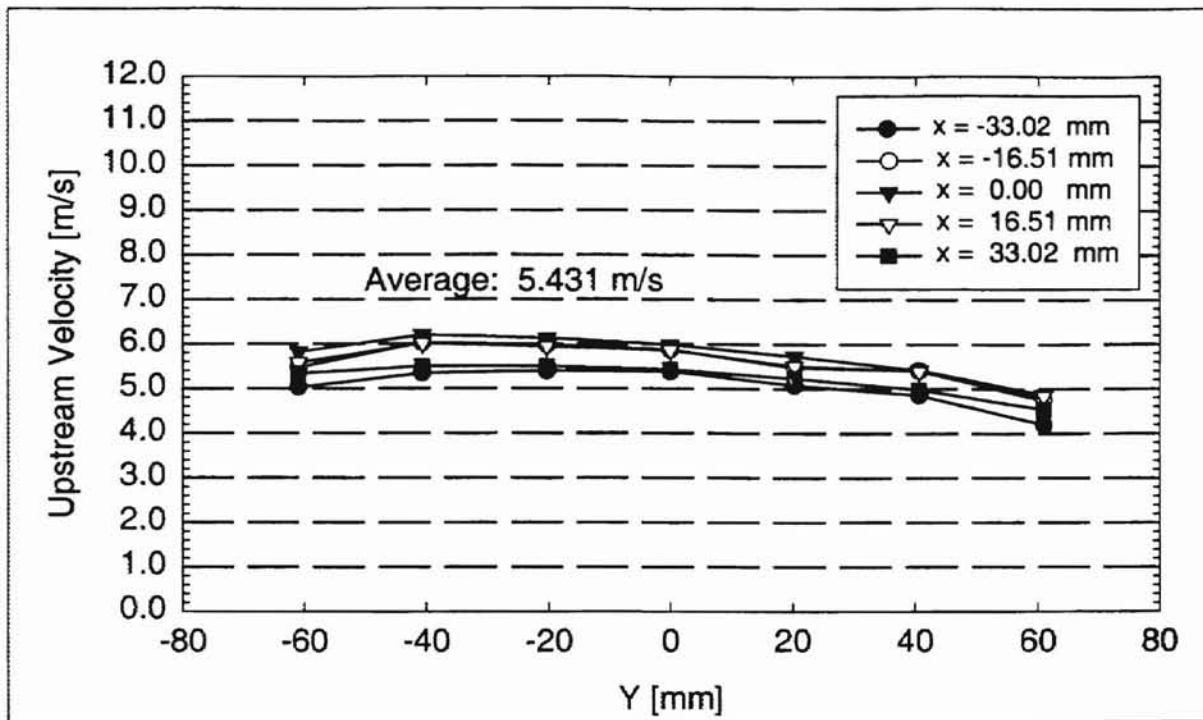


Figure 6.19 Upstream Velocity Distribution for Test No. NESH125.3 at Low Humidity and an Air Flow Rate of 187.7 m³/hr.

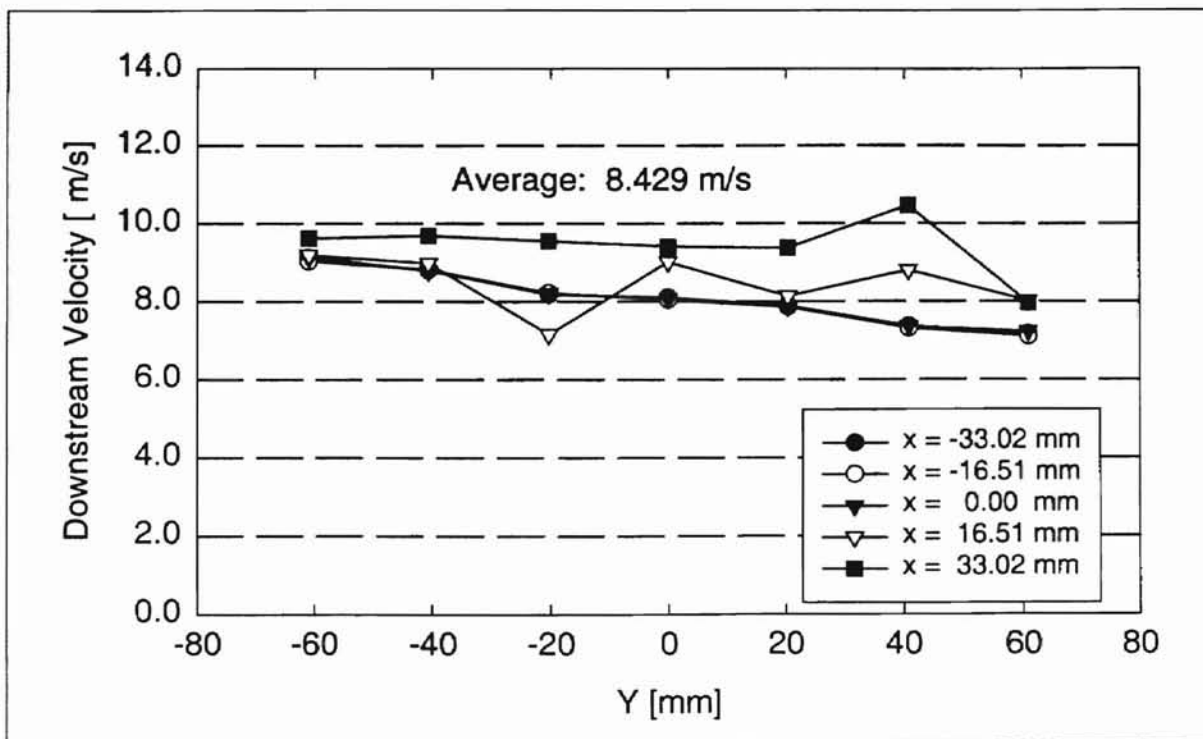


Figure 6.20 Downstream Velocity Distribution for Test No. NESH125.3 at Low Humidity and an Air Flow Rate of 187.7 m³/hr.

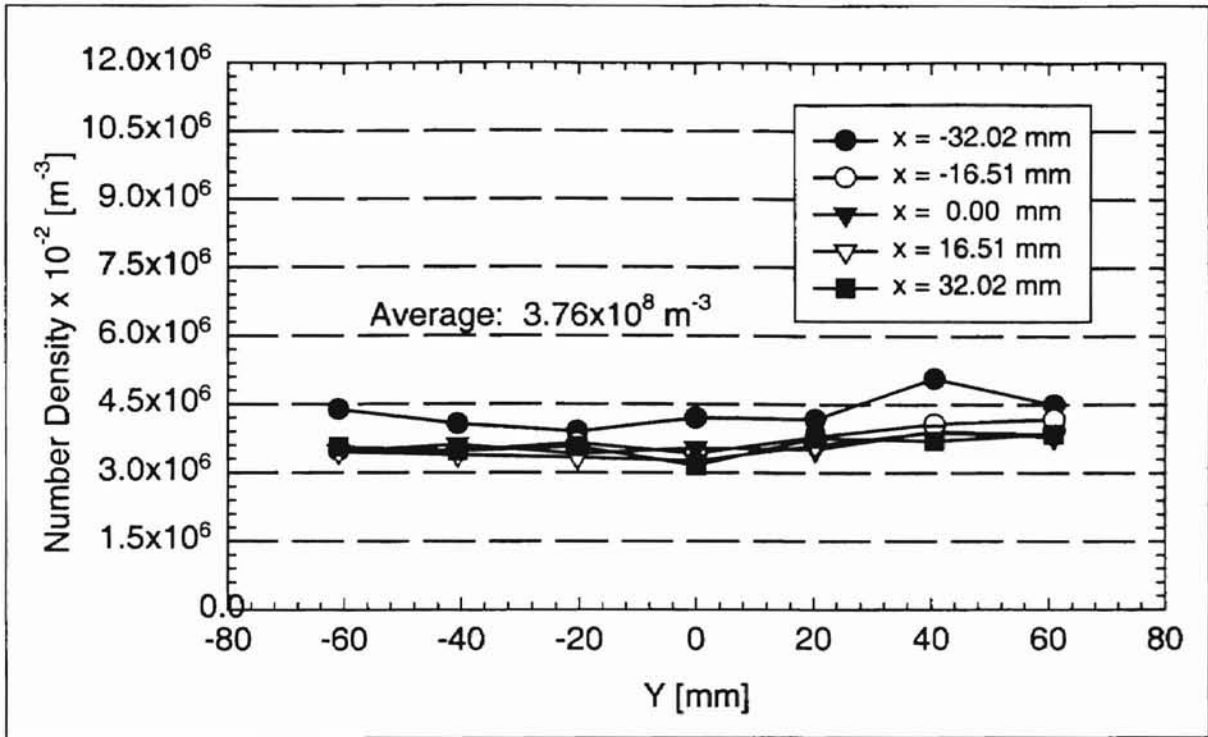


Figure 6.21 Upstream Number Density Distribution for Test No. NESH125.3 at Low Humidity and an Air Flow Rate of $187.7 m^3/hr$.

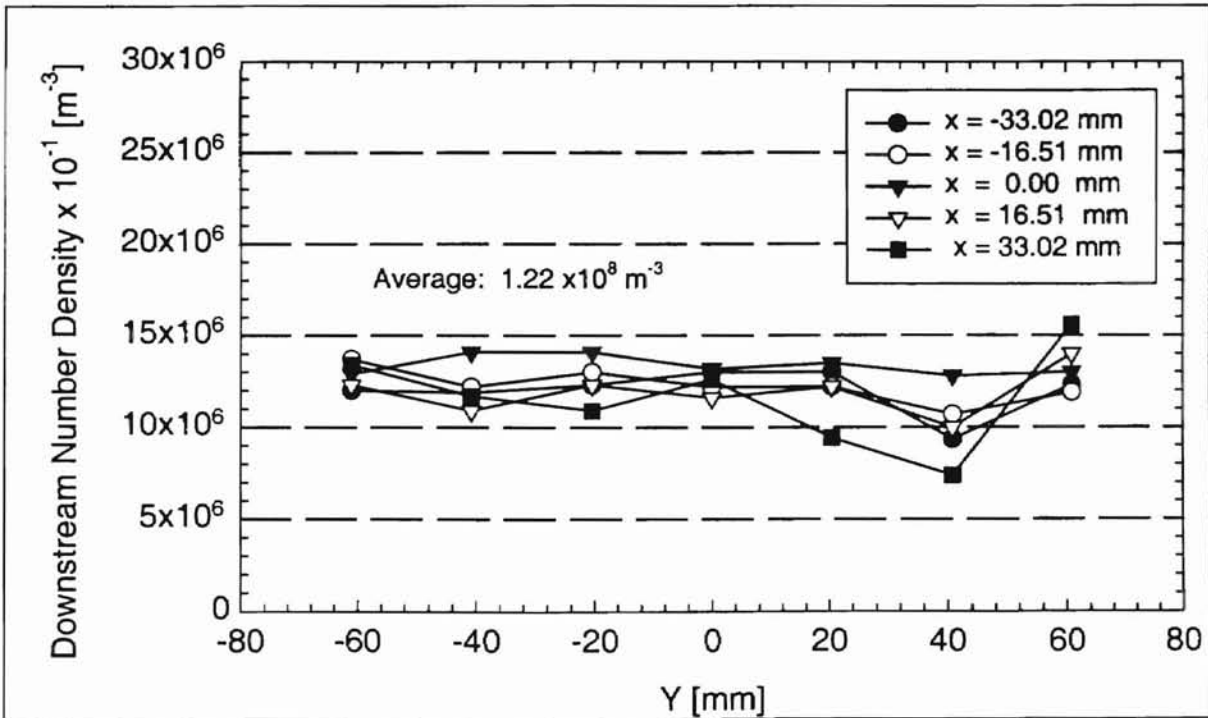


Figure 6.22 Downstream Number Density Distribution for Test No. NESH125.3 at Low Humidity and an Air Flow Rate of $187.7 m^3/hr$.

Figure 6.23 shows the efficiency profile of the model A13192 filter at an air flow rate of 187.7 m³/hr at a low humidity. The local efficiency with an average value of 67.08%, varies from a minimum value of 58% (at grid point location of X = 0.00 mm and Y = -20 mm) to a maximum of about 80% (at grid location X = -33.02 mm and Y = 40 mm).

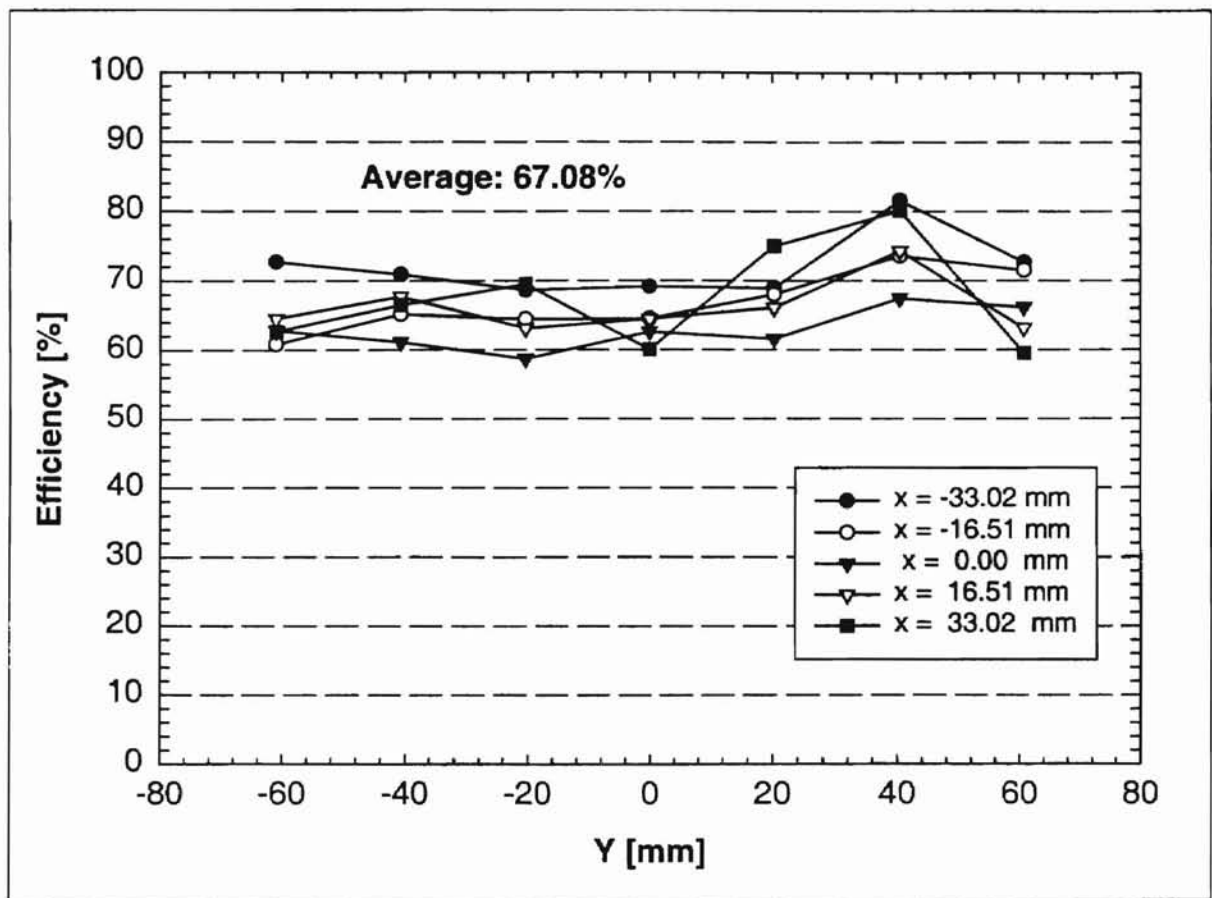


Figure 6.23 Filtration Efficiency Distribution for Test No. NESH125.3 at Low Humidity and an Air Flow Rate of 187.7 m³/hr.

6.2.2 High Humidity Effects

To investigate high humidity effects on the filtration efficiency of the A13192 filters following the experimental procedures and setup of Chapter IV using neutralized PSL particles, the relative humidity of the air flow for all of the flow rates was maintained above 70% as tabulated in the summary of Table 6.3. In this study, high humidity was found to have an influence on the efficiency of fibrous filters at all air flow rates by enhancing the adhesion between the aerosol particles and the filter fibers.

In this subsection, a brief discussion of the experimental results of velocity, number density and efficiency profiles for a low air flow rate of 13.53 m³/hr at a relative humidity of 85% will be presented. Plots of the most important filter performance parameter namely, the overall filtration efficiency of the filter at low and high relative humidities as a function of flow rate and pressure drop across the filter will also be presented and discussed.

6.2.2.1 Velocity, Number Density and Efficiency Profiles

The velocity profiles upstream and downstream of the filter for 13.53 m³/hr are provided in Figs. 6.24 and 6.25. The respective average velocities for the upstream and downstream velocity profiles are 0.227 m/s and 0.363 m/s. The velocity profile upstream of the filter is more symmetric and uniform than the downstream velocity distribution. The downstream velocity profile varies from a minimum of 0.15 m/s (at the X = 33.02 mm and Y = 40 mm grid point) to 0.57 m/s (at the X = -33.02 mm and Y = -20 mm grid point) near the wall. Thus the trends in the velocity distributions for high humidities are not different from the velocity distribution for the low humidity tests plotted in Figs. 6.14

and 6.15 conducted at the same flow rate ($13.53 \text{ m}^3/\text{hr}$). The corresponding upstream and downstream number density profiles (obtained from measurements upstream and downstream of the filter), as shown in Figs. 6.26 and 6.27, have average number densities of 2.41×10^9 and $1.52 \times 10^9 \text{ m}^{-3}$ respectively. While performing experimental tests to calculate downstream number densities at high and low humidities, the observation of the author was that the time taken to collect a specific number of samples (by the LDA system) for a particular air flow rate at high humidity was higher than that required to collect the same number of samples for the same air flow at low humidity. This suggests that there was less PSL particle penetration per unit time through the Dayco-Purolator A13192 fibrous filter at high humidity than at low humidity. Most of the number density distributions downstream of the filter were also found to be nonuniform and unsymmetric with respect to the geometric centerline of the filter.

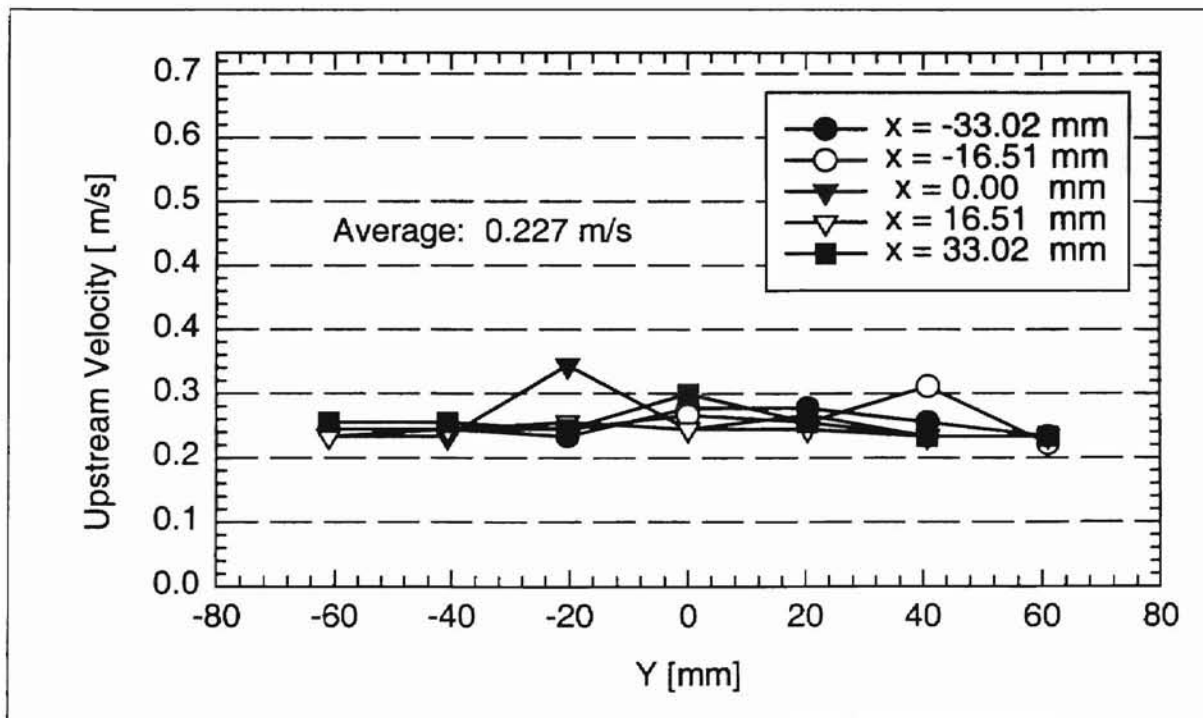


Figure 6.24 Upstream Velocity Distribution for Test No. NESH10.4 at High Humidity and an Air Flow Rate of $13.53 \text{ m}^3/\text{hr}$.

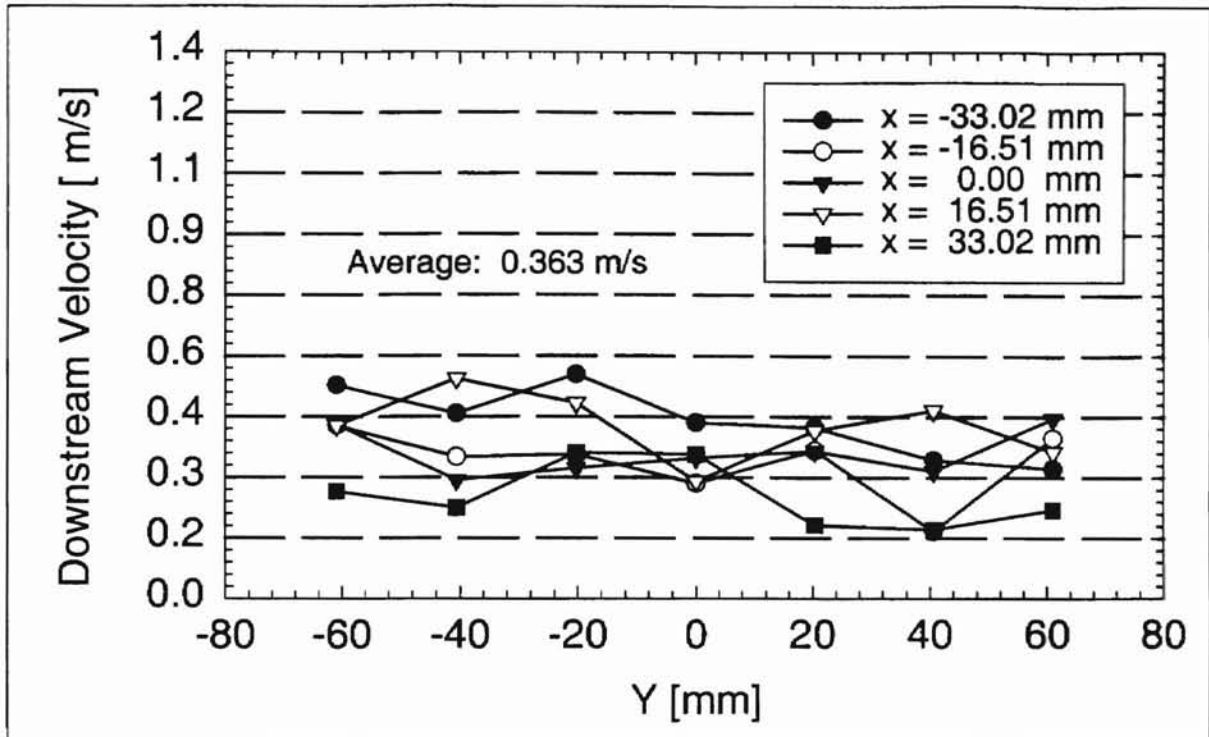


Figure 6.25 Downstream Velocity Distribution for Test No. NESH10.4 at High Humidity and an Air Flow Rate of 13.53 m³/hr.

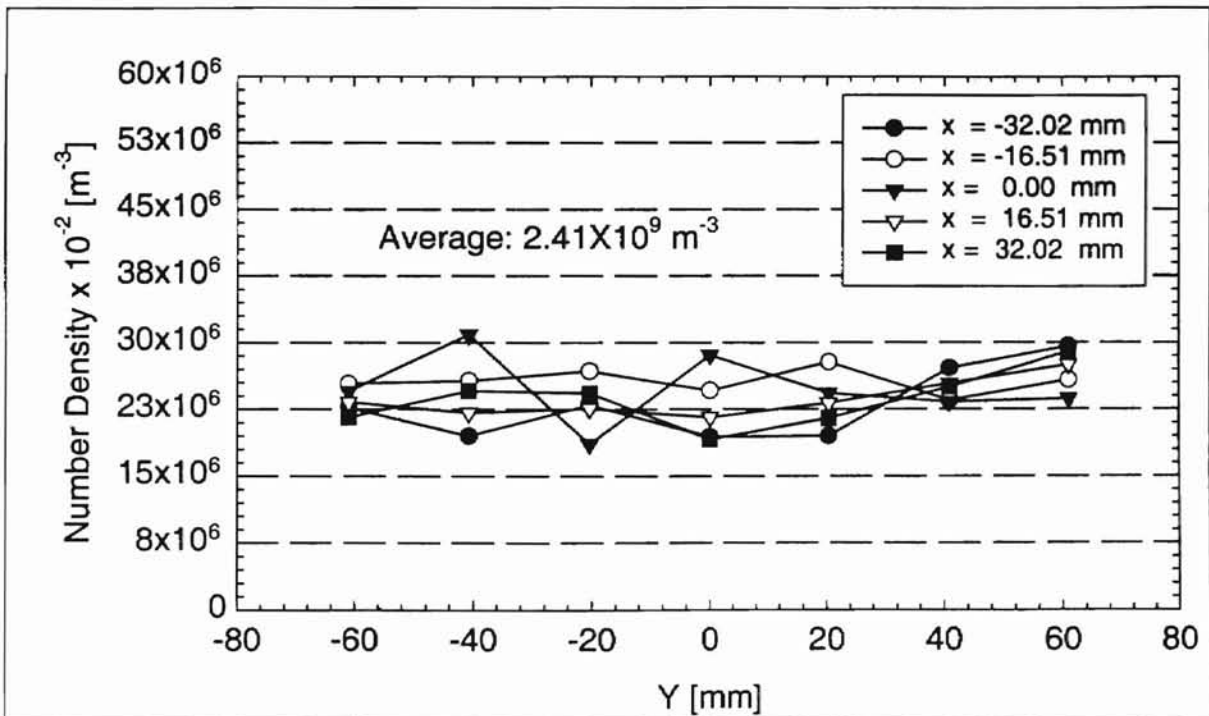


Figure 6.26 Upstream Number Density Distribution for Test No. NESH10.4 at High Humidity and an Air Flow Rate of 13.53 m³/hr.

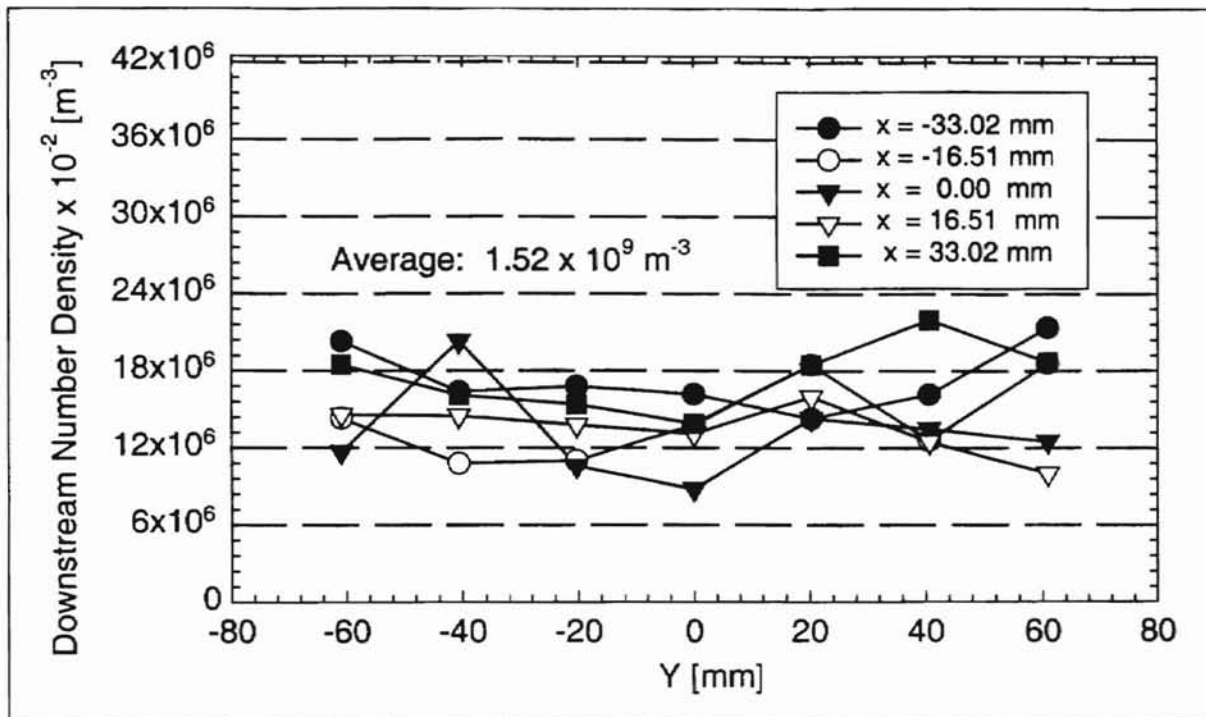


Figure 6.27 Downstream Number Density Distribution for Test No. NESH10.4 at High Humidity and an Air Flow Rate of $13.53 \text{ m}^3/\text{hr}$.

Figure 6.28 shows the efficiency profile for an air flow rate of $13.53 \text{ m}^3/\text{hr}$ at high humidity. The local efficiency distribution varies between the 10% minimum at the center of the filter and the 70% maximum efficiency at the $X = -33.02 \text{ mm}$ and $Y = -60 \text{ mm}$ grid point. This nonuniformity is attributed to the nonuniformity in the local number density distributions (from grid point to grid point) due to very small changes in the upstream or downstream velocities or run (sample collection) time. Thus at low flow rates for a very small percentile change in the local upstream or downstream number densities due to variations in the collection time or average velocity of the particles, there is a marked change in the corresponding local efficiency of the filter [Jadbabaei, 1997].

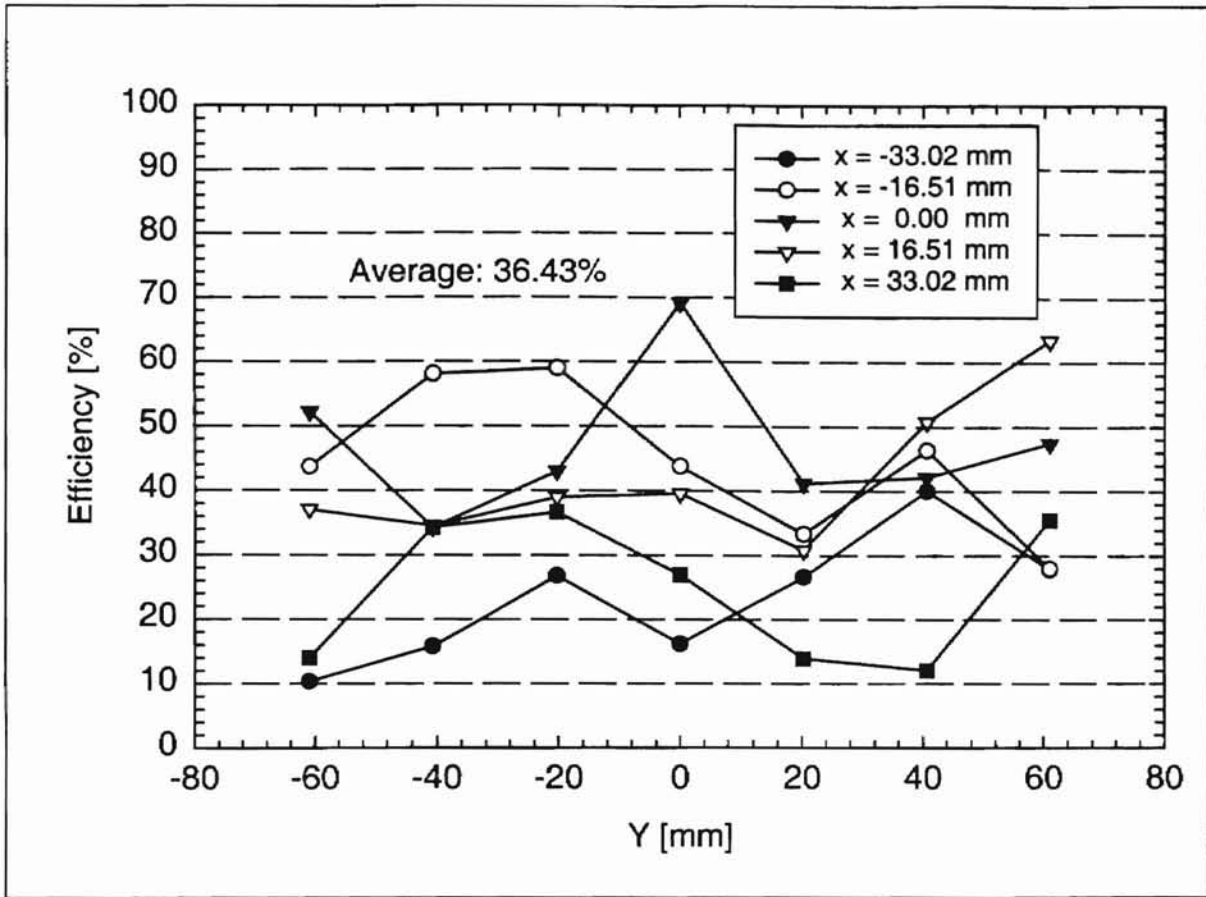


Figure 6.28 Filtration Efficiency Distribution for Test No. NESH10.4 at High Relative Humidity and an Air Flow Rate of $13.53 \text{ m}^3/\text{hr}$.

6.2.2.2 Efficiency Variation with Flow Rate and Pressure Drop

Figure 6.29 shows the variation in the overall efficiency for the model A13192 fibrous filter as a function of flow rate of the contaminant loaded air at both low and high relative humidities for electrostatically neutral PSL particles. At higher humidities, the filtration efficiency is higher than at low humidities. Thus, humidity affects filtration efficiency of fibrous filters even at high flow rates, unlike electrostatic charge, which influences filtration efficiency at low flow rates. The increase in efficiency as the flow rate increases is mainly due to the dominance of inertial impaction at high flow rates.

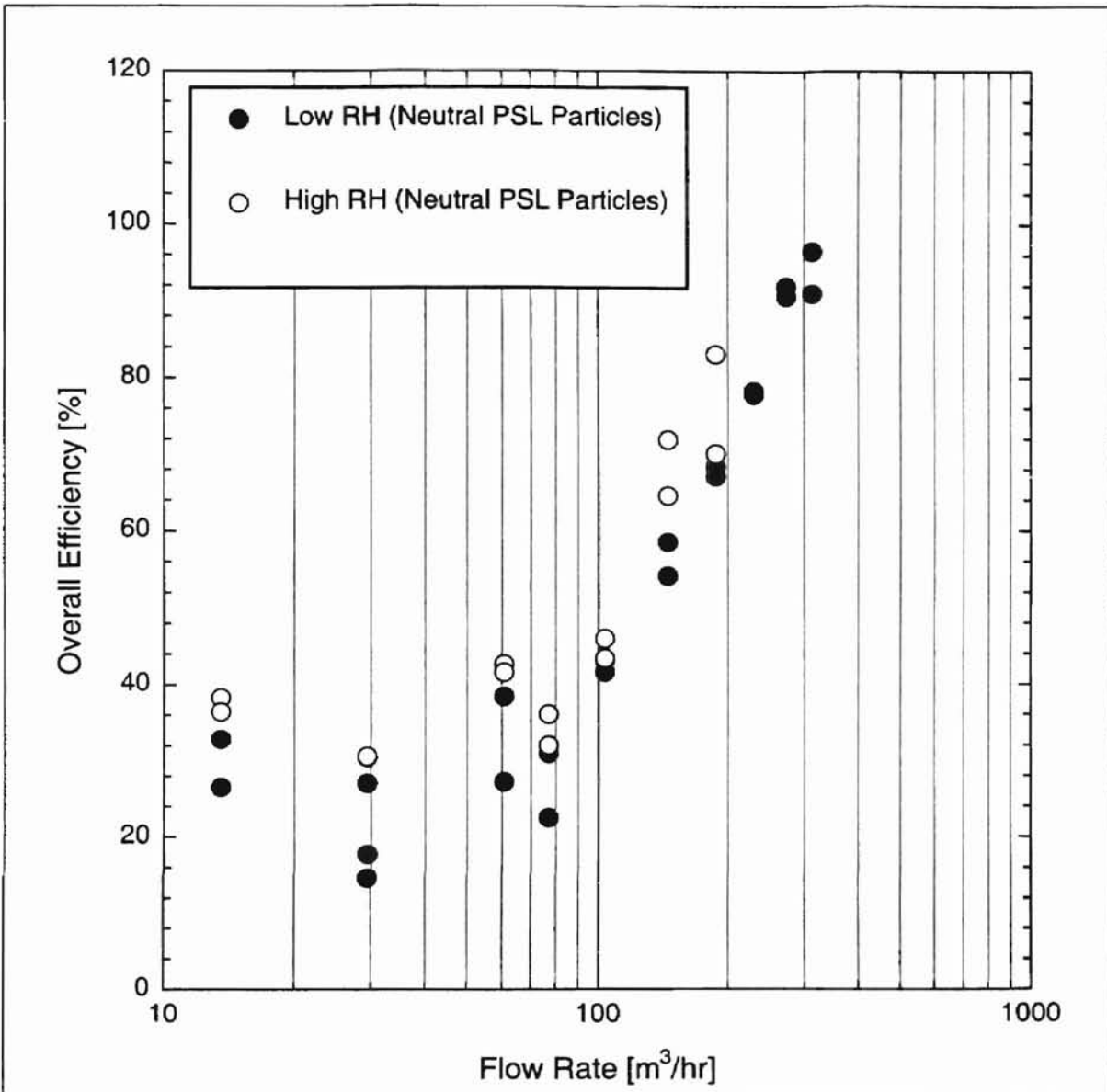


Figure 6.29 Humidity Effects on Fibrous Filtration Efficiency Using Electrostatically Neutral PSL Particles (Summer, 1998).

Figure 6.30 shows the variation of overall efficiency with pressure drop. The experimental filtration efficiencies of several A13192 Dayco-Purolator fibrous filters were plotted against their corresponding pressure drops across the filters (measured using a water-manometer). Similar to the experimental results for the electrostatic charge effects at low humidity, results for the high and low humidity tests using neutralized particles show that the initial filtration efficiency of the filter is also closely associated to

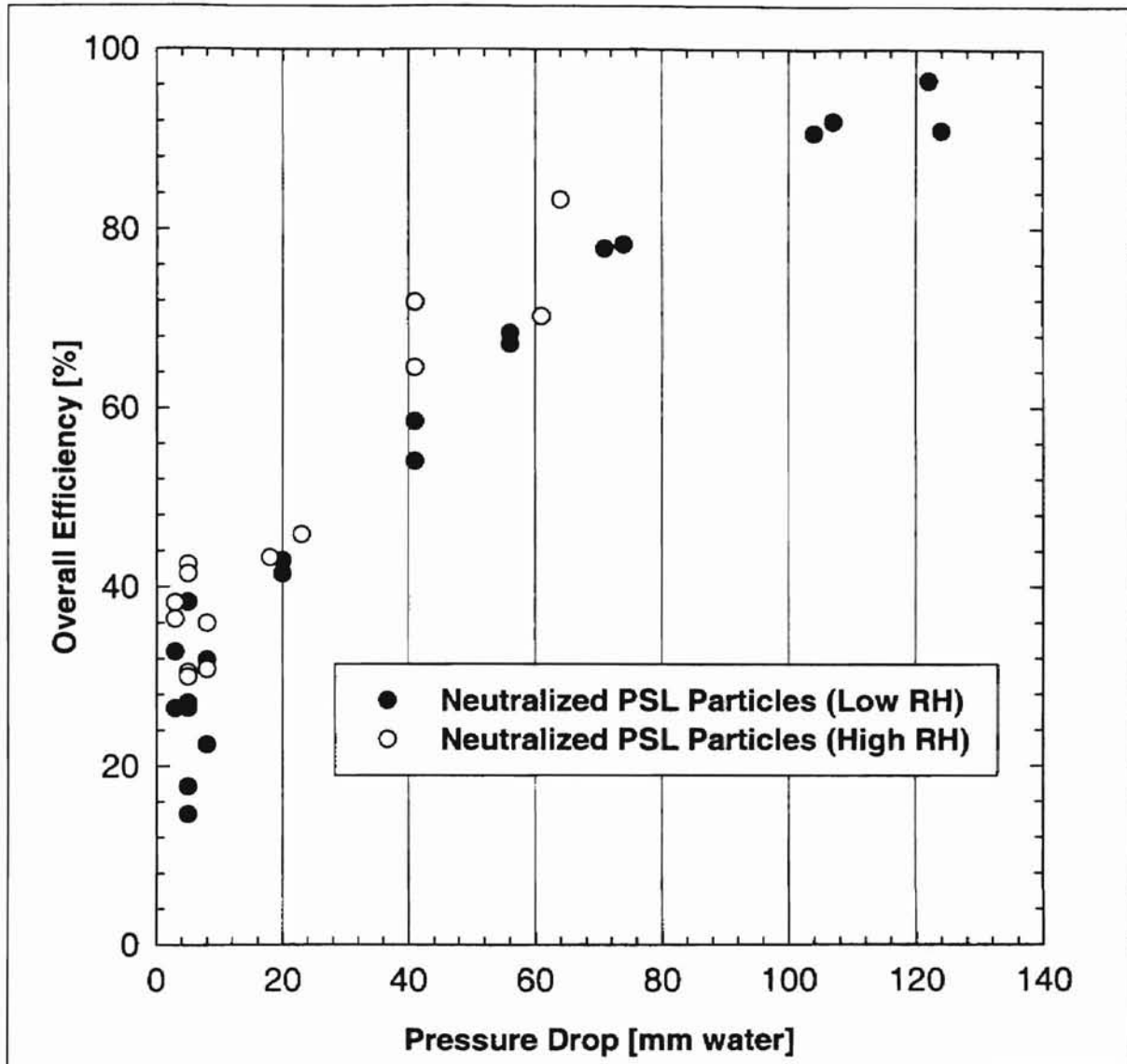


Figure 6.30 Humidity Effects on Fibrous Filtration: Filter Efficiency Variation with Pressure Drop for Electrostatically Neutral Filter and Particles.

to the initial pressure drop across the filter. Thus high initial pressure drop implies high initial filter efficiency, though high pressure drop across the filter is undesirable from a filter performance point-of-view. On the other hand, the pressure drop, Δp , across the filter is dependent upon the flow rate. The pressure drop also increases almost quadratically (refer to the empirical equation of Eq. (3-25) of Chapter III and Figure 4.18 of Chapter IV) with increasing flow rate.

6.3 Single Fiber Efficiency

The total single fiber efficiency for the Dayco-Purolator A13192 pleated filters is calculated from the overall filtration efficiency equation (Eq. 3.19) after rearranging it and solving for the total single fiber efficiency. The total single fiber efficiency has been defined as the efficiency of a single fiber due to all possible filtration mechanisms. For all experiments that involve charged aerosol particles, the total single fiber efficiency is a cumulative effect of more than one filtration mechanism including electrostatic charge, whose effect may depend upon the flow rate of the air. However, comparison of the total single fiber efficiencies for the electrostatically neutralized versus charged aerosol (PSL) particles with neutral filters indicate that the electrostatic charge contribution to the total single fiber efficiency of the filter (calculated to three decimal places) have been found minimal (see Tables 6.2 and 6.4 or Fig. 6.33).

The single fiber efficiency of the pleated filter in this study has been calculated by modeling the pleated filter as a flat filter with a normal area equal to the unfolded filter area with a depth (height) of 30 mm. The effective solidity (packing density) of the filter has been calculated as 0.153 from previous estimates of the packing density of the filter by Jadbabaei [1997] based on Duran's [1995] estimated data. Jadbabaei's approach to modeling the pleated filter with an equivalent flat filter that has the same efficiency and unfolded area as that of the pleated filter was the basis for calculating his single fiber efficiency results for the filter. However, instead of using the 30 mm actual pleat height (thickness) of the pleated filter or other values commensurate with the packing density as the thickness of his equivalent flat filter model, he chose 700 μm (the filter paper's unfolded thickness) as the thickness of the filter model with a packing density of 0.153.

However, in modeling a pleated filter with a known filter thickness and packing density with an equivalent flat filter, the inverse relation between filter thickness and packing density needs to be strictly followed, that is, one has to bear in mind that the volume of the solid fibers remains constant. Thus, the author feels there is no consistency in his approach. It seems that there is a discrepancy between his model and its application. Duran [1995] had estimated the packing density of the unfolded filter paper as 0.345. Jadbabaei [1997] calculated the effective packing density of the model filter using the above recommended (estimated) value by establishing corresponding packing density ratios [refer to Jadbabaei, 1997].

In this study, a packing density of 0.153 and a filter thickness equal to the pleated filter's depth or pleat height of 30 mm has been used in calculating the single fiber efficiencies from the experimental overall efficiencies. In Figure 6.31, the humidity effects on the single fiber efficiency for the electrostatically neutral filters and particles are shown as a function of the Stokes number. The single fiber efficiency steadily increases with the Stokes number for air flow rates at high and low humidities. This suggests that inertial impaction plays an important role and is more responsible for the increasing filtration efficiencies of fibrous filters. At a given flow rate, filtration efficiencies are higher at high humidity than at lower humidity. This implies that high humidity enhances the adhesion of aerosol particles to the fibers of the filter. Thus under monitored humidity and temperature conditions both upstream and downstream of the filter, it may not be difficult to estimate the amount of water moisture absorbed by the filter at each constant flow rate in order to establish new adhesion models as a function of the humidity of the air flow. The procedure for calculating a single fiber efficiency from

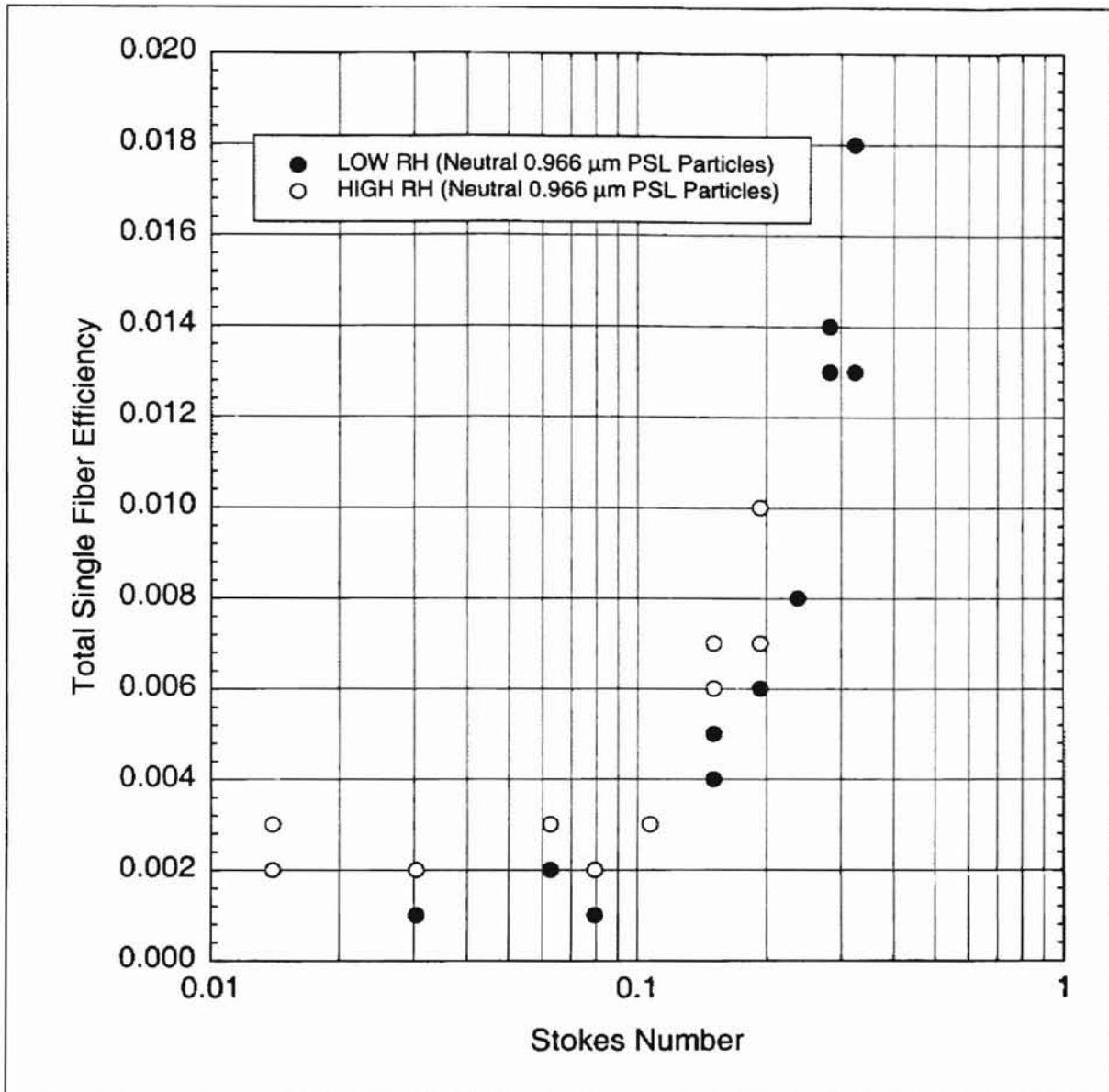


Figure 6.31 Humidity Effects: Total Single Fiber Efficiency Versus Stokes Number for Dayco-Purolator A13192 Filters Using Neutralized 0.966 μm Diameter PSL Particles.

the experimental overall efficiency is presented in Appendix K.

Figure 6.32 shows the total single efficiencies obtained from this model for the electrostatically charged particles. All of the single fiber efficiency results calculated from the present study are lower than Jadbabaei's results by more than a factor of 10.

This is mainly due to the difference in modeling the Dayco-Purolator A13192 pleated automotive air filters.

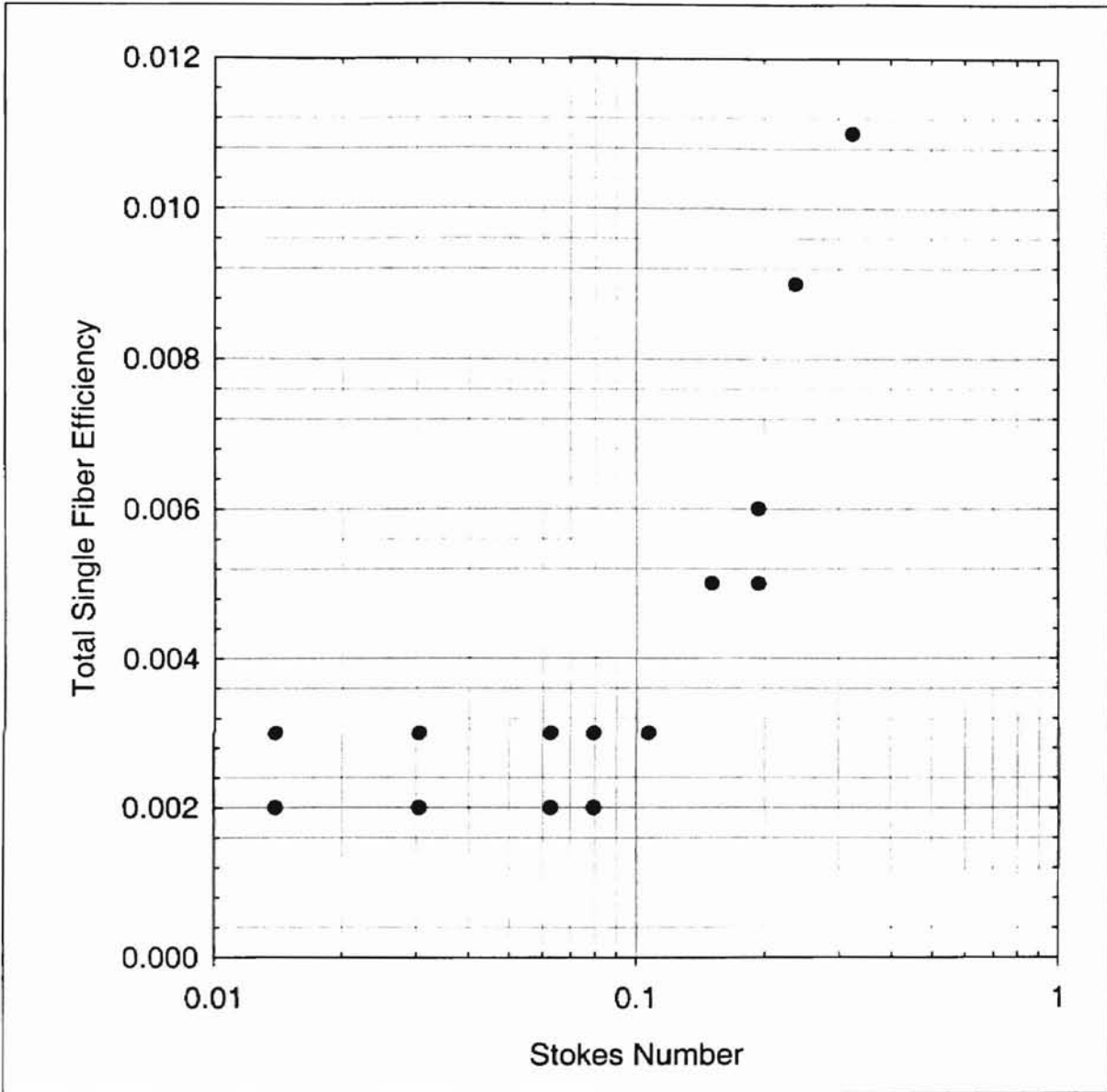


Figure 6.32 Total Single Fiber Efficiency for Dayco-Purolator A13192 Filters Using Electrostatically Charged 0.966 μm Diameter PSL Particles in the Small Angle Diffuser Housing at Low Humidity.

Figure 6.33 shows the comparative results for the total single fiber efficiencies for both the electrostatic charge and humidity effects. The differences in the single fiber

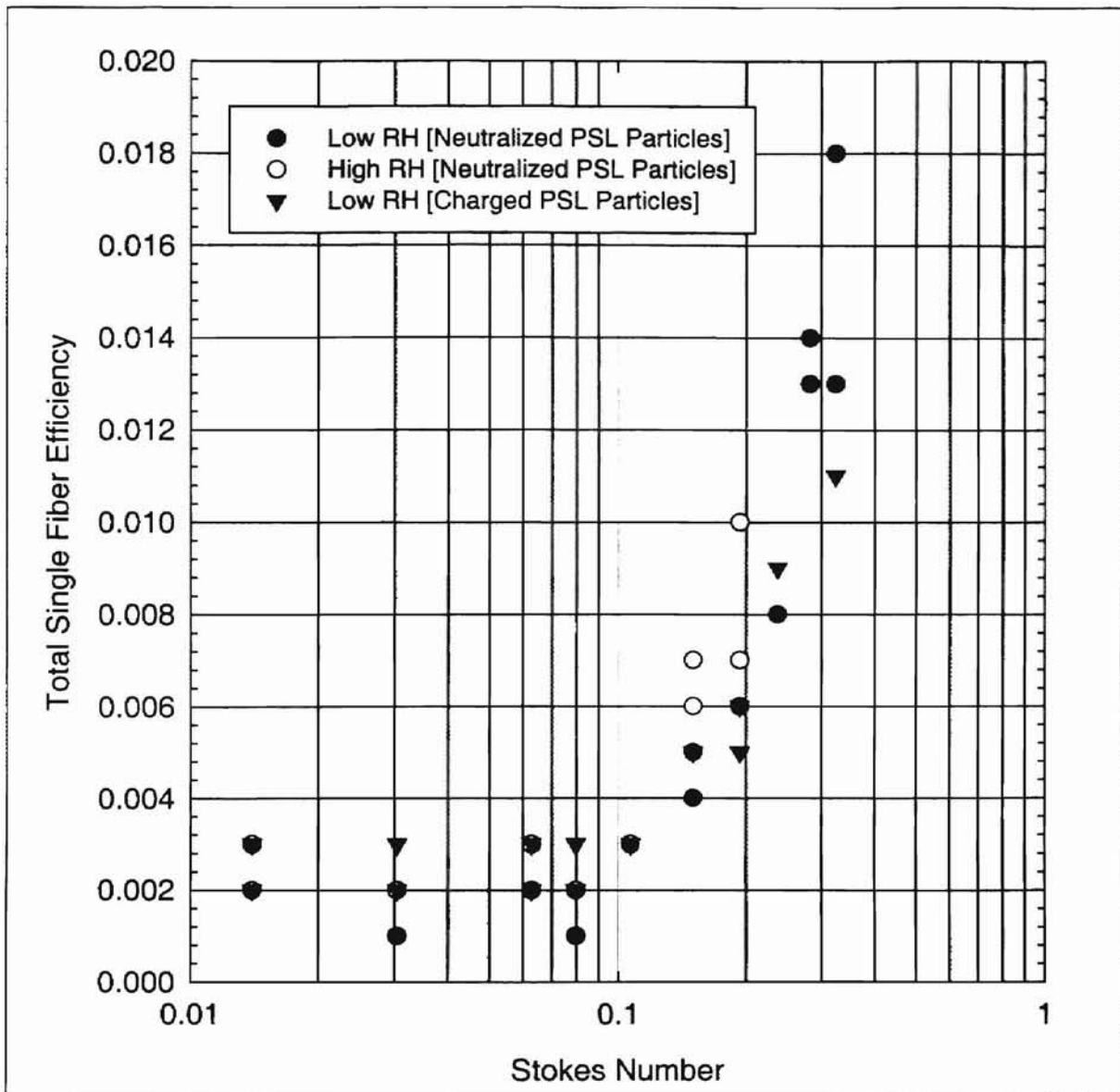


Figure 6.33 Single Fiber Efficiencies Versus Stokes Number for Charged and Neutralized 0.966 μm Diameter PSL Particles at Different RH for the Dayco-Purolator A13192 Filter (Small Angle Diffuser Housing).

efficiencies for both the electrostatically charged and neutral PSL particles at low air flow rates and low relative humidity are not discernible in the plot up to three decimal places.

However, the single total fiber efficiency for each of the air flow rates at high humidity is much higher than the total single fiber efficiency of the pleated filter with charged and neutral PSL particles and air flow rates at low humidity.

6.4 Comparison of Results

In this section, a comparison of the overall filtration efficiency results of Sections 6.1 and 6.2 will be done using theoretical perfect adhesion models of Duran [1995] and previous experimental results from Jadbabaei [1997] here at the School of Mechanical and Aerospace Engineering.

6.4.1 Comparison with Theoretical Results

The variation of the efficiencies of the pleated fibrous filters for the electrostatic and humidity effects as a function of Stokes number is shown in Fig. 6.34. The comparison of the experimental results of the present study with the theoretical model based on perfect adhesion [Duran, 1995] show that the efficiencies for both the electrostatic and humidity effects are underestimated for lower flow rates while the model overpredicts the results for higher flow rates. At a particular flow rate (Stokes number), the overall efficiency of the pleated filter at high humidity is higher than the overall efficiency of the same filter at the same flow rate (Stokes number) at low humidity. The overall efficiency for high air flow rate (Stokes number) measured at high humidity tends to approach the theoretical model closer than the overall efficiency results for charged particles at low humidity. Since most theoretical filtration efficiency models are based on two-dimensional flow analyses, they generally underpredict or overpredict the experimental results by making many simplifying assumptions.

Duran's [1995] theoretical model does not take account of electrostatic charge effects. His model mainly deals with the investigation of the most important filtration mechanisms namely, interception and inertial impaction.

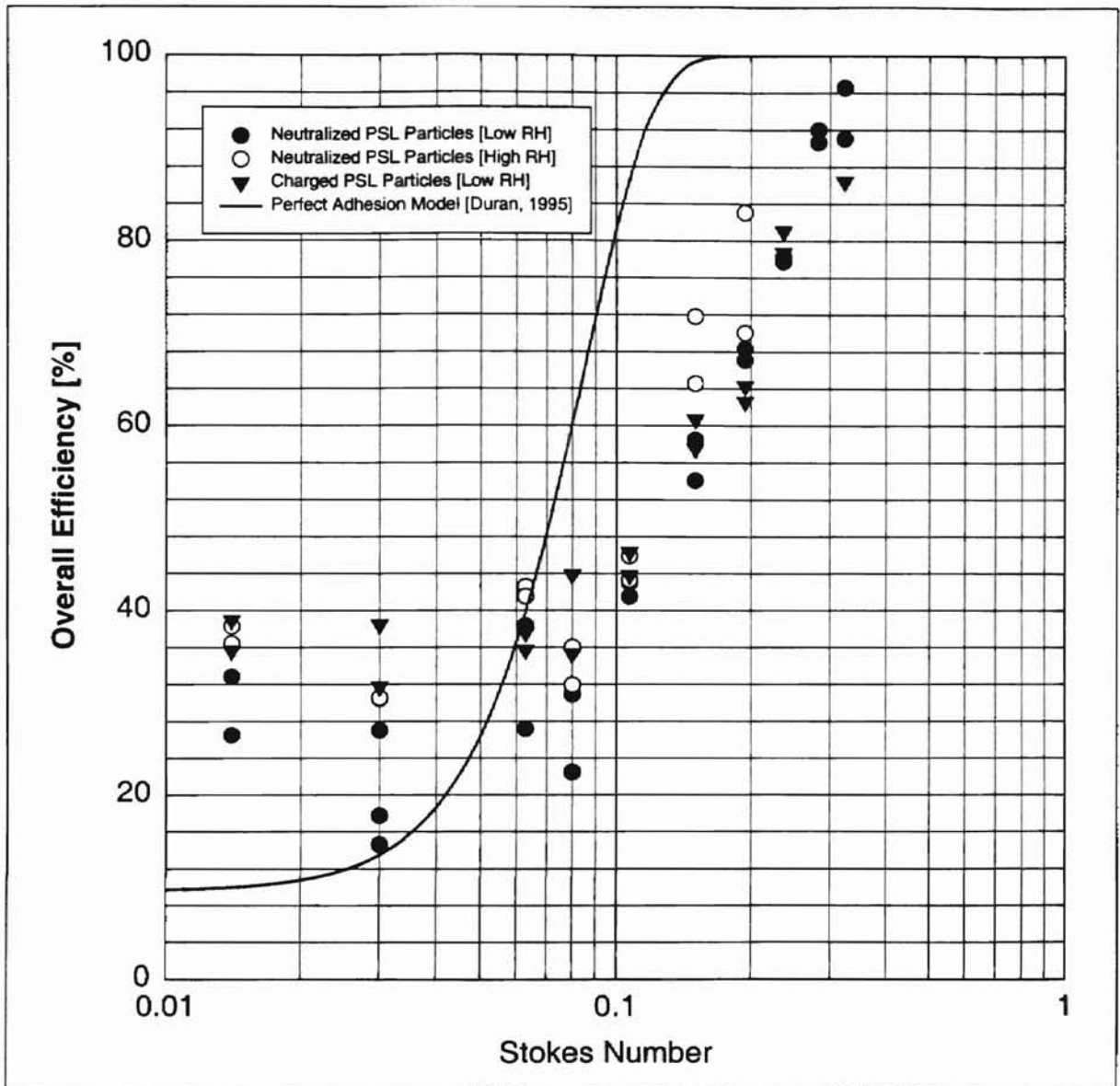


Figure 6.34 Comparison of Experimental Results of Present Study (Humidity and Electrostatic Charge Effects) with a Theoretical Model Based on Perfect Adhesion Theory [Duran, 1995] for Interception Parameter = 0.018, Fiber Diameter = 51.7 μm , and Packing Density = 0.23.

On the other hand, Fig. 6.35 shows the overall filtration efficiency variation as a function of the air flow rate through the filter. The overall efficiency versus air flow plot follows trends similar to that of the variation of overall efficiency with Stokes number, for Stokes number itself is a function of the air flow rate. Thus, the overall efficiency of

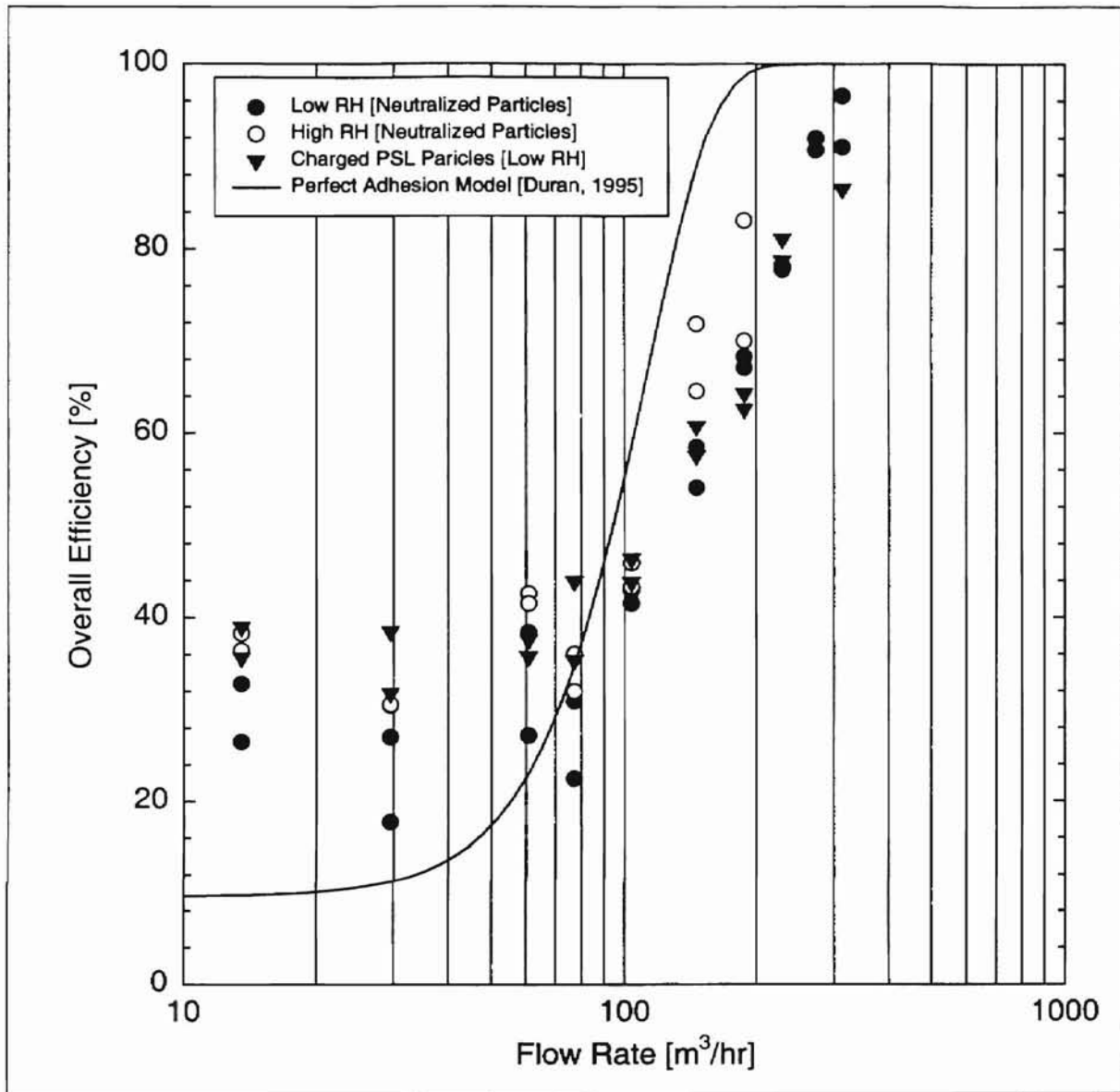


Figure 6.35 Comparison of Experimental Filtration Efficiency Results with a Theoretical Model Based on Perfect Adhesion [Duran, 1995] for $0.966 \mu\text{m}$ Diameter Particles and A13192 Filter with Interception Parameter = 0.018, Fiber Diameter = $51.7 \mu\text{m}$, and Packing Density = 0.23].

the A13192 filter depends upon the humidity, electrostatic charge and flow rate of air (face velocity). However, filtration efficiency by impaction (inertial effect) remains the most dominant filtration mechanism, while high humidity still plays a significant role in enhancing the filtration efficiency of filters more than electrostatic charge effects.

6.4.2 Comparison with Previous Experimental Studies

Jadbabaei [1997] performed filtration measurements on the same Dayco-Purolator A13192 automotive fibrous air filters, using $0.966 \mu\text{m}$ particles without neutralizing the PSL particles or controlling (monitoring) the humidity of the air inside the duct. Thus Fig. 6.36 shows the plot of the present experimental study and Jadbabaei's [1997] result.

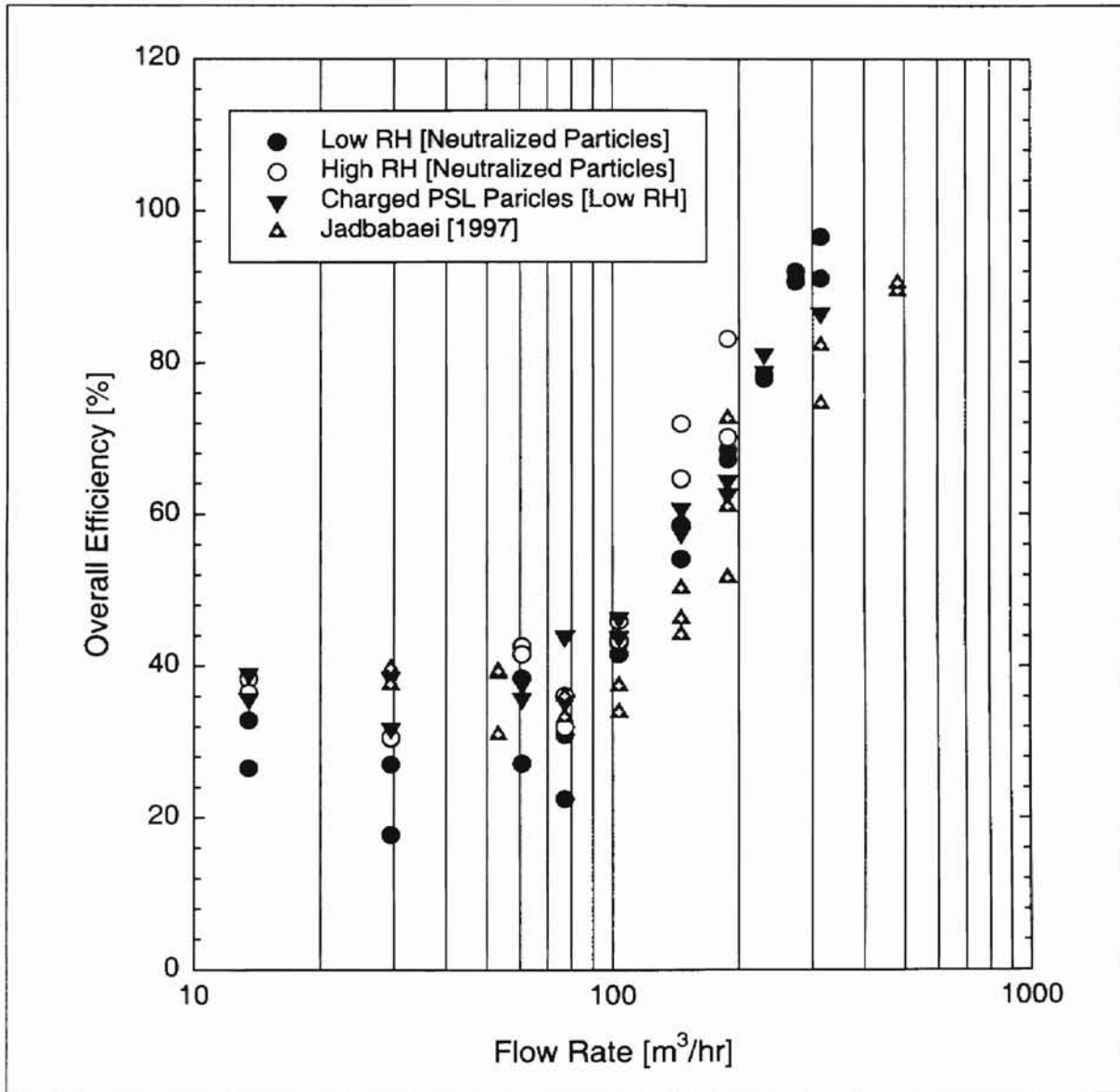


Figure 6.36 Comparison of Filtration Efficiencies for the Model A13192 Filter Using $0.966 \mu\text{m}$ Charged and Neutral Particles at High and Low Air Humidities with Jadbabaei's [1997] Results.

The efficiency of the filter in this study at higher flow rates is much higher than that of Jadbabaei's. A close investigation of the previous results of Jadbabaei and the present study for higher flow rates shows that the average velocities of the particles and pressure drops across the filter in this study were both much higher than Jadbabaei's. However, except for some points, most of the experimental results tend to follow the theoretical "S" shaped curve. The high filtration efficiency results in the present study suggest that there might have been possible leakage in Jadbabaei's experimental setup, specifically in the old filter housing (later replaced by a new one). Leakage can give rise to low pressure drop across the filter and low average velocities of the air and particles, yielding low filtration efficiency. To exclude or avoid any error in the air flow rate that may give rise to variations in efficiency due to variations in number density and velocity distribution, the TSI flow meter sensor was cleaned using alcohol and ether prior to the filtration experiments. The temperature of the air before/after the TSI flow meter sensor was also monitored as per the recommendation of Jadbabaei [1997]. The calibrations of the TSI flow meter by other authors in 1996 and later by Jadbabaei [1997] were also found consistent.

Thus, at a laboratory level, one can infer from this study that high humidity enhances the efficiency of fibrous filters more than the effect of the electrostatic charge carried by the moderately charged spherical polystyrene latex (PSL) particles at lower concentrations. However, this electrostatic charge (generated during the atomization of suspensions of the PSL particles or the triboelectric effects of the PSL particles as they flow through the filter and filter housing) at a low humidity influences the efficiency of fibrous filters at very low air flow rates.

CHAPTER VII

SUMMARY, CONCLUSIONS AND RECOMMENDATIONS

In this chapter the summary and conclusions from the present study as well as recommendations for future work are presented.

7.1 Summary

The summary of the experimental work on the stability of the Laser Doppler Anemometry (LDA) system, number density measurement, electrostatic charge and humidity are outlined in this section using the small angle diffuser housing of Fig. 4.13.

7.1.1 The Stability of the LDA System

- Extensive work on the stability of the Laser Doppler system has shown that the stability of the laser power is dependent upon the temperature of the room, and mainly upon temperature variations around the laser tube-fiber drive setup (especially the couplers, breadboard and supporting table). Induced vibration by the blower and air currents around the fiber drive unit do not appear to show any significant effects on the stability of the laser power.
- Provided that the cooling water temperature and pressure remain within

the safe operating ranges of the LDA system as recommended by the supplier [Aerometrics, 1992], the temperature of the incoming cooling water to the laser tube and humidity variations of the air around the laser system or the room in general do not affect the stability of the laser power [refer to Chapters IV and V].

7.1.2 Number Density Measurements

1. The most important parameters that affect number density are the number of samples, the sampling (sample collection) time, the average velocity of the particles and the cross-sectional area of the probe volume (perpendicular to the direction of air flow). All are related by Eq. (4-1) of Chapter IV.

- a. Average Velocity of Particles

- At any grid location, experimental results show that the variation in the average velocity of the particles with time as measured by the LDA data acquisition system (due to changes in temperature or the subsequent laser power variation) is insignificant. Hence the change in number density due to variation in the average velocity with time is negligible for a given grid point and air flow rate.
- For all of the electrostatic and humidity effect results for the small angle diffuser housing, the velocity distribution upstream of the filter has been found uniform. However, the velocity distribution downstream of the filter is not uniform, due to recirculation zones near the edges of the rubber seal.

b. Sample Collection Time

- The data collection or sampling time is the time necessary to detect the contaminant particle samples as they pass through the probe volume. This is the parameter that is most influenced by the stability of the laser power. When the laser power changes due to temperature variation at the couplers, the time necessary for collecting the particles also changes (for a previously chosen set of DSA parameters). In most cases, the sample collection time becomes longer as some weak light signals reflected from the flowing particles are rejected as noise (unwanted signals) owing to decreasing laser power (due to changes in temperature at and around the couplers). Thus high collection time implies lower number density, which can seriously affect the local efficiency measurements.

c. Cross-sectional area of probe volume

- The cross-sectional area of the probe volume perpendicular to the air flow for calculating the particle concentration (number density) is assumed to be constant. However, there are variations in the cross-sectional area of the probe volume due to temperature fluctuations, if the temperature is not stabilized within a certain acceptable range.

2. The concentration of particles (number densities) significantly depends upon the stability of the laser power, which in turn depends upon the temperature. A temperature variation of about 1°C can result in up to a 25% variation in the number density measurements at 103.7 m³/hr, which can significantly affect

the local and overall filtration efficiency measurements. This is attributed to changes in the cross-sectional area of the probe volume through which the particles pass for detection.

3. For the small angle diffuser housing, number densities upstream of the filter are more uniform than the downstream number densities. Nonuniform downstream number density distribution is connected to the nonuniform downstream velocity distribution. The nonuniformity of downstream velocity is due to the recirculation zones around the edges of the filter since the rubber seal to which the filter paper is embedded creates an abrupt area reduction on the downstream side of the filter. Otherwise, the downstream number densities for all of the electrostatic and humidity tests are more or less uniform for the central region of the filter.

7.1.3 Electrostatic Charge Generation and Voltage Measurement

Before examining the effects of electrostatic charge on the filtration efficiency of the fibrous automotive air filters, some measurements were performed on the presence, amount, polarity and time dependence of the electrostatic charge voltage of the atomized particles (contaminants) flowing through the duct and the small angle diffuser housing. The electrostatic charge voltage measurements were conducted by atomizing different diameter PSL particles, NaCl, and glass beads at different concentrations. The experimental observation and results are summarized as follows:

1. The amount (level) of electrostatic charge voltage depends upon
 - particle concentration,

- nature or type of particles,
 - size (diameter) of particles,
 - humidity and flow rate of the dispersing medium (air in this case).
2. The dependence of charge polarity upon the type of the contaminant particles:
- A solution of sodium chloride salt (NaCl) in distilled water and its atomization into preheated air to generate dry crystals (particles) produces no electrostatic charge.
 - The atomization and drying of spherical polystyrene latex (PSL) particles generates charge with negative polarity.
 - The atomization of solutions of glass beads with a size distribution (polydisperse) and various concentrations show charge with a positive polarity.
 - The flow of preheated room air at low humidity produces charge with positive polarity only at the filter. This implies that the concentration of the contaminant particles that are present in the air and the filter material determines the polarity based on the triboelectric series/order of the materials as discussed in Chapter III and Chapter V.
3. The time dependence of electrostatic voltage:
- Electrostatic voltage level measurements at both constant air flow and particle atomization rate show that the accumulation or growth of charge at different locations within the duct/filter housing in the ungrounded state is dependent upon time.

- Experiments on discharging electrostatic charge potential after stopping both the flow of preheated air and atomization of the contaminating particles by the atomizer show that there is a steady decrease of electrostatic charge voltage with time from the surfaces of the filter housing and duct. Even closer observations reveal that the rate of electrostatic charge discharge is related to the rate of increase or change in humidity inside the duct/filter housing. Thus when the relative humidity inside the housing remains constant, then the electrostatic charge voltage tends to remain constant for some time. According to studies (see literature review) made on the electrical conductivity of materials, it is possible that high humidity inside the room around the external surface of the plexiglass housing also plays a significant role in the discharging process of the surface charge.

4. Neutralizing/minimizing electrostatic charge:

- To investigate electrostatic charge effects on the efficiency of the Dayco-Purolator A13192 automotive air filters, neutralization of the atomized and dry particles is essential. Hence measurement of electrostatic charge voltage using an electrostatic field meter for each flow rate shows that covering the upper half of the filter housing with aluminum foil and its subsequent grounding, together with a metallic filter support, fixtures and structure, appears to effectively discharge triboelectric potential. However, firm contact between the aluminum foil and the surface of the filter housing is needed in order to enhance the effective neutralization of the charge. Electrostatic charge voltage readings for most of the experiments have been zero at the filter. However, in

some cases, there have been rare electrostatic charge voltage measurements not exceeding 50 v for an intermediate flow rate at a low humidity, for which the corresponding electrostatic charge voltage could have been 750 v in the ungrounded state.

7.1.4 Humidity Measurements

Prior to the measurement of humidity effects on the efficiency of the filter, consistency measurements on the variation of humidity and temperature of the air that flows through the duct and filter housing have been performed and closely monitored at different locations both upstream and downstream of the filter.

1. At any location along the duct and filter housing (assuming a constant heat supply), humidity and temperature vary with flow rate. As the flow rate increases, the humidity and temperature approach that of room conditions. The lowest humidity is recorded in the intermediate flow rate region between 30 and 103 m³/hr, where the temperature reaches its peak value.
2. Humidity and temperature variations with time at constant flow rates show that the time taken to reach steady-state conditions (humidity and temperature) at low flow rates (less than 30 m³/hr) is much longer than that at intermediate and high flow rates (greater than 77.1 m³/hr). Experiments on the temperature and humidity measurements upstream and downstream of the filter at low flow rates show that it takes between 1 and 2 hours to reach steady-state conditions.
3. By calculating and establishing absolute humidity variation with time (following the definitions and procedures of Appendices F and G) from the

experimental time dependent relative humidity measurements of the air upstream and downstream of the filter, it is possible to estimate the moisture carried by the air before and after it enters the filter using numerical integration techniques. Thus in order to estimate the amount of moisture absorbed by the filter under special conditions, one has to use the mass balance of the moisture from the knowledge of the upstream and downstream moisture content of the air (see Subsections 5.3.4 and 5.3.5 of Chapter V).

4. A fibrous air filter can be modeled as a medium constantly exchanging moisture with the air flowing through it. This modeling can help to understand the adhesion of particles in fibrous air filtration and the development of new adhesion models or corroborate existing models.

7.2 Conclusions

After establishing the necessary conditions (consistency measurements related to LDA instrumentation, humidity and electrostatic voltage levels at different flow rates) and devising methods to minimize electrostatic charge at the filter, the experimental investigation of the electrostatic charge and humidity effects was carried out. Both the effects of electrostatic charge and humidity on the efficiency of fibrous filters for the 0.966 μm PSL particles were carried out as parallel and independent studies by controlling or monitoring each parameter in the duct (relative humidity of air, electrostatic charge voltage, air flow rate, etc.).

From the filtration efficiency measurements in this study, the following conclusions can be drawn:

1. The effect of electrostatic charge on the efficiency of fibrous filters in this study has been found to be very minimal; and this effect is confined only to low flow rates (less than $77.1 \text{ m}^3/\text{hr}$), when compared to efficiencies measured using the electrostatically neutralized PSL particles in the air flow at low humidity (less than 50% relative humidity). For a given flow rate at low humidity, there is no such a significant (marked) difference in the efficiencies of a fibrous filter using electrostatically charged versus neutralized PSL particles. Thus, one can infer that electrostatic charge effects on the efficiency of the fibrous filters tend to vanish as the flow rate increases. In the literature, it is believed that at high flow rates, the electrostatic, diffusive, and interception mechanisms of filtration diminish and the inertial impact dominates.
2. A comparison of the efficiencies of the Dayco-Purolator A13192 fibrous air filter at high and low humidities in the absence of electrostatic charge shows that the efficiencies of the fibrous filters are higher at high humidity than at low humidity. Thus adhesion of particles appears to be enhanced by humidity.
3. Comparison of the efficiencies between the effects of humidity and electrostatic charge at a given flow rate shows that the filter has the highest efficiency at high humidity of all the efficiencies measured in the presence and absence of electrostatic charge at low humidity.
4. From the experimental results for filtration efficiency at high and low humidities, one can conclude that humidity affects filtration efficiency independent of the flow rate/Stokes number, while the electrostatic charge

effect is limited to the low flow rate region (less than $77.1 \text{ m}^3/\text{hr}$ with a corresponding average face velocity of 0.932 m/s). However, at extremely high flow rates (greater than $313.8 \text{ m}^3/\text{hr}$) with filter face velocity much higher than 3.793 m/s , high humidity may not always enhance efficiency by favoring adhesion. It is possible that, under extreme conditions, entrainment effects may be enhanced by excessive water moisture that may be formed at the junction of the filter fibers to reduce the adhesion probability of the particles.

5. Previous research work here in the School of Mechanical and Aerospace Engineering shows that the efficiency of fibrous filters suffered a lot of inconsistencies at low flow rates. From this study, one can have a glimpse of some of the main factors responsible for these inconsistencies. The most dominant factor has been high and uncontrolled humidity in the whole flow rate region. However, electrostatic charge effects at low humidity (low flow rate region) still may not be neglected. The selection of unoptimized particle concentrations (greater or equal to 10 ml suspension at 10% solids of $0.966 \mu\text{m}$ PSL particles per 1000 ml solution) that can affect the visibility (detection) of the particles by the LDA system can also be sited as an additional factor that can give rise to erroneous or inconsistent efficiency results.
6. Under special and controlled conditions, it is possible to estimate the amount of water absorbed by a filter by numerical integration techniques from the knowledge of air condition (humidity and temperature data as function of time) upstream and downstream of the filter. This procedure can help assess particle adhesion models in fibrous air filtration processes as a function of humidity.

7. Variation in the efficiency of the filter at low flow rates ((less than $77.1 \text{ m}^3/\text{hr}$) or face velocities less than 0.932 m/s) is very sensitive to changes in number densities upstream and downstream of the filter. Thus errors in the efficiency measurement of the filters is higher at low flow rates than at high flow rates.
8. Jadbabaei's [1997] experimental results show lower efficiency values in the high flow rate region as compared to the results of the present study at a given flow rate. This marked difference (variation) in the efficiencies is attributed to the following possible factors:
 - The initial pressure drop across the filter for most of the flow rates in this study were higher than Jadbabaei's, because the old filter housing has been replaced by a new one. Thus the filtration efficiency measurements on the old filter housing might have suffered higher leakage. Leakage causes low initial pressure drop, which in turn implies lower efficiency due to lower inertial impaction. Since filtration efficiency at high flow rates is due to inertial impaction, for a given flow rate when the pressure drop across the filter decreases due to leakage or improper sealing, the filter face velocity decreases leading to low inertial impaction.
 - The fact that laser stability tremendously affects the experimental efficiency measurement results and humidity has never been controlled or monitored by any other previous researcher are some of the possible factors. Thus, in this study, the author has introduced many measures to stabilize the laser power after long experimental work, as indicated in the consistency measurements of this thesis work.

7.3 Recommendations for Future Work

The author would like to suggest the following recommendations for future work in fibrous filtration efficiency measurements in general, and for electrostatic charge and humidity effects on filtration efficiency in particular.

1. In fibrous filtration, since charge neutralization is an important task, it is advisable to study the present charge neutralization/discharging mechanism and setup further. In addition to using aluminum foil covering, installing grounded conducting ducts upstream of the filter before and after the mixing box (mounted at the top end of the upper part of the diffuser housing) may easily help reduce the electrostatic charge of the particles as they flow past the experimental set up.
2. Monitoring the electrostatic charge discharging mechanism may be made possible by installing a circuit to measure the current or voltage during the discharging process of the mixing box or the surface of the aluminum-covered small angle diffuser housing.
3. To do more studies on the effect of electrostatic charge on filtration, it is advisable to use a high voltage air ionizer to charge or increase the electrostatic charge of the already electrostatically charged PSL particles by exposing them further to unipolar ions. Figure 7.1 shows a schematic drawing of a high voltage ionizer, which may be used for this purpose.
4. In this study, the overall effects of humidity on the efficiency of filters have been found to be highly important in enhancing the efficiency of filters. Hence it is important that the humidity of the inlet air before reaching the filter be controlled and monitored so that the repeatability or consistency of the experimental results are guaranteed.

5. It is important that the particle concentration for low flow rates (less than $77.1 \text{ m}^3/\text{hr}$) be reduced to an optimum value (from 10 ml to 5 ml or less of PSL particle suspensions at 10% solids by weight to prepare one liter of solution) by establishing more experimental results. It may also be advisable to increase the solution or particle concentration for those high flow rates (above $230 \text{ m}^3/\text{hr}$). At high flow rates due to low particle concentration, the run time or sample collection time has been found to exceed 200 seconds for measurements down stream of the filter. At this particle counting rate, filter plugging may result in nonuniform (unsymmetric with respect to the centerline of the filter) local filtration efficiency measurements of the filter, which can lead to erroneous conclusions about the performance A13192 fibrous air filters.
6. To avoid incorrect and inconsistent air flow measurements by the TSI flow meter due to temperature changes in the room and dust deposits at the sensor of the TSI flow meter, it is important to install a manometer at the Venturi meter ahead of the flow meter. Thus by calibrating the manometer it would be easy to tell and verify how accurately the TSI flow meter is measuring the flow rate. A thermometer may also be installed to monitor the temperature of the air ahead of the TSI flow meter sensor. The TSI flow meter sensor may need to be regularly cleaned and calibrated once a year depending upon the operation hours.
7. During the experiment, the author was able to observe some grouping and regrouping of the filter pleats when the temperature and flow rate of the air exceeded $50 \text{ }^\circ\text{C}$ and $273 \text{ m}^3/\text{hr}$, respectively. Under these conditions, it seems that this can affect the local distribution of the efficiency of the filter. Thus the workable design face velocity of

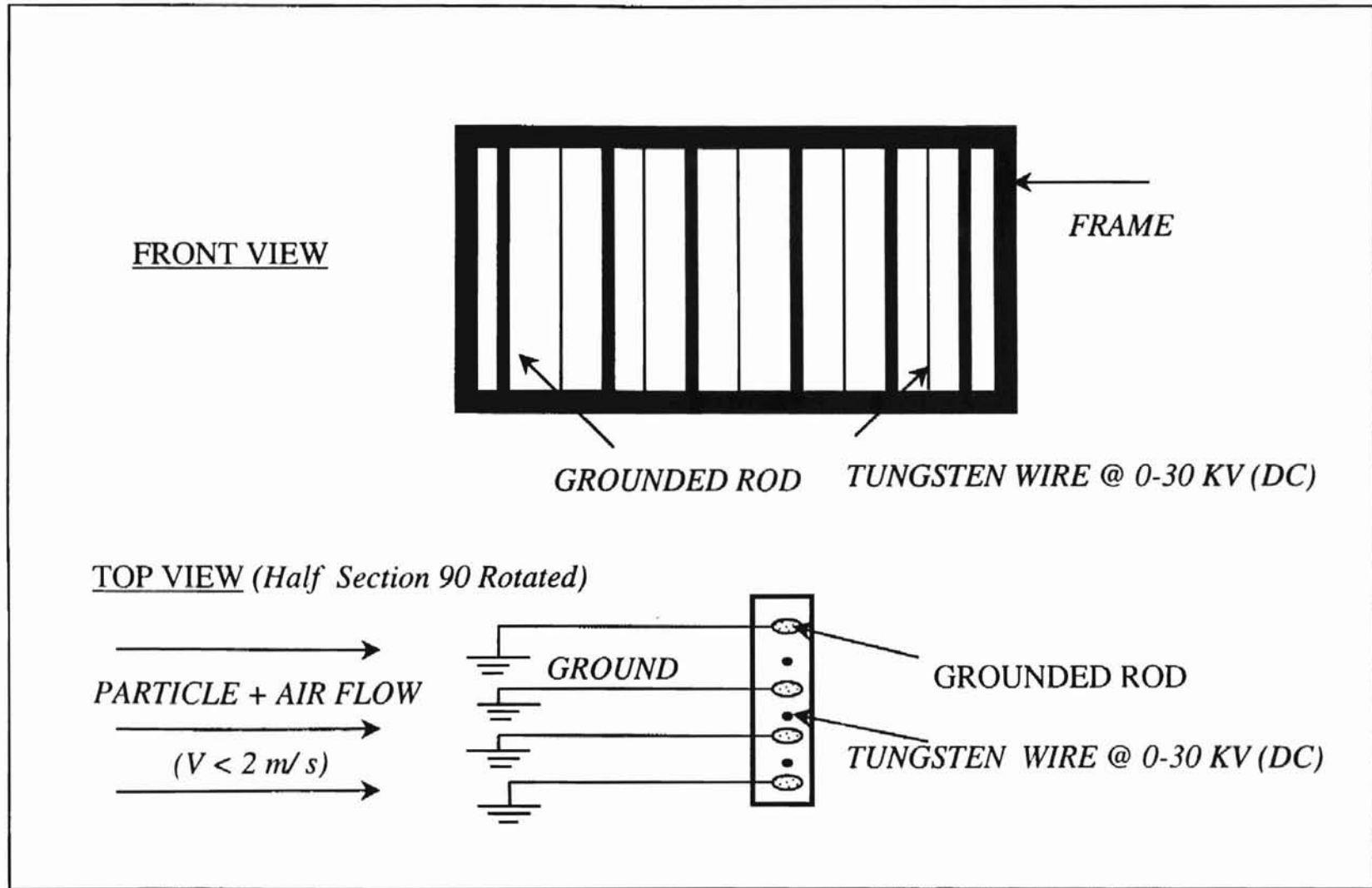


Figure 7.1 Schematic Drawing of an Electrostatic Charger/Ionizer.

the filter should not exceed 3.307 m/s at 273 m³/hr of air flow rate and temperature above 50 °C. It was also observed that this irregular regrouping (elastic structural deformation) of the filter pleats was eliminated a few hours later, provided that the filter was subjected to room conditions or by stopping the preheated air flow through the filter inside the filter housing.

8. Leakage in the filter housing could arise due to cracks and improper clamping (sealing) of the flanges of the upper and lower parts of the filter housing, and filter positioning and alignment inside the filter housing. To overcome leakage problems in addition to soap test by pressurizing the filter housing, it is advisable to establish a pressure drop versus flow rate curve ahead of the actual filtration efficiency measurements [as discussed in the experimental procedures in Chapter IV]. Using this curve as a reference, the initial pressure drop measured prior to the execution of each experiment would indirectly indicate if there was/was not any leakage for that specific flow rate.
9. Eliminating or reducing the recirculation zones downstream of the filter is advisable by improving the geometry (size) of the bottom part of the housing or minimizing the rubber sealing underneath the filter that abruptly reduces the filter cross-sectional area through which the air flows. Since the air flow downstream of the filter (as it leaves the filter) produces jets of air at high velocity (compared to upstream velocity), it may be important to investigate this jet effects on the velocity distribution and concentration of particles (downstream of the filter) using CFD models.

REFERENCES

- Adachi, M., Pui, D. Y. H. and Liu, B. Y. H. (1990a), "Aerosol Charge Neutralization by a Corona Ionizer," *Aerosols: Science, Industry, Health, and Environment*, Proceedings of the Third International Aerosol Conference, Kyoto, Japan, September 24–27, Vol. I, pp. 442-445.
- Adachi, M., Pui, D. Y. H., Romay, F. J., and Liu, B. Y. H. (1990b), "High Efficiency Unipolar Charger Using Alpha-ray Radioactive Source," *Aerosols: Science, Industry, Health, and Environment*, Proceedings of the Third International Aerosol Conference, Kyoto, Japan, September 24–27, Vol. I, pp. 439-441.
- Aerometrics Inc. (A Division of TSI Inc.) (1992), Doppler Signal Analyzer for Phase Doppler Particle Applications User's Manual, Sunnyvale, CA, draft 2.
- Al-Sarkhi, A., Yao, S. H. and Chambers, F. W. (1997), "Flow Distribution Dependence on Housing Geometry for Tangential Inlet Automotive Air Filter Housings," *Advances in Filtration and Separation Technology - Advancing Filtration Solutions*, Proceedings of the Annual National Technical Conference of the American Filtration and Separations Society, Minneapolis, Minnesota, April 29 – May 2, pp. 210-215.
- American Society for Testing and Materials (1989), "ASTM F 1215-89, Standard Test Method for Determining the Initial Efficiency of a Flat sheet Filter Medium in an Air Flow Using Latex Spheres," Annual Book of ASTM Standards, Vol. 14.02.
- Anand S. (1997), "Filtration Efficiency Measurements on Pleated Filters," M. S. Thesis, School of Mechanical and Aerospace Engineering, Oklahoma State University, Stillwater, Oklahoma.
- Anand, S., Jadbabaei, F. M. and Dougherty, R. L. (1997), "Comparison of Filtration Efficiency Measurements for Pleated and Flat Sheet Filters," presented at the 1997 SAE International Congress and Exposition, SAE Technical Paper #970671, *Topics in Automotive Filtration Design (SP-1252)*, Conference of SAE Inc., February 24-27 Detroit, MI.
- Benarie, M. (1963), "Einfluss der Porenstruktur auf den Abscheidegrad in Faserfiltern," *Staub*, Vol. 29, No. 2, pp. 74-78.

Bensch, L. E. (1977), "The Influence of Electrostatic Charge on the Filtration of Hydraulic Fluids by Fibrous Filters," Ph.D. Dissertation, School of Mechanical and Aerospace Engineering, Oklahoma State University, Stillwater, Oklahoma.

Bouguila, N. Coelho, R. and Navarre, D. (1993), "Electrostatic Painting of Insulating Surfaces," *IEE Transactions on Industry Applications*, Vol. 29, No. 4, July/August.

Brown, R. C. (1993), Air Filtration: An Integrated Approach to the Theory and Applications of Fibrous Filters, Pergamon Press, Oxford, England.

Bugli, N. J. (1997), "Filter Performance Requirements for Engine Air Induction Systems," SAE Technical Paper #970556, *Topics in Automotive Filtration Design (SP-1252)* SAE, Inc., Warrendale, PA.

Chapman Catalog (1997), Static Elimination Systems, Portland, Maine, USA.

Chen, D. R., Pui, D. Y. H. and Tang, Y. M. (1996), "Filter Pleating Design for Cabin Air Filtration," SAE Technical Paper #960941, *Aspects of Automotive Filtration (SP-1165)*, Conference SAE Inc., Warrendale, PA.

Chen, Y. K. and Yu, C. P. (1993), "Particle Deposition from Duct Flows by Combined Mechanisms," *Aerosol Science and Technology*, Vol. 19, pp. 389 - 395.

Chubb, J. N. (1993), "Calibration of Instruments for Electrostatic Measurements," Presented at the IEE Colloquium, *Computing and Control Division Colloquium on Significance of Calibration*, February 23, London, England.

Crawford, M. (1976), Air Pollution Control Theory, McGraw Hill, New York, N. Y.

Davies, C. N. (1952), "The Separation of Airborne Dust and Particles," *Proceedings of The Institute of Mechanical Engineers (Part B)*, Vol. 1b, pp. 185 - 213.

Davies, C. N. (1966), Aerosol Science, Academic Press, New York, N. Y.

Davies, C. N. (1973), Air Filtration, Academic Press, New York, N. Y.

Davies, W. T. (1994), "Air Filtration Efficiency Testing," *TAPPI Journal*, Vol. 77, Part 1, Feb. 94, pp. 221-226.

Dickey, G. D. (1961), Filtration, Reinhold Publishing Corp., New York, N. Y.

Drain, L. E. (1980), The Laser Doppler Technique, John Willey & Sons, New York, N. Y.

Duran, R. (1995), "Improvement of Flow Uniformity and Modeling of Filtration Efficiencies for Automotive Air Filter Test Housings," M.S. Thesis, School of Mechanical and Aerospace Engineering, Oklahoma State University, Stillwater, Oklahoma.

Durkin, W. J. (1993), "Electrostatic Measurements on Plastic Webs," presented at the Industrial Applications Society Annual Meeting, Oct. 2-8, Vol. 3, pp. 1728 – 1736.

Electro-tech Systems, Inc. Catalog (1996), Electrostatic Elimination, Testing Laboratory and Environmental Control, Glenside, PA, USA.

Electro-tech Systems, Inc. (1998) User's Guide Static Meter 210, Glenside, PA, USA.

Fodor, J. (1979), "Improving Utilization of Potential I. C. Engine Life by Filtration," **Tribology International**, Vol. 12, pp. 127-129.

Fodor, J. (1982), "Improving the Economy of I. C. Engines by Controlling the Contaminants Through Filtration," *World Filtration Congress III*, pp. 707-711.

Frederick, E. R. (1996), Utilizing Electrical Effect in Nonaqueous Filtration, Filter Media Specification, Pittsburgh, PA.

Friedlander, S. K. (1958), "Theory of Aerosol Filtration," **Industrial Engineering Chemistry**, Vol. 50, pp. 1161-1164.

Fuchs, N. A. (1964), The Mechanics of Aerosols, Pergamon Press, Oxford, England.

Gerald, C. F. and Wheatley, P. O. (1994), Applied Numerical Analysis, Addison Wesley, New York, N. Y.

Gibson, N. (1971), "Static in Liquids," *Static Electrification*, Proceedings of the third Conference on Static Electrification, Organized by Static Electrification Group of the Institute of Physics, London, England, May, Series No. 11, pp. 71-83.

Gillespie, T. (1955), "The Role of Electric Forces in the Filtration of Aerosols by Fiber Filters," **Journal of Colloid Science**, Vol. 10, pp. 299-314.

Greenkorn, R. A. (1983), Flow Phenomena in Porous Media: Fundamentals and Applications in Petroleum, Water, and Food Production, Marcel Dekker, Inc., New York and Basel.

Gustavsson, J. (1996), "Cabin Air Filters: Performances and Requirements," SAE Technical Paper #960941, *Aspects of Automotive Filtration (SP-1165)*, SAE Inc., Warrendale, PA.

Hamaker, H. C., (1937), "The Van Der Waals Attraction between Spherical Particles," **Physica**, Vol. 4, pp. 1058+.

Harrop, J. A. (1969), "The Effect of Fiber Configuration on the Efficiency of Aerosol Filtration," Ph.D. Thesis, Loughborough University of Technology, Loughborough, England.

Henry, P. S. H. (1971), "Risks of Ignition Due to Static on Outer Clothing," *Static Electrification*, Proceedings of the Third Conference on Static Electrification, Organized by Static Electrification Group of the Institute of Physics, London, England, May, Series No. 11, pp. 71-83.

Hinds, W. C. (1982), Aerosol Technology: Properties, Behavior and Measurement of Airborne Particles, John Wiley & Sons Inc, New York, N. Y.

Hsieh, Ker-Ching, Wu, T., Connors, P., and Tang, Y. M. (1996), "Performance Enhanced Electret Media," SAE Technical Paper #960534, *Aspects of Automotive Filtration (SP-1165)*, SAE, Inc., Warrendale, PA.

Igwe, G. J. I. (1987), Needle Felts in Gas and Dust Filtration: Design of Mechanically-bonded Filters, John Wiley & Sons, New York, N. Y.

Jadbabaei, F. M. (1997), "Filtration Efficiency Measurements on Pleated Filters," M.S. Thesis, School of Mechanical and Aerospace Engineering, Oklahoma State University, Stillwater, Oklahoma.

Jaroszcyk, T. (1987), "Experimental Study of Nonwoven Filter Performance Using Second Order Orthogonal Design," **Particulate Science and Technology**, Vol. 5, No. 3, pp. 271-287.

Jaroszcyk, T. and Wake, J. (1991), "Critical Aerosol Velocity in Nonwoven Filtration," *TAPPI Proceedings*, Nonwoven Conference, pp. 125-135.

Jaroszcyk, T., Ptak, T. J., Fallon, S. L. and Wake, J. (1993a), "Particulate and Odor Control Systems in Car Ventilation Systems," SAE Technical Paper #930014, SAE, Inc., Warrendale, PA.

Jaroszcyk, T., Wake, J. and Connor, M. J. (1993b), "Factors Affecting the Performance of Engine Air Filters," American Society of Mechanical Engineers, *Energy Sources Technology* Conference and Exhibition, Houston, Texas.

Jaroszcyk, T., Ptak, T. J. and Wake, J. (1994), "An Experimental Evaluation of the Factors Influencing the Performance of Car Interior Air Filters," SAE #940321, International Congress and Exposition, Detroit, MI.

Kalatoor, S., Legare, P. and Smith, S. (1997), "Filtration Efficiency of Automotive Cabin Air Filter Media Subjected to Different Aerosols Under Various Environmental Conditions," SAE Technical Paper #970669, *Topics in Automotive Filtration Design (SP-1252)*, SAE, Inc., Warrendale, PA.

Khan, A. M. (1990), "Offset Screen and Pseudo-Diffusion Models for Prediction of Filtration Phenomena in Real Fibrous Filter Media," Ph.D. Dissertation, Mechanical Engineering Department, University of Rhode Island, Kingston, Rhode Island.

Khan, A. M. (1995), "Historical Review of Filtration Theories in Fibrous Media," *Advances in Filtration and Separation Technology - Shape up the Future*, Proceedings of the Annual National Technical Conference of the American Filtration and Separations Society, Nashville, Tennessee, Nashville, April 23 – 26, Vol. 9, pp. 200-223.

Kline, S. J. and McClintock, F. A. (1953), "Describing Uncertainties in Single-Sample Experiments," **Mechanical Engineering**, January, Vol. 75, pt. 2, pp. 3-8.

Landahl, H. D. and Hermann, R. G. (1949), "Sampling of Liquid Aerosols by Wires, Cylinders, and Slides, and the Efficiency of Impaction of the Droplets," **Journal of Colloidal Science**, Vol. 4, pp. 103-136.

Langmuir, I. (1942), "Report on Smokes and Filters," Section I US Office of Scientific Research and Development Report, no. 865, part IV.

Lee, K. W. (1977), "Filtration of Submicron Aerosols by Fibrous Filters," Ph.D. Thesis, University of Minnesota, Twin Cities, Minnesota.

Lee, S. E. (1996), "In-Vehicle Performance of New and Used Automotive Cabin Air Filters," SAE Technical Paper #960541, *Aspects of Automotive Filtration (SP-1165)*, Conference of SAE Inc., Warrendale, PA.

Liang, F. (1997), "Particle Counting and Sizing with LDV for Automotive Air Filters," Ph.D. Thesis, School of Mechanical and Aerospace Engineering, Oklahoma State University, Stillwater, Oklahoma.

Liang, F., Natarajan, B., Tian, Y. and Dougherty, R. L. (1995), "Local Efficiency Measurements Applicable to Both Automotive Engine and Cabin Filtration," **Particulate Science and Technology**, Vol. 12, No. 4, April, pp. 333-350.

Lindeken, C. L., Morgan, R. L. and Petrock, K. F. (1963), **Health Physics**, Vol. 9, pp. 305+.

Liu, B. Y. H. and Pui, D. Y. H. (1974), "Electrical Neutralization of Aerosols," **Journal of Aerosol Science**, Vol. 5, pp. 465-472.

Liu, G., Tebutt, C. B., Duran, R. and Chambers, F. W. (1995), "Filter Inlet Redistribution with Filter Loading," *Advances in Filtration and Separation Technology - Shape Up the Future*, Proceedings of the Annual National Technical Conference of the American Filtration and Separations Society, Nashville, Tennessee, Nashville, April 23 – 26, Vol. 9, pp. 159-163.

Matteson, M. J. (ed.), (1987), Filtration - Principles and Practices, Marcel Dekker, New York, New York.

Maus, R. and Umhauer, H. (1996), "Determination of the Fractional Efficiencies of Fibrous Filter Media by Optical In - Situ Measurements," **Aerosol and Technology**, Vol. 24, April, pp. 161-173.

McAteer, O. J. (1989), Electrostatic Discharge Control, McGraw Hill, New York, N. Y.

McDonald, B., Gogins, M., Rothman, J. and Scott, J. (1997), "Discriminating Tests for Automobile Cabin Air Filter Media," SAE Technical Paper #970670, *Topics in Automotive Filtration Design (SP-1252)*, Conference of SAE Inc., February 24-27 Detroit, MI.

McQuiston, F. C. and Parker, J. D. (1994), Heating, Ventilating, and Air Conditioning: Analysis and Design, John Wiley and Son, New York, N. Y.

Natanson, G. L. (1957), "Deposition of Aerosol Particles by Electrostatic Attraction upon a Cylinder Around which They Are Flowing," **Dokl. Akad. Nauk SSSR**, Vol. 112, pp. 696-699 (in Russian), *Hungarian Studies in English Translation*, 7222 (1977).

Natarajan, B. (1995), "Local Efficiency Measurements of Automotive Air Filters Using Laser Doppler Velocimetry," M.S. Thesis, School of Mechanical and Aerospace Engineering, Oklahoma State University, Stillwater, Oklahoma.

Natarajan, B., Liang, F., Williams, J. C., and Dougherty, R. L. (1995), "Local Efficiency Measurements Flat Filter Media: Application to Automotive Cabin and Engine Air Filters," *Advances in Filtration and Separation Technology - Shape Up the Future*, Proceedings of the Annual National Technical Conference of the American Filtration and Separations Society, Nashville, Tennessee, April 24-26, Nashville, Tennessee.

Newman, R. A. (1994), "Uniformity of Air Flow in Automotive Air Filter Test Housing and Its Effects on the Efficiency of Fibrous Filters," M.S. Thesis, School of Mechanical and Aerospace Engineering, Oklahoma State University, Stillwater, Oklahoma.

Nicholson, R. M. and Weisert, L. E. (1986), "A Review of the Use of SAE Standard J726 in Heavy Duty Engine Air Cleaner Testing," **Fluid Filtration: Gas**, ASTM STP 975, American Society for Testing and Materials, Philadelphia, Vol. 1, pp. 266-274.

Orr, C. (1977), Filtration: Principles and Practices Part I, Marcel Dekker, Inc., New York, N. Y.

Pich, J. (1966), "Theory of Aerosol Filtration by Fibrous and Membrane Filters," Aerosol Science, C.N. Davies, ed., Academic Press, New York, New York, pp. 223-285.

Pich, J. (1977), "Gas Filtration Theory," Filtration Principles and Practices, C. Orr, ed. Marcel Dekker, Inc., New York, N. Y. pp. 2-167.

Pich, J. (1987), Filtration - Principles and Practices, M.J. Matteson, ed., Marcel Dekker, New York, N. Y.

Poon, W. S. and Liu, B. Y. H. (1997a), "A Bimodal Loading Test for Engine and General Purpose Air Cleaning Filters," presented at 1997 SAE International Congress and Exposition, SAE Technical Paper #970674, *Topics in Automotive Filtration Design (SP-1252)*, February 24-27, Detroit, MI.

Poon, W. S. and Liu, B. Y. H. (1997b), "Dust Loading Behavior of Engine and General Purpose Air Cleaning Filters," presented at 1997 SAE International Congress and Exposition, SAE Technical Paper #970676, *Topics in Automotive Filtration Design (SP-1252)*, February 24-27, Detroit, MI.

Ptak, T. J. and Jaroszczyk, T. (1990), "Theoretical-Experimental Aerosol Filtration Model for Fibrous Filters at Intermediate Reynolds Numbers," Proceedings of the Fifth World Filtration Congress, Nice, France, pp. 566-572.

Ptak, T. J., Wake, J. and Jaroszczyk, T. (1994), "An Experimental Evaluation of the Factors Influencing the Performance of Car Interior Air Filters," SAE Technical Paper #930014, Conference of SAE, Inc., Warrendale, PA.

Reinhart, C. O. and Weisert, L. E. (1983), "Measurement of Engine Air Cleaner Efficiency Using Airborne Particle Size Analysis," SAE Technical Paper #831262, International Off-Highway Meeting and Exposition, Milwaukee, Wisconsin, September.

Rodman, C. A. and Lessmann, R. C. (1988), "Automotive Nonwoven Filter Media: Their Constructions and Filter Mechanisms," **Tappi Journal**, April, pp. 161-168.

Sabnis, R. D. (1993), "Effects of Non-Uniform Air Flow Through Filters on Filtration Efficiency," M. S. Thesis, School of Mechanical and Aerospace Engineering, Oklahoma State University, Stillwater, Oklahoma.

Sabnis, R. D., Cai, Q. and Chambers, F. W. (1994a), "Diagnosis of the Flow Fields in a Housing for Automotive Air Filter Performance Testing," AIAA Paper #94-0117, AIAA 32nd Aerospace Sciences Meeting, Reno, Nevada.

Sabnis, R. D., Cai, Q. and Chambers, F. W. (1994b), "Flow Distribution Effects Upon Air Filter Performance Measurements," SAE 1994 Transactions, **Journal of Engines**, Section 3, pp. 386-397.

Saxena, P. (1998), "Comparison of Filtration Efficiency of Pleated Filters for Different Particles," M.S. Thesis, School of Mechanical and Aerospace Engineering, Oklahoma State University, Stillwater, Oklahoma.

Shobokshy, E. and Mohammed, S. (1994), "Computer Simulation of Monodisperse Aerosol Collection in Fibrous Filters," **Aerosol Science and Technology**, Vol. 20, pp. 149-160.

Society of Automotive Engineers (1987), "SAE J726 Air Cleaner Test Code - SAE Recommended Practice," Society of Automotive Engineers Hand Book, SAE, Inc., Warrendale, PA.

Society of Automotive Engineers (1993), "SAE J1669 Passenger Compartment Air Filter Test Code - SAE Recommended Practice," Proposed Draft, SAE, Inc., Warrendale, PA.

Society of Automotive Engineers (1997), "SAE J1141 Air Cleaner Elements - SAE Recommended Practice," Society of Automotive Engineers Hand Book, SAE, Inc., Warrendale, PA.

Society of Automotive Engineers (1998), "SAE J726 Air Cleaner Test Code - SAE Recommended Practice," Society of Automotive Engineers Hand Book, SAE, Inc., Warrendale, PA.

Srinivasan, R. (1999), "Efficiency of Pleated Filters for Different Particle Sizes and Particle Sizing Techniques," (a Tentative Topic), M.S. Thesis, School of Mechanical and Aerospace Engineering, Oklahoma State University, Stillwater, Oklahoma.

Stenhouse, J. I. T. (1975), "Filtration of Air by Fibrous Filters," **Filtration and Separation**, May/June, pp. 268-274.

Stern, S. T., Zeller, H. W. and Schekman, A. I. (1960), "The Aerosol Efficiency and Pressure Drop of a Fibrous Filter at Reduced Pressures," **Journal of Colloid Interface Science**, Vol. 15, pp. 546-562.

Stinson, J. A., Meyers, M. N., Jaroszczyk, T. and Verdegan, B. M. (1988), "Temporal Changes in Oil and Air Filter Performance Due to Dust Deposition," **Filtration and Separation**, Sept./Oct., pp. 368-371.

Sudarshan, T. S. and Jaitly, N. C. (1988), "In-situ Insulator Surface Charge Measurement in Dielectric Bridged Vacuum Gaps Using an Electrostatic Probe," *IEEE Transactions on Electrical Insulation*, April, Vol. 23, No. 2, pp. 261-271.

Tien, C., (1989), Granular Filtration of Aerosols and Hydrosols, Butterworths, Boston, MA.

Wake, J. and Jaroszczyk, T. (1991), "Experimental Study of Dust Filtration in Surface-Type Nonwovens," **Particulate Science and Technology**, Vol. 9, No. 1-2, pp. 31-44.

Walker, M. and Ptak, T. J. (1996), "Particulate Filter Performance in the North American Environment," SAE Technical Paper #960940, *Aspects of Automotive Filtration (SP-1165)*, Conference of SAE, Inc., Warrendale, PA.

Watrasiwicz, B. M., and Rudd, M. J. (1976), Laser Doppler Measurements, Butterworths & Co., London, England.

Whitby, K. T. (1973), "On the Multimodal Nature of Atmospheric Aerosol Size Distributions," **Particle Technology**, Publication No. 218, pp. 576-585.

Whitby, K. T. and Liu, B. Y. H. (1966), "The Electrical Behavior of Aerosols," Aerosol Science, C.N. Davies, ed. Academic Press, New York, New York, pp. 59-86.

Whitby, K. T., Lundgren, D. A., Jordan, R. C. and McFarland, A. R. (1961), "Evaluation of Air Cleaners for Occupied Spaces," **Journal of Air Pollution Control Association**. Vol. 11, No. 11, pp. 503-515.

Williams, J. C. (1996), "In-Situ Measurements of Local Efficiency for Flat Automotive Air Filter Media," M.S. Report, School of Mechanical and Aerospace Engineering, Oklahoma State University, Stillwater, Oklahoma.

Wilson, W. E. (1977), "General Motors Sulfate Dispersion Experiment: Summary of EPA Measurements," **Journal of Air Pollution Control Association**, Vol. 27, No. 1, pp. 225-234.

Yeh, H. C. (1972), "A Fundamental Study of Aerosol Filtration by Fibrous Filters," Ph.D. Thesis, University of Minnesota, Twin Cities, Minnesota.

Yeh, H. C. and Liu, B. Y. H. (1974), "Aerosol Filtration by Fibrous Filters - I. Theoretical," **Aerosol Science**, Vol. 5, pp. 191-204.

Young, J. H., Bunn, J. M. and Henson, W. H. (1963), "Humidity and Moisture Problems Associated with the Handling and Storage of Cured Tobacco," *Humidity and Moisture: Measurement and Control in Science and Industry*, presented at the International Symposium on Humidity and Moisture, Washington D.C. USA, 1963, Vol. II, pp 231-238, 1963.

Zimon, A. D. (1969), Adhesion of Dust and Powder, Plenum Press, New York, N. Y.

APPENDICES

APPENDIX A

LETTER TO NATARAJAN ET AL. FROM E. R. FREDERIC

E.R. Frederick
294 Sunset Rd.
Pittsburgh, PA 15237
(412) 364-3529

March 11, 1996

Mr. B. Natarajan et al.
School of Mechanical and
Aerospace Engineering
Oklahoma State University
Stillwater, OK 74078

Dear Mr. Natarajan and Coauthors:

I've noted with interest your recent article entitled "Local Efficiency Measurements Over Flat Filter Media: Application To Automotive Cabin And Engine Filters" in October's Fluid/Particle Separation Journal. I have no comments concerning your finding except to suggest that consideration might also be directed to electrical effects in the collection process. In fact, isn't it possible that the lower efficiency at lower flow rates can be attributed directly to this phenomenon?

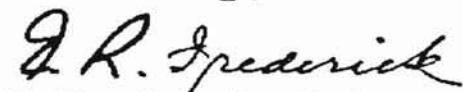
If essentially all normally produced particulates reaching filters are charged, as reported by White (1) and others, and if the common (man-made fiber content) media respond upon contact with these or even uncharged particles to develop their inherent-triboelectric (TE) polarities, should not these electrical effects be considered in all filtration processes? My extensive laboratory scale experimental studies as reported (2) and verified in industrial applications that involved a large number: (over 50) and a large variety of particulates, clearly demonstrated the presence and influence of triboelectric charging on the filtration process. Only because we learned early during our studies that reuse of dusts destroys charge effects were we in a position to show how these effects of triboelectric charging influences the overall operation. Actually, I have evidence to show that the reuse of a test dust led to misinformation by a prestigious investigator who with others were responsible for providing fallacious data. Some of my more current articles are also listed below under (3) that may deserve examination and consideration.

As a result of my earlier experience in filter media evaluation and specification with results demonstrating the (TE) variability of presumably identical commercial media, I've now developed processes whereby the TE polarities of some fibers/fabrics may be predictably adjusted. Accordingly, in cooperation with a producer of a very special, high surface area fiber; a unique bi-polar filter is being developed to provide what is expected to be "THE SUPERIOR FILTER TYPE MEDIA".

Page 1 of 2

If you, your coauthors and Advisor(s) are interested in this special filter, it should be possible for us to provide samples sometime soon for consideration and evaluation. Whether you are or not so inclined, kindly provide your appraisal regarding the influence or potential influence of electrostatic effects in fiber or fabric filtration as used in industrial applications, commercial air house hold, cabin or engine filters.

Sincerely,



E.R. Frederick

- (1) Frederick, E. R., "HOW DUST FILTER SELCTION DEPENDS ON ELECTROSTATICS", Chem. Eng. 68: 107-114 (1961)
- (2) White, H. J., Addison-Wesely Publishing Co. Palo Alto, CA.
- (3) Frederik, E. R., "ELECTROSTATIC EFFECTS IN FABRIC FILTRATION": Filtration News, 13(1): 36 - 37 (1995).
- (4) Frederik, E. R., " THE INFLUENCE OF 'OTHER' PHYSICAL PROPERTIES OF PARTICULATE MATTER ON FILTRATION PERFORMANCE", Filtration News, 13(3): 48-51 (1995).
- (5) Frederik, E. R., "ELECTRICAL EFFECTS IN FABRIC FILTRATION: FUNDAMENTAL CONCEPTS"; Filtration News, 13 (6): 30 - 31 (1995) And 13(6) 46 - 47 (1995) and 14(1): 24 - 25, 32 - 64 (1996).
- (6) Frederik, E. R., "AN OVERVIEW OF ELECTROSTATIC EFFECTS IN BAGHOUSE TECHNOLOGY", Kenote Address – The User and Fabric Filtration Equipment VII, Proceedings of an International Specialty Conference of the Air and Waste Management Association, Toronto, CA September 12 - 14, 1994, Pages 7-18.

APPENDIX B

SWEPT VOLUME TECHNIQUE

The swept volume technique described in Chapter IV was developed by Liang [1997] in order to determine the concentration of particles (number density), N_i , upstream and downstream of the filter from the number of particles counted (n_i), their average measured velocity (V_i), length of time (t_i) taken to detect these particles, and the cross-sectional area of the probe volume (A_p) perpendicular to the flow. As the particles travel with a mean velocity of V_i for a duration of time t_i , they travel a distance of $L_s = V_i t_i$ as shown in Fig. B-1. Thus the swept volume technique derives its name from the volume swept by the distance the particles travel and the projected (cross-sectional) area of the probe volume normal to the path of the flow of particles. Hence the swept (generated) volume is equal to $L_s A_p$. The method assumes that all of the particles crossing the probe volume have a velocity equal to the average velocity of all samples measured at a location (grid point) i . Thus the number density (particle concentration) is calculated by

$$N_i = \frac{n_i}{V_i t_i A_p} \quad (\text{B-1})$$

The cross-sectional area of the probe volume is $3.803746137 \times 10^{-8} \text{ m}^2$ as calculated from the data of Table 4.1 (Chapter IV) using $A_p = (\pi/4)L_{pv} d_{pv}$, where L_{pv} and d_{pv} are the major and minor diameters of the ellipse as shown in Fig. 4.2b of Chapter IV. Anand [1997] and Saxena [1998] have quoted a wrong value of A_p as $3.25 \times 10^{-11} \text{ m}^2$.

Figure B.1 shows the concept of the swept volume [Jadbabaei, 1997]. A closer look at Eq. (B-1) indicates that, for very low velocities, like those measured near the walls of the housing, the number density tends to an erroneously large value. Jadbabaei [1997] explains this observation from a physical point-of-view and discusses a number of different methods to overcome this difficulty. It has been explained in Chapter VI that, in regions downstream of the filter where there is a recirculating flow, the average velocity of the particles is close to zero, since the velocity distribution is comprised of both positive and negative velocity values. This technique assumes that the velocity is unidirectional and perpendicular to the cross-sectional area of the probe volume. However, this technique fails due to very low velocities in the recirculation zones downstream of the filter. Jadbabaei [1997] suggests the use of several methods to offset this problem.

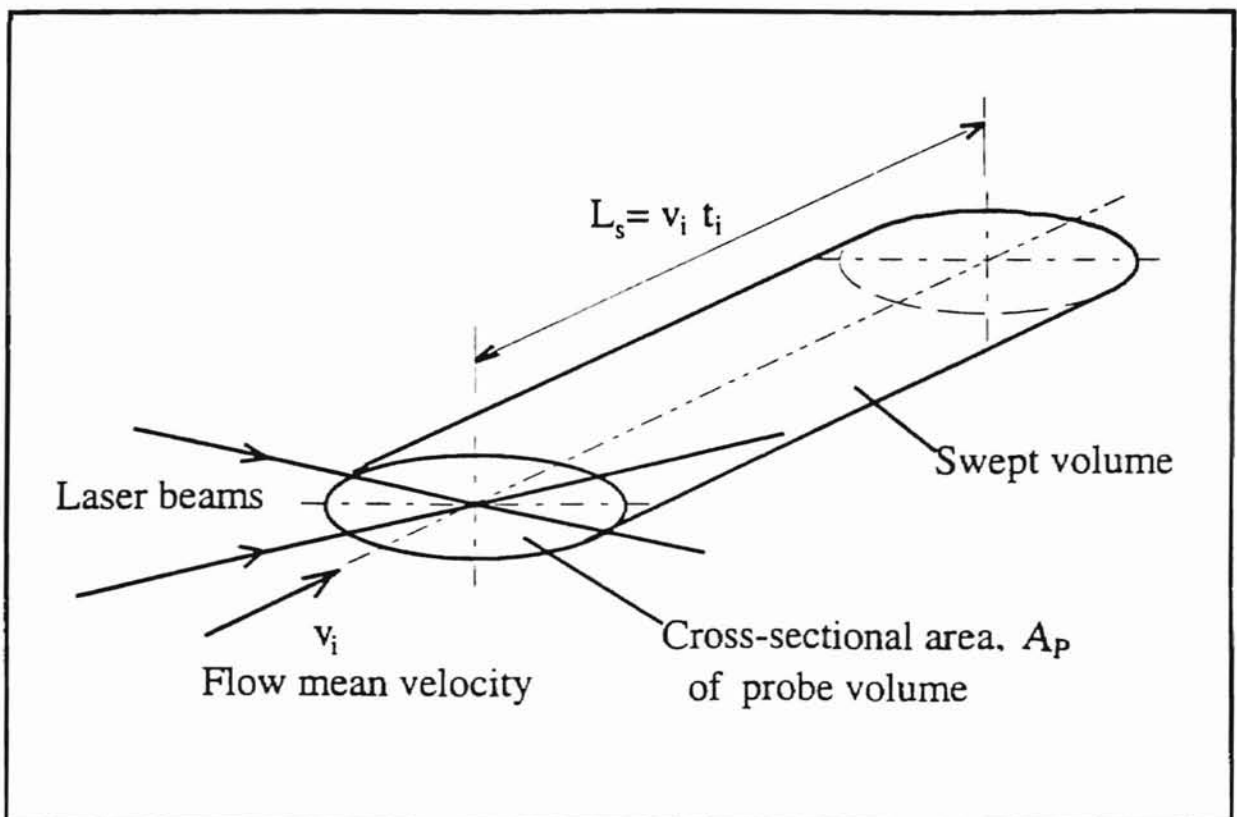


Figure B.1 Swept Volume Technique [Liang, 1997].

APPENDIX C

ERROR ANALYSIS

The errors or uncertainties in the overall efficiency of the filter discussed in Chapter VI were based on a simple analysis of the variation in the number density calculation. Anand [1997] and Saxena [1998] have presented the prediction of the uncertainties in their experimental filtration efficiency measurements using error analysis as proposed by Kline and McClintock [1953]. This was based on the assumption of a random error in number density measurements. Thus the error in number density due to errors in particle count, n_i , velocity, V_i , time, t_i , and cross-sectional area of probe volume, A_p has been shown [Anand, 1997] to be equal to

$$\frac{dN_i}{N_i} = \left[\left(\frac{dn_i}{n_i} \right)^2 + \left(\frac{dV_i}{V_i} \right)^2 + \left(-\frac{dt_i}{t_i} \right)^2 + \left(-\frac{dA_p}{A_p} \right)^2 \right]^{1/2} \quad (\text{C-1})$$

where the number density is defined as follows:

$$N_i = \frac{n_i}{V_i t_i A_p} \quad (\text{C-2})$$

On the other hand, the filtration efficiency based on number density or particle count (concentration) is given as

$$\eta_i = \frac{N_{iup} - N_{idown}}{N_{iup}} = 1 - \frac{N_{idown}}{N_{iup}} = 1 - R_d \quad (\text{C-3})$$

where N_{iup} and N_{idown} are the upstream and downstream number densities, respectively. Thus the error in the measured efficiencies will be predicted by the following equation [for the derivation, refer to Anand, 1997]:

$$\frac{d\eta_i}{\eta_i} = \frac{N_{idown}}{N_{iup}} \left[(c_e)^2 + (c_e)^2 \right]^{1/2} = \sqrt{2}(c_e)R_d \quad (C-4)$$

where c_e is the fractional error values for the upstream and downstream number densities assuming both fractional errors are of the same magnitude. It is defined as follows:

$$c_e = \frac{\Delta N_{iup}}{N_{iup}} = \frac{\Delta N_{idown}}{N_{idown}} = \frac{dN_i}{N_i} \quad (C-5)$$

where ΔN_{iup} and ΔN_{idown} are the deviations (errors) in the upstream and downstream number densities.

Anand [1997] assumed an error of 2% for the cross-sectional area of the probe volume of the LDA system. However, this might be more than 2% if one sees the errors in calculating the cross-sectional area of the probe volume by approximating it as a perfect ellipsoid and without any corrections to the variation in the cross-sectional area of the probe volume. The cross-sectional area is subject to variations due to laser power fluctuations associated with the problems of coupling the laser beams to the fiber optic cables as discussed in Chapter IV. Thus assuming a maximum error of 7.5% in the cross-sectional area of the probe volume would not be an exaggeration. Similarly the percentage errors in particle count (due to noise), time for data collection, and velocity can be assumed as 5%, 2%, and 2%, respectively. Following the above error assumptions, the error in number density becomes (from Eq. (C-1))

$$\frac{dN_i}{N_i} = \left[(0.05)^2 + (-0.02)^2 + (-0.02)^2 + (-0.075)^2 \right] = 0.0945, \text{ or } 9.45\% \quad (C-6)$$

Substituting this 9.45% number density error into the equation for efficiency error in Eq. (C-4), the general error equation for filtration efficiency measurement reduces to:

$$\frac{d\eta_i}{\eta_i} = \sqrt{2}(0.0945)R_d = (0.1262)R_d \quad (\text{C-7})$$

Therefore it is possible to find the experimental overall and local filtration efficiency errors using Eq. (C-4).

APPENDIX D

ELECTROSTATIC CHARGE EFFECTS:

VELOCITY, NUMBER DENSITY AND EFFICIENCY RESULTS FOR 0.966 μm DIAMETER PSL PARTICLES IN THE SMALL ANGLE DIFFUSER HOUSING

In this appendix, other test results in addition to those discussed in Chapter VI are presented. These test results were performed on the 0.966 μm diameter PSL particles under monitored conditions (humidity, temperature, and electrostatic charge voltage, pressure drop, etc.) for all of the flow rates. The results presented herein are the upstream and downstream local velocity measurements, the upstream and downstream local number densities, and the local efficiencies for each flow rate. These results were used to evaluate the effect of electrostatic charge at low humidities by enhancing (maximizing) electrostatic charge as much as possible and comparing them with the experimental results obtained at low humidities without electrostatic charge (refer to Appendix E). For all of the experimental results presented herein, the filter housing was left ungrounded.

The tests have been alphanumerically designated to specify the electrostatic charge condition, flow rate, and the type of housing used. ESH40.1 stands for the experimental test performed to investigate electrostatic charge (E) effects at an air flow rate of 40 scfm (60.81 m^3/hr) without grounding the 'Small Angle Diffuser Housing' (SH), that houses the filter (see Figs. 4.13 and 4.15 of Chapter IV). The numeral 1, after

the decimal point, refers to this being the first experimental test conducted for that flow rate. Summaries of test conditions for all cases are given in Tables 6.1 and 6.2 of Chapter VI.

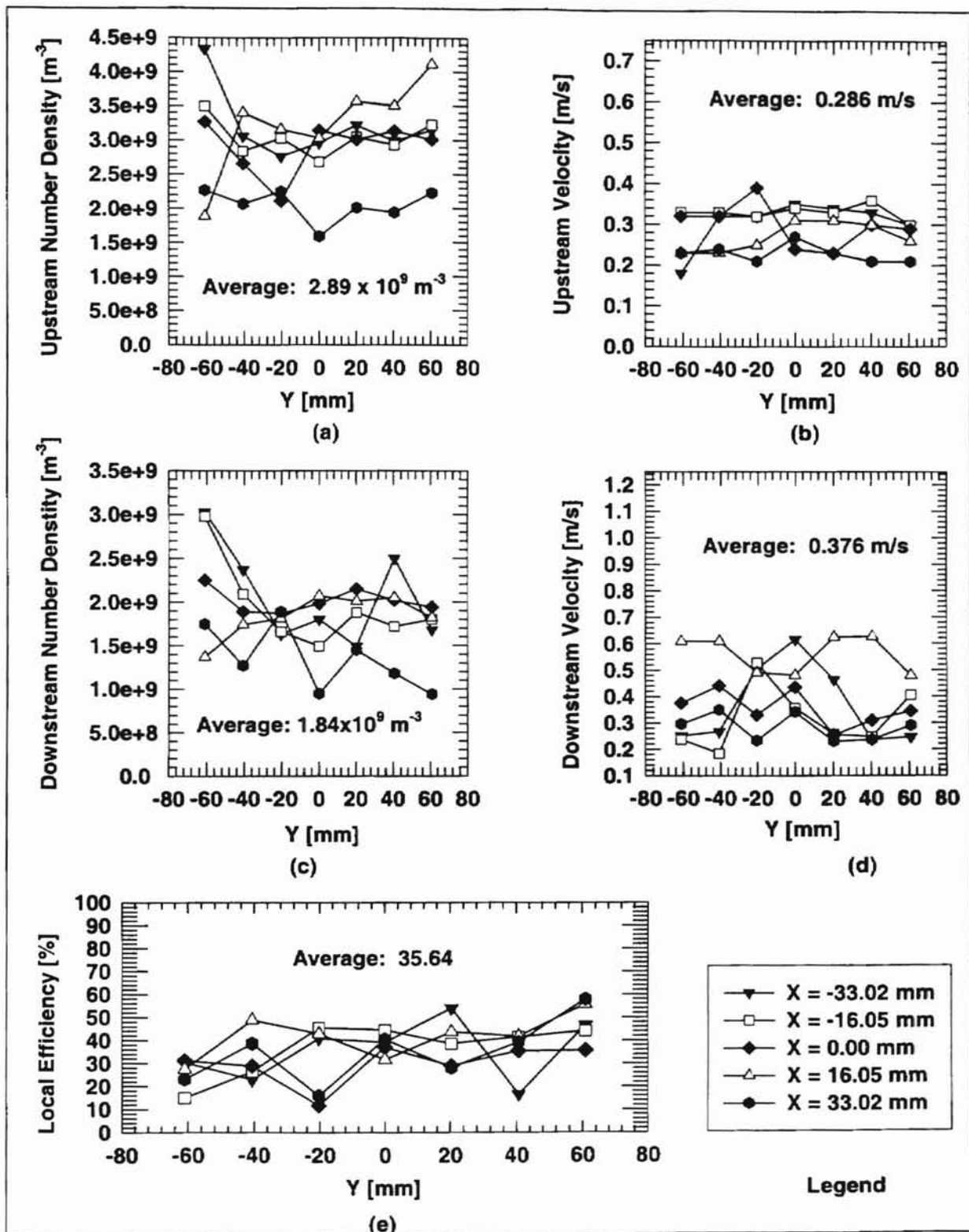


Figure D.1 Electrostatic Charge Effect on Efficiency of Pleated Fibrous Filter:
 (a) Upstream No. Density, (b) Downstream No. Density, (c) Upstream Velocity,
 (d) Downstream Velocity, (e) Local Efficiency. Pressure Drop Δp [mm Water] = 3,
 RH = 43.5%, Temperature [$^{\circ}C$] = 38, Electrostatic Voltage at Filter [v] = 100.
 Air Flow Rate = 13.5 m^3/hr , Test # ESH10.1, Test Date: 08/20/98.

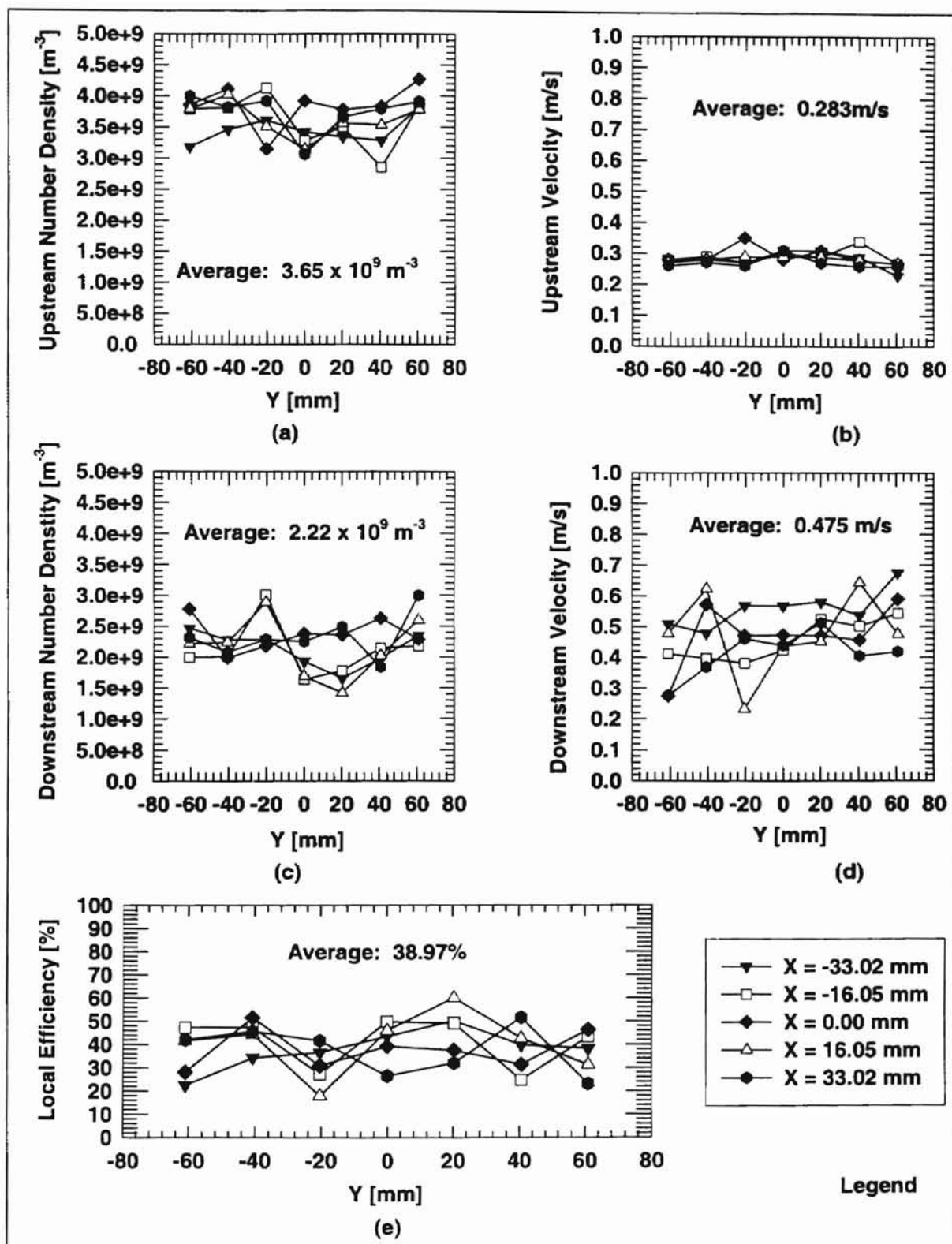


Figure D.2 Electrostatic Charge Effect on Efficiency of Pleated Fibrous Filter:

(a) Upstream No. Density, (b) Downstream No. Density, (c) Upstream Velocity, (d) Downstream Velocity, (e) Local Efficiency. Pressure Drop Δp [mm Water] = 3, RH = 39%, Air Temperature [°C] = 39, Electrostatic Voltage at Filter [v] = 150, Air Flow Rate = 13.5 m³/hr, Test # ESH10.2, Test Date: 08/20/98.

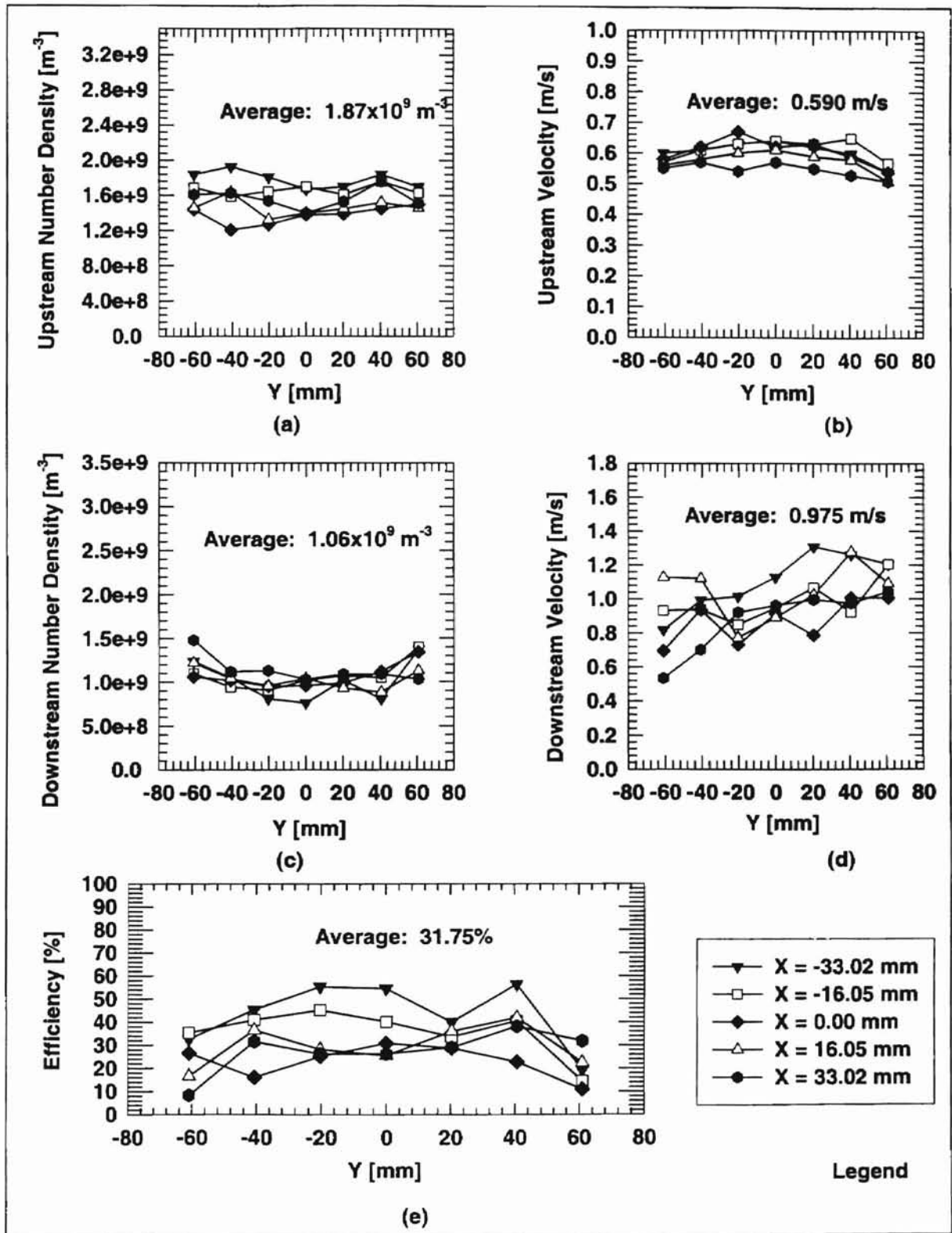


Figure D.3 Electrostatic Charge Effect on Efficiency of Pleated Fibrous Filter:
 (a) Upstream No. Density, (b) Downstream No. Density, (c) Upstream Velocity,
 (d) Downstream Velocity, (e) Local Efficiency. Pressure Drop Δp [mm Water] = 3,
 RH = 33%, Air Temperature [$^{\circ}C$] = 43, Electrostatic Voltage at Filter [v] = 150,
 Air Flow Rate = $29.5 m^3/hr$, Test # ESH20.1, Test Date: 08/21/98.

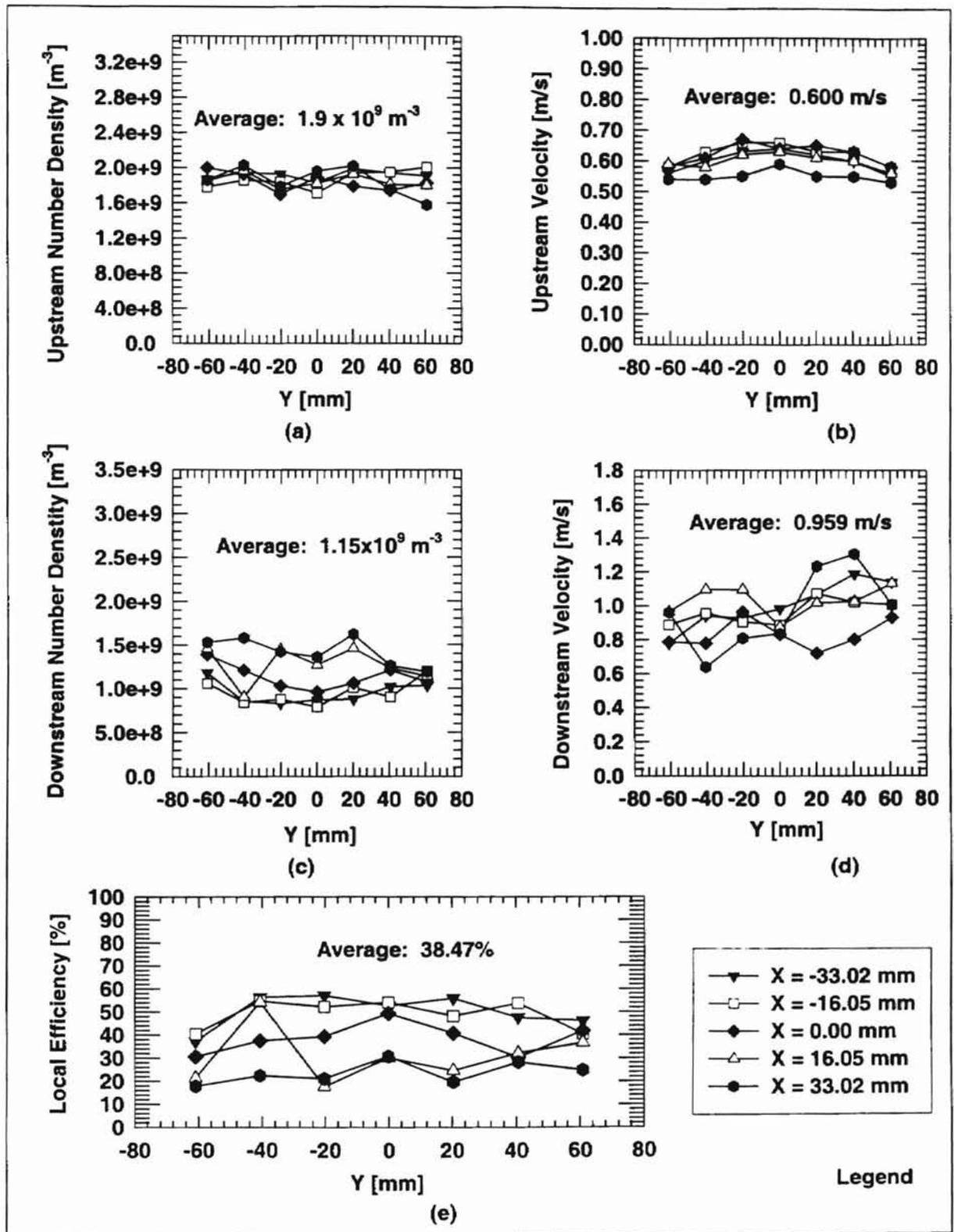


Figure D.4 Electrostatic Charge Effect on the Efficiency of Pleated Fibrous Filter:
 (a) Upstream No. Density, (b) Downstream No. Density, (c) Upstream Velocity,
 (d) Downstream Velocity, (e) Local Efficiency. Pressure Drop Δp [mm Water] = 3,
 RH = 32%, Air Temperature [°C] = 44, Electrostatic Voltage at Filter [v] = 200,
 Air Flow Rate = 29.5 m³/hr, Test # ESH20.2, Test Date: 08/21/98.

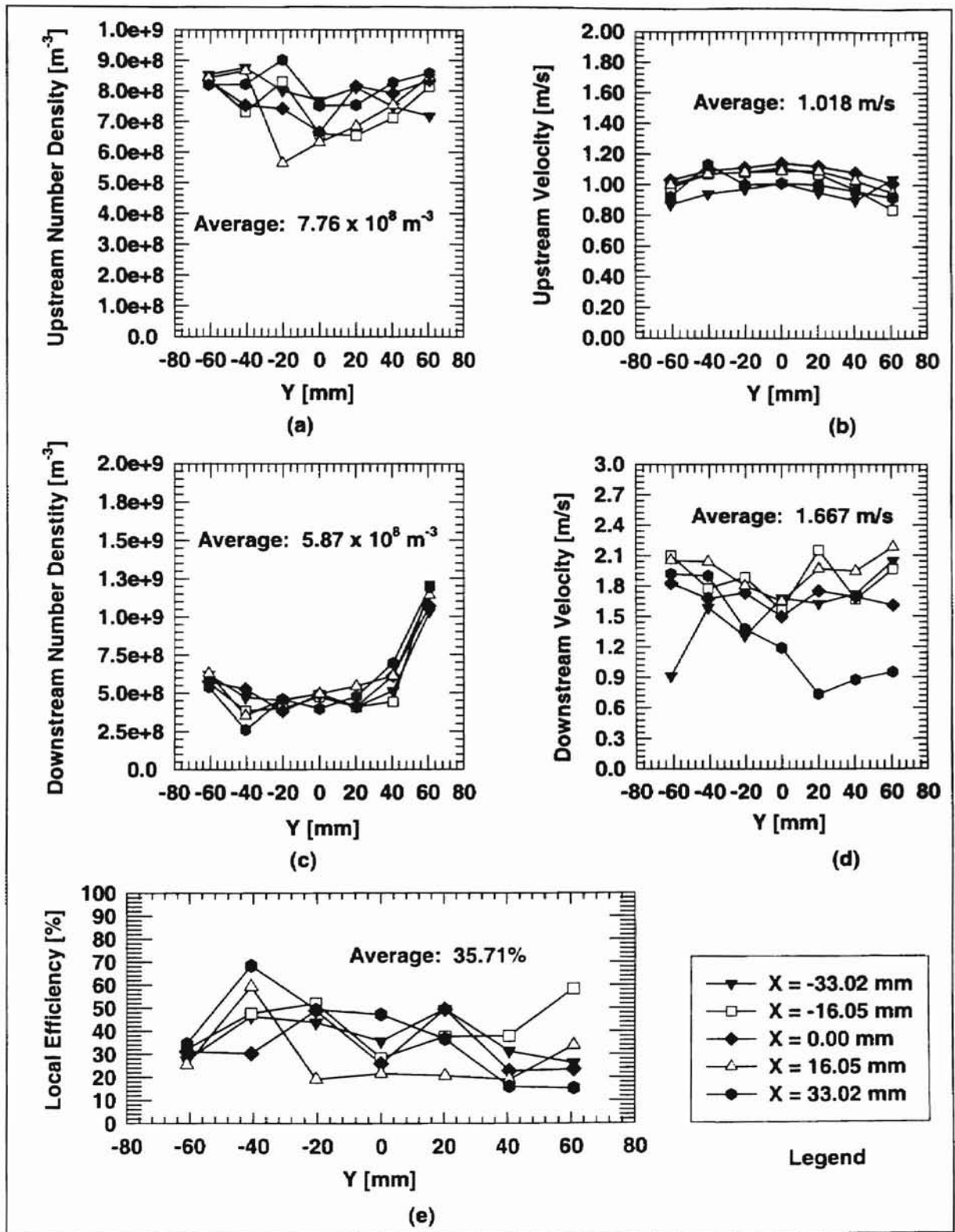


Figure D.5 Electrostatic Charge Effect on Efficiency of Pleated Fibrous Filter:
 (a) Upstream No. Density, (b) Downstream No. Density, (c) Upstream Velocity,
 (d) Downstream Velocity, (e) Local Efficiency. Pressure Drop Δp [mm Water] = 3,
 RH = 33%, Air Temperature [$^{\circ}C$] = 52, Electrostatic Voltage at Filter [v] = 200,
 Air Flow Rate = $60.81 m^3/hr$, Test # ESH40.1, Test Date: 08/22/98.

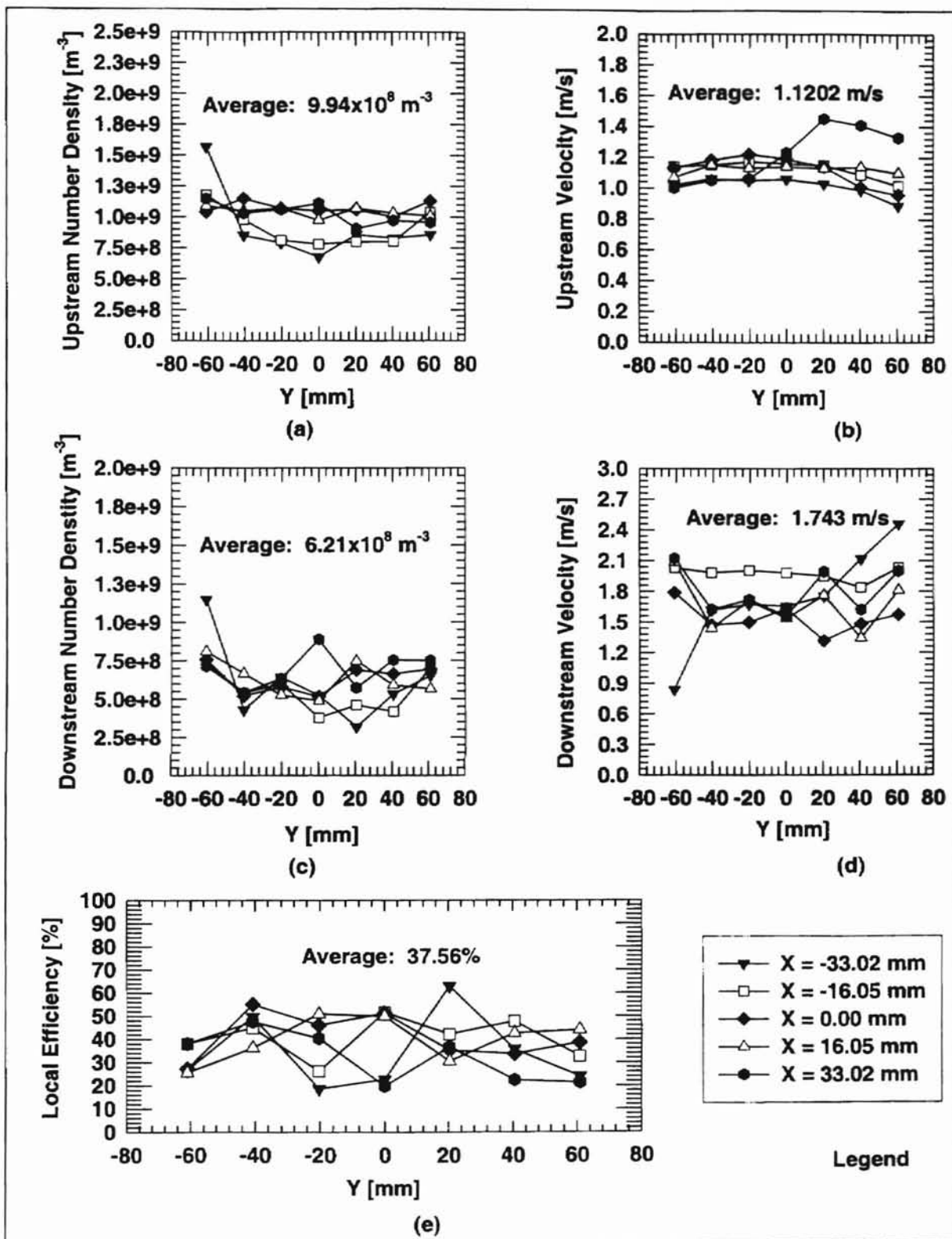


Figure D.6 Electrostatic Charge Effect on Efficiency of Pleated Fibrous Filter:
 (a) Upstream No. Density, (b) Downstream No. Density, (c) Upstream Velocity,
 (d) Downstream Velocity, (e) Local Efficiency. Pressure Drop Δp [mm Water] = 5,
 RH = 33%, Air Temperature [$^{\circ}C$] = 49.5, Electrostatic Voltage at Filter [v] = 200,
 Air Flow Rate = 60.81 m^3/hr , Test # ESH40.2, Test Date: 08/22/98.

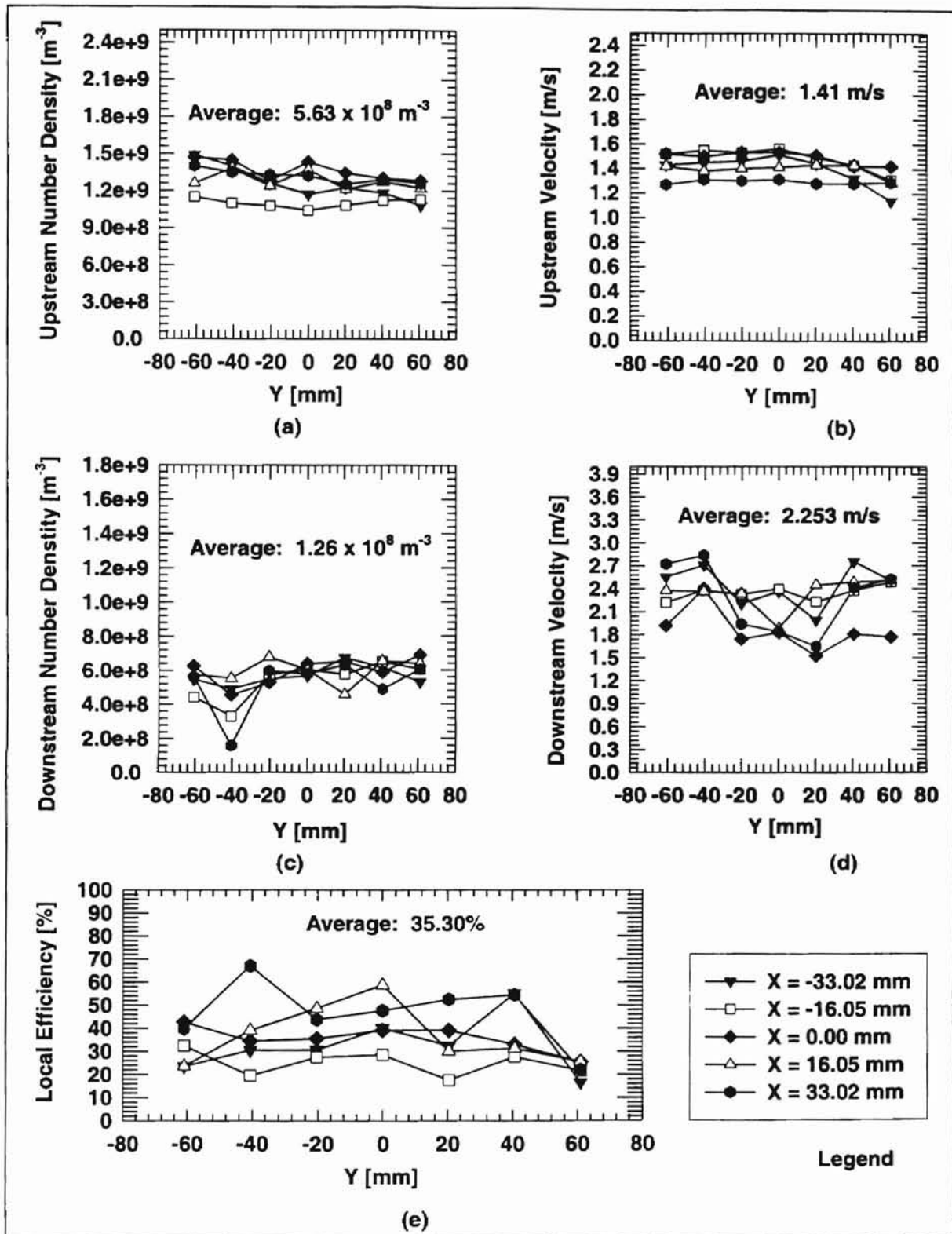


Figure D.7 Electrostatic Charge Effect on Efficiency of Pleated Fibrous Filter:

(a) Upstream No. Density, (b) Downstream No. Density, (c) Upstream Velocity, (d) Downstream Velocity, (e) Local Efficiency. Pressure Drop Δp [mm Water] = 5, RH = 35%, Air Temperature [$^{\circ}C$] = 52, Electrostatic Voltage at Filter [v] = 500, Air Flow Rate = $77.1 m^3/hr$, Test # ESH50.1, Test Date: 08/23/98.

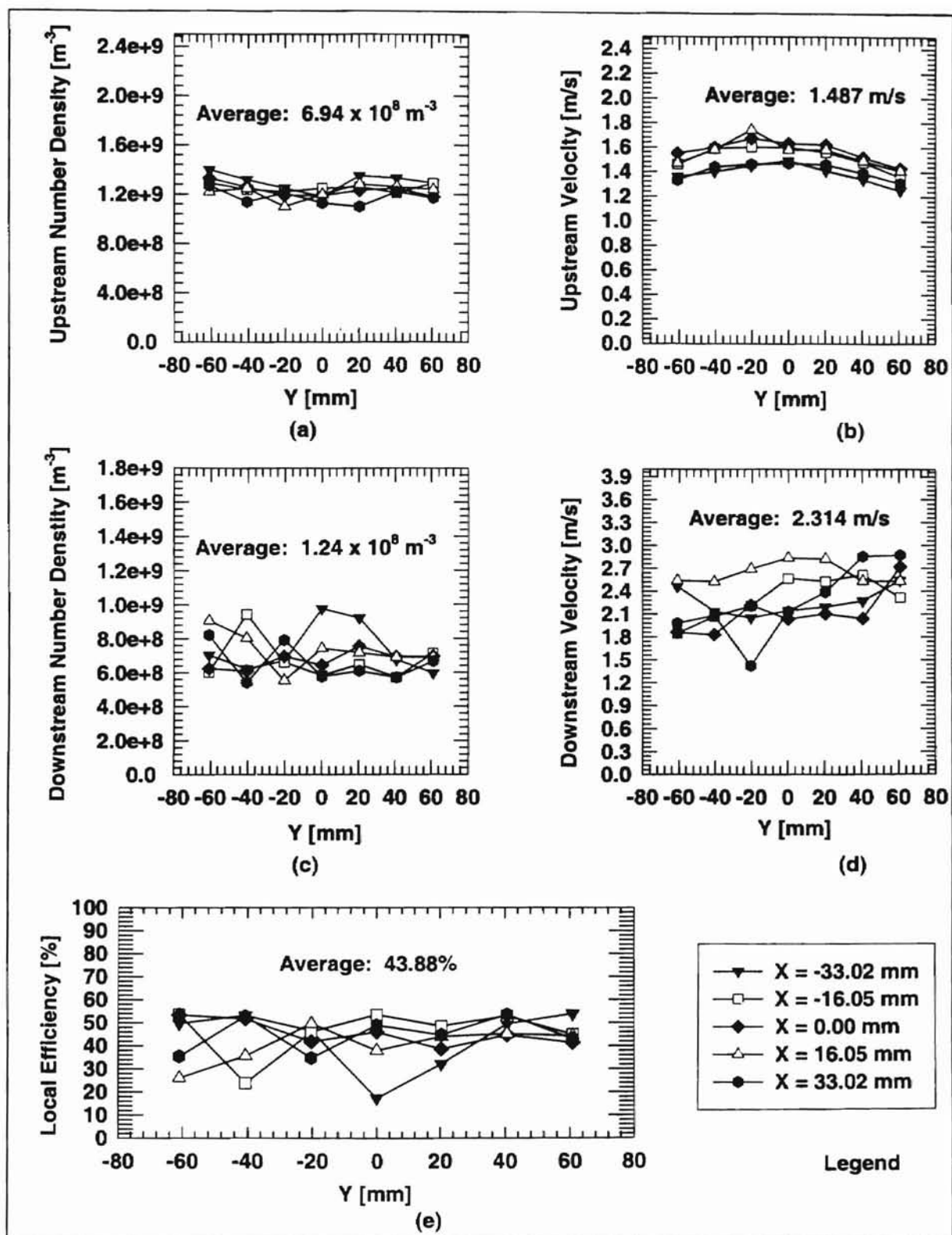


Figure D.8 Electrostatic Charge Effect on Efficiency of Pleated Fibrous Filter: (a) Upstream No. Density, (b) Downstream No. Density, (c) Upstream Velocity, (d) Downstream Velocity, (e) Local Efficiency. Pressure Drop Δp [mm Water] = 8, RH = 35%, Air Temperature [$^{\circ}C$] = 52, Electrostatic Voltage at Filter [v] = 750, Air Flow Rate = 77.1 m^3/hr , Test # ESH50.2, Test Date: 08/13/98.

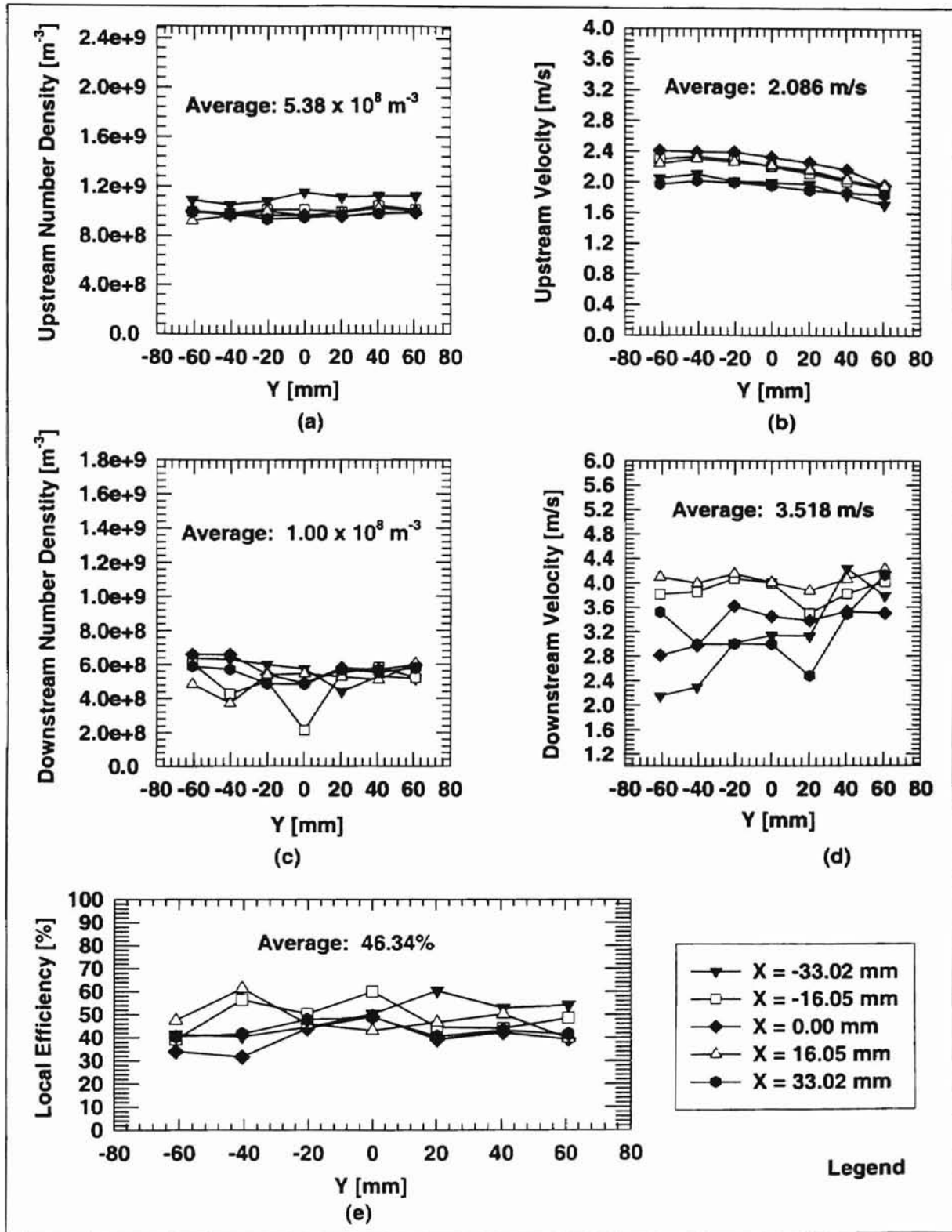


Figure D.9 Electrostatic Charge Effect on Efficiency of Pleated Fibrous Filter:
 (a) Upstream No. Density, (b) Downstream No. Density, (c) Upstream Velocity,
 (d) Downstream Velocity, (e) Local Efficiency. Pressure Drop Δp [mm Water] = 13,
 RH = 39%, Air Temperature [$^{\circ}C$] = 47, Electrostatic Voltage at Filter [v] = 750,
 Air Flow Rate = 103.7 m^3/hr , Test # ESH75.1, Test Date: 08/24/98.

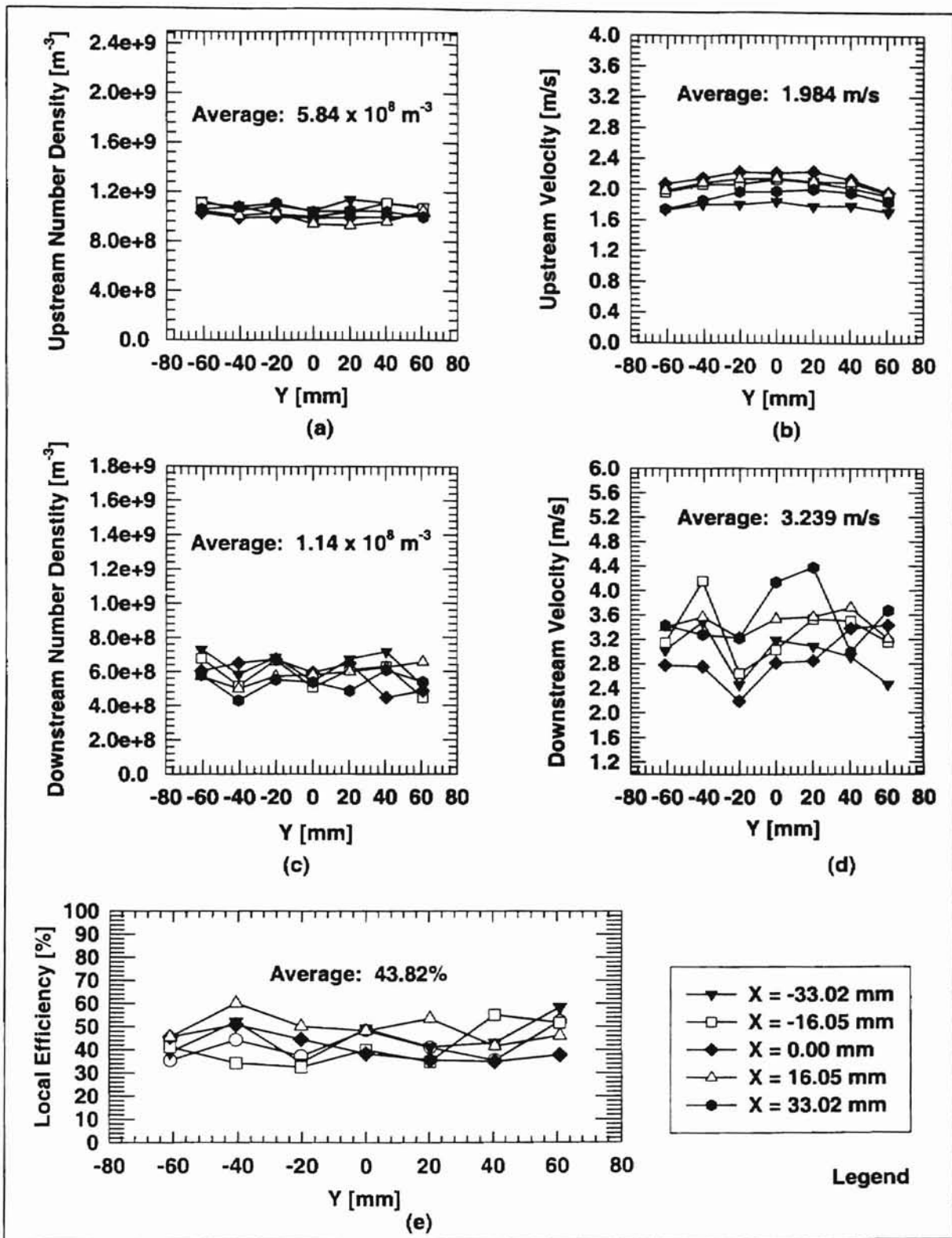


Figure D.10 Electrostatic Charge Effect on Efficiency of Pleated Fibrous Filter: (a) Upstream No. Density, (b) Downstream No. Density, (c) Upstream Velocity, (d) Downstream Velocity, (e) Local Efficiency. Pressure Drop Δp [mm Water] = 13, RH = 39%, Air Temperature [$^{\circ}C$] = 48, Electrostatic Voltage at Filter [v] = 750, Air Flow Rate = $103.7 m^3/hr$, Test # ESH75.2, Test Date: 08/24/98.

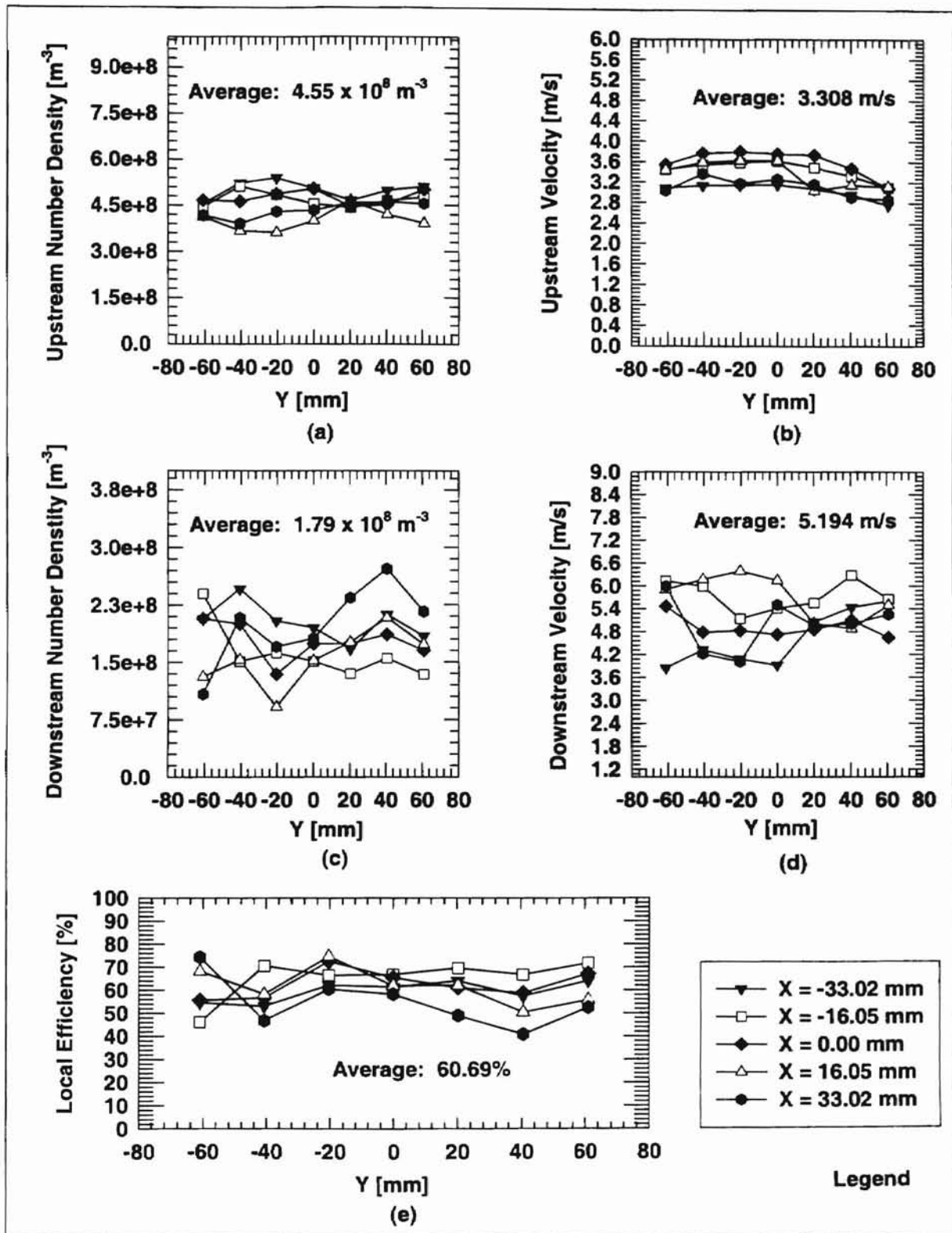


Figure D.11 Electrostatic Charge Effect on Efficiency of Pleated Fibrous Filter:
 (a) Upstream No. Density, (b) Downstream No. Density, (c) Upstream Velocity,
 (d) Downstream Velocity, (e) Local Efficiency. Pressure Drop Δp [mm Water] = 30,
 RH = 42%, Air Temperature [$^{\circ}C$] = 43, Electrostatic Voltage at Filter [v] = 500,
 Air Flow Rate = $145.7 m^3/hr$, Test # ESH100.1, Test Date: 08/25/98.

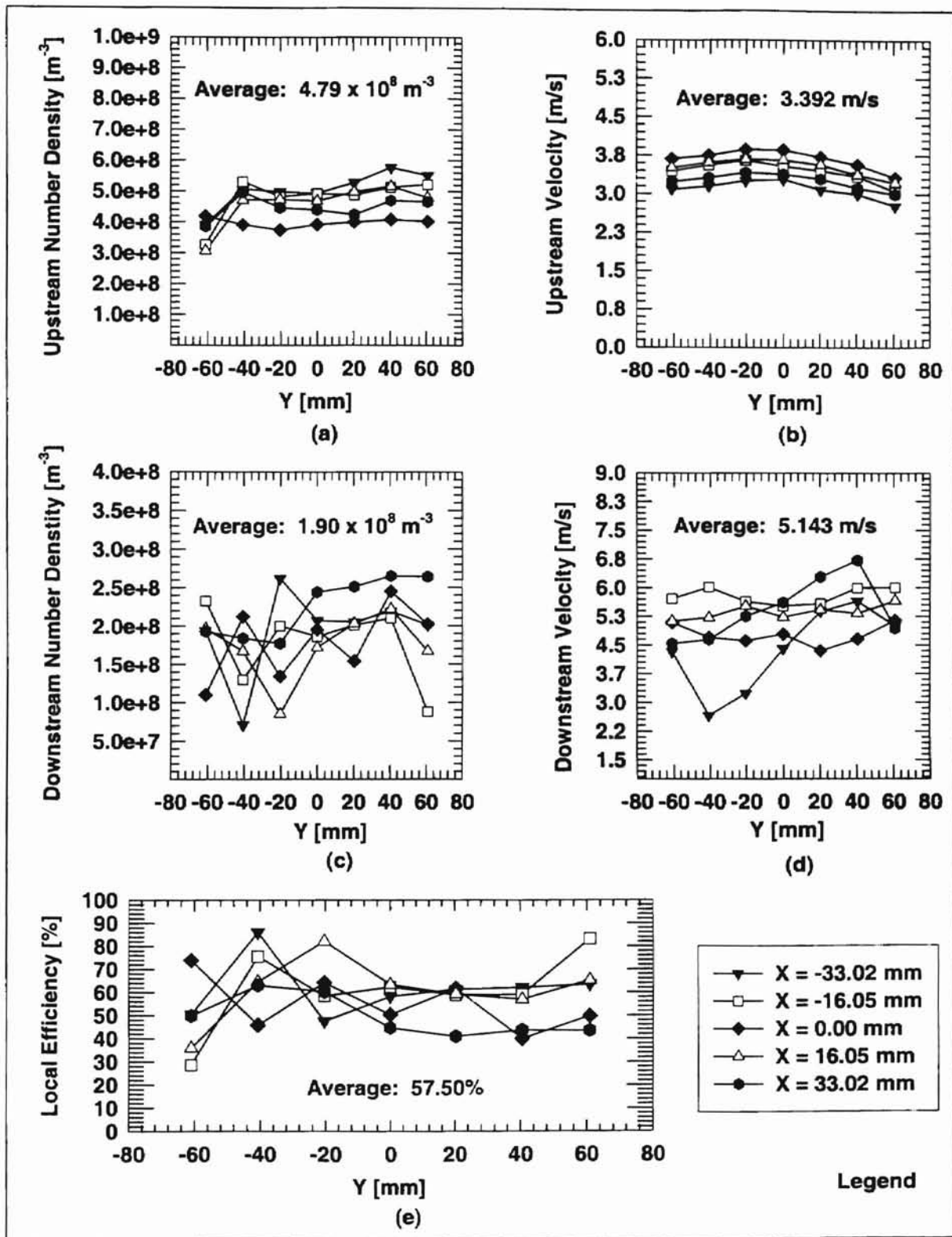


Figure D.12 Electrostatic Charge Effect on Efficiency of Pleated Fibrous Filter:
 (a) Upstream No. Density, (b) Downstream No. Density, (c) Upstream Velocity,
 (d) Downstream Velocity, (e) Local Efficiency. Pressure Drop Δp [mm Water] = 30,
 RH = 42%, Air Temperature [$^{\circ}C$] = 42, Electrostatic Voltage at Filter [v] = 500,
 Air Flow Rate = $145.7 m^3/hr$, Test # ESH100.2, Test Date: 08/25/98.

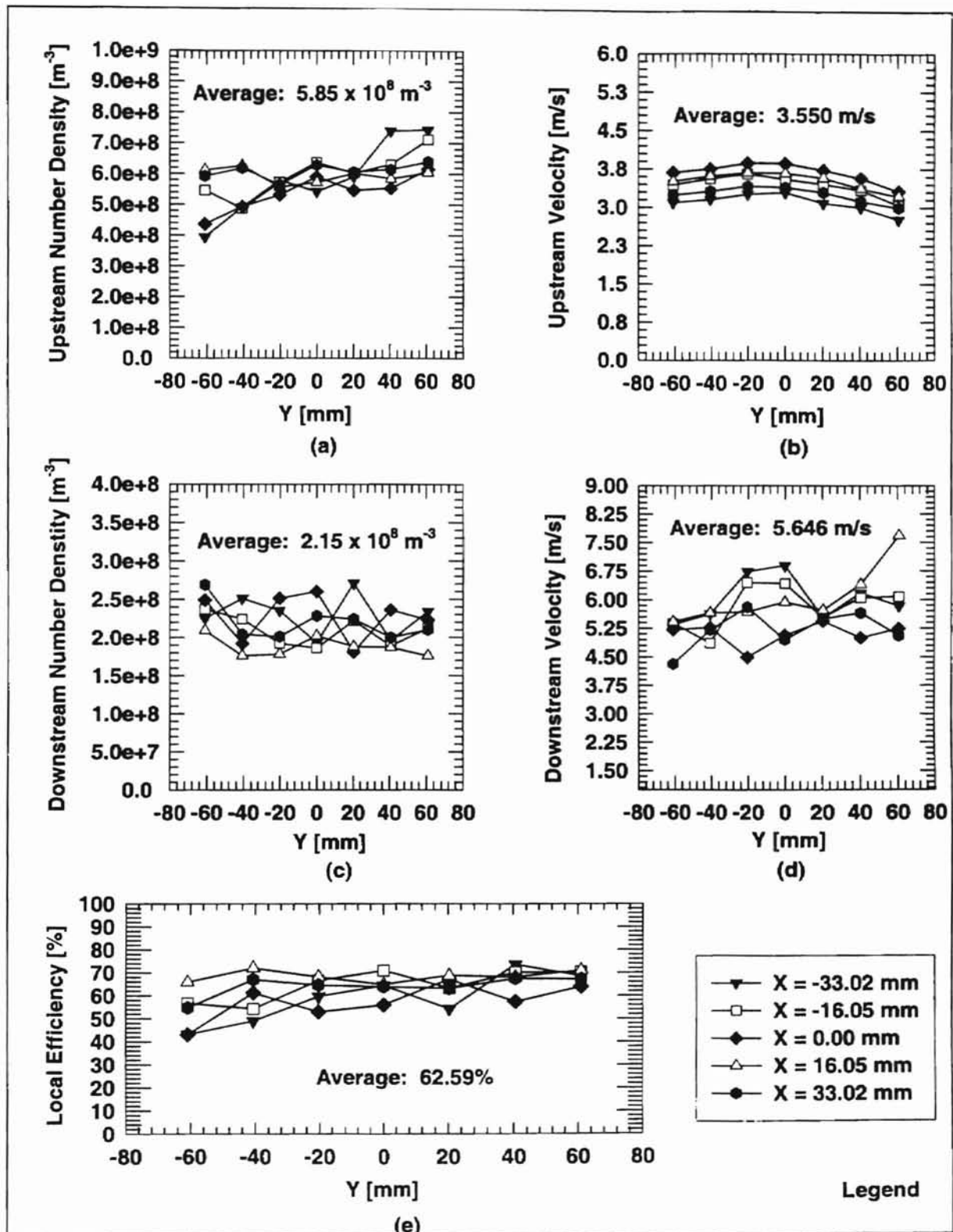


Figure D.13 Electrostatic Charge Effect on Efficiency of Pleated Fibrous Filter:
 (a) Upstream No. Density, (b) Downstream No. Density, (c) Upstream Velocity,
 (d) Downstream Velocity, (e) Local Efficiency. Pressure Drop Δp [mm Water] = 38,
 RH = 45%, Air Temperature [$^{\circ}C$] = 37, Electrostatic Voltage at Filter [v] = 500,
 Air Flow Rate = $187.7 m^3/hr$, Test # ESH125.1, Test Date: 08/28/98.

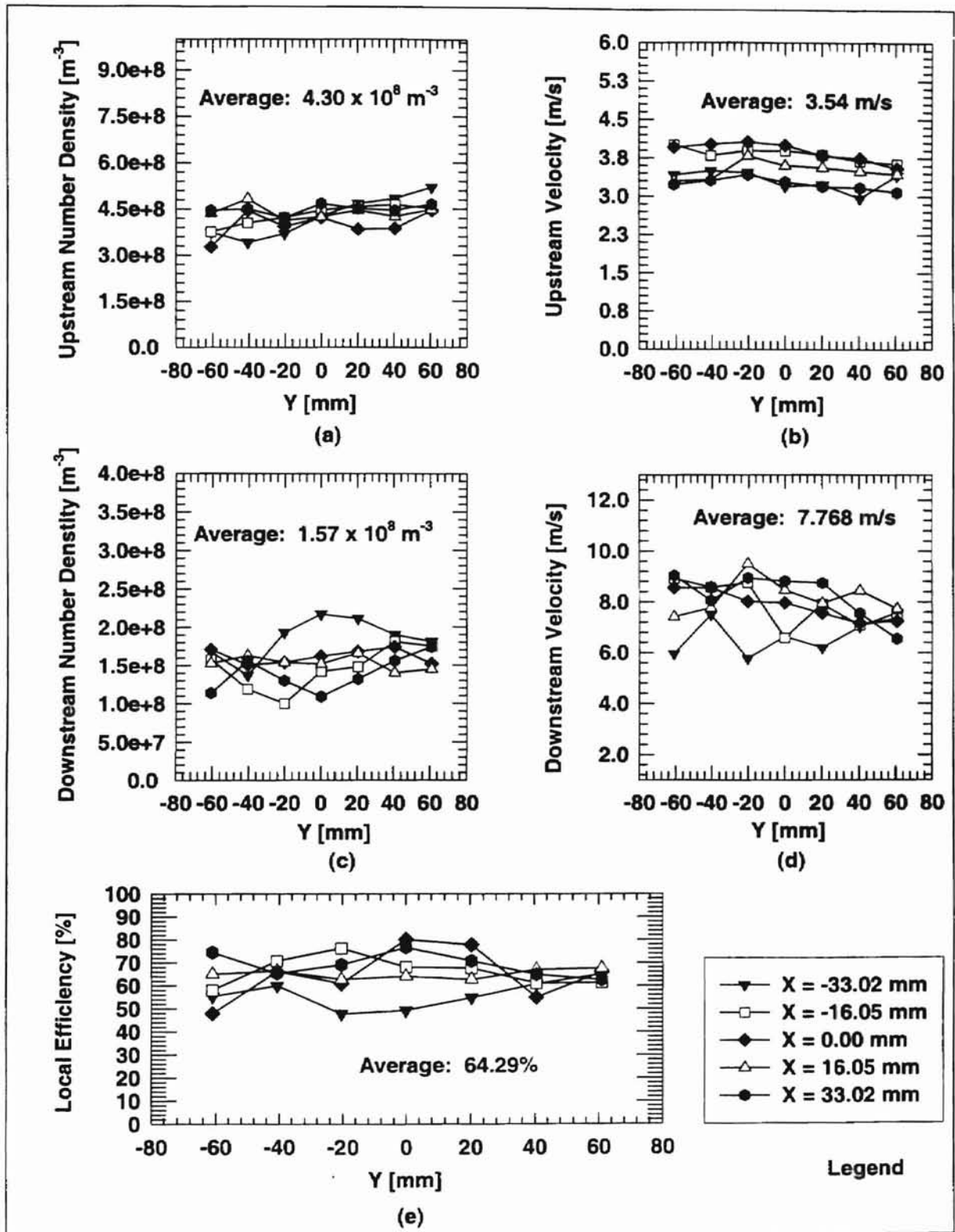


Figure D.14 Electrostatic Charge Effect on Efficiency of Pleated Fibrous Filter:
 (a) Upstream No. Density, (b) Downstream No. Density, (c) Upstream Velocity,
 (d) Downstream Velocity, (e) Local Efficiency. Pressure Drop Δp [mm Water] = 38,
 RH = 45%, Air Temperature [°C] = N/A, Electrostatic Voltage at Filter [V] = 500,
 Air Flow Rate = 187.7 m³/hr, Test # ESH125.2, Test Date: 08/28/98.

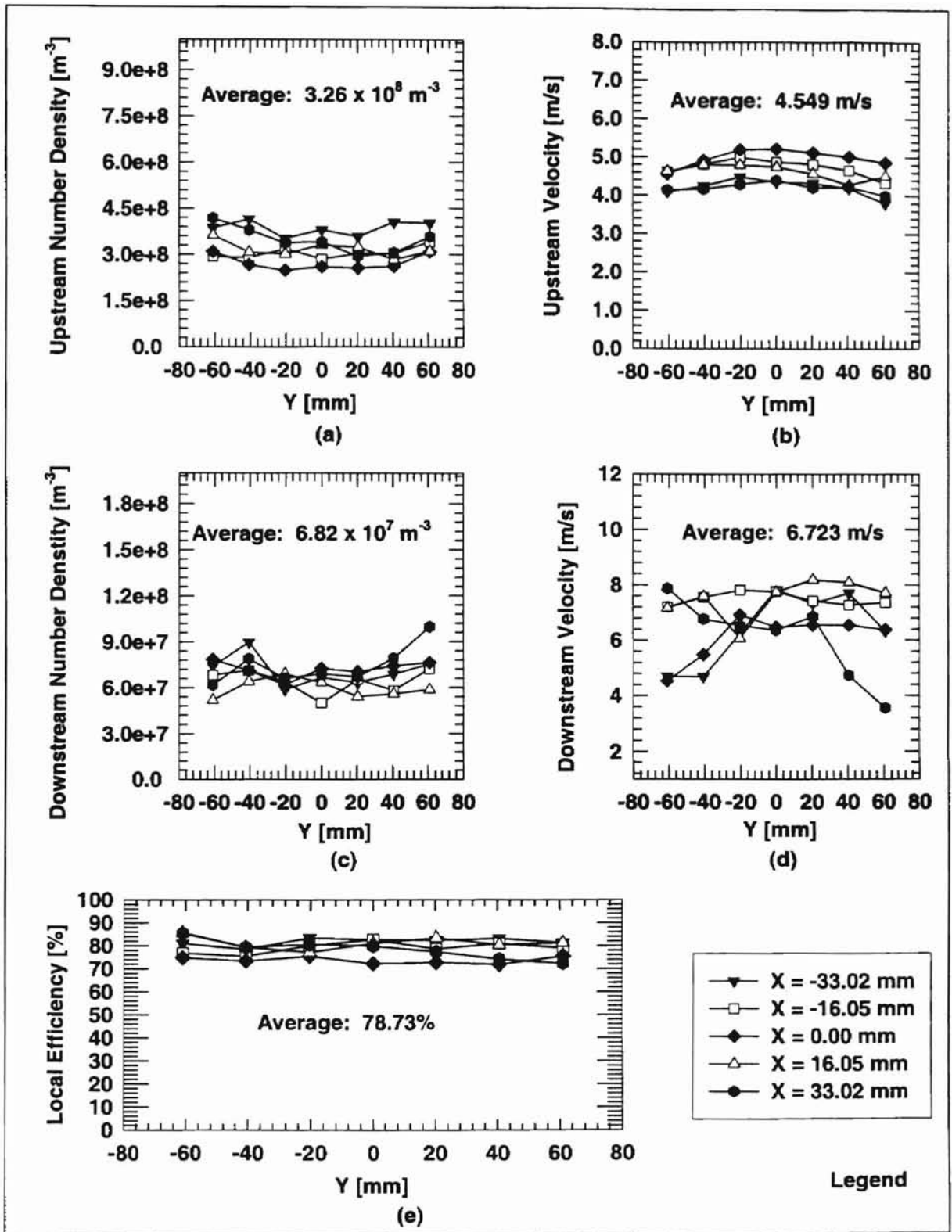


Figure D.15 Electrostatic Charge Effect on Efficiency of Pleated Fibrous Filter:
 (a) Upstream No. Density, (b) Downstream No. Density, (c) Upstream Velocity,
 (d) Downstream Velocity, (e) Local Efficiency. Pressure Drop Δp [mm Water] = 48,
 RH = 50%, Air Temperature [$^{\circ}C$] = N/A, Electrostatic Voltage at Filter [v] = 400,
 Air Flow Rate = 229.7 m^3/hr , Test # ESH150.1, Test Date: 08/27/98.

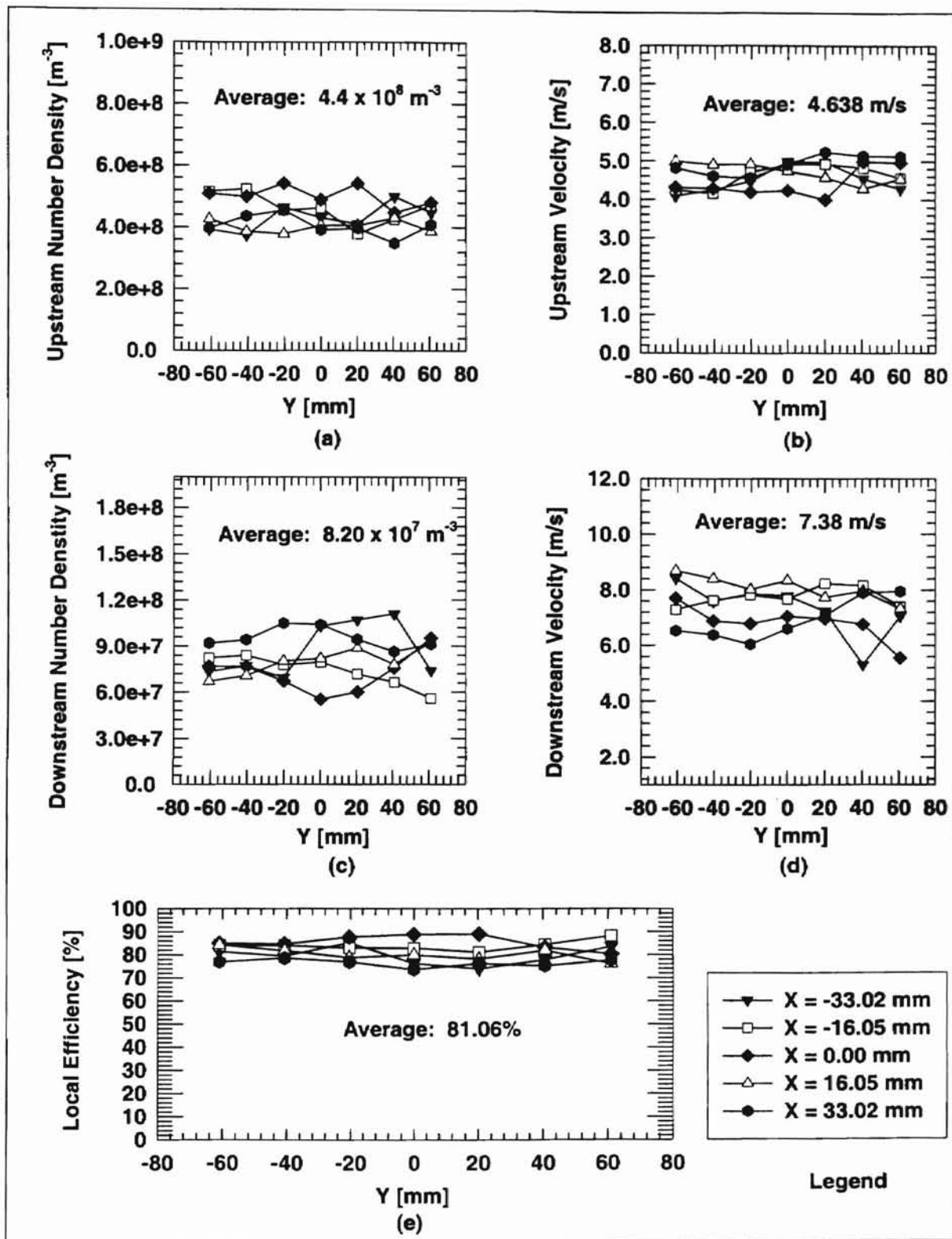


Figure D.16 Electrostatic Charge Effect on Efficiency of Pleated Fibrous Filter:
 (a) Upstream No. Density, (b) Downstream No. Density, (c) Upstream Velocity,
 (d) Downstream Velocity, (e) Local Efficiency. Pressure Drop Δp [mm Water] = 48,
 RH = 50%, Air Temperature [$^{\circ}C$] = 34, Electrostatic Voltage at Filter [v] = 400,
 Air Flow Rate = $229.7 m^3/hr$, Test # ESH150.2, Test Date: 08/27/98.

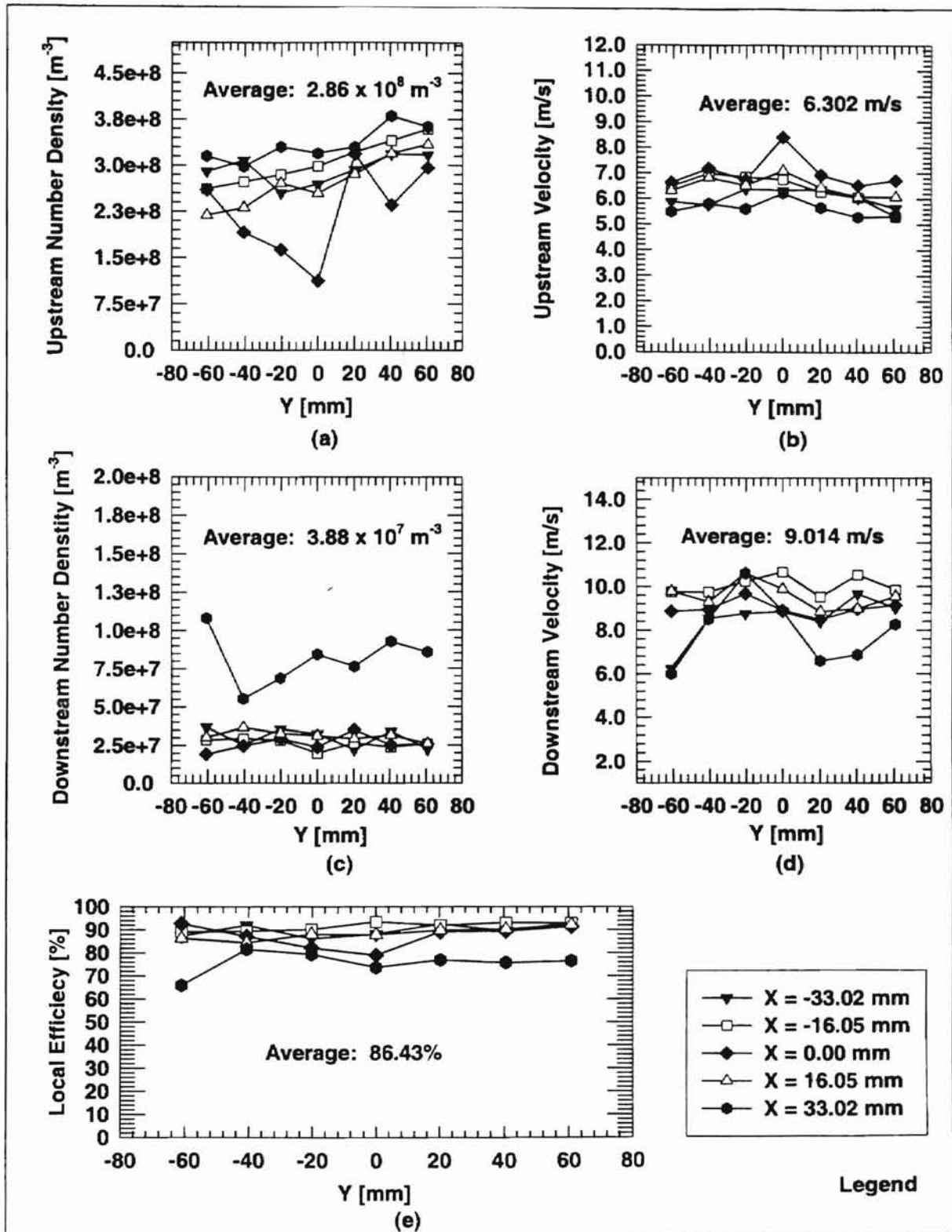


Figure D.17 Electrostatic Charge Effect on Efficiency of Pleated Fibrous Filter:
 (a) Upstream No. Density, (b) Downstream No. Density, (c) Upstream Velocity,
 (d) Downstream Velocity, (e) Local Efficiency. Pressure Drop Δp [mm Water] = 122,
 RH = 50%, Air Temperature [$^{\circ}C$] = 31, Electrostatic Voltage at Filter [v] = 500,
 Air Flow Rate = $313.8 m^3/hr$, Test # ESH200.1, Test Date: 08/27/98.

APPENDIX E

HUMIDITY EFFECTS:

VELOCITY, NUMBER DENSITY AND EFFICIENCY RESULTS FOR 0.966 μm DIAMETER PSL PARTICLES IN THE SMALL ANGLE DIFFUSER HOUSING

Test results for investigating the humidity effects are provided in this appendix. The results are performed at low and high humidities. As discussed in Chapter VI and in the consistency measurement section of Chapter V, low humidity refers to relative humidities below 50% and high humidity refers to those humidity values above 70%. All tests were performed using the 0.966 μm diameter PSL particles under monitored conditions (humidity, temperature, electrostatic charge voltage, pressure drop, etc.) for all of the flow rates. These tests were designed to evaluate the effect of humidity by minimizing/controlling electrostatic charge effects. Those experimental results conducted at low humidities (less than 50%) using electrostatically neutralized particles and neutral filter were also used for comparison with the results of Appendix D to investigate electrostatic charge effects. To minimize/control the unwanted electrostatic charge effects at the filter, the filter housing was grounded as per Fig. 4.15 of Chapter IV. The upstream and downstream local velocity measurements, upstream and downstream local number densities, and local filtration efficiencies are presented herein.

The experimental tests on the effect of humidity using electrostatically neutralized

PSL particles for each flow rate are alphanumerically designated. For example, NESH10.4 designates a test carried out on electrostatically neutralized particles at 10 scfm (13.53 m³/hr) in the small angle diffuser housing. Thus NE stands for an electrostatically neutralized condition (PSL particles, housing, and filter) and SH stands for the small angle diffuser housing in which the test was conducted. The numeral 4 after the decimal point indicates the fourth test conducted to test humidity effects at the indicated flow rate at either low (less than 50%) or high (greater than 70%) relative humidity. A Summary of test conditions for all of the tests shown in this appendix is given in Tables 6.3 and 6.4.

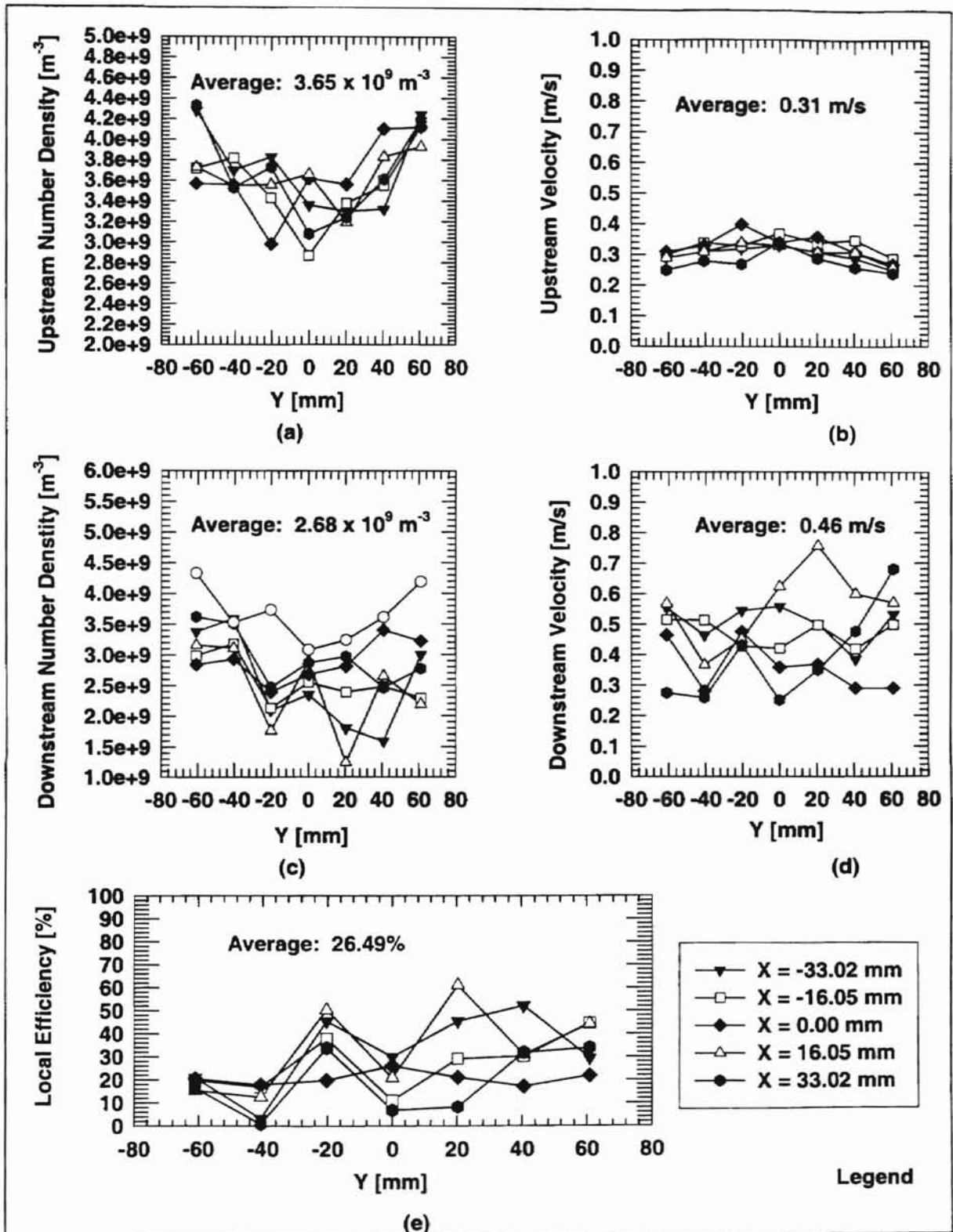


Figure E.1 Humidity Effect on Efficiency of Electrostatically Neutral Pleated Fibrous Filter: (a) Upstream No. Density, (b) Downstream No. Density, (c) Upstream Velocity, (d) Downstream Velocity, (e) Local Efficiency. Pressure Drop Δp [mm Water] = 3, RH = 43.5%, Air Temperature [$^{\circ}C$] = 38, Air Flow Rate = $13.5 m^3/hr$, Test # NESH10.1, Test Date: 03/22/98.

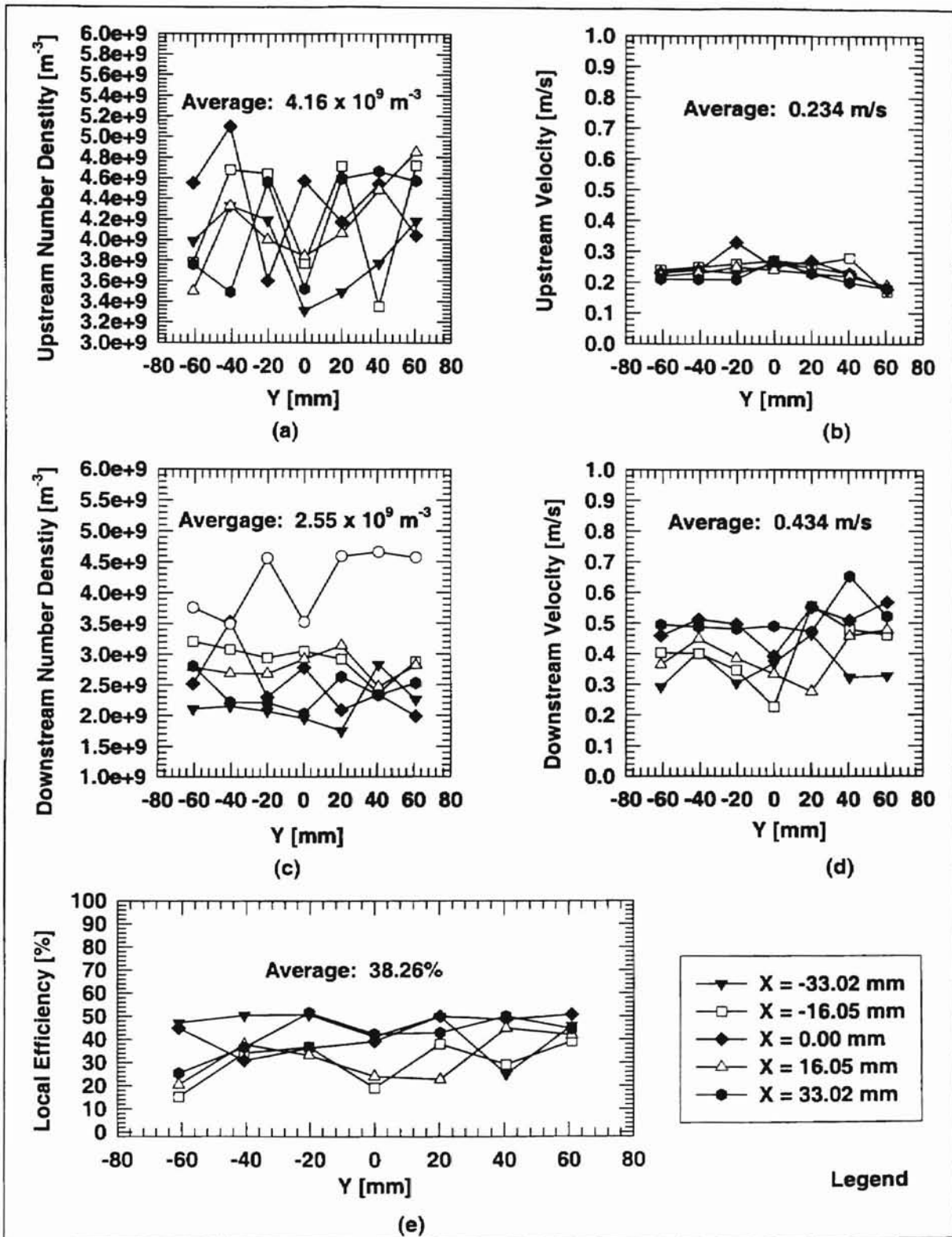


Figure E.2 Humidity Effect on Efficiency of Electrostatically Neutral Pleated Fibrous Filter: (a) Upstream No. Density, (b) Downstream No. Density, (c) Upstream Velocity, (d) Downstream Velocity, (e) Local Efficiency. Pressure Drop Δp [mm Water] = 3, RH = 95%, Air Temperature [$^{\circ}C$] = 27, Air Flow Rate = $13.5 m^3/hr$, Test # NESH10.2, Test Date: 03/22/98.

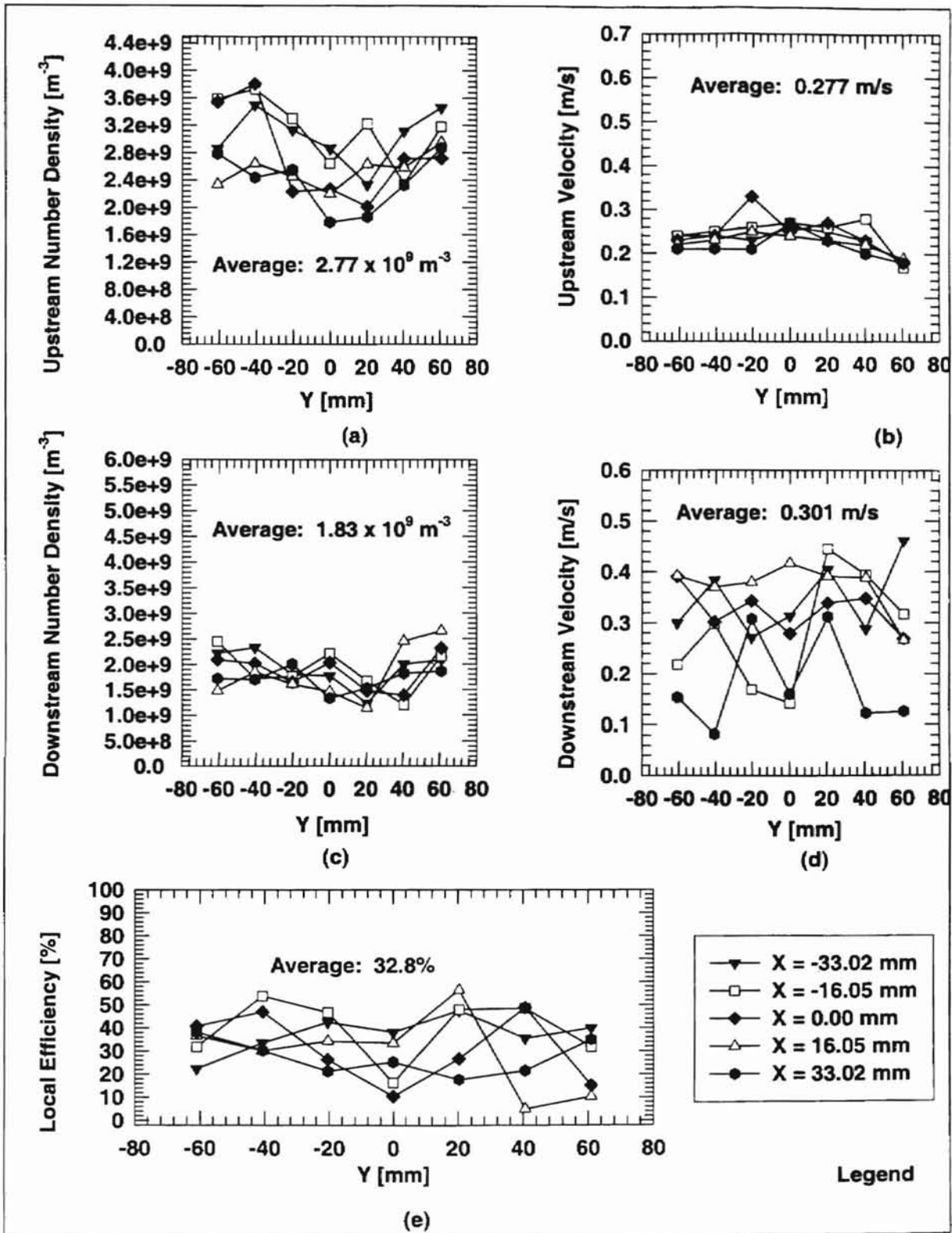


Figure E.3 Humidity Effect on Efficiency of Electrostatically Neutral Pleated Fibrous Filter: (a) Upstream No. Density, (b) Downstream No. Density, (c) Upstream Velocity, (d) Downstream velocity, (e) Local Efficiency. Pressure Drop Δp [mm Water] = 3, RH = 45%, Air Temperature [$^{\circ}C$] = 39, Air Flow Rate = 13.5 m^3/hr , Test # NESH10.3, Test Date: 08/15/98.

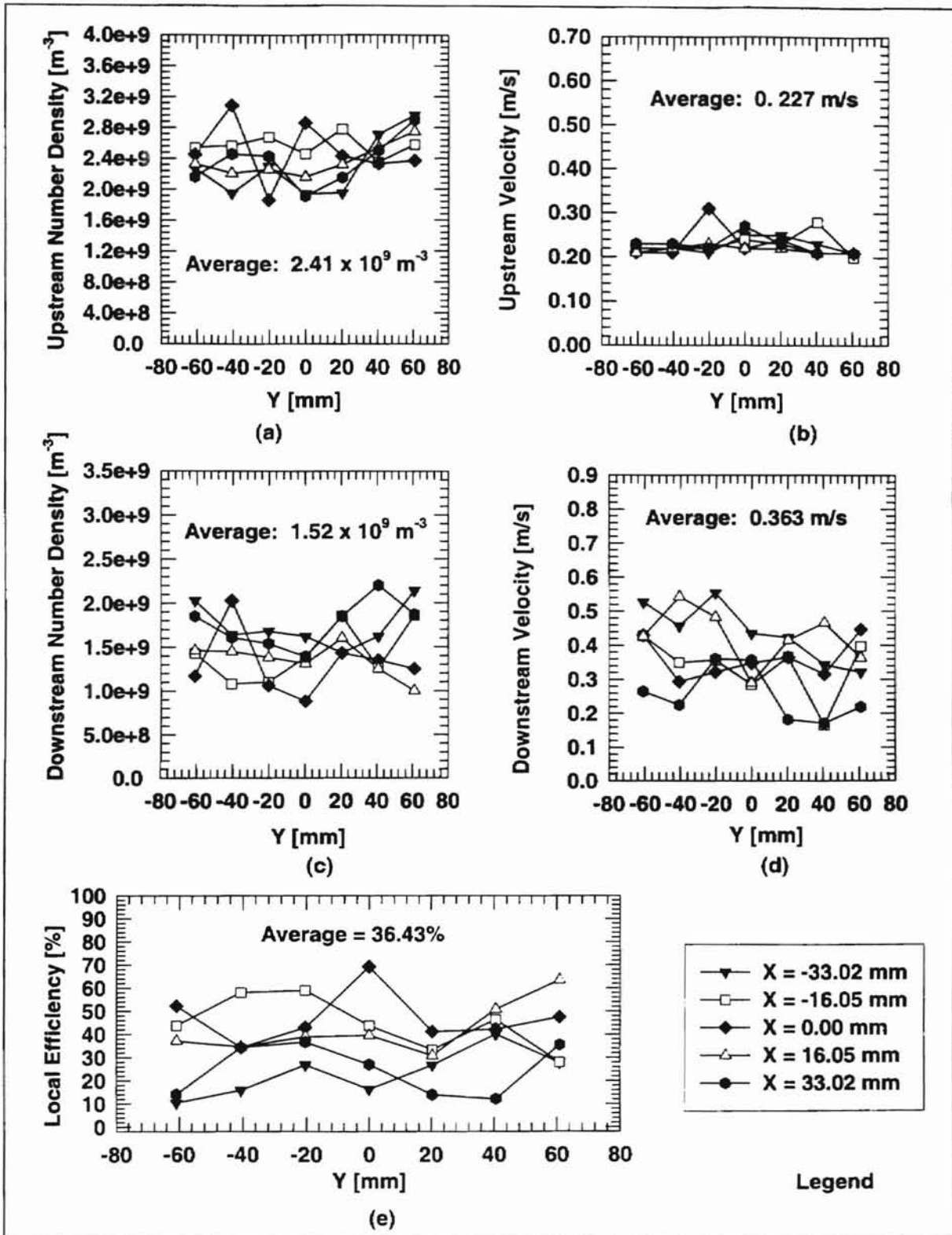


Figure E.4 Humidity Effect on Efficiency of Electrostatically Neutral Pleated Fibrous Filter: (a) Upstream No. Density, (b) Downstream No. Density, (c) Upstream Velocity, (d) Downstream Velocity, (e) Local Efficiency. Pressure Drop Δp [mm Water] = 3, RH = 85%, Air Temperature [$^{\circ}C$] = 29, Air Flow Rate = 13.5 m^3/hr , Test # NESH10.4, Test Date: 08/15/98.

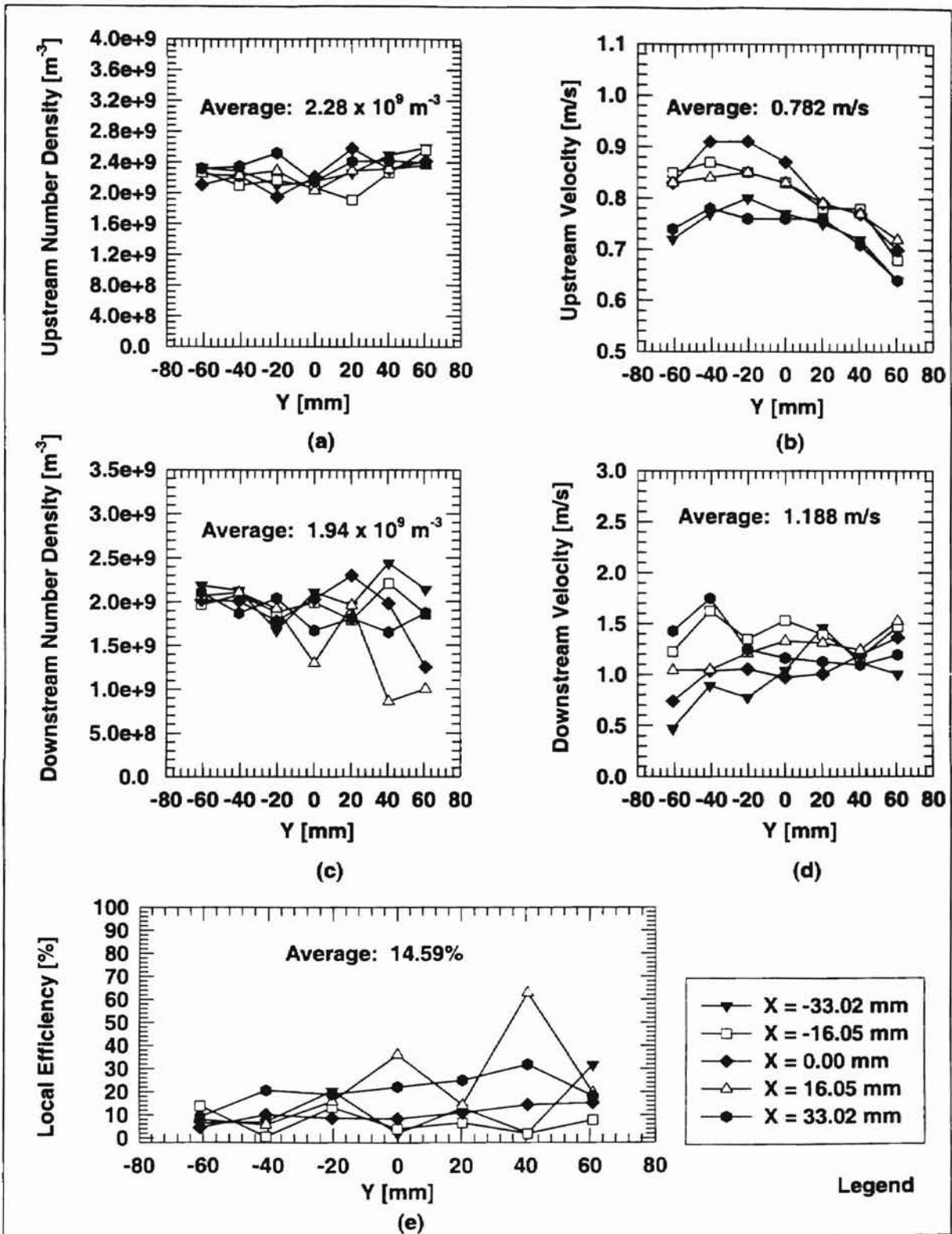


Figure E.5 Humidity Effect on Efficiency of Electrostatically Neutral Pleated Fibrous Filter: (a) Upstream No. Density, (b) Downstream No. Density, (c) Upstream Velocity, (d) Downstream Velocity, (e) Local Efficiency. Pressure Drop Δp [mm Water] = 5, RH = 35%, Air Temperature [$^{\circ}C$] = 43, Air Flow Rate = $29.5 m^3/hr$, Test # NESH20.1, Test Date: 06/18/98.

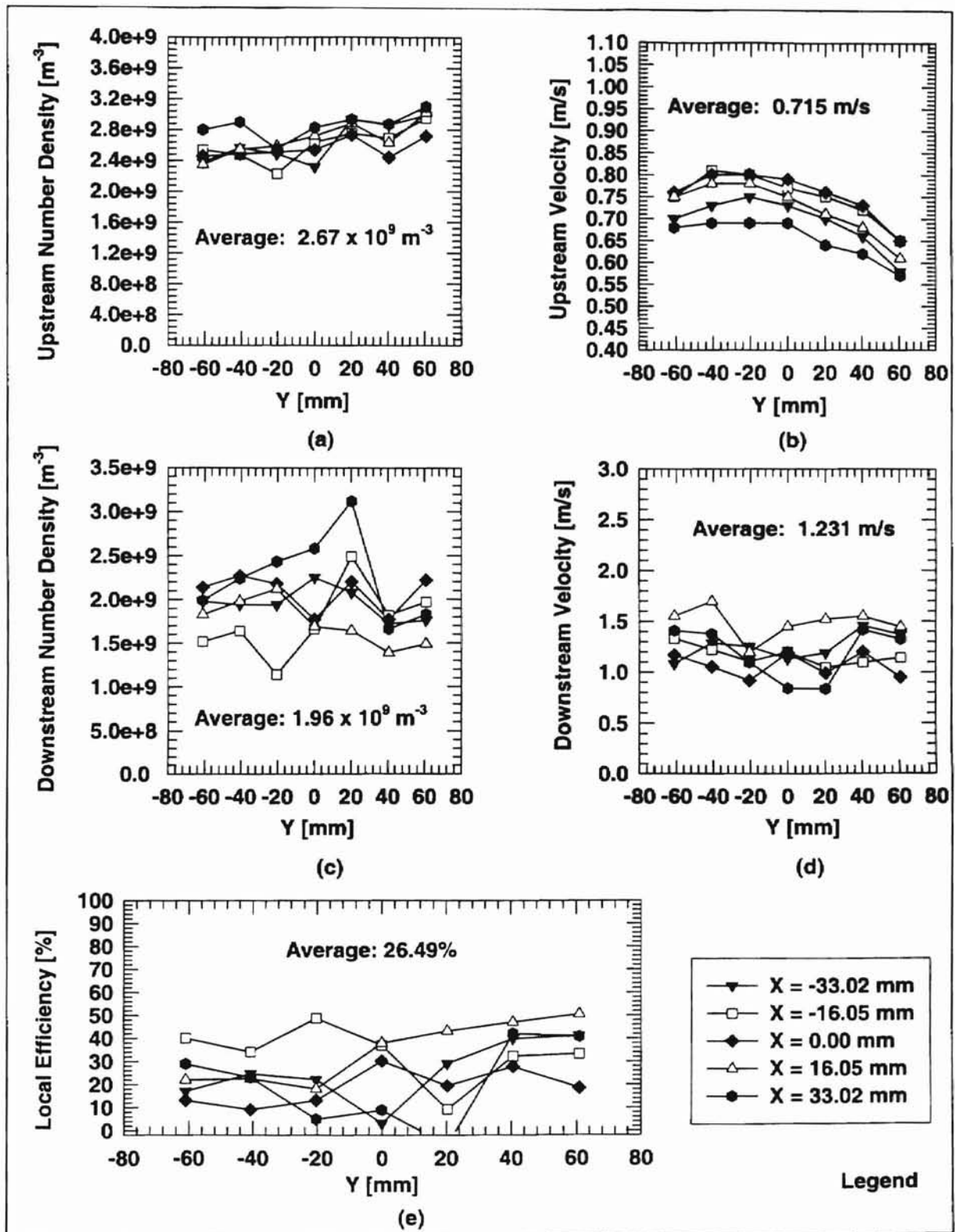


Figure E.6 Humidity Effects on Efficiency of Electrostatically Neutral Pleated Fibrous Filter: (a) Upstream No. Density, (b) Downstream No. Density, (c) Upstream Velocity, (b) Downstream Velocity, (e) Local Efficiency. Pressure Drop Δp [mm Water] = 5, RH= 31.5%, Air Temperature [$^{\circ}C$] = 48, Air Flow Rate = 29.5 m^3/hr , Test # NESH20.2, Test Date: 07/06/98.

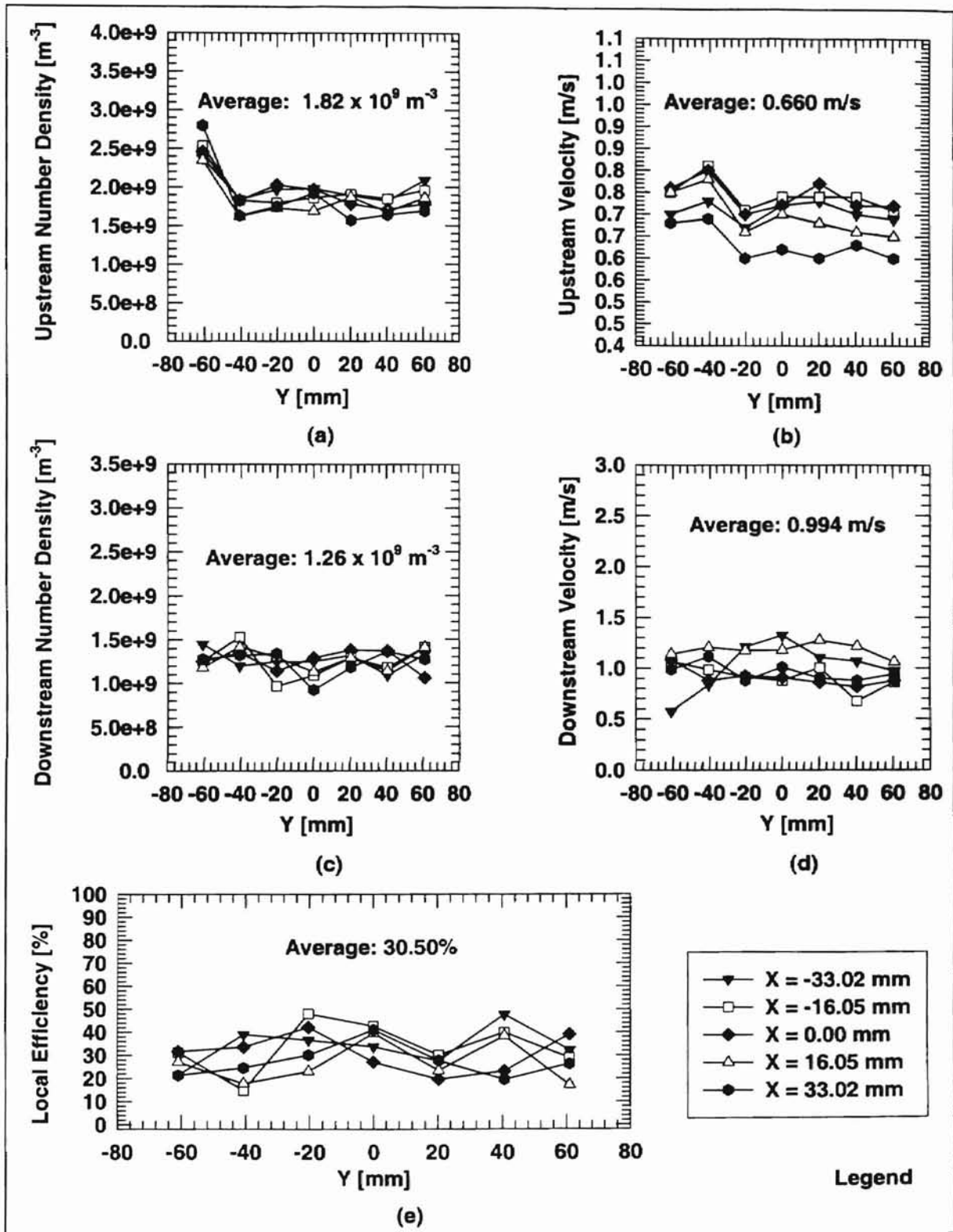


Figure E.7 Humidity Effect on Efficiency of Electrostatically Neutral Pleated Fibrous Filter: (a) Upstream No. Density, (b) Downstream No. Density, (c) Upstream Velocity, (d) Downstream Velocity, (e) Local Efficiency. Pressure Drop Δp [mm Water] = 5, RH = 79%, Temperature [$^{\circ}C$] = 35, Air Flow Rate = $29.5 m^3/hr$, Test # NESH20.3, Test Date: 07/06/98.

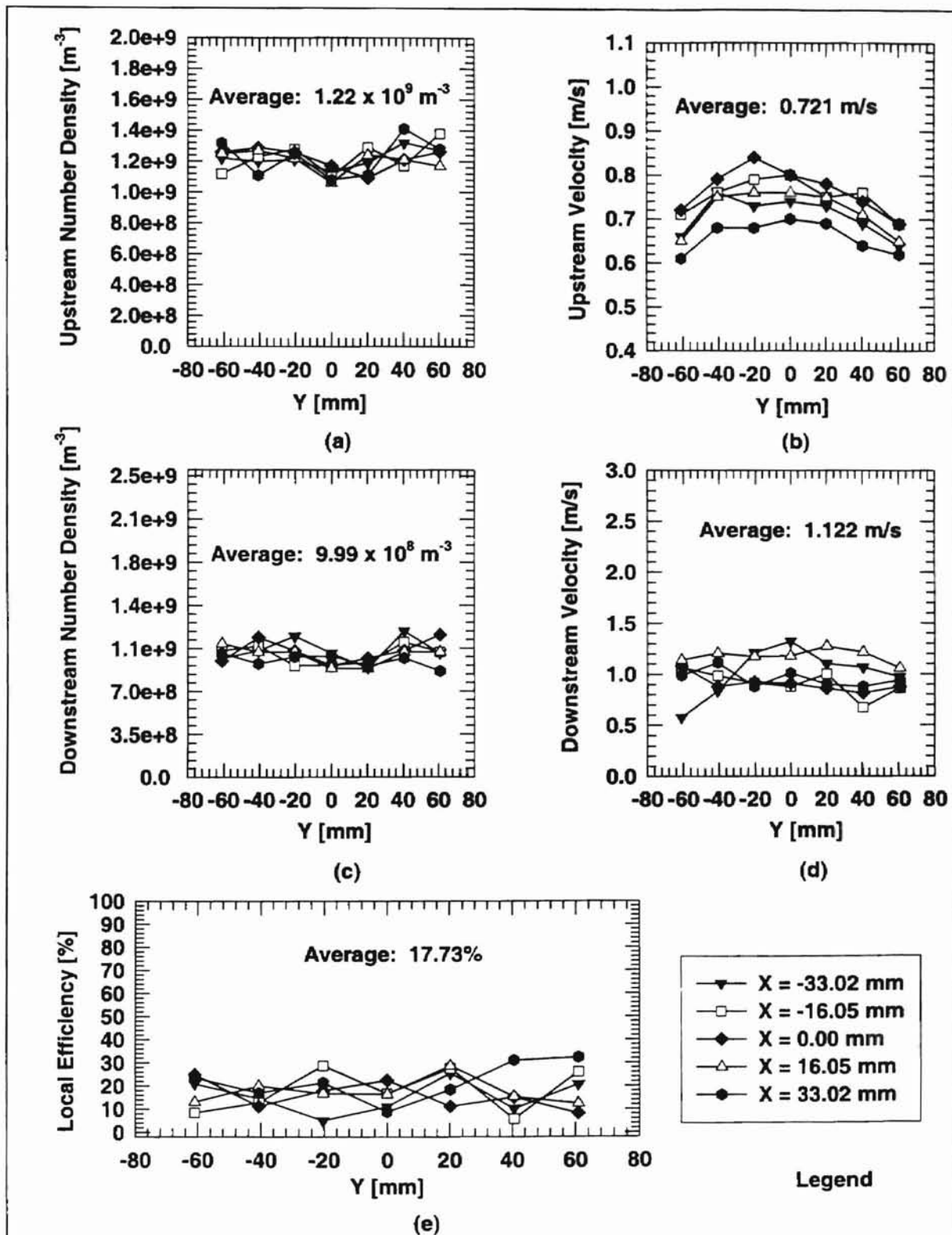


Figure E.8 Humidity Effect on Efficiency of Electrostatically Neutral Pleated Fibrous Filter: (a) Upstream No. Density, (b) Downstream No. Density, (c) Upstream Velocity, (d) Downstream Velocity, (e) Local Efficiency. Pressure Drop Δp [mm Water] = 5, RH = 33%, Air Temperature [$^{\circ}C$] = 43, Air Flow Rate = $29.5 m^3/hr$, Test # NESH20.4, Test Date: 06/22/98.

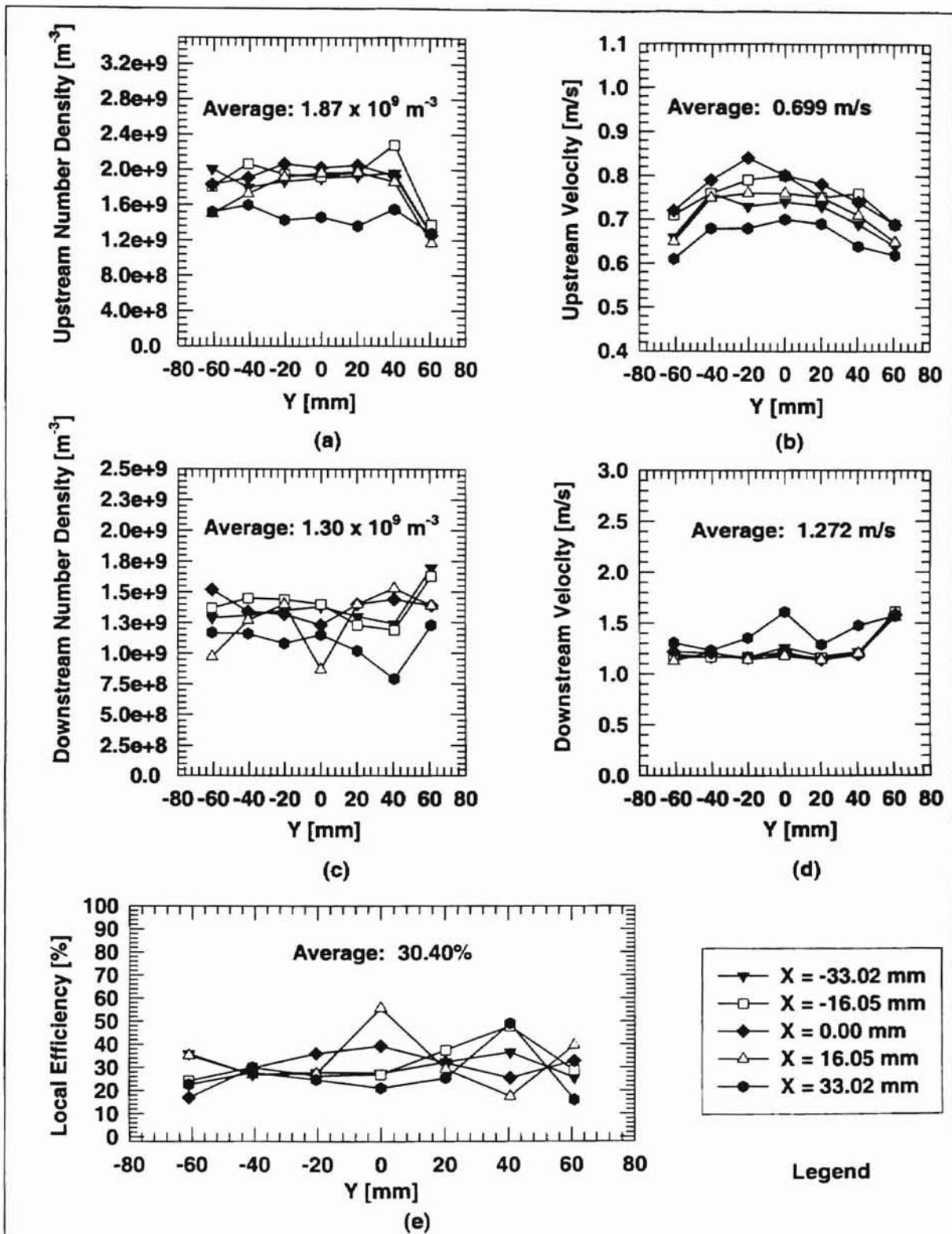


Figure E.9 Humidity Effect on Efficiency of Electrostatically Neutral Pleated Fibrous Filter: (a) Upstream No. Density, (b) Downstream No. Density, (c) Upstream Velocity, (d) Downstream Velocity, (e) Local Efficiency. Pressure Drop Δp [mm Water] = 5, RH = 80%, Air Temperature [$^{\circ}C$] = 31, Air Flow Rate = $29.5 m^3/hr$, Test # NESH20.5, Test Date: 07/22/98.

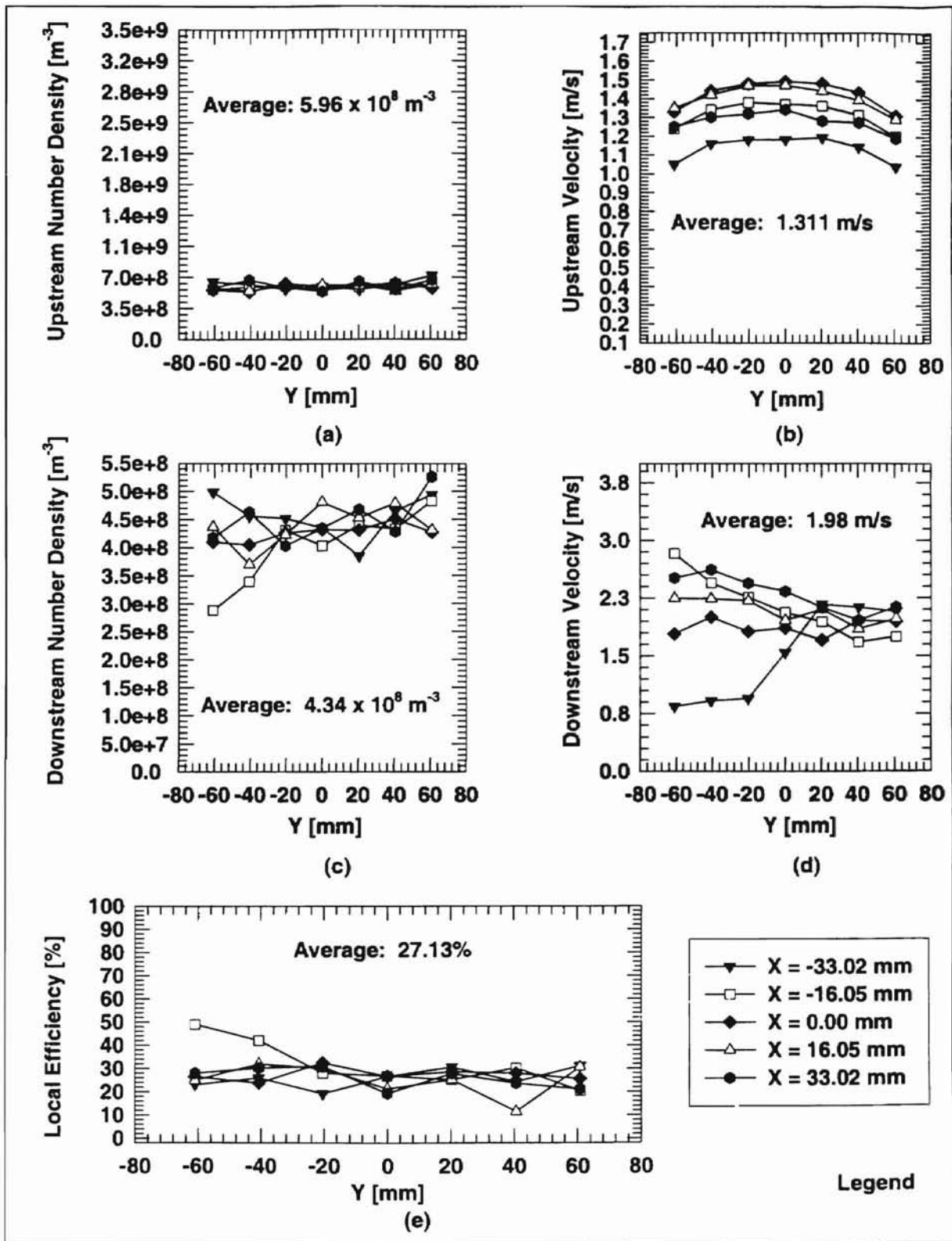


Figure E.10 Humidity Effect on Efficiency of Electrostatically Neutral Pleated Fibrous Filter: (a) Upstream No. Density, (b) Downstream No. Density, (c) Upstream Velocity, (d) Downstream Velocity, (e) Local Efficiency. Pressure Drop Δp [mm Water] = 5, RH = 17%, Air Temperature [$^{\circ}C$] = 55, Air Flow Rate = $60.81 m^3/hr$, Test # NESH40.1, Test Date: 03/01/98.

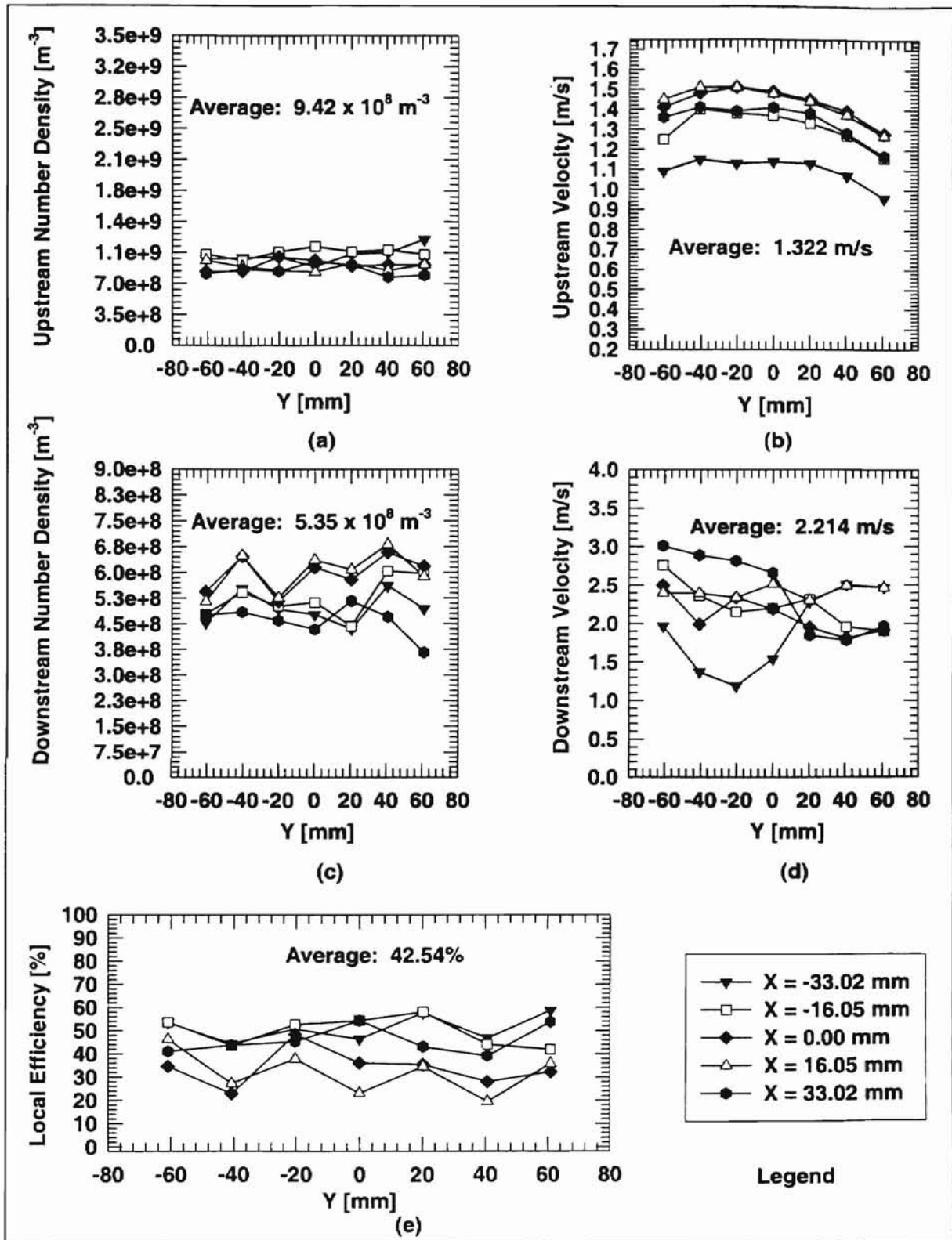


Figure E.11 Humidity Effect on Efficiency of Electrostatically Neutral Pleated Fibrous Filter: (a) Upstream No. Density, (b) Downstream No. Density, (c) Upstream Velocity, (d) Downstream Velocity, (e) Local Efficiency. Pressure Drop Δp [mm Water] = 5, RH = 85%, Air Temperature [$^{\circ}C$] = 37, Air Flow Rate = 60.81 m^3/hr , Test # NES40.2, Test Date: 03/05/98.

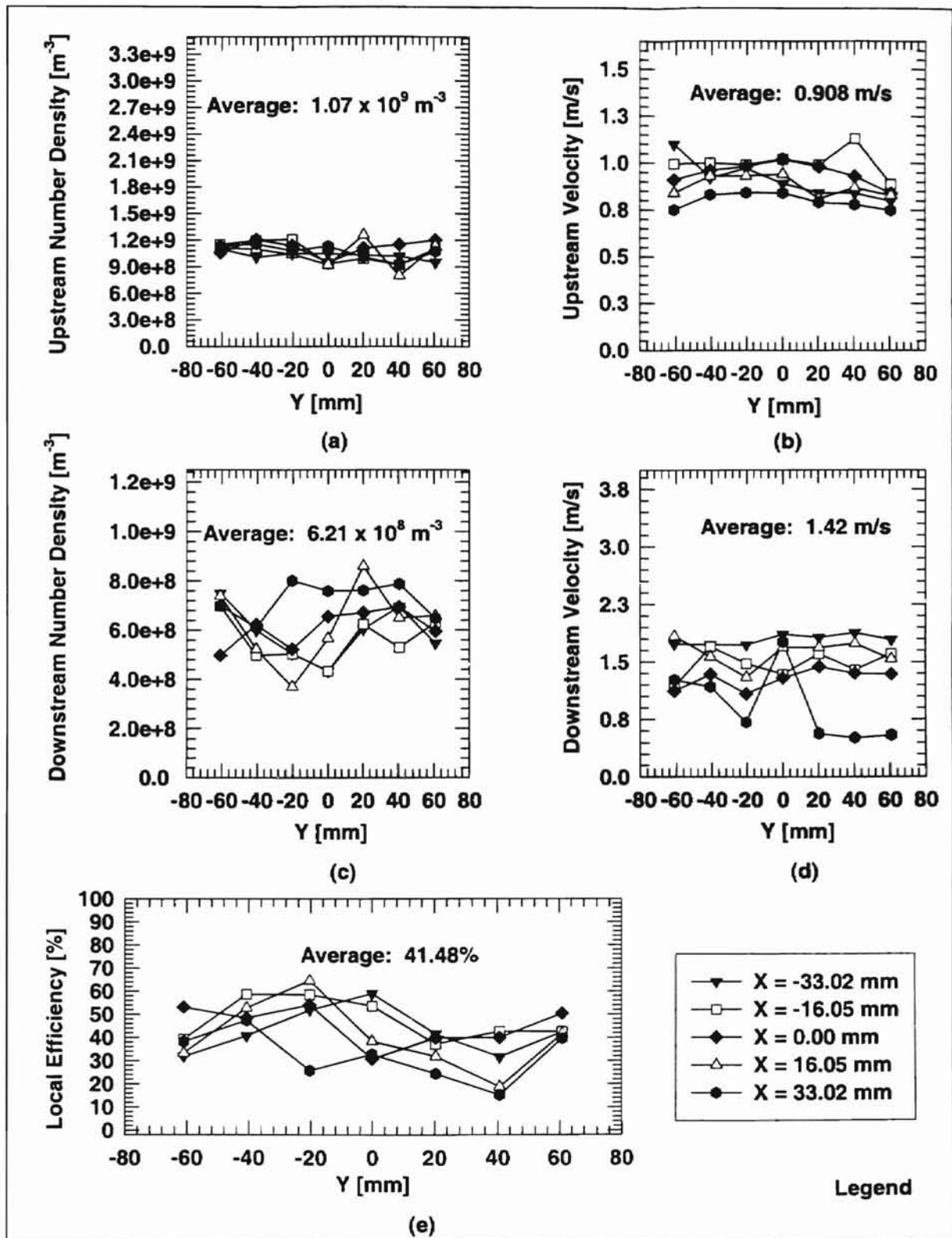


Figure E.12 Humidity Effect on Efficiency of Electrostatically Neutral Pleated Fibrous Filter
 (a) Upstream No. Density, (b) Downstream No. Density, (c) Upstream Velocity,
 (d) Downstream Velocity, (e) Local Efficiency. Pressure Drop Δp [mm Water] = 5,
 RH = 85%, Air Temperature [$^{\circ}C$] = 38, Air Flow Rate = 60.81 m^3/hr , Test # NESH40.3,
 Test Date: 08/16/98.

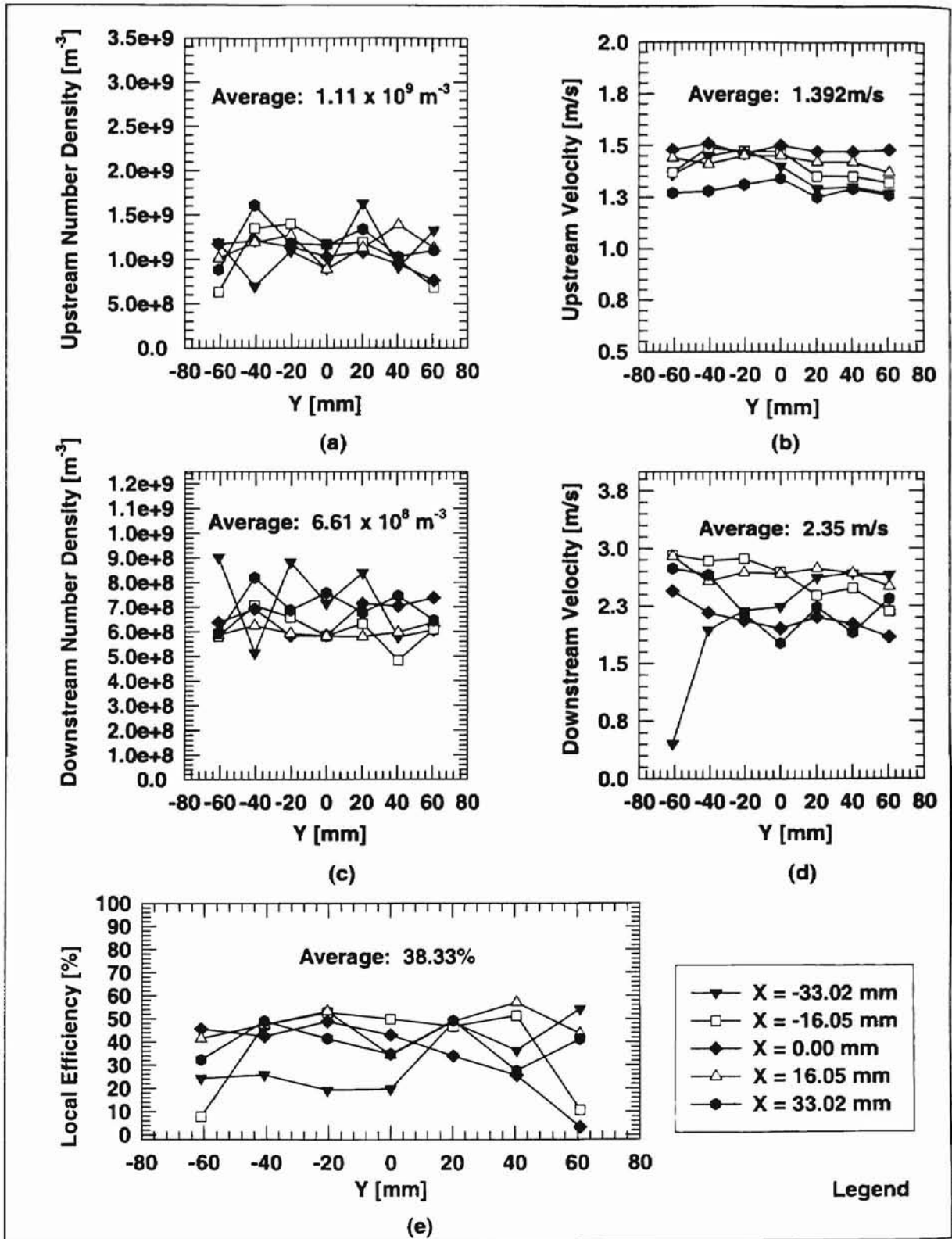


Figure E.13 Humidity Effect on Efficiency of Electrostatically Neutral Pleated Fibrous Filter: (a) Upstream No. Density, (b) Downstream No. Density, (c) Upstream Velocity, (d) Downstream Velocity, (e) Local Efficiency. Pressure Drop Δp [mm Water] = 5, RH = 35%, Air Temperature [$^{\circ}C$] = 53, Air Flow Rate = $60.81 m^3/hr$, Test # NESH40.4, Test Date: 06/22/98.

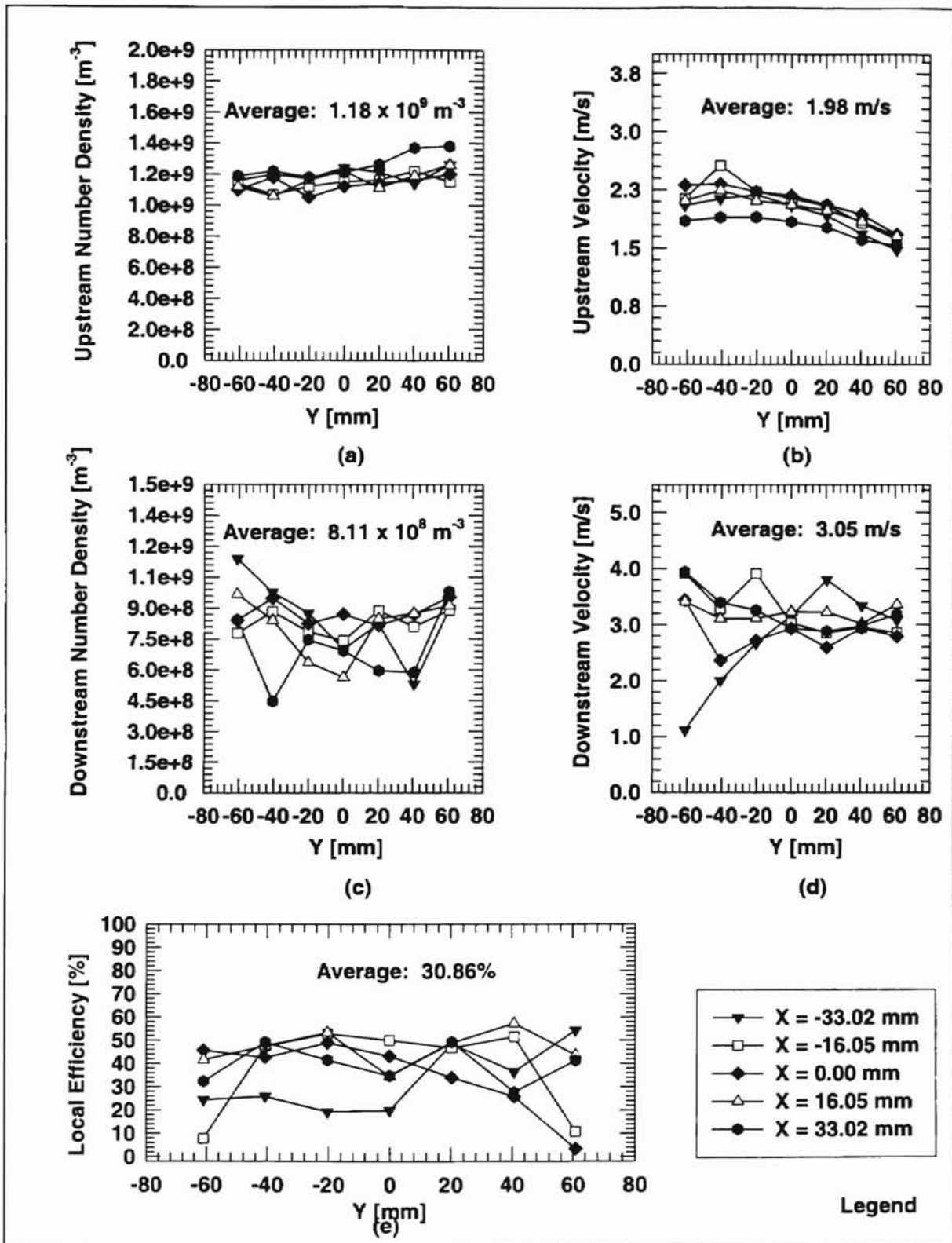


Figure E.14 Humidity Effect on Efficiency of Electrostatically Neutral Pleated Fibrous Filter: (a) Upstream No. Density, (b) Downstream No. Density, (c) Upstream Velocity, (d) Downstream Velocity, (e) Local Efficiency. Pressure Drop Δp [mm Water] = 5, RH = 42%, Air Temperature [$^{\circ}C$] = 46, Air Flow Rate = $77.1 m^3/hr$, Test # NESH50.1, Test Date: 06/11/98.

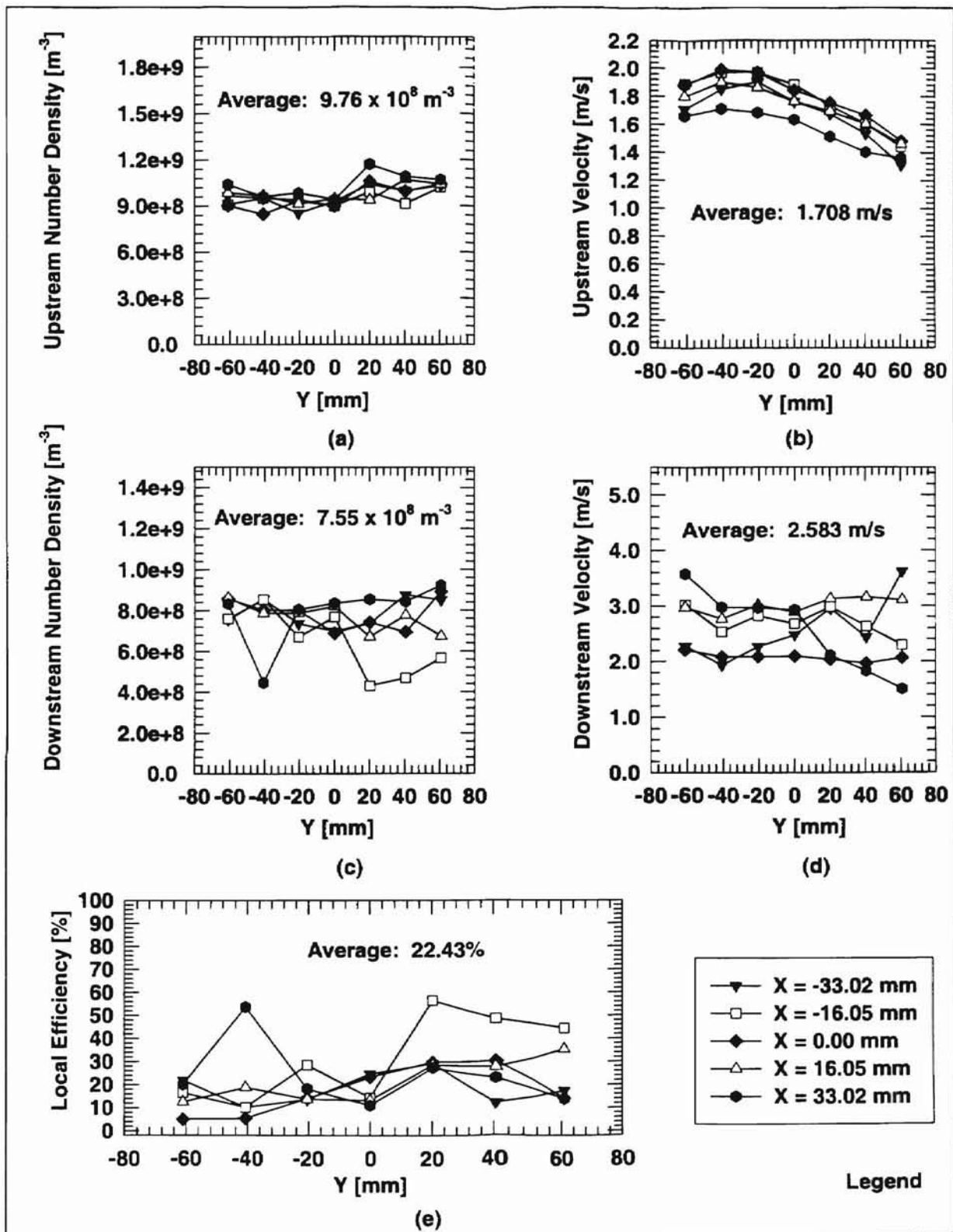


Figure E.15 Humidity Effect on Efficiency of Electrostatically Neutral Pleated Fibrous Filter: (a) Upstream No. Density, (b) Downstream No. Density, (c) Upstream Velocity, (d) Downstream Velocity, (e) Local Efficiency. Pressure Drop Δp [mm Water] = 8, RH = 35%, Air Temperature [$^{\circ}C$] = 53, Air Flow Rate = $77.1 m^3/hr$, Test # NESH50.2, Test Date: 06/13/98.

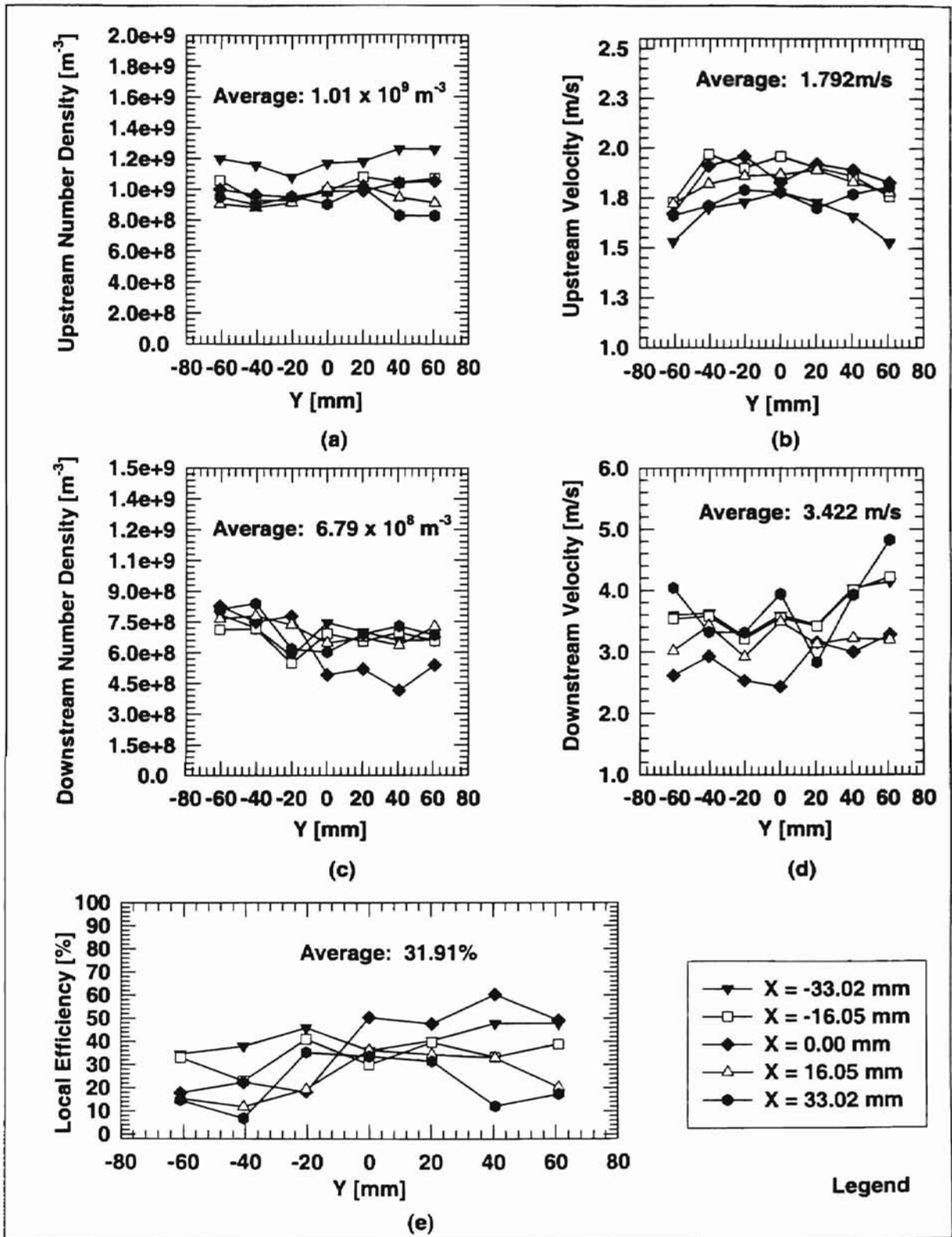


Figure E.16 Humidity Effect on Efficiency of Electrostatically Neutral Pleated Fibrous Filter: (a) Upstream No. Density, (b) Downstream No. Density, (c) Upstream Velocity, (d) Downstream Velocity, (e) Local Efficiency. Pressure Drop Δp [mm Water] = 8, RH = 80%, Air Temperature [°C] = 34, Air Flow Rate = 77.1 m³/hr, Test # NESH50.3, Test Date: 06/13/98.

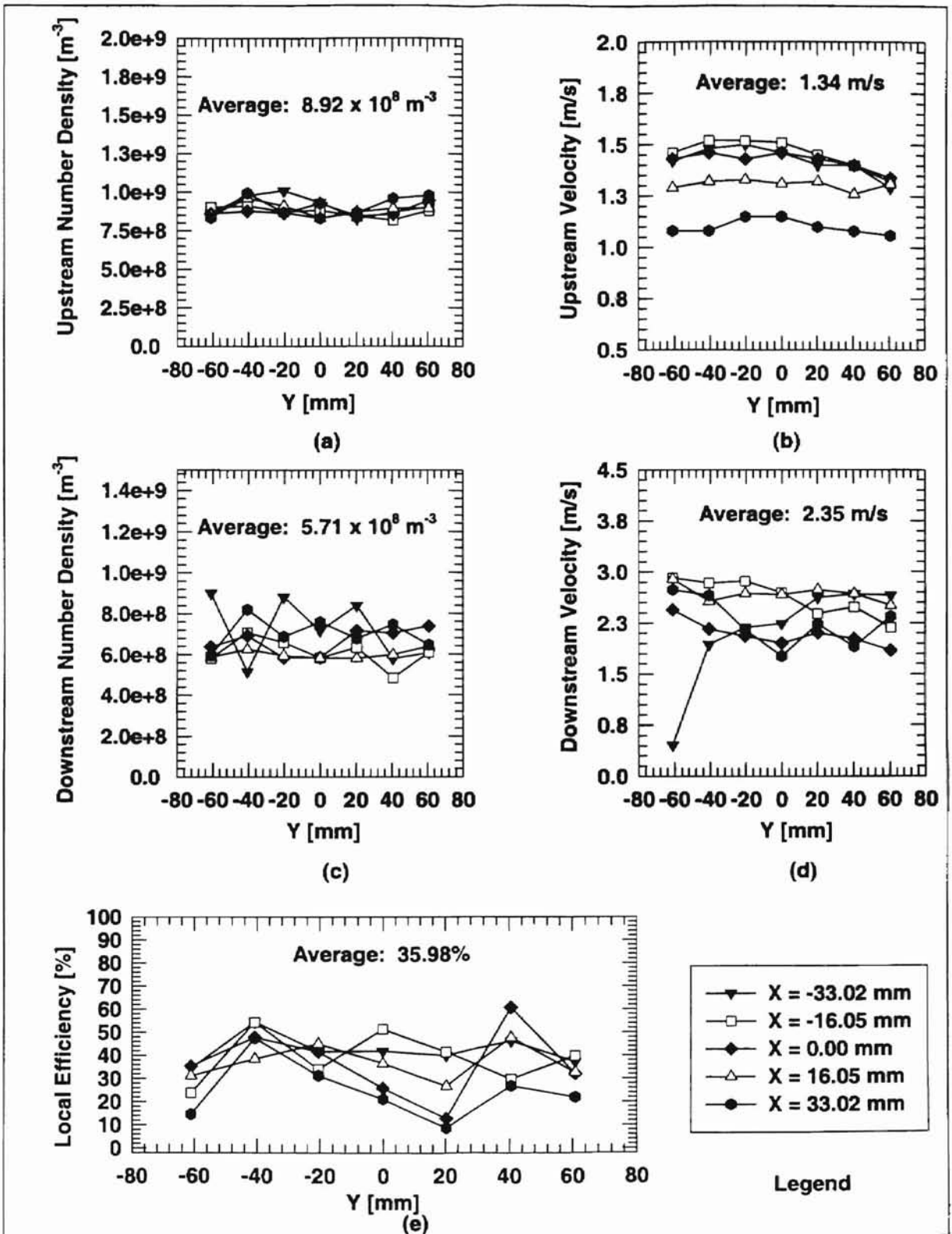


Figure E.17 Humidity Effect on Efficiency of Electrostatically Neutral Pleated Fibrous Filter: (a) Upstream No. Density, (b) Downstream No. Density, (c) Upstream Velocity, (d) Downstream Velocity, (e) Local Efficiency. Pressure Drop Δp [mm Water] = 8, RH = 85%, Air Temperature [$^{\circ}C$] = 35, Air Flow Rate = $77.1 m^3/hr$, Test # NESH50.4, Test Date: 08/16/98.

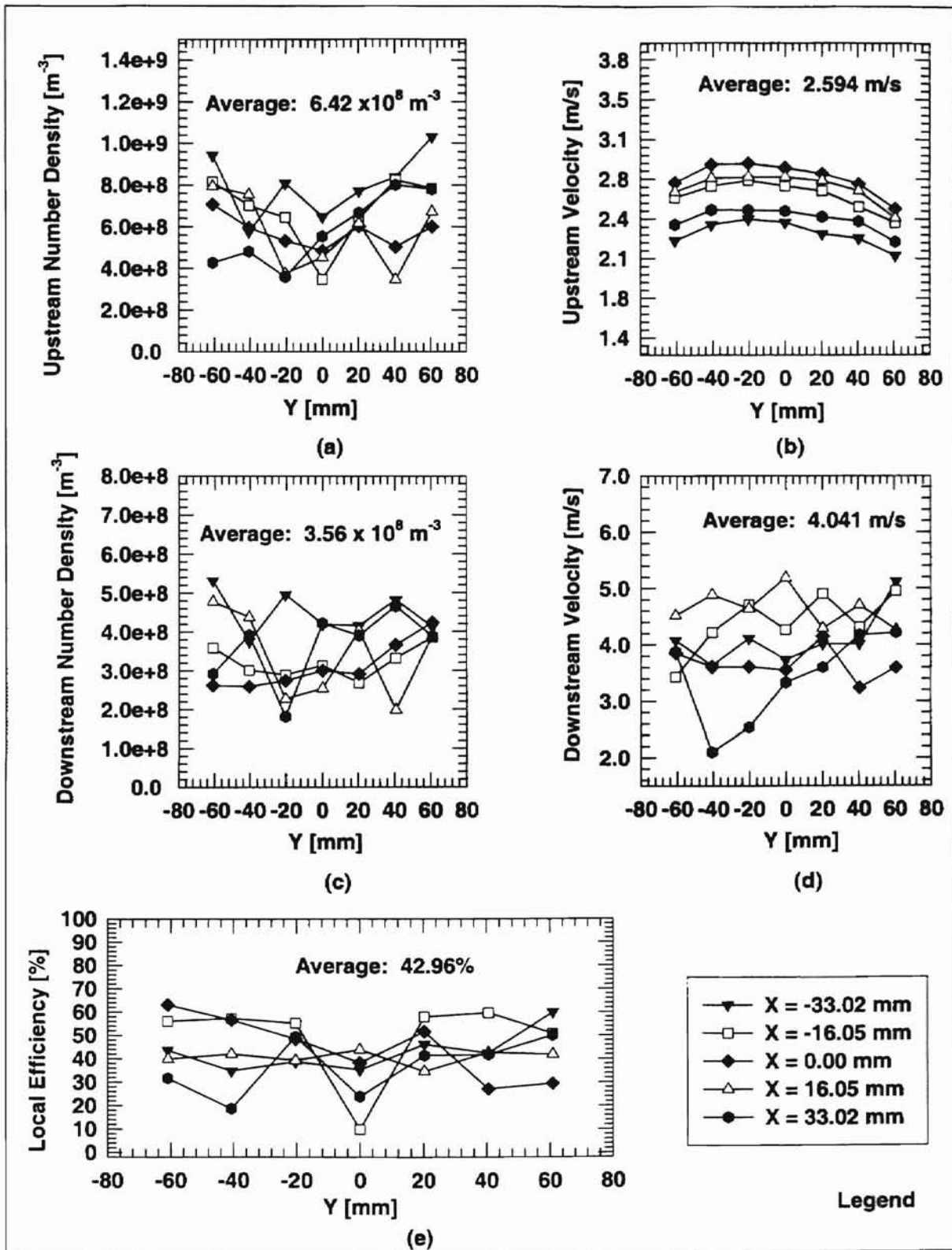


Figure E.18 Humidity Effect on Efficiency of Electrostatically Neutral Pleated Fibrous Filter: (a) Upstream No. Density, (b) Downstream No. Density, (c) Upstream Velocity, (d) Downstream Velocity, (e) Local Efficiency. Pressure Drop Δp [mm Water] = 23, RH = 35%, Air Temperature [$^{\circ}C$] = 47, Air Flow Rate = 103.7 m^3/hr , Test # NESH75.1, Test Date: 06/09/98.

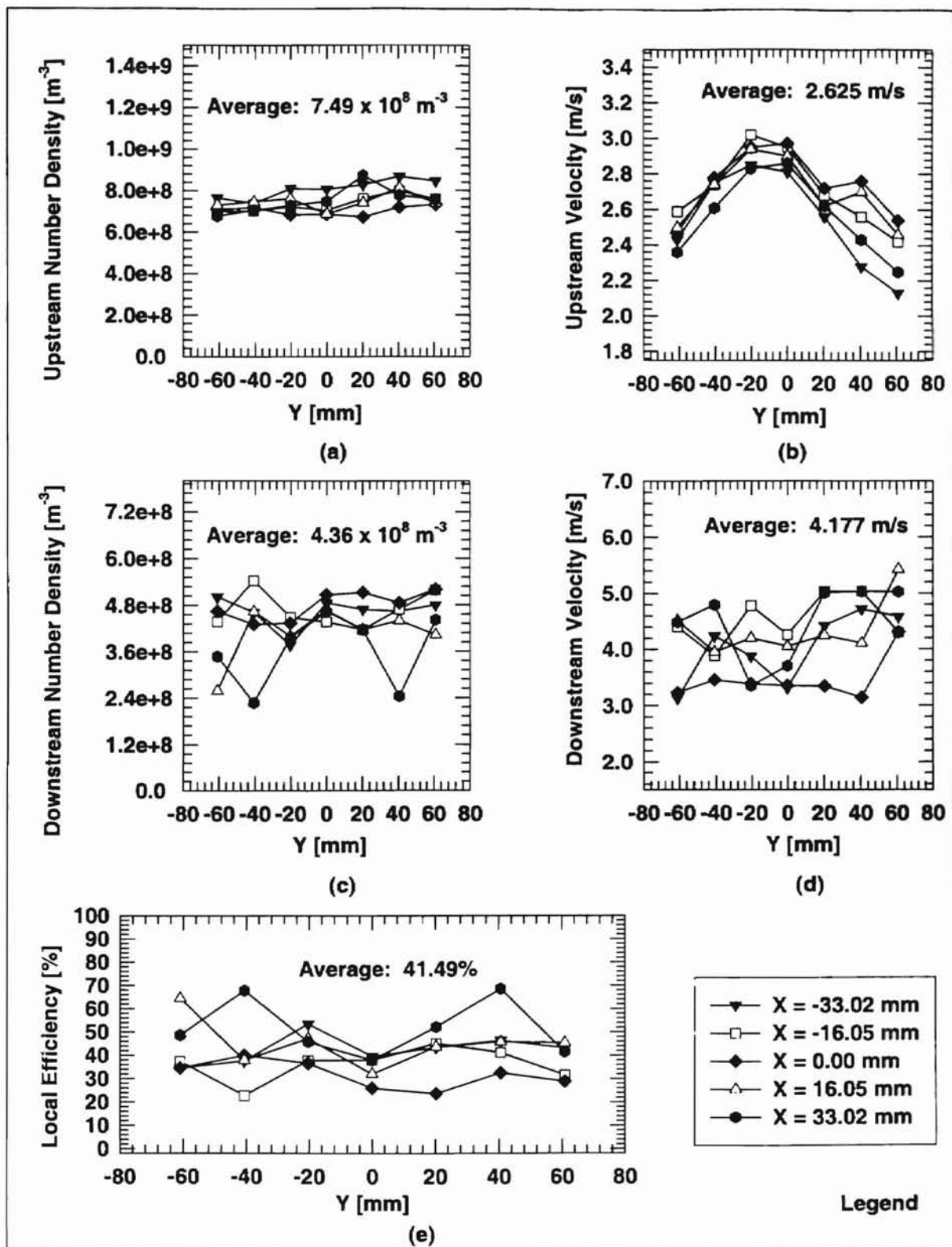


Figure E.19 Humidity Effect on Efficiency of Electrostatically Neutral Pleated Fibrous Filter: (a) Upstream No. Density, (b) Downstream No. Density, (c) Upstream Velocity, (d) Downstream Velocity, (e) Local Efficiency. Pressure Drop Δp [mm Water] = 18, RH = 45%, Air Temperature [$^{\circ}C$] = 44, Air Flow Rate = 103.7 m^3/hr , Test # NESH75.2, Test Date: 06/09/98.

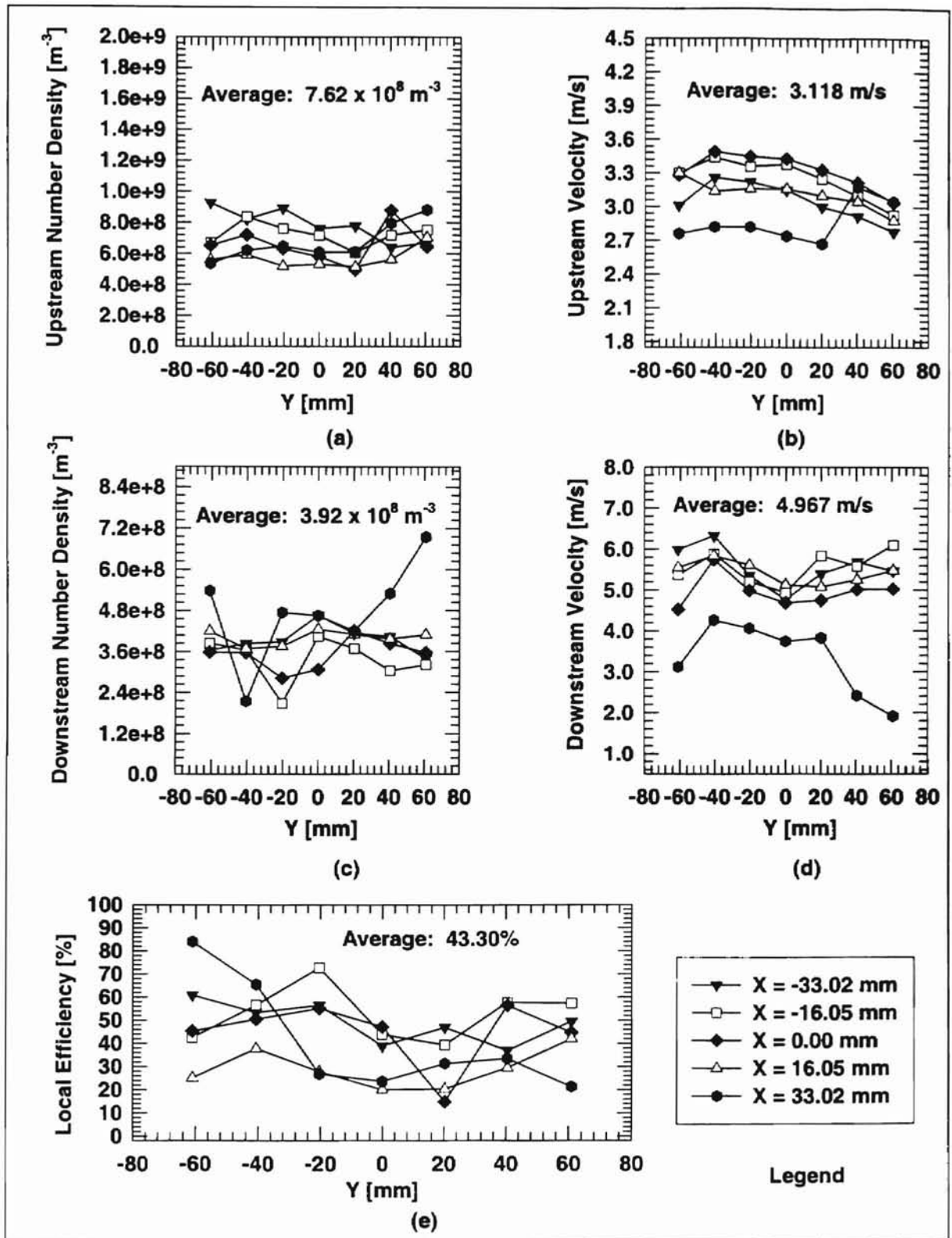


Figure E.20 Humidity Effect on Efficiency of Electrostatically Neutral Pleated Fibrous Filter: (a) Upstream No. Density, (b) Downstream No. Density, (c) Upstream Velocity, (d) Downstream Velocity, (e) Local Efficiency. Pressure Drop Δp [mm Water] = 23, RH = 80%, Air Temperature [$^{\circ}C$] = 34, Air Flow Rate = $103.7 m^3/hr$, Test # NESH75.3, Test Date: 06/09/98.

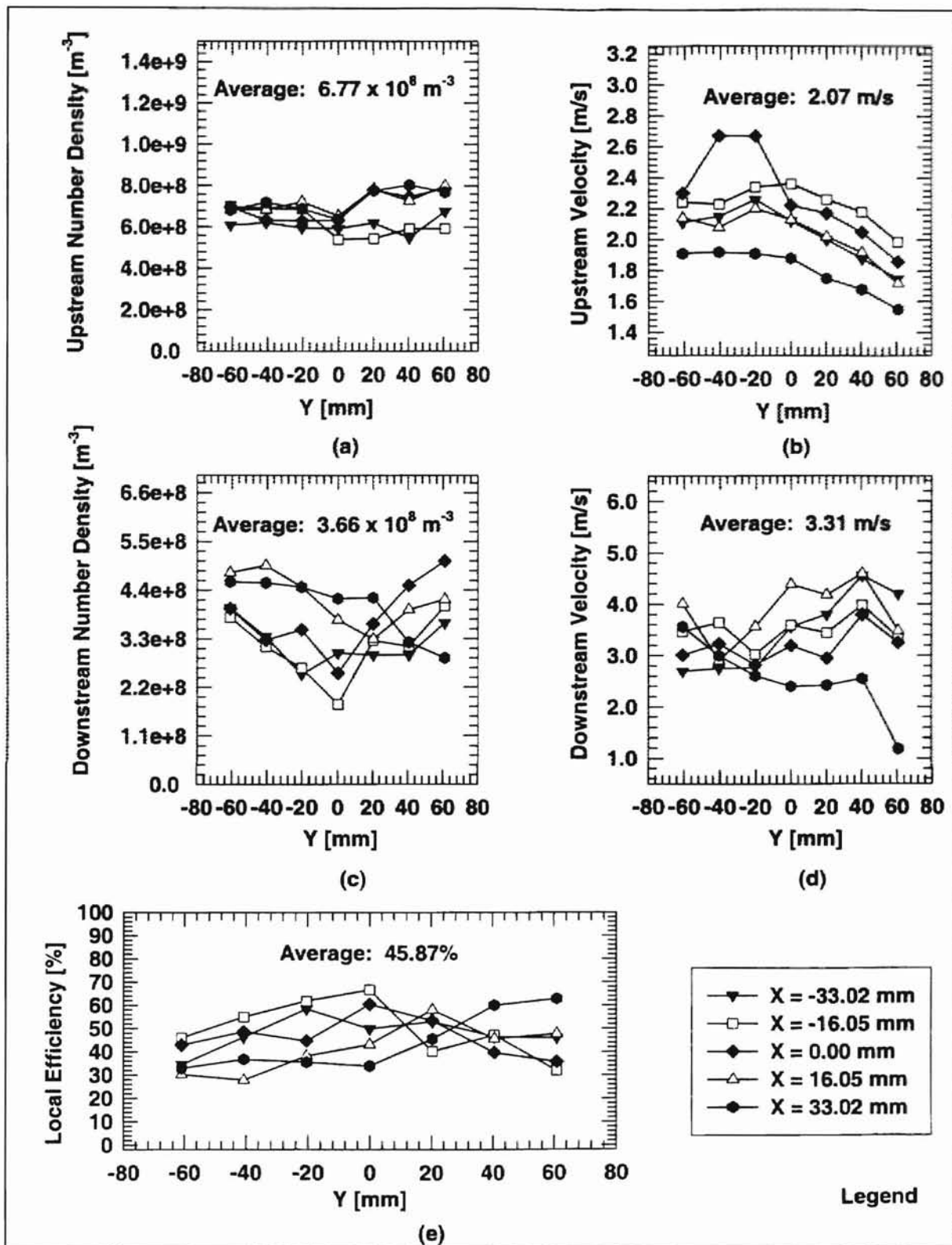


Figure E.21 Humidity Effect on Efficiency of Electrostatically Neutral Pleated Fibrous Filter: (a) Upstream No. Density, (b) Downstream No. Density, (c) Upstream Velocity, (d) Downstream Velocity, (e) Local Efficiency. Pressure Drop Δp [mm Water] = 23, RH = 80%, Air Temperature [$^{\circ}C$] = 31, Air Flow Rate = $103.7 m^3/hr$, Test # NES75.4, Test Date: 08/17/98.

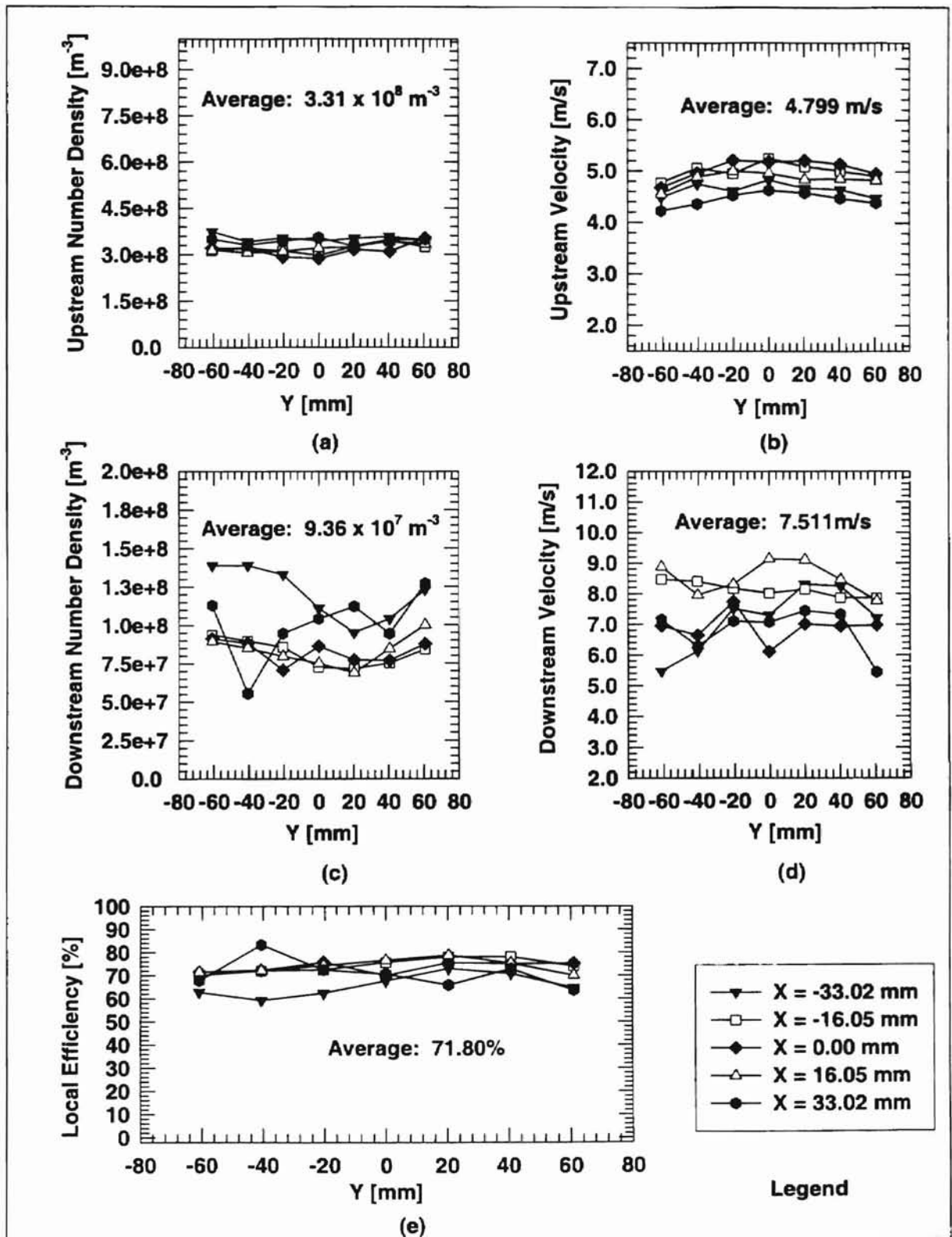


Figure E.22 Humidity Effect on Efficiency of Electrostatically Neutral Pleated Fibrous Filter: (a) Upstream No. Density, (b) Downstream No. Density, (c) Upstream Velocity, (d) Downstream Velocity, (e) Local Efficiency. Pressure Drop Δp [mm Water] = 41, RH = 73%, Air Temperature [$^{\circ}C$] = 33, Air Flow Rate = $145.7 m^3/hr$, Test # NESH100.1, Test Date: 06/25/98.

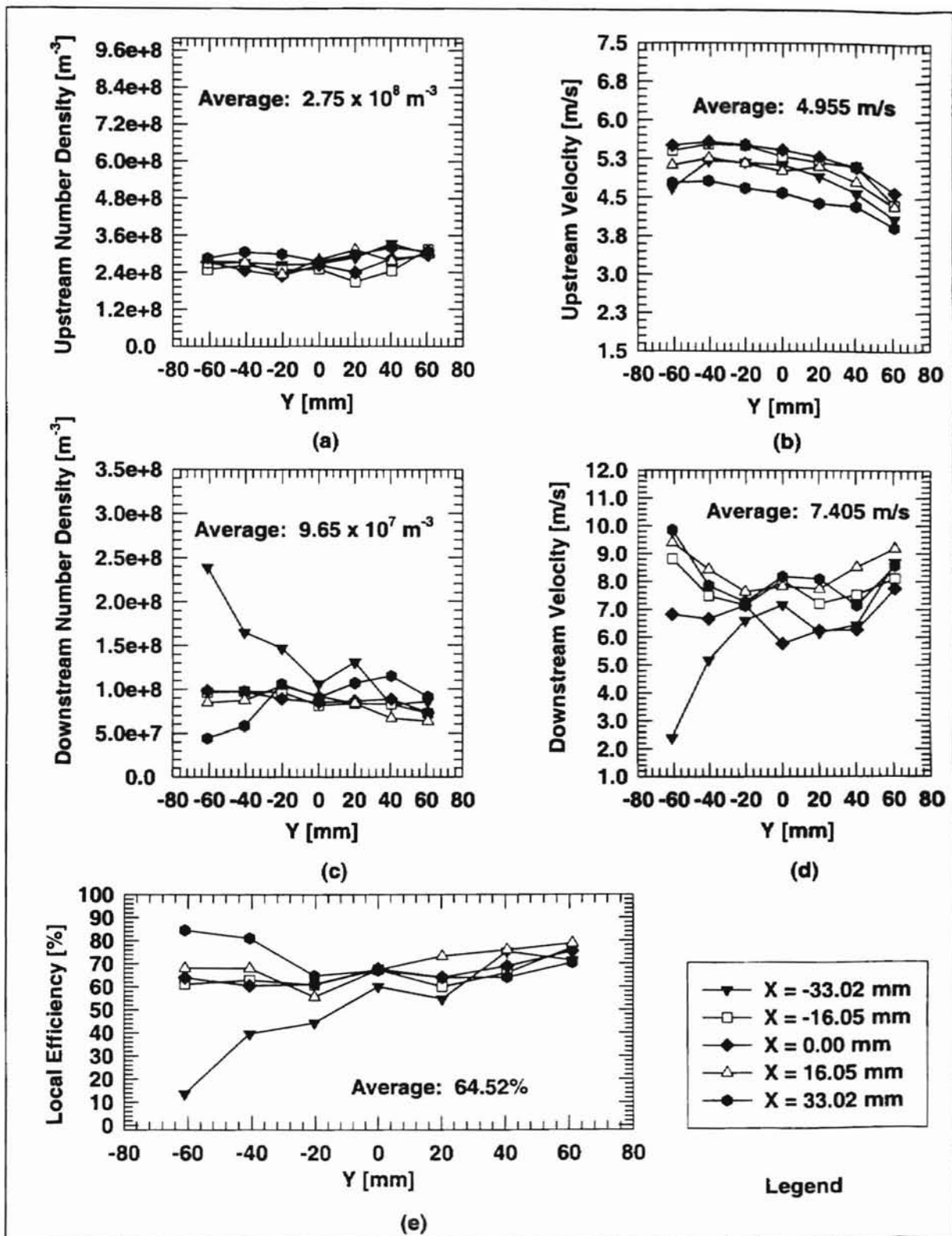


Figure E.23 Humidity Effect on Efficiency of Electrostatically Neutral Pleated Fibrous Filter: (a) Upstream No. Density, (b) Downstream No. Density, (c) Upstream Velocity, (d) Downstream Velocity, (e) Local Efficiency. Pressure Drop Δp [mm Water] = 43, RH = 74%, Air Temperature [$^{\circ}C$] = 33, Air Flow Rate = $145.7 m^3/hr$, Test # NESH100.2, Test Date: 06/25/98.

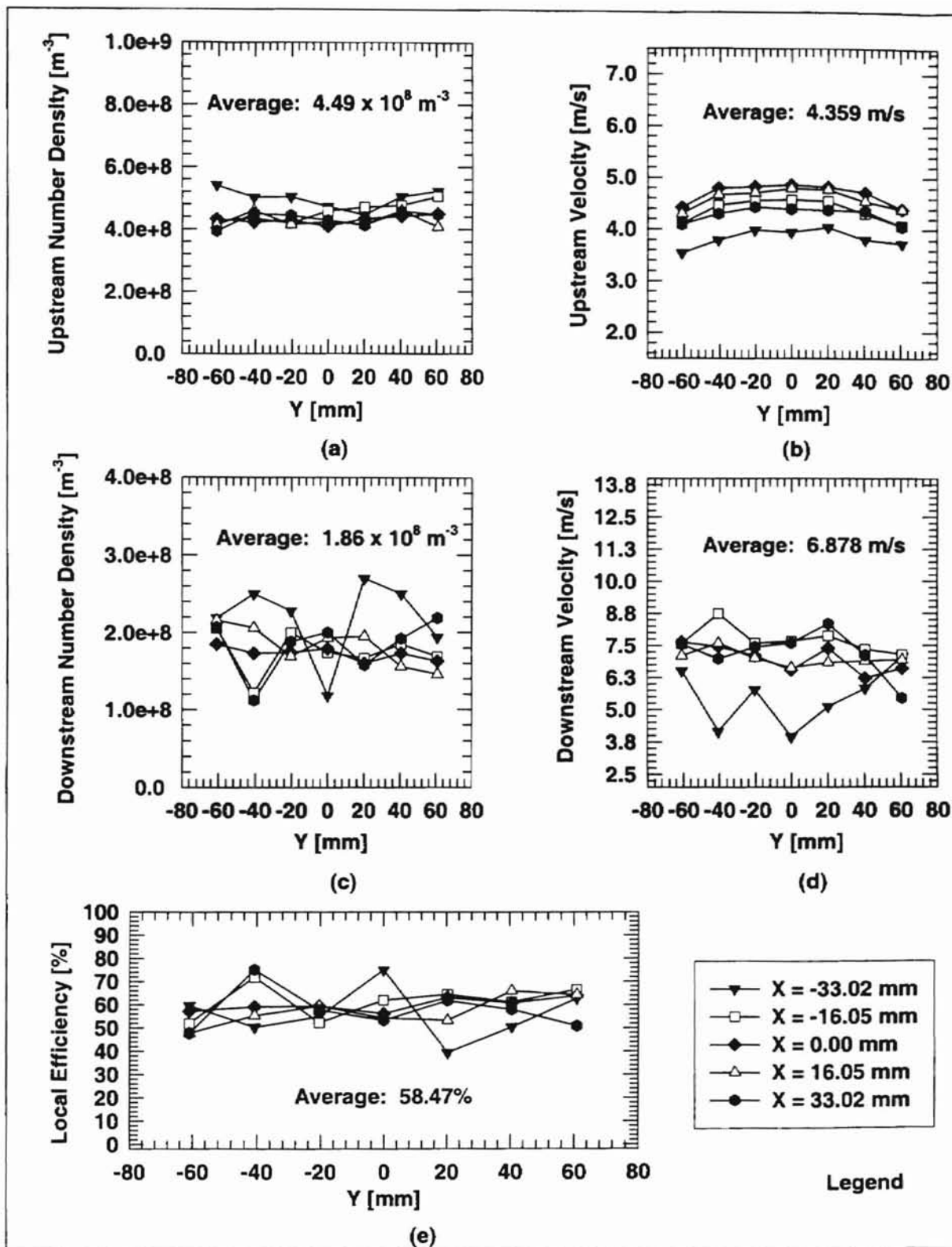


Figure E.24 Humidity Effect on Efficiency of Electrostatically Neutral Pleated Fibrous Filter: (a) Upstream No. Density, (b) Downstream No. Density, (c) Upstream Velocity, (d) Downstream Velocity, (e) Local Efficiency. Pressure Drop Δp [mm Water] = 40, RH = 35%, Air Temperature [$^{\circ}C$] = 40, Air Flow Rate = $145.7 m^3/hr$, Test # NESH100.3, Test Date: 07/12/98.

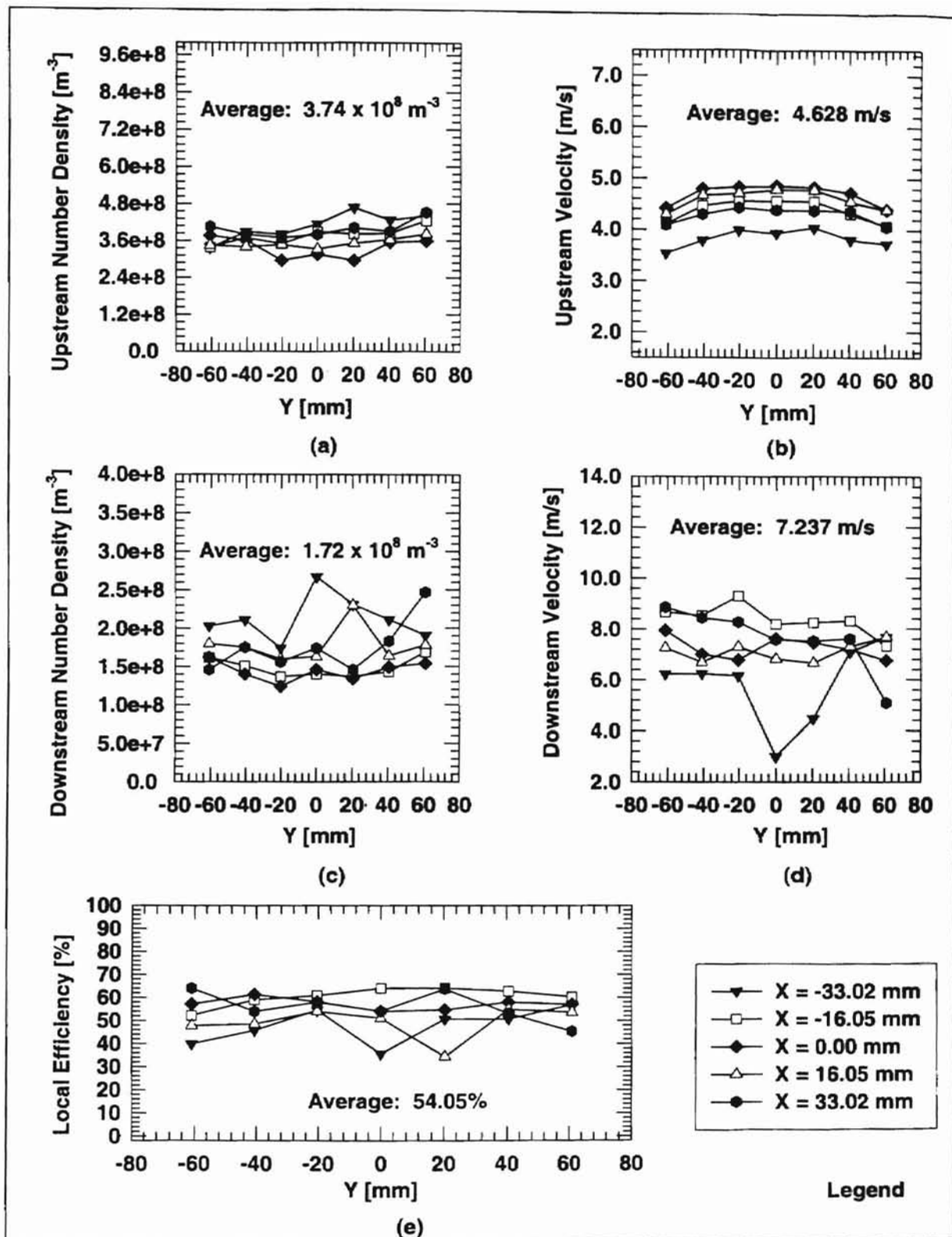


Figure E.25 Humidity Effect on Efficiency of Electrostatically Neutral Pleated Fibrous Filter: (a) Upstream No. Density, (b) Downstream No. Density, (c) Upstream Velocity, (d) Downstream Velocity, (e) Local Efficiency. Pressure Drop Δp [mm Water] = 41, RH = 38%, Air Temperature [$^{\circ}C$] = 39, Air Flow Rate = $145.7 m^3/hr$, Test # NESH100.4, Test Date: 07/13/98.

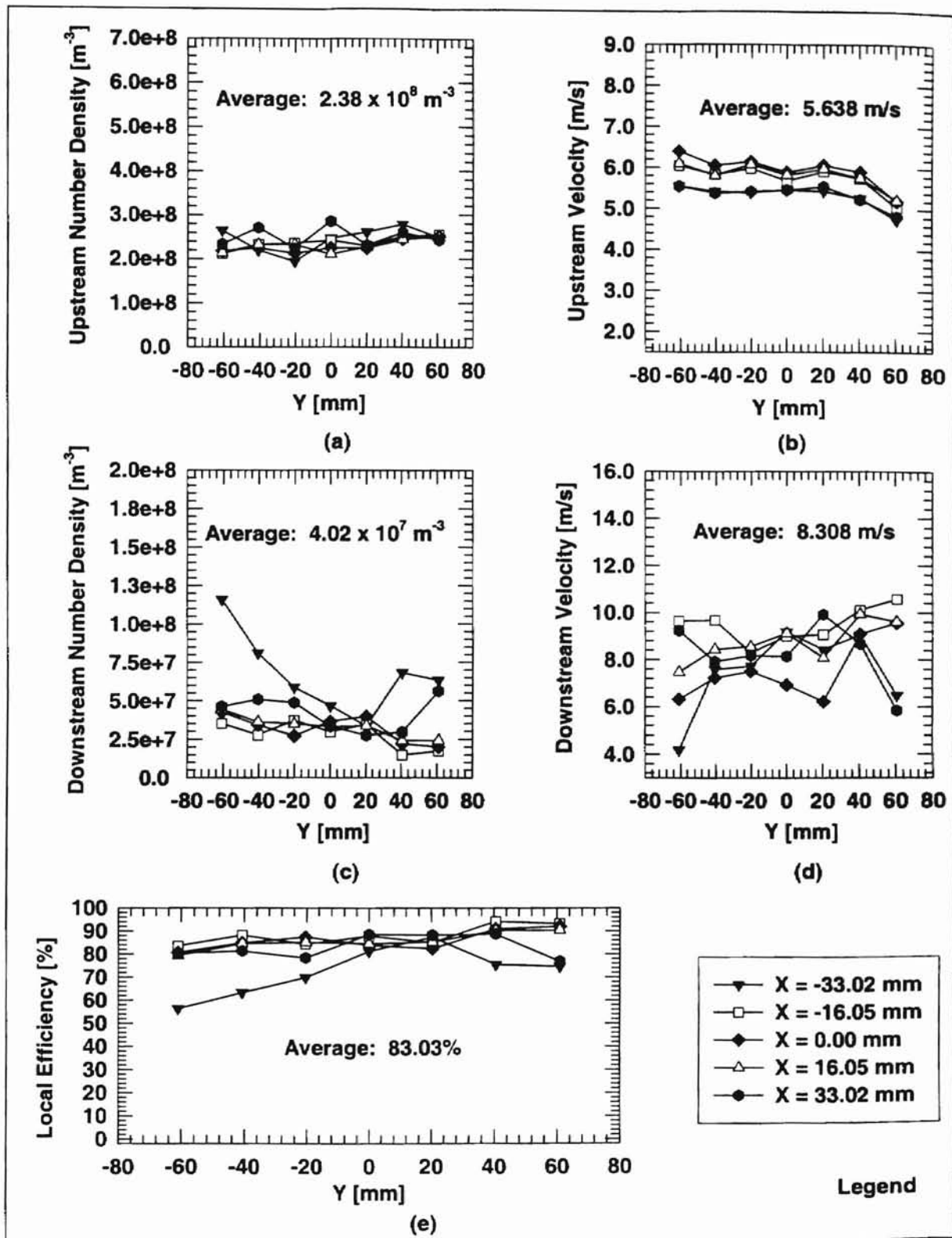


Figure E.26 Humidity Effect on Efficiency of Electrostatically Neutral Pleated Fibrous Filter: (a) Upstream No. Density, (b) Downstream No. Density, (c) Upstream Velocity, (d) Downstream Velocity, (e) Local Efficiency. Pressure Drop Δp [mm Water] = 64, RH = 87%, Air Temperature [°C] = 28, Air Flow Rate = 187.7 m³/hr, Test # NESH125.1, Test Date: 06/29/98.

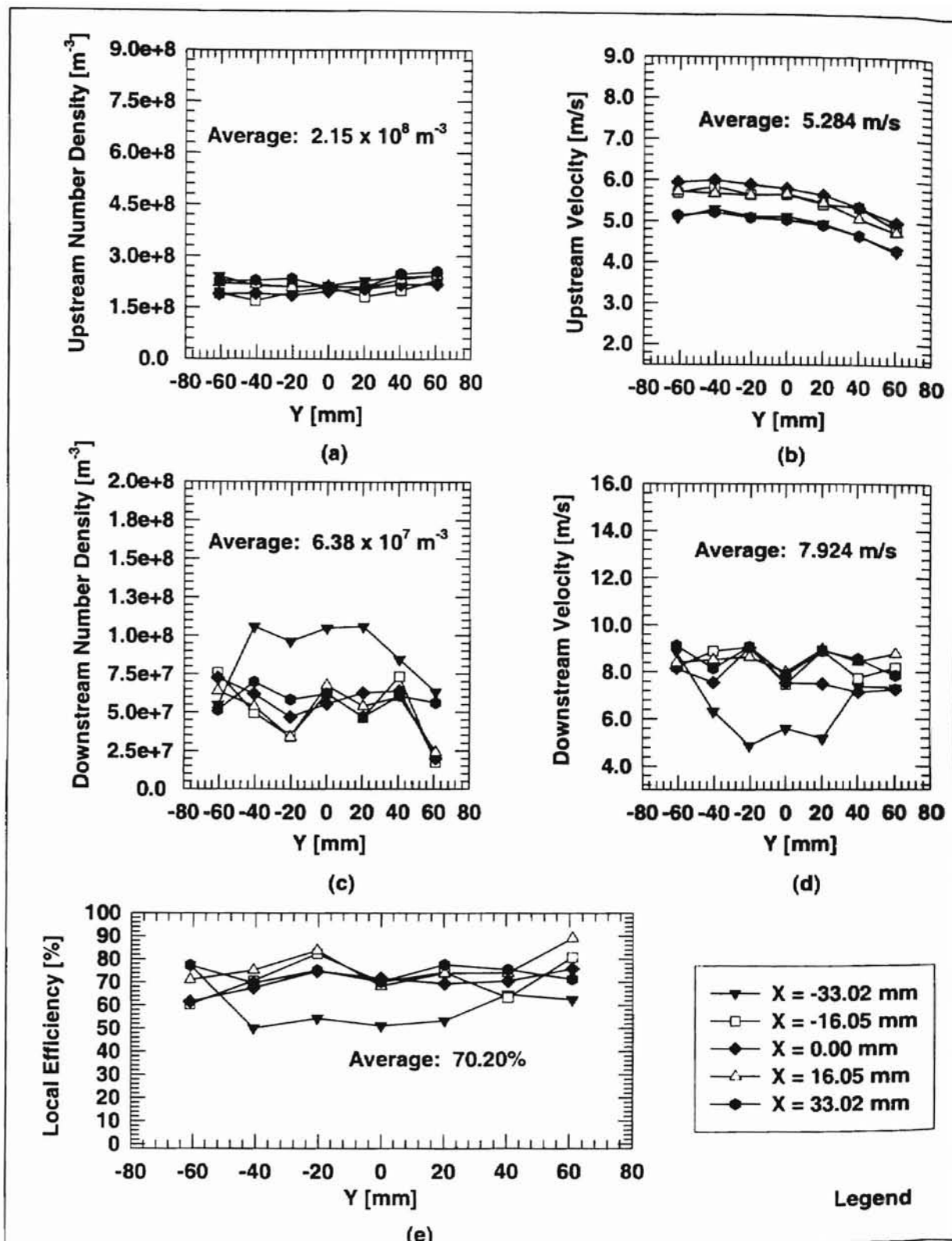


Figure E.27 Humidity Effect on Efficiency of Electrostatically Neutral Pleated Fibrous Filter
 (a) Upstream No. Density, (b) Downstream No. Density, (c) Upstream Velocity,
 (d) Downstream Velocity, (e) Local Efficiency. Pressure Drop Δp [mm Water] = 61,
 RH = 80%, Air Temperature [$^{\circ}C$] = 28, Air Flow Rate = $187.7 m^3/hr$, Test # NESH125.2,
 Test Date: 06/30/98.

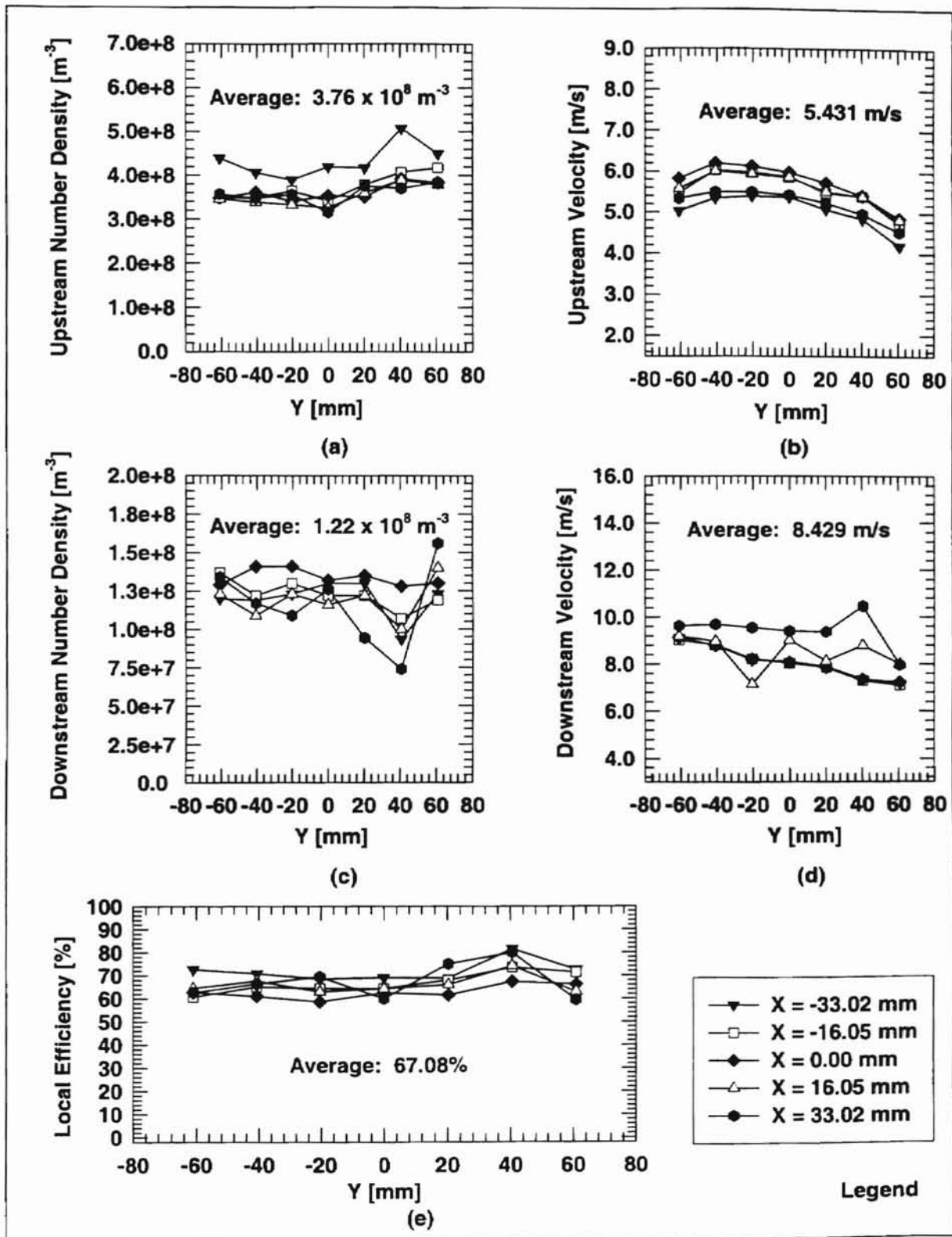


Figure E.28 Humidity Effect on Efficiency of Electrostatically Neutral Pleated Fibrous Filter: (a) Upstream No. Density, (b) Downstream No. Density, (c) Upstream Velocity, (d) Downstream Velocity, (e) Local Efficiency. Pressure Drop Δp [mm Water] = 56, RH = 43%, Air Temperature [$^{\circ}C$] = 37, Air Flow Rate = $187.7 m^3/hr$, Test # NESH125.3, Test Date: 07/11/98.

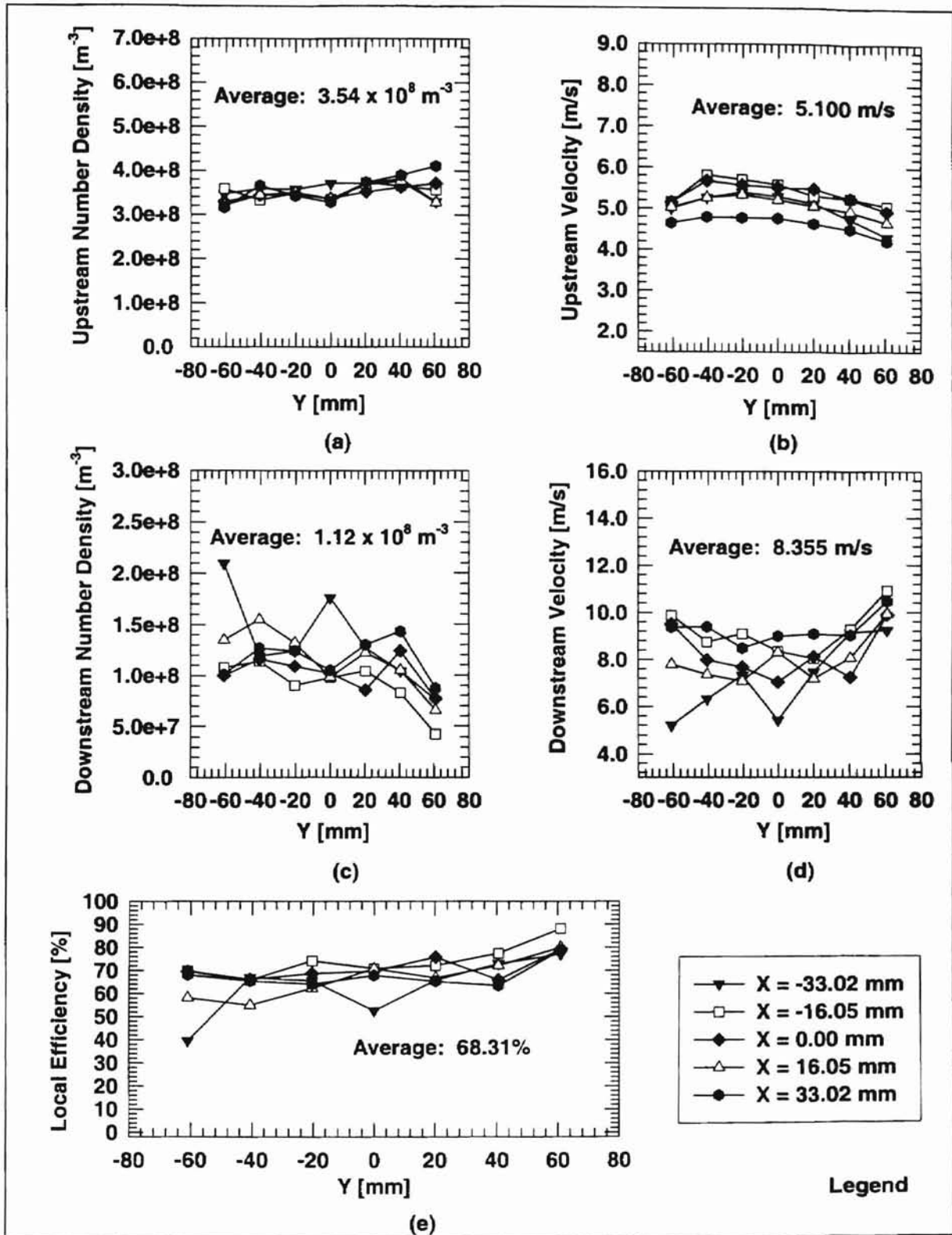


Figure E.29 Humidity Effect on Efficiency of Electrostatically Neutral Pleated Fibrous Filter: (a) Upstream No. Density, (b) Downstream No. Density, (c) Upstream Velocity, (d) Downstream Velocity, (e) Local Efficiency. Pressure Drop Δp [mm Water] = 56, RH = 48%, Air Temperature [°C] = 37, Air Flow Rate = 187.7 m^3/hr , Test # NESH125.4, Test Date: 07/12/98.

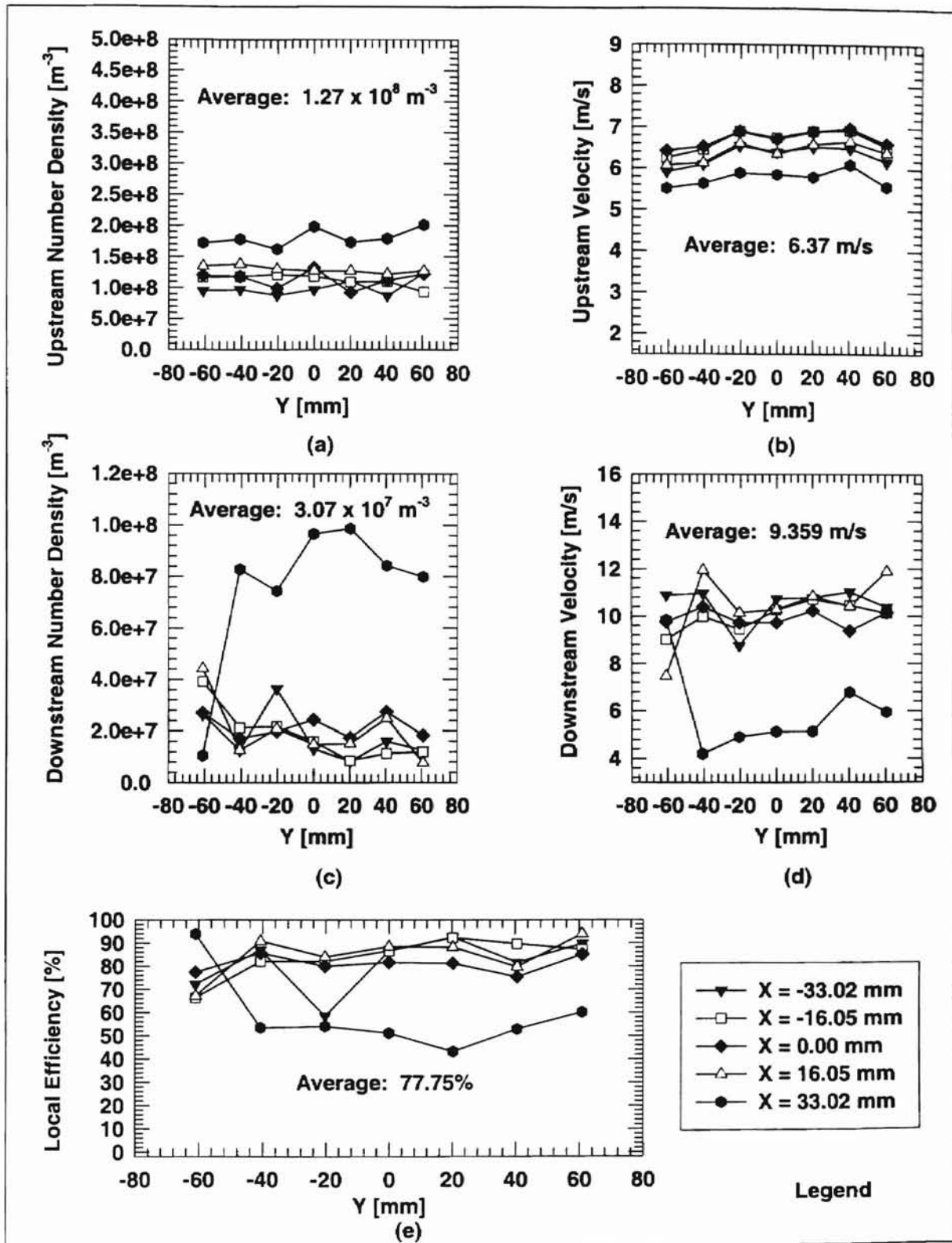


Figure E.30 Humidity Effect on Efficiency of Electrostatically Neutral Pleated Fibrous Filter: (a) Upstream No. Density, (b) Downstream No. Density, (c) Upstream Velocity, (d) Downstream Velocity, (e) Local Efficiency. Pressure Drop Δp [mm Water] = 74, RH = 43.5%, Air Temperature [$^{\circ}C$] = 35, Air Flow Rate = $229.7 m^3/hr$, Test # NESH150.1, Test Date: 07/02/98.

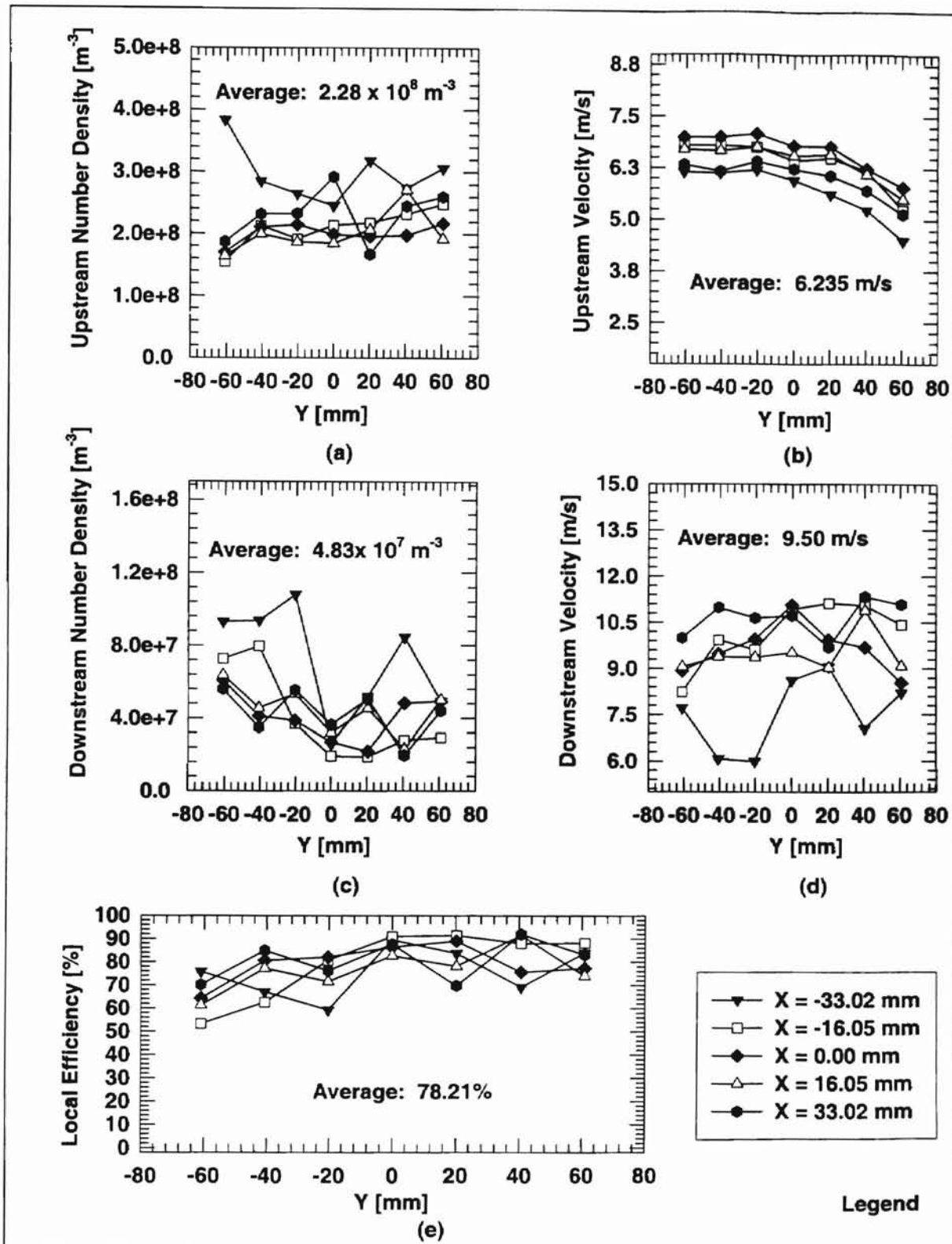


Figure E.31 Humidity Effect on Efficiency of Electrostatically Neutral Pleated Fibrous Filter: (a) Upstream No. Density, (b) Downstream No. Density, (c) Upstream Velocity, (d) Downstream Velocity, (e) Local Efficiency. Pressure Drop Δp [mm Water] = 71, RH = 43.5%, Air Temperature [$^{\circ}\text{C}$] = 36, Air Flow Rate = $229.7 \text{ m}^3/\text{hr}$, Test # NESH150.2, Test Date: 07/11/98.

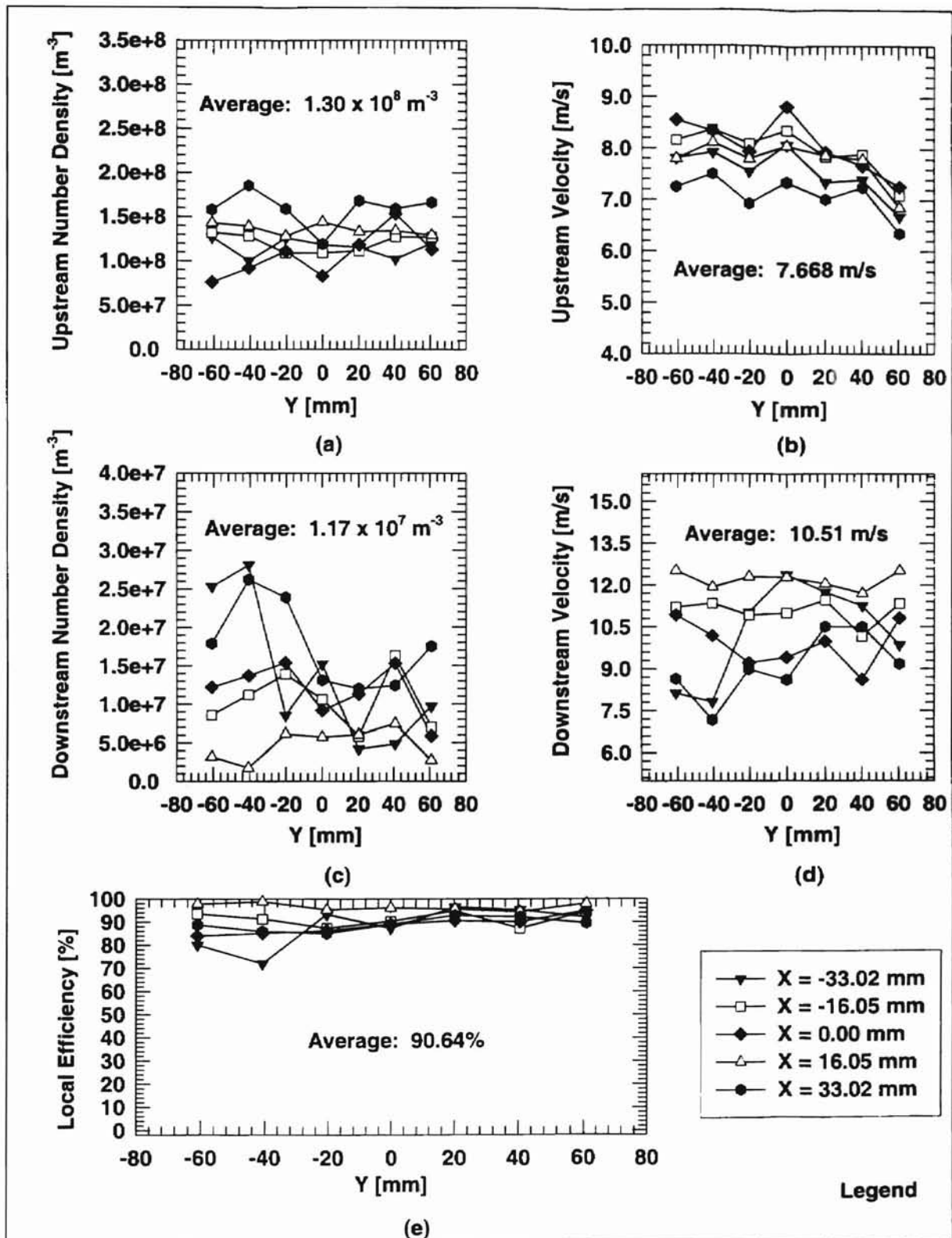


Figure E.32 Humidity Effect on Efficiency of Electrostatically Neutral Pleated Fibrous Filter: (a) Upstream No. Density, (b) Downstream No. Density, (c) Upstream Velocity, (d) Downstream Velocity, (e) Local Efficiency. Pressure Drop Δp [mm Water] = 104, RH = 43.5%, Air Temperature [$^{\circ}C$] = 35, Air Flow Rate = $273.6 m^3/hr$, Test # NESH175.1, Test Date: 07/02/98.

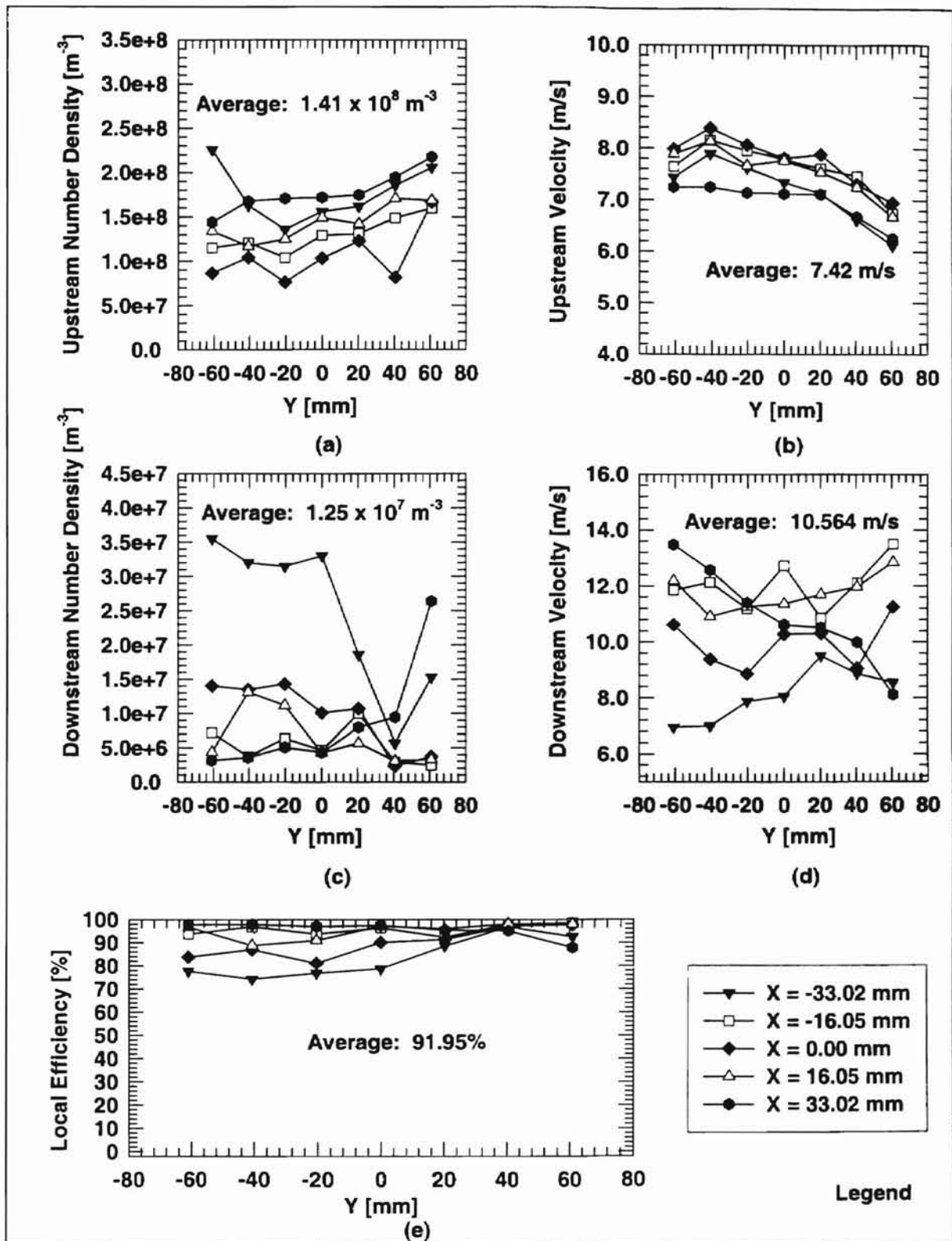


Figure E.33 Humidity Effect on Efficiency of Electrostatically Neutral Pleated Fibrous Filter: (a) Upstream No. Density, (b) Downstream No. Density, (c) Upstream Velocity, (d) Downstream Velocity, (e) Local Efficiency. Pressure Drop Δp [mm Water] = 107, RH = 48.5%, Air Temperature [°C] = 35, Air Flow Rate = 273.6 m³/hr, Test # NESH175.2, Test Date: 07/07/98.

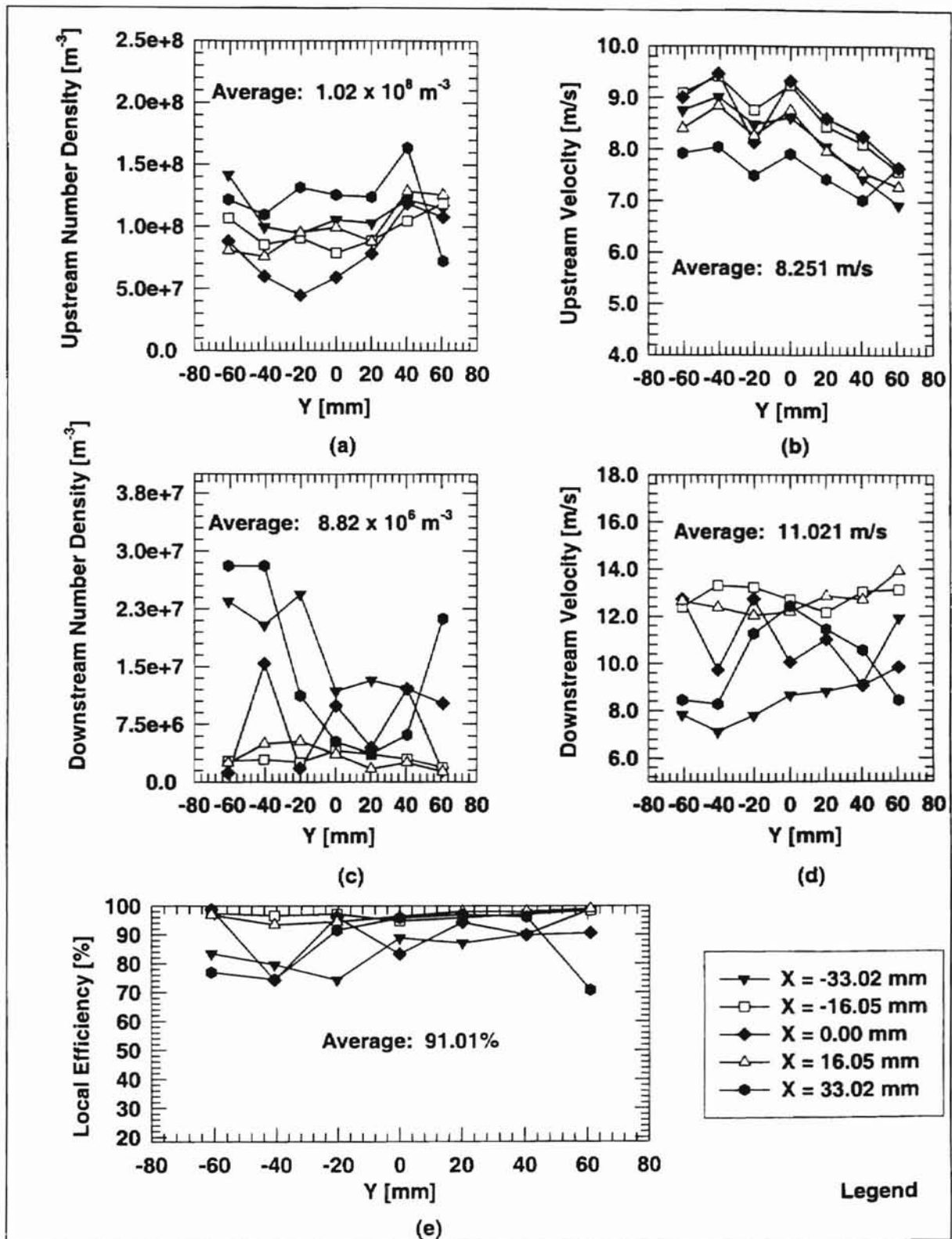


Figure E.34 Humidity Effect on Efficiency of Electrostatically Neutral Pleated Fibrous Filter
 (a) Upstream No. Density, (b) Downstream No. Density, (c) Upstream Velocity,
 (d) Downstream Velocity, (e) Local Efficiency. Pressure Drop Δp [mm Water] = 122,
 RH = 45%, Air Temperature [$^{\circ}C$] = 34, Air Flow Rate = $313.8 m^3/hr$, Test # NESH200.1,
 Test Date: 07/03/98.

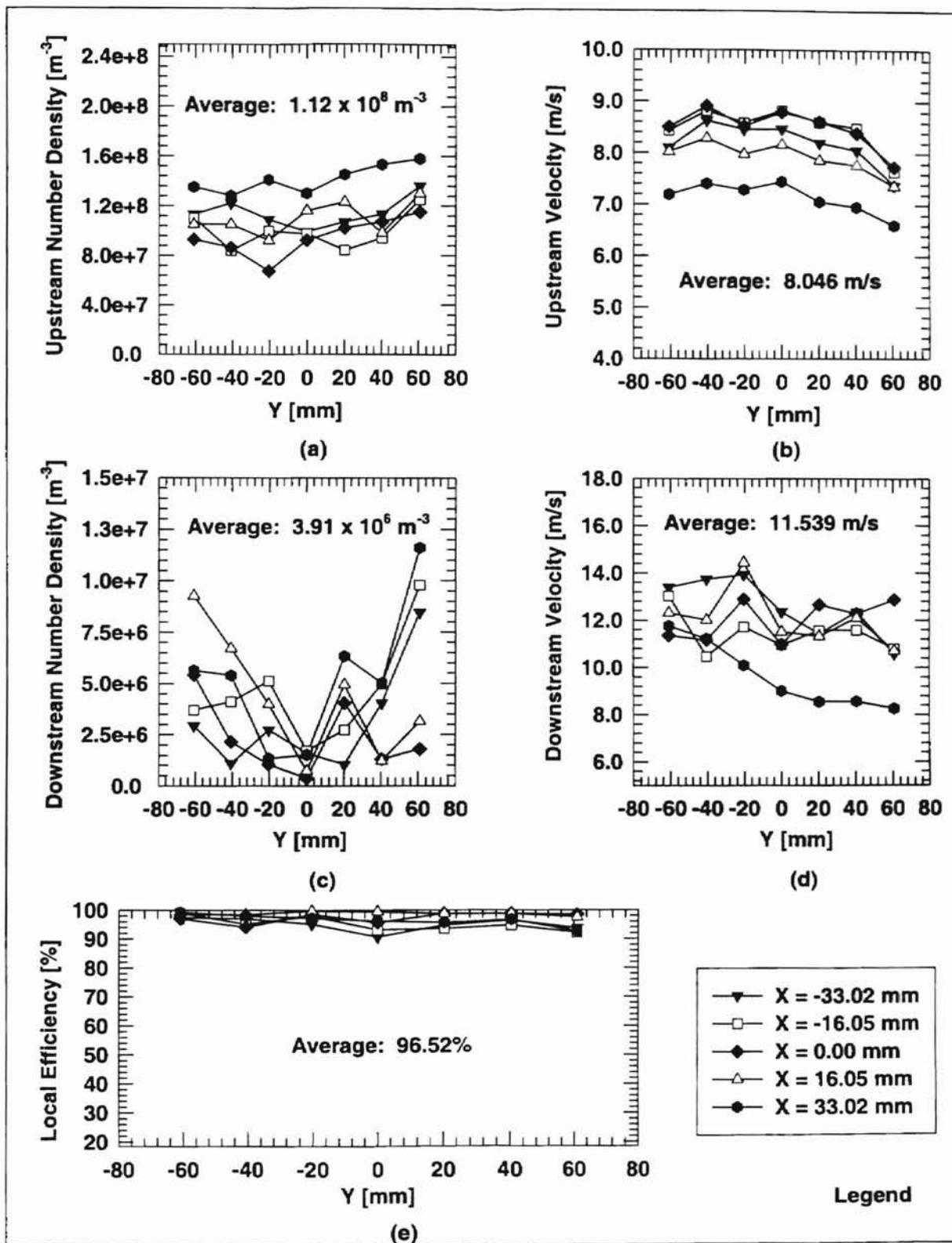


Figure E.35 Humidity Effect on Efficiency of Electrostatically Neutral Pleated Fibrous Filter: (a) Upstream No. Density, (b) Downstream No. Density, (c) Upstream Velocity, (d) Downstream Velocity, (e) Local Efficiency. Pressure Drop Δp [mm Water] = 124, RH = 44%, Air Temperature [$^{\circ}C$] = 32, Air Flow Rate = $313.8 m^3/hr$, Test # NESH200.2, Test Date: 07/04/98.

APPENDIX F

BASIC TERMS AND DEFINITIONS RELATED TO HUMIDITY MEASUREMENTS

Presented herein (in this appendix) are the definitions of some basic terms in hygrometry/psychrometry that might be used frequently in the determination of moisture in the air and subsequently moisture content of the filter, using the procedures outlined in Appendix G and Chapter V.

Saturated Air: Air that cannot carry any more water vapor at its given temperature is called saturated air. The partial pressure due to the water vapor in the moist air is the vapor pressure, p_v . The partial pressure of water vapor at the saturation point is called the saturation vapor pressure, p_{sat} .

Humidity: This indicates the presence of moisture or water vapor in air. Some of the important parameters of humidity are defined next.

1. Humidity Ratio (Ω): This is also called the absolute humidity. Moist air is regarded as a mixture of water vapor and dry air. The humidity ratio pertaining to a sample of moist air is the ratio of the mass of water vapor contained in the sample to the mass of dry air with which the water vapor is associated.

The humidity ratio, Ω , is defined as [McQuiston and Parker, 1994]:

$$\Omega = \frac{m_v}{m_a} \quad (F-1)$$

$$m_{ma} = m_v + m_a \quad (F-2)$$

where m_a is mass of dry air in a sample of moist air, m_v is the mass of water vapor in that sample of moist air, and m_{ma} is the total mass of that moist air.

2. **Relative Humidity:** This indicates how close a given sample of air is to the saturated condition. It is equal to the ratio of the partial pressure of the water vapor, p_v to the partial pressure of water vapor, p_{sat} , which would saturate the air at the specified temperature.

$$RH = \frac{P_v}{P_{sat}} \quad (F-3)$$

3. **Dew point:** This is the temperature at which water vapor starts to condense from a given sample of moist air at a constant pressure.

4. **Dry-bulb Temperature:** This is the temperature of a moist air sample measured using a thermometer inside that sample of air.

5. **Wet-bulb Temperature:** It is the temperature indicated by a thermometer on the hygrometer whose bulb is kept wet (100% saturated moist air) by a piece of wet cloth.

Gas Law:

The gas law is an equation that governs the state of real or ideal gases and vapors given by,

$$p_g V_g = z \left(\frac{m_g}{M_g} \right) RT \quad (F-4)$$

where V_g is the volume of gas, M_g is the molecular weight of the gas, m_g is the mass of the gas, R is the universal gas constant, T is the absolute temperature of the gas, p_g is the pressure of the gas, and z is the compressibility factor of the gas. When $z = 1$, then Eq. (F-4) reduces to the ideal or perfect gas equation as follows:

$$p_g V_g = \left(\frac{m_g}{M_g} \right) RT \quad (\text{F-5})$$

The gas constants R_a and R_v of dry air and water vapor, respectively, can be found as follows:

$$(a) R_a = \frac{R}{M_a} \quad (b) R_v = \frac{R}{M_v} \quad (\text{F-6}),$$

where M_a and M_v are the molecular weights of air and water vapor, respectively.

The molecular weights of air and water vapor are 28.965 and 18.015 kg /mole respectively. The universal gas constant R is 8314 J/(kg-mole-K). Hence, from Eq. (F-6), $R_a = 287$ J/kg-K, and $R_v = 462$ J/kg-K.

The equation for humidity ratio in Eq. (F-1) can be expressed in terms of the partial pressures by solving for m_a and m_v from the gas equation (assuming the same volume and temperature for each) as follows:

$$\Omega = \frac{m_v}{m_a} = \frac{R_a p_v}{R_v p_a} = \frac{287 p_v}{462 p_a} = 0.622 \frac{p_v}{p_t - p_v} \quad (\text{F-7})$$

where p_t is the total pressure of the moist air, and p_a is the partial pressure of the air.

Psychrometric Chart: This is the chart that relates relative humidity, humidity ratio, wet-bulb temperature and dry-bulb temperature (psychrometric charts are found in most thermodynamics books, for example, the reader may refer to McQuiston and Parker, 1994).

APPENDIX G

MOISTURE ESTIMATION PROCEDURE

Appendix G is devoted to the procedure for the estimation of moisture in the air upstream and downstream of the filter for a period of time during the experimental filtration process (at a constant flow rate) in order to estimate the amount of moisture that might be absorbed /given up by the filter. The author believes that the estimation of the amount of moisture absorbed by a filter will help to understand, improve, develop or corroborate existing particle adhesion models due to condensed water films. Some literature (see Section 3.9 of Chapter III) discusses the role of water films on the enhancement of the adhesion of particles to the filter fibers as the water film deposits between surfaces of the fibers and particles.

The procedure for calculating the moisture content in air assumes that the relative humidity and dry bulb temperature of the air (flowing across the filter) as a function of time are known from direct measurements during the filtration process. Thus the procedure for calculating the moisture content of the air upstream or downstream of the filter from the data is as follows:

- 1) Transforming relative humidity, RH, into absolute humidity (mass of water vapor per unit mass of moist air), AH:
 - use a set of steam tables to find the saturated vapor pressure, p_{sat} , at the given temperature of air;

- use the relation $RH = \frac{P_v}{P_{sat}}$ to calculate p_v ;
- next calculate the humidity ratio:

$$\Omega = \frac{m_v}{m_a} = \frac{R_a p_v}{R_v p_a} = \frac{287 p_v}{462 p_a} = 0.622 \frac{p_v}{p_t - p_v} \quad (G-1)$$

- calculate AH using Ω , by

$$AH = \frac{m_v}{m_v + m_a} = \frac{\Omega m_a}{\Omega m_a + m_a} = \frac{\Omega}{1 + \Omega} \quad (G-2)$$

It is also possible to use the psychrometric chart for finding the humidity ratio [McQuiston and Parker, 1994] so that the absolute humidity can be calculated from Eq. (G-2). The air temperature, which is considered the dry-bulb temperature and the relative humidity, RH, are sufficient to give the corresponding humidity ratio from which the corresponding absolute humidity (AH) value can be easily calculated.

2) Estimating Moisture:

Finding the area under the curve by integration yields an estimate of the total moisture in the air, which is actually done using numerical integration methods applied to the corresponding absolute humidity and time data or the plot as shown in Fig. G-1.

For example, using the trapezoidal rule [Gerald and Wheatley, 1994], by subdividing the interval between the two limits of integration [time bounds] a_1 and b_1 into i subintervals, the estimated moisture content is

$$M_v = \rho_{ma} Q \int_{a_1}^{b_1} AH(t) dt = \frac{\Delta t}{2} [AH_1 + 2AH_2 + 2AH_3 + \dots + 2AH_{i-1} + AH_i] \quad (G-3)$$

where ρ_{ma} and Q are the density and volume flow rate of the moist air (mixture), and Δt

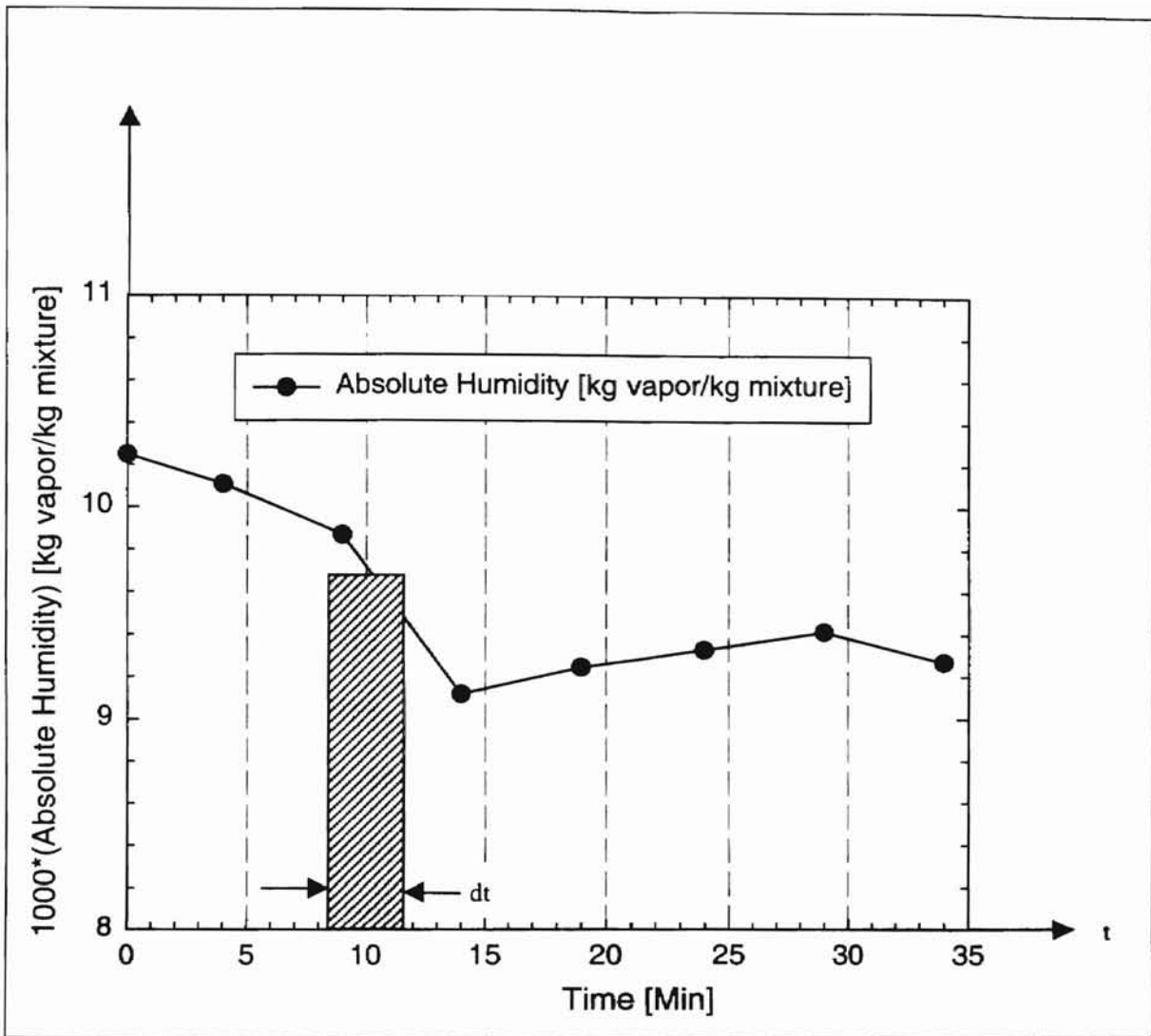


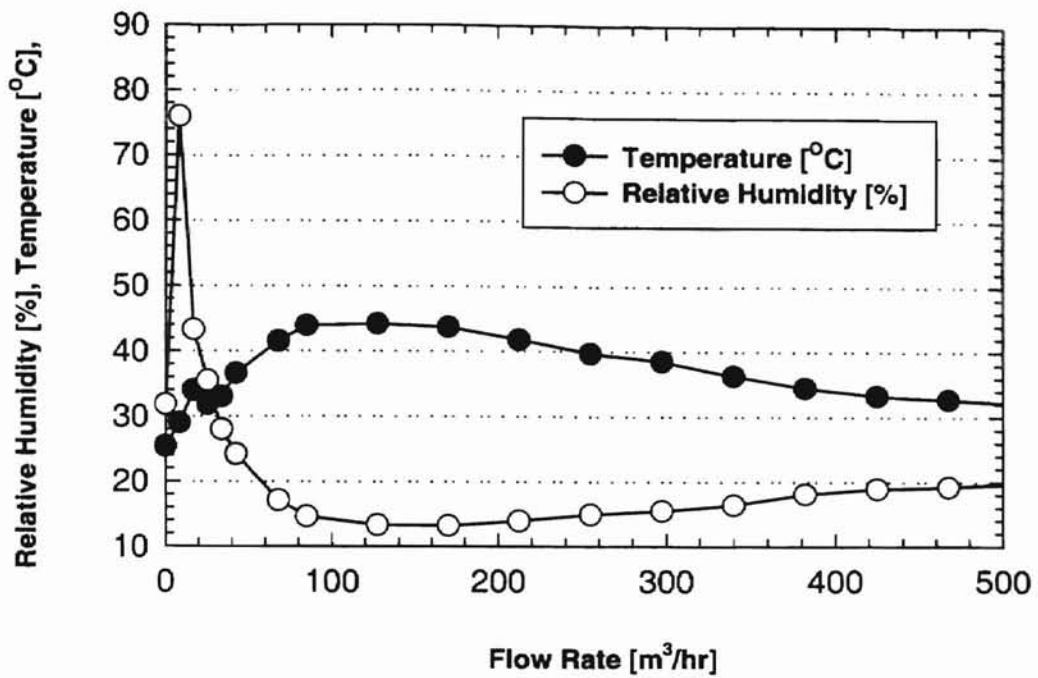
Figure G-1 Absolute Humidity Variation with Time at a Constant Air Flow Rate.

is the time step. Once the time dependent humidity and temperature curves are known, one can obtain the corresponding absolute humidity versus time plot to calculate the amount of moisture. Thus by calculating the moisture content of the air upstream and downstream of the filter using this procedure for moisture determination, it might be possible to evaluate the amount of moisture absorbed by the dry filter (depending upon the prior conditions of the air and filter) under special and controlled conditions. [Note: In Eq. (G-1), $p_t = 1$ atmosphere (760 mm Hg) was used as an approximation to the atmospheric pressure in Stillwater (740 mm Hg) to calculate the humidity ratio.]

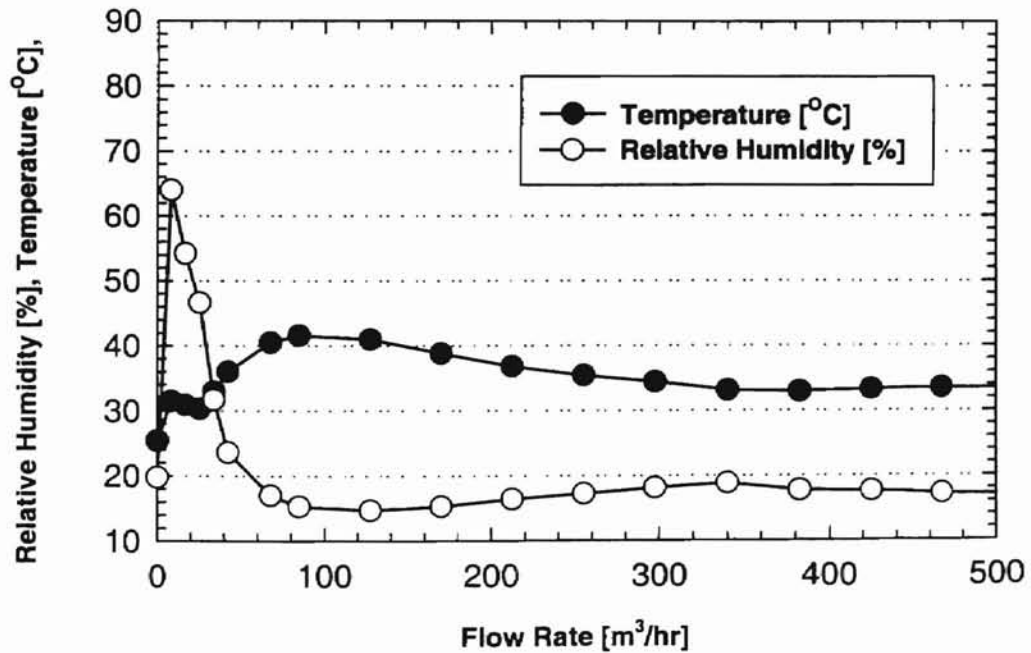
APPENDIX H

HUMIDITY MEASUREMENTS

In Appendix H, the humidity measurements that were made prior to the investigation of humidity effects on the efficiency of the fibrous A13192 Dayco-Purolator automotive filters to investigate the repeatability of the humidity of the measurements are presented. More than fifty different humidity measurements were performed at the immediate upstream and downstream sides of the filter as well as before the entrance of the air flow into the mixing box using a digital model Omega RH21 thermometer-hygrometer. The plots show the variation of humidity with flow rate and the dependence of humidity upon time for a particular flow rate. These measurements were made for several cases to simulate how humidity changes during the actual filtration process. In some cases, the humidity measurements were done with or without the supply of heat or atomization of distilled water to simulate the drying and atomization of the solution of suspension of PSL particles.



(a)



(b)

Figure H.1 Temperature and Humidity Variations Downstream of Filter As a Function of Air Flow Rate:
 (a) without Both Heat Addition and Atomization of Distilled Water
 (b) with Both Heat Addition and Atomization of Distilled Water.

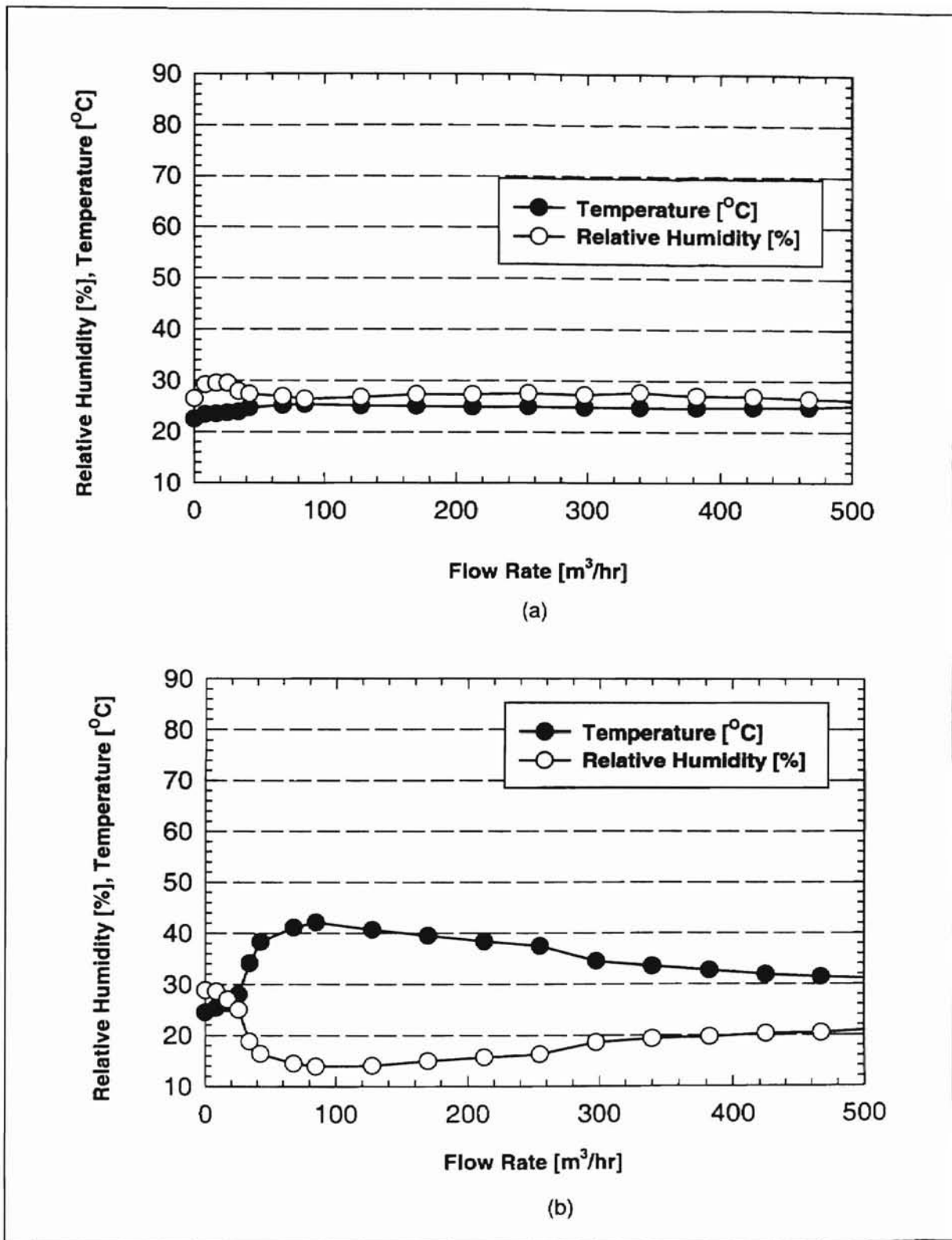


Figure H.2 Temperature and Humidity Variations Downstream of Filter As a Function of Air Flow Rate:
 (a) without Heat Addition and Atomization of Distilled Water
 (b) with Heat Addition But No Atomization of Distilled Water.

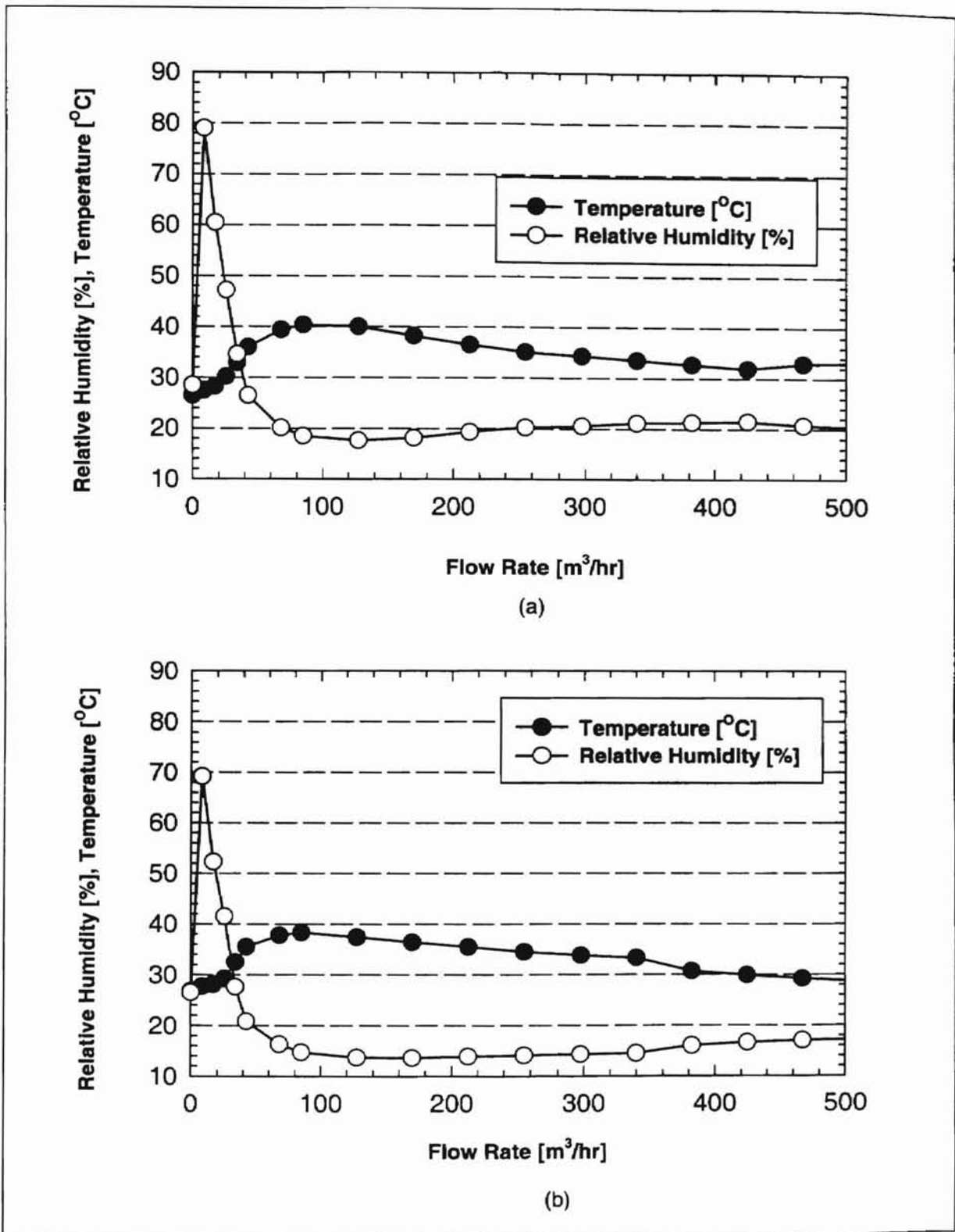
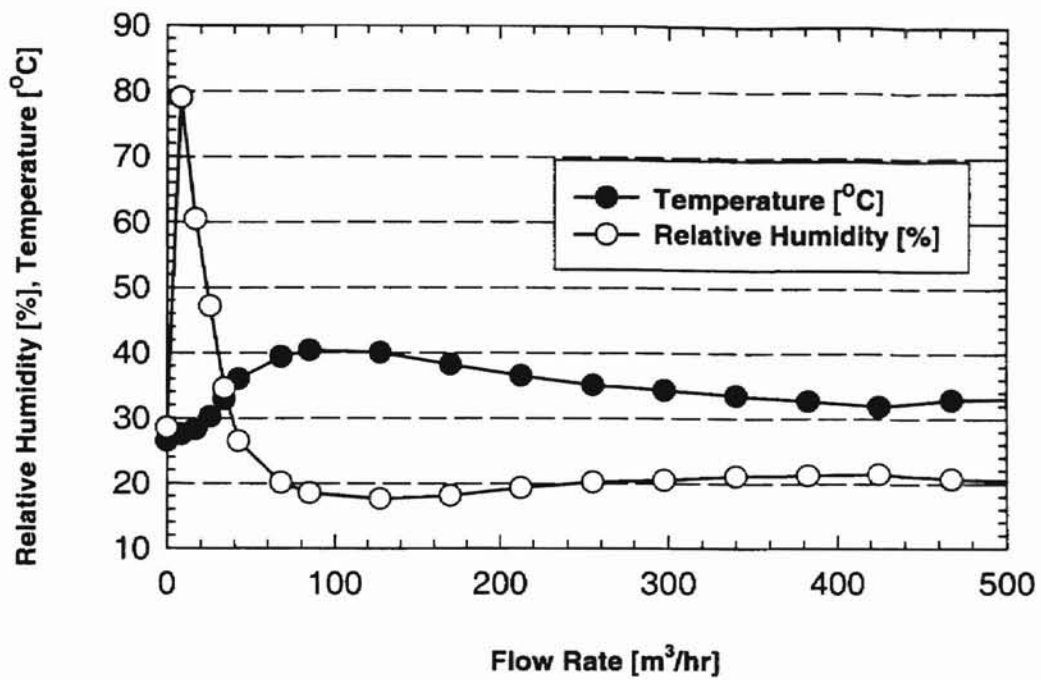
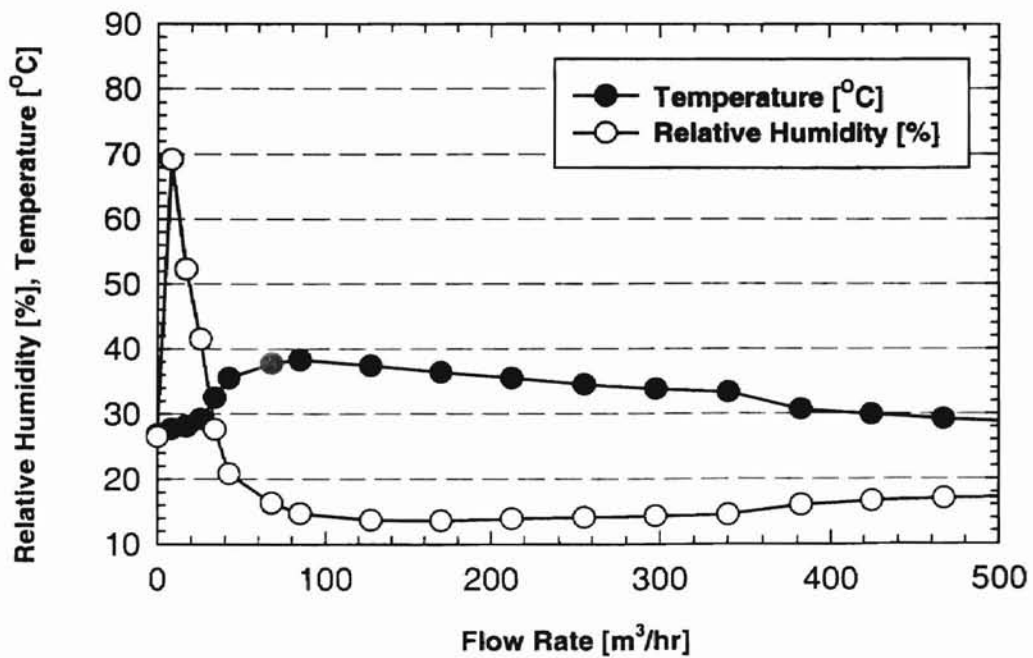


Figure H.3 Temperature and Humidity Variations Upstream of Filter As a Function of Air Flow Rate:
 (a) with Both Heat Addition and Atomization of Distilled Water
 (b) with Both Heat Addition and Atomization of Distilled Water.

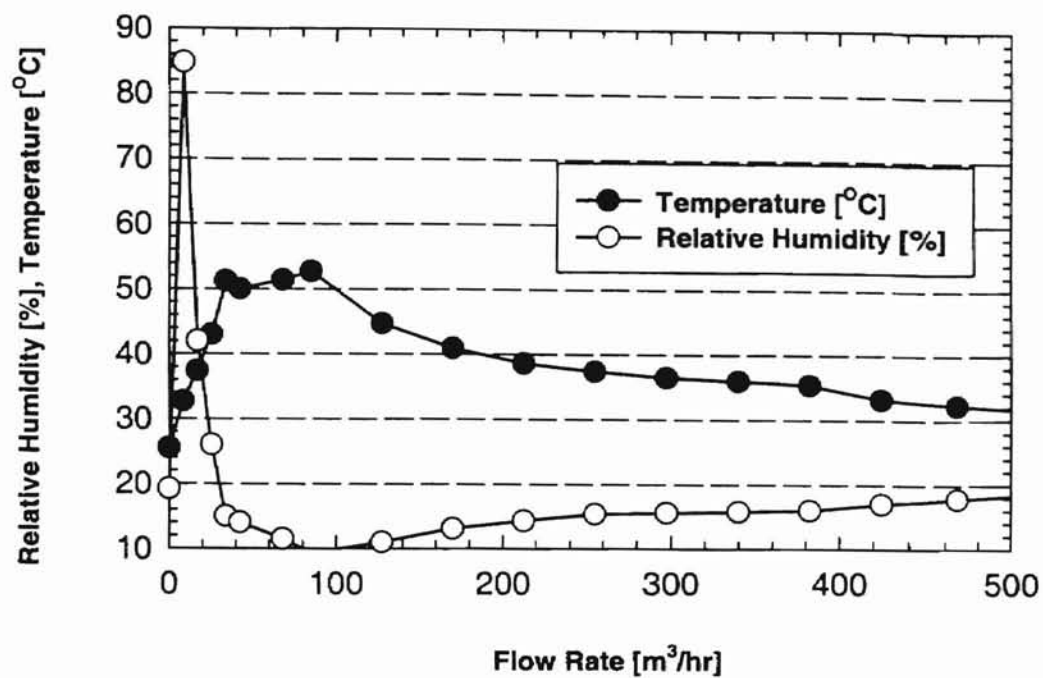


(a)

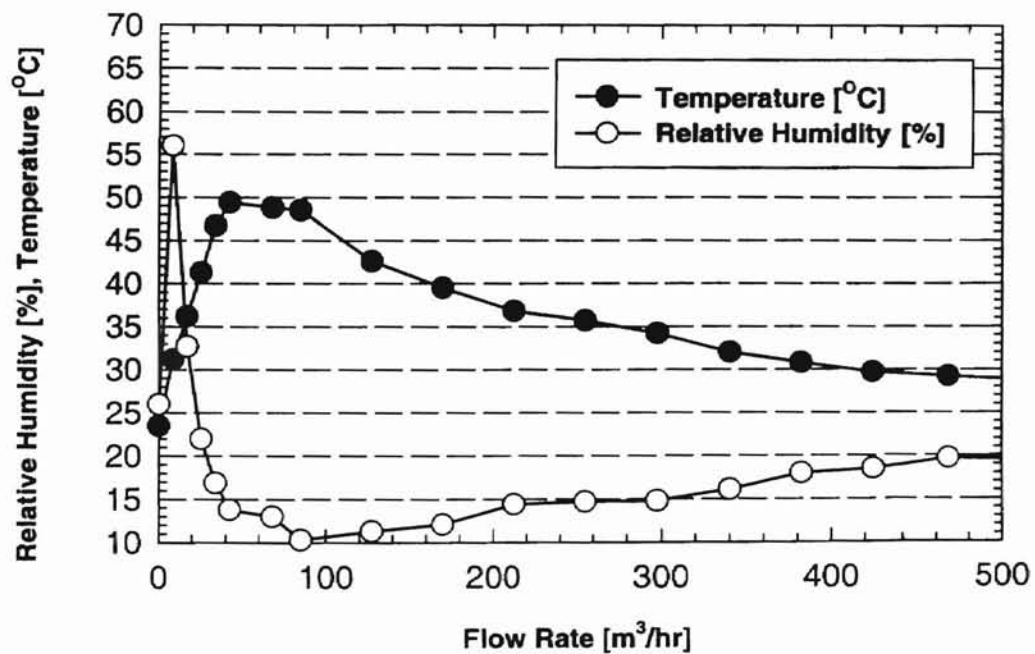


(b)

Figure H.4 Temperature and Humidity Variations Upstream of Filter As a Function of Air Flow Rate:
 (a) with Heat Addition and Atomization of Distilled Water
 (b) with Heat Addition and Atomization of Distilled Water.

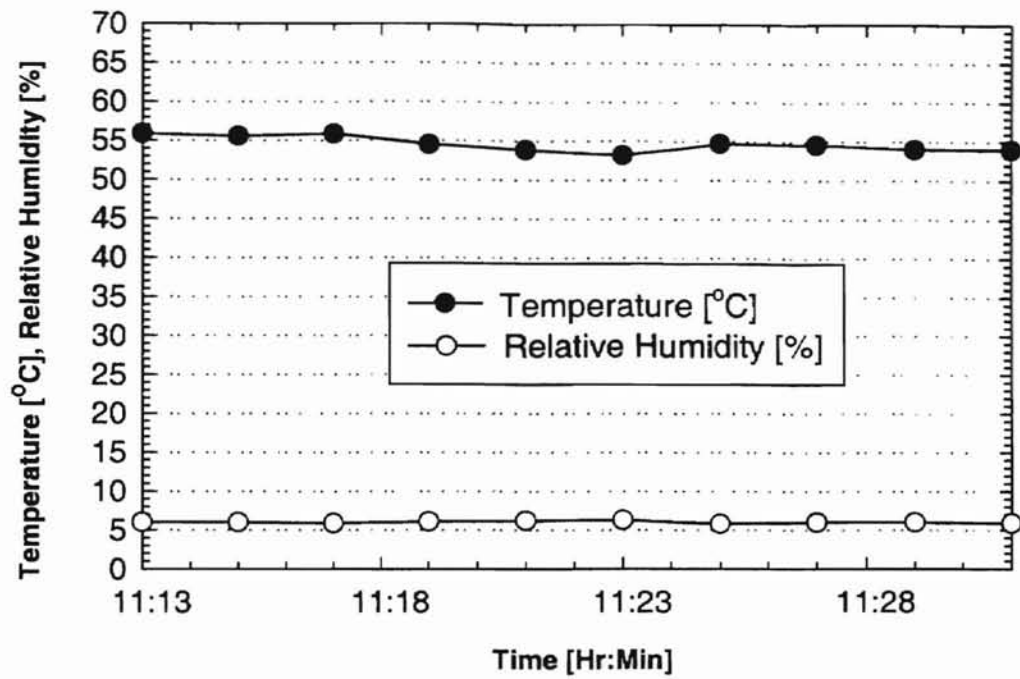


(a)

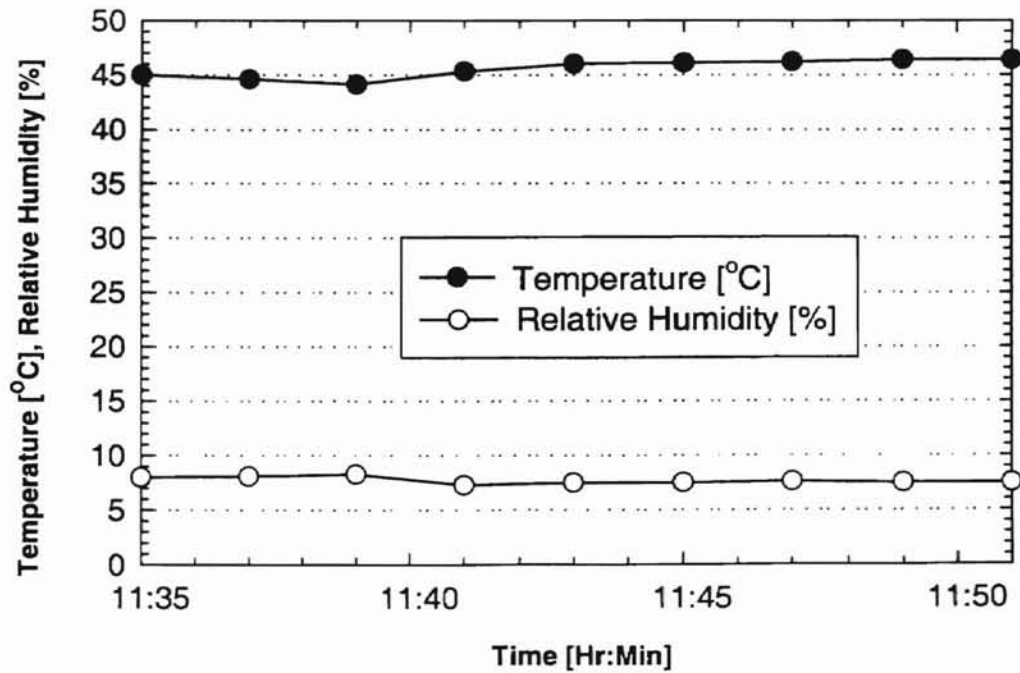


(b)

Figure H.5 Temperature and Humidity Variations Near Mixing Box As a Function of Air Flow Rate:
 (a) with Both Heat Addition and Atomization of Distilled Water
 (b) with Heat Addition and Atomization of Distilled Water.



(a)



(b)

Figure H.6 Temperature and Humidity Variations of Preheated Air As a Function of Time:
 (Heater on, But without the Atomization of Distilled Water; Date: 01/23/98)
 (a) at an Air Flow Rate of 77 m³/hr (b) at an Air Flow Rate of 103 m³/hr.

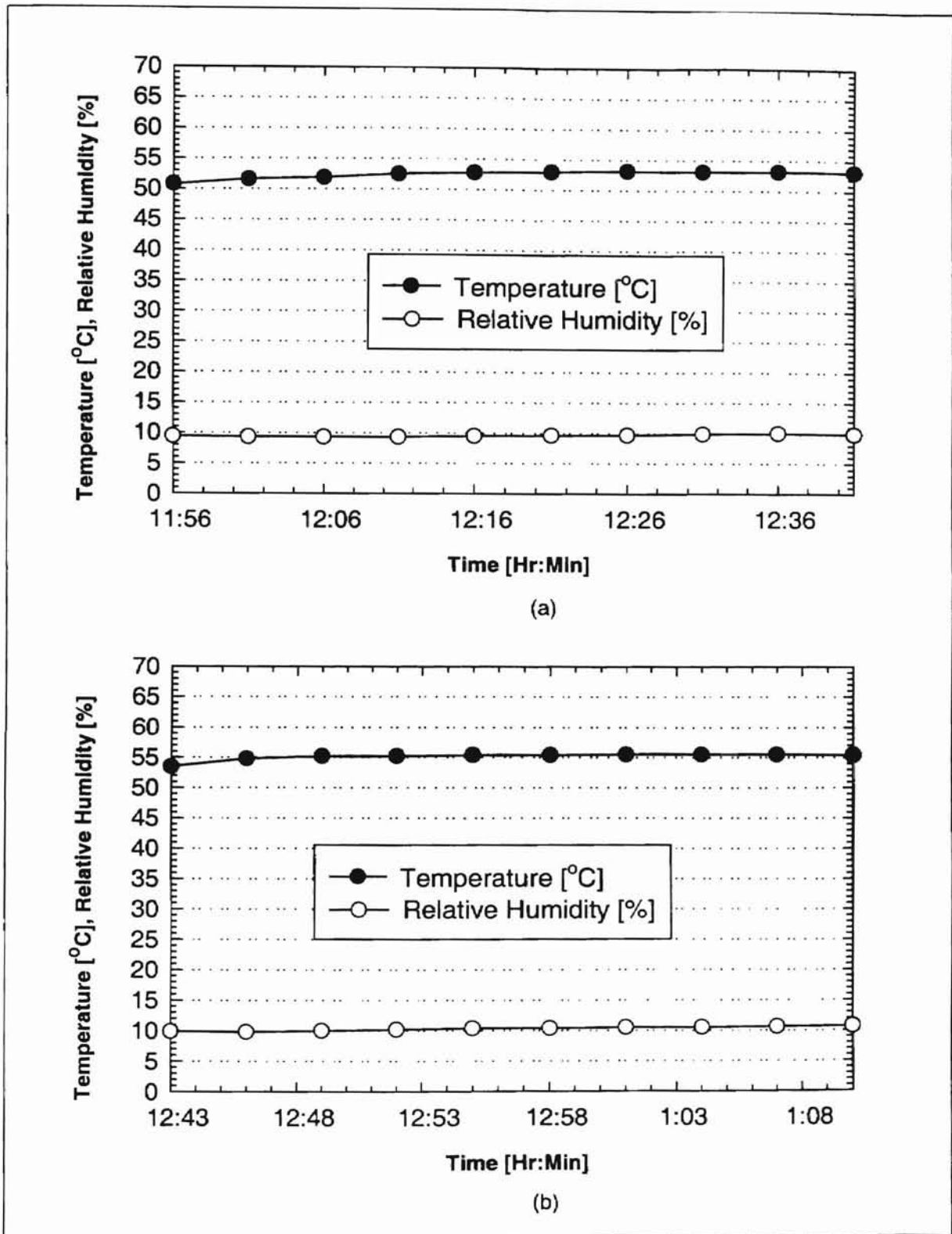
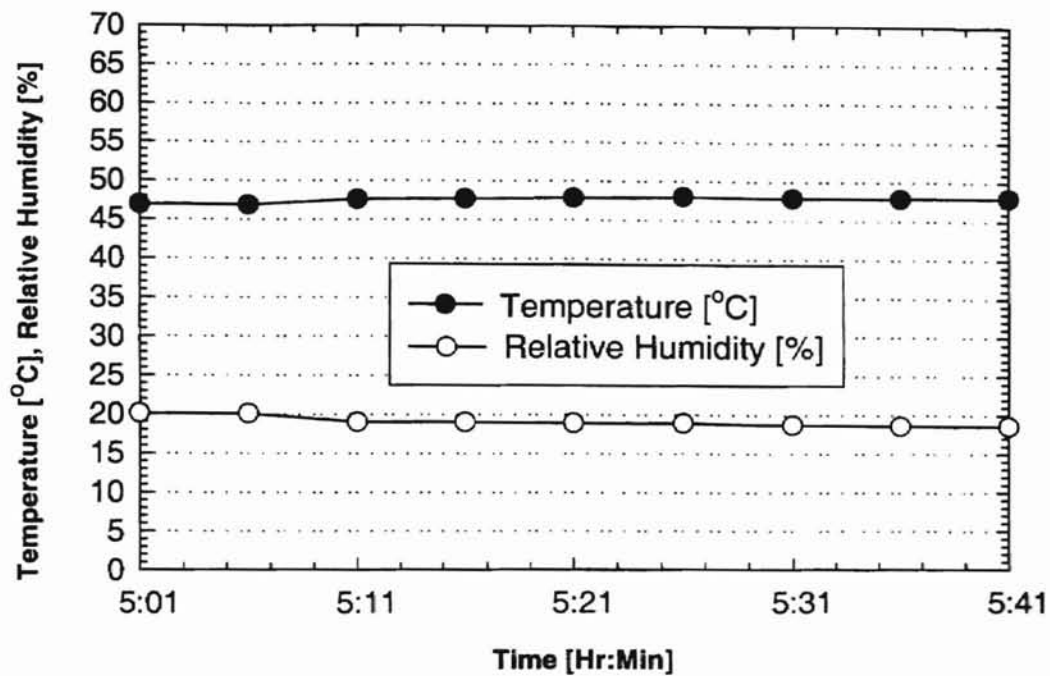
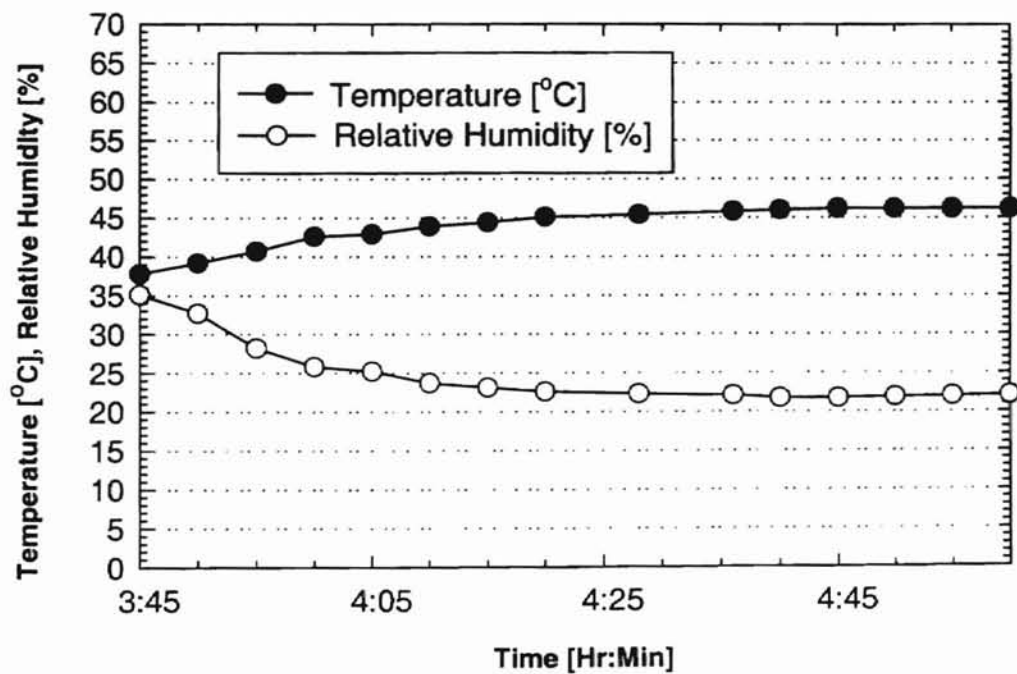


Figure H.7 Temperature and Humidity Variations of Preheated Air As a Function of Time Downstream of Filter (Heater on, But without Atomization of Distilled Water): (a) at an Air Flow Rate of 15 m³/hr (b) at an Air Flow Rate of 29 m³/hr.



(a)



(b)

Figure H.8 Temperature and Humidity Variations As a Function of Time Upstream of Filter (with Heat Addition, But without Atomization of Distilled Water): (a) at an Air Flow Rate of 15 m³/hr (b) at an Air Flow Rate of 13 m³/hr.

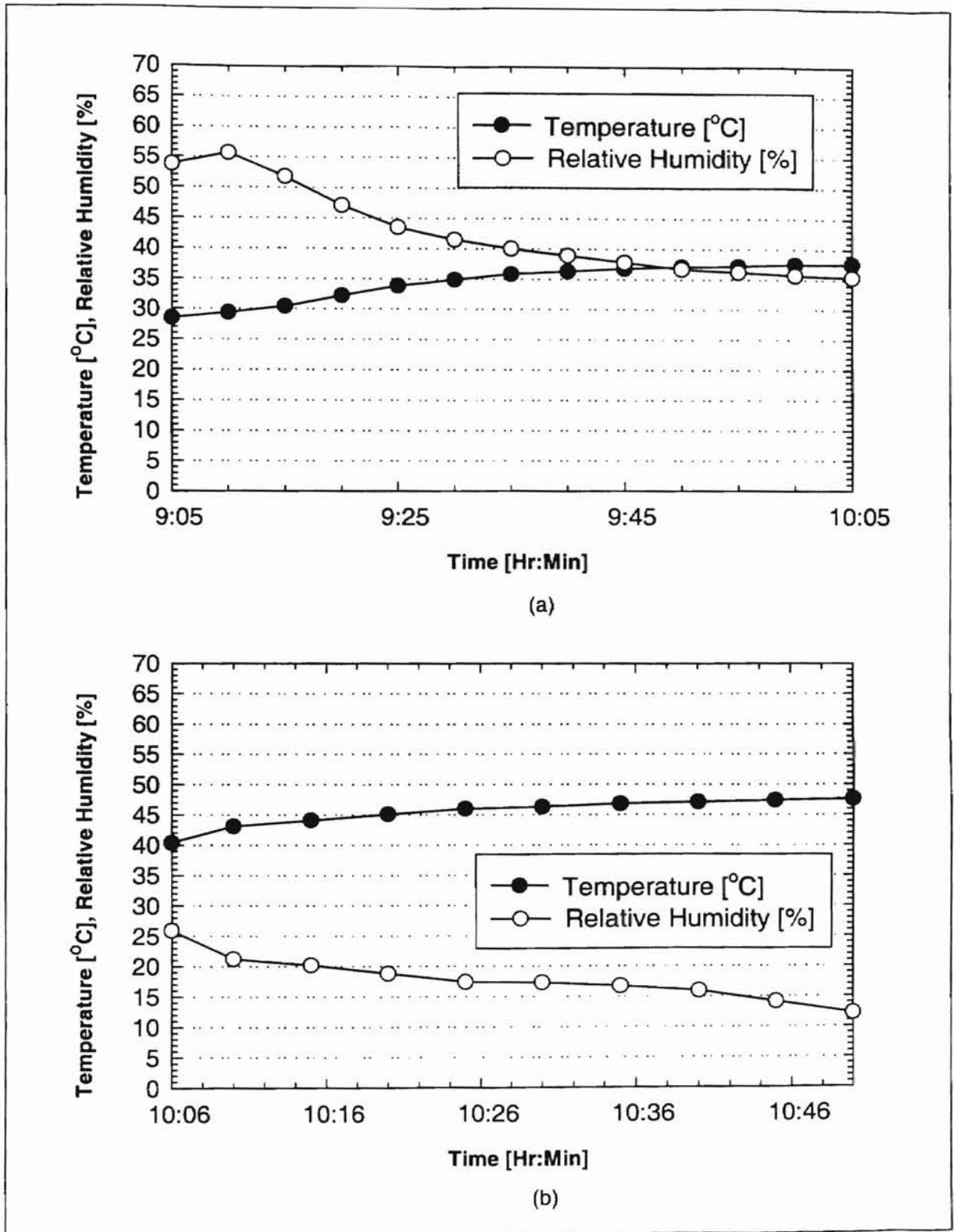


Figure H.9 Temperature and Humidity Variations As a Function of Time Downstream of Filter (Heater on, But without the Atomization of Distilled Water): (a) at an Air Flow Rate of 12 m³/hr (b) at an Air Flow Rate of 17 m³/hr.

APPENDIX I

STOKES NUMBER CALCULATION

The Stokes number in Tables 6.2 and 6.4 of Chapter VI have been calculated using Eq. (2-53) of Chapter II, which is rewritten as

$$St = \frac{\rho_p D_p^2 U_0 C_c}{18 D_f \mu} \quad (\text{I-1})$$

where St is the Stokes number, D_p is particle diameter, ρ_p is particle density, D_f is fiber diameter, μ is the viscosity of air, C_c is the Cunningham correction factor and U_0 is the velocity of air upstream of the fiber far removed from it.

An example on the calculation of Stokes number is presented after listing the values of the variables as follows:

- Density of the PSL particles (ρ_p) is within the range of 1000 to 1050 kg/m³.
- Cunningham slip corrections factor (C_c): This is calculated using Eq. (I-2) from Eq. (2-48) of Chapter II as follows:

$$C_c = 1 + 2.52 \frac{\lambda}{D_p} \quad (\text{I-2})$$

where λ is the mean free path of air molecules. The value of λ is 0.065 μm at normal temperature and pressure (NTP) of 20 °C and 1 atmosphere, respectively.

- Air viscosity (μ): Excluding humidity effects the viscosity of dry air at 20 °C and 1 atmosphere, $\mu = 18.1 \times 10^{-6}$ Pa-s.
- Air velocity (U_0), which is dependent upon the flow rate is approximated by the face velocity. For example, the velocity (0.164 m/s) upstream of the filter for test ESH10.1 (with a flow rate of 13.53 m³/hr, Table 6.2 of Chapter VI) based on the folded filter/duct cross-sectional area was used.
- Fiber diameter D_f : The average fiber diameter has been estimated to be 38 μm by Natarajan [1995], and subsequently used by others [Anand, 1997; Jadbabaei, 1997 and Saxena, 1998].

Hence substituting the values of the parameters in to Eq. (I-1), the Stokes number will be:

$$\text{St} = \frac{(1.165)[(0.966)(10^{-6})]^2(1000)(0.164)}{18(18.1)(10^{-6})(38)(10^{-6})} = 0.0144$$

APPENDIX J

LIST OF EQUIPMENT

1. 5 Watt Argon Ion Laser: Coherent, Model Innova 70-A, Serial No. P/S 92K-1758
2. Remote Control for the Laser: Coherent, Model I-70, Serial No. 92411171
3. Fiber Drive: Aerometrics, Inc., Model FBD1240, Serial No. 026
4. Bragg Cell: IntraAction, Inc., Model ME-40H, Serial No. 3247
5. Photomultiplier Tubes: Aerometrics, Inc., Model RCM2200L, Serial No. 029
6. Doppler Signal Analyzer: Aerometrics, Inc., Model DSA3220, Serial No. 044
7. Computer and Monitor: Impression 3, IBM compatible 80486 DX2, 66 MHz
8. Computer for Traverse System and MS-Excel Data Acquisition Files: Gateway 2000, IBM compatible, 80486, 33 MHz
9. Laser Transceiver: Aerometrics, Inc., Model XRV1212, Serial No. 001
10. Three Stepper Motors (Sanyo Denki, Type: 103-850-11)
11. Oscilloscope: Hewlett Packard, Model 54501A
12. Plexiglass Test Housings: a) Similar to SAE J1669 Small Angle Diffuser Housing, b) Standard J726 housing, c) Simulated Automotive Filter housing
13. Pleated Test Filters: Dayco-Purolator, Inc., A13192 (formerly AF3192)
14. TSI Mass Flow Sensor: TSI, Model 2018, Serial No. 30644
15. Atomizer: TSI Model 9306, six-jet atomizer

16. SAE J726 Air Stand, Purolator Products, Inc.
17. Rival Compact Heater, Model T114 (1250 w)
18. Electric Heater [with 1300 w and 1500 w Capacity]
19. Stepper Motor Drives, Model CMD-40
20. 24 V DC - 6 A Power Supply (Acme Electronics)
21. Connector 3 for Digital Output, Model PCLD-780
22. Ultrasonic Humidifier: Pollenex, Model SH55R
23. Omega RH20/RH21 Digital Temperature and Humidity meters
24. SunBeam Mechanical Thermometer-hygrometer
25. Electro-Tech Systems, Inc., Model 210 Static Meter
26. Room Air Conditioner: Cooling Capacity 12600 Btu/hr
27. Polystyrene Latex (PSL) Particles: 0.497, 0.966, 2.04 μm particles, accuracy (99.99%), Duke Scientific; \$700 for 100 ml of the particles in a 10% solution
28. Glass Beads: 1.59 μm diameter beads, Standard Deviation: 0.304, Powder Technologies Inc.; \$50 for 25 gm of the particles

APPENDIX K

SINGLE FIBER EFFICIENCY CALCULATION

The total single fiber efficiency, E_s , due to one or more filtration mechanisms acting simultaneously for the deposition of a particle on the model A13192 fibrous automotive filter can be calculated from the experimental filtration efficiency results. The single and overall efficiencies are mathematically related by Eq. (3-19) of Chapter III as follows:

$$E = 1 - e^{-\left(\frac{4 \alpha E_s}{\pi(1-\alpha)D_f}\right)L} \quad (\text{K-1})$$

where E is the overall experimental filter efficiency, D_f is the fiber diameter, α is the packing density and L is the depth or thickness of the filter. After rearranging Eq. (K-1) and solving for E_s , one obtains the equation for the total single fiber efficiency E_s due to all possible mechanisms of filtration that compete for the deposition of the particles as

$$E_s = -\frac{\pi(1-\alpha)D_f}{4\alpha L} \ln(1-E) \quad (\text{K-2})$$

In order to use equation (K-2), one needs to model the pleated filter. In this study, the pleated filter was modeled by a flat filter with the same overall efficiency and dimensions as the pleated filter. Thus, while the height and width (that constituted the normal flow area) of the real pleated filter remained as the dimensions (height and width) for the flat filter model, the depth of the flat filter model was also selected to be equal to the pleat

height of the pleated filter. However, the only challenge left to use Eq. (K-2) was finding the flat filter model's packing density from the known (estimated) parameters of the unfolded pleated filter. Thus using the pleated filter's unfolded filter thickness as 700 μm and its packing density as 0.345, the packing density for the flat filter model was calculated by establishing the corresponding packing density ratios for the two filters. Accordingly the flat filter model's packing density was found to be 0.153. Hence, since all of the parameters in Eq. (K-2) are known, it is possible to solve for the total single fiber efficiency of the model filter. For example, the single fiber efficiency for the experimental filtration test of ESH100.1 performed on the electrostatic charge effect is has been calculated as follows:

- Fiber diameter: $D_f = 38 \mu\text{m}$
- Packing density: $\alpha = 0.153$
- Flat filter model thickness: $L = 30 \text{ mm} = .03 \text{ m}$
- Efficiency of flat filter model: $E = 60.69\%$

Substituting the above values into Equation (K-2) yields

$$E_s = -\frac{\pi(1-0.153)(38 \times 10^{-6})}{4(0.153)(.03)} \ln(1-60.69\%) = 0.005$$

A summary of all the single fiber efficiencies for both the electrostatic and humidity effects are presented in Tables 6.2 and 6.4, respectively.

APPENDIX L

LANGMUIR'S SINGLE FIBER EFFICIENCY EQUATION FOR DIFFUSION

In this appendix the step by step simplifications and approximations made to derive the simplified and reduced single fiber efficiency equation due to diffusion of Eq. (2-40) will be provided.

To begin with, Eq. (2-39) of Chapter II has been rewritten as follows:

$$E_D = \frac{1}{2(2 - \ln \text{Re})} \left[2(1 + A_1) \ln(1 + A_1) - (1 + A_1) + \frac{1}{1 + A_1} \right] \quad (\text{L-1})$$

$$\text{where, } A_1 = 1.308 \left[(2 - \ln \text{Re})^{1/3} / \text{Pe}^{1/3} \right] \quad (\text{L-2})$$

Assumption: A_1 tends to zero (or $A_1 \ll 1$) and $\text{Pe} \gg 1$

The first step is to approximate $\ln(1+A_1)$ in the first term within the bracket using a truncated Maclaurin series expansion (power series expansion about zero) as follows:

$$\ln(1 + A_1) = A_1 - \frac{A_1^2}{2} \quad (\text{L-3})$$

Substituting Eq. (L-3) into Eq. (L-1) yields

$$E_D = \frac{1}{2(2 - \ln \text{Re})} \left[2 \left((1 + A_1) \left(A_1 - \frac{A_1^2}{2} \right) \right) - (1 + A_1) + \frac{1}{1 + A_1} \right]$$

Upon choosing $(1 + A_1)$ as a common denominator and expanding the numerator of the above equation one obtains,

$$E_D = \frac{1}{2(2 - \ln \text{Re})} \frac{\left[2 \left((1 + 2A_1 + A_1^2) \left(A_1 - \frac{A_1^2}{2} \right) \right) - (1 + 2A_1 + A_1^2) + 1 \right]}{(1 + A_1)}$$

$$E_D = \frac{1}{2(2 - \ln \text{Re})} \frac{\left[\left((2 + 4A_1 + 2A_1^2) \left(A_1 - \frac{A_1^2}{2} \right) \right) - 2A_1 - A_1^2 \right]}{(1 + A_1)}$$

Further simplification and collection of like terms yields,

$$E_D = \frac{1}{2(2 - \ln \text{Re})} \frac{2A_1^2 - A_1^4}{(1 + A_1)} = \frac{1}{2(2 - \ln \text{Re})} \frac{2A_1^2 \left(1 - \frac{A_1^2}{2} \right)}{1 + A_1} \quad (\text{L-4})$$

The division of $\left(1 - \frac{A_1^2}{2} \right)$ by $(1 + A_1)$ yields $(1 - A_1) + \frac{A_1^2}{2(1 + A_1)}$

Thus Eq. (L-4) becomes

$$E_D = \frac{1}{2(2 - \ln \text{Re})} 2A_1^2 \left((1 - A_1) + \frac{A_1^2}{2(1 + A_1)} \right) = \frac{1}{2(2 - \ln \text{Re})} \left[2A_1^2 - 2A_1^3 + \frac{A_1^4}{1 + A_1} \right] \quad (\text{L-5})$$

Investigating and comparing the first, second, and third terms in the above equation, Eq. (L-5), and using the assumption that $A_1 \ll 1$ (or approaches zero), then the terms of higher order can be dropped to yield the following approximate reduced equation:

$$E_D = \frac{2A_1^2}{2(2 - \ln \text{Re})} = \frac{A_1^2}{(2 - \ln \text{Re})} \quad (\text{L-6})$$

upon substituting the value of A_1 from Eq. (L-2), one obtains the final approximation equation of Eq. (2-40) as:

$$E_D = 1.71 \frac{1}{(2 - \ln \text{Re})^{1/3}} \text{Pe}^{-2/3} \quad (\text{L-7})$$

APPENDIX M

SINGLE FIBER EFFICIENCY EQUATION FOR INTERCEPTION

The simplified and reduced single fiber efficiency equation for particle deposition due to the interception mechanism is presented in Eq. (2-45) of Chapter II. The objective of this appendix is to show how this reduced equation can be obtained from the general equation, Eq. (2-44a), of Chapter II.

For the Kuwabara model, the single fiber efficiency due to interception [Brown, 1993] is rewritten from Eq. (2-44a) as follows:

$$E_R = \frac{1}{2Ku} \left\{ 2(1 + N_R) \ln(1 + N_R) - (1 + N_R)(1 - \alpha) + (1 + N_R)^{-1}(1 - \alpha/2) - \frac{\alpha}{2}(1 + N_R)^3 \right\} \quad (\text{M-1})$$

$$Ku = -\frac{1}{2}\alpha \ln(\alpha) - 0.75 + \alpha + \frac{\alpha^2}{4} \quad (\text{M-2})$$

where Ku is the Kuwabara hydrodynamic constant, α is the packing density and $N_R (= D_p/D_f)$ is the dimensionless intensity of deposition called interception parameter.

Assumption: N_R is small (approaches zero), or $N_R \ll 1$.

Initially $\ln(1 + N_R)$ is approximated by a truncated power series expansion.

$$\ln(1 + N_R) = N_R - \frac{N_R^2}{2} \quad (\text{M-3})$$

Substitution of Eq. (M-3) into Eq. (M-1) yields,

$$E_R = \frac{1}{2Ku} \left\{ 2(1 + N_R) \left(N_R - \frac{N_R^2}{2} \right) - (1 + N_R)(1 - \alpha) + \frac{(1 - \alpha/2)}{(1 + N_R)} - \frac{\alpha}{2}(1 + N_R)^3 \right\}$$

Choosing $(1 + N_R)$ as a common denominator:

$$E_R = \frac{1}{2Ku} \left\{ 2 \frac{(1 + 2N_R + N_R^2)}{(1 + N_R)} \left(N_R - \frac{N_R^2}{2} \right) - \frac{(1 + 2N_R + N_R^2)}{(1 + N_R)} (1 - \alpha) + \frac{(1 - \alpha/2)}{(1 + N_R)} - \frac{\alpha}{2} \frac{(1 + N_R)^4}{(1 + N_R)} \right\}$$

Upon expansion, it yields:

$$E_R = \frac{1}{2Ku} \frac{\left\{ (2N_R + 4N_R^2 + 2N_R^3 - N_R^2 - 2N_R^3 - N_R^4) - (1 + 2N_R + N_R^2)(1 - \alpha) + (1 - \alpha/2) - \frac{\alpha}{2}(1 + N_R)^4 \right\}}{(1 + N_R)}$$

The term $(1 + N_R)^4$ is expanded as $(1 + N_R)^4 = 1 + 4N_R + 6N_R^2 + 4N_R^3 + N_R^4$

After collecting like terms and further simplification, the equation reduces to

$$E_R = \frac{1}{2Ku} \frac{\left(2N_R^2 - 2\alpha N_R^2 - N_R^4 - 2\alpha N_R^3 - \frac{\alpha N_R^4}{2} \right)}{(1 + N_R)} \quad (\text{M-4})$$

A close look at the numerator of Eq. (M-4) and comparing the orders of the bracketed terms, taking into account the fact that N_R and α are small, one can drop the last three terms to get

$$E_R = \frac{1}{2Ku} \frac{(2N_R^2 - 2\alpha N_R^2)}{(1 + N_R)} \quad (\text{M-5})$$

Thus the approximate reduced equation is presented in Eq. (M-6) [Brown, 1993] as:

$$E_R = \frac{N_R^2(1 - \alpha)}{Ku} \quad (\text{M-6})$$

APPENDIX N

CALIBRATION OF HUMIDITY AND TEMPERATURE MEASUREMENTS

The humidity and temperature measurements of the air flow inside the duct and the filter housing at different locations were performed either with Omega RH20/RH21 digital humidity and temperature sensors or a SunBeam mechanical thermometer-hygrometer device. In most cases, prior to the actual filter performance (air filtration) tests, the model Omega RH20 and RH21 humidity and temperature sensors were used in order to monitor or simulate the humidity and temperature variations of the air flow as a function of both time and flow rate. During the simulation, the air flow was subjected to different conditions (for instance, atomizing distilled water, pre-heating the air or injecting mists from an ultrasonic humidifier). However, during the actual filter performance (air filtration) tests, due to the RH20/RH21 humidity and temperature sensors' limited/restricted environmental working conditions, the SunBeam thermometer-hygrometer was used to monitor the humidity and temperature of the air flow under dusty conditions. Thus, ensuring the calibration of the Omega model RH20 and RH21 and the SunBeam devices was an essential part of the humidity and temperature measurement task.

The Omega model RH20 humidity and temperature sensor was factory calibrated when it arrived shortly before the humidity and temperature measurements began. On the

other hand, there was a need to calibrate both the Omega model RH21 humidity and temperature sensors and the SunBeam device.

Description of Omega Model RH20/RH21 Humidity and Temperature Sensors: The relative humidity sensor consists of a double sided, gold plated plastic foil which is mounted in a perforated plastic or metal housing. The foil functions as a dielectric of a plate capacitor, and the gold-plating on both sides of the foil acts as electrodes. The dielectric constant of the foil and capacitance of the sensor are sensitive to both humidity and temperature. Whenever the capacitance changes, these changes are converted into a d.c. voltage signal. On the other hand, the temperature sensor of the humidity-temperature probe consists of a platinum RTD (Resistance Temperature Detector) sensor. The working principle is based on the change in electrical resistance as the temperature changes (the reader is advised to read the Omega RH20/RH21 user's guide).

The calibration of the RH21 temperature and humidity sensors and the SunBeam mechanical thermometer-hygrometer were performed as follows:

a) The Calibration of the Omega RH21 humidity and Temperature Sensors

1) The Humidity sensor

Generally, the calibration of the Omega RH 21 humidity sensor is performed by preparing saturated aqueous solutions and maintaining the solution in equilibrium with the air space above it. Thus for the calibration of the humidity sensor, two solutions were prepared in order to simulate the upper and lower humidities of (76%) and (11%), using sodium chloride (NaCl) and lithium chloride (LiCl) salts, respectively. The Omega RH20/RH21 user's guide has been strictly followed to go through the calibration process.

2) Temperature Sensor

The temperature sensor was calibrated against the factory calibrated Omega RH20 temperature sensor by subjecting the probes of the two instruments to an air flow inside the mixing box with and without a heat supply in order to achieve a wider range of temperature. Both of the temperature sensors within the respective probes (placed in the air flow inside the mixing chamber) showed the same temperature reading, accurate to within ± 0.1 °C at a given air flow rate.

b) The Calibration of the SunBeam Thermometer-Hygrometer

The calibration of the SunBeam thermometer-hygrometer device was performed using the already calibrated Omega RH20/RH21 temperature and humidity meters. Figures N-1 and N-2 show the calibration results for the humidity and

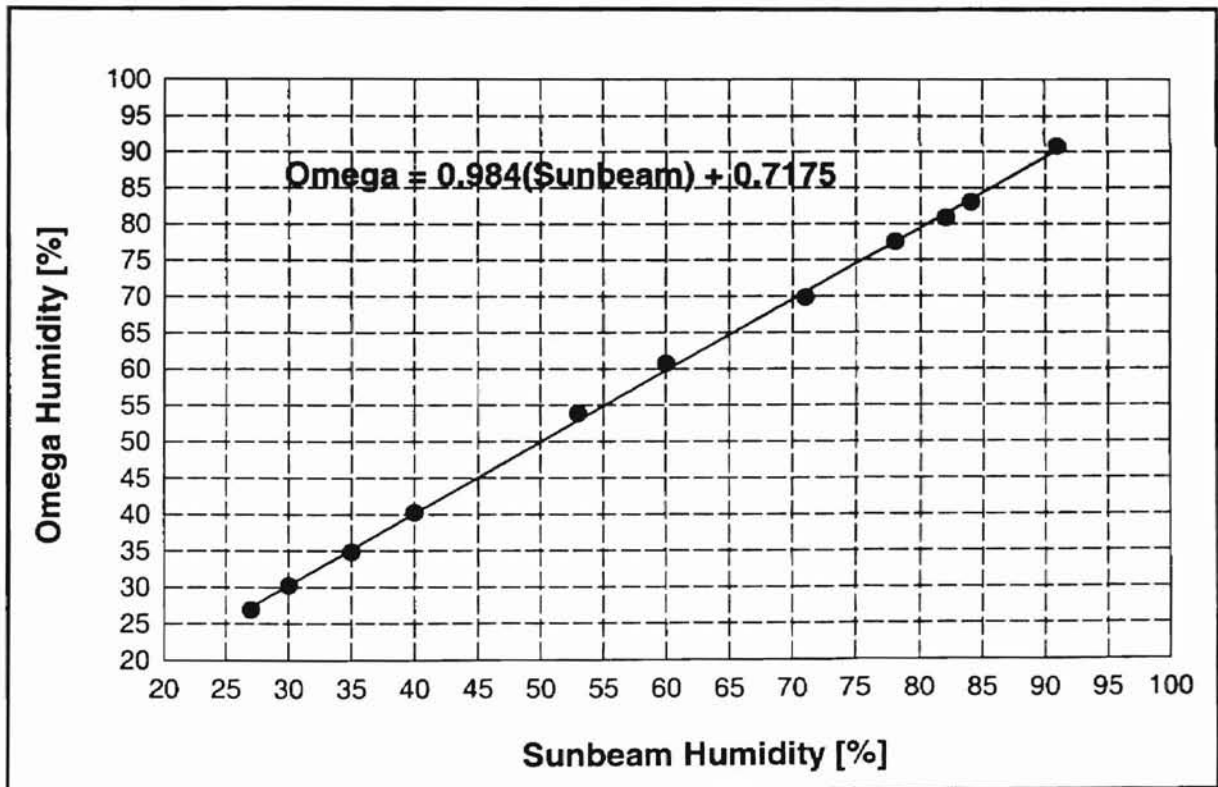


Figure N-1 Humidity Calibration Curve for SunBeam Based on Omega RH20 Humidity Sensor (Date: 07/14/98).

temperature. During the calibration, the RH21 (temperature and humidity sensors) and the SunBeam (temperature-humidity measuring device) were placed together in the mixing box and were exposed to different air flow rates (greater than 30 m³/hr) of a preheated air with varying humidities and temperatures.

For air flow rates above 30 m³/hr, the average response time for the devices was within 1 to 3 minutes. The higher the flow rate, the shorter the response time recorded.

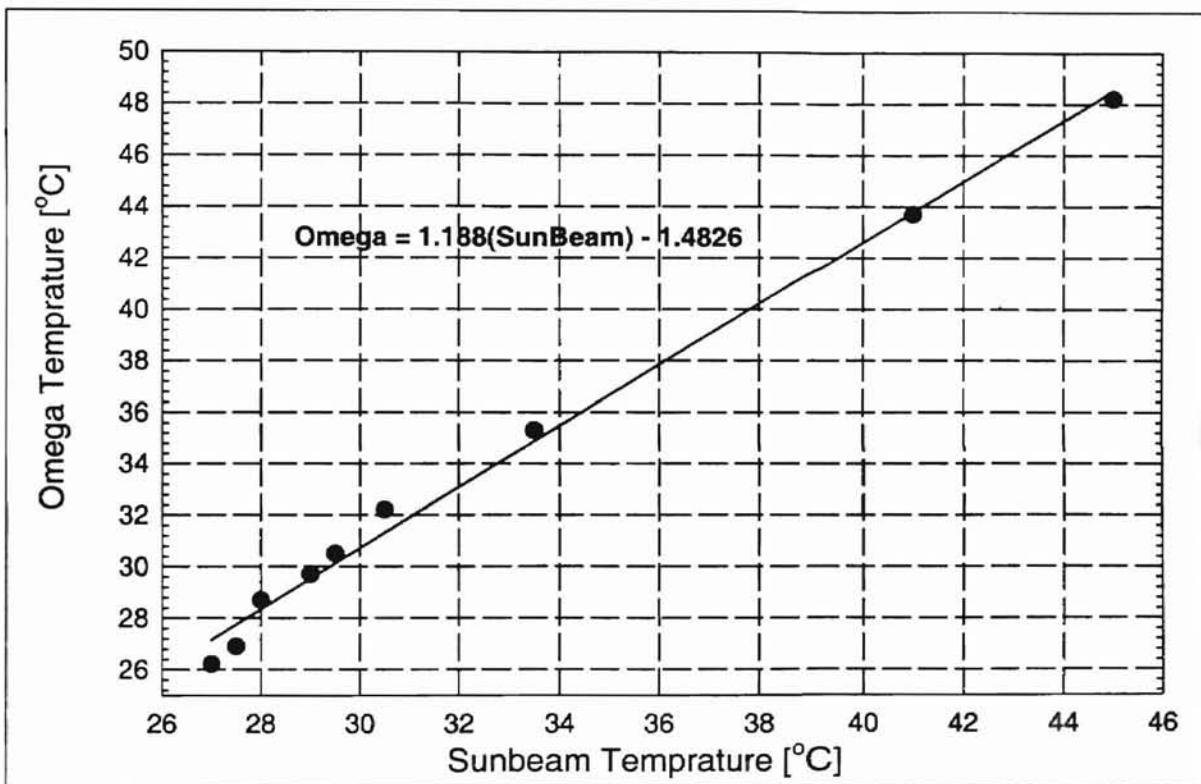


Figure N-2 Temperature Calibration Curve for SunBeam Based on Omega RH20 Temperature Sensor (Date: 07/14/98).

APPENDIX O

ELECTROSTATIC CHARGE VOLTAGE MEASUREMENTS

In this study, electrostatic charge voltage or simply electrostatic voltage refers to the voltage due to the electrostatic charge resident upon the surface of the plexiglass housing and mixing box or the charged particles inside the flowing air along the PVC duct and filter housing. The electrostatic charge voltage in the charged aerosol laden air flow and on the plexiglass surface (due to the atomization of suspensions of particles or the triboelectric effects) was measured using the model 210 static field meter (manufactured by Electro-tech Systems, Inc.). The electrostatic voltage was measured at different locations along the filter housing (upstream and downstream of the filter) and at the mixing box. The model 210 static meter is a non-contacting hand held meter designed to locate and accurately indicate the magnitude and polarity of the electrostatic fields produced by charged objects. Although the meter is calibrated at 500 and 5000 volts at a measuring distance of two inches, it can be used for measuring virtually any electrostatic field by increasing the distance between the meter and the charged surface. It can also be used wherever a true non-contact electrometer type measurement is required [Electro-tech Systems, Inc., 1996].

The accuracy of the electrostatic voltage measurement depends upon the following factors [Electro-tech Systems, Inc., 1998]:

- 1) the magnitude of the average charge distribution,
- 2) the predominant polarity of the charge,
- 3) the distance between the surface of the charged object being measured and the detector,
- 4) the size and shape of the object in relation to the field of view of the detector (static meter).

The author, while strictly adhering to the procedures in the user's guide, has also taken the following additional cautionary measures necessary to measure the electrostatic charge voltage accurately:

- (a) The model 210 static meter was mounted to a wooden plank using aluminum duct tape allowing a free length of two inches in front of the detector. This would help to avoid any damage to the detector due to excessive voltage as result of human error in maintaining a minimum two-inch distance between the surface of the object (in this case the plexiglass housing) and the detector (static meter).
- (b) The use of vinyl duct tape (for sealing purposes) near or at the surface of the plexiglass where measurements were taken was avoided as much as possible in order to minimize measurement errors due to the unwanted electrostatic charge on the surface of the duct tape that would arise due to sliding friction or any residual charge.
- (c) Electrostatic voltage measurements were taken at least twice for improved accuracy and at times the average of the two or more reading would be taken as the final reading.

- (d) The static meter was attached to the ground using the grounding jack for reliable and consistent measurement purposes.
- (e) Measurements were taken first by establishing a zero potential far ahead of the charged surface (plexiglass) to be measured by holding the read button depressed (turned on) and then moving towards the object until the distance between the detector and the object was two inches [Electros-tech Systems, Inc., 1998]. At times, to check the repeatability of the electrostatic charge voltage measurements, the meter would be first brought to the surface and held at two-inch distance (with the read button turned on) and then withdrawn, yielding the same magnitude of electrostatic charge voltage reading. Although both techniques give the same magnitude of electrostatic voltage, the latter would give an opposite charge polarity [Electro-tech Systems, Inc., 1998].
- (f) Efforts were also made to avoid any electrostatic charge generation between the surface of the plexiglass housing and the wooden plank (upon which the static meter was mounted) due to sliding or rubbing friction.

Calibration of the Model 210 Static Meter

The calibration of the static field meter had been performed at the factory. Although the manufacturer recommended that the calibration to be done by the factory, it was also possible to calibrate the instrument here in the laboratory provided all of the necessary equipment was available. Some of the equipment necessary for the calibration of the instrument is listed in the user's guide [Electro-tech Systems, Inc., 1998].

VITA

Tadesse Gebreegziabher

Candidate for the Degree of

Master of Science

Thesis: ELECTROSTATIC CHARGE AND HUMIDITY EFFECTS ON THE EFFICIENCY OF FIBROUS AUTOMOTIVE AIR FILTERS USING LASER DOPPLER ANEMOMETRY

Major Field: Mechanical Engineering.

Biographical:

Personal Data: Born in Adua, Tigray, Ethiopia, on January 1, 1964, son of Asamenesh Gebreselassie and Gebreegziabher Berhe.

Educational: Graduated from Atse Yohannes IV Comprehensive Secondary School, Mekele, Ethiopia in March 1981. Received Bachelor of Science degree in Mechanical Engineering from Addis Ababa University, Addis Ababa, Ethiopia in July 1986. Successfully completed and participated in both theoretical and practical Training in "Diesel Engine Maintenance and Repair Course for Mechanical Engineers," in Shanghai, China in 1990. Completed the requirements for the Master of Science degree with a major in Mechanical Engineering at Oklahoma State University in July 1999.

Experience: Employed by Oklahoma State University as a graduate research assistant from January, 1997 to May, 1999; worked as a Mechanical Engineer with Ethiopian Beverages Corporation, Ministry of Industry from October 1986 to July 1990.

Professional Memberships: Student Member, ASME and AIAA.